Topological phases and criticality
in low-dimensional systems
with disorder and interactions

Zur Erlangung des akademischen Grades eines
DOKTORS DER NATURWISSENSCHAFTEN (Dr. rer. nat.)

von der KIT-Fakultät für Physik
des Karlsruher Instituts für Technologie (KIT)
genehmigte
Dissertation

von

M. Sc. Jonas F. Karcher
aus Karlsruhe

Introduction

The mathematical concept of topology dates back to 1736, when Leonhard Euler presented his paper [1] on the seven bridges of Königsberg. He proved that it was not possible to find a path that crosses each bridge exactly once. This proof only depended on connectivity properties in an abstracted graph representing the city. The lengths of bridges and roads do not appear in this abstracted picture and can be varied arbitrarily without changing the answer. This thesis deals with topological gapped condensed matter systems, that can be characterized by a topological winding number. Smooth deformations (respecting certain symmetries) like disorder or varying couplings without closing the bulk gap leave this winding number invariant. More specifically, for non-interacting gapped fermions the topological phases that can occur are classified according to the "10-fold way" [2–5]. This classification is tied to the Riemannian symmetric spaces [6], which directly appear in the description of disordered systems: as the transfer matrix ensembles and as the non-linear sigma model (NLSM) manifold [7–9].

The world we live in can be described best using three spatial dimensions. In condensed matter physics, many applications nevertheless consider lower dimensional systems. The quantum Hall systems introduced in more detail below are famous examples of surface physics with important applications. In the context of topological materials, surfaces and edges are particularly interesting, since there are gapless modes at a topological phase boundary protected by the bulk-boundary corresponence [10, 11]. The work in Chap. 4 touches this question, surface states in a topological superconductor are found to be critical throughout the superconducting gap, despite the topological protection being defined strictly only at the band center. Another exciting example of potential applications of low dimensional physics are Majorana bound states (MBS) appearing at the edges of topological wires [12–15]. One idea is to use these as an ingredient of a universal quantum computer, since the quantum states of the Majoranas are protected by topology and robust to local impurities. Such low-dimensional systems are prone to Anderson localization in presence of arbitrarily weak disorder [9, 16]. One can understand Anderson localization as constructive interference catastrophe of multiple scattering event return paths. One mechanism to escape this fate is (weak) antilocalization due to spin orbit coupling, that introduces dephasing. In such systems metallic phases and metal-insulator transitions are possible in two dimensions (2D). Another mechanism relies on topology. At the transition between topologically distinct phases, there must be gapless degrees of freedom and criticality [17–19]. Despite the general tendency towards localization, low dimensional systems at a topological transition remain critical in presence of disorder [2, 10, 11]. This would be an example of a (topological) insulator-insulator Anderson transition (AT).

At an AT, there is multifractality determining the statistics of eigenstates [9]. The wavefunctions are neither spread over a large extent of the system like in a metal nor localized to a finite localization volume like in an insulator. Instead they can be thought to occupy fractal dimensional portions of the system. This serves as a hallmark of such a transition and can be used to pinpoint its position in the phase diagram [20, 21]. In experiments, the direct observation of multifractality remains challenging. Recently, there was progress for electrons in disordered semiconductors [22] and experiments on superconductor-insulator transition in disordered films [23, 24].

A paradigmatic example of topological transitions in physics is the integer quantum Hall effect

discovered in 1980 by Klaus von Klitzing [25]. The Hall conductance is precisely quantized in integer multiples of e^2/h. These integers can be understood as topological winding number of the system. By varying the magnetic field a transition between two distinct phases is driven. In presence of disorder, multifractal spectrum and longitudinal conductance assume universal values. The integer quantum Hall systems reside in class A and have superconducting counterparts in classes C, D: the spin quantum Hall (SQH) systems and the thermal quantum Hall (TQH) systems, where spin (thermal) current is quantized. These systems host the 2D quantum Hall type phases. In Chap. 3, the multifractality in SQH systems is studied in detail.

The interplay of topology, multifractality and interactions gives rise to surprising phenomena. Formally, the "10-fold way" classification can be extended to include weak interactions [26–28]. In that sense topological phases are robust towards weak interactions. At phase boundaries in disordered systems however there is Anderson-transition criticality. Multifractality can enhance the impact of interactions, in 2D superconductor systems, it has been shown to drive the system away from criticality by spontaneous symmetry breaking [29, 30]. A similar setting can be found in the Majorana and complex fermion wires under investigation in Chap. 2.

In the following paragraphs, more detailed introductions to the particular systems addressed in this thesis follow. The central questions analyzed and answered here are formulated.

Disorder and interaction in chiral chains   Topological one-dimensional (1D) systems are considered a potential platform for quantum computing [12–15], as topology protects the qubit state from local, uncorrelated noise.

In this part of my thesis a disordered interacting generalization [31] of the Kitaev chain [32], which is such a topological 1D system of Majorana fermions, is explored. Potential realizations of this system are vortex lattices [33–35] in a thin film topological superconductor. Another possibility are superconductor-ferromagnet structures along quantum spin Hall edges [36]. The effective low energy theory in InGaAs nanowires on top of a superconductor in a magnetic field is described by a Kitaev Hamiltonian [37].

The Majorana model is compared to that of complex fermion hopping on a chain with the chemical potential tuned to zero [38, 39]. In absence of interactions both models exhibit the same infinite randomness physics [38, 40]. With interactions, the complex fermions remain at the infinite randomness fixed point, whereas the Majoranas either localize or show a different kind of criticality depending on the sign of the interaction term [41]. The main aim in Chap. 2 is to understand the fundamental difference between Majoranas and complex fermions in 1D.

Generalized multifractality in Spin Quantum Hall systems   Low dimensional disordered systems have a natural tendency to localize. More precisely, in symmetry class AI, $d = 2$ is the lower critical dimension, systems in this class localize in presence of arbitrarily weak disorder. In the other symmetry classes, there is a wealth of escape mechanisms from localization [9]. These are related to topology or conventional weak antilocalization physics. A famous example is the plateau transition in the integer quantum Hall effect.

Many critical theories attempting to describe the integer quantum-Hall plateau transition have been formulated [42–50]; in particular, various versions of the Wess-Zumino-Novikov-Witten (WZNW) theory were proposed. These kinds of theories constrain the multifractal spectrum to be parabolic, determined by a single parameter. On the numerical side, the multifractal spectrum is very close to parabolicity [51]; however, a high-precision numerics indicates small deviations [52, 53].

The work in this part investigates a superconducting counterpart of the integer quantum Hall transition—the spin quantum Hall (SQH) transition [54, 55]. The multifractal spectrum can be studied analytically in special points by mapping to classical percolation [56–58]. By numerical studies Refs. [58] and very recently Ref. [59] found clear (although relatively weak) deviations from parabolicity. These deviations hint to a possible violation of local conformal invariance (LCI)[60]. The quest in Chap. 3 is to derive the theory describing generalized multifractality for the SQH transition. This theory should be formulated in a way allowing an extension to other critical points in 2D. A fundamental question arising is, whether SQH criticality satisfies or violates LCI.

Disordered Surfaces of time reversal invariant topological superconductors In this part of my work in Chap. 4, a novel phenomenon in time-reversal invariant topological superconductors is described. The surface theories of the bulk TSCs under consideration can be described by 2D Dirac models [8]. These are equivalent to Wess–Zumino–Novikov–Witten (WZNW) nonlinear sigma models, modified by the addition of the nonzero quasiparticle energy. At zero energy (the surface Dirac point), these models are also quantum critical, and have been long understood thanks to the exact solution via conformal field theory [61–68]. By contrast, the finite-energy behaviour of the WZNW models still evades analytical treatment.

In particular, finite-energy states in class AIII Dirac surface of the U(1) symmetric TSC with winding number $\nu = 1$ appear to share the multifractal spectrum and the distribution of the Landauer conductance associated with the integer quantum Hall (IQH) plateau transition in class A [9, 51, 69–74]. Further the TSC with full spin SU(2) symmetry (class CI) has finite-energy surface states [75] mimicing the class C SQH phenomenology precisely [9, 54–58, 76, 77]. At this point one can ask the questions (i) does this generalize to higher winding numbers ν? and (ii) does the TSC in class DIII display any kind of criticality related to the thermal quantum hall transition in class D [78–85]?

Structure of this Thesis

This thesis consists of three content chapters dealing with 1D wires (Chap. 2), 2D quantum Hall systems (Chap. 3) and surfaces of 3D bulk time reversal invariant topological superconductors (Chap. 4). Additionally there is an exhaustive introduction (Chap. 1) to all fundamentals necessary to understand the systems and methods studied in this thesis.

Disorder and interaction in chiral chains This first chapter is devoted to chiral topological chains.

1. The models are introduced in Sec. 2.2 complemented by an exhaustive discussion of better understood limiting cases. The aim is to understand the behavior of fermionic and Majorana versions for different coupling strengths, in other words determining and understanding the phase diagram.

2. Having introduced the models, one can directly perform density matrix renormalization group (DMRG) numerics. In Sec. 2.3 the results from Ref. [86] are reviewed. Both the clean and the disordered theories are considered. The analytically understood limits of the models serve as benchmark for the numerics. The most remarkable finding is that interaction drastically changes the physics in the disordered Majorana chain. The effect is sign dependent: for repulsive interaction there is localization, for attractive interaction disorder becomes effectively weakened

and the chain is critical. From the behavior of the correlation functions a spontaneous symmetry breaking can be made responsible for the localization.

3. In order to understand the numerically extracted phase diagram and phenomenology, I performed two complementary RG approaches. These are (a) a momentum space RG treating disorder perturbatively and (b) an exact treatment of disorder analyzing the interaction matrix elements at perturbative level. In method (a) disorder flows to strong coupling quickly, which means that method (b) is more appropriate to gain new insight on the system.

4. By combining the RG treatment of interaction with a numerical study of wave-function correlations at the infinite-randomness fixed point, we identify a relevant operator in the case of the Majorana chain. No such operator exists in the case of the complex fermionic chain in view of the cancellation between Hartree and Fock contributions.

Key result to this chapter is the fundamental difference between interacting disordered Majoranas and complex fermions. A disordered Majorana chain is instable towards arbitrarily weak interaction, repulsive interaction has the most dramatic localizing effect, whereas in a chain of complex fermions is stable to short range interaction.

Generalized multifractality in Spin Quantum Hall systems   The above mentioned studies [58, 59] are extended to the generalized multifractal spectrum:

1. In the conformal field theory framework for multifractality 3.2 the impact of local conformal invariance (LCI) on the multifractal spectrum is investigated. The argument given in Ref. [60] can be extended to generalized multifractality assuming Abelian fusion of the pure-scaling composite operators in addition to local conformal invariance. In this case, the generalized-multifractality spectrum must exhibit "generalized parabolicity", i.e. is parametrized (for a given critical point) by a single constant. This proof is shown in Section 3.2.

2. A construction of pure-scaling composite operators for the σ-model of class C, invoking the Iwasawa decomposition (Sec. 3.3) is presented. It is proven explicitly that the constructed composite operators obey Abelian fusion rules.

3. There is an infinite number of pure-scaling operators families. By using one-loop renormalization group of the class C NLSM, one further alternative family (invariant with respect to the action of the symmetry group of the σ-model) is derived in Sec. 3.5.

4. In Sec. 3.6 and Sec. 3.7 a "translation" of the scaling operators to the language of eigenstates of the Hamiltonian is performed. Explicit expressions for eigenstate correlators exhibiting pure scaling and thereby making the generalized multifractal spectrum accessible are determined. Using the SU(2) version of the Chalker-Coddington network model in class C, I numerically verify that these are indeed the proper scaling operators and determine the corresponding exponents. Very remarkably, there is a *strong violation* of the generalized parabolicity of the generalized-multifractality spectrum. In combination with the results proven in 1., this points out to a violation of the local conformal invariance at the SQH transition. This is a rather surprising conclusion, but the analytical results in 5. eliminate the possibility of different explanations.

5. By exploiting the percolation mapping of the SQH transition, the violation of generalized parabolicity is verified analytically in Sec. 3.8.

Two points in above list should be emphasized. Reference [87] contains the construction from 2.,4. for class A. In class C considered here a lot more technical obstacles occur. This is related to the additional "spin" structure of the wavefunctions here. Second, the points 1.,5. imply directly violation of the local conformal invariance at the SQH critical point.

Disordered Surfaces of time reversal invariant topological superconductors Here disordered surfaces of bulk TSCs are considered.

1. The finite energy multifractal spectrum of wave function fluctuations and the distribution of the Landauer conductance in the class AIII Dirac surface theory appears to match the universal values associated with the integer quantum Hall transition (IQHT) in class A [88]. This is surprising for a number of reasons. First, the critical state associated with the IQHT typically obtains only with fine-tuning of the magnetic field or particle density. This is because the IQHT is a quantum phase transition separating topologically distinct plateaus. Instead, at the surface of a TSC, every finite-energy state appears to feature its own plateau transition. Second, the quantum Hall effect lacks time-reversal symmetry (TRS), yet the findings in Ref. [88] show an energy-stacking of IQHT states without TRS breaking.

2. For the TSC with full spin SU(2) symmetry (class CI), the finite-energy surface states [75] mimic the class C *spin* QHT phenomenology precisely (see Sec. 1.5.3).

3. The TSC unrestricted by spin symmetry shows non-universal behavior. This is hypothesized to be related to the thermal QHT in class D (see Sec. 1.5.3).

These key numerical findings for class AIII, CI, and DIII finite-energy surface theories [75, 88, 89] are summarized in this chapter. Novel results for the Kubo conductivity for class CI and AIII surface states from Ref. [90] are shown as well.

The 2D Dirac surface models studied here are equivalent to WZWN nonlinear sigma models [8], modified by the addition of the nonzero quasiparticle energy. Many works (like Ref. [50]) conjectured that quantum Hall criticality is described by a WZNW CFT. The results in Chap. 3 indicate that such a description is not possible for the SQH case. The results of this chapter and the numerical works reviewed in it instead suggest, that the WZNW theory in presence of the energy perturbation (breaking even global conformal invariance) seems to flow to a Pruisken like theory, exhibiting QH criticality.

Contents

1 Chapter 1

Fundamentals

In this chapter, the theoretical concepts underlying the problems considered in this thesis are introduced. In Sec. 1.1 (field theoretic) methods for tackling low-dimensional systems are introduced. The concepts of Anderson transitions and multifractality are outlined in Sec. 1.2. In the cases of interest in this thesis, the transitions are induced by topology (Sec. 1.3). Finally having introduced the necessary concepts and methods, a detailed overview of criticality in low dimensions is given (Sec. 1.4, Sec. 1.5).

1.1 Methods

In this section methods for analyzing low-dimensional problems are discussed. Among them (local) conformal field theory (Sec. 1.1.2) is a powerful tool restricted to $(1+1)$D or $(2+0)$D. For 1D problems Sec. 1.1.1 introduces a further technique restricted to this dimension, the Jordan Wigner transformation. The renormalization group analysis 1.1.3 and field theoretic techniques for disorder averages (Sec. 1.1.4) are applicable in arbitrary spatial dimension. However, the non-linear sigma model (Sec. 1.1.4.4) and the transfer matrix (Sec. 1.1.4.3) are particularly useful in low dimensions.

1.1.1 Special techniques in 1D

For presenting the methods in this chapter, I closely follow Ref. [91].

1.1.1.1 Jordan-Wigner Transformation

Any fermionic model can be mapped to a spin$-\frac{1}{2}$ chain via the Jordan-Wigner (JW) transformation. The spin operators are related to complex fermionic creators/annihilators as follows:

$$\sigma_j^+ = e^{i\pi \sum_{k<j} \hat{n}_k} c_j^\dagger, \qquad\qquad c_j^\dagger = \prod_{k<j} \sigma_k^z \sigma_k^+, \qquad (1.1)$$

$$\sigma_j^- = e^{i\pi \sum_{k<j} \hat{n}_k} c_j, \qquad\qquad c_j = \prod_{k<j} \sigma_k^z \sigma_k^-, \qquad (1.2)$$

$$\sigma_j^z = 2\hat{n}_j - 1. \qquad (1.3)$$

The exponential is the so-called Jordan-Wigner string, the transformation is non-local. For physical (i.e. local) models, all terms in the Hamiltonian contain an even number of fermion operators, which leads to local spin models.

For Majorana operators, the transformation reads:

$$\sigma_j^x = \left(\prod_{k<j} i\gamma_{2k}\gamma_{2k+1}\right)\gamma_{2j}, \qquad\qquad \gamma_{2j} = \prod_{k<j}\sigma_k^z\sigma_j^x, \qquad (1.4)$$

$$\sigma_j^y = \left(\prod_{k<j} i\gamma_{2k}\gamma_{2k+1}\right)\gamma_{2j+1}, \qquad\qquad \gamma_{2j+1} = \prod_{k<j}\sigma_k^z\sigma_j^y, \qquad (1.5)$$

$$\sigma_j^z = i\gamma_{2j}\gamma_{2j+1}. \qquad (1.6)$$

It is assumed that neighboring majoranas are paired to a fermion via $c_k = \gamma_{2k} + i\gamma_{2k+1}$.

1.1.1.2 Bosonization

One of the peculiarities in one dimension is that the partition function of right- and left-moving fermions with a linear spectrum $\epsilon_{R/L,k} = v_F(\pm k - k_F)$ is equal to that of a single boson. This means that a many-body fermionic problem may equivalently be described in terms of bosons.
This is especially helpful when fermionic density-density interactions are considered, since there is an exact mapping to a bosonic non-interacting Hamiltonian. The bosons are then simply given by the particle hole exitations. A slightly changed basis related directly to the density $\rho_{R/L}$ in real space

$$\nabla\Phi(x) = -\pi(\rho_R(x) + \rho_L(x)), \qquad (1.7)$$
$$\nabla\Theta(x) = \pi(\rho_R(x) - \rho_L(x)) \qquad (1.8)$$

no longer has bosonic commutation relations, however Φ and Θ are canonically conjugated:

$$[\Phi(x_1), \Theta(x_2)] = i\frac{\pi}{2}\text{sign}(x_2 - x_1), \qquad (1.9)$$

$$[\Phi(x_1), \nabla\Theta(x_2)] = i\pi\delta(x_2 - x_1). \qquad (1.10)$$

The fermionic creators and annihilators contain Φ and Θ as phases. The subscript $r = \pm = R/L$ distinguishes right and left movers:

$$\psi_r(x) = U_r\frac{1}{2\pi\alpha}e^{irk_F x}e^{-i(r\Phi(x)-\Theta(x))}. \qquad (1.11)$$

The U_r are the so called Klein-factors that are simply numbers satisfying majorana algebra for all purposes considered here.

Fermionic Density-Density Interaction The spinless fermionic Hamiltonian with short range density-density interaction

$$H = \int \text{d}x\left[v_F(\Psi_R^\dagger\nabla\Psi_R - \Psi_L^\dagger\nabla\Psi_L) + g_4(\rho_R\rho_R + \rho_L\rho_L) + g_2\rho_L\rho_R\right] \qquad (1.12)$$

can be brought to quadratic form in the bosonic basis via the transformation introduced above:

$$H = \frac{1}{2\pi} \int \mathrm{d}x \left[uK(\nabla\Theta)^2 + \frac{u}{K}(\nabla\Phi)^2 \right]. \tag{1.13}$$

The parameters K and u of this Hamiltonian are the Luttinger parameter controlling the asymptotics of all correlation functions and the velocity of exitations. The dependence on g_4, g_2 and v_F can be worked out after a bit of simple algebra. This becomes important for the RG analysis in Chap. 2, where the density-density interaction term can be treated exactly by the above Luttinger Liquid description.

1.1.2 Conformal field theory

For the proof on constraints of the multifractal spectrum due to local conformal invariance and abelian fusion in Chap. 3 some fundamentals in conformal field theory are crucial.

I closely follow Ref. [92] to give an overview of the constraints of global conformal invariance to correlation functions.

1.1.2.1 Global conformal invariance

In a space of arbitrary dimension, the (global) conformal transformations:

1. translations $T_a : \mathrm{r} \to \mathrm{r} + a$

2. dilations $D_\lambda : \mathrm{r} \to \lambda\mathrm{r}$

3. rotations $R_M : \mathrm{r} \to M\mathrm{r}$ with M orthogonal

4. special conformal transformation $S_b : \mathrm{r} \to I \circ T_b \circ I(\mathrm{r})$, with inversion $I : \mathrm{r} \to \frac{\mathrm{r}}{|\mathrm{r}|^2}$

leave the metric tensor $g_{\mu\nu}$ invariant:

$$g'_{\mu\nu}(\mathrm{r}') = \Lambda(\mathrm{r})g_{\mu\nu}(\mathrm{r}). \tag{1.14}$$

This work sticks to Euclidean space, for Minkowski spacetime one needs to include boosts in the rotation group.

Why are low dimensions special? A small conformal coordinate transformation $\mathrm{r}_\mu \to \mathrm{r}_\mu + \epsilon_\mu$ changes the metrics as:

$$g_{\mu\nu}(\mathrm{r}) \to g_{\mu\nu} - (\partial_\mu\epsilon_\nu + \partial_\nu\epsilon_\mu). \tag{1.15}$$

The scale invariance condition Eq. (1.14) implies:

$$\partial_\mu\epsilon_\nu + \partial_\nu\epsilon_\mu = f(\mathrm{r})g_{\mu\nu}. \tag{1.16}$$

For a flat space ($\partial_\rho g_{\mu\nu} = 0$) this can be simplified to:

$$f(\mathrm{r}) = \frac{2}{d}\partial_\rho\epsilon^\rho. \tag{1.17}$$

Using Eq. (1.16) again yields:

$$2\partial^2 \epsilon_\mu = (2 - d)\partial_\mu f. \tag{1.18}$$

Applying ∂_μ once more and contracting, one finds:

$$(1 - d)\partial^2 f = 0. \tag{1.19}$$

In $d \geq 3$ this implies $f(\mathrm{r})$ is a linear function of the coordinate r and is restricted to the above global conformal transformations.

For $d = 1$, the condition (1.16) is trivially satisfied, since there is one coordinate. Consequently, any smooth coordinate change f is conformal in 1D.

In $d = 2$, the RHS in (1.18) cancels to zero, which means that the constraints on ϵ reduce to the Cauchy-Riemann differential equations. One can see this easily by writing $z = \mathrm{r}_1 + i\mathrm{r}_2$ and $\bar{z} = \mathrm{r}_1 - i\mathrm{r}_2$. The metric in these holomorphic and antiholomorphic coordinates then is

$$g_{\mu\nu} = \begin{pmatrix} 0 & \frac{1}{2} \\ \frac{1}{2} & 0 \end{pmatrix}, \qquad\qquad g^{\mu\nu} = \begin{pmatrix} 0 & 2 \\ 2 & 0 \end{pmatrix}. \tag{1.20}$$

Eq. (1.16) then becomes

$$\partial_{\bar{z}}\epsilon(z, \bar{z}) = 0, \qquad\qquad \partial_z \bar{\epsilon}(z, \bar{z}) = 0, \tag{1.21}$$

which are the Cauchy-Riemann equations.

One point correlation function   A basic notion of CFT is that of a quasiprimary operator $\phi(r)$. Such operators transform in a specific way under global conformal transformations, and the results summarized in this section are derived assuming the quasiprimary nature of all operators involved. In a (unitary) CFT the expectation value $\langle\,.\,\rangle$ of any nontrivial quasiprimary field with scaling dimension $x > 0$ in the infinite space is zero:

$$\left\langle \phi(\mathrm{r}) \right\rangle = \delta_{x,0}. \tag{1.22}$$

Only the identity operator $\mathbb{1}$ has vanishing dimension and $\left\langle \mathbb{1} \right\rangle = 1$.

Two point correlation function   A correlation function of two fields transforms as

$$\langle \phi_1(\mathrm{r}_1)\phi_2(\mathrm{r}_2) \rangle = \left| \frac{\partial \mathrm{r}'}{\partial \mathrm{r}} \right|^{x_1/d}_{\mathrm{r}=\mathrm{r}_1} \left| \frac{\partial \mathrm{r}'}{\partial \mathrm{r}} \right|^{x_2/d}_{\mathrm{r}=\mathrm{r}_2} \langle \phi_1(\mathrm{r}'_1)\phi_2(\mathrm{r}'_2) \rangle \tag{1.23}$$

under conformal transformations $\mathrm{r} \to \mathrm{r}'$.

Dilation invariance $\mathrm{r} \to \lambda \mathrm{r}$ implies:

$$\langle \phi_1(\mathrm{r}_1)\phi_2(\mathrm{r}_2) \rangle = \lambda^{x_1 + x_2} \langle \phi_1(\lambda \mathrm{r}_1)\phi_2(\lambda \mathrm{r}_2) \rangle. \tag{1.24}$$

From rotational and translational invariance, one can infer that

$$\langle \phi_1(\mathrm{r}_1)\phi_2(\mathrm{r}_2) \rangle = f(|\mathrm{r}_1 - \mathrm{r}_2|), \tag{1.25}$$

where f must be a homogeneous function $f(\mathrm{r}) = \lambda^{x_1 + x_2} f(\lambda \mathrm{r})$.

This fixes f to the form:

$$\langle \phi_1(\mathrm{r}_1)\phi_2(\mathrm{r}_2) \rangle = \frac{C_{12}}{|\mathrm{r}_1 - \mathrm{r}_2|^{x_1 + x_2}}. \tag{1.26}$$

Finally, the special conformal symmetry forces either $x_1 = x_2$ or $C_{12} = 0$.

Three point correlation function   Imposing translational, rotational and dilation invariance on the correlator of three fields one finds:

$$\langle \phi_1(\mathrm{r}_1)\phi_2(\mathrm{r}_2)\phi_3(\mathrm{r}_3)\rangle = \frac{C_{123}^{(abc)}}{\mathrm{r}_{12}^a \mathrm{r}_{23}^b \mathrm{r}_{13}^c}. \tag{1.27}$$

Here the dilations force $a + b + c = x_1 + x_2 + x_3$.

Finally the special conformal transformation gives a set of constraints:

$$\begin{array}{ll} a + c = 2x_1 & a = x_1 + x_2 - x_3 \\ a + b = 2x_2 \Leftrightarrow b = x_2 + x_3 - x_1 \\ b + c = 2x_3 & c = x_3 + x_1 - x_2 \end{array} \tag{1.28}$$

This again determines the correlation function up to the prefactor C_{123}:

$$\langle \phi_1(\mathrm{r}_1)\phi_2(\mathrm{r}_2)\phi_3(\mathrm{r}_3)\rangle = \frac{C_{123}}{\mathrm{r}_{12}^{x_1+x_2-x_3} \mathrm{r}_{23}^{x_2+x_3-x_1} \mathrm{r}_{13}^{x_3+x_1-x_2}}. \tag{1.29}$$

This restrictive power of the global conformal invariance diminishes in higher orders.

Higher order correlation functions   Beginning with four point functions, certain so called anharmonic ratios of the coordinates are conformally invariant by themselves and can therefore appear arbitrarily in correlation functions. In fourth order, there are two anharmonic ratios η, η'. So an arbitrary function of two variables $f(\eta, \eta')$ appears in the correlation function:

$$\langle \phi_1(\mathrm{r}_1)\phi_2(\mathrm{r}_2)\phi_3(\mathrm{r}_3)\phi_4(\mathrm{r}_4)\rangle = f\left(\frac{\mathrm{r}_{12}\mathrm{r}_{34}}{\mathrm{r}_{13}\mathrm{r}_{24}}, \frac{\mathrm{r}_{12}\mathrm{r}_{34}}{\mathrm{r}_{23}\mathrm{r}_{14}}\right) \prod_{i<j}^4 \mathrm{r}_{ij}^{x/3-x_i-x_j}, \tag{1.30}$$

where $x = \sum_i x_i$.

Operator product expansions   Fields ϕ_i, ϕ_j at nearby points r_1, r_2 can fuse together:

$$\phi_i(r_1)\phi_j(r_2) = \sum_k C_k^{ij}(r_1, r_2, r)\phi_k(r), \tag{1.31}$$

where r is a point close to r_1, r_2 and $C_k^{ij}(r_1, r_2, r)$ are structure constants. This formula is particularly useful, when almost all of the $C_k^{ij}(r_1, r_2, r)$ are zero.

1.1.2.2 Local conformal invariance in 2D

One can use the Laurent representation to express any small local conformal transformation as

$$z' = z + \varepsilon(z), \qquad\qquad \varepsilon(z) = \sum_{-\infty}^{\infty} c_n z^{n+1}. \tag{1.32}$$

In contrast to the higher dimensional case, this contains an infinite number of generators:

$$\ell = -z^{n+1}\partial_z, \qquad\qquad \bar{\ell} = -\bar{z}^{n+1}\partial_{\bar{z}} \tag{1.33}$$

These fulfill special commutation relations.

Witt algebra   The conformal algebra can be thought of as two copies of the infinite Virasoro algebra:

$$[\ell_n, \ell_m] = (n - m)\ell_{n+m},$$
$$[\bar{\ell}_n, \bar{\ell}_m] = (n - m)\bar{\ell}_{n+m},$$
$$[\ell_n, \bar{\ell}_m] = 0. \tag{1.34}$$

The six dimensional global conformal subalgebra is generated by $\ell + \bar{\ell}$ and $i(\ell - \bar{\ell})$ for $n = -1, 0, 1$.

Primary fields   Given a field with scaling dimension Δ and planar spin s, the holomorphic and antiholomorphic dimensions are:

$$h = \frac{1}{2}(\Delta + s), \qquad\qquad \bar{h} = \frac{1}{2}(\Delta - s). \tag{1.35}$$

In this work, one can restrict to $s = 0$, and $h = \bar{h}$.

Primary fields (of dimension $(h, \bar{h})$) transform as

$$\phi'(w, \bar{w}) = \left(\frac{\mathrm{d}w}{\mathrm{d}z}\right)^{-h} \left(\frac{\mathrm{d}\bar{w}}{\mathrm{d}\bar{z}}\right)^{-\bar{h}} \phi(z, \bar{z}) \tag{1.36}$$

under all local conformal transformations $z \to w$.

Correlation functions   The four point correlator slightly simplifies, one cross ratio $\eta = \dfrac{x_{12}x_{34}}{x_{13}x_{24}}$ is sufficient in the parametrization (1.30):

$$\langle \phi_1(x_1)\phi_2(x_2)\phi_3(x_3)\phi_4(x_4) \rangle = f(\eta, \bar{\eta}) \prod_{i<j}^{4} z_{ij}^{h/3 - h_i - h_j} \bar{z}_{ij}^{\bar{h}/3 - \bar{h}_i - \bar{h}_j}. \tag{1.37}$$

In Sec. 3.2 use will be made of this technical formalism in the proof that local conformal invariance and a complete family of operators satisfying abelian fusion in a field theory describing a multifractal system imply generalized parabolicity of the multifractal spectrum.

Bosonization   The bosonic free fields introduced above in Sec. 1.1.1.2 are an example of a conformal field theory with central charge $c = 1$ (see Ref. [91]). The holomorphic field is given by $\phi(z = x + it) = \Phi(t, x) - \Theta(t, x)$ and the antiholomorphic field is $\phi(\bar{z} = x - it) = \Phi(t, x) + \Theta(t, x)$ in terms of the notation introduced above.

1.1.3 Momentum space renormalization group

In Chaps. 2 and 3 momentum space RG-analyses are performed. The basic principle are outlined in the following lines. Consider a general action $S[\phi]$ with couplings (g_i) of a field ϕ living on momenta $|k| < \Lambda$. The ultraviolet (UV) cutoff Λ is typically given by the reciprocal lattice spacing $\Lambda \sim a^{-1}$ for condensed matter applications. The physical reason is that it is meaningless to consider fluctuations on scales much smaller than the lattice constant a. In the infrared (IR), the sample size L cuts the range of momenta $L^{-1} \lesssim |k|$.

The partition sum for such an action $S[\phi]$ reads:

$$Z = \int \mathcal{D}\phi \exp\left(-S[\phi]\right). \tag{1.38}$$

Usually one is interested in the long range behavior $L \gtrsim r \gg a$ corresponding to slow momenta $k \ll \Lambda$. Momentum space RG provides a way to derive an effective action that does no longer depend on the exact microscopic details $k \sim a^{-1}$. A reduced cutoff $\tilde{\Lambda} = \Lambda e^{-\ell}$ is chosen. This splits the field $\phi = \phi^> + \phi^<$ in fast $\phi^>$ and slow components $\phi^<$ containing only $\Lambda > k > \tilde{\Lambda}$ and $\tilde{\Lambda} > k$ respectively. The momentum shell $\tilde{\Lambda} < |k| < \Lambda$ is then eliminated by integrating over the fast degrees of freedom $\phi^<$. at the expense of renormalized coupling $(\tilde{g}_i(\ell))$. The procedure can be iterated until the one of the g_i reaches the strong coupling regime, or the cutoff reaches an external scale like the system size or temperature. This is described in more detail in the next paragraph.

First, the field is split in fast and slow momentum components $\phi = \phi^> + \phi^<$ at the reduced cutoff $\Lambda e^{-\ell}$. Let $S_0 = D(\nabla \phi)^2$ be the kinetic part of the action S. In S_0, the field components $\phi^>$ and $\phi^<$ do not mix, since they live in different parts of momentum space and S_0 is diagonal in momentum space. This of course generalizes straightforwardly to arbitrary dispersions. One prepares to integrate out the field by expanding the exponential. For this step, all couplings are assumed to be small:

$$
\begin{aligned}
Z &= \int \mathcal{D}\phi^< \mathcal{D}\phi^> \exp\left(-S_0[\phi^>] - S_0[\phi^<] - S_1[\phi^>, \phi^<]\right) \\
&= \int \mathcal{D}\phi^< \mathcal{D}\phi^> \exp\left(-S_0[\phi^>] - S_0[\phi^<] -\right)\left(1 - S_1[\phi^>, \phi^<] + \frac{1}{2}S_1[\phi^>, \phi^<]^2 + \ldots\right).
\end{aligned}
\tag{1.39}
$$

For this reason, one needs to stop the RG at strong coupling, since one cannot justify this step in that case.

In the next step, one can perform the Gaussian integral over the fast modes $\phi^>$. By re-exponentiating (still assuming the couplings to be small) one finds a new effective action:

$$
\begin{aligned}
Z &= \int \mathcal{D}\phi^< \exp\left(-S_0[\phi^<]\right)\left(1 - \langle S_1[., \phi^<]\rangle_> + \frac{1}{2}\langle, S_1[., \phi^<]\rangle_> + \ldots\right) \\
&= \int \mathcal{D}\phi^< \exp\left(-S_0[\phi^<]\right) \exp\left(-\langle S_1[., \phi^<]\rangle_> + \frac{1}{2}(\langle S_1[., \phi^<]^2\rangle_> - \langle S_1[., \phi^<]\rangle_>^2) + \ldots\right) \\
&= \int \mathcal{D}\phi^< \exp\left(-\tilde{S}[\phi^<]\right).
\end{aligned}
\tag{1.40}
$$

In order to compare $\tilde{S}[\phi^<]$ and $S[\phi^<]$ one needs to rescale $\tilde{\Lambda} \to \Lambda$. Then one can read off how the couplings in S change: $(g_i) \to (\tilde{g}_i)$ for a scale change ℓ. By considering infinitesimal scale changes ℓ differential equations for the (g_i) can be derived. These RG flow equations describe the evolution of the couplings from small to larger scales. Starting from the microscopic bare $(g_i(\ell = 0))$ one can in principle obtain $(g_i(\ell))$ at arbitrary length scales. The procedure is only valid to the point, where a coupling becomes large $(g_i \sim 1)$. This prevents the RG step based on integrating out a free fast field shown above.

The fixed points of the RG flow equations are of special physical interest, since they can persist to arbitrary large length scales. If a physical system is at criticality, it becomes scale invariant [92]. Therefore critical points in the phase diagram of the system appear as fixed points in the RG equation.

To first order in the couplings, the RG equations around a fixed point (FP) usually look like:

$$\frac{\mathrm{d}g_i'}{\mathrm{d}\ell} = d_i g_i' + \mathcal{O}(g_j^2), \tag{1.41}$$

where a basis change $g_i \to U_{ij}g_j'$ might be necessary to bring the equations to above form.

Couplings with

- $d_i > 0$ are called relevant

- $d_i = 0$ are marginal, one distinguishes marginally (ir)relevant by looking at higher orders in (g_i)

- $d_i < 0$ are irrelevant

One may then keep the most relevant couplings for further analysis with more sophisticated methods.

In the case that there are no relevant couplings for a given set of parameters, a stable fixed point of the theory is reached. Fixed points with m irrelevant and $n - m$ relevant couplings can be thought of as m dimensional phase boundaries in the full n dimensional parameter space.

1.1.4 Dealing with disorder

When treating models analytically, one usually assumes the disorder potential (or generic coupling) to be Gaussian distributed. Then arbitrary moments of the disorder potential V can be expressed in terms of the first and second moment:

$$\langle V(x) \rangle = 0, \qquad\qquad \langle V(x)V(x') \rangle_V = K(x - x'). \tag{1.42}$$

In general the predictions derived for these models under the Gaussian assumption are valid for generic disorder ensembles, except for pathological special cases [40]. A formal justification for this can be derived using the central limit theorem, Gaussian disorder corresponds to infinitely many and infinitely dense impurities [93]. The special case $K(x - x') = D\delta(x - x')$, where every momentum component of the disorder kernel $K_k = D$ is present, is called Gaussian white noise.

In the language of field theory a random field $V(x)$ is coupled to the density ρ of system. It appears linear in the action $S = S_0 + S_{\mathrm{dis}}$.

$$Z[V] = \int \mathcal{D}(\psi, \bar{\psi}) \exp\left(-S_0[\psi, \bar{\psi}] - \int \mathrm{d}^d x \mathrm{d}\tau V(x)\rho(x, \tau)\right) \tag{1.43}$$

In this setting, any observable depends on the configuration of V, one has to average over all configurations of V:

$$\langle O \rangle_V = \int \mathcal{D}(V) \frac{1}{Z[V]} \int \mathcal{D}(\psi, \bar{\psi}) O[\psi, \bar{\psi}] \exp\left(-S[V, \psi, \bar{\psi}]\right) \exp\left\{-\int \mathrm{d}^d x \mathrm{d}^d x' V(x)K(x - x')V(x')\right\} \tag{1.44}$$

The partition sum $Z[V]$ is in the denominator of any expectation value of observables. Performing the integral over configurations V is not straightforward at this stage. In this thesis, two distinct methods for this disorder averaging step are used.

1.1.4.1 Replicas

The so called replica trick is used to perform the disorder averages in Chap. 3. A short sketch of the underlying concept is given here. The partition sum $Z[V]$ in the denominator of the expectation value for the observable O

$$\langle O \rangle_{S[V]} = \frac{1}{Z[V]} \int \mathcal{D}(\psi, \bar{\psi}) O[\psi, \bar{\psi}] \exp\left(-S[V, \psi, \bar{\psi}]\right) \tag{1.45}$$

may be formally rewritten as product of $n-1$ Zs in the limit n to zero:

$$\frac{1}{Z} = \lim_{n \to 0} Z^{n-1} = \lim_{n \to 0} \underbrace{Z \ldots Z}_{n-1 \text{ times}} . \tag{1.46}$$

The argument V indicating dependence on the disorder configuration V is suppressed in this line.

In the average of an observable the action is then replicated $n - 1 + 1$ times from the denominator $(n-1)$ and the expectation value (1). The disorder can be integrated out yielding the following quartic term mixing the replicas in the effective action:

$$\langle O \rangle_V = \lim_{n \to 0} \int \prod_{a=1}^{n} \left[\mathcal{D}(\psi_a, \bar{\psi}_a) \right] O(\psi_1) \exp(-S_{\text{eff}}), \tag{1.47}$$

$$S_{\text{eff}}[\psi_a, \bar{\psi}_a] = \sum_{a=1, b=1}^{n} S_0(\psi_a, \bar{\psi}_a) - \int \mathrm{d}x \mathrm{d}x' \mathrm{d}\tau \mathrm{d}\tau' \rho[\psi_a(x, \tau), \bar{\psi}_a(x, \tau)] \rho[\psi_b(x', \tau'), \bar{\psi}_b(x', \tau')] K(x - x'). \tag{1.48}$$

In pathological special cases, the limit $n \to 0$ is not well-defined. For non-interacting systems, there a more controlled analytical approach.

1.1.4.2 Supersymmetry

Without interaction, it does not matter whether one writes the functional integral in terms of Grassman (fermions) or ordinary complex variables (bosons). There is no difference between bosons and fermions at single-particle level. The partition sum Z is given by (one over) the determinant of the matrix in the exponential for fermions (bosons). Writing the model in terms of Grassman $(\psi, \bar{\psi})$ and ordinary complex variables (ϕ^*, ϕ) at the same time, Z is fixed to one:

$$Z = \int \mathcal{D}(\psi, \bar{\psi}, \phi^*, \phi) \exp\left(\bar{\psi}(H_0 + V)\psi + \phi^*(H_0 + V)\phi\right) = 1. \tag{1.49}$$

Averaging over V again gives an effective interaction that is elastic and mixes bosons and fermions. Observables are written either in bosonic or fermionic form. This method is used in Chap. 1. The work in Chap. 3 can be safely restricted to just the bosonic sector of the action.

1.1.4.3 Transfer Matrix Method

Another way to derive the topological classification in one dimension (Tab. 1.1, column $d = 1$) is to look at the transfer matrix ensembles arising in the different symmetry classes. The set-up is a 1D-system of finite length L with N channels attached to ideal leads at both ends in the limit $N \ll L$.

The $2N \times 2N$ transfer matrix M relates the N right movers and N left movers in the right lead to the $2N$ modes in the left lead. Current conservation implies that in general $M \in U(N, N)$.

Imposing the constraints of the symmetry class on M, each space of transfer matrices can be related to a (Cartan) symmetric space [9]. In table 1.1 one may observe, that the symmetric spaces of the Hamiltonians are just shifted down by one to obtain the transfer matrix spaces. This is a consequence of Bott-periodicity [3].

The intuitive reason why the transfer matrix is such a useful tool is as follows. For a given boundary condition at one end of the wire, the transfer matrix gives the solution of the Schrödinger equation (without boundary conditions) at the other end. Checking that the actual boundary conditions at both leads are respected, eigenmodes of the wire are obtained. Away from criticality, the eigenvalues t_i usually behave exponentially in L. Hence it is natural to defined the Lyapunov exponents [94] $\lambda_i = \frac{1}{L} \ln t_i$. The sign of the λ_i determines at which end of the wire the modes sit: the exponentially decaying solution has to be chosen (normalization of the wave function). A vanishing exponent λ_i indicates critical states at that energy, extended over a large part of the wire.

Restricting to one chiral subspace, the sign of λ_i is well-defined and each sign configuration corresponds to a different component in the symmetric space [95]. That way it can be seen nicely how different chiral topological phases have different edge mode structure. This approach is used in Chap. 2. In the next section a method particularly useful in 2D follows.

1.1.4.4 The non-linear sigma model

In this section the non-linear sigma model (NLσM) is derived for disordered non-interacting fermions in d dimensions. The generalization to bosons or the supersymmetric case is straightforward. I will follow the book of Efetov [96] and Ref. [97] closely. First, one needs to write the action of the system to extract the retarded and advanced Green's function. It is then most convenient to use field integration variables in a form respecting the symmetries of the Hamiltonian [98]. For integration over disorder, the replica trick can be employed. The arising effective interaction term can be decoupled with a Hubbard-Stratonovich transformation of the appropriate momentum transfer channels. Integrating out the fermions leaves us with an action $S[Q]$ depending only on the Hubbard-Stratonovich field. Deriving the low energy theory of $S[Q]$, one finds that Q satisfies the non-linear constraint $Q^2 = \mathbb{1}$. In general, $S[Q]$ is a non-linear sigma model over the symmetric space of the corresponding symmetry class [98].

Our starting point is the time independent disordered action $S[\psi, \bar{\psi}, V]$:

$$S[\psi, \bar{\psi}, V] = \int \mathrm{d}^d r \, \bar{\psi} \left(-\hat{\omega} + H_0 + V + i0\tau_3 \right) \psi \equiv \int \mathrm{d}^d r \bar{\psi} G^{-1} \psi. \tag{1.50}$$

The fields $\bar{\psi}, \psi$ are fermionic and in this line the Green's function G of the system described by $H_0 + V$ is introduced. The disorder potential V couples to the density. The field ψ is chosen to carry an advanced/retarded index τ. This ensures the appropriate $\pm i0$ prescription of the Green's function:

$$\langle \bar{\psi}_\omega^R(r_1) \psi_\omega^R(r_2) \rangle_{S[\psi, \bar{\psi}, V]} = G^R(r_1, r_2; \omega). \tag{1.51}$$

Expectation values non-diagonal in frequency and retarded/advanced space vanish.

Depending on the symmetry class, G satisfies certain linear constraints. As an example consider spinless fermions with time reversal symmetry $\mathcal{T}^2 = 1$. Let $\mathcal{T}$ act as transposition, then the Green's

function obeys $G^T = G$:

$$S[\psi, \bar{\psi}, V] = \frac{1}{2} \int \mathrm{d}^d r \left[\bar{\psi} G^{-1} \psi - \psi^T \left(G^{-1} \right)^T \bar{\psi}^T \right] = \frac{1}{2} \int \mathrm{d}^r \bar{\Psi} G^{-1} \Psi. \tag{1.52}$$

In this step the doubled fields $\Psi = (\psi, \bar{\psi}^T)_\sigma$ and $\bar{\Psi} = (\bar{\psi}, -\psi^T)_\sigma$ are introduced. The time reversal operation acts as $\bar{\Psi} = -\Psi^T i\sigma_2$ on the doubled fields.

Integrating out the disorder following the steps of Sec. 1.1.4.1, one obtains the replicated action:

$$S_{\mathrm{eff}}[\psi, \bar{\psi}] = \frac{1}{2} \sum_a \int \mathrm{d}^d r \bar{\Psi}_a G_0^{-1} \Psi_a + \frac{1}{16\pi\nu\tau} \sum_{ab} \int \mathrm{d}^d r \bar{\Psi}_a \Psi_a \bar{\Psi}_b \Psi_b. \tag{1.53}$$

A Hubbard-Stratonovich transformation makes this action quadratic in Ψ again. One can do so exactly using a field containing all momentum components. Since a low energy/momentum theory is of interest here, the focus rather is on the processes with low momentum transfer. There are three channels: direct, exchange and cooper.

$$\int \mathrm{d}^d r \bar{\Psi}_a \Psi_a \bar{\Psi}_b \Psi_b = \sum_{p_1, p_2, q} \left[\left(\bar{\Psi}_{a,p_1} \Psi_{a,-p_1+q} \right) \left(\bar{\Psi}_{b,p_2} \Psi_{b,-p_2-q} \right) \right.$$
$$\left. + \left(\bar{\Psi}_{a,p_1} \Psi_{a,p_2} \right) \left(\bar{\Psi}_{b,-p_2-q} \Psi_{b,-p_1+q} \right) + \left(\bar{\Psi}_{a,p_1} \Psi_{a,p_2} \right) \left(\bar{\Psi}_{b,-p_1+q} \Psi_{b,-p_2-q} \right) \right] \tag{1.54}$$

The time reversal operation forces the last two terms (exchange, cooper) to coincide:

$$\left(\bar{\Psi}_{b,-p_1+q} \Psi_{b,-p_2-q} \right) = \left(\bar{\Psi}_{b,-p_1+q} \Psi_{b,-p_2-q} \right)^T = \left(\bar{\Psi}_{b,-p_2-q} (\sigma_2)^2 \Psi_{b,-p_1+q} \right) = \left(\bar{\Psi}_{b,-p_2-q} \Psi_{b,-p_1+q} \right). \tag{1.55}$$

The direct channel can be safely neglected, since it corresponds to scattering off impurities at low momentum transfer. The other two channels are associated with Diffuson and Cooperon in the diagrammatic treatment and can be expected to give the dominant contributions.

Our decoupled action reads:

$$e^{-S_{\mathrm{eff}}[\psi, \bar{\psi}]} = \int \mathcal{D}Q \, \exp \left[-\frac{\pi\nu}{8\tau} \int \mathrm{d}^d r \, \mathrm{tr} Q^2 - \frac{1}{2} \mathrm{d}^d r \bar{\Psi} \underbrace{\left(G_0^{-1} + \frac{i}{2\tau} Q \right)}_{\equiv G^{-1}[Q]} \Psi \right]. \tag{1.56}$$

At this point, one can integrate over the fermions:

$$Z = \int \mathcal{D}[\psi, \bar{\psi}] e^{-S_{\mathrm{eff}}[\psi, \bar{\psi}]}$$
$$= \int \mathcal{D}Q \exp \left[-\frac{1}{2} \mathrm{tr} \log \left(H_0 + \frac{i}{2\tau} Q + \Sigma_3 \hat{\omega} + i0\tau_3 \right) + \frac{\pi\nu}{8\tau} \int \mathrm{d}^d r \, \mathrm{tr} \, Q^2 \right] \tag{1.57}$$

The action for the Q field then is:

$$S[Q] = -\frac{1}{2} \mathrm{tr} \log \left(\underbrace{H_0 + \Sigma_3 \hat{\omega} + i0\tau_3}_{\equiv G_0^{-1}} + \frac{i}{2\tau} Q \right) + \frac{\pi\nu}{8\tau} \int \mathrm{d}^d r \, \mathrm{tr} \, Q^2. \tag{1.58}$$

Up to neglecting the direct interaction channel, this action is exact. This comes at the expense of arbitrary high order interaction terms contained in the Q expansion of the logarithm.

The next step is to find a quadratic low energy theory. Let us first look for the saddle point of this action:

$$
S[Q_0 + \delta Q] = \operatorname{tr} \log \left(\underbrace{H_0 + \Sigma_3 \hat{\omega} + i0\tau_3 + \frac{i}{2\tau} Q_0 + \frac{i}{2\tau} \delta Q}_{\equiv G^{-1}[Q]} \right) + \frac{\pi\nu}{8\tau} \int \mathrm{d}^d r \ \operatorname{tr} \left(Q_0^2 + 2Q_0 \delta Q + \delta Q^2 \right),
$$

$$
\sim \sum_q (\delta Q)_{-q} \left(2L^d (Q_0)_q - \lambda \sum_p G^{-1}[Q_0]_{p,p+q} \right). \tag{1.59}
$$

An ansatz diagonal in retarded/advanced and time reversal space is chosen: $(Q_0)_p \equiv \Lambda$. Then the stationarity criterion reduces to:

$$
\pi\nu\Lambda = \frac{i}{L^d} \sum_p \frac{1}{\hat{\omega} - \xi_p + i0\tau_3 + \frac{i}{2\tau}\Lambda} \tag{1.60}
$$

Choosing $\Lambda = \tau_3$ is a solution of this equation. In fact there is a whole group G that leaves these mean field equations invariant. One can equivalently put $(Q_0)_p \equiv g\Lambda g^{-1}$ for any $g \in G$. Here for spinless fermions with time-reversal invariance $G = Sp(4n)$.

One can decompose $Q = g\Lambda g^{-1}$ with a spatially slowly fluctuating $g \in G$ to find the low energy field theory around the saddle point. The second term gives a constant contribution, since $Q^2 = 1$.

Under the trace, the matrices in the logarithm effectively commute and one can employ $\operatorname{tr} \log(AB) = \operatorname{tr} \log(A) + \operatorname{tr} \log(B)$:

$$
\operatorname{tr} \log \left(G_0^{-1}[\Sigma_3 \hat{\omega} + i0\tau_3] + Q \right) = \operatorname{tr} \log \left(G_0^{-1}[\Sigma_3 \hat{\omega} + i0\tau_3](1 + G_0[\Sigma_3 \hat{\omega} + i0\tau_3]Q) \right)
$$

$$
= \operatorname{tr} \log \left(G_0^{-1}[\Sigma_3 \hat{\omega} + i0\tau_3] \right) + \operatorname{tr} \log \left(1 + G_0[\Sigma_3 \hat{\omega} + i0\tau_3]Q \right). \tag{1.61}
$$

The first term gives a constant contribution to the action, the second term is expanded up to second order in Q:

$$
\operatorname{tr} \log \left(1 + G_0[\Sigma_3 \hat{\omega} + i0\tau_3]Q \right) = \operatorname{tr} \left(G_0[\Sigma_3 \hat{\omega} + i0\tau_3]Q \right) - \frac{1}{2} \operatorname{tr} \left(G_0[\Sigma_3 \hat{\omega} + i0\tau_3]Q G_0[\Sigma_3 \hat{\omega} + i0\tau_3]Q \right). \tag{1.62}
$$

From symmetry reasoning and due to the constraint $Q^2 = \mathbb{1}$, the terms in the soft-mode action are:

$$
S[Q] = \frac{\pi\nu}{2} \int \mathrm{d}^d r \ \operatorname{tr} \left[c_D \left(\nabla Q \right)^2 - c_\omega Q \right]. \tag{1.63}
$$

By comparison to the diffusion propagator and by computing $\nu = \langle G \rangle_{\text{dis}}$ one can fix c_D and c_ω to:

$$
S[Q] = \frac{\pi\nu}{2} \int \mathrm{d}^d r \ \operatorname{tr} \left[\frac{D}{4} \left(\nabla Q \right)^2 - \hat{\omega} Q \right]. \tag{1.64}
$$

This construction works analogous for the nine other symmetry classes. In Sec. 3.7.2 the sigma model for class C is derived. Driven to criticality by a topological term (see Sec: 1.5.3), it describes the statistics of critical wave functions in Spin Quantum Hall systems.

1.2 Anderson transitions and Multifractality

In general, low dimensional systems ($d \leq 2$) tend to localize in presence of disorder. By thinking about arbitrarily weak impurities in the system as shallow potentials one can intuitively understand this within elementary quantum mechanics: a shallow well still has at least one bound state in $d = 1, 2$ no matter how weak the potential. Bound states are exponentially localized. Formally this means that there is a localization length ξ that is much smaller than the system size L. In the thermodynamic limit $\xi/L \overset{L \to \infty}{\to} 0$. Wave functions at nearby energies are not correlated, they sit in different wells of the random potential and have an overlap exponentially suppressed with distance. The conductance g of such insulating systems decays exponentially with L. It was therefore surprising that chiral wires with an odd number of channels [99–101] can have perfectly transmitting eigenchannels. The average conductance scales as a power law with L [99]. The mechanism behind this is topological protection (which is discussed below in Sec. 1.3): the system is at the boundary of two topologically distinct phases and therefore has to remain critical. There is no finite localization length $\xi(L) \sim \sqrt{L}$, yet the wave functions are not fully delocalized as in a metal.

Another route to escape localization is considering larger dimensions $d > 2$ and sufficiently weak disorder. Neglecting topological effects, in $d > 2$ the system is a diffusive metal for weak disorder W and an insulator at strong disorder. At $W^*(d)$ there is a metal insulator transition where the wavefunctions exhibit multifractality. The critical disorder strength $W^*(d)$ grows with d [9].

1.2.1 Multifractality

In my thesis I adopt the notation from Ref. [9] for the context of multifractality (MF). Critical disordered systems can be characterized by the scaling of the distribution of powers of the wave function $|\psi|^2$, the so called inverse-participation ratios $\mathcal{P}_q$:

$$\mathcal{P}_q \equiv \langle \int d^d \mathbf{r} \, |\psi(\mathbf{r})|^{2q} \rangle_{dis} \sim L^{-\tau_q}. \tag{1.65}$$

With $\langle . \rangle_{dis}$ the disorder average is indicated and d is the spatial dimension of the system with linear size L. For large system size $L \to \infty$, the multifractal exponents τ_q are self-averaging [9]. In a good metal, the wave function is spread across the entire d dimensional system. Normalization of ψ then implies that $|\psi(r)| \propto L^{-d/2}$ for all r. Plugging this into the definition, one obtains $\mathcal{P}_q \propto L^{(1-q)d}$ in the metal, i.e. $\tau_q^{\text{metal}} = (q-1)d$. In general the function τ_q is non-decreasing ($\tau_q' \geq 0$) and convex ($\tau_q'' \leq 0$) with $\tau_0 = -d$ and $\tau_1 = 0$ (normalization of ψ).

The anomalous dimensions

$$\Delta_q \equiv \tau_q - d(q-1) \tag{1.66}$$

are defined relative to the scaling of a completely delocalized metallic wave function. In contrast the perfect insulator has $\mathcal{P}_q$ that do not scale with L at all. This means all τ_q^{ins} vanish identically for $q > 0$. The converse is not true: for chiral wires considered in Chap. 2 all τ_q for $q > 0$ are zero at a critical point, yet the systems are not insulating. The wave functions show nontrivial spatial correlations $\langle |\psi(r)|^2 |\psi(0)|^2 \rangle \propto r^{-3/2}$ [39] and the localization length diverges with system size.

Boxing   Numerically it can be favorable to subdivide a $(L)^d$ system into N^d boxes of size b, where $N \equiv L/b$. The box probability $\mu_i \equiv \int_{b_i} d^d \mathrm{r} \, |\psi_0(\mathrm{r})|^d$ shows scaling behavior suitable to extract τ_q:

$$\sum_{i=1}^{N^d} (\mu_i)^q \sim \left(\frac{b}{L}\right)^{\tau_q}. \tag{1.67}$$

This kind of boxing is essential to handle negative values of q (where exact zeros of the wavefunction have drastic effects) and correlated disorder (where one needs to restrict the analysis to boxes larger than the disorder correlation length). In Chap. 4, the multifractal spectra of Dirac Hamiltonians with correlated disorder are extracted using this method and compared to universal predictions for two classes of theories, which are reviewed in Sec. 1.5.5 and Sec. 1.5.3.

1.2.1.1 Symmetries of (generalized) MF spectra

Due to the finite energy stacking in Chap. 4 one cannot properly access the local density of states in a meaningful way. The analysis of LDOS moments and more generic composite objects of Green's functions is a powerful tool used in the other Chapters 2, 3. Multifractality implies the presence of infinitely many relevant (in the RG sense) operators at the fixed point of an Anderson transition (AT). In Chap. 2 the RG (ir)relevance of a multifractal interaction matrix element is probed. Contrastingly a task in Chap. 3 is to find combinations of Green's functions in order to probe (in principle) the entire multifractal spectrum.

The anomalous dimensions Δ_q defined above in Eq. (1.66) are in linear relation with the scaling exponents x_q of moments of the local density of states (LDOS) $\nu(\mathrm{r})$:

$$\overline{\nu^q(\mathrm{r})} \propto L^{-x_q}, \qquad\qquad x_q = \Delta_q + q x_1. \tag{1.68}$$

Here x_1 describes the scaling of the average LDOS: $\rho \equiv \overline{\nu(r)} \propto L^{-x_1}$, and $x_0 = 0$.

The MF exponents have the beautiful symmetry property [102]:

$$x_q = x_{q_* - q}, \tag{1.69}$$

where q^* only depends on the symmetry class (with $q_* = 1$ for Wigner-Dyson classes).

It turns out that the notion of LDOS MF exponents x_q can be generalized to more complicated composite objects of Green's functions showing pure scaling (in Sec. 3.6 such are explicitly constructed in the class C NLσM). The generalized MF dimensions x_λ can be labeled with a weight $\lambda = (q_1, q_2, \ldots, q_n)$ and are invariant under the action of the so called Weyl group W:

$$x_{w\lambda} = x_\lambda, \qquad\qquad \forall w \in W. \tag{1.70}$$

The weights λ label irreducible representations of the NLσM supersymmetric space G/K, this is motivated below. The corresponding Weyl group W is generated by the following inversions and permutations in weight space. Their action on the weight $\lambda = (q_1, q_2, \ldots, q_n)$ is as follows:

(i) sign inversion of $\tilde{q}_j \equiv q_j + c_j/2$ for any $j \in \{1, 2, \ldots, n\}$:

$$q_j \to -c_j - q_j. \tag{1.71}$$

(ii) interchange of $\tilde{q}_i = q_i + c_i/2$ and $\tilde{q}_j = q_j + c_j/2$ for some pair $i, j \in \{1, 2, \ldots, n\}$:

$$q_i \rightarrow q_j + \frac{c_j - c_i}{2}; \qquad\qquad q_j \rightarrow q_i + \frac{c_i - c_j}{2}. \tag{1.72}$$

The parameters c_i only depend on the manifold G/K. In particular, $c_j = 1 - 2j$ for class A, and $c_j = 1 - 4j$ for class C. The leading MF dimensions x_q corresponds to weights $\lambda = (q)$ in this notation.

When all of the q_i are non-negative integers, one can translate a Green's function pure-scaling composite object C_λ into a pure-scaling operator $\mathcal{O}_\lambda$ in the NLσM framework (by analytic continuation one can then extend this to generic complex q_i in certain cases, see Sec. 3.7). In this case $\lambda = (q_1, q_2, \ldots, q_n)$ forms a highest weight under the action of the Lie algebra of G. With the usual procedure [103] one can relate multipoint functions with sigma model operators:

$$\overline{C_{\lambda_1}(r\ r_1) \ldots C_{\lambda_n}(r\ r_n)} = \left\langle \mathcal{O}_{\lambda_1}(r_1) \ldots \mathcal{O}_{\lambda_n}(r_n) \right\rangle. \tag{1.73}$$

The angular brackets indicate expectation value w.r.t. the NLσM action.

Postponing details to later sections, let us mention here important properties of the operators $\mathcal{O}_\lambda$ that result from their explicit construction and the symmetry relation (1.69):

1. There are families $\mathcal{O}_\lambda$ of exact scaling operators in the σ model at its critical fixed point:

$$\left\langle \mathcal{O}_\lambda(r) \right\rangle \sim L^{-x_\lambda}, \tag{1.74}$$

   their scaling dimension is x_λ.

2. There are $\mathcal{O}_{\lambda_j}, \lambda_j = (-c_1, \ldots, -c_j)$ with vanishing scaling dimension

$$x_{\lambda_j} = 0, \qquad\qquad \left\langle \mathcal{O}_{\lambda_j}(r) \right\rangle = 1, \tag{1.75}$$

   even though it describes the scaling of a nontrivial moment of the LDOS, and, thus, is different from the identity operator $\mathcal{O}_0$.

3. The $\mathcal{O}_\lambda$ satisfy the fusion rule $\mathcal{O}_\lambda \mathcal{O}_{\lambda'} \sim \sum_\mu C_\mu^{\lambda, \lambda'} \mathcal{O}_\mu$.

These properties point out the resemblance of MF spectra and field theory, compare Ref. [104].

There are special families of operators $\mathcal{P}_\lambda$ that satisfy an Abelian OPE (1.31):

$$\mathcal{P}_\lambda(r_1) \mathcal{P}_{\lambda'}(r_2) \propto r_{12}^{x_{\lambda+\lambda'} - x_\lambda - x_{\lambda'}} \mathcal{P}_{\lambda+\lambda'} \left(\frac{r_1 + r_2}{2} \right) + \ldots \tag{1.76}$$

In Sec. 3.3, such families are constructed for the bosonic class C NLσM. For generic λ there are infinitely many pure scaling operators $\mathcal{P}'_\lambda$ that do not share this fusion property (other gradientless operators appear on RHS). An example is given in Sec. 3.5.

1.2.2 CFT and Multifractality

This technical section dealing with the conformal field theory description of multifractal observables is an excerpt from Ref. [105]. Heavy use of the notation in Sec. 1.1.2 is made. The formalism introduced here is employed in Chap. 3 to prove the parabolicity constraint imposed by local conformal invariance and abelian fusion.

Here, a general discussion of multifractality at Anderson transitions (ATs) is presented, including definitions of multifractal (MF) observables, their correlation functions, the MF spectra of scaling dimensions, and relation to the field-theoretical renormalization group (RG). One central issue for us is a description of MF correlation functions in terms of conformal field theory (CFT). As discussed below, such a description in general does not hold, in view of the system-size dependence of the MF correlation functions. At the same time, a certain subclass of MF correlators satisfying a "neutrality" condition (1.83) is consistent with conformal invariance.

1.2.2.1 Multifractal multipoint functions and RG

Equation (1.74) can be understood from an RG point of view. One needs to run the RG from the microscopic scale a up to the scale L, and a one-point function at this scale becomes a number of order one. The result of the RG is the appearance of the scale factor L/a raised to the power $-x_q$, which is exactly Eq. (1.74). Similar arguments determine the behavior of multi-point functions. Let us consider the two-point function $\left\langle \mathcal{O}_{q_1}(r_1)\mathcal{O}_{q_2}(r_2) \right\rangle$. Now one can run the RG up to the scale $r_{12} = |r_1 - r_2|$, which results in the renormalization factor $r_{12}^{-x_{q_1}-x_{q_2}}$. At this scale the two operators fuse to $\mathcal{O}_{q_1+q_2}$. Then one can renormalize further up to scale L, which results in the additional factor $(L/r_{12})^{-x_{q_1+q_2}}$. Finally, at this scale the correlator is of order unity, and one gets

$$\left\langle \mathcal{O}_{q_1}(r_1)\mathcal{O}_{q_2}(r_2) \right\rangle \sim r_{12}^{-x_{q_1}-x_{q_2}} \left(\frac{L}{r_{12}} \right)^{-x_{q_1+q_2}} = r_{12}^{x_{q_1+q_2}-x_{q_1}-x_{q_2}} L^{-x_{q_1+q_2}}. \tag{1.77}$$

The same result is obtained from the Abelian OPE (1.76) combined with Eq. (1.74) applied to the expectation value of $\mathcal{O}_{q_1+q_2}$.

Next consider the three-point function $\left\langle \mathcal{O}_{q_1}(r_1)\mathcal{O}_{q_2}(r_2)\mathcal{O}_{q_3}(r_3) \right\rangle$. To apply the RG argument, one needs to know the hierarchy of distances between the three points. For example, let us assume that r_{12} is the smallest distance: $r_{12} \ll r_{13} \simeq r_{23} \ll L$. Then there will be three stages of RG and two fusions resulting in

$$\left\langle \mathcal{O}_{q_1}(r_1)\mathcal{O}_{q_2}(r_2)\mathcal{O}_{q_3}(r_3) \right\rangle \sim r_{12}^{-x_{q_1}-x_{q_2}-x_{q_3}} \left\langle \mathcal{O}_{q_1+q_2}(r_1/r_{12})\mathcal{O}_{q_3}(r_3/r_{12}) \right\rangle$$

$$\sim r_{12}^{-x_{q_1}-x_{q_2}-x_{q_3}} \left(\frac{r_{13}}{r_{12}} \right)^{-x_{q_1+q_2}-x_{q_3}} \left(\frac{L}{r_{13}} \right)^{-x_{q_1+q_2+q_3}} = r_{12}^{x_{q_1+q_2}-x_{q_1}-x_{q_2}} r_{13}^{x_{q_1+q_2+q_3}-x_{q_1+q_2}-x_{q_3}} L^{-x_{q_1+q_2+q_3}}. \tag{1.78}$$

Similar expressions are obtained in other cases when the distances between the points satisfy different inequalities. It is also easy to generalize these expressions to higher multipoint functions. In particular, it should be clear from the discussion above that a generic n-point MF function $\left\langle \prod_{i=1}^{n} \mathcal{O}_{q_i}(r_i) \right\rangle$, when considered as a function of system size L at fixed pairwise distances r_{ij} (all much smaller than L) will scale with L as

$$\left\langle \mathcal{O}_{q_1}(r_1)\ldots\mathcal{O}_{q_n}(r_n) \right\rangle \propto L^{-x_{q_1+\cdots+q_n}}. \tag{1.79}$$

1.2.2.2 Relation of MF multipoint functions and CFT correlators

A quick comparison of MF correlators with those in a CFT indicates that not all MF multipoint functions can be represented as CFT correlators. For example, even the one-point function (1.74)

is consistent with Eq. (1.22) only if $x_q > 0$. It is easy to see that for an extended range of q the dimensions are negative $x_q < 0$. (In fact, $x_q < 0$ holds for any q satisfying $q < 0$ or $q > q_*$.) In addition there is a non-trivial operator $\mathcal{O}_{q_*}$, distinct from the identity operator, whose dimension is zero, and whose expectation value in the infinite system is one, see Eq. (1.75). This indicates that one cannot expect all aspects of MF multipoint functions to be describable by a CFT.

The reader is encouraged to look at the two-point function (1.77). In general, it is L-dependent, at variance with Eqs. (1.25) and (1.26). One has to notice the following: one can choose $q_2 = -q_1$, and then the dimension $x_{q_1+q_2} = x_0 = 0$. This implies that with this choice the two-point function stops depending on the system size:

$$\left\langle \mathcal{O}_{q_1}(r_1)\mathcal{O}_{-q_1}(r_2) \right\rangle \sim r_{12}^{-x_{q_1}-x_{-q_1}} \left(\frac{L}{r_{12}} \right)^{-x_0} = r_{12}^{-x_{q_1}-x_{-q_1}}. \tag{1.80}$$

Then the system size can be taken to infinity, and the two-point function can be compared with a two-point function in a critical field theory. One can see that the above form is consistent with requirements of rotational, translational and scale invariance, Eq. (1.25), but not with conformal invariance, Eq. (1.26), since the dimensions $x_{q_1} \neq x_{-q_1}$.

However, the presence of the special operator $\mathcal{O}_{q_*}$ allows us to make another choice. Indeed, if one chooses the special value $q_2 = q_* - q_1$, the dimension $x_{q_1+q_2} = x_{q_*} = 0$. In this case one has

$$\left\langle \mathcal{O}_{q_1}(r_1)\mathcal{O}_{q_*-q_1}(r_2) \right\rangle \sim r_{12}^{-x_{q_1}-x_{q_*-q_1}} \left(\frac{L}{r_{12}} \right)^{-x_{q_*}} = r_{12}^{-2x_{q_1}}. \tag{1.81}$$

This two-point function is independent of the system size and is consistent with the CFT form

$$\left\langle \phi_{q_1}(r_1)\phi_{q_*-q_1}(r_2) \right\rangle_{\text{CFT}} \sim r_{12}^{-2x_{q_1}}, \tag{1.82}$$

since the two operators involved have the same dimensions.

This discussion and the scaling (1.79) suggest that CFT may apply only to such multipoint MF functions $\left\langle \mathcal{O}_{q_1} \dots \mathcal{O}_{q_n} \right\rangle$ where the sum of the indices q_i is equal to q_* (a sort of "neutrality" condition):

$$\sum_{i=1}^{n} q_i = q_*. \tag{1.83}$$

An alternative choice $\sum_i q_i = 0$ leads to MF multipoint functions that are well defined in the infinite system, but are inconsistent with conformal invariance.

To illustrate this point, let us make the choice (1.83) in the three-point function (1.78):

$$\left\langle \mathcal{O}_{q_1}(r_1)\mathcal{O}_{q_2}(r_2)\mathcal{O}_{q_*-q_1-q_2}(r_3) \right\rangle \sim r_{12}^{x_{q_1+q_2}-x_{q_1}-x_{q_2}} r_{13}^{-2x_{q_1+q_2}}. \tag{1.84}$$

If the general CFT expression (1.29) is specified to the case here and the symmetry relation (1.69) is used one gets

$$\left\langle \phi_{q_1}(r_1)\phi_{q_2}(r_2)\phi_{q_*-q_1-q_2}(r_3) \right\rangle_{\text{CFT}} \sim r_{12}^{x_{q_1+q_2}-x_{q_1}-x_{q_2}} r_{13}^{x_{q_2}-x_{q_1}-x_{q_1+q_2}} r_{23}^{x_{q_1}-x_{q_2}-x_{q_1+q_2}}. \tag{1.85}$$

If one now assumes that the arrangement of points satisfies the inequality $r_{12} \ll r_{13} \simeq r_{23}$, one can replace $r_{23} \approx r_{13}$, and the three-point function simplifies to

$$\left\langle \phi_{q_1}(r_1)\phi_{q_2}(r_2)\phi_{q_*-q_1-q_2}(r_3) \right\rangle_{\text{CFT}} \sim r_{12}^{x_{q_1+q_2}-x_{q_1}-x_{q_2}} r_{13}^{-2x_{q_1+q_2}}, \tag{1.86}$$

which is the same as Eq. (1.84). On the other hand, the choice $\sum_i q_i = 0$ leads to inconsistent expressions. The MF three-point function (1.78) in this case becomes

$$\left\langle \mathcal{O}_{q_1}(r_1)\mathcal{O}_{q_2}(r_2)\mathcal{O}_{-q_1-q_2}(r_3) \right\rangle \sim r_{12}^{x_{q_1+q_2}-x_{q_1}-x_{q_2}} r_{13}^{-x_{q_1+q_2}-x_{-q_1-q_2}}, \tag{1.87}$$

while the CFT expression (1.29) reduces to a different form

$$\left\langle \phi_{q_1}(r_1)\phi_{q_2}(r_2)\phi_{-q_1-q_2}(r_3) \right\rangle_{\mathrm{CFT}} \sim r_{12}^{x_{-q_1-q_2}-x_{q_1}-x_{q_2}} r_{13}^{-2x_{-q_1-q_2}}. \tag{1.88}$$

This shows that m-point correlation functions of CFT can be related to m-point MF correlation functions in an infinite system under the condition $\sum_{i=1}^{m} q_i = q_*$. Let us return to the MF multipoint functions with indices q_i that do not satisfy this condition. As discussed above, they in general scale with L and thus should be considered in a finite system. Such generic m-point MF functions in a finite system can be related to $m + 1$-point CFT functions in an infinite system by adding another field to ensure the condition $\sum_{i=1}^{m+1} q_i = q_*$.

As the simplest example, let us consider the two-point function (1.82) (defined in an infinite system) and place the operator $\phi_{q_*-q_1}$ at a large distance L (which is not the system size) from the point $r_1 = 0$. Then one can rewrite the two-point function as

$$L^{x_{q_1}} \left\langle \phi_{q_1}(0)\phi_{q_*-q_1}(L) \right\rangle_{\mathrm{CFT}} \sim L^{-x_{q_1}}. \tag{1.89}$$

This has the same form as the scaling of a one-point MF correlation function in a system of size L, Eq. (1.74). Similarly, if one places the operator $\phi_{q_*-q_1-q_2}$ in the three-point function (1.85) at a distance $L \gg r_{12}$ from the points r_1 and r_2, one can replace $r_{13} \approx r_{23} \approx L$, which yields

$$\left\langle \phi_{q_1}(r_1)\phi_{q_2}(r_2)\phi_{q_*-q_1-q_2}(L) \right\rangle_{\mathrm{CFT}} \sim r_{12}^{x_{q_1+q_2}-x_{q_1}-x_{q_2}} L^{-2x_{q_1+q_2}}. \tag{1.90}$$

This can be rewritten as

$$L^{x_{q_1+q_2}} \left\langle \phi_{q_1}(r_1)\phi_{q_2}(r_2)\phi_{q_*-q_1-q_2}(L) \right\rangle_{\mathrm{CFT}} \sim r_{12}^{x_{q_1+q_2}-x_{q_1}-x_{q_2}} L^{-x_{q_1+q_2}}, \tag{1.91}$$

which is exactly the same as Eq. (1.77). Thus, a three-point CFT function, which describes a three-point MF function with $q_1 + q_2 + q_3 = q_*$ in an infinite system, can also be related to a two-point MF function (with arbitrary q_1 and q_2) in a finite system. It is natural to expect that such relations continue to hold for higher multi-point correlators. For example, the four-point function $L^{x_{q_1+q_2+q_3}} \left\langle \phi_{q_1}(r_1)\phi_{q_2}(r_2)\phi_{q_3}(r_3)\phi_{q_*-q_1-q_2-q_3}(L) \right\rangle_{\mathrm{CFT}}$ should reduce to the three-point function (1.78) in the appropriate limiting case of separation of scales $r_{12} \ll r_{13} \sim r_{23} \ll L$.

A brief recapitulation of the results so far follows. First of all, there are multi-point MF correlation functions (1.79) with $\sum_i q_i \neq 0, q_*$ that explicitly contain the system size L, exemplifying strong infrared fluctuations that may grow with L. Secondly, there are MF correlators with $\sum_i q_i = 0$ that can be considered in an infinite system, consistent with scale invariance, but inconsistent with conformal invariance. Finally, there are "good" MF correlators satisfying the neutrality condition $\sum_i q_i = q_*$ that are consistent with conformal invariance.

This analysis can be extended to the generalized MF correlation functions $\langle \mathcal{O}_{\lambda_1}(r_1)\mathcal{O}_{\lambda_2}(r_2)\ldots \rangle$ involving the much broader class of gradientless operators $\mathcal{O}_\lambda$, with $\lambda = (q_1, q_2, \ldots, q_n)$, see Sec. 1.2.1.1. Again, almost all such correlation functions are infrared-singular with respect to the system size L, i.e., depend on L in a power-law fashion. There is a subset of them that exhibits L-independence.

And within this subset, there is a still smaller subset of correlators whose scaling is consistent with conformal invariance. Specifically, the corresponding condition is $\sum_i \lambda_i = (-c_1, -c_2, \dots, -c_n) \equiv -\rho_b$.

This consistency is not a guarantee of conformal invariance at ATs. While there is a wide-spread folklore that scale invariance and locality imply conformal invariance, this is not the case in general, see Ref. [106] for a comprehensive discussion of the relation between the two. All currently existing or even envisioned proofs of conformal invariance following from scale invariance involve certain technical assumptions such as unitarity (reflection positivity) of the field theory and discreteness of the spectrum of scaling dimensions. These assumptions are certainly violated in any viable theory of ATs, so conformal invariance is not guaranteed to be a feature of ATs.

Understanding the difference of scale and conformal invariance is especially important in two dimensions, where conformal invariance is particularly powerful due to the existence of an infinite-dimensional Virasoro symmetry. In Sec. 3.2 one can see that assuming local conformal invariance in two dimensions together with Abelian fusion leads to very stringent restrictions on the spectra of MF exponents.

1.3 Symmetry Classes and Topology

Here the famous topological classification completed by Altand and Zirnbauer in Ref. [7] is introduced. That is more precisely non-interacting fermionic gapped local Hamiltionians with disorder (that can be represented as matrices with dimension L^d) are considered. A short overview is given of how far this classification is stable towards weak interaction.

Random matrix theory was introduced by Wigner [107] and generalized by Dyson [108]. The Wigner-Dyson classification is complete if one demands the symmetry and topological protection to be present over the whole energy spectrum. Weakening this requirement to the discrete symmetry being present at a single energy in the spectrum leads to further symmetry classes. Among these are the chiral classes [109, 110]. In condensed matter context, these are relevant for systems at half filling. Here the Fermi energy is the special point in the spectrum where the additional symmetry is present. Altand and Zirnbauer finally extended this theory to the superconducting Bogolyubov-de-Gennes Hamiltonian ensembles [7] with effectively broken particle conservation.

In the following, the Altland-Zirnbauer symmetry classes are introduced briefly. It is sketched how to find the number of topologically distinct phases in each class. Further, it is summarized how weak interactions influence this. In Chap. 2 a superconducting wire in with anomalous time reversal and particle hole symmetry (class BDI) is considered. The spin quantum Hall systems that are studied in Chap. 3 reside in class C. The last chapter 4 deals with time reversal invariant superconductors with different degrees of spin rotational symmetry (classes AIII, CI, DIII).

1.3.1 Fermionic Disordered Hamiltonians

Let $\mathcal{H}$ be an ensemble of hermitian quadratic matrices representing fermionic non-interacting gapped local Hamiltionians. $\mathcal{H}$ can be interpreted as a manifold. Depending on the symmetries shared by all $H \in \mathcal{H}$, one can make general statements about the number of (path) connected components of this manifold. Intuitively, there is no way from one to a distinct (path) connected component tuning the parameters of the system (without closing the gap in the system or breaking the defining symmetries of the ensemble).

Usually symmetries in quantum mechanics act as unitary operators U on the observables. If the system possesses the symmetry acting as unitary U, the Hamiltonian is invariant: $H = U^\dagger H U$. However symmetries can also be represented by antiunitary operators commuting with the Hamiltonian

like time reversal $\mathcal{T}$. The spectrum of the Hamiltonian H is preserved by these symmetries. Moreover one can weaken this requirement and generalize to symmetries that are present at a single special energy. Examples are the antiunitary particle-hole $\mathcal{P}$ symmetry anticommuting with H and the unitary chiral symmetry $\mathcal{C}$ anticommuting with H. Anticommutating the symmetry means the spectrum is symmetric around zero energy:

$$[\mathcal{U}, H] = 0, \qquad\qquad \{\mathcal{C}, H\} = 0, \qquad\qquad (1.92)$$

$$[\mathcal{T}, H] = 0, \qquad\qquad \{\mathcal{P}, H\} = 0. \qquad\qquad (1.93)$$

The chiral symmetry $\mathcal{C}$, particle-hole symmetry $\mathcal{P}$ and time reversal symmetry $\mathcal{T}$ introduced in the preceding lines are different from the conventional unitary symmetries and it turns out that their presence or absence is sufficient to characterize the different ensembles of Hamiltionians.

As one can easily see, the conventional unitary commuting symmetries $\mathcal{U}$ *factor out* of the classification. The reason is that H and $\mathcal{U}$ have common eigenspaces, more precisely there exists a convenient basis where H is block diagonal. In formal mathematical language, the symmetries represented by unitary commuting U form a group G. All Hamiltonians H in the ensemble can be decomposed into irreducible representations with respect to the action of G. In the irreducible blocks, the elements of G act trivial (multiplication by a phase). Each block then needs to be classified individually depending on the presence or absence of the anomalous symmetries $\mathcal{C}, \mathcal{P}, \mathcal{T}$.

These are either absent or unique and present and square to $\mathcal{T}^2 = \pm 1$, $\mathcal{P}^2 = \pm 1$ and $\mathcal{C}^2 = 1$. One can convince oneself of this by supposing there are two distinct time reversal symmetries $\mathcal{T}, \mathcal{T}'$. In general an antiunitary operator decomposes into a unitary operator and the complex conjugation $\mathcal{K}$: $\mathcal{T} = U\mathcal{K}$ and $\mathcal{T}' = U'\mathcal{K}$ with U, U' unitary. By exploiting that H must also commute with $\mathcal{T}'\mathcal{T}$

$$0 = [\mathcal{T}, H] = [\mathcal{T}', H] = [\mathcal{T}'\mathcal{T}, H] = [U'U^*, H], \qquad\qquad (1.94)$$

one finds a unitary operator $U'U^*$ commuting with H.

Since the block is assumed to be irreducible this means $U'U^*$ must be the identity up to a phase. In this sense $\mathcal{T}$ is equivalent to $\mathcal{T}'$. Further by choosing $\mathcal{T}' = \mathcal{T}$ one can show $\mathcal{T}^2 = \pm 1$: Then $\mathcal{T}^2 = UU^* = \lambda \mathbb{1}$. Since UU^* is real symmetric $\lambda \in \{-1, 1\}$. The cases $\mathcal{P}, \mathcal{C}$ follow analogously. The full rigorous proof is given in Ref. [111].

Since the presence of both $\mathcal{T}$ and $\mathcal{P}$ in a block implies the existence of $\mathcal{C} = \mathcal{T}\mathcal{P}$, there are $10 = 3 \cdot 3 \cdot 2 - 2 \cdot 4$ possible combinations of these symmetries. These are the ten Altland-Zirnbauer classes (Tab. 1.1).

Each class is associated to the ensemble of hermitean matrices $\mathcal{H}$ obeying the corresponding symmetries. Interpreted as a group theoretic manifold, these from Riemannian symmetric spaces that are either connected (0), have two components ($\mathbb{Z}_2$) or infinitely many ($\mathbb{Z}$). The so called Cartan labels A, AIII, AI, ... are the historical name of the ten infinite families of symmetric spaces introduced by Elie Cartan [6]. Depending on the dimension d of the system described by H, this is sufficient to determine if and how many distinct topological phases there can be (see tab. 1.1).

1.3.2 Topological Invariants and Dimensionality

Given a general ensemble of Hamiltonians, the question arises what constraints locality and the dimension of space impose. A matrix element between two sites i, j has to decay sufficiently fast $H_{i,j} \to 0$ as the distance between them becomes large $\text{dist}(i, j) \to \infty$. The function dist depends on the dimensionality d. If (almost) all Hamiltonians in the ensemble satisfy such a property for a metric dist with an associated dimension d, one can say that this ensemble is local in d dimensions.

Class	$\mathcal{T}$	$\mathcal{P}$	$\mathcal{C}$	$d=1$	$d=2$	$d=3$	Realization	Fermion NLσM
C	0	-1	0	-	$\mathbb{Z}$	-	SQH	$\mathrm{Sp}(4n)/\mathrm{U}(2n)$
A	0	0	0	-	$\mathbb{Z}$	-	IQH	$\mathrm{U}(2n)/\mathrm{U}(n)\otimes\mathrm{U}(n)$
D	0	+1	0	$\mathbb{Z}_2$	$\mathbb{Z}$	-	MZM, TQH	$\mathrm{O}(2n)/\mathrm{U}(n)$
CI	+1	-1	1	-	-	$\mathbb{Z}$	3D TSC	$\mathrm{Sp}(4n)\otimes\mathrm{Sp}(4n)/\mathrm{Sp}(4n)$
AIII	0	0	1	$\mathbb{Z}$	-	$\mathbb{Z}$	3D TSC, chiral TI	$\mathrm{U}(2n)\otimes\mathrm{U}(2n)/\mathrm{U}(2n)$
DIII	-1	+1	1	$\mathbb{Z}_2$	$\mathbb{Z}_2$	$\mathbb{Z}$	3D TSC (^{3}He-B)	$\mathrm{O}(2n)\otimes\mathrm{O}(2n)/\mathrm{O}(2n)$
AI	+1	0	0	-	-	-	-	$\mathrm{Sp}(4n)/\mathrm{Sp}(2n)\otimes\mathrm{Sp}(2n)$
AII	-1	0	0	-	-	$\mathbb{Z}_2$	2D, 3D TIs	$\mathrm{O}(2n)/\mathrm{O}(n)\otimes\mathrm{O}(n)$
BDI	+1	+1	1	$\mathbb{Z}$	-	-	MZM	$\mathrm{U}(2n)/\mathrm{Sp}(2n)$
CII	-1	-1	1	$\mathbb{Z}$	-	$\mathbb{Z}_2$	3D chiral TI	$\mathrm{U}(2n)/\mathrm{O}(2n)$

Table 1.1: Modified from Ref. [90]. The 10-fold way classification for strong (fully gapped), d-dimensional symmetry-protected topological phases of fermions, i.e. topological insulators (TIs) and topological superconductors (TSCs) [2–5]. The 10 classes are defined by different combinations of the three *effective* discrete symmetries $\mathcal{T}$ (time–reversal), $\mathcal{P}$ (particle–hole), and $\mathcal{C}$ (chiral or sublattice). For a d-dimensional bulk, any deformation of the clean band structure that preserves $\mathcal{T}$, $\mathcal{P}$ and $\mathcal{C}$ and does not close a gap preserves the topological winding number. For a $(d-1)$-dimensional edge or surface theory, the equivalent statement is that any static deformation of the surface (quenched disorder) that preserves $\mathcal{T}$, $\mathcal{P}$ and $\mathcal{C}$ also preserves the "topological protection" against Anderson localization. Of particular interest here are classes C, A, D on one hand, and classes CI, AIII, DIII on the other. Classes C, A, and D are topological in $d=2$, and describe the spin (SQHE), integer or charge (IQHE), and thermal (TQHE) quantum Hall effects; all three can be realized as TSCs with broken T. Classes CI, AIII, and DIII are topological in $d=3$, and can describe 3D time-reversal-invariant TSCs. (In this case, the physical time-reversal symmetry appears as the *effective* chiral symmetry S in the table [2, 112].) The column "spin sym." denotes the amount of spin SU(2) symmetry preserved for TSC realizations of these 6 classes. The 3D TSCs can host 2D massless Dirac (CI, AIII) or Majorana (DIII) surface theories. The last column gives the symmetry structure of the non-linear sigma model (NLσM) description (see Sec. 1.1.4.4) for each class, in terms of fermionic replicas [9].

This mathematical property is already sufficient to reduce the general classification problem of the Hamiltonian ensembles to classifying a Dirac operator defined on a compact space [3] that can then be tackled with real/complex K-theory. This gives insights about the number of boundary modes in d dimensional topological insulators see (tab. 1.1).

The problem is essentially reduced to determining how many topologically distinct mass terms can be added to the corresponding Dirac's equation.

1.3.3 Nonlocal Discrete Symmetries

The presence of non-local symmetries modifies the above results [113]. These symmetries further restrict the choices of the mass term and therefore modify the classification. For a simple disordered chain as investigated here there are no such additional symmetries.

1.3.4 Interactions

The topological classification discussed above is not stable towards weak interactions in general. Arbitrarily small interactions can in principle open gaps between distinct phases [27]. For $\mathcal{T}$-invariant Majorana chains (non-int: BDI) this has been investigated by Fidkowski and Kitaev [26]. It is found that the interaction can only gap between phases $n \in \mathbb{Z}$ and $m = n \mod 8$. The proof uses matrix product states, which ties it to 1D systems.

In general, $\mathbb{Z}$ is broken down to $\mathbb{Z}_\nu$ in odd dimensions, where ν is a power of two [28]. These results do not apply to strong interactions, where symmetry breaking can occur. As one can see in Sec. 2.5, disorder introduces wave function multifractality that enhances interaction matrix elements. In one of the models discussed there, an interaction term becomes relevant and induces spontaneous symmetry breaking even for weak interaction. The topologically protected criticality goes away.

1.4 Criticality in 1D

The considerations before in Sec. 1.3 dealt with the question whether a system with given anomalous symmetries can in principle be in a topologically nontrivial phase. In this section, the setting is that a concrete (non-interacting local 1D) Hamiltonian is given. An overview is given how to obtain a winding number that enumerates the different phases as function of the parameters of the given Hamiltonian. From this, a full phase diagram of the system may be constructed. Here, only non-interacting chiral Quasi-1D lattices with a gap, like the dimerized model (with interaction treated at mean field level) investigated in Sec. 2.2.2.4, are considered. While this picture does not lead to many new insights into the topological transition in the disordered case, it is amusing to note that the RG flow away from this critical line is of Khmelnitskii-Pruisken type. This is a further connection between the works presented in the following chapters.

1.4.1 Perfectly conducting channels: A, C, D, AII, DIII

In Sec. 1.5.3, the quantum Hall like topological systems in 2D are introduced. Interpreting the edge of such systems between topologically distinct phases (indices p, q) as a 1D wire, one obtains $p - q$ perfectly transmitting channels. In these wires, backscattering is suppressed totally [9].

The same mechanism also exists in wires of classes AII, DIII or edges of quantum spin Hall systems (AII). There is a distinct type of topological criticality in 1D having drastic impact on conductivity and wavefunctions that is exhaustively discussed in the following.

1.4.2 Chiral Symmetry: AIII, BDI, CII, D, DIII

Commuting unitary symmetries can be used to bring H in block diagonal form. The chiral symmetry is a unitary anticommuting symmetry. Still, by choosing a basis where $\mathcal{C} = \sigma_x \mathrm{K}$ the Hamiltonians H can be brought to block off-diagonal form:

$$H = \begin{pmatrix} 0 & h \\ h^\dagger & 0 \end{pmatrix}. \tag{1.95}$$

This is the most general form, the off-diagonal entries are related by hermiticity. The 2×2 structure depicted is the one the σ_x matrix acts in. This will be denoted as chiral basis in the following.

In Tab. 1.1, one can see that these classes support distinct topological phases in 1D. In presence of disorder, the properties at criticality (topological transition) are universal for all classes [114]:

- broad distribution of g:

$$-\langle \ln g \rangle \sim \sqrt{L}, \qquad\qquad \langle (\ln g)^2 \rangle \sim L \tag{1.96}$$

- broad distribution of localization length

$$\xi_{\mathrm{typ}} \sim |\ln \varepsilon|, \qquad\qquad \xi_{\mathrm{av}} \sim |\ln \varepsilon|^2 \tag{1.97}$$

- the near $\varepsilon \approx 0$ wave function

$$\langle |\psi(x)\psi(0)|^q \rangle \sim L^{-1} |x|^{-\frac{3}{2}} \tag{1.98}$$

  is a stretched exponential localized at x_0 with a secondary maximum at x appearing with probability $\sim (x - x_0)^{-\frac{3}{2}}$

- the density of states

$$\rho(\varepsilon) \sim \frac{1}{|\varepsilon \ln^3 \varepsilon|} \tag{1.99}$$

  is strongly singular

All these properties can be understood from the infinite randomness physics perspective, see Sec. 2.5 for a discussion.

1.4.2.1 Winding numbers

In the following, the formalism used to describe topological winding numbers in chiral wires in classes AIII, BDI, CII, D, DIII is sketched. Peculiarities arising due to the $\mathbb{Z}_2$ classification of classes D, DIII are not discussed here, the reader is referred to Ref. [115].

Clean case Without disorder, one can work with the band structure of the model. The approach described here follows the work of Schnyder *et. al.* [2]. Let $u_n(k)$ be the Bloch states of the system. The projector P on the occupied states can then be used to define the operator $Q = 2P - \mathbb{1}$, that gives 1 for a particle and -1 for a hole. The idea behind this is that Q corresponds to the Hamiltonian with each energy continuously deformed to ± 1 (the Fermi level is set to zero energy). Topology is diffeomorphism invariant, to extract topological properties, it is sufficient to restrict to Q:

$$P = \sum_{n\text{ filled}} \left|u_n(k)\right\rangle \left\langle u_n(k)\right|, \qquad\qquad Q(k) = 2P(k) - 1. \qquad (1.100)$$

Since P is a projector, Q is unitary. The following expression is the winding number of the unitary Q [2], that serves as topological index:

$$N[Q] = \frac{1}{2\pi} \int_0^{2\pi} \mathrm{d}k \, \mathrm{tr}\left(Q^{-1}(k)\partial_k Q(k)\right) = \frac{1}{2\pi} \int_0^{2\pi} \mathrm{d}k \, \partial_k \mathrm{tr}\left(\ln Q(k)\right). \qquad (1.101)$$

This can be motivated by the following facts: $N[Q]$ is locally constant which is shown by rewriting the equation in terms of the ln. The first homotopy group of the U(n) is $\pi_1(\mathrm{U}(n)) = \mathbb{Z}$, so $N[Q]$ can range over all integers.

For the chiral classes (AIII, BDI, CII), H can be brought to block form (1.95), so Q may be replaced by one chiral block h. Comparison to the transfer matrix formalism then yields that the number of negative eigenvalues of Q corresponds to the number of negative Lyapunov exponents. This proves that $N[Q]$ defined above is indeed the topological index.

Since this heavily relies on the existence of a Brillouin zone, that is to say (discrete) translational invariance, it cannot be used in presence of disorder.

1.4.2.2 Generalization to Disorder

Refs. [115, 116] point out that the key is to define the topological index in terms of how the sample reacts to twisting the boundary conditions. I will briefly summarize this formalism in the following lines.

For bipartite Hamiltonians possessing a chiral symmetry P one can define a non-unitary transformation T_ϕ:

$$P_{s,s'} = (-1)^s \delta_{s\,s'}, \qquad (1.102)$$

$$(T_\phi)_{s,s'} = \exp\left(-i\frac{s}{L}\phi P_{s,s'}\delta_{s\,s'}\right). \qquad (1.103)$$

The application of T_ϕ to the Hamiltonian effectively twists the boundary condition of the wave functions ψ:

$$H_\phi = T_\phi H T_\phi, \qquad\qquad \psi_\phi(s) = \exp\left(i\frac{s}{L}\phi(-1)^s\right)\psi(s). \qquad (1.104)$$

With the transformation of the eigenfunctions, one can formulate the Green's function G_ϕ of the sample with boundaries twisted by a phase ϕ. Then the following formula generalizes the index introduced above:

$$\chi = \frac{1}{4\pi} \ln\left(\frac{G_{2\pi}}{G_0}\right). \qquad (1.105)$$
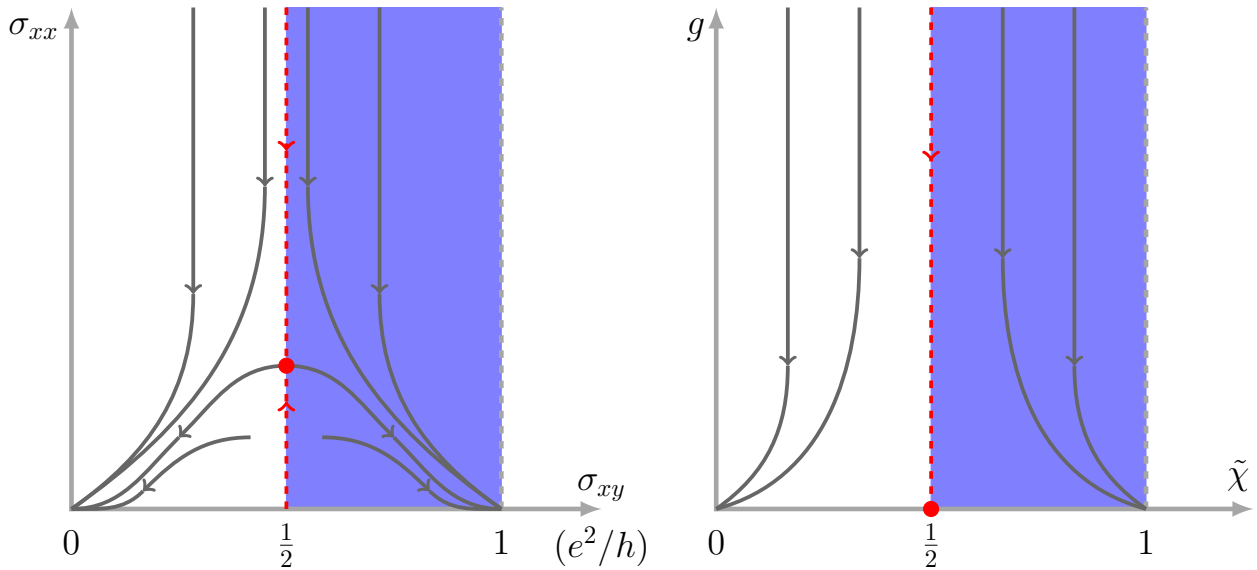
Figure 1.1: *Left panel:* Khmelnitzkii-Pruisken flow [117–119] of longitudinal and transverse conductance $(\sigma_{xx}, \sigma_{xy})$ in the 2D IQHE. Non half-integer σ_{xy} (x axis) flows (gray arrows) to the nearest integer as the system size L increases. Meanwhile, σ_{xx} (y axis) reaches zero. For half-integer valued σ_{xy} (red dashed lines), one is at the boundary of two topologically distinct phases (0, 1: white, blue) *Right panel:* RG flow of Khmelnitzkii-Pruisken type [115] of the conductance g and the bare index $\tilde{\chi}$ of a disordered topological chiral wire. $(g, \tilde{\chi})$ correspond to $(\sigma_{xx}, \sigma_{xy})$ in IQHE. Non half-integer $\tilde{\chi}$ (x axis) flows to the nearest integer. Meanwhile, the conductance g (y axis) reaches zero exponentially fast in L. For half-integer valued $\tilde{\chi}$ (red dashed lines), one is at the boundary of two topologically distinct phases (0, 1: white, blue). On the critical lines g decays algebraically with L. In contrast to the Khmelnitzkii-Pruisken flow there is no finite g^* at the transition.

The "bare" index $\tilde{\chi}$ defined this way is not locally constant, in presence of disorder there is no reason why it has to be an integer. For short samples, $\tilde{\chi}$ can take arbitrary real values. In the thermodynamic limit $L \to \infty$ there are only two possibilities for $\chi \equiv \tilde{\chi}(L \to \infty)$:

- $\chi \in \mathbb{Z}$: the system is a (topological) Anderson insulator, the conductance g approaches zero exponentially fast $g \propto e^{-L/\xi}$

- $\chi \in \mathbb{Z} + \frac{1}{2}$: the system is at the boundary of two distinct phases and therefore critical, the conductance decays algebraically $g \propto L^{-\alpha}$

Using field theoretical methods these results are obtained by showing that $(g, \tilde{\chi})$ have a similar two-parameter flow diagram as the $(\sigma_{xx}, \sigma_{xy})$ Khmelnitzkii-Pruisken flow [117–119] in the integer quantum Hall effect (IQHE), see fig. 1.1. From the field theoretical point of view this is since in a chiral non-linear σ-model (NLσM) a Θ-term is allowed. A brief sketch of the derivation follows in the next section.

Supersymmetric field theory   The winding number defined in Eq. (1.105) can be expressed in terms of the supersymmetric partition function $Z[\phi_1, \phi_0]$:

$$Z[\phi_1, \phi_0] = \left\langle \int \mathcal{D}(\overline{\psi}, \psi) \exp\left\{ i\overline{\psi}\hat{G}_\phi\psi \right\} \right\rangle \tag{1.106}$$

$$\hat{G}_\phi = \mathrm{diag}(G_{-i\phi_0}, G_{\phi_1})_{bf}. \tag{1.107}$$

The phases ϕ_1, ϕ_0 are twists of the boundary condition in the fermionic and bosonic sectors. They act as a source term and the "bare index" $\tilde{\chi}$ can be found by integration/differentiation of Z in the usual way:

$$\tilde{\chi} = \frac{1}{4\pi} \int_0^{2\pi} \mathrm{d}\phi \left\langle \frac{\partial_\phi \det\left(G_\phi\right)}{\det\left(G_\phi\right)} \right\rangle \tag{1.108}$$

$$= \frac{1}{4\pi} \int_0^{2\pi} \mathrm{d}\phi_1 \partial_{\phi_1} \left. Z(\phi_1, \phi_0) \right|_{\phi_0 = i\phi_1}. \tag{1.109}$$

As discussed in Sec. 1.1.4.2, due to supersymmetry fixing $Z = 1$ the disorder may be averaged over. The emerging quartic effective interaction terms are decoupled using a Hubbard-Stratonovich transformation. The domain of the integration variable Q thereby depends on the symmetry class. The remaining quadratic action $S[\overline{\psi}, \psi, Q]$ is quadratic in the supervector ψ which can be integrated over at this point.

The partition function can then be written only in terms of Q: $Z = \int \mathcal{D}Q \exp\left(-S[Q]\right)$. The action reads:

$$S[Q] = \frac{1}{2w^2} \mathrm{str}(Q^+ Q^-) + \mathrm{str}\ln \begin{pmatrix} i\eta - Q^+ & -\hat{h}_+ \\ -\hat{h}_- & i\eta - Q^- \end{pmatrix}. \tag{1.110}$$

The dependence on the twist angles ϕ is hidden in this expression. However one has to keep in mind that it affects the boundary conditions of the Q field. At this stage one needs to find the quadratic low energy/momentum theory. To this end a saddle-point expansion of $S[Q]$ needs to be performed. For this purpose the parametrization $Q = \Sigma T$, where Σ is the self-consistent Born-approximation (SCBA) self-energy and T describes slow fluctuations living in the saddle point manifold is convenient.

Expanding the action in the slow fluctuations T one finds, using the standard gradient expansion of the trace logarithm:

$$Z[\phi = 0] = \int \mathcal{D}T \exp\left(a_1 \mathrm{str}(T\partial T^{-1}) + a_2 \mathrm{str}(T\partial^2 T^{-1}) + \ldots \right). \tag{1.111}$$

Remembering the ϕ dependence of the boundary conditions $T(L) = e^{2i\phi}T(0)e^{2i\phi}$, one finds the general formula for $Z[\phi]$.

One can fix the constants a_1, a_2, by computing the index $\tilde{\chi}$ with Eq. (1.109), this implies $a_1 = 2\tilde{\chi}$. The corresponding term in the action can be identified as the topological winding number. Similar considerations relate the a_2 coefficient to the conductance $g = a_2$. Knowing the microsopic details of the model, one can compute a_1, a_2 on the other hand. These bare parameters in the action undergo an RG flow analogous to Khmelnitskii-Pruisken flow in the 2D quantum Hall like phases.

1.5 Criticality in 2D

The chapters 3 and 4 are concerned with 2D systems. Ref. [9] describes the mechanisms to escape criticality in 2D, which are directly relevant to these studies. Additionally, in Chap. 4 numerical evidence for a further mechanism in surfaces of bulk STI is shown. The results are recapitulated in the language of the NLσM, in terms of the renormalization of the first coefficient in Eq. (1.64), $\beta(t) \equiv \dfrac{\mathrm{d}t}{\mathrm{d}\ln L}$ with $t = \dfrac{1}{2\pi g} = \dfrac{\rho D}{2\pi}$ in $d = 2 + \epsilon$ dimensions. In an insulating/metallic system β is negative/positive, the conductivity becomes smaller/larger with increasing system size. Zeros of the beta function correspond to criticality and multifractal behavior.

1.5.1 Broken spin rotation invariance: positive β function

The classes AII, D, DIII have a positive $\beta(t < t^*)$ function at small t in 2D. This means there can be a stable metallic phase depending on the parameters of the system. At weak disorder the conductance $\sim t^{-1}$ is typically large, if $t < t^*$ is reached, t scales to zero in the RG flow, i.e. the system is metallic. In the opposite strong disorder limit, t is large and the system becomes insulating. At t^* there is a metal-insulator transition. With the techniques introduced in Chap. 3 one can construct the observables revealing the generalized multifractal spectrum in these classes and study its properties numerically. Preliminary results [120] indicate violation of generalized parabolicity in these classes.

1.5.2 Chiral classes: vanishing β function

The sigma model of the chiral classes (AIII, CII, BDI) shows a peculiarity: Gade and Wegner found the β function does not renormalize at *any* order in t [109, 110]! This means the conductance t^{-1} is exactly marginal in RG sense and serves as a parameter labeling different fixed points. In addition to the terms in Eq. (1.64), there is also the Gade term, that affects the renormalization of the LDOS, which typically becomes strongly singular.

1.5.3 2D Quantum Hall type topological phases

In the time reversal breaking classes (A, C, D) one has an integer classified second homotopy group $\pi_2(\mathcal{M}_F) = \mathbb{Z}$ which means the θ term

$$iS_{\text{top}}(Q) = i\Theta N[Q], \qquad\qquad N[Q] = \frac{i}{8\pi}\int \mathrm{d}^2 r\, \mathrm{tr}Q\partial_x Q\partial_y Q \qquad (1.112)$$

may appear in the NLσMs of these classes. The integer $N[Q]$ is the winding number of the Q field configuration.

Integer Quantum Hall criticality A paradigmatic example of topological phase transition is the integer quantum Hall effect in the unitary Wigner-Dyson class A.

The Hall conductivity σ_{xy} of a 2D electron gas at sufficiently low temperature develops plateaus quantized in units of e^2/h. Given the background introduced in Sec. 1.3, one can think about the plateaus as distinct topological phases, with the winding number given by the number of conductance quanta observed at the plateau. The nature of the criticality emerging at the topological transition (between the plateaus) is still an open problem.

In the NLσM picture, the IQHE is described by a Khmelnitskii-Pruisken two parameter RG flow[118, 119]. The NLσM has an additional topological term:

$$S[Q] = \frac{1}{8} \int \mathrm{d}^2 r \, \mathrm{tr} \left[-\sigma_{xx} (\nabla Q)^2 + 2\sigma_{xy} Q \partial_x Q \partial_y Q \right] \tag{1.113}$$

that measures the winding number of the Q field. The coefficient is the effectively quantized transverse conductivity σ_{xy}. The flow diagram shown in Fig. 1.1 can however only be verified with a perturbative RG analysis, when σ_{xx} is large. The fixed points occur at strong coupling $\sigma_{xx} \sim 1$, where the RG is not controlled any more.

An open question is whether the multifractal spectrum is parabolic:

$$\Delta_q = \theta \, q(1-q). \tag{1.114}$$

Studies [51] of the Chalker-Coddington network model (see Sec. 1.5.3.1) indicate approximately parabolic multifractality with $\theta \simeq 1/4$ in Eq. (1.114). The longitudinal conductivity is known to be $\sigma_{\mathrm{IQHPT}}^{xx} \simeq 0.58 \pm 0.02$ [74] from numerical Kubo computations. Later studies [53] find substantial deviations from parabolicity. Together with the arguments presented in Sec. 3.2 this indicates violation of local conformal invariance at the IQH critical point.

Spin Quantum Hall criticality   The SQH transition is well-studied numerically with the network model [58, 77]. Certain observables can be studied analytically by a mapping to 2D classical percolation (Ref. [54–58, 76] and an extension of that work in Sec. 3.8). The conductance distribution and exact average longitudinal conductivity $\sigma_{\mathrm{SQH}}^{xx} = \sqrt{3}/2$ have been determined analytically in Ref. [76]. For certain multifractal exponents there are exact analytical results available compatible with $\theta = 1/8$ in Eq. (1.114) (assuming approximate parabolicity). The work done by me and collaborators in Ref. [105] is extended in Chap. 3 showing the strong violation of generalized parabolicity in the subleading multifractal spectrum. This confirms high precision numerical studies [59], that find a nonzero quartic term in in the leading Δ_q.

Thermal Quantum Hall criticality   In class D one can formulate a large variety of distinct network models and Hamiltonians [78–84], since there apparently is non-universality. In most models, the topological phase transition is hidden by a broad thermal metal wedge in the phase diagram separating the phases. In this region the system is weakly antilocalizing. The conjectured thermal quantum Hall transition is therefore difficult to observe.

In Chap. 4 numerical evidence for the conjecture, that finite energy 3D time reversal invariant topological superconductor (TSC) surface states match the phenomenology of quantum Hall criticality is presented. Chap. 3 focuses on the class C NLσM and the multifractal spectrum in SQH transitions.

1.5.3.1 Chalker-Coddington network model

IQH   The IQHE in a smooth random potential can be modeled with the Chalker-Coddington network (CCN) [121]. Smooth here means that the correlation length of the potential is large. The electrons then can be assumed to drift along equipotential lines. Deep in a topological phase, each of the electrons performs cyclotron motion around its orbit in this picture. Increasing the energy to the percolation threshold enables tunneling processes at the saddle points of the potential between the closed orbits. This way electrons can delocalize at criticality.
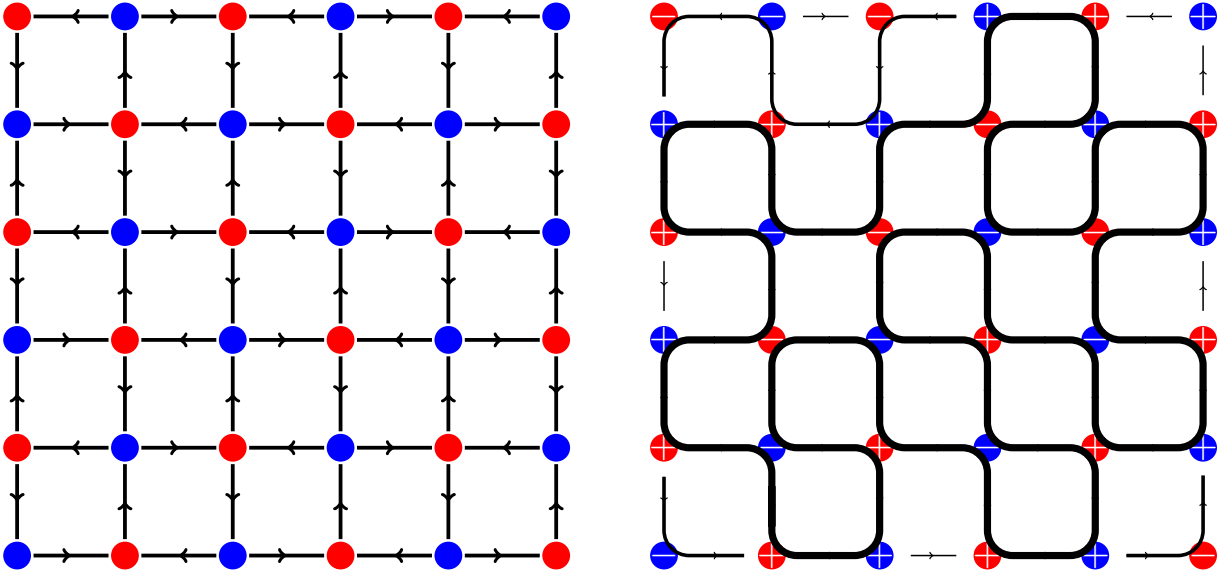
Figure 1.2: *Left panel:* Network model defined on square lattice. Each node has two incoming and outgoing links. There is an amplitude to turn right and one to turn left at a node (red or blue dot). Traveling along a link e_i shown as directed arrow in the sketch accumulates a phase $U_i \in G$.

Right panel: In the $G =$ SU(2) version of the CC network model, disorder average reduces the computation of certain observables to the sum over self-avoiding loops. This reduces the quantum mechanical problem to studying probabilities in classical percolation. The configuration is shown as $+, -$ in the nodes. Paths separate $+$ from $-$ regions. The closed loop in the part of the network shown is highlighted by a bold line. By considering an infinite area or applying periodic boundary conditions, all paths form closed loops.

In the CCN, one assumes a square grid of nodes that are the "saddle points" of the random potential. At each node, there are two outgoing and incoming links. The distance to criticality is encoded in the scattering amplitudes $\pm \cos \theta$, $\pm \sin \theta$ between the links. In each discrete time evolution step, one such scattering event occurs and the electron traversing a link e acquires a random $G = \mathrm{U}(1)$ phase $e^{i\phi_e}$ with $\phi_e \in [0, 2\pi]$ uniformly.

By choosing different G, one can realize the other quantum hall like phases in 2D.

SQH The defining symmetry in class C implies that the evolution operator $\mathcal{U}$ satisfies the property $\mathcal{U} = \sigma_y \mathcal{U}^* \sigma_y$ in addition to unitarity. This means that the phases on the links e are in $G = \mathrm{SU}(2)$. The average over these phase groups is amenable to an analytical treatment.

An important result was obtained in Ref. [58]: expressions involving $n \leq 3$ Green's functions at the same finite broadening can be mapped to classical percolation.

One can restrict to paths satisfying the following two conditions in these cases:

- each network link is visited either zero or two times

- each node is visited zero, two or four times, the sum over (i) $\cdot \cos^4 \theta$, (ii) $\cdot \sin^4 \theta$, (iii) $\cdot (-\sin^2 \theta \cos^2 \theta)$ can be reduced to the sum over (i) $\cdot \cos^2 \theta$, (ii) $\cdot \sin^2 \theta$

These statements imply, that the sum over quantum mechanical amplitudes averaged over disorder can be restricted to the sum over closed loops that can be interpreted as classical percolation hulls, see Fig. 1.2.

Class D network models By using $G = \mathrm{O}(1)$ in analogy to the cases discussed above, one does not find a topological transition [9]. Each of the (-1) network factors distributed with concentration p is a topological defect, that cannot be gotten rid of by a continuous deformation [79]. These defects completely destroy localization, such that the $\mathrm{O}(1)$ network model is always in the metallic phase. In class D it is important how to introduce disorder, other network models show a different phase diagram. The fermionic counterpart of the Random Bond Ising Model [80] for example does not contain this metallic phase. In the Cho-Fisher model [71] the metal phase appears at strong defect concentration. At low concentration, there two topologically distinct phases, it is not fully established whether there is a direct topological transition, or the thermal metal wedge in the phase diagram persists to arbitrarily weak disorder and "hides" the topological transition.

1.5.4 Topological $\mathbb{Z}_2$-theta term

The NLσM in the symplectic metal class AII and its superconducting analog class CII also have nontrivial second homotopy group $\pi_2(\mathcal{M}_F) = \mathbb{Z}_2$. Since this is a subgroup of $\mathbb{Z}$, the parameter Θ in front of the winding number is restricted to the values $0, \pi$. The action (1.112) then is sensitive only to $N[Q]$ even or odd. Graphene with long range disorder can be described by a Dirac model with random scalar potential which in turn maps to a NLσM with such a $\Theta = \pi$ topological term [122].

1.5.5 Wess-Zumino-Novikov-Witten (WZNW) models

In Chap. 4 disordered surfaces of time-reversal invariant topological superconductors (AIII, CI, DIII) are investigated. As it turns out, the critical surface states can be described by a NLσM with fermionic manifold $\mathcal{M}_F = H \times H/H$ with H being $\mathrm{U}(n)$, $\mathrm{Sp}(n)$ or $\mathrm{O}(n)$, respectively. In general, topology of

the bulk manifests itself by a topological term in the corresponding surface NLσMs [9–11]. In the case considered here a Wess-Zumino term $S_{\text{WZ}}(g)$ is emerges in the action (1.64) due to the topological nontrivial bandstructure of the clean model.

In order to write down the Wess-Zumino term, one needs to extend $g(x, y)$ to the third dimension $g(x, y, s)$:

$$iS_{\text{WZ}}(g) = \frac{ik}{24\pi} \int \mathrm{d}^2 r \int_0^1 \mathrm{d}s \, \epsilon_{\mu\nu\lambda} \text{Str}(g^{-1}\partial_\mu g)(g^{-1}\partial_\nu g)(g^{-1}\partial_\lambda g). \tag{1.115}$$

As usual ϵ is the Levi-Civita symbol and k the level of the theory. The topological ambiguity of above integral arising since $g(x, y, s)$ is not unique forces k to take integer values. At this point a comment on existence and uniqueness of this extension are in order. The second homotopy group of H is trivial, $\pi_2(H) = 0$. This means that given two arbitrary maps $f_1, f_2 : S_2 \to H$ one can interpolate between them continuously, there is a continuous $F : S_2 \times [0, 1] \to H$ such that $f(x, y, s = 0) = f_1(x, y)$ and $f(x, y, s = 1) = f_2(x, y)$. By identifying the sphere and the $2d$ plane, one is guaranteed a map $g(x, y, s)$ interpolating between $g(x, y, s = 1) = g(x, y)$ and the constant map to identity $g(x, y, s = 0) = 1$. The extension is not unique, nevertheless the choice of a specific extension leaves observables invariant. Maps $g : S_3 \to H$ are classified by the third homotopy group $\pi_3(H) = \mathbb{Z}$, hence $iS_{\text{WZ}}(g)$ is defined up to a phase $nk2\pi i$ with integer n. Since this is an integer multiple of 2π observables are not affected.

By employing advanced CFT methods, one can extract multifractality, LDOS and conductance at criticality in these models. See Tab. 1.2 for an overview and references.

At zero energy the (generalized) multifractal spectrum is strictly parabolic (1.114). Consequently, the infinite set of multifractal scaling dimensions is solely described by a single parameter θ. A fundamental question addressed in this thesis, is which 2D Anderson transitions exhibit (generalized) parabolicity. For a more specific and comprehensive discussion of WZNW models with finite energy perturbation see Sec. 4.2.2.

1.5.6 Stacking in TSC surfaces

In Chap. 4 numerical evidence is gathered that TSC surface states away from the particle hole symmetric point ensuring topological protection remain critical. Moreover independent of the energetic distance from the center of the spectrum they share the same critical properties. These are truly distinct from Gade-Wegner criticality introduced above in Sec. 1.5.2 and Wess-Zumino criticality (see Sec. 1.5.5) at zero energy.

The conventional expectation was that finite energy $\varepsilon \neq 0$ breaks the defining chiral S symmetry, producing a standard Wigner-Dyson class, so that [9] CI $\to$ AI (Anderson localized), AIII $\to$ A (Anderson localized), and DIII $\to$ AII (Anderson localized or weak antilocalization).

Even more surprisingly than this conventional expectation being violated, the criticality exhibited resembles Quantum Hall critical phenomenology. Therefore the numerics presented in Chap. 4 supports the conjectures AIII $\to$ A, CI $\to$ C and DIII $\to$ D at relating time reversal invariant TSC at finite energy with QH critical systems fine tuned to the critical point. Refs. [50, 126] claim that the QH Pruisken model (1.113) could flow to a deformed WZNW. This would imply local conformal invariance of the corresponding QH critical theory, which can be completely ruled out for the SQH transition (see Sec. 3.9 for a discussion) and is unlikely for the IQH transition (Ref. [53]). The numerical data presented in this work instead suggests that apparently the TSC surface WZNW flows to a Pruisken model in presence of the energy perturbation breaking conformal invariance.

	AIII	CI	DIII
ν	$\mathbb{Z}$	$2\mathbb{Z}$	$\mathbb{Z}$
x_1/z	$\frac{\pi-\nu^2\lambda_A}{\pi(2\nu^2-1)+\nu^2\lambda_A}$ [67]	$\frac{1}{2|\nu|+3}$ [63]	$-\frac{1}{2|\nu|-3}$ $(|\nu|\geq 3)$ [61, 123]
$\theta(\varepsilon=0)$	$\frac{|\nu|-1}{\nu^2}+\frac{\lambda_A}{\pi}$ [64, 65, 67]	$\frac{1}{|\nu|+2}$ [64, 65, 124]	$\frac{1}{|\nu|-2}$ $(|\nu|\geq 3)$ [61]
$\sigma^{xx}(\varepsilon=0)$	$\frac{\nu}{\pi}$	$\frac{\nu}{\pi}$	$\frac{\nu}{\pi}$

Table 1.2: Summary of properties for Wess–Zumino–Novikov–Witten criticality at zero energy. The parameter ν is the level of the theory and the scaling of the density of states is $\rho(\varepsilon) \propto |\varepsilon|^{x_1/z}$. The WZNW model is locally conformally invariant, by the arguments reviewed and generalized in Sec. 3.2 the multifractal spectrum is strictly parabolic, $\Delta_q = -\theta\, q(1-q)$. The level determines the curvature θ. The longitudinal surface conductivity σ^{xx} (for spin or heat transport at the boundary of the TSC, in units of the appropriate conductance quantum [2, 125]) is quantized. In class AIII, there is a peculiarity: the abelian disorder strength λ_A, which is defined in Eqs. (4.10) and (4.11). The additional parameter λ_A is RG-marginal and addresses a continuum of distinct zero-energy fixed points [64, 65, 67].

2 Chapter 2

Disorder and interaction in chiral chains: Majoranas vs complex fermions

In this chapter, I study the low-energy physics in topological chains of (real) Majorana fermions and complex fermions in the presence of both interactions and disorder. Numerically there is qualitatively a drastically distinct behavior between these systems, despite the fact they are (up to the total number of degrees of freedom) equivalent in the non-interacting limit.

While in the non-interacting limit both models are equivalent (in particular, belong to the same symmetry class BDI and flow towards the same infinite-randomness critical fixed point), their behavior differs drastically once interaction is added. Density-matrix renormalization group (DMRG) calculations show that the complex-fermion chain remains at the non-interacting fixed point. On the other hand, the Majorana fermion chain experiences a spontaneous symmetry breaking and localizes for repulsive interaction.

In order to understand the phenomena observed in the DMRG numerics, an RG analysis treating interaction perturbatively is performed. The appropriate RG fixed point to study is of infinite-randomness type. The interaction matrix elements from which the scaling dimension can be inferred are given by two-point wavefunction correlators. Both numerically and analytically the critical eigenstate correlations are studied. The Majorana chain is driven away from the infinite randomness fixed point by a strongly relevant interaction operator. The interaction is irrelevant in the complex fermionic chain.

The contents of this chapter are based on Ref. [86], a work performed by collaborators and myself.

2.1 Introduction

Topological states of matter represent one of the central directions of the contemporary condensed matter physics [127]. Systems with topological order are usually characterized by a gap in the bulk and "metallic" states at the boundaries. These boundary states are robust against disorder-induced Anderson localization as long as the disorder is not strong enough to close the gap in the bulk[122, 128–130].

One-dimensional (1D) systems with topological phases are considered a potential platform for quantum computing[12–15], as the quantum state is stored non-locally and cannot be destroyed by local, uncorrelated noise (as long as the noise is not strong enough to close the bulk gap). For non-interacting systems, the symmetry classification (see Sec. 1.3) by Altland and Zirnbauer [131] combined with the analysis of topologies [2, 3, 132, 133], extended also to various spatial symmetries [134, 135], has pro-

vided a systematic picture of possible topological states. Despite the progress on extending this classification to include weak interactions [26–28], it is still a formidable task to determine which topological phases are present in a given interacting systems. While non-interacting topological phases are robust against disorder-induced localization, this is not always the case for topological states in interacting systems, see discussion in Sec. 1.3. In particular, in 2D superconductor systems, the combined effect of disorder and interactions has been shown to break entirely the topological protection [29, 30]. The underlying mechanism is that disorder renders the interaction relevant in the renormalization-group (RG) sense; see also Refs. [136, 137] for related physics. The fact that the interplay of interaction and disorder may crucially affect the physics has been known for a while [138]; recent works show that it is also of central importance for topological states of matter.

In this work, the effect of disorder and interaction on the low energy physics of a chain of Majorana quasiparticles commonly called Kitaev chain [32] is explored. Note that usually one studies the gapped Kitaev chain, with zero-dimensional Majorana bound states at its ends. In particular attention is payed to the combined effect of disorder and interaction on a gapless Majorana chain representing a one-dimensional wire with counterpropagating Majorana modes. The most local interaction one can have in this system is a four-point Majorana interaction [31]. Disorder is introduced by choosing the hopping parameters from a random distribution. This model could potentially be realized by vortex lattices [33–35] in a thin film topological superconductor. In general, chains of parafermions such as Majoranas can also be realized in superconductor-ferromagnet structures along quantum spin Hall edges [36]. Further, the (gapped) Kitaev chain Hamiltonian has been realized as an effective low energy theory in InGaAs nanowires on top of a superconductor in a magnetic field [37]. A gapless Majorana chain can be realized on the edge of an array of such wires [41]. Other platforms for generating Majorana chains include chains of magnetic atoms on top of a superconductor [139], as well as cold atoms in optical lattices [140]. The phase diagram of a clean interacting Kitaev chain was studied in Ref. [31].

The Majorana model is compared to that of complex fermion hopping on a chain with the chemical potential tuned to zero [38, 39]. In spin language (see Sec. 1.1.1), this model is equivalent to the random bond XXZ model. In the absence of interaction, both Majorana and complex-fermion models belong to the symmetry class BDI and are largely equivalent. The only difference between them is that in the case of complex fermions each pair of states related through chiral symmetry represent two independent single body states, while in the case of the Majorana chain each pair represents a single state. However, the situation changes dramatically once one adds interaction. In the case of complex fermions, previous work based on real-space RG analysis showed that weak interactions are irrelevant in the RG sense [38, 40] and thus do not change the low energy properties of the system. This system flows into a peculiar critical infinite-randomness fixed point. For the interacting disordered Majorana chain, the behavior turns out to be very different. It is shown that interaction drives the system away from the infinite randomness fixed point, which leads to localization in the case of (even weak) repulsive interaction. The localization of a disordered Majorana chain with moderately strong repulsive interaction was observed previously in Ref. [41]. Further it is explained why the above two similar models behave so drastically different once interaction is added.

The outline of this chapter is as follows. The models are defined in Sec. 2.2. Further, previously known results on the models are reviewed. In Sec. 2.3, the numerical results obtained with the density matrix renormalization group[141] (DMRG) code OSMPS [142] are presented. First the clean interacting Majorana chain driven out of criticality by staggering in order to explore emerging topological phases is considered. Then the DMRG study of the combined effect of disorder and interaction follows, both for complex fermions and for Majoranas. In the case of complex fermions, the properties of a

random chain are not essentially influenced by interaction, in consistency with previous results. On the other hand, the observations indicate that the interacting disordered Majorana chain localizes even for weak repulsive interaction. This localization is accompanied by a spontaneous breaking of symmetry between two topological phases that manifests itself in correlation functions. To shed light on the physical origin of these results, in Sec. 2.4 and 2.5 two complementary approaches are employed. Specifically, in Sec. 2.4 momentum-space RG methods (introduced in Sec. 1.1.3) are used to investigate the effect of weak disorder on the interacting clean models. It is shown that disorder in both models is strongly relevant rendering the clean fixed point unstable. The complementary approach in Sec. 2.5 follows, where the start is from an exact treatment of disorder (which drives the system into the infinite-randomness fixed point) and the interaction considered as perturbation. By combining the RG treatment of interaction with a numerical study of wave-function correlations (see Sec. 1.2.1) at the infinite-randomness fixed point, a relevant operator is identified in the case of the Majorana chain. No such operator exists in the case of the complex fermionic chain in view of the cancellation between Hartree and Fock contributions. This explains why the Majorana fermion chain is unstable with respect to weak interaction, while the complex fermion chain is stable.

2.2 Models

In this Section two 1D models to be considered in this chapter are defined: that of complex fermions, Sec. 2.2.1, and of Majoranas, Sec. 2.2.2. Briefly some previous results relevant to this work are reviewed.

2.2.1 Complex Fermion chain

The vanilla chiral wire is a spinless fermionic chain where the chemical potential is tuned to zero,

$$H = \sum_j t_j(c_j^\dagger c_{j+1} + h.c.). \tag{2.1}$$

Every hopping term is between an even (e) and an odd (o) site. The Hamiltonian possesses therefore a sublattice symmetry which is represented by the operator $\mathcal{S} = \tau_z$, where τ_z is the Pauli matrix operating on the even-odd subspace. By using the local $U(1)$ gauge freedom, the hopping matrix elements t_j can always be chosen as reals. This implies a time reversal symmetry represented by complex conjugation $\mathcal{T} = \mathcal{K}$ with $\mathcal{T}^2 = 1$. Further, the system possesses in addition the particle hole symmetry $\mathcal{P}$ expressed by $\mathcal{P} = \mathcal{K}\tau_z$, with $\mathcal{P}^2 = 1$. These symmetries place the model in the BDI symmetry class.

Disorder is introduced by making the hopping matrix elements random. This does not change the symmetry classification. The most local interaction that can be added to this model is a two-point nearest-neighbor density-density interaction. To keep the system at half filling, a chemical potential proportional to the interaction strength has to be included. Since later it becomes clear that the sublattice structure of the interaction is important, we generalize the interaction to act on sites separated by a distance r:

$$H = \sum_j t_j(c_j^\dagger c_{j+1} + h.c.) + g \sum_j p_j p_{j+r}, \tag{2.2}$$

$$p_j = c_j^\dagger c_j - \frac{1}{2}. \tag{2.3}$$

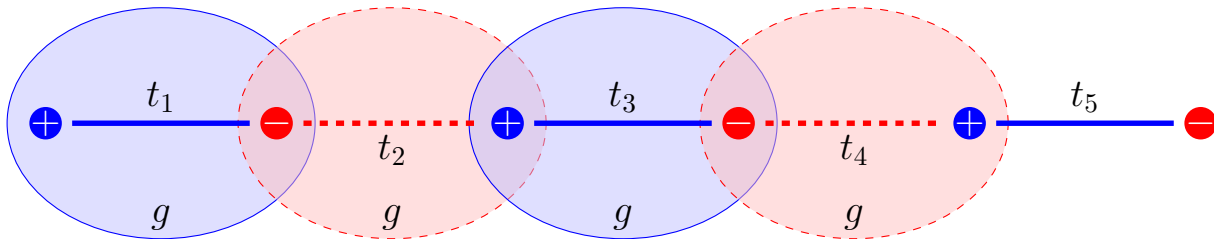The couplings of this model for $r = 1$ are sketched in Fig. 2.1.

Figure 2.1: Figure taken from Ref. [86]. Sketch of the couplings of the complex-fermion chain with Hamiltonian (2.2) and $r = 1$. Couplings starting on odd sites are solid, those starting on even sites are dashed. Odd sites have blue color and are labeled by $+$, while even sites have red color and are labeled by $-$. The first few quartic interaction terms involving the sites j and $j + 1$ are indicated by blue (odd j) and red (even j) ellipses.

2.2.1.1 Spin representation

Using the Jordan-Wigner transformation, one can map the model (2.2) onto a random-bond, spin-$\frac{1}{2}$ XXZ chain:

$$H_{\text{spin}} = \sum_j t_j(\sigma_j^x \sigma_{j+1}^x + \sigma_j^y \sigma_{j+1}^y) + g\sigma_j^z \sigma_{j+r}^z. \tag{2.4}$$

The $U(1)$ gauge freedom in the fermionic model corresponds to the spin-rotation symmetry in the XY plane. While the two models (2.2) and (2.4) are equivalent, the Jordan-Wigner transformation is non-local, and so is the mapping between the correlation functions. The spin representation turns out to be particularly suitable for the DMRG analysis and will be used in this chapter.

2.2.1.2 Symmetries and topology

To show that the interaction does not change the symmetry class, the many body generalizations of the above symmetries $\mathcal{T} = \hat{U}_T \mathcal{K}, \mathcal{P} = \hat{U}_P \mathcal{K}, \mathcal{C} = \hat{U}_C$ are considered, see Ref. [143]. They can be obtained by defining the action of the symmetry operators on the creation and annihilation operators:

$$\hat{T}c_j\hat{T}^{-1} = (U_T)_{j,i}c_i = c_j, \tag{2.5}$$

$$\hat{P}c_j\hat{P}^{-1} = (U_P)_{j,i}c_i^\dagger = (-1)^j c_j^\dagger, \tag{2.6}$$

$$\hat{C} = \hat{T} \cdot \hat{P}. \tag{2.7}$$

This defines the action of $\hat{T}, \hat{P}, \hat{C}$ on all operators and states in the Fock space. In this many-body formulation, the time-reversal symmetry $\hat{T}$ and chiral symmetry $\hat{C}$ are represented by anti-unitary operators, while the particle hole symmetry $\hat{P}$ is represented by a unitary operator. In contrast to the single body symmetry operators $\mathcal{P}$ and $\mathcal{C}$, the many body symmetry operators $\hat{P}, \hat{C}, \hat{T}$ all commute with the Hamiltonian.

Now one can analyze the symmetries of the Hamiltonian (2.2). First, all couplings are real, implying that $\hat{T}$ commutes with H. Second, the term $-1/2$ in Eq. (2.3), which corresponds to a proper choice of the chemical potential ensures that the model is invariant under $\hat{P}$. Further, the operators $\hat{T}$ and $\hat{P}$ square to unity. The interacting model belongs therefore to the symmetry class BDI. It was shown that 1D interacting systems of complex fermions belonging to this symmetry class (in absence of pairing terms) have a $\mathbb{Z}_4$ topological invariant [28].

2.2.1.3 Clean limit

Here the clean limit is briefly discussed. If all matrix elements t_j are equal, $t_j = t$, and the interaction g is not too strong, the low-energy theory of the XXZ model (2.4) is the Luttinger liquid. This is a conformal field theory with central charge $c = 1$. For the case of nearest-neighbor interaction, $r = 1$, the corresponding condition is[144] $|g| < t$. For $|g| > t$ the system is gapped.

One can drive the system away from the critical line by introducing a staggering, $t_{2j} = t_e$ and $t_{2j+1} = t_o$, with $t_e \neq t_o$. This will in general open a gap. More precisely, investigating the RG relevance of the corresponding term in the bosonization language (see analysis in Sec. 2.4 below), one finds that the staggering immediately opens a gap for $-1 < g/t < 0.7$, i.e., almost in the whole range of g/t corresponding to a critical theory. The gapped phases with $t_e > t_o$ and $t_e < t_o$ are topologically distinct. This can be easily seen by observing that in the limit $t_e \to \infty$, the fermion at the first site decouples from the rest of the chain, thus representing a topological zero mode. This zero mode will persist for $t_e > t_o$ (although it will spread over a few sites). In the opposite case, $t_o \to \infty$, there is no zero mode. The $c = 1$ critical theory (Luttinger liquid) thus represents a boundary between two topologically distinct phases.

2.2.1.4 Noninteracting limit

Consider now a non-interacting system ($g = 0$) but in the presence of disorder, i.e. with random hopping matrix elements t_j. This breaks translational symmetry $j \to j + 1$ for a given realization of disorder. However, if the distributions of even t_{2j} and odd t_{2j+1} matrix elements are the same, the system remains self-dual with respect to the transformation $j \to j + 1$. In spin language, the model corresponds to a disordered XY chain. Analytically, the problem can be treated with a real space RG procedure [38]. At the self-dual point, the system is critical despite an RG flow towards strong disorder. This very peculiar fixed point is termed infinite-randomness fixed point. By considering the scaling of the disorder-averaged entanglement entropy, one can define an effective central charge $c_{\text{eff}} = \ln 2$ characterizing this critical state [145–147].

2.2.2 Majoranas

To introduce the second model—the one that is which is of the central interest for this work—one starts with a 1D chain of spinless fermions of length L with superconducting pairing matrix elements Δ_j, hopping $\tilde{t}_j$ and local chemical potential μ_j. The pairing and hopping are chosen to be real. The Hamiltonian reads

$$
\begin{aligned}
H &= \sum_{j=1}^{L} \mu_j c_j^\dagger c_j + \tilde{t}_j (c_j^\dagger c_{j+1} + c_{j+1}^\dagger c_j) \\
&+ \Delta_j (c_j c_{j+1} + c_{j+1}^\dagger c_j^\dagger).
\end{aligned} \tag{2.8}
$$

Now one rewrites each pair of fermionic creation and annihilation operators in terms of two Hermitian Majorana operators $\gamma_j = \gamma_j^\dagger$:

$$
c_j = (\gamma_{2j} + i\gamma_{2j+1})/2; \qquad c_j^\dagger = (\gamma_{2j} - i\gamma_{2j+1})/2. \tag{2.9}
$$

The Majorana operators obey the commutation relations

$$
\{\gamma_i, \gamma_j\} = 2\delta_{ij}; \qquad \gamma_i^2 = 1. \tag{2.10}
$$
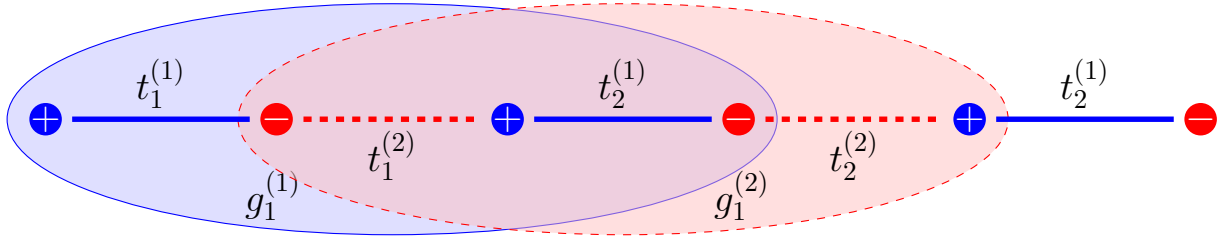
Figure 2.2: Figure taken from Ref. [86]. Sketch of the couplings in the Majorana Hamiltonians (2.13),(2.17). Couplings t_{2j} are dashed, t_{2j+1} solid. Odd sites have blue color and are labeled by $+$, while even sites have red color and are labeled by $-$. The first two quartic interaction terms with couplings $g_1^{(1)}$ and $g_1^{(2)}$ are indicated by a blue and a red ellipse, respectively. Translation by one site swaps even and odd hopping and interaction terms.

Each Majorana operator represents half a degree of freedom. The Hamiltonian becomes now

$$
\begin{aligned}
H &= \frac{i}{2}\sum_{j=1}^{L}[\mu_j\gamma_{2j}\gamma_{2j+1} + (-\tilde{t}_j + \Delta_j)\gamma_{2j+1}\gamma_{2j+2} \\
&+ (\tilde{t}_j + \Delta_j)\gamma_{2j}\gamma_{2j+3}].
\end{aligned}
\tag{2.11}
$$

If the hopping and pairing terms are chosen such that $\tilde{t}_j = -\Delta_j$, this simplifies to

$$
H = \sum_{j=1}^{2L} it_j\gamma_j\gamma_{j+1},
\tag{2.12}
$$

where the notations $t_{2j} = \mu_j/2$ and $t_{2j+1} = -\tilde{t}_j$ were introduced. This model is known as Kitaev chain[32].

The symmetries of the non-interacting Hamiltonian (2.8) are inspected in the following lines. The pairing terms in Hamiltonian (2.8) break the global $U(1)$ symmetry to the parity $\mathbb{Z}_2$. As usual for Bogolyubov-de Gennes models, the Hamiltonian has a particle hole symmetry $\mathcal{P} = \mathcal{K}$. Since all couplings are real, the system has time reversal symmetry $\mathcal{T} = \tau_z\mathcal{K}$. Both symmetry operators square to unity, thus the model belongs to class BDI. The product of those two symmetries yields the sublattice symmetry $\mathcal{C} = \tau_z$.

In the following, the interaction term is included. Since $\gamma_n^2 = 1$, the most local interaction term couples four neighboring Majoranas [31]:

$$
H = \sum_{j=1}^{2L} it_j\gamma_j\gamma_{j+1} + \sum_{j=1}^{2L} g_j\gamma_j\gamma_{j+1}\gamma_{j+2}\gamma_{j+3}.
\tag{2.13}
$$

Below it will be allowed for randomness in the hopping matrix elements t_j. If the values of the interaction g_j as well as the distribution of hopping matrix elements t_j is the same for even and odd sites, the model is self-dual under translation by one side.

2.2.2.1 Symmetry and topology

The symmetries $\mathcal{T}, \mathcal{P}$ and $\mathcal{C}$ can be extended to the many-body setting in analogy with discussion in Sec. 2.2.1.2 for the case of complex fermions. In terms of Majorana operators the symmetries read

$$\hat{T}\gamma_j\hat{T}^{-1} = (-1)^j\gamma_j, \tag{2.14}$$

$$\hat{C}\gamma_j\hat{C}^{-1} = \gamma_j, \tag{2.15}$$

$$\hat{S} = \hat{T} \cdot \hat{C}. \tag{2.16}$$

It is worth mentioning that for Bogolyubov-de Gennes Hamiltonians the particle-hole symmetry is not a true many-body symmetry but rather a constraint related to the Fermi statistics, see discussion in Ref. [148]. This puts the model in interacting symmetry-class BDI with $\mathbb{Z}_8$ topological classification, see Ref. [26].

While the Hamiltonian (2.13) contains only nearest-neighbor Majorana hopping t_j, any odd-range hopping is in principle permitted by symmetry. In particular, as it is discussed below, the interaction generates third nearest neighbor hopping on the mean-field level. An even-range hopping would couple Majoranas from the same sublattice and break the chiral symmetry and the time-reversal symmetry. Similarly, any interaction term containing an even number of Majorana operators belonging to even sites (and thus an even number of operators from odd sites), is consistent with the $\hat{T}$ and chiral symmetries.

2.2.2.2 Spin representation

The interacting Kitaev chain (2.13) can be mapped onto a spin-$\frac{1}{2}$-chain by means of Jordan-Wigner transformation (see Sec. 1.1.1):

$$
\begin{aligned}
H &= \sum_{j=1}^{L} t_j^{(1)}\sigma_j^x - \sum_{j=1}^{L} t_j^{(2)}\sigma_j^z\sigma_{j+1}^z \\
&- \sum_{j=1}^{L} g_j^{(1)}\sigma_j^x\sigma_{j+1}^x - \sum_{j=1}^{L} g_j^{(2)}\sigma_j^z\sigma_{j+2}^z.
\end{aligned}
\tag{2.17}
$$

Here $t_j^{(1)}$ and $t_j^{(2)}$ correspond respectively to odd (t_{2j-1}) and even (t_{2j}) hopping matrix elements of Eq. (2.13), and similarly for the interaction couplings g. The couplings of this model are sketched in Fig. 2.2.

It is interesting to note that the odd couplings $g_j^{(1)}$ and $t_j^{(1)}$ couple in the spin language to x components, and the the odd couplings $g_j^{(2)}$ and $t_j^{(2)}$ to z components. Translation by one site (even-odd transformation) exchanges $g_j^{(1)} \leftrightarrow g_j^{(2)}$ and $t_j^{(1)} \leftrightarrow t_j^{(2)}$. Models related by this transformation are dual, although this duality is less obvious in the spin representation than in the Majorana representation.

The spin representation will be used for the DMRG analysis below.

2.2.2.3 Noninteracting limit

In the non-interacting limit ($g = 0$) the Hamiltonian (2.17) describes the transverse Ising model. In the clean translational-invariant case (no staggering, $t^{(1)} = t^{(2)}$) the system is critical with a 1D Majorana low-energy theory and central charge $c = \frac{1}{2}$. In the presence of random hopping, the model is at the

infinite-randomness fixed point [40] as noted above in the context of complex fermions in Sec. 2.2.1.4. The difference between the two models in the absence of interaction is that two single-particle states of the complex-fermion model correspond to a single state of the Majorana model. As a consequence, the effective central charge at the infinite-randomness fixed point is halved, $c = (\ln 2)/2$.

2.2.2.4 Clean limit

For the case of interacting model with homogenous couplings, $t_j = t$ and $g_j = g$, Rahmani et al. [31] have determined the phase diagram:

- *Strong interaction.* The system is gapped for very strong interactions of both signs ($g > 250$ or $g < -2.86$). The translation symmetry gets spontaneously broken, and the transition between the topologically distinct phases is of first order type.

- *Attractive interaction.* There is a critical phase up to very strong interactions $0 < g < 250$. The low energy theory is a single Majorana mode with central charge $c = \frac{1}{2}$. This phase is controlled by the same fixed point as the transverse Ising model and therefore dubbed Ising phase.

- *Weak repulsive interaction.* For the case of repulsive interaction ($g < 0$), the Ising phase is stable for sufficiently weak interactions, $g > -0.28$.

- *Intermediate repulsive interaction.* For repulsive interaction of intermediate strength, $-2.86 < g < -0.28$, a phase emerges with coexisting Luttinger-liquid and Majorana modes. Alternatively, one can say that a single Majorana mode of the non-interacting theory is promoted to three Majorana modes, which can be understood already by mean-field level treatment of the interaction. The central charges in this phase is $c = \frac{3}{2}$.

2.3 DMRG results

In this section an overview over the DMRG numerics from Ref. [86] performed by one of my collaborators is given. For DMRG methods, spin models are most convenient. Therefore the spin representations, Eq. (2.4) and Eq. (2.17) of the models are employed. The software OSMPS [142] was used for the calculations. The maximum bond dimension was chosen to be 512, states with weight smaller than 10^{-8} were truncated.

2.3.1 Interacting Majorana chain with staggering

This section presents the numerical DMRG results obtained by my collaborator in Ref. [86]. The analytical reasoning in the next sections are based on these findings.

The main numerical observations are that disorder drives an interacting Majorana chain into different localized phases if the interaction is repulsive. To obtain an overview over possible localized phases in the Majorana model, first consider the clean model driven out of criticality by introducing staggering is considered. The parameters of the Hamiltonian, Eq. (2.17) are chosen equal to $t_i^{(1)} = t_1$, $t_i^{(2)} = t_2$, $g_i^{(1)} = g_1$, and $g_i^{(2)} = g_2$. The system size is fixed to $L = 96$ spin sites (which corresponds to $2L = 192$ Majorana sites). Parameters are chosen in such a way that the relation $g_1/t_1 = g_2/t_2$ is maintained; a short-hand notation g/t is used for this ratio. The DMRG simulations explore the range $-4 < g/t < 1$ of the interaction strength, varying the staggering, $0 < t_1/t_2 = g_1/g_2 < \infty$. For the staggering region

$0 < t_1/t_2 < 1$, the hopping $t_1 = 1$ is fixed and t_2 is varied, while for staggering above the self-dual line $1 < t_1/t_2 < \infty$, $t_2 = 1$ is fixed and t_1 is varied.

The system with a given value of staggering t_1/t_2 is related to the system with inverse staggering via duality transformation. In the Majorana representation, this transformation corresponds simply to a translation by one lattice site. On the other hand, in the spin language of Eq. (2.17) the duality transformation is much less trivial (and, in particular, non-local).

In the MPS representation the (von Neumann) entanglement entropy between two subsystems split by a bond is readily available [142, 149]. In a critical 1D system of length L with open boundary conditions, the bond entropy scales as a function of bond position x as [150]

$$S(x) = \frac{c}{6} \ln \left(\frac{2L}{\pi} \sin \frac{\pi x}{L} \right) + \gamma \qquad (2.18)$$

where c is the central charge and γ the topological entanglement entropy. The slope of the dependence of the entanglement entropy on the scaling function entering Eq. (2.18) can thus be used to extract the central charge of the system. In gapped systems, the entanglement entropy saturates, i.e., $c = 0$.

In order to identify critical lines and regions, the central charge defined according to Eq. (2.18) is plotted in Fig. 2.3 via a color map in the parameter plane spanned by the interaction strength g/t and the staggering t_1/t_2. Further, in Fig. 2.4 the long-range spin-spin correlation $\langle \sigma_{L/4}^z \sigma_{3L/4}^z \rangle$ are shown. This plot helps to differentiate between topologically distinct gapped regions. Figure 2.5 provides an overview over results that are discussed in more detail below. In this figure, numbers from 1 to 6 label different regions; the corresponding distance dependences of spin correlations is shown (with the same labels) in Fig. 2.6. On the self-dual line, $t_1/t_2 = 1$, the range of interaction strength $-4 < g/t < 1$ can be divided, in agreement with Ref. [31], into three intervals: the $c = \frac{1}{2}$ Ising phase for attractive and relatively weak repulsive interaction, $g/t > -0.28$, the $c = \frac{3}{2}$ phase where the Ising sector coexists with a Luttinger liquid sector for repulsive interaction in the interval $-0.28 > g/t > -2.9$, and a gapped phase for even stronger repulsive interaction, $g/t < -2.9$. This distinction remains useful also for understanding of phases in the presence of staggering, as discussed below.

2.3.1.1 Attractive and weak repulsive interaction

In the absence of staggering, $t_1/t_2 = 1$, the system remains in the non-interacting Ising phase for attractive interaction and for repulsive interaction, $-g/t < 0.28$, as was found in Ref. [31]. Indeed, one can observe in Fig. 2.3 that on the self-dual line the system is critical with a central charge of $\frac{1}{2}$ at this range of interactions. At finite staggering the system is gapped, with two topologically distinct phases (labeled 2 and 3 in Fig. 2.5) that can be distinguished by the behavior of the spin-spin correlator. For staggering $t_1/t_2 = g_1/g_2 > 1$, which corresponds to the topologically trivial phase in the fermionic picture, it decays quickly with distance, see Fig. 2.4 and the top left panel of Fig. 2.6. On the other hand, in the symmetry-broken phase in the spin language, $t_1/t_2 = g_1/g_2 < 1$ (which is topologically non-trivial in the fermion language), the correlator saturates at a constant value of order unity at large distance, Fig. 2.4 and the bottom left panel of Fig. 2.6. On the critical line $t_1/t_2 = g_1/g_2 = 1$, the correlator decays slowly (algebraically), as expected, see middle left panel of Fig. 2.6.

2.3.1.2 Intermediate repulsive interaction

For stronger repulsive interaction $-0.28 < g < -2.9$, the clean system without staggering exhibits a Luttinger liquid sector in addition to the Ising sector as has been already pointed out in Sec. 2.2.2.4.
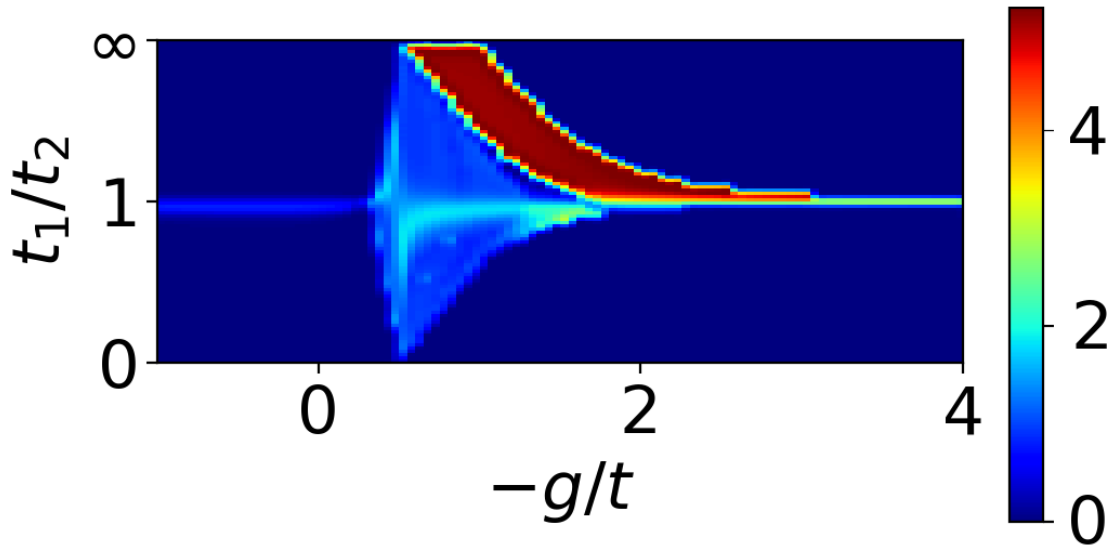
Figure 2.3: Figure modified from Ref. [86]. Central charge c of the clean interacting Majorana chain vs interaction strength $g_1/t_1 = g_2/t_2 \equiv g/t$ and staggering $t_1/t_2 = g_1/g_2$. On the self-dual line (no staggering, i.e., $t_1/t_2 = 1$), the results agree with Ref. [31]: the central charge is $c = \frac{1}{2}$ for $-g/t \lesssim 0.28$ and is then $c = \frac{3}{2}$ until the system becomes gapped at strong repulsive interaction, $-g/t > 2.9$. In the Ising phase, the system is gapped everywhere apart from the critical line (i.e., by any staggering $t_1/t_2 \neq 1$). On the other hand, in the Ising+LL phase, adding staggering produces an extend critical region with $c = 1$, see also a schematic phase diagram in Fig. 2.5. The red patch is a peculiar region where determination of c by means of Eq. (2.18) breaks down, see Ref. [86] for more detail. In fact, this phase is gapped (as is also clear by inspecting its dual, $t_1/t_2 \to t_2/t_1$), i.e., the properly defined central charge is zero.

In this paper we will call this phase "Ising + LL" phase, where "LL" stands for "Luttinger liquid". In Ref. [31] this phase is called the "floating" phase, in analogy to a similar phase in the anisotropic next nearest neighbor Ising model. It is characterized by a central charge of $c = \frac{3}{2}$. Our numerical data in Fig. 2.3 confirm this behavior.

As Fig. 2.3 demonstrates, the staggering does not immediately lead to a gapped system in this interaction range. Instead, there is an extended region of finite staggering with a central charge of $c = 1$ around the no-staggering line. This can be understood as a result of the Luttinger-liquid sector being stable to weak staggering, with the Ising sector becoming gapped. An argument based on RG analysis is given in Sec. 2.4. More precisely, there are two such phases with $c = 1$, labeled 5 and 6 in Fig. 2.5, which are separated by the line with $c = 3/2$ (label 4).

In these extended critical regions, the spin-spin correlator is an oscillating function of distance, as detailed in Fig. 2.6. The oscillation decay above the no-staggering line (label 6, top right panel), while their amplitude remains constant below this line (label 5, bottom right panel). On the line without staggering, the oscillations decay very slowly (label 4, middle right panel). The non-decaying oscillation in the extended critical region below the self-dual line are also visible in Fig. 2.4.

At extreme staggering $t_1/t_2 = 0$, the model reduces to the longitudinal Ising model. This model exhibits a first order transition at the point $g/t = 0.5$. The critical region with central charge $c = 1$
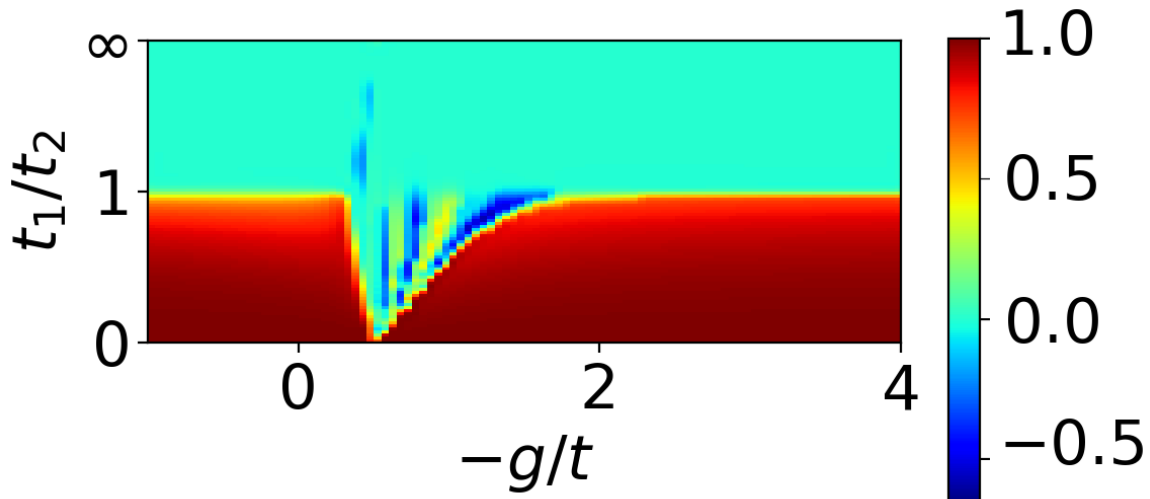
Figure 2.4: Figure modified from Ref. [86]. The $\langle \sigma^z_{24} \sigma^z_{48} \rangle$ correlator between spins on the sites $i = 24$ and $i = 48$ for the clean interacting Majorana chain as a function of interaction strength $g_1/t_1 = g_2/t_2 \equiv g/t$ and staggering $t_1/t_2 = g_1/g_2$. In the gapped phases (cf. Figs. 2.3 and Fig. 2.5) the correlator is equal to zero above the self-duality line and to unity below this line, thus helping to distinguish two topologically distinct phases. In the critical region with $c = 1$ around the Ising + LL phase the correlator shows an oscillatory behavior, cf. Fig. 2.6, right panels.

is separated from the gapped region of the Ising phase by a line connecting this point ($g/t = 0.5$ and $t_1/t_2 = g_1/g_2 = 0$; marked by a black dot in Fig. 2.5) with the point of the Lifshitz transition on the critical line ($g/t \approx -0.28$ and $t_1/t_2 = g_1/g_2 = 1$; marked by a red star in Fig. 2.5). Additionally, there is a vertical critical line (red) connecting the black dot to its dual. This line is also clearly visible in the picture of the central charge, Fig. 2.3, as it has a central charge of $c = \frac{3}{2}$.

At variance with the horizontal $c = \frac{3}{2}$ line that is determined by the condition of no staggering, the vertical $c = \frac{3}{2}$ line is not fixed by any simple symmetry. Thus additional checks were performed to verify its position. First, in order to exclude finite-size effects, considered twice larger systems ($L = 192$) are considered in this part of the phase diagram. The results demonstrated that neither the obtained value $c = \frac{3}{2}$ nor the position of the line change with L. This implies that the vertical $c = \frac{3}{2}$ line is indeed a property of the system in the thermodynamic limit. Second, the precise location of the line was looked at more carefully and found that it is not exactly at $-g/t = 0.5$, although very close to it. As an example, it was found that the $c = \frac{3}{2}$ line crosses the horizontal line $t_1/t_2 = 0.72$ at $-g/t \approx 0.45$. This indicates that the "vertical" $c = \frac{3}{2}$ line is not exactly straight but rather shows a small deviation from the line $-g/t = 0.5$.

Analogous to the horizontal (no-staggering) critical line, the value $c = \frac{3}{2}$ can be understood as a superposition of a Luttinger liquid ($c = 1$) and a Majorana mode ($c = \frac{1}{2}$) due to a topological phase boundary.

To shed light on the reason for the emergence of the vertical $c = \frac{3}{2}$ line, I performed a mean-field analysis by generalizing that of Ref. [151] to the problem. In this way, one can approximately mapped an interacting fermionic Hamiltonian to a non-interacting (mean-field) one and obtained the condition for gap closing. This condition yields a two-dimensional surface in the whole (three-dimensional) space
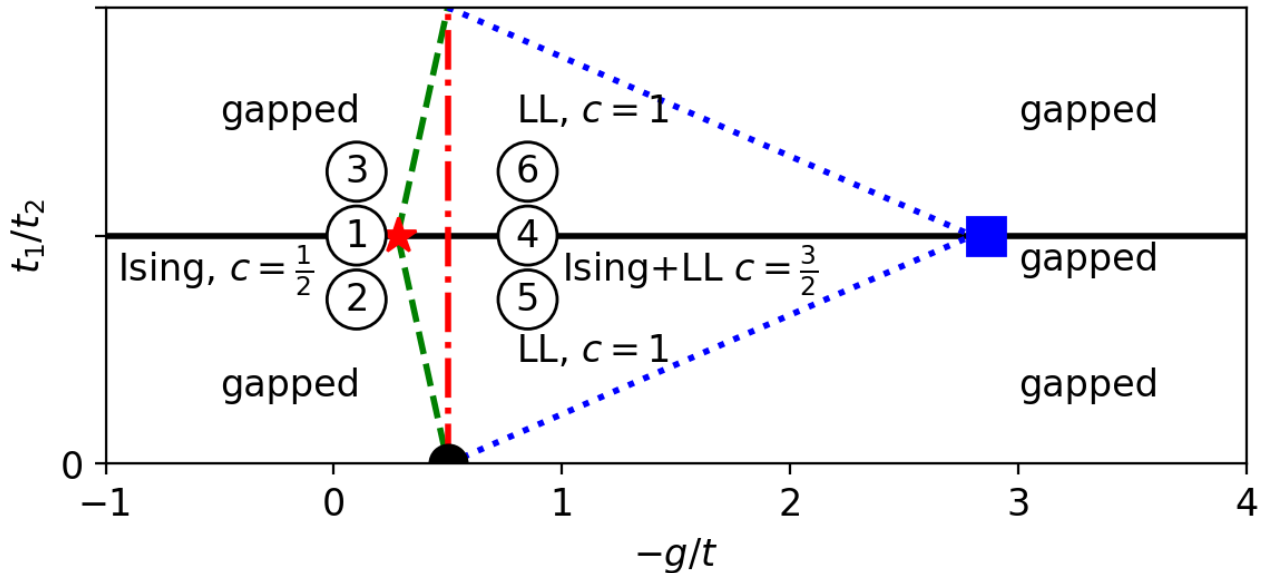
Figure 2.5: Figure taken from Ref. [86]. Schematic phase diagram of the clean interacting Majorana chain in the plane spanned by the interaction strength $g_1/t_1 = g_2/t_2 \equiv g/t$ and the staggering t_1/t_2. The labels from 1 to 6 correspond to the plots of the spin-spin correlator as a function of distance in Fig. 2.6 which are labeled in the same way. For $-g/t \lesssim 0.28$ the system on the self-dual line ($t_1/t_2 = 1$) is in the Ising phase with central charge $c = 1/2$ (label 1). Introducing staggering yields two topologically distinct gapped phases (labels 2 and 3). At the point $-g/t \approx 0.28$ (marked by a red star) the system undergoes a Lifshitz transition into the Ising+LL phase with $c = 3/2$ (label 4). This Ising+LL phase intersects the projection plane also in the vertical line at $-g/t = 0.5$ (red dashed-dotted line). For intermediate interactions, a not too strong staggering leaves the system gapless but reduces its central charge down to $c = 1$ (Luttinger liquid phases; bounded by green dashed and blue dotted lines, labels 5 and 6). These lines are drawn schematically, their exact form has not been determined. The black dot on the bottom of the diagram ($g_1/g_2 = t_1/t_2 = 0$ and $-g/t = 0.5$) marks the first-order transition in the longitudinal Ising model. The blue square at $-g/t \approx 2.9$ on the self-duality line $t_1/t_2 = 1$ is the point of the transition to a gapped phase. The phase diagram is symmetric with respect to the duality transformation that links points with the same value of g/t and inverse values of t_1/t_2.

of parameters (t_2/t_1, g_1/t_1, and g_2/t_1). The surface can be computed numerically. One can observe numerically that this two-dimensional surface intersects the two-dimensional surface determined by the condition $t_1/t_2 = g_1/g_2$ (that is used in the DMRG numerics) on two lines – the horizontal and the vertical ones. The numerically obtained position of the vertical line is close to $-g/t = 0.5$. With the superimposed extended Luttinger liquid phase, one has $c = \frac{3}{2}$ on these lines. In analogy with the horizontal line, the vertical line corresponds to the gap closing in the Ising sector, which corresponds to a phase boundary between topologically distinct phases.

Another interesting point is the red patch appearing in the upper plane seemingly violating the duality of the model. This is more than a numerical artifact and has to do with corrections to the scaling form of the entanglement entropy (2.18) in gapped phases. In the Appendix of Ref. [86] a more detailed discussion can be found.

2.3.1.3 Strong repulsive interaction

With increasing strength of repulsive interaction $-g/t$, the extended critical region around the no-staggering line gradually shrinks, see Fig. 2.3. For sufficiently strong interaction $-g/t > 2.9$ this region vanishes and, moreover, the line of no-staggering becomes gapped.

2.3.2 Interacting Majorana chain with disorder

In this part, the DMRG numerics that introduce disorder in the interacting Majorana chain model are presented. The hopping t_j was chosen as random independent variables, with a homogeneous distribution over the interval $[0.5, 1.5]$. All hopping matrix elements have now the same distribution, so that there is no staggering.

In general, critical lines can move in phase space as function of disorder strength [152, 153]. However, the critical line at no staggering is pinned by self-duality. Therefore, it should remain critical in the presence of both disorder and interaction unless spontaneous symmetry breaking takes place, see a more detailed discussion in Sec. 2.3.2.2 below.

Since the average value of the hopping matrix elements is unity, the value of the interaction g has now the same meaning as g/t in the analysis of the clean system. Three different ranges of interaction strength were considered: (i) attractive interaction $0 < g < 250$, (ii) weak repulsive interaction $0 > g > -0.28$ and (iii) medium repulsive interaction $-0.28 > g > 2.86$. The effective central charge in these regions of interaction was calculated by analyzing the disorder-averaged entanglement entropy via Eq. (2.18).

2.3.2.1 Attractive interaction

For attractive interaction $0 < g < 250$, the clean system is in the Ising phase[31] with a central charge of $\frac{1}{2}$, see Sec. 2.3.1.1 and left panel of Fig. 2.7. On the other hand, the disordered non-interacting system has an effective central charge of $c_{\text{eff}} = \frac{\ln 2}{2} \approx 0.35$ as was found in Ref. [146]. The numerics confirms this value.

Remarkably, in the presence of both disorder and interaction, the central charge returns to the value of the clean system $c_{\text{eff}} = \frac{1}{2}$, see Fig. 2.7 (right panel). For higher attractive interaction, the disorder averaging requires less samples in order to give a smooth function of the entanglement entropy vs scaling function than for lower interaction. This serves as an additional indication that disorder does not play an important role for the Majorana chain with attractive interaction.
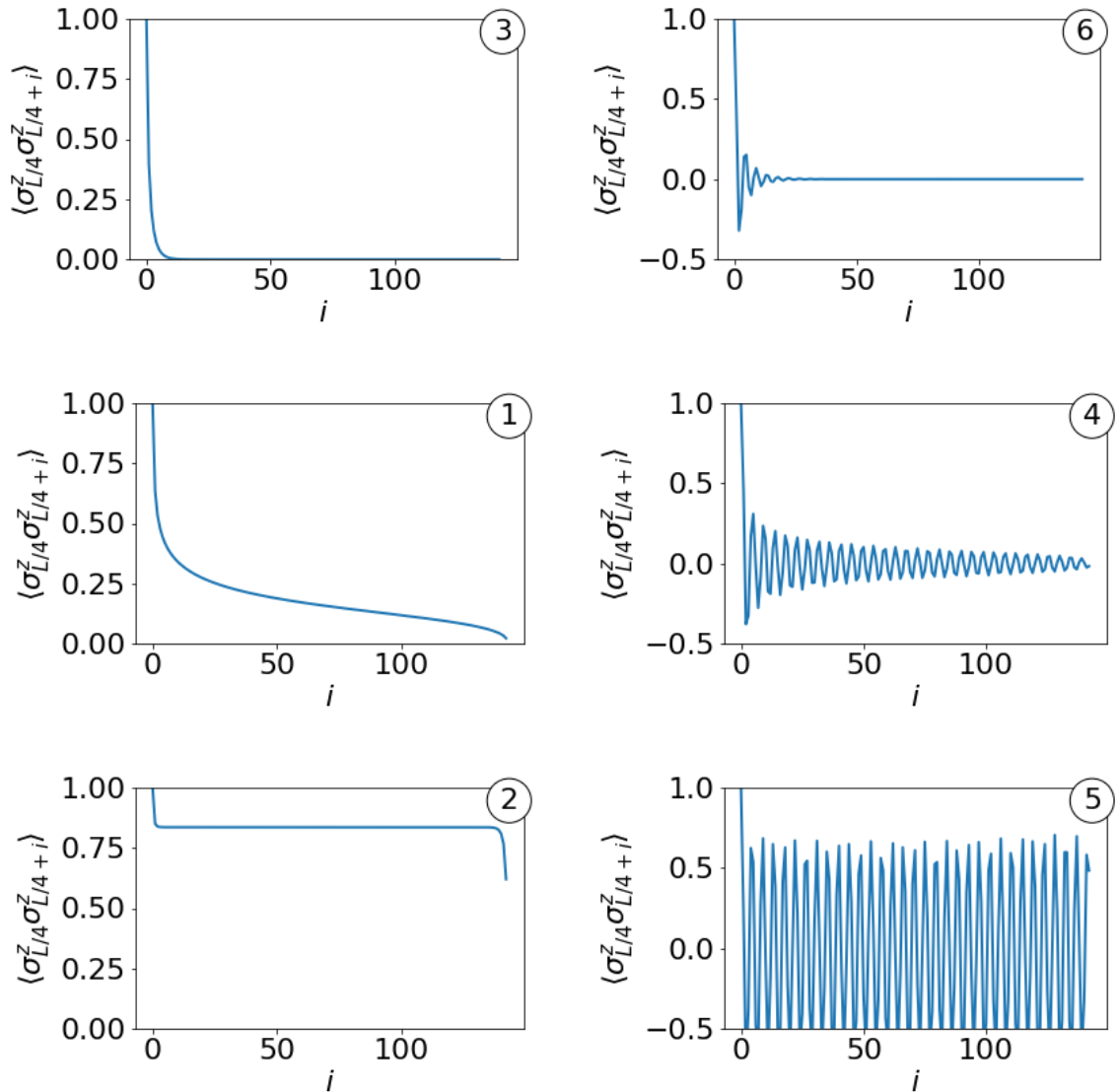
Figure 2.6: Figure taken from Ref. [86]. Spin-spin correlator $\langle \sigma^z_{L/4}\sigma^z_{L/4+i}\rangle$ for the clean Majorana chain in spin formulation, Eq. (2.17), at weak repulsive interaction $g/t = -0.10$ (left) and medium repulsive interaction $g/t = -0.85$ with no staggering, $t_1/t_2 = 1$ (middle), and staggering $t_1/t_2 = 1.39$ (top) and $t_1/t_2 = 0.72$ (bottom). The labels from 1 to 6 correspond to those in Fig. 2.5. The system size is $L = 190$, in the indices $L/4$ denotes the integer part $[190/4] = 47$. In the case of weak repulsive interaction, the correlator is strictly positive, while in the case of medium repulsive interaction, the correlator oscillates as a function of distance and can take on negative values. On the self-dual line (middle), both correlators decay slowly (presumably algebraically) to zero. Above the self-dual line the correlators decay in both regimes quickly (presumably exponentially) to zero. Below the self-dual line, the correlator becomes constant for weak repulsive interaction and oscillates with a constant amplitude for medium repulsive interaction. The drop of the correlator in the bottom left panel (with label 2) near $i = 3L/4$ (i.e., at the right end of the curve) is a boundary effect.
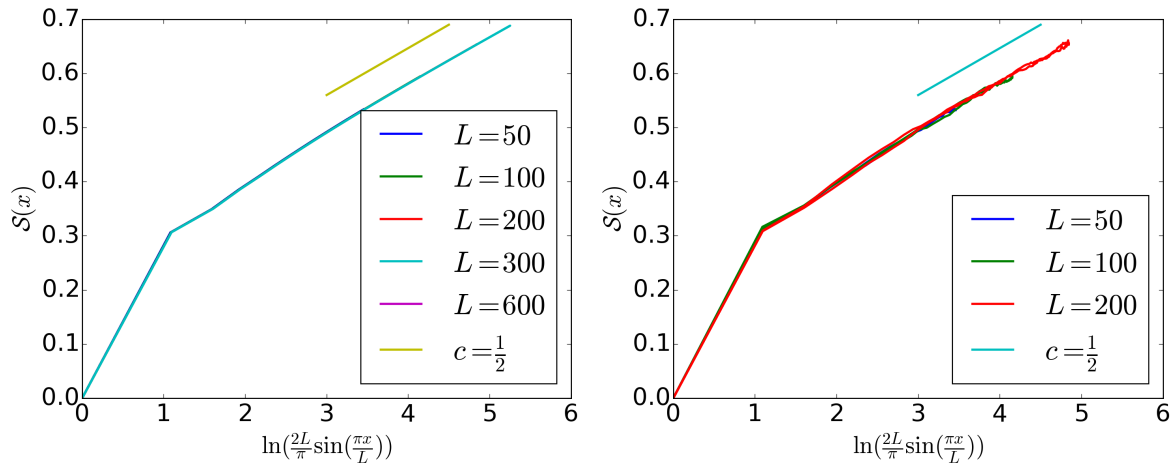
Figure 2.7: Entanglement entropy of the clean (left) and disordered (right) Majorana chain with attractive interaction $g = 1$ vs the scaling function Eq. (2.18) for different system sizes. For the clean system, the central charge is $c = \frac{1}{2}$ in agreement with Ref. [31]. For the disordered system, the effective central charge is also found to be $c = \frac{1}{2}$.

2.3.2.2 Weak repulsive interaction

The clean system stays critical with $c = \frac{1}{2}$ for weak repulsive interaction [31], $-0.28 < g < 0$, see Sec. 2.3.1.1 and the left panel of Fig. 2.8. An important finding was that adding disorder leads to localization, see right panel of Fig. 2.8. This appears to happen for arbitrarily weak repulsive interaction and arbitrarily weak disorder. Due to duality, the critical lines have to be mirror symmetric around the self-dual line with respect to staggering. This holds also when the system is disordered. For this reason, the critical line cannot simply bend away from the self dual line. If the system localizes on the self-dual line, there are therefore two possibilities: (i) the critical line splits up into two lines with equal central charge, leaving a gapped region around the self-dual line, or (ii) the critical line terminates, and the transition between the region above and below the self-dual line becomes first order. It is shown in Appendix A.3 by treating the interaction at the mean-field level that the criticality is pinned to the self-dual line for all interaction values and disorder strengths. This excludes the option (i), thus implying that the possibility (ii) is realized.

Thus one can conclude that, for a disordered system with repulsive interaction, the symmetry gets spontaneously broken, and the system undergoes a first-order transition on the self-dual line. This is also reflected in the distance dependence of the spin correlation function. Specifically, it was found that, depending on the disorder configuration, this correlation function shows one of two types of behavior: it either very quickly decays to zero or fluctuates around a value of order unity. This is illustrated in Fig. 2.9 where the results for two disorder configurations are shown. These two types of behavior correspond to two topologically distinct phases, as is clear from the comparison of two panels of Fig. 2.9 with the top left and bottom left panels of Fig. 2.6. In the latter figure, the topologically distinct phases were induced by staggering (in a clean model) breaking explicitly the symmetry with respect to the duality transformation. One can now see that adding disorder breaks spontaneously the symmetry of the system on the no-staggering line, placing it into one of the two topologically distinct phases. The transition between these two topological phases becomes thus first order.

Figure 2.8: Entanglement entropy of the clean (left) and disordered (right) Majorana chain with weak repulsive interaction $g = -0.1$ vs the scaling function Eq. (2.18) for different system sizes. In the clean system, the central charge stays at $c = \frac{1}{2}$, while in the disordered case the entanglement entropy saturates indicating localized behavior.


Figure 2.9: Spin-spin correlator $\langle \sigma_{L/4}^z \sigma_{L/4+i}^z \rangle$ of the Majorana chain with weak repulsive interaction $g = -0.1$ at length $L = 200$. The two panels represent two different disorder configurations. In the left panel, the correlator decays quickly to zero, which is analogous to the behavior in the presence of staggering $g_1/g_2 = t_1/t_2 > 1$, see top right panel of Fig. 2.6. In the right panel, the correlation function fluctuates, staying of order $O(1)$. This is similar to the region with staggering $g_1/g_2 = t_1/t_2 < 1$, see bottom right panel of Fig. 2.6. This behavior reflects the fact that disorder breaks spontaneously the symmetry with respect to duality transformation, placing the system in one of two topological phases.
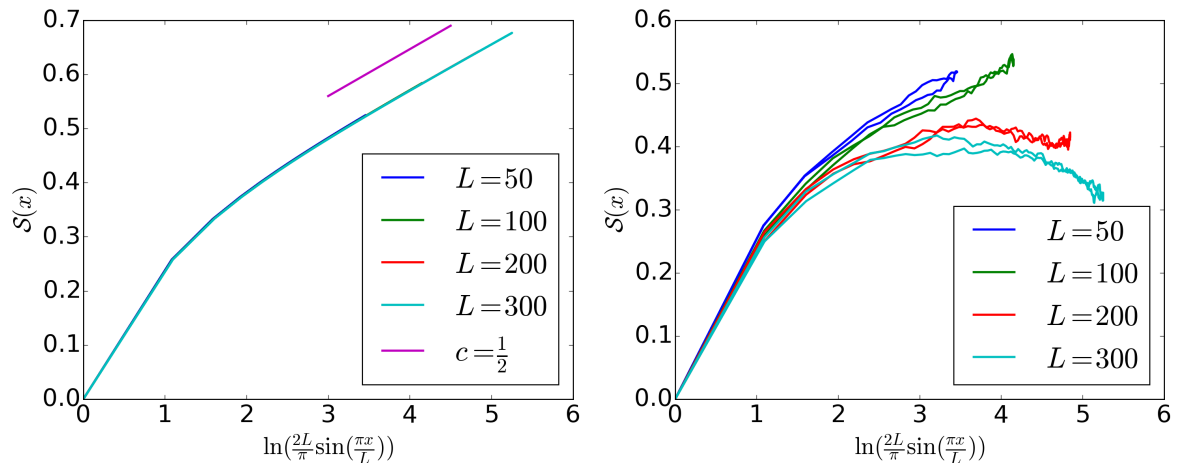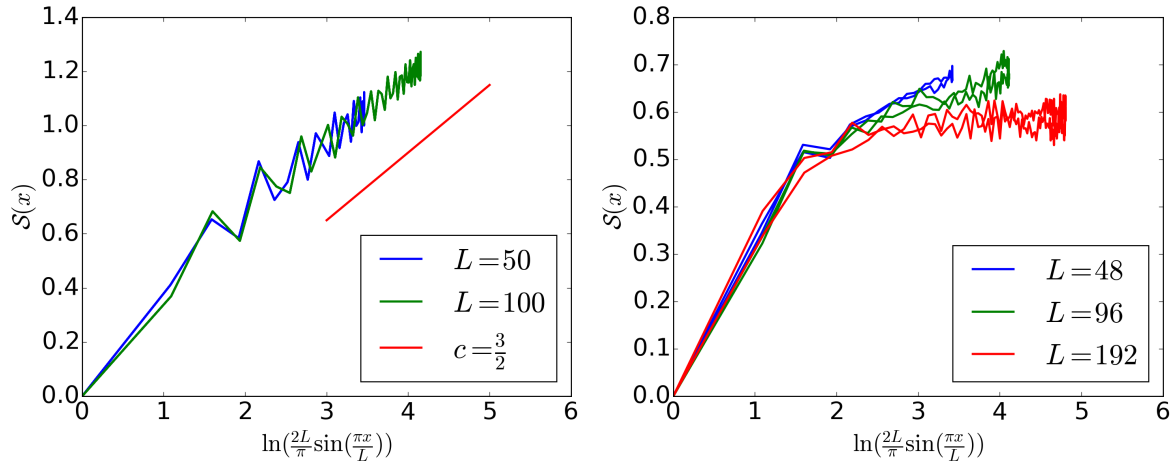
Figure 2.10: Entanglement entropy of the clean (left) and disordered (right) Majorana chain with medium repulsive interaction $g = -0.5$ vs the scaling function Eq. (2.18). The central charge of the clean system is $\frac{3}{2}$ as predicted [31]. On the other hand, the entanglement entropy saturates for the disordered case, implying localization.

2.3.2.3 Medium repulsive interaction

If the repulsive interaction is in the interval $-2.86 < g < -0.28$ the clean system is in the Ising+LL[31] phase which is characterized by a central charge of $\frac{3}{2}$, see Sec. 2.3.1.2 and left panel of Fig. 2.10. The results show that, similar to the case of weak repulsive interaction, disorder leads to localized behavior also in this range of interaction, see right panel of Fig. 2.10. This was also found in Ref. [41].

As in the case of weak repulsive interaction, the spontaneous symmetry breaking by disorder can be visualized by inspecting the spin-spin correlation function for individual realizations of disorder. Again two distinct types of behavior were found that are illustrated in Fig. 2.11: oscillations without decay or with a quick decay. The behavior shown in the left panel of Fig. 2.11 corresponds to that in the clean model in the Ising+LL phase with staggering $g_1/g_2 = t_1/t_2 < 1$, see bottom right panel of Fig. 2.6, while the behavior shown in the right panel of Fig. 2.11 corresponds to that in the clean model with staggering $g_1/g_2 = t_1/t_2 > 1$, see top right panel of Fig. 2.6. Thus, the symmetry between the two topological phases gets broken spontaneously by disorder in full analogy with the weak-repulsion regime. A comparison of Figs. 2.9 and 2.11 reveals an interesting difference between the weak-repulsion and intermediate-repulsion topological phases. Specifically, in the latter case the correlator shows oscillations around zero, thus changing sign.

2.3.3 Disordered Fermionic chain

It has been found that the (sufficiently weak) interaction for a disordered interacting fermionic chain, Eq. (2.2), does not modify the behavior of the disordered system in Ref. [86]. Both for $r = 1$ and $r = 2$ the interacting system remains critical and has the central charge $c = \ln 2$ characteristic for the infinite-randomness fixed point. The interaction must be RG irrelevant.
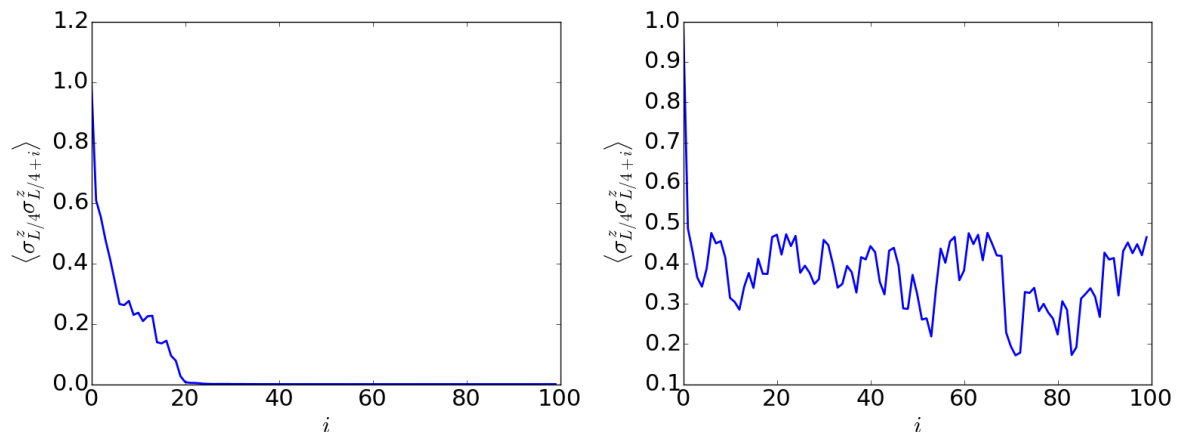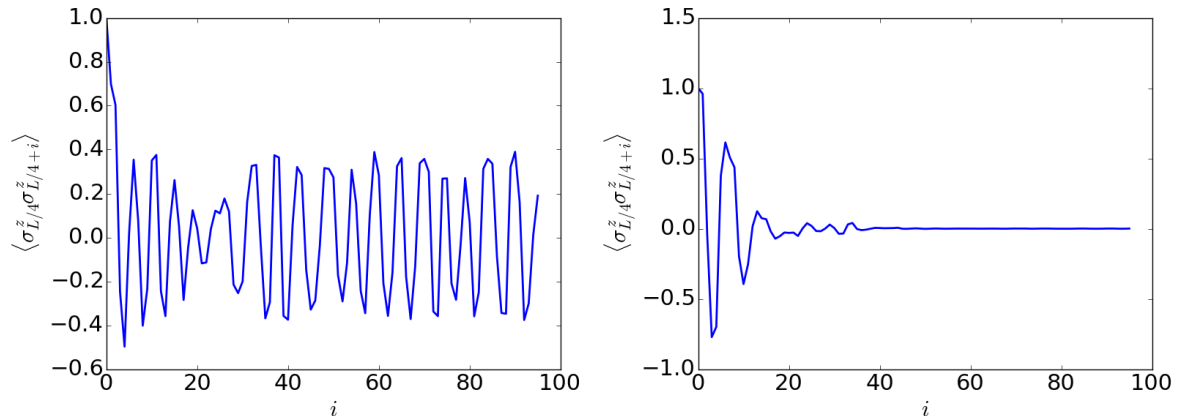
Figure 2.11: Spin-spin correlators $\langle \sigma^z_{L/4} \sigma^z_{L/4+i} \rangle$ of the Majorana chain for medium repulsive interaction $g = -0.5$ with length $L = 200$. Two panels show results for two different disorder configurations that lead to vastly different behavior. In the plot for the first disorder configuration, the spin correlator oscillates around zero with an amplitude essentially independent of distance. This behavior is analogous to the one induced by staggering in the region below the self-dual line, see bottom right panel of Fig. 2.6. For the other disorder configuration, the spin-spin correlator oscillates and quickly drops to zero. This behavior corresponds to the one induced by staggering in the region above the no-staggering line, see top right panel of Fig. 2.6. The disorder thus breaks spontaneously the symmetry between the two topologically distinct phases. In both phases, the correlator takes negative values for some distances, at variance with the case of weak repulsive interaction, Fig. 2.9.

2.4 Renormalization group around the clean fixed point

Numerical results of Sec. 2.3.2 for a disordered interacting Majorana chain indicate that in the presence of disorder an interaction of either sign becomes relevant. To get the corresponding analytical insight, one has to consider a model with both interaction and disorder, which is an extremely challenging problem. In this Section this problem is approached by starting from a clean interacting Majorana chain and exploring the effect of weak disorder.

The stability of the clean fixed points of the interacting fermionic and Majorana models can be probed by a weak-disorder momentum-space RG analysis, which is introduced in Sec. 1.1.3. For this purpose, the low-energy theory is considered in the continuum limit. In the case of the complex fermionic chain, this is a Luttinger liquid (LL) theory. In the Majorana case, it is either a Majorana theory ($c = \frac{1}{2}$, Ising phase) or a Majorana theory with an additional LL sector ($c = \frac{3}{2}$, Ising +LL phase), depending on the interaction strength. The density-density parts of the interaction are quadratic in Luttinger theory and renormalize the Luttinger parameter K.

In these continuum theories, disorder appears as a random-mass term. Choosing nonzero average of the mass or a constant non-vanishing mass corresponds to staggering. By including such terms, one can draw conclusions about the stability with respect to staggering, which is another goal of the present section. This should help understanding the appearance of extended gapless phases that were found by DMRG numerical analysis in Sec. 2.3.1.

It is shown below that at any of the fixed points of the clean Majorana chain (Ising or Ising +

LL), the disorder becomes relevant and flows to the strong-coupling regime. This happens also for the complex-fermion fixed point (Luttinger liquid) if the interaction is not too strong. This will lead to the complementary analysis in Sec. 2.5, where disorder is treated exactly and the interaction as a perturbation.

2.4.1 Majorana: $c = 1/2$ fixed point

The continuum decomposition in slow modes $\gamma_{R/L}$ of the lattice Majorana operators γ_j is

$$\gamma_j = \gamma_R + (-1)^j \gamma_L. \tag{2.19}$$

For a Majorana low energy theory disorder corresponds to a random-mass term of the form:

$$S_m^{\mathrm{maj}} = \int \mathrm{d}\tau \mathrm{d}x \; m(x)\gamma_R(\tau, x)\gamma_L(\tau, x). \tag{2.20}$$

A constant mass $m(x) = m_0$ corresponds to a staggering; it directly opens a gap of size m_0.

The disorder is assumed to be Gaussian white noise with $\langle m(x)m(y) \rangle = D\delta(x - y)$; one can also include a staggering by introducing a non-zero mean $\langle m(x) \rangle = m_0$. Treating the disorder by using the replica trick, one straightforwardly finds that the term generated by disorder has (upon disorder averaging) the scaling dimension 1 and is therefore relevant in the RG sense. This term drives the system away from the clean fixed point. However, this does not necessarily mean that the system becomes gapped. For example, in the non-interacting case (and in the absence of staggering) the system flows to the critical infinite-randomness fixed point [40]. It means, however, that an analysis based on RG around the clean fixed point is insufficient to understand the infrared physics of the problem and suggests a complementary approach as implemented in Sec. 2.5.

Finally it should be noted that no relevant interaction term can be written down in a Majorana low-energy theory. Indeed, the interaction should involve at least four Majorana operators with scaling dimension $\frac{1}{2}$ each and two derivatives with dimension -1. The most relevant term thus has scaling dimension -2 and is strongly irrelevant.

2.4.2 Complex fermions: Luttinger liquid ($c = 1$) fixed point

Lattice operators c_j are related to their continuum versions $\psi_{R/L}$ as follows

$$c_j = i^j \psi_R + (-i)^j \psi_L. \tag{2.21}$$

In the presence of interaction $g \neq 0$, bosonization has to be employed. Here the following conventions relating the fermionic fields $\psi_{R/L}$ to the bosonic fields ϕ, θ are used:

$$\psi_{R/L} = U_{R/L} \exp\left(\phi \pm \theta\right). \tag{2.22}$$

The Klein factors $U_{R/L}$ are not important in any of the following considerations.

The exact dependence of the Luttinger parameter K on the parameters of the lattice model is known[144]:

$$g/t = -\cos\left(\pi/2K\right). \tag{2.23}$$

Disorder and staggering introduce a mass term of the form:

$$S_m^{\mathrm{LL}} = \int \mathrm{d}\tau \mathrm{d}x \, m(x)(\psi_R^\dagger(\tau, x)\psi_L(\tau, x) + h.c.). \tag{2.24}$$

The scaling dimension of a constant mass term is $2 - K$. This means that it is relevant for $K < 2$, which corresponds, in terms of the microscopic parameters, to the interval $-1 < g/t < 0.7$ covering almost the whole range of critical theories, $|g/t| < 1$.

The scaling dimension of the quartic term generated by disorder, as obtained by the replica field-theory approach, is $3 - 2K$. It depends thus on the Luttinger parameter K whether the disorder is relevant or not. Specifically, for $g/t < 0.5$ the disorder is relevant, while for $0.5 < g/t < 1$ the model remains at the clean fixed point in the presence of weak disorder. The latter prediction has been checked by DMRG [86] for the scaling of the entanglement entropy at strong attractive interaction, $g = 0.8$, and sufficiently weak disorder. One finds $c = 1$, as expected for the system at the Luttinger-liquid fixed point. Around the non-interacting limit, i.e. for K sufficiently close to unity, the disorder is strongly relevant, as expected.

The allowed interaction terms are discussed briefly as perturbations to the Luttinger liquid fixed point. They are of three types. First, the density-density interaction is marginal and simply modifies the value of K. Second, terms that are of higher order in ψ or contain gradients are strongly irrelevant. Finally, the staggering yields sine and cosine terms that are relevant in a range of K (in particular, around the weak-interaction point $K = 1$). On the self-dual line, these latter terms are absent.

2.4.3 Majorana chain: Ising+Luttinger liquid ($c = 3/2$) fixed point

This subsection turns to the $c = \frac{3}{2}$ fixed point of the clean Majorana chain that emerges in a range of medium-strength repulsive interactions, as discussed above. It was suggested in Ref. [31] that, at this fixed point, the low-energy theory consist of Majorana and Luttinger-liquid sectors, see also Sec. 2.2.2.4 and 2.3.1.2. This can be understood by considering the quadratic form of the action including the third-nearest-neighbor hopping which is generated by mean-field treatment of the interaction (or, alternatively, under RG flow):

$$H = i \sum_j \left[t_j \gamma_j \gamma_{j+1} + t' \gamma_j \gamma_{j+3} \right]. \tag{2.25}$$

The third-nearest-neighbor hopping term modifies the dispersion such that there are now three Majorana modes, or, equivalently, a fermionic mode emerge in addition to the Majorana mode. The lattice Majorana operator γ_j then has the following low-energy decomposition [31]:

$$\begin{aligned} \gamma_j = {}& 2\gamma_L + 2(-1)^j \gamma_R \\ & + \exp(-ik_0 j)\Psi_L^\dagger + \exp\left(+i(k_0 + \pi)j\right)\Psi_R^\dagger + h.c. \, , \end{aligned} \tag{2.26}$$

where k_0 is the effective Fermi momentum. The interaction $g\gamma_j \gamma_{j+1}\gamma_{j+2}\gamma_{j+3}$ generates now the density-density interaction of the fermions Ψ_R, Ψ_L. To treat this interaction exactly, the bosonization approach is employed. Another interaction term couples the resulting Luttinger liquid to the Majoranas with strength g', see Eq. (A.2).

Next, the stability with respect to staggering is discussed. The kinetic term $\gamma_j \gamma_{j+1}$ has oscillatory components with wave vectors $k_i = 0$, k_0, $k_0 + \pi$, $2k_0$, $2k_0 + \pi$, and π. A constant mass term $m(x) = m$

Table 2.1: The RG scaling dimension and relevance range of couplings in the low-energy theory of the Ising+LL phase. Forward scattering is gauged away, see Appendix A.1. The five remaining (dimensionless) coupling constants corresponding to disorder are labeled y_{k_i}, where k_i refers to the momentum component. The dimensionless interaction strength is denoted by $y' = g'au^{-1}$, where a is the lattice spacing and u the LL velocity. The clean Ising+LL phase of the Majorana chain is characterized by $K < 1$ and remains stable with respect to coupling between the Ising and LL sectors as long as [31] $\frac{1}{4} < K < 1$.

coupling	dimension	relevant in
y_{k_0}	$2 - \frac{1}{2}(K + K^{-1})$	$0.27 < K < 3.8$
$y_{k_0+\pi}$	$2 - \frac{1}{2}(K + K^{-1})$	$0.27 < K < 3.8$
y_{2k_0}	$3 - 2(K + K^{-1})$	$0 < K < 2$
$y_{2k_0+\pi}$	$3 - 2K$	$K < 1.5$
y_π	$3 - 2K^{-1}$	$0.67 < K$
y'	$1 - K^{-1}$	$1 < K$

describing staggering couples to the π-component of the kinetic term:

$$S_m = \int \mathrm{d}^2r \left[-8m\gamma_L\gamma_R + 4m\cos k_0 \cos 2\theta \right]. \tag{2.27}$$

The Majoranas are then immediately gapped out. On the other hand, the cosine term in the Luttinger-liquid sector is relevant only for $K > \frac{1}{2}$. There is therefore a region of the interaction strength where the Luttinger liquid is stable towards staggering. This explains the existence of the extended gapless phase with $c = 1$ observed numerically, see Fig. 2.3 and the schematic phase diagram in Fig. 2.5.

Now the effect of disorder that is treated as a weak perturbation is analyzed. Combining the oscillatory components of the kinetic term $\gamma_j\gamma_{j+1}$ (with the six wave vectors listed above) with the corresponding Fourier components of the random mass yields non-oscillatory contributions. One therefore gets six independent disorder couplings D_{k_i} that coincide at the beginning of the RG flow but renormalize differently. Details on implementation of the RG procedure are presented in Appendix A.1. In Eq. (A.1), the disorder-induced terms in the action (with the replica formalism used to average over disorder) are presented. While the forward scattering D_0 cannot be gauged away straightforwardly, a more detailed calculation shows that it does not change the results presented here.

In Table 2.1, the scaling dimensions of the disorder couplings resulting from the corresponding RG equations are listed. They determine the range of K in which the disorder-induced terms are RG-relevant. One can observe that at least one of the couplings is relevant for any value of K, i.e. the disorder always drives the system aways from the clean fixed point. In analogy with the conventional Giamarchi-Schulz RG [154], the RG equations for the disorder-induced couplings are complemented by the flow equation for the Luttinger constant K:

$$\frac{\partial K}{\partial \ell} = -\frac{1}{2}\left[K^2 - \frac{(1+K^2)(3-2K)}{2} \right] y_{2k_0+\pi}$$
$$+ \frac{1}{2}\left[1 - \frac{(1+K^2)(3-2/K)}{2} \right] y_\pi. \tag{2.28}$$

Here $y_{2k_0+\pi} = \pi^{-1}D_{2k_0+\pi}au^{-2}$ and $y_\pi = 16\cos^2 k_0 D_\pi au^{-2}$ are dimensionless coupling constants for the disorder-induced terms with momentum component k_i in terms of lattice spacing a and Luttinger-liquid velocity u. In Eq. (2.28), kept only the contribution of the couplings $y_{2k_0+\pi}$ and y_π to the renormalization of K has been kept. In principle, the other couplings y_{k_i} also contribute to this renormalization; however, they are less relevant for K around unity, so that their contributions have been neglected.

A brief summary of main conclusions that can be drawn from this RG is as follows. First, the Ising+LL clean fixed point is stable towards interaction. Indeed, this phase is characterized by a repulsive interaction, hence $K < 1$, so that the y' coupling is irrelevant. In fact, a higher order coupling between the LL and Majorana sectors becomes relevant for very strong interaction [31], $K < 1/4$, so that the range of stability in the absence of disorder is $1/4 < K < 1$. Second, over an extended parameter regime, the staggering is irrelevant in agreement with the numerical results of Sec. 2.3.1.2, see Fig. 2.3. Third, and most importantly, the disorder at the Ising+LL fixed point always runs to strong coupling. In other words, this fixed point is unstable with respect to disorder.

The results obtained in Sec. 2.4 demonstrate that the weak-disorder analysis is not sufficient for Majorana chain, both in the $c = 1/2$ and $c = 3/2$ phases of the clean system. The RG relevance of disorder is also supported by the analysis in Appendix A.3 where the exact treatment of disorder is combined with mean-field treatment of the interaction. The disorder is also RG relevant for the complex-fermion chain if the interaction is not too strong. These results motivate one to perform in Sec. 2.5 a complementary analysis. One can start there from an exact treatment of disorder and will include interaction as a weak perturbation.

2.5 Strong randomness fixed point: Eigenfunction statistics and effect of interactions

In Sec. 2.4, one could see that the combined effect of interaction and disorder cannot be understood as a perturbation around the clean interacting fixed point. Specifically, it has been established that disorder is strongly relevant at the clean fixed point, thus quickly increasing under RG. It is known that, in the absence of interaction, this RG flow leads to the critical infinite-randomness fixed point. It is thus a natural question whether this fixed point is stable or not with respect to interaction. This question is addressed in the present section. The analysis has much in common with the investigation of stability of 2D surface states of disordered topological superconductors with respect to interaction [29, 30]. A closely related physics controls the enhancement of superconducting and ferromagnetic instabilities by disorder in 2D systems [137, 155]. Further, there are close connections with the analysis of the anomalous scaling dimension of interaction in context of the study of decoherence and the dynamical critical exponent at the quantum-Hall transition with short-range interaction[156–158].

In the clean system, the relevance or irrelevance of an operator can be often established by a relatively straightforward power counting. As an example, this was done in Sec. 2.4 to show that interactions are RG-irrelevant at the clean fixed point of the Majorana chain. In the presence of disorder, the situation is much more complex, since the multifractal nature of wavefunctions as well as a non-trivial scaling of the density of states have to be taken into account. Formally, this disorder-induced renormalization of the interaction U can be expressed by an RG equation of the form [29, 30]

$$\frac{\mathrm{d}\ln U}{\mathrm{d}\ln L} = x_1 - x_2^{(U)}. \tag{2.29}$$

Here x_1 is the scaling dimension of the density of states of a non-interacting system, with $x_1 > 0$ and $x_1 < 0$ corresponding to the cases of vanishing and diverging density of states, respectively. Further, $x_2^{(U)}$ is the scaling dimension of the four-fermion interaction operator with respect to the non-interacting theory. For a detailed derivation of Eq. (2.29) the reader is referred to Appendix C of Ref. [30]. If the right-hand side of Eq. (2.29) is positive, the interaction is relevant at the non-interacting fixed point; otherwise it is irrelevant.

For a short-range interaction, and in the case when cancellations of the Hartree-Fock type (see below) are not operative, the scaling dimension $x_2^{(U)}$ is equal to the dimension x_2 of the squared density of states (which is also a local four-fermion operator). For the clean system x_2 is simply equal to $2x_1$ but for a disordered system one has in general $x_2 < x_1$ in view of multifractality (characterizing strong fluctuations of the density of states) [30, 87, 159]. Specifically,

$$x_2 = \Delta_2 + 2x_1, \tag{2.30}$$

where $\Delta_2 < 0$ is the anomalous dimension of the fourth moment of the eigenfunction ($\langle U_{i\alpha}^4 \rangle$ in the notations used below). In this situation of the maximally relevant interaction (no suppression due to Hartree-Fock cancellation or other reasons), Eq. (2.29) takes the form

$$\frac{\mathrm{d}\ln U}{\mathrm{d}\ln L} = -x_1 - \Delta_2. \tag{2.31}$$

The sum of two exponents $-x_1$ and $-\Delta_2$ in the r.h.s. of Eq. (2.31) determines the scaling with L of the product νC_H of the density of states ν and the Hartree-type correlation function C_H [defined in Eq. (2.48) below] for $r = 0$.

In general, $x_2^{(U)} \geq x_2$ since the effect of the interaction can be suppressed due to Hartree-Fock-type cancellation. In this generic situation, one has, in analogy with Eq. (2.30),

$$x_2^{(U)} = \Delta_2^{(U)} + 2x_1, \tag{2.32}$$

where $\Delta_2^{(U)}$ is the anomalous dimension of the eigenstate correlation function C_{HF} corresponding to the matrix element of the interaction (and thus taking into account possible Hartree-Fock-type cancellations; see, e.g., Eq. (2.47) for the case of complex fermions below). Substituting Eq. (2.32) into Eq. (2.29), one gets

$$\frac{\mathrm{d}\ln U}{\mathrm{d}\ln L} = -x_1 - \Delta_2^{(U)}. \tag{2.33}$$

The sum of the exponents $-x_1$ and $-\Delta_2^{(U)}$ in the r.h.s. of Eq. (2.33) corresponds to the scaling with L of the product νC_{HF} of the density of states and the correlation function C_{HF}. Below the explicit form of this correlation function is determined by inspecting the expectation value of the interaction operator and analyze the scaling of the product νC_{HF} with L for the models of complex fermions (Sec. 2.5.2) and for the Majorana model (Sec. 2.5.3).

If $-x_1 - \Delta_2^{(U)} < 0$, the interaction is RG-irrelevant, i.e., the non-interacting fixed point is stable with respect to inclusion of not too strong interaction. In the opposite case, $-x_1 - \Delta_2^{(U)} > 0$, the interaction is RG-relevant and drives the system away from the non-interacting fixed point. It was found in previous works on the effect of interaction at critical points of higher spatial dimensionality ($d > 1$, with a particular focus on 2D systems)[29, 30, 136, 137, 156–158] that both these scenarios can

be realized. Whether the interaction is relevant or irrelevant depends on the specific non-interacting critical theory considered (i.e., spatial dimensionality as well as symmetry and topology class). As is shown below, both scenarios are also realized in the context of the present work (1D critical systems of class BDI): the interaction is irrelevant in the case of complex fermions and relevant in the Majorana model.

The present problem has much in common with $d > 1$ Anderson-localization critical points studied in previous works where the multifractality induces strong correlations between eigenstates at different spatial points and different energies (often referred to as Chalker scaling). In fact, critical singularities are particularly strong in the present case. In the more conventional situation, both the density of states ν and the eigenstate correlation function C_{HF} (and, correspondingly, their product) exhibit a power-law scaling with L, so that the indices x_1 and $\Delta_2^{(U)}$ are constant (i.e., independent on L). On the other hand, below it can be seen that in the present problem ν and (in the complex-fermion case) C_{HF} scale exponentially with $\sqrt{L}$, which means that x_1 and $\Delta_2^{(U)}$ are L-dependent and increase (by absolute value) at large L as $\sqrt{L}/\ln L$. This is a manifestation of the fact that the 1D critical point studied here is characterized by very strong multifractality. The sign of $-x_1 - \Delta_2^{(U)}$ at large L is of interest here, since it controls the behavior (increase or decrease) of νC_{HF} in the limit $L \to \infty$.

For systems of the symmetry class BDI in one dimension with an odd number of channels, the density of states at low energies ϵ exhibits the well known Dyson singularity[39, 101, 160, 161]:

$$\nu(\epsilon) \sim \frac{1}{\epsilon |\ln \epsilon|^3}. \tag{2.34}$$

One can use this result to calculate the position of the n-th level in a system of the length L:

$$\int_0^{\epsilon_n} \nu(\epsilon) \mathrm{d}\epsilon = \frac{n}{L}, \tag{2.35}$$

which yields

$$\epsilon_n \sim \exp\left(-c\sqrt{\frac{L}{n}}\right), \qquad\qquad c = O(1). \tag{2.36}$$

The scaling (2.36) is verified numerically for the model with the nearest-neighbor hopping matrix elements uniformly distributed over the interval $t_j \in [0, 1]$. The numerical data shown in Fig. 2.12 fully confirm the analytical prediction, with the coefficient $c \approx 0.5$. Thus, one can write down the density of states around the lowest energy state ϵ_1 as a function of the length L:

$$\nu(0, L) \sim \frac{\exp\left(c\sqrt{L}\right)}{L^{\frac{3}{2}}}. \tag{2.37}$$

This behavior is not of power-law type, i.e., it is not characterized by a critical exponent in the usual sense. One can define, however, an L-dependent scaling exponent $x_1(L) = -\partial \ln \nu / \partial \ln L$, with the result

$$-x_1(L) = c\frac{\sqrt{L}}{\ln(L)} - \frac{3}{2}. \tag{2.38}$$
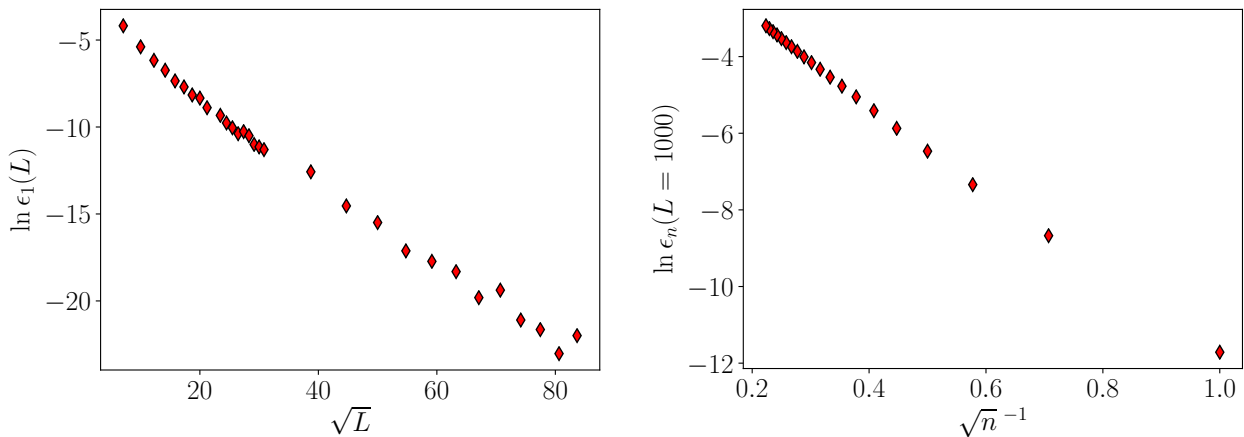
Figure 2.12: Figure taken from Ref. [86]. Numerical verification of Eq. (2.36) for the scaling of energies of the low-lying single-particle states. *Left:* Average energy of the lowest eigenstate ϵ_1 as a function of the square root of the system size, confirming the scaling $-\ln \epsilon_1 \propto \sqrt{L}$. *Right:* average energy ϵ_n of the n-th eigenstate vs $1/\sqrt{n}$ in a system of size $L = 1000$, confirming the scaling $-\ln \epsilon_n \propto n^{-1/2}$ for sufficiently low energies. Combination of the scaling behavior observed in both panels confirms Eq. (2.36).

The result (2.38) for the scaling dimension of the density of states is valid both for the Majorana and complex fermions, since these models are equivalent in the absence of interaction. (The only difference is that the number of states is halved in the case of Majoranas.) On the other hand, it will be shown that the scaling dimension $\Delta_2^{(U)}$ of the interaction is completely different in these two models. The scaling of interaction by a will be explored by a numerical approach, supporting the results by analytical arguments.

2.5.1 Scaling of interaction

In order to determine the scaling of the interaction operators, the interaction matrix elements are expressed in terms of linear combinations of products of single-particle eigenfunctions. These expression in terms of the eigenfunctions are then numerically averaged over the disorder. The numerical results will be also supported by analytical considerations (Appendix 2.5.4).

One can start by writing the most general non-interacting Hamiltonian of a 1D system of size L of symmetry class BDI [159]:

$$H = \frac{1}{2} \left(\begin{array}{cc} \mathbf{c}_A^\dagger & \mathbf{c}_B^\dagger \end{array} \right) \left(\begin{array}{cc} 0 & \underline{h} \\ \underline{h} & 0 \end{array} \right) \left(\begin{array}{c} \mathbf{c}_A \\ \mathbf{c}_B \end{array} \right), \tag{2.39}$$

where $\underline{h}$ is a real matrix and $c_{A,B}$, $c_{A,B}^\dagger$ are onsite operators acting on the two sublattices. In the case of the complex fermionic chain, these are fermionic creation and annihilation operators, in the case of the Majorana chain one has $c_A = \gamma_A = c_A^\dagger$ and $c_B = i\gamma_B = -c_B^\dagger$, where $\gamma_{A,B}$ are the real Majorana operators in Eq. (2.12). Diagonalizing the $L \times L$ matrix in Eq. (2.39), one can rewrite the Hamiltonian

in the basis of operators which correspond to the single particle excitations of the system,

$$H = \frac{1}{2} \begin{pmatrix} \mathbf{d}_+^\dagger & \mathbf{d}_-^\dagger \end{pmatrix} \begin{pmatrix} \underline{\epsilon} & 0 \\ 0 & -\underline{\epsilon} \end{pmatrix} \begin{pmatrix} \mathbf{d}_+ \\ \mathbf{d}_- \end{pmatrix}, \tag{2.40}$$

$$c_i = \sum_\alpha U_{i,\alpha} d_\alpha. \tag{2.41}$$

Here $\underline{\epsilon}$ is a diagonal matrix with eigenvalues $0 < \epsilon_1 < \epsilon_2 < \ldots < \epsilon_{L/2}$. In the case of complex fermions, the eigenvectors $U_{i\alpha}$ are just the conventional single-particle wavefunction $\Psi_\alpha(i)$. The ground state $|\Omega\rangle$ of the Hamiltonian can be written in terms of the operators d and the zero-particle state $|0\rangle$:

$$|\Omega\rangle = \prod_{\alpha, \epsilon_\alpha < 0} d_\alpha^\dagger |0\rangle. \tag{2.42}$$

This immediately yields the action of the d operators on the ground state:

$$d_\alpha |\Omega\rangle = 0 \qquad \text{for } \epsilon_\alpha > 0, \tag{2.43}$$

$$d_\alpha^\dagger |\Omega\rangle = 0 \qquad \text{for } \epsilon_\alpha < 0. \tag{2.44}$$

A general q-body interaction operator can be expressed as sum of products of annihilation and creation operators of the following type:

$$\hat{O} = \prod_{i=1}^{q} c_{a_i}^\dagger \prod_{j=q+1}^{2q} c_{a_j}$$

$$= \sum_{\{\alpha_i, \alpha_j\}} \prod_{i=1}^{q} U_{a_i, \alpha_i} d_{\alpha_i}^\dagger \prod_{j=q+1}^{2q} U_{a_j, \alpha_j} d_{\alpha_j}. \tag{2.45}$$

The expectation value of the operator $\hat{O}$ over any eigenstate of a non-interacting system can now be calculated by substituting Eq. (2.41) into Eq.(2.45):

$$\langle \hat{O} \rangle = \sum_{\{\alpha_i, \alpha_j\}} \prod_{i,j} U_{a_i, \alpha_i} U_{a_j, \alpha_j} \left\langle \prod_{i=1}^{q} d_{\alpha_i}^\dagger \prod_{j=q+1}^{2q} d_{\alpha_j} \right\rangle. \tag{2.46}$$

The expectation value that stands as a last factor on the right-hand side of Eq. (2.46) is non-zero only if the states α_i and α_j are pairwise identical; in this case, it is equal to $+1$ or -1, depending on parity of the permutation of indices. The right-hand side of Eq. (2.46) thus represents an algebraic sum of products of single-particle eigenfunctions.

The terms in Eq. (2.46) are therefore the matrix elements of the interaction operator expressed as products of the eigenvector amplitudes $U_{i\alpha}$. For the conventional case of two-body interaction, $q = 2$, Eq. (2.46) reduces, in accordance with the Wick theorem, to a sum over pairs of states α_1, α_2. For a given choice of sites $a_1, \ldots a_4$ and eigenstates α_1, α_2, there will be two different terms in Eq. (2.46) (plus analogous terms obtained by an interchange $\alpha_1 \leftrightarrow \alpha_2$), that have a meaning of Hartree and Fock terms. These two terms correspond to the order of subscripts $\alpha_1 \alpha_2 \alpha_1 \alpha_2$ and $\alpha_1 \alpha_2 \alpha_2 \alpha_1$ of d operators in Eq. (2.46). As usual, the Fock term will enter with a relative minus sign due to Fermi statistics. Below one can see that, in close analogy with Refs. [156–158], a major cancellation between the Hartree and Fock terms will play a crucial role for the RG-irrelevance of the interaction in the

case of complex fermions. In the case of Majorana system, there is a third term, originating from the following order of indices $\alpha_1\alpha_1\alpha_2\alpha_2$, as discussed in detail in Sec. 2.5.3. It has a meaning of the Cooper term, and its emergence it is not surprising since Majorana excitations are characteristic for superconducting systems. As is shown below, the presence of this term spoils the cancellation, making the total interaction matrix element relevant in the RG sense.

In general, the disorder averaged value of matrix elements under consideration is a function of the system size and of the energies of the $q = 2$ eigenvectors involved. To obtain the scaling of these functions numerically, matrices of the form Eq. (2.39) for different system sizes were generated and the lowest 20 eigenvectors calculated. Then for each pair of eigenvectors the corresponding matrix elements entering Eq. (2.46) were calculated. This procedure yields pairs of energies and the associated matrix elements, which then have to be averaged over disorder configurations. This is done by making a histogram and averaging the matrix elements over each energy bin. It is worth emphasizing that for the cases of logarithmic dependence of the matrix elements on energy, the correct choice of averaging procedure is crucial. In these cases, the bin sizes are chosen such that the number of data points is the same in every bin.

Even though here one is dealing with eigenstates of a non-interacting problem, the corresponding numerical analysis is a rather challenging endeavour. This is particularly true in the regime of strong Hartree-Fock cancellations that plays a central role below. In this situation, the default double precision that provides approximately 15 decimal digits is by far insufficient. As will be shown below, the Hartree and Fock terms can be the same within hundreds of digits for large systems. The calculations have therefore been performed with at least 500 decimal digit floating point arithmetics.

Since for large ($L \gg 1$) systems full diagonalization becomes slow (typically $\mathcal{O}(L^3)$)) and memory intensive (at least $\mathcal{O}(L^2)$)), a transfer matrix approach is chosen to compute the first few eigenvectors U_{i,ϵ_i}. The characteristic polynomial $\lambda(\epsilon)$ is evaluated by L column expansions in $\mathcal{O}(L^2)$. The first 20 eigenenergies ϵ_i closest to zero are obtained as roots of $\lambda(\epsilon)$. The ϵ_i are plugged into the transfer matrix equation (A.3) to find U_{i,ϵ_i}.

For all following calculations, the hopping parameters are chosen to be uniformly distributed over the interval $t_j \in [0, 1]$.

2.5.2 Complex fermion chain

Start with the model of the complex fermionic chain described by Hamiltonian Eq. (2.2). Due to chiral symmetry, each state with positive energy has a partner state with negative energy. For zero chemical potential, in the non-interacting ground state all states of negative energy are occupied and all of positive energy are free. The relevance of the interaction in the infrared limit is controlled by its matrix elements evaluated on low-lying eigenstates. To obtain the appropriate eigenstate correlation function, the expectation value of the interaction, Eq. (2.46) is inspected. For each pair of sites i, j, one has a contribution

$$
\begin{aligned}
\langle c_i^\dagger c_{i+r}^\dagger c_i c_{i+r} \rangle &= \sum_{\alpha\beta\gamma\delta} U_{i\alpha} U_{i\beta} U_{i+r,\gamma} U_{i+r,\delta} \langle d_\alpha^\dagger d_\beta^\dagger d_\gamma d_\delta \rangle \\
&= \sum_{\{\alpha\beta\}} \Big(U_{i\alpha} U_{i\alpha} U_{i+r,\beta} U_{i+r,\beta} \\
&\quad - U_{i\alpha} U_{i\beta} U_{i+r,\alpha} U_{i+r,\beta} \Big),
\end{aligned}
\tag{2.47}
$$

with the summation in the last expression going over pairs of filled states. The two terms in brackets after the last equality sign in Eq. (2.47) correspond to the conventional Hartree and Fock diagrams. Define the corresponding correlation functions of two single-particle eigenfunctions as functions of energies, distance, and system size:

$$C_{\mathrm{H}}(\epsilon_\alpha, \epsilon_\beta, r, L) = \langle U_{i\alpha} U_{i\alpha} U_{i+r,\beta} U_{i+r,\beta} \rangle_{\mathrm{dis}}, \tag{2.48}$$

$$C_{\mathrm{F}}(\epsilon_\alpha, \epsilon_\beta, r, L) = \langle U_{i\alpha} U_{i\beta} U_{i+r,\alpha} U_{i+r,\beta} \rangle_{\mathrm{dis}}, \tag{2.49}$$

$$C_{\mathrm{HF}}(\epsilon_\alpha, \epsilon_\beta, r, L) = \langle U_{i\alpha} U_{i\alpha} U_{i+r,\beta} U_{i+r,\beta}$$
$$- U_{i\alpha} U_{i\beta} U_{i+r,\alpha} U_{i+r,\beta} \rangle_{\mathrm{dis}}, \tag{2.50}$$

where $\langle \ldots \rangle_{\mathrm{dis}}$ denotes the disorder averaging. Below, the scaling of the full correlation function $C_{\mathrm{HF}} = C_{\mathrm{H}} - C_{\mathrm{F}}$ is analyzed in order to determine the scaling exponent $\Delta_2^{(U)}$ of the interaction. It was verified in Refs. [156–158] that this scaling dimension also controls the scaling of interaction matrix elements also in the second order of the perturbation theory. Thus it is expected that the analysis of the scaling of the correlation function (2.50) with energy and the distance is sufficient for establishing the relevance or irrelevance of the interaction near the non-interacting fixed point.

The following comment concerning the r dependence is in order here. The DMRG results presented above dealt with short range interaction $r \sim 1$ only. At the same time, one may be also interested in effects of long-range interaction, in which case one needs to know the scaling of correlations functions of the type (2.50) with r. Furthermore, the analysis of correlations of eigenstates at the infinite-randomness fixed point constitutes by itself a very interesting problem (with r dependence being an important ingredient), as it represents a remarkable example of strong-coupling Anderson-localization critical point (see also a discussion in Sec. 2.6). Since the r dependence of the correlation functions (2.48), (2.49), (2.50) can be tackled by the same approach, below the correlation functions not only for $r \sim 1$ but also for arbitrary r are analyzed. In the end, when the RG relevance of the short-range interaction is studied, the focus is on the correlations at $r \sim 1$. This comment applies also to the Majorana chain, Sec. 2.5.3.

2.5.2.1 Single-wavefunction correlations

Terms where the two wavefunctions are identical, i.e. $\alpha = \beta$, do not contribute to the interaction matrix element C_{HF} as the Hartree and Fock terms cancel each other exactly. Nevertheless, it is useful to start the analysis by considering the single-wavefunction correlations for two reasons. First, they can be particularly well understood analytically and can serve as a benchmark to the numerical calculations. Second, it can be seen below that some of properties of the single-wavefunction correlations translate to correlations of two eigenstates that are important for the interacting models. The two-point, single-wavefunction correlation function C_2 is defined to be:

$$C_2(\epsilon_\alpha, r, L) = \langle U_{i\alpha} U_{i\alpha} U_{i+r,\alpha} U_{i+r,\alpha} \rangle_{\mathrm{dis}}. \tag{2.51}$$
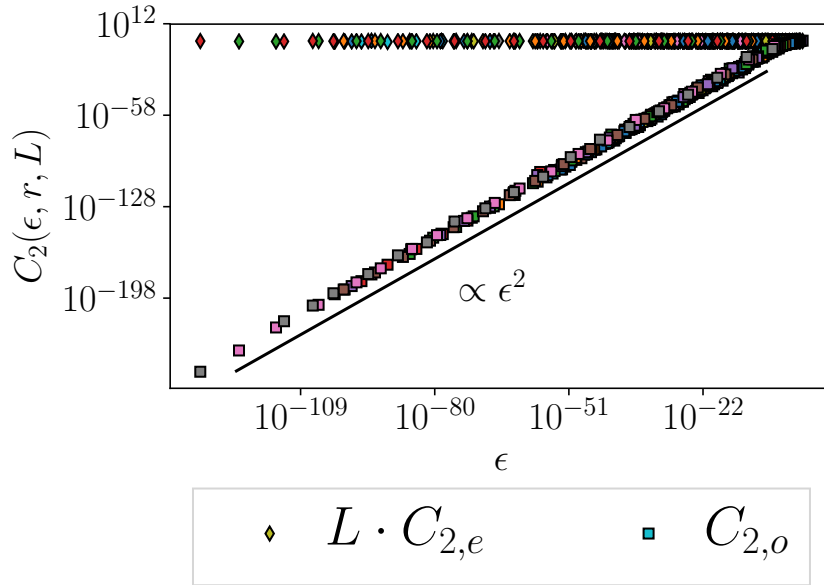
Figure 2.13: Figure taken from Ref. [86]. Single-wavefunction correlation function for short even distance, $LC_2(\epsilon, r = 2, L)$, and short odd distance, $C_2(\epsilon, r = 1, L)$, vs energy ϵ in systems with size L from 100 to 10000 (distinct colors). For $r = 2$ the correlation function is independent on energy, while for $r = 1$ it scales as ϵ^2 (and thus is strongly suppressed at low energy), as predicted analytically.
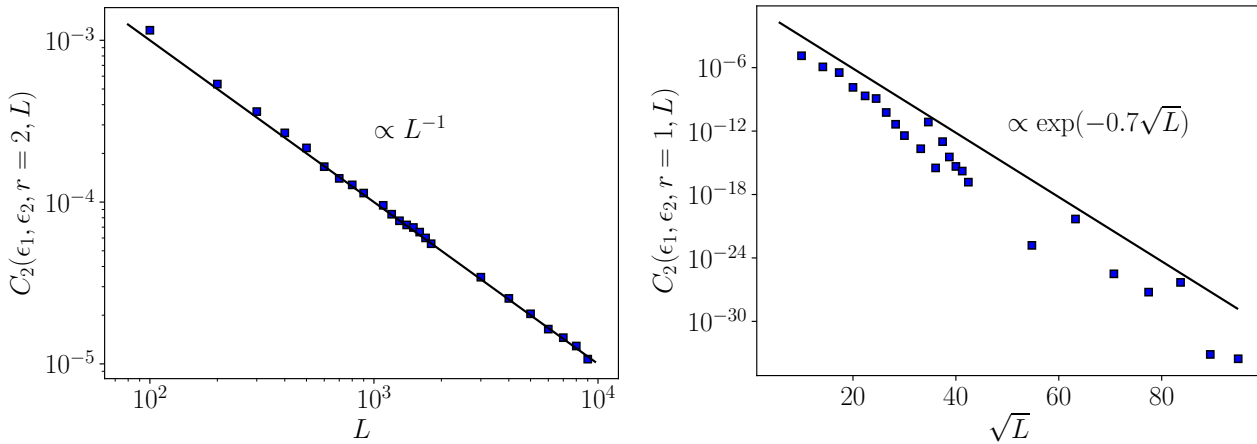
Figure 2.14: Figure taken from Ref. [86]. Single-wavefunction correlation function for short even distances $C_2(\epsilon_1, r = 2, L)$ (left panel) and short odd distances $C_2(\epsilon_1, r = 1, L)$ (right panel) vs system size L. For $r = 2$ the data confirm the analytically predicted scaling, $C_2 \sim L^{-1}$, see first line of Eq. (2.53). For odd distance, the correlation function decreases quickly with L since the lowest energy ϵ_1 approaches zero exponentially fast, $\epsilon_1 \sim \exp\{-c\sqrt{L}\}$ and in view of $C_2 \propto \epsilon_1^2$, see Appendix A.2.

For zero energy, the wavefunction U_r can be expressed exactly in terms of a given realization of

disorder [39]. The zero-energy wavefunctions belong entirely to one of the two sublattices (i.e., vanish on the other sublattice). If one looks at the wave function moments at a single point, their scaling is similar to that of a fully localized wavefunction[39, 159]:

$$\langle U_r^{2q} \rangle \sim \frac{1}{L}, \tag{2.52}$$

for $q > 0$. At the same time, the spatial decay of the correlation function C_2 at zero energy is only algebraic, which is a property of a critical system [39]:

$$C_2(0, r, L) \sim \begin{cases} r^{-\frac{3}{2}} L^{-1}, & \text{r even;} \\ 0 & \text{r odd.} \end{cases} \tag{2.53}$$

For finite energy, this formula for even-r correlations is expected to hold as long as the distance r is smaller than the localization length, $r \lesssim \xi_\epsilon$. The latter was predicted [39] to scale with energy as

$$\xi_\epsilon \propto |\ln \epsilon|^2. \tag{2.54}$$

Using Eq. (2.36) with $n = 1$, one can see that $\xi_\epsilon \sim L$ for the lowest eigenstate.

As to odd-distance correlations, they are not exactly zero for a non-zero energy ϵ. Indeed, the absence of odd-distance correlations, Eq. (2.53), is a consequence of the chiral symmetry which is exact at $\epsilon = 0$ but is violated at non-zero energy and gets progressively more strongly broken when the energy increases. Thus, the odd-r correlations should be strongly suppressed relative to even-r correlations at low energies, with the suppression becoming stronger with lowering energy. As shown in Appendix A.2, the corresponding suppression factor is $\sim \epsilon^2$ for odd $r \sim 1$.

Now the analytical predictions are confronted with numerical simulations. In Fig. 2.13 the numerically obtained energy dependence of the correlation function C_2 is shown for fixed $L = 1200$ and fixed small separation r. Specifically, $r = 2$ is chosen for the even case and $r = 1$ for the odd case. It is seen that the even-distance correlations are essentially independent of ϵ. This is the expected behavior: indeed, for $r \sim 1$, the condition $r \ll \xi_\epsilon$ is fulfilled as long as $|\ln \epsilon| \gg 1$, i.e., essentially in the whole range of $\ln \epsilon$. On the other hand, the odd-distance correlations strongly increase with energy. Specifically, the data unambiguously demonstrate the ϵ^2 behavior of $C_2(\epsilon, r, L)$ for small odd r discussed above and derived analytically in Appendix A.2. It is worth emphasizing the enormously broad range of variation of the energy ϵ and the correlation function C_2 (odd r) in Fig. 2.13: about 130 and 260 orders of magnitude, respectively!

Finally, in Fig. 2.14 the dependence of the correlation function $C_2(\epsilon_1, r, L)$ on the system size L is shown for even ($r = 2$) and odd ($r = 1$) distance. In the even case, the correlation function does not depend on energy for small r, so that the fact that ϵ_1 is different from zero and varies with L is of no importance. The expected result is given by the first line of Eq. (2.53). The numerical data in the right panel of Fig. 2.14 confirm the predicted L^{-1} scaling. For odd r the decay of $C_2(\epsilon_1, r, L)$ with L should be exponentially fast due to $C_2(\epsilon, r, L) \sim \epsilon^2$ and the fact that the energy ϵ_1 approaches zero exponentially with increasing L, see Eq.(2.36). This yields the analytical expectation $C_2(\epsilon_1, r, L) \sim \exp\left(-2c\sqrt{L}\right)$, in full agreement with the data in the right panel of Fig. 2.14.

2.5.2.2 Two wavefunction correlations

Matrix elements for two-wavefunction correlations, Eqs. (2.48)–(2.50), are calculated using two eigenstates with different energies for a given disorder configuration, and then averaging over disorder. The

energy levels are on average distributed as $\epsilon_n \sim \exp\left(-c\sqrt{L/n}\right)$, which means that, for $L \gg 1$ and $n \sim 1$, one of the energies will almost always be much larger than the other one. Since the energy breaks the chiral symmetry, it is expected that the matrix elements will essentially depend only on the larger of the two energies and only weakly on the lower one.

The correlation functions at criticality depend thus on the (larger) energy ϵ, the length L and the distance r. As for the single-eigenstate correlation function, Sec. 2.5.2.1, the behavior for even and odd distances r is very different. At low energy ϵ, and short even distances, it is natural to expect that C_H behaves, in similarity with with C_2, as a power-law in r and L. Such a power-law behavior is also analogous to that of eigenfunction correlation functions at critical points of localization-delocalization transitions in systems of higher dimensionality, see Ref. [159]. As to the expected for of the energy dependence, recall that, at the critical point that is studied, the logarithm of the energy scales as a power law of the length, see Eq. (2.36). Therefore, it is natural to expect a power-law scaling of C_H with respect to $\ln \epsilon$. Therefore, for short even distances r and low energy ϵ, the correlation function C_H is expected to have the scaling form (see also [162]):

$$C_H(0, \epsilon, r, L) \sim \frac{|\ln \epsilon|^\alpha}{r^\beta L^\gamma}, \qquad r - \text{even}. \tag{2.55}$$

This equation should hold at criticality, so that the necessary condition is $r \lesssim \xi_\epsilon$. Now the exponents α, β, and γ are determined by a numerical analysis. The numerical results are supported by analytical considerations (details of which are presented in Appendix 2.5.4) yielding the values of the exponents α and γ.

To find the exponent α in the critical scaling of C_H, Eq. (2.55), in the right panel of Fig. 2.15 the dependence of correlation functions is shown at small even distance ($r = 2$) and fixed L on the energy. The slope yields $\alpha = 1$. To determine γ, in the left panel of the same figure the dependence on the system size L is plotted. Here the correlation functions are evaluated for two lowest eigenstates, so that the energy ϵ is equal to $\epsilon_2 = \exp\left(-c\sqrt{L/2}\right)$. The obtained scaling of C_H is L^{-2}; taking into account the $|\ln \epsilon_2| \sim L^{1/2}$ factor originating from the energy dependence of C_H, on finds that $\gamma = 2$. The scaling of C_H in the critical regime is thus given by

$$C_H(0, \epsilon, r, L) \sim \frac{|\ln \epsilon|}{L^2 r^{\frac{3}{2}}}, \qquad r - \text{even}. \tag{2.56}$$

The Fock correlation function C_F for even r is found to behave in exactly the same way. This is what should be expected: indeed, a particular case of a small even r is $r = 0$, for which C_H and C_F are identically the same. The $|\ln \epsilon| L^{-2}$ scaling of C_H and C_F for even r is confirmed also by an analytical calculation of the averaged square of the Green function, see Appendix 2.5.4 for details.

As was discussed above, the effect of the interaction is controlled by the scaling of the Hartree-Fock correlation function $C_{HF} = C_H - C_F$. As the data in Fig. 2.15 clearly demonstrate, this function is strongly suppressed (for small even r) as compared to C_H and C_F. This is also what is expected analytically: as shown in Appendix A.2, the suppression factor is $\sim \epsilon^4$. If the correlation function is evaluated for two lowest eigenstates, the suppression factor becomes $\sim \epsilon_2^4 \sim \exp\left(-4c\sqrt{L/2}\right)$. These analytical predictions are fully confirmed by the numerical results, see Fig. 2.15.

Figure 2.15: Figure taken from Ref. [86]. Hartree, Fock, and Hartree-Fock correlation functions $C_H(\epsilon_1, \epsilon, r = 2, L)$, $C_F(\epsilon_1, \epsilon, r = 2, L)$, and $C_{HF}(\epsilon_1, \epsilon, r = 2, L)$ for a small even distance ($r = 2$). *Upper left:* Scaling of C_H, C_F with L at $\epsilon = \epsilon_2$. The slope yields the power-law scaling $\sim L^{-3/2}$, implying a relation $\gamma - \alpha/2 = 3/2$ for the exponents in Eq. (2.55). *Upper right:* Scaling with energy at fixed $L = 4000$. The slope implies the scaling $\sim |\ln \epsilon|$ for C_H, implying the exponent $\alpha = 1$ in Eq. (2.55). In both panels, the Fock correlation function is nearly equal to the Hartree one, which is a characteristic feature of the critical regime for even r. As a result, C_{HF} shown in lower panels is strongly suppressed with respect to C_H and C_F. *Lower left:* Scaling of C_{HF} with L at $\epsilon = \epsilon_2$. *Lower right:* Scaling of C_{HF} with energy for L from 100 to 10000. The slope agrees with the analytical prediction $C_{HF} \propto \epsilon^4$.

The considerations now turn to the critical behavior of the correlation functions at odd r. One expects that odd-distance correlation functions C_H and C_F are suppressed with respect to their even-r counterparts. The reason for this is the same as for the the single-eigenfunction correlation function C_2, Sec. 2.5.2.1: odd-r correlations necessarily involve wavefunctions on different sublattices. As shown in Appendix A.2, the suppression factor for C_H and C_F with odd r is the same ($\sim \epsilon^2$) as for C_2. Again, this translates into an exponential suppression with respect to L.

This expectation is fully supported by the numerical results shown in Fig. 2.16. Note that, in the case of odd r, the Fock term is considerably smaller than the Hartree one (even though the dominant

scaling factor is the same). This, the Hartree-Fock cancellation is not operative and $C_{HF} \simeq C_H$.
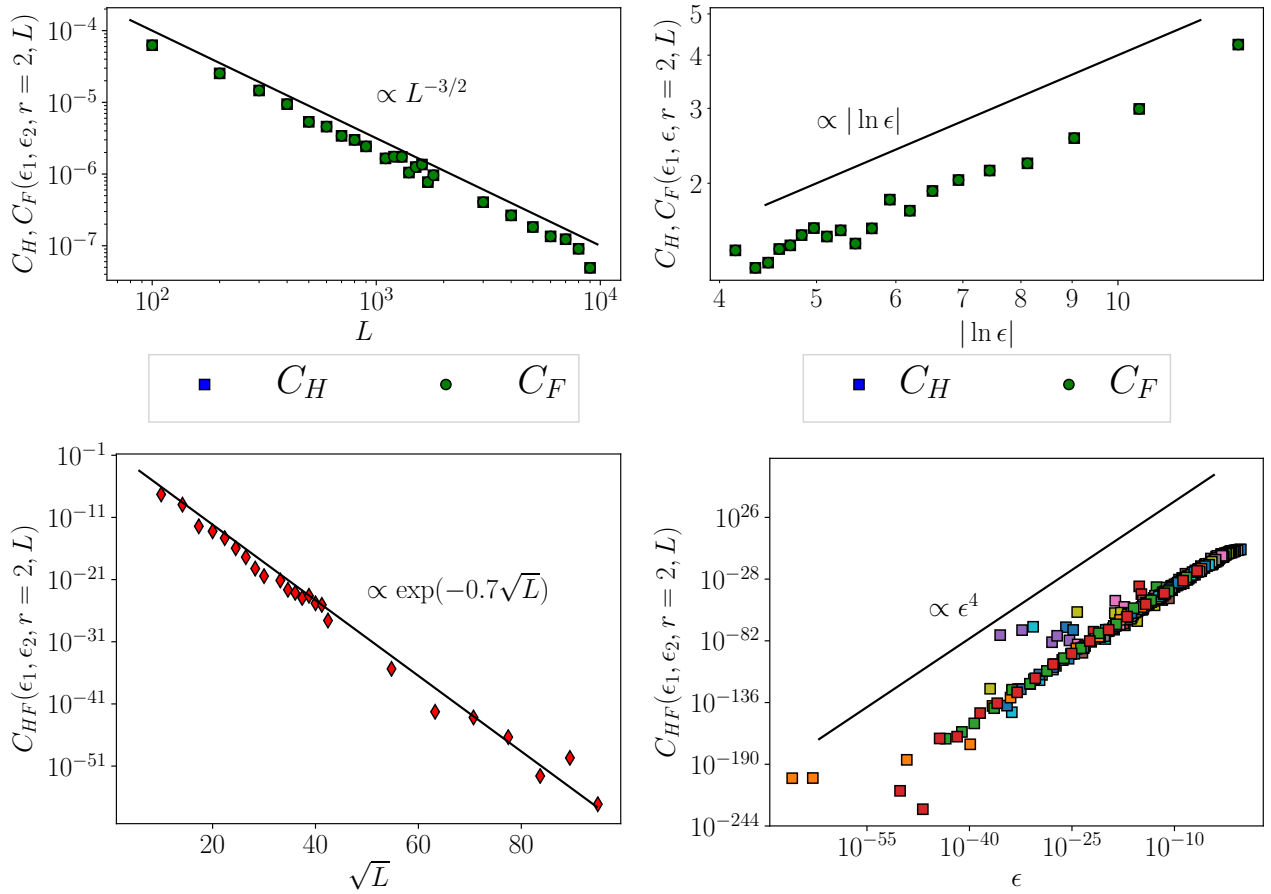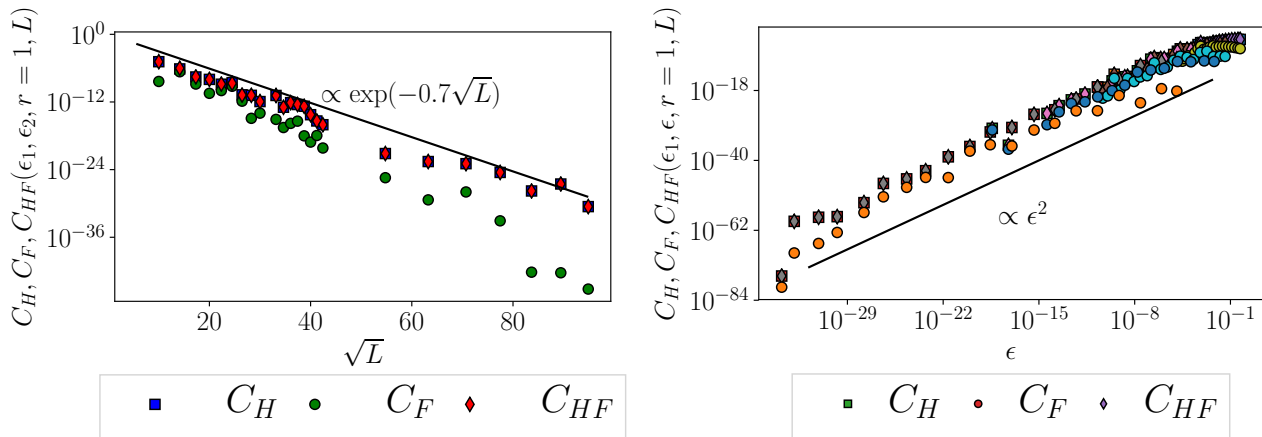

Figure 2.16: Figure taken from Ref. [86]. Hartree, Fock, and Hartree-Fock correlation functions $C_H(\epsilon_1, \epsilon, r = 1, L)$, $C_F(\epsilon_1, \epsilon, r = 1, L)$, and $C_{HF}(\epsilon_1, \epsilon, r = 1, L)$ for a small odd distance ($r = 1$). *Left:* Scaling with L at $\epsilon = \epsilon_2$. *Right:* Scaling with energy. Different colors represent different lengths from 100 to 10000. In both panels, the Fock correlation function is much smaller than the Hartree one, so that $C_{HF} \simeq C_H$. The dominant scaling for both C_H and C_F is $\sim \epsilon^2$ (which translates into an exponential length dependence in the left panel). The data for the Fock term suggest an additional power-law dependence on length.

One thus finds that the Hartree-Fock correlation function C_{HF} is strongly suppressed at criticality (i.e., at short distances r and low energies, so that $r \ll \xi_\epsilon$). This is valid both for even distances (due to cancellation between Hartree and Fock terms) and for odd distances (due to different sublattices entering). The suppression factor is $\sim \epsilon^4$ for even r and $\sim \epsilon^2$ for odd r.

One can return now to the question of RG relevance of the interaction which is determined by Eq. (2.29). The right-hand-side of this equation characterizes the scaling of the product of the interaction matrix element and the density of states with the system size L. The matrix element to be used here is the Hartree-Fock correlation function, see Eqs. (2.47) and (2.50). If this product increases (decreases) with L, the interaction is relevant (respectively, irrelevant). The density of states increases exponentially with $\sqrt{L}$ according to Eq. (2.37) or, equivalently, as $1/\epsilon$ with energy (up to logarithmic correction), see Eq. (2.34). On the other hand, the Hartree-Fock correlation function decreases as ϵ^2 (odd r) or ϵ^4 (even r). Thus, the suppression of the Hartree-Fock correlation function is stronger than the increase of the density of states, and the product decays as a power of ϵ (and thus exponentially with respect to $\sqrt{L}$). To illustrate this, in Fig. 2.17 the product $\nu(L)C_{HF}(\epsilon_1, \epsilon_2, r, L)$ is plotted for small even and odd distances ($r = 2$ and $r = 1$, respectively) as a function of L. One can see that both functions decrease exponentially with $\sqrt{L}$ as expected. This implies that the interaction in Eq. (2.2) is irrelevant in the presence of disorder, and the system stays critical (at the infinite-randomness fixed point), at least for sufficiently weak interaction. This is in agreement with the DMRG results presented in Sec. 2.3 and with real-space-RG findings of Refs. [38, 40].

Above the focus was on the behavior of two-eigenstate correlation functions at criticality ($r \ll \xi_\epsilon$), since such functions emerge when one explores the effect of short-range interaction ($r \sim 1$). On the

other hand, the behavior of the correlation functions at $r \gtrsim \xi_\epsilon$ may be of interest in other contexts. This behavior is briefly discussed in the Appendix of Ref. [86].
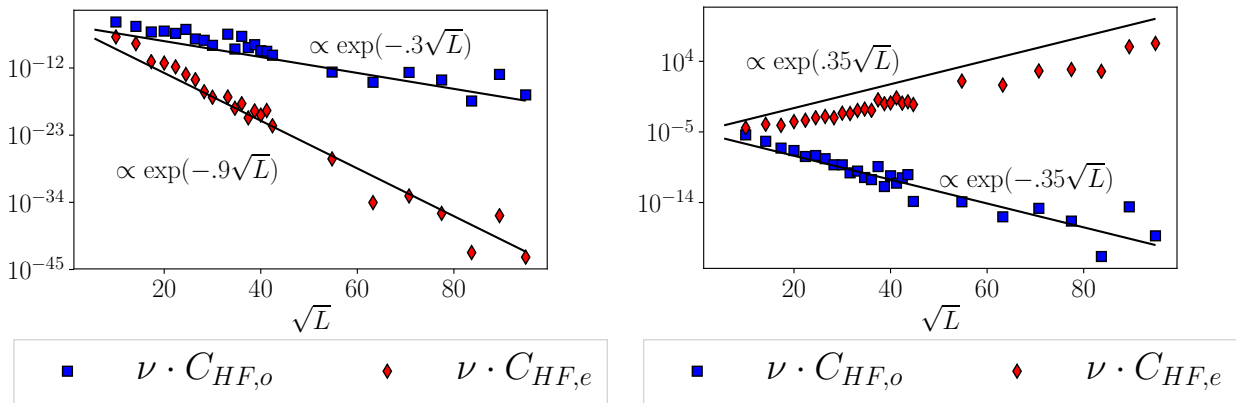
Figure 2.17: *Left panel:* Figure taken from Ref. [86]. RG irrelevance of interaction at the infinite-randomness fixed point of the complex-fermion chain. Product $\nu(L)C_{HF}(\epsilon_1, \epsilon_2, r, L)$ of the Hartree-Fock matrix element at criticality multiplied by the density of states plotted versus the system size L, for odd ($r = 1$, blue symbols) and even ($r = 2$, red symbols). Both for even and odd distances, the product decreases quickly with L (as an exponential of $\sqrt{L}$), implying that the interaction is irrelevant.
Right panel: Figure taken from Ref. [86]. RG (ir)relevance of interaction at the infinite-randomness fixed point of the majorana chain. Product $\nu(L)C_{HF,\{e,o\}}(\epsilon_1, \epsilon_2, r, L)$ of the Hartree-Fock correlation function and the density of states is plotted versus the system size L. Blue symbols: $\nu C_{HF,o}$ for $r = 2$ quickly decreases with L, implying RG irrelevance of the corresponding interaction terms. Red symbols: $\nu C_{HF,e}$ for $r = 4$ quickly increases with L, indicating RG relevance of the corresponding interaction term.

2.5.3 Majorana chain

Now the attention turns to the Majorana model. The simplest interaction term in this model was presented in Eq. (2.13). However, as was already mentioned before, any fourth order interaction term containing an even number of Majoranas on even sites (and an even number of those on on odd sites) is consistent with the symmetries of the Hamiltonian. In fact, such terms will be generated by RG even if one starts from the simplest term only as in Eq. (2.13).

The interaction in Eq. (2.13) is generalized by introducing a distance r separating two nearest-neighbor pairs of Majoranas:

$$H_{\text{int}} = \sum_{j=1}^{L} \gamma_j \gamma_{j+1} \gamma_{j+r} \gamma_{j+r+1}. \tag{2.57}$$

($r \geq 2$ is assumed to be even but it is not particularly important here.) Such a term is analogous to the odd-r interaction term in the case of complex fermions, see Eq. (2.3), since it involves two operators on even sites and two on odd sites.

The Majorana operators γ_i can be expressed in terms of the Bogoliubov operators d_α using the definitions $c_A = \gamma_A = c_A^\dagger$ and $c_B = i\gamma_B = -c_B^\dagger$, and then diagonalizing the Hamiltonian matrix, see Sec. 2.5.1. At variance with the complex fermion case, these $2L$ Bogolyubov operators are not independent: each operator is related to its chiral conjugate with inverse sign of the energy, $d_\alpha^\dagger = d_{\bar\alpha}$. Thus, one can express the Majorana operators by using only wavefunctions and Bogolyubov operators associated with positive energies:

$$\gamma_j = \sum_{\epsilon_\alpha > 0} U_{\alpha,j}(d_\alpha + d_\alpha^\dagger) \qquad (j \text{ even}), \qquad (2.58)$$

$$\gamma_j = \sum_{\epsilon_\alpha > 0} iU_{\alpha,j}(d_\alpha - d_\alpha^\dagger) \qquad (j \text{ odd}). \qquad (2.59)$$

Via the same token, the whole Hilbert space of the problem is obtained by acting with operators $d_\alpha^\dagger$ with $\epsilon_\alpha > 0$ on the vacuum state.

Substituting Eq. (2.59) into an interaction term in (2.57), one can evaluate the expectation value of the interaction term over any basis state of the non-interacting Fock space. For example, averaging over the non-interacting vacuum (that is annihilated by all d_α with positive energies), one gets

$$\langle \gamma_k \gamma_{k+1} \gamma_{k+r} \gamma_{k+r+1} \rangle$$
$$= - \sum_{\alpha > 0; \beta > 0} \Big(U_{k,\alpha} U_{k+1,\alpha} U_{k+r,\beta} U_{k+r+1,\beta}$$
$$+ U_{k,\alpha} U_{k+1,\beta} U_{k+r,\alpha} U_{k+r+1,\beta}$$
$$- U_{k\alpha} U_{k+1\beta} U_{k+r,\beta} U_{k+r+1,\alpha} \Big). \qquad (2.60)$$

Three terms here correspond to the expansion of a Pfaffian that is a general form of the Majorana Wick's theorem[163].

The matrix element in Eq. (2.60) consists of three terms. The first of them is similar to a Hartree term in the sense that amplitudes of each eigenstates enter at spatial points separated by a minimal distance (one site). The other two terms are similar to Fock terms. In full analogy with the case of complex fermions, correlation functions depending on two energies $\epsilon_\alpha, \epsilon_\beta$, distance r, and the system size L are defined:

$$C_{H,o}(\epsilon_\alpha, \epsilon_\beta, r, L) = \langle U_{k,\alpha} U_{k+1,\alpha} U_{k+r,\beta} U_{k+r+1,\beta} \rangle_{\text{dis}}, \qquad (2.61)$$

$$C_{F,1,o}(\epsilon_\alpha, \epsilon_\beta, r, L) = \langle U_{k,\alpha} U_{k+1,\beta} U_{k+r,\alpha} U_{k+r+1,\beta} \rangle_{\text{dis}}, \qquad (2.62)$$

$$C_{F,2,o}(\epsilon_\alpha, \epsilon_\beta, r, L) = \langle U_{k,\alpha} U_{k+1,\beta} U_{k+r,\beta} U_{k+r+1,\alpha} \rangle_{\text{dis}}, \qquad (2.63)$$

$$C_{HF,o}(\epsilon_\alpha, \epsilon_\beta, r, L) = \langle U_{k,\alpha} U_{k+1,\alpha} U_{k+r,\beta} U_{k+r+1,\beta}$$
$$+ U_{k,\alpha} U_{k+1,\beta} U_{k+r,\alpha} U_{k+r+1,\beta}$$
$$- U_{k,\alpha} U_{k+1,\beta} U_{k+r,\beta} U_{k+r+1,\alpha} \rangle_{\text{dis}}. \qquad (2.64)$$

The subscript "o" serves to indicate that, as was explained above, these correlation functions bear analogy with odd-r correlations introduced for the model of complex fermions.

The same analytical consideration as were used in the case of correlation functions (2.48) - (2.50) with odd r suggest that all the correlation functions (2.61) - (2.64) should be suppressed by the factor $\sim \epsilon^2$. Now it is shown by numerical analysis that the correlation functions (2.61) - (2.64) indeed behave in a way very similar to the correlation functions (2.48) - (2.50) with odd r. One can observe that

in the critical regime of not too large r (the condition is $r \ll \xi_\epsilon$) the function $C_{F,1,o}$ dominates. It is also seen that the magnitude of this term is quite small. To understand the source of this smallness and its parametric dependence, in Fig. 2.18 the dependence of the correlation functions on system size L and on the energy ϵ is shown. The right panel clearly shows the ϵ^2 scaling that is expected from the analytical argument and is fully analogous to the scaling in Fig. 2.16. This is translated into an exponential scaling with respect to $\sqrt{L}$ of correlation functions evaluated on two lowest- energy states, as is seen in the left panel of Fig. 2.18 and is again in full analogy with the corresponding behavior in Fig. 2.16.
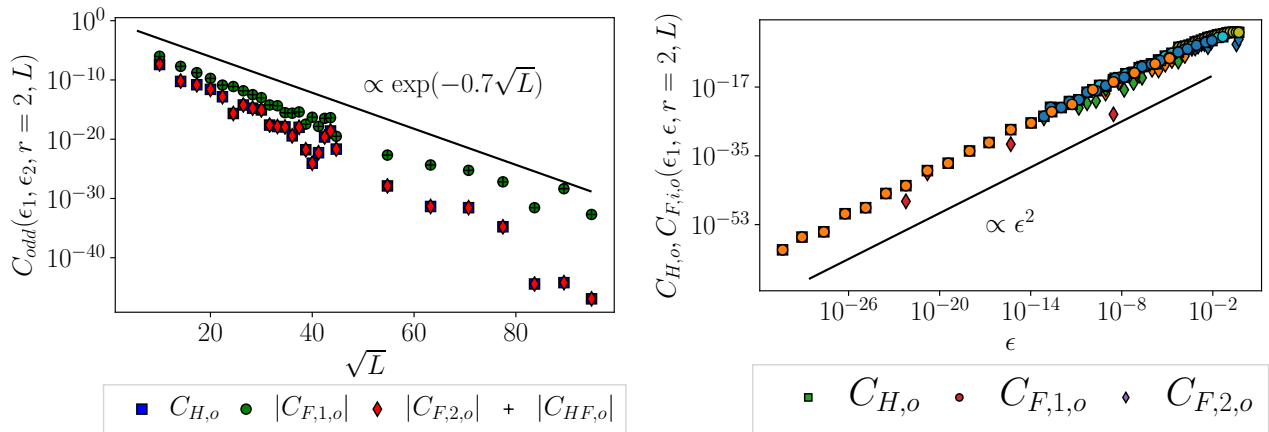
Figure 2.18: Figure taken from Ref. [86]. *Left:* Scaling of the correlation functions $C_{H,o}(\epsilon_1, \epsilon_2, r = 2, L)$, $C_{F,1,o}(\epsilon_1, \epsilon_2, r = 2, L)$, $C_{F,2,o}(\epsilon_1, \epsilon_2, r = 2, L)$, $C_{HF,o}(\epsilon_1, \epsilon_2, r = 2, L)$, Eqs. (2.61) - (2.64) with respect to system size L. *Right:* Scaling of the same correlation functions with energy. Different colors represent L from 100 to 10000. The data clearly demonstrated the ϵ^2 scaling that is also expected analytically.

The ϵ^2 scaling of the correlation functions (2.61) - (2.64) implies the RG irrelevance of the corresponding interaction term. Indeed, the density of states increases only as $1/\epsilon$ with logarithmic correction, see Eq. (2.34), and thus the suppression of the interaction wins over the increase of the density of states. This will be verified numerically below (Fig. 2.17). As explained above, the reason behind the ϵ^2 suppression of the matrix elements is the fact that both even and odd sites are involved. This tells one which correlation functions may escape such a suppression: those that involve sites of one sublattice only, i.e., with all distances between the sites being even. Thus such a generalized interaction term is considered:

$$\hat{O} = \gamma_k \gamma_{k+2} \gamma_{k+r} \gamma_{k+r+2}, \tag{2.65}$$

with an even $r \geq 4$. Such a term is allowed by symmetries and will be generalized by RG from the original interaction. This leads to introducing the corresponding generalization of the correlation

functions (2.61) - (2.64):

$$C_{H,e}(\epsilon_\alpha, \epsilon_\beta, r, L) = \langle U_{k,\alpha} U_{k+2,\alpha} U_{k+r,\beta} U_{k+r+2,\beta} \rangle_{\text{dis}}, \tag{2.66}$$

$$C_{F,1,e}(\epsilon_\alpha, \epsilon_\beta, r, L) = \langle U_{k,\alpha} U_{k+2,\beta} U_{k+r,\alpha} U_{k+r+2,\beta} \rangle_{\text{dis}}, \tag{2.67}$$

$$C_{F,2,e}(\epsilon_\alpha, \epsilon_\beta, r, L) = \langle U_{k,\alpha} U_{k+2,\beta} U_{k+r,\beta} U_{k+r+2,\alpha} \rangle_{\text{dis}}, \tag{2.68}$$

$$\begin{aligned} C_{HF,e}(\epsilon_\alpha, \epsilon_\beta, r, L) = \langle &U_{k,\alpha} U_{k+2,\alpha} U_{k+r,\beta} U_{k+r+2,\beta} \\ &+ U_{k,\alpha} U_{k+2,\beta} U_{k+r,\alpha} U_{k+r+2,\beta} \\ &- U_{k,\alpha} U_{k+2,\beta} U_{k+r,\beta} U_{k+r+2,\alpha} \rangle_{\text{dis}}. \end{aligned} \tag{2.69}$$

The subscript "e" indicates that all distances between the sites involved are even, in analogy with correlation functions (2.48) - (2.50) at even r.

In view of the analogy that has just been emphasized, one can expect that (i) the correlation function $C_{H,e}$ scales similarly to C_H, (2.48), and (ii) the correlation functions $C_{F,1,e}$ and $C_{F,2,e}$ scale in the same way and, moreover, are equal in the leading order to $C_{H,e}$, in analogy with the corresponding behavior of C_F, (2.49). However, since now there are three terms rather than two, the strong Hartree-Fock compensation should not happen, leaving one with $C_{HF,e} \simeq C_{H,e}$. These expectation are fully supported by the numerical simulations. In Fig. 2.19 it is shown that the r dependence of the correlation functions (2.66) - (2.69) evaluated on two lowest-energy eigenstates in a system of size $L = 400$. All four correlations functions $C_{H,e}$, $C_{F,1,e}$, $C_{F,2,e}$, and $C_{HF,e}$ are nearly equal in the critical regime (not too large r) and show the $r^{-3/2}$ scaling in analogy with C_H and C_F. In fact, the overall behavior of the correlation function $C_{H,e}$ ($C_{F,1,e}$ and $C_{F,2,e}$) in Fig. 2.19 is remarkably similar to that of C_H (respectively, C_F) in Fig. 2.15. Now one can turn to the scaling of the correlation functions (2.66) - (2.69) with energy ϵ and length L, see Fig. 2.19. The figure is very similar to the upper two panels of Fig. 2.15 and confirms that $C_{H,e}$, $C_{F,1,e}$, and $C_{F,2,e}$ scale exactly in the same as C_H with even r, (2.56). Since the Hartree-Fock compensation is not operative now, the correlation function $C_{HF,e}$ scales in the same way.
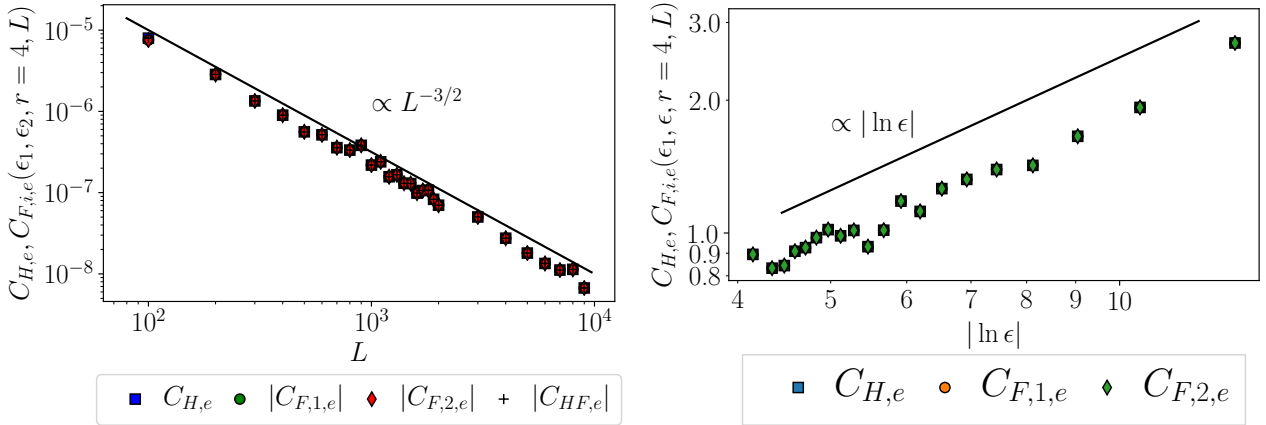
Figure 2.19: Figure taken from Ref. [86]. Correlation functions (2.66)-(2.69) with $r = 4$. *Left:* Scaling with the system size L of the correlation functions evaluated on two lowest-energy eigenstates. The slope corresponds to a power law with an exponent $3/2$. *Right:* Dependence on energy at fixed $L = 4000$. The slope corresponds to the $|\ln \epsilon|$ scaling. The total scaling with L and ϵ is therefore the same as for the complex-fermion correlation function C_H with even r, Eq. (2.56).

Since the correlation function $C_{HF,e}$ decreases with L in a power-law fashion only, and the density of states increases in an exponential way, they product should clearly increase exponentially. This is explicitly demonstrated in Fig. 2.17. For comparison, it is also show there that the product $\nu C_{HF,e}$ decreases with increasing L as discussed above. The exponential increase of $\nu C_{HF,e}$ indicates the RG relevance of the corresponding interaction term. This explains why the interaction drives the system away from the the infinite-randomness fixed point and establishes the spontaneous symmetry breaking and localization, as exhibited by the DMRG results, Sec. 2.3.2.

At this point, the following comment is in order. The completeness of eigenstates in combination with the chiral symmetry implies that $\sum_{\epsilon_\alpha > 0} U_{k,\alpha} U_{k+r,\alpha}$ is equal to zero for any even $r \neq 0$. As a result, the correlation functions (2.66) - (2.69) are zero when summed over all states with positive energies. Exactly such sums will arise if the expectation of the interaction (2.65) is calculated over the vacuum state (or, more generally, over any Fock-space basis state). However, what actually is of interest here is not this expectation value but rather the effect of non-diagonal matrix elements of the interaction. In more conventional problems, it turns out that it is sufficient to study the scaling of the expectation value to understand the effect of the interaction. It turns out that the situation with the term of the type (2.65) in the present problem is more delicate. The full analysis of the effect of non-diagonal matrix elements of such an interaction at the infinite-randomness fixed point is a very challenging task that will be left to future work. The expectation is that two properties of the correlation functions (2.66) - (2.69) that have been identified above—namely, (i) the contributions that, when multiplied with the density of states, strongly increase with L and (ii) the absence of Hartree-Fock cancellation of such contributions—will be also key ingredients of such a more sophisticated analysis, thus governing the RG relevance of the interaction for the disordered Majorana chain.

2.5.4 Analytical approach to wave function correlations

In this subsection analytical results for the scaling of eigenfunction correlation functions at the infinite-randomness fixed point are provided. These results complement, support, and explain the corresponding numerical results in Sec. 2.5.

In Ref. [39] the average of one Green's function in a non-interacting 1D model of class BDI was computed by means of supersymmetry formalism that allowed to map the problem onto quantum mechanics of a $SU(1|1)$ spin. In order to obtain directly the correlation functions of two eigenstates, one would need to average products of two Green's functions with the corresponding energy and spatial arguments. While the mapping on a supersymmetric quantum mechanics can be generalized to this situation, the solution of the corresponding problem becomes extremely difficult. For this reason, below a slightly different approach is chosen. By using the supersymmetry technique, the averaged square of the Green's function at an imaginary frequency is calculated. This average is related, by virtue of a spectral decomposition, to the two-eigenstates correlation functions. The resulting conclusions on the scaling of the two-eigenstates correlations are in agreement with the numerical findings in Sec. 2.5.

Following the formalism of Ref. [39] and map the original lattice model with random hopping onto a continuous model of a Dirac fermion with random mass, cf. Sec. 2.4.1. The latter is considered to be delta-correlated and gaussian-distributed disorder, with the strength W (which sets the ultraviolet cutoff for the critical theory and can be set to unity). Within the mapping onto the supersymmetric quantum mechanics, the averaged Green's function at an imaginary frequency $i\omega$ and with coinciding spatial arguments is obtained from the ground state of the corresponding effective Schrödinger equation.

In agreement with Ref. [39], one obtains:

$$\langle G(i\omega)\rangle_{\text{dis}} = \frac{a_1 W}{i\omega |\ln(\omega/a_0 W)|^2}. \tag{2.70}$$

The constants a_1 and a_0 can be by a numerical solution of the effective Schrödinger equation of the supersymmetric quantum mechanics; the results are $a_1 = 1$ (which holds with a very high accuracy and is apparently exact) and $a_0 \simeq 0.8$. Extending this analysis to the averaged square of the Green's function, one obtains

$$\langle G(i\omega)G(i\omega)\rangle_{\text{dis}} = \frac{a_2 W}{\omega^2 |\ln(\omega/a_0 W)|^2}, \tag{2.71}$$

where $a_2 = 1/3$ (which again holds numerically with a very high accuracy and should thus be exact). Equations (2.70) and (2.71) are derived in the continuum-limit approximation to the effective Schrödinger equation. By a numerical solution of the exact (discrete) equation, it was verified that they hold with an outstanding accuracy. Specifically, as shown in Fig. 2.20, the relative correction to Eq. (2.70) is of the order ω and that to Eq. (2.71) is of the order ω^2. This means, in particular, that all orders of expansion of Eqs. (2.70) and (2.71) in $1/|\ln\omega|$ are fully reliable.
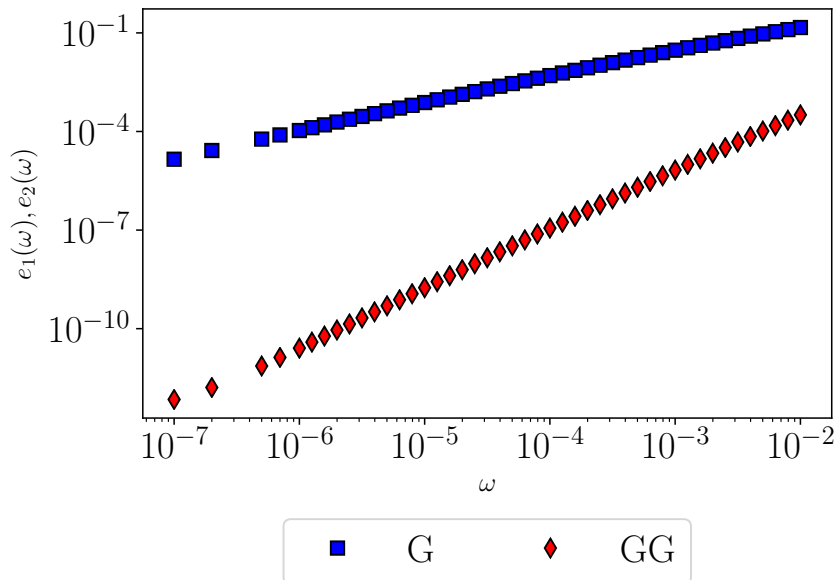
Figure 2.20: Figure taken from Ref. [86]. In this plot, the validity of Eqs. (2.70) and (2.71) for $\langle G(i\omega)\rangle_{\text{dis}}$ and $\langle G(i\omega)G(i\omega)\rangle_{\text{dis}}$ derived in a continuum-limit approximation to the effective Schrödinger equation is verified numerically. For this purpose, the numerically computed $e_1(\omega) = i\omega\langle G(i\omega)\rangle_{\text{dis}} - |\ln(\omega/a_0)|^{-2}$ and $e_2(\omega) = 3\omega^2\langle G(i\omega)G(i\omega)\rangle_{\text{dis}} - |\ln(\omega/a_0)|^{-2}$ are plotted. The disorder strength is set $W = 1$. The constant $a_0 \simeq 0.8$ is determined to minimize the errors e_i. It can be seen that $e_1(\omega) \propto \omega$ and $e_2(\omega) \propto \omega^2$.

Now these results are connected to the correlation functions of eigenstates $\psi_\alpha(r)$ (which are continuum limit counterparts of the states $\psi_{i\alpha}$ studied numerically in Sec. 2.5. Since all arguments of

Green's functions that considered here are equal (they are set to $r = 0$), only eigenstates at this point will enter. Using the spectral decomposition of the single-particle Green's function, one gets

$$\langle G(i\omega) \rangle_{\text{dis}} = \sum_\alpha \left\langle \frac{\psi_\alpha^2(0)}{i\omega - \epsilon_\alpha} \right\rangle_{\text{dis}}$$

$$= \int d\epsilon\, L\, \nu(\epsilon) \frac{\langle \psi_\alpha^2(0) \rangle_{\text{dis}}}{i\omega - \epsilon}. \tag{2.72}$$

The average entering here is $\langle \psi_\alpha^2(0) \rangle_{\text{dis}} = L^{-1}$ due to eigenfunction normalization. Further, the density of states is

$$\nu(\epsilon) \simeq \frac{c^2}{\epsilon |\ln(\epsilon/\Lambda)|^3}, \tag{2.73}$$

see Eq. (2.34), where $c \sim 1$ is the constant defined in Eq. (2.36) and $\Lambda \sim 1$ is an ultraviolet cutoff. Substituting this in Eq. (2.72), one gets

$$\langle G(i\omega) \rangle_{\text{dis}} = c^2 \left[\frac{1}{i\omega |\ln \omega/\Lambda|^2} + \frac{\ln 2}{i\omega |\ln \omega/\Lambda|^3} \right.$$

$$+ \left. \mathcal{O}(\omega^{-1} |\ln \omega|^{-4}) \right]. \tag{2.74}$$

One can see that Eq. (2.74) is in full agreement with the result (2.70) of the supersymmetric calculation. Indeed, not only the leading behavior agrees but also Eq. (2.70) can be expanded to bring it to the form (2.74). This confirms that the formula (2.73) for the density of states that was used when deriving Eq. (2.74) from the spectral decomposition (2.72) is correct. One can, of course, also obtain (2.73) by performing an analytical continuation of Eq. (2.70). Note, however, that different models of disorder were used in the numerical and analytical calculations, so that numerical value of the coefficient c^2 in Eq. (2.73) cannot be directly obtained from the analytical result.

Having satisfied ourselves that the spectral decomposition works properly for $\langle G(i\omega) \rangle_{\text{dis}}$, one can turn to $\langle G(i\omega) G(i\omega) \rangle_{\text{dis}}$ that provides information about correlations of different eigenfunctions. The spectral decomposition now yields

$$\langle G(i\omega) G(i\omega) \rangle_{\text{dis}} = \sum_\alpha \left\langle \frac{\psi_\alpha^4(0)}{(\epsilon_\alpha - i\omega)^2} \right\rangle_{\text{dis}}$$

$$+ \sum_{\alpha \neq \beta} \left\langle \frac{\psi_\alpha^2(0) \psi_\beta^2(0)}{(\epsilon_\alpha - i\omega)(\epsilon_\beta - i\omega)} \right\rangle_{\text{dis}}. \tag{2.75}$$

In Sec. 2.5, the following scaling of the eigenstates correlation functions entering Eq. (2.75) is found numerically: $\langle \psi_\alpha^4(0) \rangle_{\text{dis}} = aL^{-1}$, Eq. (2.53), and $\langle \psi_\alpha^2(0) \psi_\beta^2(0) \rangle_{\text{dis}} = bL^{-2} \ln \epsilon_>$, Eq. (2.56), where a and b are numerical coefficients, and $\epsilon_>$ is the larger of the two energies ϵ_α and ϵ_β. Substituting them into Eq. (2.75) and rewriting the sum over energies as integrals with the density of states (2.73), one obtains

$$\langle G(i\omega) G(i\omega) \rangle_{\text{dis}} = c^2 \left[\frac{a}{i\omega^2 |\ln \omega/\Lambda|^2} + \frac{a - (2/3)bc^2}{i\omega^2 |\ln \omega/\Lambda|^3} \right.$$

$$+ \left. \mathcal{O}(\omega^{-1} |\ln \omega|^{-4}) \right]. \tag{2.76}$$

The two leading terms of Eq. (2.76) fully correspond to the expansion of the result (2.71) of the supersymmetry-formalism calculation. This proves that the numerically found values of the exponents, $\alpha = 1$ and $\gamma = 2$, in the scaling of eigenstate correlations, Eq. (2.56), are indeed exact.

2.6 Summary

In this part of the work the chief aim was understanding the behavior of disordered wires of Majoranas and complex fermions in the presence of interaction. The models studied both belong to symmetry class BDI and are completely equivalent (except for the smaller Majorana Hilbert space) in the non-interacting limit. In particular, the low energy theory is governed by the infinite-randomness fixed point. The intriguing question whether there is a fundamental difference between the Majorana and complex fermions version of the problem was answered: they behave drastically distinct! Additionally, the analysis presented above yields insight on the origin of this difference.

As mentioned above in 1D there are more methods available than in higher dimensions. Here the full force of DMRG, bosonization, SCBA topological indices with mean field decoupled interaction and infinite randomness RG were used.

The statistical properties of eigenfunction correlations in systems controlled by the infinite-randomness fixed point were studied. A similar analysis is performed in Chap. 3, where multifractal eigenstate correlations in spin quantum Hall systems are investigated. Here, it directly permits conclusions on the (ir)relevance of interaction at the perturbative level. The main results from this work are:

(1) Together with my collaborators, I have determined phase diagrams and drew conclusions about their observable properties (spin order, criticality). As basis of this, DMRG simulations of the models were employed. This provided access to the entanglement entropy and the spin-spin correlation functions. In detail:

(i) The topological phase diagram of the Majorana chain was studied by artificially introducing staggering. In Fig. 2.3 the central charge, obtained from the scaling of the entanglement entropy, is visualized in parameter space and in Fig. 2.4 a spin-order phase diagram is shown. Using the correspondence of spin order of the Jordan Wigner dual and topological order in the original model, one obtains the full topological phase diagram shown in Fig. 2.5. Additionally the observed central charges allow conclusions on the type of criticality at the phase boundaries. On the average translational symmetric line, up to moderate interaction, the numerics shows Ising (central charge $c = \frac{1}{2}$) criticality. For moderate repulsive interaction the DMRG simulations show Ising+LL ($c = \frac{3}{2}$) criticality in agreement with Ref. [31]. The critical line is surrounded by gapped topologically distinct phases and an extended patch of LL ($c = 1$) criticality. The Ising sector that is still gapped in this phase, it is therefore natural to assume that topological protection persists, despite there are gapless LL degrees of freedom. The strongly interacting gapped phases show a rich phenomenology of density waves with different wave vectors.

(ii) Gapped topological phases are robust towards weak disorder, however the phase boundaries depend on disorder strength in general. When turning on disorder in the DMRG analysis it is therefore most convenient to stay on the pinned self dual critical line in the phase diagram. The results obtained depend on the sign of interaction: for attractive interaction, the scaling of the entanglement reveals the system is still at criticality. Interestingly, the data in Fig. 2.7 suggests a central charge that (within the numerical accuracy) agrees with clean Ising criticality ($c = \frac{1}{2}$) despite the presence of disorder. For repulsive interaction on the other hand the system localizes for weak repulsion (saturating entanglement entropy). Even in the localized phase there is rich phenomenology: spin correlation functions Figs. 2.9, 2.10 and 2.11 show signs of topological ordering for half of the disorder configurations. In the other half, the ordering is absent. The most probable explanation for this is that repulsive interaction and disorder lead to spontaneous breaking of the translational symmetry.

(iii) Confirming the well known result in spin chains for nearest neighbor density-density interaction, DMRG indicates disordered interacting complex fermions behave the same way as in the non-

interacting case. Investigations of the entanglement [86] yield an effective central charge $c \approx \ln 2$, which is a smoking gun pointing to infinite-randomness physics.

(2) I performed two kinds of RG analysis to understant the numericals results from (1): (i) First, I have developed a Giamarchi-Schulz like weak-disorder RG. Fig. 2.3 indicates there are three clean critical theories in the phase diagram: $c = \frac{1}{2}$ (Ising), $c = \frac{3}{2}$ (Ising+LL) and $c = 1$ (LL). The disorder is strongly RG-relevant and quickly flows towards the strong-disorder regime driving the system away from the clean FP. The RG flow becomes uncontrolled before reaching the infrared behavior.

(ii) Since the disorder flows to strong coupling, an RG analysis starting at the non-interacting infinite-randomness fixed point seemed natural. The effect of the interaction was investigated perturbatively from that point. To this end, the scaling of the interaction matrix elements had to be determined. I studied the eigenfunction statistics in great detail. The difference between LDOS moments and generic composite objects of eigenfunctions is maximally pronounced in the sense that a single wavefunction looks localized and nontrivial correlations appear only with several points and wavefunctions. Further there was a strong even/odd sublattice effect in all correlation functions studied. Using high precision numerics, the correlation functions for both Hartree and Fock terms are computed. Due to the singular LDOS, both terms grow quickly with increasing system size. However because there is a strong cancellation between the two terms, their difference vanishes rapidly. Since this is even faster than the divergence of the LDOS, the interaction is RG-irrelevant in the complex fermionic chain.

Contrarily in the Majorana model the interaction terms are spread over four sites. The unsuppressed matrix elements with even separation scale similarly to the two point function C_H introduced before in Eq. (2.56) [86]. Due to non-conservation of particle number in the Majorana case there are three non-vanishing contributions from Wick's theorem in the matrix elements of the interaction. Since these are each of the same magnitude (in leading order), there is no cancellation in the Majorana system. Consequently such interaction terms are strongly relevant at the infinite randomness fixed point. This explains the drastic difference of behavior between Majoranas and complex fermions seen in the DMRG numerics.

3 Chapter 3
Generalized multifractality in Spin Quantum Hall systems

In this chapter, I coin the term generalized multifractality *characterizing the scaling of arbitrary eigenstate composite observables at Anderson-localization critical points opposed to leading multifractality dealing with local density of states (LDOS) moments only.*

The spin quantum Hall (SQH) transition in superconductors with anomalous particle-hole symmetry (class C) is central to this chapter. Many of the mathematical constructions for pure-scaling eigenoperators and observables generalize straightforwardly to the other symmetry classes. In order to explore generalized multifractality in SQH (and other) systems, I derive the pure-scaling observables in the field theoretical framework of the non-linear sigma model (NLSM). Then a "translation" in terms of eigenstate observables has to be found. Having obtained these, I perform numerical studies of the network models for SQH and IQH transitions. As expected, the results show pure scaling in the corresponding observables, which allows me to find the generalized multifractal spectrum. Remarkably the spectrum at the SQH critical point strongly deviates from generalized parabolicity. These numerical indices imply violation of the local conformal invariance (LCI) at this critical point.

Finally I give analytical arguments showing violations from generalized parabolicity explicitly in certain scaling exponents. This is sufficient to proof that SQH criticality does not obey LCI.

This section closely follows my publication Ref. [105].

3.1 Motivation

Anderson localization in disordered systems belongs to the most fundamental phenomena in condensed matter physics [164, 165]. In particular, Anderson transitions between localized and delocalized phases (or between topologically distinct localized phases) [9] attract much attention. This interest was additionally enhanced by development of the symmetry classification of disordered systems [7, 98, 111] (see Sec. 1.3), which has further extended the scope of Anderson transitions (in particular, to the area of disordered superconductors); see [9] for review. A general discussion of Anderson transition and multifractality can be found in Sec. 1.2 and Sec. 1.2.1.

A remarkable hallmark of critical points of Anderson transitions is the multifractality characterizing the statistics of eigenfunctions and of the local density of states (LDOS). Multifractality of critical eigenstates at various Anderson-transition critical points has been extensivlely explored analytically and numerically [9]. It was demonstrated that the multifractality can be efficiently employed to

determine the position of the critical point of the Anderson transition and the critical index of the localization length [20, 21]. It was also shown that the multifractality survives in the presence of Coulomb interaction [166]. Recently, the multifractality was used as an efficient tool to detect and explore the emergent criticality of 2D surface states of topological superconductors [75, 88–90].

Direct experimental measurement of multifractality is a highly non-trivial task. Experimental observations of multifractality near metal-insulator transition were reported for sound waves [167] and electrons in disordered semiconductors [22]. Strong fluctuations of the local density of states qualitatively analogous to multifractality were observed in experiments on superconductor-insulator transition in disordered films [23, 24].

Recent works on interplay of multifractality and interactions have additionally emphasized the importance of multifractality. In particular, it was predicted that the multifractality may enhance the critical temperature T_c of superconductiors in three-dimensional [168–170] and two-dimensional (2D) [171–175] systems. The multifractal enhancement of T_c in 2D superconductors was indeed observed experimentally [176, 177]. Further, it was shown that the multifractality drives instabilities of surface states of topological superconductors [61, 124] and leads to broad distribution of Kondo temperatures in disordered metals with magnetic impurities [178–180].

It was shown in Refs. [181–185] that, within the non-linear σ model (which constitutes the field theory of Anderson localization), the distribution of LDOS in Wigner-Dyson classes possesses a symmetry relating the probabilities of values ν and ν^{-1} (with the average LDOS normalized to unity). This was used in Ref. [102] to derive exact symmetry relations between multifractal exponents at Anderson transitions in the Wigner-Dyson classes. It was later shown in Ref. [186] that these relations can be understood as a manifestation of Weyl-group symmetry associated with the σ-model manifold and can be extended to unconventional symmetry classes. In Ref. [87], a general classification of composite operators without gradients was developed, which extends that of Refs. [187–189]. Further, in Ref. [87] multiple symmetry relations between scaling exponents of composite operators were derived, which all follow from the Weyl-group symmetry. Finally, Ref. [87] determined a "translation" of these composite operators to eigenfunction correlation functions for the symmetry class A (unitary Wigner-Dyson class).

The scaling of the whole set of composite operators characterizing critical eigenstates extends the conventional notion of multifractality (which refers only to leading exponents τ_q characterizing moments $|\psi(\mathbf{r})|^{2q}$ of eigenstate amplitude). I will thus term it *"generalized multifractality"*. The subleading multifractal exponents manifest themselves in dephasing and broadening of localization transition in an interacting system with a short-range interaction that is irrelevant in the renormalization-group sense [158, 190, 191].

The spatial dimensionality $d = 2$ plays a special role in the context of Anderson localization. In the most conventional symmetry class AI (orthogonal Wigner-Dyson class), $d = 2$ is the lower critical dimension, so that a 2D system is always in the localized phase (although with an exponentially large localization length for weak disorder). The situation is, however, different in other symmetry classes, with a wealth of 2D Anderson-localization critical points [9]. Emergence of these critical points is related either to peculiarities of the perturbative expansion (e.g., antilocalization in Wigner-Dyson symplectic class AII) or to topology. A paradigmatic example of the localization-transition critical point associated with topology is the plateau transition in the quantum Hall effect (which belongs to the Wigner-Dyson unitary class A).

Multifractality at the quantum-Hall plateau transition and, more generally, physics of the corresponding fixed point, has been attracting much interest. On the numerical side, the multifractal spectrum is very close to parabolicity [51]; however, a high-precision numerics indicates small devia-

tions [52, 53]. Many papers have attacked the problem of the character of the critical theory [42–50]; in particular, various versions of the Wess-Zumino-Novikov-Witten (WZNW) theory were conjectured. Quite generally, such WZNW-type theories lead to a parabolic multifractality spectrum as for free Gaussian fields. Another important argument in favor of parabolic multifractality was provided by Ref. [60]. In was shown in that work that, for 2D Anderson transitions, the assumption of local conformal invariance, in combination with an assumption of Abelian fusion of composite operators, leads to an exactly parabolic multifractal spectrum of moments of the local density of states: the exponent τ_q is a quadratic function of q. A further interesting connection between WZNW models and quantum Hall criticality is explored in Chap. 4.

The present work deals with a superconducting counterpart of the quantum Hall transition—the spin quantum Hall (SQH) transition [54, 55]. It was found that mapping to percolation allows one to obtain some critical exponents for the SQH transition exactly [56–58]. The multifractality spectrum at the SQH critical point was studied numerically in Refs. [58, 77] and very recently in Ref. [59]. It was found [58, 59] that the spectrum exhibits clear (although relatively weak) deviations from parabolicity. These deviations are very interesting physically since, in combination with results of Ref. [60], they hint to a possible violation of local conformal invariance.

In this work, I present a detailed analysis of the generalized multifractality at the SQH critical point, supporting and complementing analytical study by numerical simulations. The key results are as follows:

1. The implications of local conformal invariance (LCI) in 2D systems for the generalized multifractal spectrum are explored. The result of Ref. [60] stating that LCI implies parabolicity of the LDOS multifractality can be extended. By assuming both LCI and Abelian fusion (1.76), one can show that the generalized-multifractality spectrum exhibits "generalized parabolicity" and is parametrized (for a given critical point) by a single constant.

2. One can develop explicitly two constructions of pure-scaling composite operators for σ-model of class C, invoking heighest-weight vectors and the Iwasawa decomposition, respectively. These composite operators both obey Abelian fusion rules. The Iwasawa decomposition is performed in Sec. 3.3. The highest weight vector construction can be found in Ref. [105].

3. Using one-loop renormalization group an alternative family of pure-scaling operators is found in Sec. 3.5 (invariant with respect to the action of the symmetry group of the σ-model and easier to connect to the wavefunctions).

4. A "translation" of the scaling operators to the language of eigenstates of the Hamiltonian is performed and explicit expressions for particularly interesting eigenstate correlators exhibiting generalized multifractality are determined in Secs. 3.6, 3.7. Using the network model of class C, it is verified numerically that these are indeed the proper scaling operators and determine the corresponding exponents. Very remarkably, there is a *strong violation* of the generalized parabolicity of the generalized-multifractality spectrum. In combination with the results proven in (i) and (ii), this points out to a violation of the local conformal invariance at the SQH transition. While this is a rather surprising conclusion, there apparently is no alternative plausible explanation of the numerical findings.

5. Exploiting the percolation mapping of certain observables in critical SQH systems, I show analytically that the generalized multifractal spectrum violates parabolicity in Sec. 3.8.

The results in (ii) and a part of analytical results in (iv) represent an extension of the class-A construction of Ref. [87] to class C. It should be emphasized, however, that this extension is far from trivial, and the situation in class C turns out to be much richer than in class A. This complexity can be traced back to the additional particle-hole degree of freedom (referred as "spin" in the term "spin quantum Hall effect") .

The mathematical constructions in the following Secs. 3.2, 3.3, 3.4, 3.5, 3.7 are excerpts from Ref. [105] slightly modified to fit notation and style of this work.

3.2 Multifractality and CFT

In this section the attention is restricted to Anderson transitions (ATs) in two dimensions. The reason is that in two dimensions, conformal symmetry is especially powerful due to local conformal invariance (LCI) and the underlying infinite-dimensional Virasoro algebra. It is commonly expected that if a 2D theory satisfies global conformal invariance, it also satisfies the—much stronger—local conformal invariance. The framework employed here relating multifractality to a field theory satisfying LCI is introduced in Sec. 1.2.2. General fundamentals on conformal field theory can be found in Sec. 1.1.2 and references therein. This infinite symmetry implies (together with the Abelian fusion) *exact* parabolicity of MF spectra [60]. After reviewing the arguments of Ref. [60] that dealt with the the leading MF spectra at the integer quantum Hall (IQH) transition, this section continues with an extension to other symmetry classes [Eq. (3.20)] and also to generalized MF exponents [Eq. (3.25)].

3.2.1 Exact parabolicity of $\triangle_q$ for the IQH transition under the assumption of local conformal invariance

Bondesan et al. [60] considered the scaling operators $\mathcal{O}_q(r)$ in the context of the IQH transition in 2D and its description in terms of the Chalker-Coddington network model. This critical point belongs to class A, so $q_* = 1$ and $x_q = \Delta_q$. The main results of [60] is that, under the assumption of local conformal invariance, exact parabolic form of the dimensions Δ_q holds:

$$\Delta_q = bq(1 - q), \tag{3.1}$$

with constant b left undetermined.

In 2D CFT, where the points are specified by complex coordinates z, the two- and three-point functions factorize into holomorphc and antiholomorphic factors (with possibly different holomorphic and antiholomorphic dimensions h and $\bar{h}$):

$$\left\langle \phi_1(z_1, \bar{z}_1)\phi_2(z_2, \bar{z}_2) \right\rangle_{\text{CFT}} \sim z_{12}^{-2h} \bar{z}_{12}^{-2\bar{h}}, \qquad \text{if } h_1 = h_2 = h \text{ and } \bar{h}_1 = \bar{h}_2 = \bar{h}, \tag{3.2}$$

$$\left\langle \phi_1(z_1, \bar{z}_1)\phi_2(z_2, \bar{z}_2)\phi_3(z_3, \bar{z}_3) \right\rangle_{\text{CFT}} \sim z_{12}^{h_3-h_1-h_2} z_{13}^{h_2-h_1-h_3} z_{23}^{h_1-h_2-h_3} \bar{z}_{12}^{\bar{h}_3-\bar{h}_1-\bar{h}_2} \bar{z}_{13}^{\bar{h}_2-\bar{h}_1-\bar{h}_3} \bar{z}_{23}^{\bar{h}_1-\bar{h}_2-\bar{h}_3}. \tag{3.3}$$

The four-point CFT correlation functions in two dimensions can be written in terms of $z_{ij} = z_i - z_j$ and the cross-ratio $\eta = z_{12}z_{34}/z_{13}z_{24}$ as follows:

$$\left\langle \phi_1(z_1, \bar{z}_1)\dots\phi_4(z_4, \bar{z}_4) \right\rangle_{\text{CFT}} = \prod_{i<j}^{4} z_{ij}^{h/3-h_i-h_j} \bar{z}_{ij}^{\bar{h}/3-\bar{h}_i-\bar{h}_j} F(\eta, \bar{\eta}), \quad h = \sum_{i=1}^{4} h_i, \quad \bar{h} = \sum_{i=1}^{4} \bar{h}_i. \tag{3.4}$$

As in higher dimensions, the function $F(\eta, \bar{\eta})$ cannot be determined from conformal symmetry alone.

To prove the exact parabolicity (3.1), Bondesan et al. considered a certain 4-point correlation function that satisfies the neutrality condition (1.83). In that work the neutrality condition (1.83) was achieved by considering $n-1$ insertions of the operators $\mathcal{O}_{q_i}$ plus one operator π_c describing a point contact in the network model [44, 192]. This operator can be written as the integral over a continuum of q values, and it always contributes the definite scaling dimension (or the fusion channel) necessary to have the correct total "charge" $q_* = 1$.

In the notations used here the relevant correlator is $\left\langle \mathcal{O}_{q_1}(z_1, \bar{z}_1) \mathcal{O}_{q_2}(z_2, \bar{z}_2) \mathcal{O}_{q_3}(z_3, \bar{z}_3) \mathcal{O}_{1-q_1-q_2-q_3}(z_4, \bar{z}_4) \right\rangle$. The operators $\mathcal{O}_q$ are expected to have $h_q = \bar{h}_q = \Delta_q/2$, and the corresponding 4-point CFT correlator is

$$\left\langle \phi_{q_1}(z_1, \bar{z}_1) \phi_{q_2}(z_2, \bar{z}_2) \phi_{q_3}(z_3, \bar{z}_3) \phi_{1-q_1-q_2-q_3}(z_4, \bar{z}_4) \right\rangle_{\text{CFT}} = \prod_{i<j}^{4} |z_{ij}|^{\Delta/3 - \Delta_{q_i} - \Delta_{q_j}} F(\eta, \bar{\eta}), \qquad (3.5)$$

$$\Delta = \Delta_{q_1} + \Delta_{q_2} + \Delta_{q_3} + \Delta_{q_1+q_2+q_3}. \qquad (3.6)$$

In the following lines the argument of Ref. [60] is briefly summarized. The authors make two essential assumptions: 1) correlation functions satisfying the neutrality condition (1.83) exhibit at the IQH transition point the local conformal invariance, with the corresponding CFT operators ϕ_q being Virasoro primaries; 2) the operators ϕ_q satisfy (the 2D variant of) the Abelian OPE (1.76):

$$\phi_{q_1}(z_1, \bar{z}_1) \phi_{q_2}(z_2, \bar{z}_2) \propto |z_{12}|^{\Delta_{q_1+q_2} - \Delta_{q_1} - \Delta_{q_2}} \phi_{q_1+q_2}(z_2, \bar{z}_2) + \dots \qquad (3.7)$$

It is important that no other primaries enter the Abelian OPE and the ellipses stand for contributions from Virasoro descendants.

The Abelian fusion immediately implies that there is only one conformal block in the correlator (3.5), that is $F(\eta, \bar{\eta}) = |f(\eta)|^2$. The holomorphic function $f(\eta)$ is present in the holomorphic factor of the correlator (3.5):

$$G(z_1, \dots, z_4) = \left\langle \phi_{q_1}(z_1) \phi_{q_2}(z_2) \phi_{q_3}(z_3) \phi_{1-q_1-q_2-q_3}(z_4) \right\rangle_{\text{CFT}} = \prod_{i<j}^{4} z_{ij}^{h/3 - h_{q_i} - h_{q_j}} f(\eta), \qquad (3.8)$$

$$h = h_{q_1} + h_{q_2} + h_{q_3} + h_{q_1+q_2+q_3}. \qquad (3.9)$$

There are three possible fusion channels in this correlator, where each of the charges q_1, q_2, and q_3 fuses with the neutralizing charge $1 - q_1 - q_2 - q_3$. These three channels lead to simple power-law singularities (branch points) of the function $f(\eta)$ at $\eta = 1, 0$ and ∞. For example, fusing q_1 with q_2, and q_3 with $1 - q_1 - q_2 - q_3$ (so that $|\eta| \ll 1$) gives

$$G(z_1, \dots, z_4) \sim z_{12}^{h_{q_1+q_2} - h_{q_1} - h_{q_2}} z_{34}^{h_{q_1+q_2} - h_{q_3} - h_{q_1+q_2+q_3}} z_{13}^{-2h_{q_1+q_2}}. \qquad (3.10)$$

On the other hand, the right-hand side of Eq. (3.8) where the distances between points are chosen appropriately ($|z_{12}|, |z_{34}| \ll |z_{13}| \approx |z_{14}| \approx |z_{23}| \approx |z_{24}|$) becomes

$$G(z_1, \dots, z_4) \sim f(\eta) z_{12}^{h/3 - h_{q_1} - h_{q_2}} z_{34}^{h/3 - h_{q_3} - h_{q_1+q_2+q_3}} z_{13}^{-2h/3}. \qquad (3.11)$$

Comparison of the two expressions gives that near $\eta = 0$

$$f(\eta \sim 0) = \eta^{h_{q_1+q_2} - h/3} [a_0 + O(\eta)]. \qquad (3.12)$$

The other two fusion channels give the forms of the singularities near the other two branch points:

$$f(\eta \sim 1) = (1 - \eta)^{h_{q_2+q_3} - h/3}[b_0 + O(1 - \eta)], \qquad f(\eta \sim \infty) = (1/\eta)^{h_{q_1+q_3} - h/3}[c_0 + O(1/\eta)]. \quad (3.13)$$

The exponents characterizing the three branch points must be related. The argument is a simple case of a more general one in Ref. [193]. Indeed, compactify the complex plane and go around all three branch points along a contour $\mathcal{C}$. Then, on the one hand, the total phase change (monodromy) of the function $f(\eta)$ acquired along the contour $\mathcal{C}$ is the product of the phases characterizing each of the branch points. On the other hand, the contour $\mathcal{C}$ can be deformed to a point by extending it to infinity, which means that the total monodromy is trivial (one). This gives the relation

$$h - h_{q_1+q_2} - h_{q_1+q_3} - h_{q_2+q_3} = M, \quad (3.14)$$

where $M \geq 0$ is a non-negative integer. Then the holomorphic function $f(\eta)$ becomes

$$f(\eta) = \eta^{h_{q_1+q_2} - h/3}(1 - \eta)^{h_{q_2+q_3} - h/3}[a_0 + a_1\eta + \cdots + a_M\eta^M]. \quad (3.15)$$

Choosing $q_1 = q_2 = q_3 = 0$, one can see that $M = 0$. This fixes the conformal block

$$f(\eta) = a_0\eta^{h_{q_1+q_2} - h/3}(1 - \eta)^{h_{q_2+q_3} - h/3}. \quad (3.16)$$

Moreover, the condition $M = 0$ gives a functional equation for the dimensions h_q:

$$h_{q_1+q_2+q_3} - h_{q_1+q_2} - h_{q_1+q_3} - h_{q_2+q_3} + h_{q_1} + h_{q_2} + h_{q_3} = 0, \quad (3.17)$$

or, for the full dimensions Δ_q,

$$\Delta_{q_1+q_2+q_3} - \Delta_{q_1+q_2} - \Delta_{q_1+q_3} - \Delta_{q_2+q_3} + \Delta_{q_1} + \Delta_{q_2} + \Delta_{q_3} = 0. \quad (3.18)$$

This equation easily leads to the result (3.1). First, it immediately implies $\Delta_0 = 0$, as it should be. Next, setting $q_1 = q$ and $q_2 = q_3 = \epsilon$, one gets

$$\Delta_{q+2\epsilon} - 2\Delta_{q+\epsilon} - \Delta_{2\epsilon} + \Delta_q + 2\Delta_\epsilon = 0. \quad (3.19)$$

Now one can expand up to second order in ϵ to get $(\Delta_q'' - \Delta_0'')\epsilon^2 = 0$. Thus $\Delta_q'' = \Delta_0'' = \text{const}$, which implies that the function Δ_q is a quadratic polynomial. A general quadratic polynomial that vanishes at $q = 0$ and satisfies the symmetry property (1.69) is exactly of the form given in Eq. (3.1).

3.2.2 Generalizations

Now one can generalize the arguments of Ref. [60] summarized in Sec. 3.2.1 in two directions.

3.2.2.1 Other symmetry classes

First, the arguments are not specific to the IQH critical point but rather apply also to 2D critical points of ATs in other symmetry classes. The assumptions are the same: (1) local conformal invariance of correlation functions satisfying the neutrality condition, and (2) Abelian fusion. Under these assumptions, the arguments can be directly extended to all five symmetry classes (A, AI, AII, CI, and C) identified in Refs. [87, 186] that exhibit the symmetry relation (1.69), with $q_* = 1$ for Wigner-Dyson classes, $q_* = 2$ for class CI, and $q_* = 3$ for class C. The result is the exact parabolicity,

$$x_q = bq(q_* - q) \quad (3.20)$$

for the simple MF spectra. (Here the term "simple" is used in the sense of opposite to "generalized".)

3.2.2.2 Generalized mulifractality

Secondly, one can obtain a generalization of this parabolic form for all gradientless scaling operators $\mathcal{O}_\lambda$ considered in [87], i.e., to generalized MF spectrum, see Sec. 1.2.1.1. As was pointed out in Sec.1.2.1.1, there is a general operator $\mathcal{O}_{-\rho_b} = \mathcal{O}_{(-c_1, -c_2, \dots)}$ with vanishing scaling dimension. Further, as is discussed in Sec. 1.2.2.2, the correlation functions satisfying $\sum_i \lambda_i = -\rho_b$ have scaling consistent with conformal invariance. Now assume, as before, that the local conformal invariance holds for these correlation functions and that $\mathcal{O}_\lambda$ are Virasoro primaries that satisfy the 2D version of the Abelian OPE (1.76). Then the arguments of Ref. [60] presented in Sec. 3.2.1 can be straightforwardly generalized to give the following equation for the dimensions x_λ:

$$x_{\lambda+\lambda'+\lambda''} - x_{\lambda+\lambda'} - x_{\lambda+\lambda''} - x_{\lambda'+\lambda''} + x_\lambda + x_{\lambda'} + x_{\lambda''} = 0. \tag{3.21}$$

[This equation is a counterpart of Eq. (3.18).] Denote by $e_i = (0, \dots, 1, \dots, 0)$ (unit in the i-th place) the standard basis in the weight space, and choose $\lambda' = \epsilon' e_i$ and $\lambda'' = \epsilon'' e_j$:

$$x_{\lambda+\epsilon'e_i+\epsilon''e_j} - x_{\lambda+\epsilon'e_i} - x_{\lambda+\epsilon''e_j} - x_{\epsilon'e_i+\epsilon''e_j} + x_\lambda + x_{\epsilon'e_i} + x_{\epsilon''e_j} = 0. \tag{3.22}$$

Then one can expand this to second order in ϵ' and ϵ'', denoting $\partial_i = \partial/\partial q_i$:

$$x_{\lambda+\epsilon'e_i} = x_\lambda + \partial_i x_\lambda \epsilon' + \frac{1}{2}\partial_i^2 x_\lambda \epsilon'^2, \qquad x_{\lambda+\epsilon''e_j} = x_\lambda + \partial_j x_\lambda \epsilon'' + \frac{1}{2}\partial_j^2 x_\lambda \epsilon''^2,$$

$$x_{\lambda+\epsilon'e_i+\epsilon''e_j} = x_\lambda + \partial_i x_\lambda \epsilon' + \partial_j x_\lambda \epsilon'' + \frac{1}{2}\partial_i^2 x_\lambda \epsilon'^2 + \frac{1}{2}\partial_j^2 x_\lambda \epsilon''^2 + \partial_i \partial_j x_\lambda \epsilon' \epsilon''. \tag{3.23}$$

Substituting these expansions into Eq. (3.22) gives $\partial_i \partial_j x_\lambda = \partial_i \partial_j x_0 = \text{const}$, which implies that x_λ is a quadratic function of q_i. Thus, it is also a quadratic function of the shifted $\tilde{q}_i = q_i + c_i/2$. But in these variables x_λ must be even due to the first type of the Weyl group actions (1.71), which restricts it to

$$x_\lambda = \sum_i b_i \tilde{q}_i^2 + B. \tag{3.24}$$

The other type of Weyl group actions (1.72), which requires invariance of x_λ with respect to the interchange $\tilde{q}_i \leftrightarrow \tilde{q}_j$ for any pair i, j, forces all coefficients b_i to be equal: $b_i = -b$. Finally, the constant B is found from the requirement $x_0 = 0$, which gives $B = b\sum_i c_i^2/4$, and

$$x_\lambda = -b\sum_i q_i(q_i + c_i) = -b(\lambda, \lambda + \rho_b). \tag{3.25}$$

Thus, the generalized dimensions are proportional to the value of the quadratic Casimir operator in the representation labeled by the highest weight λ. Now choosing $\lambda = qe_1$, one can see that the constant b is the same as in the simple MF spectrum (3.20). The generlized MF spectrum (3.25) is thus parametrized by a single constant b. For the result (3.25) the term "generalized parabolicity" will be used.

3.2.2.3 Generalized parabolicity of generalized MF spectra as a hallmark of local conformal invariance at 2D ATs

Now two conditions under which the generalized parabolicity of generalized MF spectra of 2D systems has been derived are discussed. Recall again that these are (1) local conformal invariance and (2) Abelian fusion.

First the second condition is discussed: the Abelian fusion of operators $\mathcal{O}_\lambda$. In Ref. [87], the operators $\mathcal{O}_\lambda$ were explicitly constructed for class A by two approaches (Iwasawa decomposition and highest-weight vectors), and the results do satisfy the Abelian fusion requirement. Furthermore, the methods of Ref. [87] can be extended to other symmetry classes. This will be done in the present paper for class C. Specifically, the Abelian fusion of the scaling operators $\mathcal{O}_\lambda$ follows from their derivation as highest-weight vectors under the action of a Lie algebra, see Ref. [105]. Furthermore, it is a consequence of the form of these operators as "plane waves" on the target space of the sigma model constructed by means of Iwasawa decomposition in Sec. 3.3. These results thus provide an explicit verification of the Abelian-fusion condition.

The situation with the assumption of the conformal invariance is much more delicate, as was already mentioned at the end of Sec. 1.2.2.2. It is not known *a priori* whether it holds (in the narrow sense explained above) at 2D critical points such as IQH or spin quantum Hall transitions. Therefore, the generalized parabolicity of spectra of generalized MF dimensions in fact serves as a hallmark for the local conformal invariance. By constructing explicitly eigenfunction correlations that correspond to $\mathcal{O}_\lambda$ operators and by determining the corresponding scaling dimensions numerically, one can thus test conformal invariance. This will be done below for the spin quantum Hall transition.

3.2.3 Beyond 2D: Non-parabolic MF spectra

While this paper focusses on 2D systems, the following comment on MF spectra beyond 2D is instructive at this point. The assumption of local conformal invariance (involving the infinite-dimensional Virasoro algebra) was crucial for the above derivation of exact parabolicity of MF spectra (both simple and generalized). This assumption may or may not hold at a 2D AT critical point. However, it definitely does not hold beyond 2D. Therefore, the derivation is certainly not applicable to systems of other spatial dimensionality. Indeed, it is well known, both analytically and numerically, that the MF spectra are in general *not parabolic*.

On the analytical side, the MF dimensions have been calculated by perturbative ε-expansion of the σ models in $2+\varepsilon$ dimensions [188, 189]. All these results give parabolic spectra in the leading term but exhibit deviations from exact parabolicity in higher orders in ε. In full consistency with the analytical predictions, numerical evaluation of MF spectra at ATs in systems of spatial dimensionality $d = 3$, 4, and 5 [21, 194–196] demonstrate significant deviations from parabolicity that grow with increasing d. Furthermore, the limit $d \gg 1$ can be addressed by using the results for the ATs on the Bethe lattice that show the MF acquires its strongest form in this limit [9], with the spectrum

$$\Delta_q \simeq d(1/2 - |q - 1/2|). \tag{3.26}$$

This spectrum is piecewise linear rather than parabolic. Numerical results indeed approach this behavior with increasing d [194, 196]. A similar evolution of the MF spectrum, from a nearly-parabolic spectrum (but still with some deviations) towards a piecewise-linear spectrum, is also found (both analytically and numerically) for the model of power-law random banded matrices [9].

In Ref. [197], it was claimed that exact parabolicity (3.1) holds for *all* ATs in the standard Wigner-Dyson classes in *any* dimension. Clearly, this statement is incorrect since it is in contradiction with the whole body of analytical and numerical results that were just reviewed. For the benefit of the reader, the crucial flaw in the argumentation of Ref. [197] is pointed out. The author of Ref. [197] obtained the relation (3.18) from an ad-hoc assumption that *all* three-point MF correlation functions are just products of simple power-law factors, see Eq. (9) in Ref. [197]. This assumption is in general incorrect. In reality, the three-point functions reduce to *different* products of power-law factors in limiting cases

that correspond to different hierarchical relations among distances between the points, as follows from general RG arguments presented in Section 1.2.2.1; see, in particular Eq. (1.78). A similar assumption of Ref. [197] for *all* multi-point MF correlation function [Eq. (19) there] is flawed for the same reason. Only in the presence of local conformal invariance in 2D systems, much stronger constraints emerge that allow one to prove the parabolicity.

3.3 Iwasawa decomposition

In this section the construction based on the Iwasawa decomposition is performed. For a bosonic NLSM manifold $\mathcal{M}_B = G/K$, this yields a family of pure scaling operators (as defined in Sec. 1.2.2) that satisfy abelian fusion (1.76). The outline of the basic steps in this approach follows. In Sec. 3.3.1 a formal construction of the Iwasawa decomposition (3.33) for the Lie algebra $\mathfrak{g}$ into the compact $\mathfrak{k}$, an abelian part $\mathfrak{a}$ and a nilpotent $\mathfrak{n}$ is given. Sec. 3.3.2 explains how this can be used to obtain a general parametrization of N-radial eigenfunctions to G/K-invariant differential operators. In Sec. 3.3.4 the Iwasawa decomposition is performed for $\mathfrak{g} = \mathfrak{so}^*(4n)$ (class C bosonic). Sec. 3.3.5 obtains the N-radial eigenfunctions in $\mathcal{M}_B = \mathrm{SO}^*(4n)/\mathrm{U}(2n)$.

3.3.1 Mathematical definition

One needs to:

1. begin with the (real) Cartan decomposition of the (real) Lie algebra $\mathfrak{g}$ of $\mathcal{M}_B$

$$\mathfrak{g} = \mathfrak{k} \oplus \mathfrak{p}, \tag{3.27}$$

which is defined by the commutation relations:

$$[\mathfrak{k}, \mathfrak{k}] \subseteq \mathfrak{k}, \qquad\qquad [\mathfrak{k}, \mathfrak{p}] \subseteq \mathfrak{p}, \qquad\qquad [\mathfrak{p}, \mathfrak{p}] \subseteq \mathfrak{k}. \tag{3.28}$$

2. choose a maximal Abelian subspace $\mathfrak{a} \subset \mathfrak{p}$.

3. consider the adjoint action $[H, .]$ of elements $H \in \mathfrak{a}$ on $\mathfrak{g}$. The eigenvectors E_α of this action satisfy

$$[H, E_\alpha] = \alpha(H) E_\alpha \tag{3.29}$$

and are called *restricted* root vectors, and the eigenvalues α are called restricted roots. The dimension m_α of the restricted root space

$$\mathfrak{g}_\alpha = \mathrm{span}\,\{E_\alpha\} \tag{3.30}$$

is called the multiplicity of the restricted root α, it holds $m_\alpha \geq 1$. Restricted roots are linear functions on $\mathfrak{a}$, and lie in the space $\mathfrak{a}^*$ dual to $\mathfrak{a}$. In the present context both $\mathfrak{a}$ and $\mathfrak{a}^*$ have dimension n. Basis elements in the space $\mathfrak{a}^*$, specified later, will be denoted in this section by e_i ($i = 1, \ldots, n$). Notice that these basis vectors were called e_i in Sections 1.2.2 and 3.2.

4. A system of positive restricted roots is defined by choosing some hyperplane through the origin of $\mathfrak{a}^*$ which divides $\mathfrak{a}^*$ in two halves, and then defining one of these halves as positive. The Weyl vector ρ is defined as the half-sum of positive restricted roots accounting for their multiplicities:

$$\rho = \sum_{\alpha > 0} m_\alpha \alpha = \sum_{i=1}^{n} c_i e_i. \tag{3.31}$$

5. The components c_i of the Weyl vector will be found later, see Eq. (3.67). Positive restricted roots generate the nilpotent Lie algebra

$$\mathfrak{n} = \sum_{\alpha > 0} \mathfrak{g}_\alpha. \tag{3.32}$$

6. The Iwasawa decomposition

$$\mathfrak{g} = \mathfrak{k} \oplus \mathfrak{a} \oplus \mathfrak{n} \tag{3.33}$$

can be thought of as real form of the complex root-space decomposition. One has

$$\mathfrak{n} = \mathfrak{p} \oplus (\mathfrak{n} \cap \mathfrak{k}). \tag{3.34}$$

of the real Lie algebra $\mathfrak{g} = \mathrm{so}^*(4n)$ into a maximal compact subalgebra $\mathfrak{k} = \mathrm{u}(2n)$ and the complementary subspace $\mathfrak{p}$.

3.3.2 N-radial eigenfunctions

The power of above Eq. (3.33) can be seen from exponentiating. This gives the Iwasawa decomposition in global form:

$$G = NAK, \tag{3.35}$$

which allows one to represent any element $g \in G$ in the form $g = nak$, with $n \in N = e^{\mathfrak{n}}$ nilpotent, $a \in A = e^{\mathfrak{a}}$ diagonal, and $k \in K = e^{\mathfrak{k}}$ compact. This factorization is unique once the system of positive restricted roots is fixed, and provides a very useful parametrization of the target space G/K. An element $a \in A$ is fully specified by n real numbers $e_i(\ln a)$, which play the role of radial coordinates on G/K. For simplicity, these radial coordinates will simply by denoted by e_i. Thus e_i may now have two different meanings: either its original meaning as a basis element in $\mathfrak{a}^*$, or the new one as an N-radial function $e_i(\ln a)$ on G/K. It should be clear from the context which of the two meanings is being used.

Using the radial coordinates, the joint N-radial eigenfunctions of the Laplace-Casimir operators on G/K take a very simple exponential form

$$\varphi_\mu(Q) = e^{(\rho + \mu)(\ln a)}, \tag{3.36}$$

where a is the a-factor in the Iwasawa decomposition of g in $Q = g\Lambda g^{-1}$, and

$$\mu = \sum_{i=1}^{n} \mu_i e_i \tag{3.37}$$

is a weight vector in $\mathfrak{a}^*$. Also use the notation

$$q_i = -(\mu_i + c_i)/2 \tag{3.38}$$

will be used, in which the exponential functions (3.36) become

$$\varphi_\mu \equiv \varphi_{(q_1, q_2, \ldots, q_n)} = \exp\left(-2 \sum_{i=1}^{n} q_i e_i\right). \tag{3.39}$$

To construct the exponential N-radial eigenfunctions explicitly as combinations of matrix elements of Q, one can use the key fact that there exists a choice of basis in which elements of $\mathfrak{a}$ and $a \in A$ are diagonal matrices, while elements of $\mathfrak{n}$ are strictly upper triangular, and elements $n \in N$ are upper triangular with units on the diagonal. This has immediate consequences for the matrix $Q\Lambda$: since elements of K commute with Λ, the Iwasawa decomposition $g = nak$ leads to $Q\Lambda = na^2\Lambda n^{-1}\Lambda$, which is a product of an upper triangular, a diagonal, and a lower triangular matrices. In this form the principal minors of the AA block of $Q\Lambda$ are simply products of diagonal elements of a^2, which are exponentials of the radial coordinates x_i on G/K. These minors are basic N-radial spherical functions on G/K which can be raised to arbitrary powers and multiplied to produce the most general exponential functions (3.36). A great advantage of this construction is that is directly gives the general positive scaling operators that can be raised to arbitrary powers and satisfy the Abelian fusion rules.

In the following details of the Iwasawa construction for the class C NLSM bosonic manifold $\mathrm{SO}^*(4n)/\mathrm{U}(2n)$ are presented.

3.3.3 Definitions and notations for the symmetric space $G/K = \mathrm{SO}^*(4n)/\mathrm{U}(2n)$

The basic vector space that is worked with here is

$$\mathbb{C}^{4n} = \mathbb{C}^2 \otimes \mathbb{C}^2 \otimes \mathbb{C}^n, \tag{3.40}$$

where the factors in the tensor product are the retarded-advanced (RA), spin, and replica spaces, in this order. A standard notation for the matrix units will be used: E_{ij} is the matrix with 1 in the i-th row and j-th column, all other entries being zero. One can write this in terms of the matrix elements: $(E_{ij})_{kl} = \delta_{ik}\delta_{jl}$. The range of indices in this definition is the dimension of the space in which E_{ij} act, and in various sections below it can be 2 for the RA space, n for the replica space, or $2n$ for the product of the spin and replica spaces. The products and commutators of matrix units are easy to find:

$$E_{ij}E_{kl} = \delta_{jk}E_{il}, \qquad\qquad [E_{ij}, E_{kl}] = \delta_{jk}E_{il} - \delta_{il}E_{kj}. \tag{3.41}$$

One can introduce an additional notation for special matrices related to the tensor product structure (3.40):

$$\Sigma_{ij} \equiv \sigma_i \otimes \sigma_j \otimes I_n. \tag{3.42}$$

Here σ_i are the usual 2×2 Pauli matrices, and the indices i and j are allowed to take the value 0, which corresponds to the identity matrix $\sigma_0 = I_2$. For example $\Sigma_{00} = I_{4n}$, and $\Sigma_{30} = \Lambda$, the usual Λ matrix from the sigma model. The notations (3.42) are different from the ones used in Sections 3.4 and 3.5. The two sets are related by

$$\tau_i = \Sigma_{i0}, \qquad\qquad \Sigma_i = \Sigma_{0i}, \qquad\qquad \tau_i\Sigma_j = \Sigma_{ij}. \tag{3.43}$$

Next, the following group involutions are defined:

$$\Theta_i(g) \equiv \Sigma_{i0}(g^{-1})^T\Sigma_{i0}, \tag{3.44}$$

These preserve multiplication of matrices, and can be applied not only to group elements g, but to any matrices, including the Q fields of the sigma model. Note that the involution Θ_1 is closely related (but not identical) with the "bar" operation defined in Eq. (3.141) in Sec. 3.5.

The definition [198] of the group $SO^*(4n)$ as the subgroup of the pseudo-unitary group $SU(2n, 2n)$ that preserves the symmetric bilinear from with the matrix Σ_{10} is used next. In this definition the elements $g \in SO^*(4n)$ satisfy

$$g^\dagger \Sigma_{30} g = \Sigma_{30}, \qquad\qquad g^T \Sigma_{10} g = \Sigma_{10}. \qquad (3.45)$$

These conditions can be rewriten using the involutions (3.44):

$$\Theta_3(g) = g^*, \qquad\qquad \Theta_1(g) = g. \qquad (3.46)$$

The sigma model field (3.111) $Q = g\Lambda g^{-1}$, where $g \in SO^*(4n)$, inherits certain symmetry properties from the constraints (3.46). Applying the involutions Θ_3 and Θ_1 to Q and using $\Theta_3(\Lambda) = \Lambda$, and $\Theta_1(\Lambda) = -\Lambda$, one gets

$$\Theta_3(Q) = Q^*, \qquad\qquad \Theta_1(Q) = -Q. \qquad (3.47)$$

Since $Q^2 = I_{4n}$, these constraints can be also written in the form

$$\Sigma_{30} Q^T \Sigma_{30} = Q^*, \qquad\qquad \Sigma_{10} Q^T \Sigma_{10} = -Q. \qquad (3.48)$$

Notice that the second constraint here is different from the one obtained in Sec. 3.4 in Eq. (3.114). Rather, it is the one that appears for the transformed matrix $\tilde{Q}$ in Eq. (3.118), see the relevant discussion and the transformation relating the two choices for Q in Sec. 3.4.

Writing Q as a block matrix in the RA space

$$Q = \begin{pmatrix} Q_{RR} & Q_{RA} \\ Q_{AR} & Q_{AA} \end{pmatrix}, \qquad (3.49)$$

one obtains constraints on the blocks:

$$Q_{RR}^\dagger = Q_{RR}, \qquad Q_{AA}^\dagger = Q_{AA}, \qquad Q_{RA}^\dagger = -Q_{AR}, \qquad (3.50)$$
$$Q_{RR}^T = -Q_{AA}, \qquad Q_{RA}^T = -Q_{RA}, \qquad Q_{AR}^T = -Q_{AR}. \qquad (3.51)$$

The anti-symmetry of the off-diagonal blocks Q_{RA} and Q_{AR} will be important in what follows.

3.3.4 Cartan decomposition and generators of SO$^*(4n)$/U$(2n)$

The group $SO^*(4n)$ is connected, so all its elements can be written as $g = e^Z$, where Z are elements of the Lie algebra $so^*(4n)$. These satisfy the infinitesimal versions of Eqs. (3.45):

$$Z^\dagger \Sigma_{30} + \Sigma_{30} Z = 0, \qquad\qquad Z^T \Sigma_{10} + \Sigma_{10} Z = 0, \qquad (3.52)$$

In terms of the Lie algebra involutions θ_i related to the group involutions (3.44)

$$\theta_i(Z) \equiv -\Sigma_{i0} Z^T \Sigma_{i0}, \qquad (3.53)$$

constraints on Z can be written as

$$\theta_3(Z) = Z^*, \qquad\qquad \theta_1(Z) = Z. \qquad (3.54)$$

If one writes the Lie algebra elements Z as block-matrices in the RA space, the constraints (3.52) imply

$$Z = \begin{pmatrix} A & B \\ -B^* & A^* \end{pmatrix}, \qquad A^\dagger = -A, \qquad B^T - B. \qquad (3.55)$$

The Cartan involution that determines the Cartan decomposition $\mathrm{so}^*(4n) = \mathfrak{k} \oplus \mathfrak{p}$ into even and odd subspaces is θ_2. It acts on generators Z as

$$\theta_2(Z) = -\Sigma_{20} Z^T \Sigma_{20} = \begin{pmatrix} A & -B \\ B^* & A^* \end{pmatrix}. \qquad (3.56)$$

This gives one a very explicit description of the Cartan decomposition:

$$\mathfrak{k} = \left\{ \begin{pmatrix} A & 0 \\ 0 & A^* \end{pmatrix}, \quad A^\dagger = -A \right\}, \qquad \mathfrak{p} = \left\{ \begin{pmatrix} 0 & B \\ -B^* & 0 \end{pmatrix}, \quad B^T = -B \right\}. \qquad (3.57)$$

As expected, the subalgebra $\mathfrak{k} = \mathrm{u}(2n)$, the Lie algebra of $K = \mathrm{U}(2n)$, the maximal compact subgroup in $G = \mathrm{SO}^*(4n)$.

Now one can separate the real and imaginary parts in Eq. (3.57):

$$\mathfrak{k} = \left\{ \begin{pmatrix} A_1 + iA_2 & 0 \\ 0 & A_1 - iA_2 \end{pmatrix}, \begin{matrix} A_1^T = -A_1 \\ A_2^T = A_2 \end{matrix} \right\}, \quad \mathfrak{p} = \left\{ \begin{pmatrix} 0 & B_1 + iB_2 \\ -B_1 + iB_2 & 0 \end{pmatrix}, \begin{matrix} B_1^T = -B_1 \\ B_2^T = -B_2 \end{matrix} \right\}. \qquad (3.58)$$

These forms allow one to write the generators of the two subsets in terms of tensors in the space (3.40). For elements in $\mathfrak{k}$, the first factor should be diagonal, so it is either I_2 or $i\sigma_3$. For the first choice (I_2), the other two tensor factors should produce a real anti-symmetric matrix, which can be done choosing one of the factors to be a symmetric matrix, and the other an anti-symmetric matrix. Likewise, for the second choice ($i\sigma_3$) one needs the other two factors to produce a real symmetric matrix, so the factors can be either simultaneously symmetric or anti-symmetric. Introducing a short-hand notation for the symmetric and anti-symmetric combinations of matrix units in the replica space

$$E_{ij}^+ = E_{ij} + E_{ji}, \qquad\qquad i \leqslant j, \qquad\qquad \frac{n(n+1)}{2} \quad \text{total}, \qquad (3.59)$$

$$E_{ij}^- = E_{ij} - E_{ji}, \qquad\qquad i < j, \qquad\qquad \frac{n(n-1)}{2} \quad \text{total}, \qquad (3.60)$$

one gets the following eight groups of generators:

$$\begin{aligned}
X_{ij}^{00} &\equiv \sigma_0 \otimes \sigma_0 \otimes E_{ij}^-, & X_{ij}^{01} &\equiv \sigma_0 \otimes \sigma_1 \otimes E_{ij}^-, & X_{ij}^{02} &\equiv \sigma_0 \otimes i\sigma_2 \otimes E_{ij}^+, & X_{ij}^{03} &\equiv \sigma_0 \otimes \sigma_3 \otimes E_{ij}^-, \\
X_{ij}^{30} &\equiv i\sigma_3 \otimes \sigma_0 \otimes E_{ij}^+, & X_{ij}^{31} &\equiv i\sigma_3 \otimes \sigma_1 \otimes E_{ij}^+, & X_{ij}^{32} &\equiv i\sigma_3 \otimes i\sigma_2 \otimes E_{ij}^-, & X_{ij}^{33} &\equiv i\sigma_3 \otimes \sigma_3 \otimes E_{ij}^+.
\end{aligned} \qquad (3.61)$$

The total number of generators here is $4n^2 = (2n)^2$, the dimension of $\mathfrak{k} = \mathrm{u}(2n)$, as it should be.

Similarly, for the elements in $\mathfrak{p}$, the first factor should be either $i\sigma_1$ or $i\sigma_2$, and for either of these choices the remaining two factors should give a real anti-symmetric matrix. This gives the following eight groups of generators:

$$Y_{ij}^{10} = i\sigma_1 \otimes \sigma_0 \otimes E_{ij}^-, \quad Y_{ij}^{11} = i\sigma_1 \otimes \sigma_1 \otimes E_{ij}^-, \quad Y_{ij}^{12} = i\sigma_1 \otimes i\sigma_2 \otimes E_{ij}^+, \quad Y_{ij}^{13} = i\sigma_1 \otimes \sigma_3 \otimes E_{ij}^-,$$
$$Y_{ij}^{20} = i\sigma_2 \otimes \sigma_0 \otimes E_{ij}^-, \quad Y_{ij}^{21} = i\sigma_2 \otimes \sigma_1 \otimes E_{ij}^-, \quad Y_{ij}^{22} = i\sigma_2 \otimes i\sigma_2 \otimes E_{ij}^+, \quad Y_{ij}^{23} = i\sigma_2 \otimes \sigma_3 \otimes E_{ij}^-.$$
$$(3.62)$$

The total number of these generators is $4n^2 - 2n = 2n(2n-1)$, which is the dimension of the space $\mathfrak{p}$.

3.3.5 Iwasawa decomposition for SO$^*(4n)/$U$(2n)$

Choose the following set of Hermitian matrices as the maximal Abelian subspace $\mathfrak{a} \subset \mathfrak{p}$:

$$\mathfrak{a} = \text{span}\left\{ H_k = i\sigma_2 \otimes i\sigma_2 \otimes E_{kk} = Y_{22,kk}/2, \quad k = 1, \ldots, n \right\}. \tag{3.63}$$

A generic element $H \in \mathfrak{a}$ is $H = \sum_{k=1}^n h_k H_k$. The basis in the dual space $\mathfrak{a}^*$ is defined as elements e_i such that $e_i(H) = h_i$. These elements will later play the role of the radial coordinates on the coset SO$^*(4n)/$U$(2n)$.

To find restricted roots and restricted root vectors, one needs to find the commutators of H with the generators (3.61) and (3.62). One needs both sets since the commutation relations (3.28) imply that

$$[\mathfrak{a}, \mathfrak{k}] \subset \mathfrak{p}, \qquad\qquad [\mathfrak{a}, \mathfrak{p}] \subset \mathfrak{k}, \tag{3.64}$$

so the eigenvectors of the adjoint action of $\mathfrak{a}$ can only be linear combinations of generators from both sets.

Straightforward computations show that the system of restricted roots consists of roots of normal length $\pm x_i \pm x_j$ ($i \neq j$) with multiplicity 4, and long roots $\pm 2x_j$ with multiplicity 1. This is the root system C_n in the usual Cartan notation. The set of positive restricted roots can be chosen as (multiplicities shown in brackets)

$$\alpha_{ij} \equiv e_i - e_j, \quad i < j \quad (4), \qquad \beta_{ij} \equiv e_i + e_j, \quad i < j \quad (4), \qquad \gamma_i \equiv 2e_i \quad (1). \tag{3.65}$$

The Weyl vector (the half-sum of positive restricted roots accounting for their multiplicities) is

$$\rho = (4n-3)x_1 + (4n-7)x_2 + \ldots + 5x_{n-1} + x_n = \sum_{j=1}^n c_j x_j, \qquad c_j = 4n + 1 - 4j. \tag{3.66}$$

In the replica limit $n \to 0$ the components of the Weyl vector become

$$c_j = 1 - 4j. \tag{3.67}$$

The positive restricted root vectors corresponding to the α, β, and γ roots are

$$E_{\alpha_{ij}}^{(1)} = X_{ij}^{00} + Y_{ij}^{22}, \qquad E_{\alpha_{ij}}^{(2)} = X_{ij}^{02} - Y_{ij}^{20}, \qquad E_{\alpha_{ij}}^{(3)} = X_{ij}^{31} - Y_{ij}^{13}, \qquad E_{\alpha_{ij}}^{(4)} = X_{ij}^{33} + Y_{ij}^{11}, \tag{3.68}$$

$$E_{\beta_{ij}}^{(1)} = X_{ij}^{01} + Y_{ij}^{23}, \qquad E_{\beta_{ij}}^{(2)} = X_{ij}^{03} - Y_{ij}^{21}, \qquad E_{\beta_{ij}}^{(3)} = X_{ij}^{30} - Y_{ij}^{12}, \qquad E_{\beta_{ij}}^{(4)} = X_{ij}^{32} + Y_{ij}^{10}, \tag{3.69}$$

$$E_{\gamma_i} = X_{ii}^{30} - Y_{ii}^{12}. \tag{3.70}$$

As was mentioned above, these vectors generate the nilpotent subalgebra $\mathfrak{n}$, and one gets the resulting Iwasawa decomposition (3.33).

3.3.6 Real scaling operators as N-radial functions

In this section I perform a unitary transformation of basis in the space (3.40) designed to bring the generators of $\mathfrak{a}$ into a diagonal form. There are infinitely many such transformations, and the one chosen has an additional useful property that the resulting positive restricted root vectors are also upper-triangular in the RA space. This is achieved with the help of the unitary matrix

$$U = \frac{1}{\sqrt{2}}(\sigma_0 \otimes E_{11} + \sigma_1 \otimes E_{12} - \sigma_2 \otimes E_{21} - i\sigma_3 \otimes E_{22}) \otimes I_n, \tag{3.71}$$

where the 2×2 matrix units E_{ij} in the spin space are used. While this is not a single tensor product in the RA and spin spaces, conjugation with this matrix,

$$T(A) \equiv UAU^{-1}, \tag{3.72}$$

keeps such single products in the basis of $\mathfrak{a}$:

$$T(H_k) = \sigma_3 \otimes \sigma_0 \otimes E_{kk}, \tag{3.73}$$

in the the saddle point

$$T(\Lambda) = -\Sigma_{12}, \tag{3.74}$$

as well as in the restricted root vectors:

$$\begin{aligned}
T(E_{\alpha_{ij}}^{(1)}) &= \sigma_0 \otimes \sigma_0 \otimes E_{ij}^- + \sigma_3 \otimes \sigma_0 \otimes E_{ij}^+ = 2E_{11} \otimes \sigma_0 \otimes E_{ij} - 2E_{22} \otimes \sigma_0 \otimes E_{ji}, \\
T(E_{\alpha_{ij}}^{(2)}) &= i\sigma_3 \otimes \sigma_1 \otimes E_{ij}^+ + i\sigma_0 \otimes \sigma_1 \otimes E_{ij}^- = 2iE_{11} \otimes \sigma_1 \otimes E_{ij} - 2iE_{22} \otimes \sigma_1 \otimes E_{ji}, \\
T(E_{\alpha_{ij}}^{(3)}) &= -i\sigma_0 \otimes \sigma_2 \otimes E_{ij}^+ - i\sigma_3 \otimes \sigma_2 \otimes E_{ij}^- = -2iE_{11} \otimes \sigma_2 \otimes E_{ij} + 2iE_{22} \otimes \sigma_2 \otimes E_{ji}, \\
T(E_{\alpha_{ij}}^{(4)}) &= i\sigma_3 \otimes \sigma_3 \otimes E_{ij}^+ + i\sigma_0 \otimes \sigma_3 \otimes E_{ij}^- = 2iE_{11} \otimes \sigma_3 \otimes E_{ij} + 2iE_{22} \otimes \sigma_3 \otimes E_{ji}, \\
T(E_{\beta_{ij}}^{(1)}) &= \sigma_1 \otimes \sigma_0 \otimes E_{ij}^- + i\sigma_2 \otimes \sigma_0 \otimes E_{ij}^- = 2E_{12} \otimes \sigma_0 \otimes E_{ij}^-, \\
T(E_{\beta_{ij}}^{(2)}) &= -\sigma_2 \otimes \sigma_1 \otimes E_{ij}^- + i\sigma_1 \otimes \sigma_1 \otimes E_{ij}^- = 2iE_{12} \otimes \sigma_1 \otimes E_{ij}^-, \\
T(E_{\beta_{ij}}^{(3)}) &= -i\sigma_1 \otimes \sigma_2 \otimes E_{ij}^+ + \sigma_2 \otimes i\sigma_2 \otimes E_{ij}^+ = -2iE_{12} \otimes \sigma_2 \otimes E_{ij}^+, \\
T(E_{\beta_{ij}}^{(4)}) &= -\sigma_2 \otimes \sigma_3 \otimes E_{ij}^- + i\sigma_1 \otimes \sigma_3 \otimes E_{ij}^- = 2iE_{12} \otimes \sigma_3 \otimes E_{ij}^- \\
T(E_{\gamma_i}) &= -2i\sigma_1 \otimes \sigma_2 \otimes E_{ii} + 2\sigma_2 \otimes i\sigma_2 \otimes E_{ii} = -4iE_{12} \otimes \sigma_2 \otimes E_{ii}.
\end{aligned} \tag{3.75}$$

As claimed, the structure in the RA space is upper triangular: in the first factor one has either E_{11} and E_{22} or E_{12}.

One can visualize the restricted root vectors for $n = 3$ as a schematic matrix diagram by indicating the matrix positions where various generators have non-zero entries. For brevity one can write $\gamma_i \equiv E_{\gamma_i}$, $\alpha^{(i)} \equiv E_{\alpha_{kl}}^{(i)}$, $\beta^{(i)} \equiv E_{\beta_{kl}}^{(i)}$ with indices suppressed since they can be inferred from the matrix grid

(uncolored cells have zero entries):

$$
T(E) = \left(\begin{array}{cccc|cccc|cccc}
x_1 & \alpha^{(14)} & & \alpha^{(23)} & & \beta^{(14)} & \gamma_1 & & \beta^{(23)} \\
 & x_2 & & & & & & \gamma_2 & \\
 & & x_3 & & \beta^{(14)} & & \beta^{(23)} & & \gamma_3 \\
\hline
 & \alpha^{(23)} & x_1 & \alpha^{(14)} & \gamma_1 & & \beta^{(23)} & & \beta^{(14)} \\
 & & & x_2 & & \gamma_2 & & & \\
 & & & x_3 & \beta^{(23)} & & \gamma_3 & \beta^{(14)} & \\
\hline
 & & & & -x_1 & & & & \\
 & & & & & -x_2 & & & \\
 & & & & \alpha^{(14)} & & -x_3 & \alpha^{(23)} & \\
\hline
 & & & & & & & -x_1 & \\
 & & & & & & & & -x_2 \\
 & & & & \alpha^{(23)} & & & \alpha^{(14)} & -x_3
\end{array}\right).
\tag{3.76}
$$

This matrix can be made upper triangular by an additional permutation π of the basis vectors that can be described explicitly as follows: for $i \in 1, \ldots, n$, one has

$$
\pi(i) = 2i - 1, \qquad \pi(n + i) = 2i, \qquad \pi(2n + i) = 4n + 2 - 2i, \qquad \pi(3n + i) = 4n + 1 - 2i.
\tag{3.77}
$$

This permutation re-sorts the diagonal entries of the matrix (3.76) as follows:

$$
x_1, \ldots, x_n, x_1, \ldots, x_n, -x_1, \ldots, -x_n, -x_1, \ldots, -x_n \quad \rightarrow \quad x_1, x_1, \ldots, x_n, x_n, -x_n, -x_n, \ldots, -x_1, -x_1.
\tag{3.78}
$$

The permutation matrix P_π that corresponds to π has the matrix elements $(P_\pi)_{ij} = \delta_{\pi(i),j}$, and can be used to permute rows and columns of a matrix M as follows:

$$
(P_\pi M)_{ij} = M_{\pi(i),j}, \qquad\qquad\qquad (M P_\pi^{-1})_{ij} = M_{i,\pi(j)}.
\tag{3.79}
$$

Then one can see that the conjugation of the matrix (3.76) by P_π makes it fully upper-triangular. Using the notation

$$
\tilde{M} \equiv P_\pi T(M) P_\pi^{-1},
\tag{3.80}
$$

for transformed matrices, one has

$$
\tilde{E} = \left(\begin{array}{cccccc|cccccc}
x_1 & & & & & & & & & & & \gamma_1 \\
 & x_1 & & & & & & & & & \gamma_1 & \\
 & & x_2 & & & & & & & \gamma_2 & & \\
 & & & x_2 & & & & & \gamma_2 & & & \\
 & & & & x_3 & & & \gamma_3 & & & & \\
 & & & & & x_3 & \gamma_3 & & & & & \\
\hline
 & & & & & & -x_3 & & & & & \\
 & & & & & & & -x_3 & & & & \\
 & & & & & & & & -x_2 & & & \\
 & & & & & & & & & -x_2 & & \\
 & & & & & & & & & & -x_1 & \\
 & & & & & & & & & & & -x_1
\end{array}\right).
\tag{3.81}
$$

In the final basis the elements of $\mathfrak{a}$ are diagonal matrices, while elements of $\mathfrak{n}$ are strictly upper triangular.

One can exploit consequences of the Iwasawa decomposition of G and the transformation T for the sigma model field Q. First of all, in the original basis where $\Lambda = \Sigma_{30}$ one can write $g = nak$ with $n \in N$, $a \in A$, and $k \in K$, and then

$$\mathcal{Q} \equiv Q\Lambda = nak\Lambda k^{-1}a^{-1}n^{-1}\Lambda = na^2\Lambda n^{-1}\Lambda. \tag{3.82}$$

Here $k\Lambda k^{-1} = \Lambda$ is used, and $a\Lambda a^{-1} = a^2\Lambda$, which is a special case of the first condition in Eq. (3.45) for a Hermitian matrix $a \in G$. Now one can perform the transformation T, Eq. (3.72), as well as the permutation P_π. Using the notation (3.80), one gets

$$\tilde{\mathcal{Q}} = \tilde{n}\tilde{a}^2\tilde{\Lambda}\tilde{n}^{-1}\tilde{\Lambda}. \tag{3.83}$$

Using Eqs. (3.74) and (3.77), one can compute the matrix

$$\tilde{\Lambda} = -P_\pi\Sigma_{12}P_\pi^{-1} = -\sigma_1 \otimes \sigma_2 \otimes \mathcal{I}_n, \tag{3.84}$$

where $\mathcal{I}_n$ is the $n \times n$ matrix with units on the "anti-diagonal", that is, $(\mathcal{I}_n)_{ij} = \delta_{i,n+1-j}$.

As should be clear from the previous discussion, the matrices $\tilde{n}$ and $\tilde{n}^{-1}$ are upper-triangular with units on the diagonals, while $\tilde{a}$ is diagonal:

$$\tilde{a} = \mathrm{diag}(e^{x_1}, e^{x_1}, \ldots, e^{x_n}, e^{x_n}, e^{-x_n}, e^{-x_n}, \ldots, e^{-x_1}, e^{-x_1}). \tag{3.85}$$

Conjugation by $\tilde{\Lambda}$ converts $\tilde{n}^{-1}$ into $\tilde{\Lambda}\tilde{n}^{-1}\tilde{\Lambda}$ which is *lower-triangular* with units on the diagonal. This results in the following structure of the AA block of the matrix $\tilde{\mathcal{Q}}$:

$$\tilde{\mathcal{Q}}_{AA} = \begin{pmatrix} 1 & * & \ldots & * & * \\ 0 & 1 & \ldots & * & * \\ \vdots & \vdots & \ddots & \vdots & \vdots \\ 0 & 0 & \ldots & 1 & * \\ 0 & 0 & \ldots & 0 & 1 \end{pmatrix} \begin{pmatrix} e^{-2x_n} & 0 & \ldots & 0 & 0 \\ 0 & e^{-2x_n} & \ldots & 0 & 0 \\ \vdots & \vdots & \ddots & \vdots & \vdots \\ 0 & 0 & \ldots & e^{-2x_1} & 0 \\ 0 & 0 & \ldots & 0 & e^{-2x_1} \end{pmatrix} \begin{pmatrix} 1 & 0 & \ldots & 0 & 0 \\ * & 1 & \ldots & 0 & 0 \\ \vdots & \vdots & \ddots & \vdots & \vdots \\ * & * & \ldots & 1 & 0 \\ * & * & \ldots & * & 1 \end{pmatrix}. \tag{3.86}$$

Determinants of the lower-right $2m \times 2m$ submatrices of $\tilde{\mathcal{Q}}_{AA}$ give the basic positive N-radial eigenfunctions

$$d_{2m} = \prod_{i=1}^{m} e^{-4x_i} = \exp\left(-4\sum_{i=1}^{m} x_i\right). \tag{3.87}$$

One can form the most general N-radial eigenfunctions as products

$$\varphi_{(q_1,\ldots,q_n)} = d_2^{(q_1-q_2)/2} d_4^{(q_2-q_3)/2} \ldots d_{2(n-1)}^{(q_{n-1}-q_n)/2} d_{2n}^{q_n/2}, \tag{3.88}$$

where one may take the q_i to be arbitrary complex numbers. It is easy to see that the product (3.88) is the same as the exponential eigenfunction (3.39), while the basic function d_{2m} is $\varphi_{(2,2,\ldots)}$ with m twos in the subscript.

Notice that the doubling of the diagonal entries e^{-2x_i} for each i in Eq. (3.86) compelled me to take determinants of sub-matrices of even size and raise the resulting functions to powers written as

$(q_i - q_{i+1})/2$. This is very similar to the appearance of minors of even size in the highest weight vector construction in Ref. [105]. Those minors were of an anti-symmetric matrix, and thus were squares of Pfaffians. In the Iwasawa formalism it is also possible to obtain directly the "Pfaffian" solutions $\varphi_{(1,1,\dots)}$. Pfaffians can be defined only for anti-symmetric matrices, so one needs to look at transformation properties of various matrices under transposition. For group elements g this property is given in the second equation in (3.45). One can use this equation to derive the following consequence:

$$T(g)^T = (U\Sigma_{10}U^T)^{-1}T(g)^{-1}(U\Sigma_{10}U^T). \tag{3.89}$$

A simple computation shows that $U\Sigma_{10}U^T = \Sigma_{10}$. Thus the rotated matrix $T(g)$ satisfies the same second equation in (3.45):

$$T(g)^{-1} = \Sigma_{10}T(g)^T\Sigma_{10}. \tag{3.90}$$

One can now look at

$$T(Q\Lambda) = T(g)T(\Lambda)T(g)^{-1}T(\Lambda) = T(g)\Sigma_{12}\Sigma_{10}T(g)^T\Sigma_{10}\Sigma_{12} = T(g)\Sigma_{02}T(g)^T\Sigma_{02}, \tag{3.91}$$

which means that $T(Q\Lambda)\Sigma_{02}$ is anti-symmetric. Now one can employ the Iwasawa decomposition $T(g) = T(n)T(a)T(k)$ and drop the last factor, since in $T(Q\Lambda)$ the group element g enters only in the product $g\Lambda g^{-1}$, and k commutes with Λ:

$$T(Q\Lambda)\Sigma_{02} = T(n)T(a)\Sigma_{02}[T(n)T(a)]^T. \tag{3.92}$$

Next, everything is restricted to the AA block using the upper triangular structure of $T(n)$ and the diagonal nature of $T(a)$ in the RA space, see Eq. (3.76). In this block $\Sigma_{02,AA} = \sigma_2 \otimes I_n$, and one has

$$T(Q\Lambda)_{AA}(\sigma_2 \otimes I_n) = T(n)_{AA}T(a)_{AA}(\sigma_2 \otimes I_n)[T(n)_{AA}T(a)_{AA}]^T. \tag{3.93}$$

One can use the property of the Pfaffians $\mathrm{Pf}(MAM^T) = \det(M)\,\mathrm{Pf}\,A$, where A is anti-symmetric and M arbitrary, to obtain

$$\mathrm{Pf}\left[T(Q\Lambda)_{AA}(\sigma_2 \otimes I_n)\right] = \det\left[T(n)_{AA}\right]\det\left[T(a)_{AA}\right]\mathrm{Pf}\,(\sigma_2 \otimes I_n). \tag{3.94}$$

Since the determinant is basis-independent, one has

$$\det\left[T(n)_{AA}\right] = \det[\tilde{n}_{AA}] = 1, \qquad \det\left[T(a)_{AA}\right] = \det[\tilde{a}_{AA}] = \prod_{i=1}^{n} e^{-2x_i}. \tag{3.95}$$

Finally, one gets the Pfaffian N-radial functions

$$p_n \equiv \varphi_{(1,1,\dots)} = \exp\left(-2\sum_{i=1}^{n} x_i\right) = \frac{\mathrm{Pf}\left[T(Q\Lambda)_{AA}(\sigma_2 \otimes I_n)\right]}{\mathrm{Pf}\,(\sigma_2 \otimes I_n)}. \tag{3.96}$$

This can be done for arbitrary number of replicas n, so one gets all basic Pfaffians this way, and the most general N-radial functions

$$\varphi_{(q_1,\dots,q_n)} = p_1^{q_1-q_2} p_2^{q_2-q_3} \dots p_{n-1}^{q_{n-1}-q_n} p_n^{q_n}. \tag{3.97}$$

One should stress again the achievement of this section: the general N-radial eigenfunctions in Eqs. (3.88) and (3.97) are parametrized by *arbitrary* complex numbers $q_1, \dots, q_n$ and satisfy the Abelian fusion. It was the combination of these two properties together with the local 2D conformal invariance that allows one to derive the generalized parabolicity (3.25) in Section 3.2.2.2.

3.4 Sigma model

In this section, the derivation of the class-C nonlinear sigma model is sketched following Ref. [105]. While doing this, notations and conventions employed throughout the following sections are introduced. Starting from the non-interacting Bogoliubov-de Gennes (BdG) Hamiltonian, one can formulate a bosonic $(2+0)$D action S_0. Then one can employ the replica trick [199, 200] to average over disorder. Following the conventional procedure of Hubbard-Stratonovich decoupling and gradient expansion [103, 201–203] described in Sec. 1.1.4.4, one arrives at the sigma model action, Eq. (3.112). The sigma-model field Q lives on the symmetric space $G/K = \mathrm{SO}^*(4n)/\mathrm{U}(2n)$. The derivation largely follows similar lines as Refs. [204–206]. For the connection to the wave function statistics in Sections 3.6, 3.7, the coupling (3.107) between the Q field of the sigma model and the bosonic field variables ϕ of the action S_0 is of crucial importance.

Systems in class C possess particle-hole and spin rotation symmetry:

$$\pi_x H^T \pi_x = -H, \qquad\qquad \sigma_i H \sigma_i = H. \tag{3.98}$$

Here π_x is the first Pauli matrix in the BdG space, and σ_i are Pauli matrices in the spin space. When written in the basis $\psi = (\psi_\uparrow, \psi_\downarrow, \psi_\uparrow^\dagger, \psi_\downarrow^\dagger)$, the Hamiltonian has the following 4×4 matrix form:

$$H_{BdG} = \begin{pmatrix} \frac{1}{2m}(p - eA)^2 - \mu & \hat{\Delta} \\ -\hat{\Delta}^* & -\frac{1}{2m}(p + eA)^2 + \mu \end{pmatrix}_\pi. \tag{3.99}$$

Here the matrix structure in the BdG space is shown explicitly (as indicated by the subscript π); each entry is a 2×2 matrix in the spin space. The matrix $\hat{\Delta}$ is antisymmetric $\hat{\Delta}^T = -\hat{\Delta}$ and $\sigma_y \hat{\Delta} \sigma_y = \hat{\Delta}$ due to spin symmetry. This implies that $\hat{\Delta} = \Delta \sigma_y$, with a complex number Δ. The kinetic term $h = -\frac{1}{2m}(p - eA)^2 + \mu$ is the same for each spin species. Note that p changes sign upon transposition.

As usual for BdG Hamiltonians with preserved spin, Eq. (3.99) decouples into two blocks. One thus gets a 2×2 matrix Hamiltonian for $\psi = (\psi_\uparrow, \psi_\downarrow^\dagger)_\sigma$:

$$H = \begin{pmatrix} \frac{1}{2m}(p - eA)^2 - \mu & \Delta \\ \Delta^* & -\frac{1}{2m}(p - eA)^2 + \mu \end{pmatrix}_\sigma. \tag{3.100}$$

Here and from now on, σ is the combined particle-hole and spin space. In general, one may have an additional matrix structure due to orbital degrees of freedom, in which case Δ is a symmetric complex matrix $\Delta^T = \Delta$. Here, one does not have additional orbital indices, so that Δ is a complex number.

In this basis, spin SU(2) and particle-hole symmetry combine into

$$H = -\sigma_y H^T \sigma_y. \tag{3.101}$$

This particle-hole symmetry squares to minus one, which is the defining property of class C. The network model that is studied numerically below is described by a scattering matrix corresponding to a Hamiltonian of this kind.

One can employ a time independent $(2 + 0)$D replicated action [199, 200] to study the statistics of wavefunctions of H. The action S is defined in such a way that the functional integral over the corresponding fields goes with the weight e^{-S}. In order to represent products of retarded and advanced Green's functions, one can double the space by introducing the additional 2×2 advanced-retarded structure labeled by τ. Further n replicas are introduced, which allows one to compute products of

m Greens functions (with $m \leq n$) at energies $\hat{\omega} = \text{diag}(\omega_1, \ldots, \omega_m, \ldots, \omega_n)$. To conveniently include finite ω_i into the action, one can double the space once more by including the additional 2×2 space Σ. This takes care of assigning each ω_i a particle-hole partner $-\omega_i$. The (complex) bosonic field ϕ has a replica index $(1, \ldots, n)$, a particle-hole index Σ and a spin index σ. One can write the action in terms of a bivector

$$\boldsymbol{\phi} = (\phi, i\sigma_y \Sigma_1 \phi^*) \tag{3.102}$$

that additionally lives in advanced-retarded τ space:

$$
\begin{aligned}
S_0 &= -i \int dr \left(\phi^\dagger \quad \phi^T i\sigma_y \Sigma_1 \right)_\tau \begin{pmatrix} H + \hat{\omega}\Sigma_3 + i0 & 0 \\ 0 & H + \hat{\omega}\Sigma_3 - i0 \end{pmatrix}_\tau \begin{pmatrix} \phi \\ +i\sigma_y \Sigma_1 \phi^* \end{pmatrix}_\tau \\
&= -i \int dr \left[\phi^\dagger H \phi + \phi^T i\sigma_y \Sigma_1 i\sigma_y H^T i\sigma_y \Sigma_1 i\sigma_y \phi^* + \phi^\dagger \hat{\omega}\Sigma_3 \phi + \phi^T i\sigma_y \Sigma_1 \hat{\omega}\Sigma_3 \Sigma_1 i\sigma_y \phi^* \right. \\
&\quad \left. + i0\phi^\dagger \phi - i0\phi^T i\sigma_y \Sigma_1 \Sigma_1 i\sigma_y \phi^* \right] \\
&= -i \int dr \left[2\phi^\dagger H \phi + 2\phi^\dagger \hat{\omega}\Sigma_3 \phi + 2i0\phi^\dagger \phi \right] .
\end{aligned} \tag{3.103}
$$

The doubling represented by the additional Pauli space Σ will be useful below to represent correlations of wavefunctions of multiple eigenstates. The full bosonic bispinor $\boldsymbol{\phi}$ satisfies the symmetry relation:

$$i\tau_1 \Sigma_1 \sigma_y \boldsymbol{\phi}^* = \boldsymbol{\phi} . \tag{3.104}$$

Up to now, I have considered a clean system, $H = H_0$. Now, one can include disorder V, so that the full Hamiltonian reads $H = H_0 + V$. The matrix V can be assumed as white-noise distributed matrix that contains all types of randomness (not involving the momentum p) respecting the class-C symmetry (3.101): spatial fluctuations of complex order parameter Δ (which couple to matrices σ_x and σ_y) and of chemical potential μ (that couples to σ_z), i.e., $V = \sum_{i=1}^3 v_i \sigma_i$. For simplicity, the disorder in all components is assumed to have the same amplitude $\sqrt{\lambda}$, so that $\langle v_i v_j \rangle = 2\lambda \delta_{i,j}$. This assumption is immaterial for the conclusions and results of this work, since they are only based on symmetries.

Disorder averages over this ensemble have the form of Gaussian integrals over the matrices V. These integrals are fully determined by the second moment [98]:

$$\int d\mu(V) \text{tr}(AV) \text{tr}(BV) = \lambda \, \text{tr}(AB - Ai\sigma_y B^T i\sigma_y). \tag{3.105}$$

To convince ourselves that Eq. (3.105) holds, it is convenient to expand the matrices A and B in terms of Pauli matrices in the σ space: $A = \sum_{i=0}^3 a_i \sigma_i$ and $B = \sum_{i=0}^3 b_i \sigma_i$. Using $\text{tr}(AB) = \sum_{i=0}^3 a_i b_i$, it is straightforward to see that both sides are equal to $2\lambda \sum_{i=1}^3 a_i b_i$.

The matrices A, B are chosen to be the combinations $\sum_{a,\Sigma,\tau} \phi_{\sigma,a,\Sigma,\tau}(r) \phi^\dagger_{\sigma',\Sigma,a,\tau}(r)$, where a is the replica index. Then one can use Eq. (3.105) to average over the disorder. As usual, the averaging results in the emergence of a quartic term in the action:

$$S_{\text{int}} = \lambda \int dr \sum_{ab,\tau\tau',\sigma\sigma',\Sigma\Sigma'} \phi_{\sigma,a,\Sigma,\tau}(r) \phi^\dagger_{\sigma',a,\Sigma,\tau}(r) \phi_{\sigma',b,\Sigma',\tau'}(r) \phi^\dagger_{\sigma,b,\Sigma',\tau'}(r) . \tag{3.106}$$

Following the conventional route, this "interaction" can be decoupled by means of a Hubbard-Stratonovich transformation involving integration over a matrix field Q. This field couples to the fields ϕ in the

following way:

$$\int dr \sum_{ab,\sigma,\Sigma\Sigma',\tau\tau'} \phi^\dagger_{\sigma a,\Sigma\tau} Q^{\tau,\tau'}_{\Sigma a,\Sigma' b} \phi_{\sigma b,\Sigma'\tau'} \, . \tag{3.107}$$

With the matrix structure in the retarded-advanced space (for which one can use the indices R and A) written explicitly, this has the form

$$\int dr \sum_{\sigma,ab,\Sigma\Sigma'} \mathrm{tr}_\tau \left[\begin{pmatrix} \phi^\dagger_{a,\Sigma,\sigma}\phi_{b,\Sigma',\sigma} & \phi^\dagger_{a,\Sigma,\sigma}(\phi^\dagger i\sigma_y)_{b,-\Sigma',\sigma} \\ (i\sigma_y\phi)_{a,-\Sigma,\sigma}\phi_{b,\Sigma',\sigma} & (i\sigma_y\phi)_{a,-\Sigma,\sigma}(\phi^\dagger i\sigma_y)_{b,-\Sigma',\sigma} \end{pmatrix} \begin{pmatrix} Q^{RR}_{\Sigma a,\Sigma' b} & Q^{RA}_{\Sigma a,\Sigma' b} \\ Q^{AR}_{\Sigma a,\Sigma' b} & Q^{AA}_{\Sigma a,\Sigma' b} \end{pmatrix} \right] . \tag{3.108}$$

Here Eq. (3.102) was used and taken into account that the matrix Σ_1 acts on the index Σ via $\Sigma \mapsto -\Sigma$. Note that the matrix Q does not carry σ indices and that this coupling explicitly respects the spin (σ) conservation.

Upon the Hubbard-Stratonovich decoupling, one gets the action:

$$S[\phi,Q] = \int dr \left[\sum_{ab,\sigma,\sigma',\tau} \phi^\dagger_{a\Sigma\tau\sigma} \left(H_0\delta_{ab}\delta_{\tau\tau'} + Q^{\tau\tau'}_{\Sigma a,\Sigma' b}\delta_{\sigma\sigma'} + \Sigma_3\hat\omega + i0\tau_3 \right) \phi_{b\Sigma'\tau'\sigma'} + \lambda^{-1}\mathrm{tr}\, Q^2 \right] . \tag{3.109}$$

The next step is to integrate over the ϕ fields. Since the action is quadratic in ϕ, this integration yields an inverse determinant, and one finally gets the action that only depends on Q:

$$S[Q] = \mathrm{tr}\log(H_0 + Q + \Sigma_3\hat\omega + i0\tau_3) + \lambda^{-1}\int dr\, \mathrm{tr}\, Q^2. \tag{3.110}$$

This action has a manifold of saddle points

$$Q = g\Lambda g^{-1}, \qquad \Lambda = \tau_3, \tag{3.111}$$

which form the target space of the nonlinear sigma model, $Q \in G/K$. For the present case of class C, this target space is $G/K = \mathrm{SO}^*(4n)/\mathrm{U}(2n)$. This form of the target space can be understood already from the symmetry of the action (3.103): transformation of ϕ that respect the symmetry constraint of ϕ and leave the main term (involving H) invariant, determine the group G, while the term proportional to $i0$ breaks this symmetry down to K.

Allowing for slow spatial fluctuations of $Q = g\Lambda g^{-1}$ around the saddle point $\Lambda = \tau_3$, one obtains the usual nonlinear sigma-model action [103, 201–206]

$$S[Q] = -\frac{\pi\rho_0}{8}\int dr\, \mathrm{tr}\left[D_0(\partial Q)^2 + 4i\left(\Sigma_3\hat\omega + i0\tau_3\right)Q \right]. \tag{3.112}$$

Here ρ_0 and D_0 are the bare (ultraviolet) values of the density of states and diffusion constant, respectively, so that $\sigma_0 = \rho_0 D_0$ is the bare spin conductivity.

The sigma-model field Q is a $4n \times 4n$ matrix in the advanced-retarded $\times$ particle-hole (equivalently, spin) $\times$ replica space [see also Eq. (3.40) below]. It satisfies two constraints. The first one is Eq. (3.111). In addition, g inherits the symmetry (3.104), yielding

$$\tau_1\Sigma_1 g^T\Sigma_1\tau_1 = g^{-1}. \tag{3.113}$$

For the Q field, this implies

$$\tau_1 \Sigma_1 Q^T \Sigma_1 \tau_1 = -Q. \tag{3.114}$$

Constraints (3.111) and (3.113) [or, equivalently, (3.111) and (3.114)] determine the sigma-model target space $G/K = \mathrm{SO}^*(4n)/\mathrm{U}(2n)$.

In the following/preceding sections dealing with the Iwasawa decomposition on G/K in Sec. 3.3, and renormalization group (RG) of generic operators composed of Q in Sec. 3.5, a slightly different parametrization of G/K related by a unitary basis rotation is used. Specifically, the two parametrizations of G/K are related by a rotation in Σ space:

$$Q = U_\Sigma^{-1} \tilde{Q} U_\Sigma, \tag{3.115}$$

where

$$U_\Sigma = \mathrm{diag}(I_{2n}, \Sigma_1 \otimes I_n)_\tau. \tag{3.116}$$

Since U_Σ commutes with τ_3, the condition (3.111) holds also for $\tilde{Q}$ without any modifications. At the same time, the condition (3.114) becomes

$$\tau_1 \Sigma_1 U_\Sigma^T \tilde{Q}^T U_\Sigma^* \Sigma_1 \tau_1 = -U_\Sigma^{-1} \tilde{Q} U_\Sigma, \tag{3.117}$$

which, by using $U_\Sigma^* \tau_1 \Sigma_1 U_\Sigma^{-1} = \tau_1 \otimes I_\Sigma$, simplifies to

$$\tau_1 \tilde{Q}^T \tau_1 = -\tilde{Q}. \tag{3.118}$$

With all indices written explicitly, this implies

$$Q_{a,b}^{AA} = \tilde{Q}_{a,b}^{AA}, \qquad Q_{a,b}^{AR} = \tilde{Q}_{a,-b}^{AR}, \qquad Q_{a,b}^{RA} = \tilde{Q}_{-a,b}^{RA}, \qquad Q_{a,b}^{RR} = \tilde{Q}_{-a,-b}^{RR}. \tag{3.119}$$

Here I have introduced a convention (to be used below) that the structure in the Σ space is represented by the sign $\pm$ of the the replicas a, b, i.e., positive replica indices $a = 1, \ldots, n$ correspond to the upper component in the Σ space, and the negative indices $-a$ to the lower component.

In the sequel, sometimes the tilde is omitted, i.e. Q for $\tilde{Q}$ is written to simplify notations. This will be explicitly pointed out in the corresponding sections when this will be done.

Before closing this section, two interrelated comments are appropriate.

1. Up to now, the manifold $G/K = \mathrm{SO}^*(4n)/\mathrm{U}(2n)$ is considered, with n being a positive integer. As is well known, the averaging over a quenched disorder requires either introducing supersymmetry or the replica trick ($n \to 0$). The supersymmetric formalism was used in Ref. [87] where the classification of composite operators was developed. At the same time, as is clear from Ref. [87], the most convenient way to build the composite operators is to use the boson-boson sector of the supersymmetric sigma-model. In this sense, the supersymmetry approach to this problem becomes very similar to using the replica trick for the bosonic fields. In other words, considering the bosonic theory only is fully sufficient for these purposes. Most of the analysis can be performed for the theory with a positive integer n. It will be pointed out below where the replica limit $n \to 0$ is essential (which could be equivalently replaced by making the theory supersymmetric).

2. In general, the sigma-model (3.112) (when written in the supersymmetric form, i.e., also with a compact sector) may contain also a topological term. In particular, this term plays a crucial role for the emergence of the critical point of the SQH transition. However, in this work, the sigma-model will be only used for determining the composite operators and for translating them to the language of wave-function correlators. This analysis is based entirely on the symmetry of the sigma model, for which the presence or absence of the topological term is fully irrelevant. The scaling of the corresponding correlation functions at the critical point of the SQH transition will be after this determined numerically.

3.5 RG

In this section, one more approach—the field-theoretic RG—is employed in order to determine the pure-scaling operators in class C. The approach is based on the invariance property of the RG transformation that works on functions (composite operators) $O[Q]$ on the symmetric space G/K. Importantly, this invariance holds to any order of RG. In view of this, eigenfunctions of one-loop RG are the pure-scaling operators, cf. previous works for class A [158] and class AI [207]. A few general word on renormalization group analysis can be found in Sec. 1.1.3.

One can use the one-loop RG to determine the class-C eigenoperators $\mathcal{P}_\lambda^C[Q]$ that are polynomials in Q. These operators correspond to Young diagrams $\lambda = (q_1, q_2, \ldots, q_n)$ with integers $q_1, \ldots, q_n$ satisfying $q_1 \geq q_2 \geq \ldots q_n > 0$. Clearly, in each order $|\lambda| \equiv q_1 + q_2 + \ldots + q_n$ of the polynomial, there is a finite number of such Young diagrams. For example, for $|\lambda| = 2$ there are two Young diagrams, (2) and (1,1); for $|\lambda| = 3$ there are three of them, (3), (2,1), and (1,1,1), and so on. Further, RG preserves the order $|\lambda|$ of the polynomial. Thus, for each $|\lambda|$, the action of RG reduces to a matrix in the corresponding subspace. Diagonalization of this matrix yields pure-scaling operators $\mathcal{P}_\lambda^C[Q]$. These operators are particularly convenient for mapping onto wave-function observables performed in Sec. 3.6. (To avoid confusion, remember that the operators $\mathcal{P}_\lambda^C[Q]$ do not satisfy the Abelian fusion, at variance with the N-radial operators (3.97) constructed in Sec. 3.3 by means of the Iwasawa decomposition.)

While the main focus is on the class C, for which $G/K = \mathrm{SO}^*(4n)/\mathrm{U}(2n)$, it is instructive to also briefly review the RG analysis for class A, for which $G/K = \mathrm{U}(n,n)/\mathrm{U}(n) \times \mathrm{U}(n)$. This allows one to point out important differences in eigenoperators between classes C and A. Furthermore, relations between the eigenoperators of both classes are established, which will be useful in Sec. 3.6 for the numerical evaluation of scaling exponents of the SQH transition.

In Sec. 3.5.1 the RG procedure is introduced and used to determine eigenoperators with the lowest non-trivial degree of polynomial, $|\lambda| = 2$. In Sec. 3.5.3 this analysis is extended to eigenoperators of higher degree, $|\lambda| > 2$; they are explicitly determined for $|\lambda| = 3$ and $|\lambda| = 4$.

Whereas the goal in this section is to determine pure-scaling operators by RG means, also the eigenvalues of the one-loop RG are calculated. Specifically, after having inspected examples of not too large $|\lambda|$ in Secs. 3.5.2 and 3.5.3, in Sec. 3.5.4 a general statement that the one-loop RG operator is proportional to Laplace-Beltrami operator on G/K is proven. This implies that eigenvalues of one-loop RG satisfy generalized parabolicity.

3.5.1 Renormalization procedure

The RG procedure is implemented in the standard way by splitting the matrix g that defines the sigma-model field $Q = g\Lambda g^{-1}$ in the slow (subscript "s") and fast (subscript "f") components, $g = g_s g_f$. (This approach is also known as background field method; e.g., recent papers [207, 208] and references

therein.) The matrix g is antiunitary, $g^{-1} = \tau_3 g^\dagger \tau_3$, and the same condition holds for g_s and g_f. The fast field

$$g_f = e^{-\mathcal{X}} = 1 - \mathcal{X} + \frac{1}{2}\mathcal{X}^2 + \dots \tag{3.120}$$

is expanded in $\mathcal{X}$. The matrix $\mathcal{X}$ does not contain the "gauge" (group K) degrees of freedom, i.e., it anticommutes with $\Lambda \equiv \tau_3$:

$$\mathcal{X} = \begin{pmatrix} 0 & X \\ X^\dagger & 0 \end{pmatrix}_\tau \tag{3.121}$$

One thus has

$$\begin{aligned} Q &= g\Lambda g^{-1} \\ &= g_s g_f \Lambda g_f^{-1} g_s^{-1} \\ &= Q_s + 2g_s \Lambda \mathcal{X} g_s^{-1} + 2g_s \Lambda \mathcal{X}^2 g_s^{-1} + \dots, \end{aligned} \tag{3.122}$$

where $Q_s = g_s \Lambda g_s^{-1}$. For the one-loop analysis, it is sufficient to keep terms up to the order $\mathcal{X}^2$.

To obtain the Gaussian fast-mode action S_f, one can expand the sigma-model action (3.112) to lowest (quadratic) order in the fast fields $\mathcal{X}$:

$$\begin{aligned} S_f[\mathcal{X}] &= \frac{\pi\sigma_0}{2} \int d^d x \left[\mathrm{tr}\,(\nabla\mathcal{X})^2 + h^2 \mathrm{tr}\,\mathcal{X}^2 \right] \\ &= \pi\sigma_0 \int d^d x \left[\mathrm{tr}\,(\nabla X^\dagger)(\nabla X) + h^2 \mathrm{tr}\, X^\dagger X \right]. \end{aligned} \tag{3.123}$$

Here the infrared cutoff h^2 that regularizes the divergence in spatial dimensionality $d \leq 2$ has been included. In $d = 2$ dimensions, the one-loop integrals are logarithmic with respect to the ratio of the ultraviolet and infrared cutoffs; in the bare theory, the ultraviolet regularization is usually provided by the lattice spacing. One can also consider the theory in $d = 2 + \epsilon$ dimensions, with $\epsilon > 0$, [188, 189]. The analysis that is performed here to determine the eigenoperators of RG is based solely on symmetry, so that it is equally applicable in any spatial dimensionality. As one can see below, the loop integral will enter as a constant I_f, whose value will be immaterial for the analysis.

Let δO be defined as the one loop renormalization contribution of an operator $O(Q)$ with respect to this fast action. It is obtained by expanding O up to second order in $\mathcal{X}$,

$$O[\mathcal{X}] = O^{(0)} + O^{(1)}[\mathcal{X}] + \frac{1}{2}O^{(2)}[\mathcal{X}, \mathcal{X}] + \dots, \tag{3.124}$$

where $O^{(n)}$ a n-linear form in $\mathcal{X}$, and then performing the Gaussian averaging $\langle \dots \rangle$ with respect to $\mathcal{X}$ with the action (3.123). One thus has

$$\delta O = \frac{1}{2} \int \mathcal{D}\mathcal{X}\, O^{(2)}[\mathcal{X}, \mathcal{X}]\, e^{-S_f[\mathcal{X}]} \equiv \frac{1}{2}\langle O^{(2)}[\mathcal{X}, \mathcal{X}] \rangle. \tag{3.125}$$

Every term in the RG flow δO thus originates from a single contraction of two fast fields and is proportional to the fast-field propagator. Since the composite operators that are considered are local, this propagator is taken at coinciding spatial points and thus involves the loop integral

$$I_f = \frac{1}{\pi\sigma_0} \int \frac{d^{2+\epsilon}p}{p^2 + h^2}. \tag{3.126}$$

At one loop level, every term in δO is thus proportional to I_f by construction. In order to determine the eigenoperators, one does not need the value of I_f, since it will simply stay as an overall prefactor in matrices that one will have to diagonalize.

3.5.2 RG for operators quadratic in Q.

I consider first the operators that are quadratic with respect to Q. The corresponding Young diagrams λ are characterized by $|\lambda| = 2$. Obviously, there are two such Young diagrams: (2) and (1,1). To derive the RG equations, one needs to look at the renormalization of the operators $\text{tr}(AQBQ)$ and $\text{tr}(AQ)\text{tr}(BQ)$ with generic matrices A and B. Using the expansion (3.122), one gets

$$
\begin{aligned}
\text{tr}(AQBQ) &= \text{tr}(Ag_s Q_f g_s^{-1} Bg_s Q_f g_s^{-1}) \\
&\simeq \text{tr}(AQ_s BQ_s) + 4\text{tr}(g_s^{-1} Ag_s \Lambda \mathcal{X} g_s^{-1} Bg_s \Lambda \mathcal{X}) \\
&\quad + 2\text{tr}(Ag_s \Lambda \mathcal{X}^2 g_s^{-1} BQ_s) + 2\text{tr}(AQ_s Bg_s \Lambda \mathcal{X}^2 g_s^{-1}), \\
&= \text{tr}(AQ_s BQ_s) + 4\text{tr}(\tilde{A}\mathcal{X}\tilde{B}\mathcal{X}) + 2\text{tr}(\tilde{B}\tilde{A}\mathcal{X}^2) + 2\text{tr}(\tilde{A}\tilde{B}\mathcal{X}^2); \\
\text{tr}(AQ)\text{tr}(BQ) &= \text{tr}(Ag_s Q_f g_s^{-1})\text{tr}(Bg_s Q_f g_s^{-1}) \\
&\simeq \text{tr}(AQ_s)\text{tr}(BQ_s) + 4\text{tr}(g_s^{-1} Ag_s \Lambda \mathcal{X})\text{tr}(g_s^{-1} Bg_s \Lambda \mathcal{X}) \\
&\quad + 2\text{tr}(Ag_s \Lambda \mathcal{X}^2 g_s^{-1})\text{tr}(BQ_s) + 2\text{tr}(AQ_s)\text{tr}(Bg_s \Lambda \mathcal{X}^2 g_s^{-1}) \\
&= \text{tr}(AQ_s)\text{tr}(BQ_s) + 4\text{tr}(\tilde{A}\mathcal{X})\text{tr}(\tilde{B}\mathcal{X}) + 2\text{tr}(\tilde{A}\mathcal{X}^2)\text{tr}(BQ_s) + 2\text{tr}(\tilde{B}\mathcal{X}^2)\text{tr}(AQ_s),
\end{aligned}
\tag{3.127}
$$

where only terms of zeroth and second order in X are retained and

$$
\tilde{A} = g_s^{-1} Ag_s \Lambda, \qquad \tilde{B} = g_s^{-1} Bg_s \Lambda. \tag{3.128}
$$

To calculate $\delta[\text{tr}(AQ)\text{tr}(BQ)]$ and $\delta\text{tr}(AQBQ)$, one should average according to Eq. (3.125) the terms of second order in $\mathcal{X}$ in Eq. (3.127). This involves the following averages (with 1,2 being the indices in the RA space):

$$
\begin{aligned}
\langle\text{tr}(\tilde{A}\mathcal{X})\text{tr}(\tilde{B}\mathcal{X})\rangle &= \left\langle \left(\text{tr}(\tilde{A}_{12}X^\dagger) + \text{tr}(\tilde{A}_{21}X)\right)\left(\text{tr}(\tilde{B}_{12}X^\dagger) + \text{tr}(\tilde{B}_{21}X)\right)\right\rangle \\
&= \tilde{A}_{12}^{\beta\alpha}\tilde{B}_{12}^{\delta\gamma}\left\langle X_{\alpha\beta}^\dagger X_{\gamma\delta}^\dagger\right\rangle + \tilde{A}_{12}^{\beta\alpha}\tilde{B}_{21}^{\delta\gamma}\left\langle X_{\alpha\beta}^\dagger X_{\gamma\delta}\right\rangle + \tilde{A}_{21}^{\beta\alpha}\tilde{B}_{12}^{\delta\gamma}\left\langle X_{\alpha\beta}X_{\gamma\delta}^\dagger\right\rangle + \tilde{A}_{21}^{\beta\alpha}\tilde{B}_{21}^{\delta\gamma}\left\langle X_{\alpha\beta}X_{\gamma\delta}\right\rangle,
\end{aligned}
\tag{3.129}
$$

$$
\begin{aligned}
\langle\text{tr}(\tilde{A}\mathcal{X}\tilde{B}\mathcal{X})\rangle &= \left\langle\text{tr}(\tilde{A}_{12}X^\dagger\tilde{B}_{12}X^\dagger + \tilde{A}_{22}X^\dagger\tilde{B}_{11}X) + \text{tr}(\tilde{A}_{11}X\tilde{B}_{22}X^\dagger + \tilde{A}_{21}X\tilde{B}_{21}X)\right\rangle \\
&= \tilde{A}_{12}^{\delta\alpha}\tilde{B}_{12}^{\beta\gamma}\left\langle X_{\alpha\beta}^\dagger X_{\gamma\delta}^\dagger\right\rangle + \tilde{A}_{11}^{\delta\alpha}\tilde{B}_{22}^{\beta\gamma}\left\langle X_{\alpha\beta}^\dagger X_{\gamma\delta}\right\rangle + \tilde{A}_{22}^{\delta\alpha}\tilde{B}_{11}^{\beta\gamma}\left\langle X_{\alpha\beta}X_{\gamma\delta}^\dagger\right\rangle + \tilde{A}_{21}^{\delta\alpha}\tilde{B}_{21}^{\beta\gamma}\left\langle X_{\alpha\beta}X_{\gamma\delta}\right\rangle,
\end{aligned}
\tag{3.130}
$$

where α, β, γ, and δ are replica indices and the convention of summation over repeated indices is used. Further, replacing $\tilde{B}$ in Eq. (3.130) by the unit matrix, one obtains

$$
\langle\text{tr}(\tilde{A}\mathcal{X}^2)\rangle = \tilde{A}_{11}^{\delta\alpha}\left\langle X_{\alpha\beta}^\dagger X_{\beta\delta}\right\rangle + \tilde{A}_{22}^{\delta\alpha}\left\langle X_{\alpha\beta}X_{\beta\delta}^\dagger\right\rangle. \tag{3.131}
$$

The analysis up to now was general and thus was applicable to both classes A and C. To proceed further, one should specify the fast-mode propagators, which are different for classes A and C.

3.5.2.1 Class A

In class A, the manifold is $G/K = \mathrm{U}(n,n)/\mathrm{U}(n) \times \mathrm{U}(n)$ and the only condition on g is pseudo-unitarity, $g^{-1} = \tau_3 g^\dagger \tau_3$. The field X in Eq. (3.121) is correspondingly a generic complex matrix with the propagator

$$\langle X_{\alpha\beta}^\dagger X_{\gamma\delta} \rangle = I_f \delta_{\alpha\delta} \delta_{\beta\gamma} \,,$$
$$\langle X_{\alpha\beta} X_{\gamma\delta} \rangle = \langle X_{\alpha\beta}^\dagger X_{\gamma\delta}^\dagger \rangle = 0 \,. \tag{3.132}$$

Using Eq. (3.132) for the propagator in Eqs.(3.129) and (3.130), one gets

$$\langle \mathrm{tr}(\tilde{A}\mathcal{X}) \mathrm{tr}(\tilde{B}\mathcal{X}) \rangle = \quad I_f \, \mathrm{tr}(\tilde{A}_{12}\tilde{B}_{21} + \tilde{A}_{21}\tilde{B}_{12}) = I_f \, \mathrm{tr} \left(\tilde{A}P_-\tilde{B}P_+ + \tilde{A}P_+\tilde{B}P_- \right)$$

$$= \quad \frac{1}{2} I_f \, \mathrm{tr}(\tilde{A}\tilde{B} - \tilde{A}\Lambda\tilde{B}\Lambda) \,; \tag{3.133}$$

$$\langle \mathrm{tr}(\tilde{A}\mathcal{X}\tilde{B}\mathcal{X}) \rangle = \quad I_f \, (\mathrm{tr}\tilde{A}_{11}\mathrm{tr}\tilde{B}_{22} + \mathrm{tr}\tilde{A}_{22}\mathrm{tr}\tilde{B}_{11})$$

$$= \quad I_f \left[\mathrm{tr} \left(\tilde{A}P_+ \right) \mathrm{tr} \left(\tilde{B}P_- \right) + \mathrm{tr} \left(\tilde{A}P_- \right) \mathrm{tr} \left(\tilde{B}P_+ \right) \right]$$

$$= \quad \frac{1}{2} I_f \left[\mathrm{tr}\tilde{A} \, \mathrm{tr}\tilde{B} - \mathrm{tr}(\tilde{A}\Lambda) \, \mathrm{tr}(\tilde{B}\Lambda) \right], \tag{3.134}$$

where the $P_\pm = \frac{\mathbb{1}\pm\Lambda}{2}$ are projectors on the advanced and retarded sectors. Substituting here now Eq. (3.128) for $\tilde{A}$ and $\tilde{B}$, one finds

$$\langle \mathrm{tr}(\tilde{A}\mathcal{X}) \mathrm{tr}(\tilde{B}\mathcal{X}) \rangle = \quad \frac{1}{2} I_f \mathrm{tr}(Q_s A Q_s B - AB) \,; \tag{3.135}$$

$$\langle \mathrm{tr}(\tilde{A}\mathcal{X}\tilde{B}\mathcal{X}) \rangle = \quad \frac{1}{2} I_f \left[\mathrm{tr}(Q_s A) \, \mathrm{tr}(Q_s B) - \mathrm{tr}A \, \mathrm{tr}B \right]. \tag{3.136}$$

Below I will focus on the choice of matrices A and B satisfying (in the replica limit $n \to 0$) $\mathrm{tr}A = \mathrm{tr}B = \mathrm{tr}(AB) = 0$, so that the Q_s-independent terms in the r.h.s. of Eqs. (3.135), (3.136) can be discarded. It is important to note, however, that these terms play only a minor role also for more generic matrices A and B: they only lead to an admixture of constant (Q-independent) terms to eigenoperators, without affecting either the quadratic-in-Q structure of eigenoperators or the corresponding eigenvalues.

Equation (3.131) yields, with the class-A propagator (3.132),

$$\langle \mathrm{tr}(\tilde{A}\mathcal{X}^2) \rangle = I_f n \, (\mathrm{tr}\tilde{A}_{11} + \mathrm{tr}\tilde{A}_{22}) = I_f n \, \mathrm{tr}\tilde{A} \,. \tag{3.137}$$

Since one is interested in the replica limit $n \to 0$, the terms of the type $\langle \mathrm{tr}(\dots \mathcal{X}^2) \rangle$ thus do not give any contribution. Using Eqs. (3.135) and (3.136) for the remaining averages in Eq. (3.127), one obtains the following RG flow (that is conveniently presented in the matrix form) for the operators $\mathrm{tr}(AQ)\mathrm{tr}(BQ)$ and $\mathrm{tr}(AQBQ)$:

$$\delta \begin{pmatrix} \mathrm{tr}(AQ)\mathrm{tr}(BQ) \\ \mathrm{tr}(AQBQ) \end{pmatrix} = (-2I_f) \cdot \underbrace{\begin{pmatrix} 0 & -1 \\ -1 & 0 \end{pmatrix}}_{=:M_2^A} \cdot \begin{pmatrix} \mathrm{tr}(AQ)\mathrm{tr}(BQ) \\ \mathrm{tr}(AQBQ) \end{pmatrix}. \tag{3.138}$$

Consequently the eigenoperators are (the superscript "A" refers to class A)

$$\mathcal{P}_{(2)AB}^A = \mathrm{tr}(AQ)\mathrm{tr}(BQ) + \mathrm{tr}(AQBQ),$$
$$\mathcal{P}_{(1,1)AB}^A = \mathrm{tr}(AQ)\mathrm{tr}(BQ) - \mathrm{tr}(AQBQ) \,, \tag{3.139}$$

with eigenvalues $2I_f > 0$ and $-2I_f < 0$, respectively. The first of them (increasing under RG) belongs to the representation (equivalently, Young diagram) $\lambda = (2)$ and the second one (decreasing under RG) to $\lambda = (1,1)$. It is important to emphasize that the eigenvalues do not depend on the choice of the matrices A and B: the operators $\mathcal{P}_{(2)}^A$ with any A and B belong to the same representation (2), and the operators $\mathcal{P}_{(1,1)}^A$ with any A and B belong to the representation $(1,1)$.

One important choice of the matrices A and B is $A = B = \Lambda$, which yields the operators

$$\begin{aligned} \mathcal{P}_{(2)}^A &= \operatorname{tr}(\Lambda Q)\operatorname{tr}(\Lambda Q) + \operatorname{tr}(\Lambda Q \Lambda Q), \\ \mathcal{P}_{(1,1)}^A &= \operatorname{tr}(\Lambda Q)\operatorname{tr}(\Lambda Q) - \operatorname{tr}(\Lambda Q \Lambda Q). \end{aligned} \tag{3.140}$$

The special feature of this choice is that the operators (3.140) are K-invariant: they are invariant with respect to rotations $Q \to UQU^{-1}$ with $U \in K$, since all such U commute with Λ.

3.5.2.2 Class C

Now the above analysis is extended to the class C. There is then an additional symmetry operation,

$$\overline{O} \equiv \tau_1 O^T \tau_1, \tag{3.141}$$

that constrains g:

$$\overline{g} = g^{-1}. \tag{3.142}$$

This means $\overline{\mathcal{X}} = -\mathcal{X}$. Since $\overline{\Lambda} = -\Lambda$, this corresponds to Q being odd with respect to the operation (3.141),

$$\overline{Q} = -Q, \tag{3.143}$$

see Eq. (3.118). Note that Q in this section is the same as $\tilde{Q}$ introduced in the end of Sec. 3.4, see Eq. (3.115).

Combining Eq. (3.121) with $\overline{\mathcal{X}} = -\mathcal{X}$, one finds that X is an antisymmetric complex matrix, $X = -X^T$. Therefore, expectation values with the Gaussian action (3.123) yield the following propagator:

$$\begin{aligned} \langle X_{\alpha\beta}^\dagger X_{\gamma\delta} \rangle &= I_f(\delta_{\alpha\delta}\delta_{\beta\gamma} - \delta_{\alpha\gamma}\delta_{\beta\delta}), \\ \langle X_{\alpha\beta} X_{\gamma\delta} \rangle &= \langle X_{\alpha\beta}^\dagger X_{\gamma\delta}^\dagger \rangle = 0. \end{aligned} \tag{3.144}$$

It is important to recall, that, as discussed in the end of Sec. 3.4, the particle-hole index Σ is included in the replica index, so that one has $2n$ replicas.

Substituting Eq. (3.144) into Eqs. (3.129), (3.130), one finds for the fast-field correlation functions

that emerge in the RG analysis (3.127), with two factors of $\mathcal{X}$ originating from different Q fields:

$$
\begin{aligned}
\langle \text{tr}(\tilde{A}\mathcal{X})\text{tr}(\tilde{B}\mathcal{X}) \rangle &= I_f \left[\text{tr}(\tilde{A}_{12}\tilde{B}_{21}) - \text{tr}(\tilde{A}_{21}\tilde{B}_{12}^T) + \text{tr}(\tilde{A}_{21}\tilde{B}_{12}) - \text{tr}(\tilde{A}_{12}\tilde{B}_{21}^T) \right] \\
&= \frac{I_f}{2} \left[\text{tr}(\tilde{A}P_-\tilde{B}P_+) - \text{tr}(\tilde{A}P_+\overline{\tilde{B}}P_-) + \text{tr}(\tilde{A}P_+\tilde{B}P_-) - \text{tr}(\tilde{A}P_-\overline{\tilde{B}}P_+) \right] \\
&= \frac{I_f}{2} \left[-\text{tr}(\tilde{A}\Lambda\tilde{B}\Lambda) + \text{tr}(\tilde{A}\tilde{B}) - \text{tr}(\tilde{A}\overline{\tilde{B}}) + \text{tr}(\tilde{A}\Lambda\overline{\tilde{B}}\Lambda) \right] ; \\
\langle \text{tr}(\tilde{A}\mathcal{X}\tilde{B}\mathcal{X}) \rangle &= \frac{I_f}{2} \left[\text{tr}(\tilde{A}_{22})\text{tr}(\tilde{B}_{11}) - \text{tr}(\tilde{A}_{22}\tilde{B}_{11}^T) + \text{tr}(\tilde{A}_{11})\text{tr}(\tilde{B}_{22}) - \text{tr}(\tilde{A}_{11}\tilde{B}_{22}^T) \right] \\
&= \frac{I_f}{2} \left[\text{tr}(\tilde{A}P_-)\text{tr}(\tilde{B}P_+) - \text{tr}(\tilde{A}P_-\overline{\tilde{B}}P_-) + \text{tr}(\tilde{A}P_+)\text{tr}(\tilde{B}P_-) - \text{tr}(\tilde{A}P_+\overline{\tilde{B}}P_+) \right] \\
&= \frac{I_f}{2} \left[\text{tr}(\tilde{A})\text{tr}(\tilde{B}) - \text{tr}(\tilde{A}\Lambda)\text{tr}(\tilde{B}\Lambda) - \text{tr}(\tilde{A}\overline{\tilde{B}}) - \text{tr}(\tilde{A}\Lambda\overline{\tilde{B}}\Lambda) \right] .
\end{aligned} \tag{3.145}
$$

Substituting now Eq. (3.128) for $\tilde{A}$ and $\tilde{B}$, one obtains

$$
\begin{aligned}
\langle \text{tr}(\tilde{A}\mathcal{X})\text{tr}(\tilde{B}\mathcal{X}) \rangle &= \frac{I_f}{2} \left[-\text{tr}(AB) + \text{tr}(AQ_sBQ_s) + \text{tr}(A\overline{B}) - \text{tr}(AQ_s\overline{B}Q_s) \right] , \\
\langle \text{tr}(\tilde{A}\mathcal{X}\tilde{B}\mathcal{X}) \rangle &= \frac{I_f}{2} \left[\text{tr}(AQ_s)\text{tr}(BQ_s) - \text{tr}(A)\text{tr}(B) + \text{tr}(A\overline{B}) + \text{tr}(AQ_s\overline{B}Q_s) \right] .
\end{aligned} \tag{3.146}
$$

In addition, Eq. (3.127) contain terms of the type (3.131), with both factors of $\mathcal{X}$ originating from the same Q field, i.e., entering in the form of $\mathcal{X}^2$. Substituting Eq. (3.144) into Eq.(3.131), one gets

$$
\langle \text{tr}(\tilde{A}\mathcal{X}^2) \rangle = I_f(-1 + 2n)\,\text{tr}\,\tilde{A} = -I_f\,\text{tr}\,\tilde{A}. \tag{3.147}
$$

In the last equality sign, the replica limit $n \to 0$ has been taken. At variance with the class A [see Eq. (3.137)], such contributions remain non-zero in the replica limit in class C. In particular, such a term is responsible for renormalization of operators of first order in Q [e.g., $\text{tr}(\Lambda Q)$] in class C:

$$
\delta\,\text{tr}(\Lambda Q) = 2\langle \text{tr}(g_s\Lambda g_s^{-1}\Lambda\mathcal{X}^2) \rangle = -2I_f\,\text{tr}(\Lambda Q). \tag{3.148}
$$

This operator belongs to the representation (1) and determines the scaling of the average LDOS. The corresponding eigenvalue is $-2I_f < 0$, which means that the average LDOS is suppressed within one-loop RG.

I return to the RG for operators that are quadratic in Q. Substituting Eqs. (3.146) and (3.147) into Eq. (3.127), one obtains the RG equations

$$
\begin{aligned}
\delta[\text{tr}(AQ)\text{tr}(BQ)] &= 2I_f \left[-\text{tr}(AB) + \text{tr}(AQBQ) - \left(-\text{tr}(A\overline{B}) + \text{tr}(AQ\overline{B}Q) \right) - 2\text{tr}(AQ)\text{tr}(BQ) \right] , \\
\delta\text{tr}(AQBQ) &= 2I_f \left[\text{tr}(AQ)\text{tr}(BQ) - \text{tr}(A)\text{tr}(B) + \left(\text{tr}(A\overline{B}) + \text{tr}(AQ\overline{B}Q) \right) - 2\text{tr}(AQBQ) \right] .
\end{aligned} \tag{3.149}
$$

In full analogy with the class A [see comment after Eq. (3.136)], one can drop constant contributions (those that do not contain Q). Furthermore, one can assume that, like the matrix Q, the matrices A to B are odd [1] with respect to the symmetry operation (3.141):

$$
\overline{A} = -A, \qquad \overline{B} = -B. \tag{3.150}
$$

---

[1] It is straightforward to check that choosing A and B to be even, $\overline{A} = A$ and $\overline{B} = B$, does not bring anything new. Specifically, the operator $\text{tr}(AQ)\text{tr}(BQ)$ is then zero, and the operator $\text{tr}(AQBQ)$ renormalizes to itself with the eigenvalue $-2I_f$ and thus belongs to the same representation (2) as the operator $\mathcal{P}_{(2)}^C$ from Eq. (3.155).

Two choices of A and B will be particularly important for us. The first one is $A = B = \Lambda$, which yields gauge-invariant operators [i.e., operators invariant with respect to the group $K = U(2n)$]. The second choice is $A = E_{aa}\Lambda$ and $B = E_{bb}\Lambda$, with E_{aa} and E_{bb} being projectors on two distinct replica indices a and b. This choice of A and B will be useful for establishing connections with wavefunction correlators in Sec. 3.6. In both cases, A and B are odd, i.e., satisfy Eq. (3.150). The RG equations (3.149) then reduce to

$$\delta \begin{pmatrix} \mathrm{tr}(AQ)\mathrm{tr}(BQ) \\ \mathrm{tr}(AQBQ) \end{pmatrix} = (-2I_f) \cdot \underbrace{\begin{pmatrix} 2 & -2 \\ -1 & 3 \end{pmatrix}}_{=:M_2} \cdot \begin{pmatrix} \mathrm{tr}(AQ)\mathrm{tr}(BQ) \\ \mathrm{tr}(AQBQ) \end{pmatrix}. \tag{3.151}$$

To determine pure-scaling operators, one writes an operator O as a linear combination

$$O = c_{(1,1)}\mathrm{tr}(AQ)\mathrm{tr}(BQ) + c_{(2)}\mathrm{tr}(AQBQ). \tag{3.152}$$

Equation (3.151) then is translated into the RG flow of the coefficients $c_{(1,1)}$ and $c_{(2)}$:

$$\delta \begin{pmatrix} c_{(1,1)} \\ c_{(2)} \end{pmatrix} = (-2I_f) \cdot \underbrace{\begin{pmatrix} 2 & -1 \\ -2 & 3 \end{pmatrix}}_{=M_2^T} \cdot \begin{pmatrix} c_{(1,1)} \\ c_{(2)} \end{pmatrix} \tag{3.153}$$

Note that M_2 from Eq. (3.151) acts transposed on the vector of coefficients. (It is necessary to emphasize this since, at variance with class A, the matrix M_2 is not symmetric for class C.) The eigenvectors of M_2^T yield the operators

$$\mathcal{P}^C_{(2)AB} = \mathrm{tr}(AQ)\mathrm{tr}(BQ) + \mathrm{tr}(AQBQ),$$
$$\mathcal{P}^C_{(1,1)AB} = \mathrm{tr}(AQ)\mathrm{tr}(BQ) - 2\mathrm{tr}(AQBQ), \tag{3.154}$$

which are eigenoperators of the RG flow with eigenvalues $-2I_f$ and $-8I_f$, respectively. The superscript "C" serves to distinguish them from class-A eigenoperators (3.139). Importantly, the coefficients in Eq. (3.154) do not depend on the choice of matrices A and B. In particular, for $A = B = \Lambda$ one finds the K-invariant pure-scaling operators to be

$$\mathcal{P}^C_{(2)} = \mathrm{tr}(\Lambda Q)\mathrm{tr}(\Lambda Q) + \mathrm{tr}(\Lambda Q\Lambda Q),$$
$$\mathcal{P}^C_{(1,1)} = \mathrm{tr}(\Lambda Q)\mathrm{tr}(\Lambda Q) - 2\mathrm{tr}(\Lambda Q\Lambda Q). \tag{3.155}$$

For another important choice mentioned above, $A = E_{aa}\Lambda$ and $B = E_{bb}\Lambda$ with two different replicas a and b, one gets the pure-scaling operators

$$\mathcal{P}^C_{(2)ab} = \mathrm{tr}(\Lambda Q_{aa})\mathrm{tr}(\Lambda Q_{bb}) + \mathrm{tr}(\Lambda Q_{ab}\Lambda Q_{ba}),$$
$$\mathcal{P}^C_{(1,1)ab} = \mathrm{tr}(\Lambda Q_{aa})\mathrm{tr}(\Lambda Q_{bb}) - 2\mathrm{tr}(\Lambda Q_{ab}\Lambda Q_{ba}), \tag{3.156}$$

where Q_{aa}, Q_{bb}, Q_{ab}, and Q_{ba} are projections of Q on the corresponding replica subspaces.

From the Weyl-symmetry relations, Sec. 1.2.1.1, one knows that the eigenoperators belonging to the representations (1) and (2) should scale in the same way under RG. These results are in full agreement with this symmetry constraint: the operators $\mathcal{P}^C_{(2)AB}$ from the representation (2) have the same eigenvalue $-2I_f$ as the operator representing the average LDOS, i.e., representation (1), see Eq. (3.148). The operator $\mathcal{P}^C_{(1,1)AB}$ that has the eigenvalue $-8I_f$ (i.e., is "more irrelevant" in the RG sense) belongs to the representation (1,1). As it is discussed below, the ratio 4 between the two eigenvalues is a manifestation of the exact generalized parabolicity that is a property of one-loop RG.

3.5.2.3 Gauge-invariant operators by K-averaging

In Sec. 3.5.2.2, the quadratic-in-Q pure scaling operators (3.154) have been determined. Two important choices of the matrices A and B were discussed. One of them was to take $A = B = \Lambda$, which yields K-invariant eigenoperators (3.155) that are linear combinations of the operators

$$O_{(2)} = \mathrm{tr}(\Lambda Q \Lambda Q), \qquad O_{(1,1)} = \mathrm{tr}(\Lambda Q)\mathrm{tr}(\Lambda Q). \tag{3.157}$$

The other choice was $A = E_{aa}\Lambda$ and $B = E_{bb}\Lambda$, which leads to the eigenoperators (3.156), which are linear combinations of

$$O_{(2)}^{ab} = \mathrm{tr}(\Lambda Q_{ab}\Lambda Q_{ba}), \qquad O_{(1,1)}^{ab} = \mathrm{tr}(\Lambda Q_{aa})\mathrm{tr}(\Lambda Q_{bb}) \tag{3.158}$$

with the same coefficients. While the operators (3.158) are not K-invariant, one can make K-invariant operators out of them by performing the averaging over the group K. This yields an alternative way to K-invariant pure-scaling operators. The result should be the same as K-invariant operators (3.155) determined above. In this subsection it is shown explicitly that this is indeed the case, which constitutes a non-trivial consistency check of this analysis.

Let $O[Q]$ be a composite operator. One can construct out of it an operator $\left\langle O[Q] \right\rangle_K$ by averaging over the group $K = \mathrm{U}(2n)$:

$$\left\langle O[Q] \right\rangle_K = \int_K d\mu(U) O[U^{-1}QU]. \tag{3.159}$$

The operator (3.159) is K-invariant, i.e., it is invariant under transformations $Q \mapsto V^{-1}QV$ with $V \in K$, as immediately follows from the invariance of the Haar measure $d\mu(U)$ on $K = \mathrm{U}(2n)$.

The elements of K commute with Λ and thus have the block-diagonal form in the retarded-advanced (τ) space, $U = \mathrm{diag}(U_1, U_2)_\tau$. In order to perform the K-averaging of the operators (3.158), one thus has to evaluate the following averages

$$\begin{aligned}
\left\langle \mathrm{tr}(\Lambda Q_{ab}\Lambda Q_{ba}) \right\rangle_K = \Big\langle &(U_1^{-1}Q_{11}U_1)_{ab}(U_1^{-1}Q_{11}U_1)_{ba} + (U_2^{-1}Q_{22}U_2)_{ab}(U_2^{-1}Q_{22}U_2)_{ba} \\
&-(U_1^{-1}Q_{12}U_2)_{ab}(U_2^{-1}Q_{21}U_1)_{ba} - (U_2^{-1}Q_{21}U_1)_{ab}(U_1^{-1}Q_{12}U_2)_{ba} \Big\rangle_K,
\end{aligned} \tag{3.160}$$

$$\begin{aligned}
\left\langle \mathrm{tr}(\Lambda Q_{aa})\,\mathrm{tr}(\Lambda Q_{bb}) \right\rangle_K = \Big\langle &(U_1^{-1}Q_{11}U_1)^{aa}(U_1^{-1}Q_{11}U_1)_{bb} + (U_2^{-1}Q_{22}U_2)_{aa}(U_2^{-1}Q_{22}U_2)_{bb} \\
&-(U_1^{-1}Q_{11}U_1)_{aa}(U_2^{-1}Q_{22}U_2)_{bb} - (U_2^{-1}Q_{22}U_2)_{aa}(U_1^{-1}Q_{11}U_1)_{bb} \Big\rangle_K.
\end{aligned} \tag{3.161}$$

Here the indices 11, 12, 21, and 22 correspond to retarded-advanced space, while a and b are two given distinct replica indices. For class A, U_1 and U_2 are independent, and $K = \mathrm{U}(n) \times \mathrm{U}(n)$. In class C, with the sigma-model field satisfying the additional symmetry constraint (3.118), one has $U_1 = U_2^*$, and $K = \mathrm{U}(2n)$. To evaluate the averages in Eqs. (3.160), (3.161), one need averages of products of matrix elements of matrices U and U^* over the unitary group $\mathrm{U}(2n)$. The required averages are as follows [209] (see also Appendix of Ref. [158]):

$$\langle U_{a\alpha}^* U_{b\beta}\rangle_{\mathrm{U}(2n)} = V_1 \delta_{ab}\delta_{\alpha\beta}, \tag{3.162}$$

$$\langle U_{a\alpha}^* U_{b\beta} U_{c\gamma}^* U_{d\delta}\rangle_{\mathrm{U}(2n)} = V_{1,1}\left(\delta_{ab}\delta_{\alpha\beta}\delta_{cd}\delta_{\gamma\delta} + \delta_{ad}\delta_{\alpha\delta}\delta_{cb}\delta_{\gamma\beta}\right) + V_2\left(\delta_{cb}\delta_{\alpha\beta}\delta_{ad}\delta_{\gamma\delta} + \delta_{ab}\delta_{\alpha\delta}\delta_{cd}\delta_{\gamma\beta}\right), \tag{3.163}$$

where V_λ are the Weingarten functions [210],

$$V_1 = \frac{1}{2n}, \qquad V_{1,1} = \frac{1}{4n^2 - 1}, \qquad V_2 = -\frac{1}{2n(4n^2 - 1)}. \tag{3.164}$$

First use Eq. (3.163) to evaluate the averages in the second line of Eq. (3.161) (denote $U_1 = U_2^* \equiv U$):

$$\left\langle (U_1^{-1} Q^{11} U_1)_{aa} (U_2^{-1} Q^{22} U_2)_{bb} \right\rangle_{\mathrm{U}(2n)}$$

$$= \left\langle U_{a\alpha}^{-1} Q_{\alpha\beta}^{11} U_{\beta a} (U^*)_{b\gamma}^{-1} Q_{\gamma\mu}^{22} (U^*)_{\mu b} \right\rangle_{\mathrm{U}(2n)}$$

$$= \left\langle U_{\alpha a}^* U_{\beta a} U_{\nu\lambda}^* U_{\sigma\rho} \right\rangle_{\mathrm{U}(2n)} \delta_{b\rho} \delta_{\sigma\gamma} \delta_{\mu\nu} \delta_{\lambda b} Q_{\alpha\beta}^{11} Q_{\gamma\mu}^{22}$$

$$= \left(V_{1,1} \left(\delta_{\alpha\beta} \delta_{aa} \delta_{\nu\sigma} \delta_{\lambda\rho} + \delta_{\alpha\sigma} \delta_{a\rho} \delta_{\nu\beta} \delta_{\lambda a} \right) + V_2 \left(\delta_{\nu\beta} \delta_{aa} \delta_{\alpha\sigma} \delta_{\lambda\rho} + \delta_{\alpha\beta} \delta_{a\rho} \delta_{\nu\sigma} \delta_{\lambda a} \right) \right) \delta_{b,\rho} \delta_{\sigma\gamma} \delta_{\mu\nu} \delta_{\lambda b} Q_{\alpha\beta}^{11} Q_{\gamma\mu}^{22}$$

$$= V_{1,1} \left(\delta_{b\rho} \delta_{\rho,b} Q_{\alpha\alpha}^{11} \delta_{\nu\gamma} Q_{\gamma\mu}^{22} \delta_{\mu\nu} + \delta_{b,a} \delta_{\sigma\gamma} \delta_{\mu\beta} \delta_{ab} Q_{\sigma\beta}^{11} Q_{\gamma\mu}^{22} \right)$$

$$\quad + V_2 \left(\delta_{b\lambda} \delta_{\lambda b} Q_{\alpha\beta}^{11} \delta_{\alpha\gamma} Q_{\gamma\mu}^{22} \delta_{\mu\beta} + \delta_{\alpha\beta} \delta_{a\rho} \delta_{\nu\sigma} \delta_{\lambda a} \delta_{b\rho} \delta_{\sigma\gamma} \delta_{\mu\nu} \delta_{\lambda,b} Q_{\alpha\beta}^{11} Q_{\gamma\mu}^{22} \right)$$

$$= V_{1,1} \mathrm{tr} \left(Q^{11} \right) \mathrm{tr} \left(Q^{22} \right) + V_2 \mathrm{tr} \left(Q^{11} \left(Q^{22} \right)^T \right)$$

$$= - V_{1,1} \left(\mathrm{tr} \left(Q^{11} \right) \right)^2 - V_2 \mathrm{tr} \left(\left(Q^{11} \right)^2 \right). \tag{3.165}$$

Further, one can calculate in the same way the terms in the second line of Eq. (3.160):

$$\left\langle (U_1^{-1} Q^{12} U_2)_{ab} (U_2^{-1} Q^{21} U_1)_{ba} \right\rangle_{\mathrm{U}(2n)}$$

$$= \left\langle U_{a\alpha}^{-1} Q_{\alpha\beta}^{12} (U^*)_{\beta b} (U^*)_{b\gamma}^{-1} Q_{\gamma\mu}^{21} U_{\mu a} \right\rangle_{\mathrm{U}(2n)}$$

$$= \left\langle U_{\alpha a}^* U_{\mu a} U_{\nu\lambda}^* U_{\sigma\rho} \right\rangle_{\mathrm{U}(2n)} \delta_{b\rho} \delta_{\sigma\gamma} \delta_{\beta\nu} \delta_{\lambda b} Q_{\alpha\beta}^{12} Q_{\gamma\mu}^{21}$$

$$= \left(V_{1,1} \left(\delta_{\alpha\mu} \delta_{aa} \delta_{\nu\sigma} \delta_{\lambda\rho} + \delta_{\alpha\sigma} \delta_{a\rho} \delta_{\nu\mu} \delta_{\lambda a} \right) + V_2 \left(\delta_{\nu\mu} \delta_{aa} \delta_{\alpha\sigma} \delta_{\lambda\rho} + \delta_{\alpha\mu} \delta_{a\rho} \delta_{\nu\sigma} \delta_{\lambda a} \right) \right) \delta_{b\rho} \delta_{\sigma\gamma} \delta_{\beta\nu} \delta_{\lambda b} Q_{\alpha\beta}^{12} Q_{\gamma\mu}^{21}$$

$$= V_{1,1} \left(\delta_{b\rho} \delta_{\rho b} Q_{\mu\beta}^{12} \delta_{\beta\nu} \delta_{\nu\gamma} Q_{\gamma\mu}^{21} + \delta_{ba} \delta_{ab} \delta_{\alpha\gamma} Q_{\alpha\beta}^{12} Q_{\gamma\nu}^{21} \delta_{\beta,\nu} \right)$$

$$\quad + V_2 \left(\delta_{b\rho} \delta_{\rho b} \delta_{\alpha\gamma} Q_{\alpha\beta}^{12} Q_{\gamma\nu}^{21} \delta_{\beta\nu} + \delta_{b,a} \delta_{\nu\gamma} \delta_{\beta\nu} \delta_{ab} Q_{\sigma\beta}^{12} Q_{\gamma\alpha}^{21} \right)$$

$$= V_{1,1} \mathrm{tr} \left(Q^{12} Q^{21} \right) + V_2 \mathrm{tr} \left(Q^{12} \left(Q^{21} \right)^T \right)$$

$$= \left(V_{1,1} - V_2 \right) \mathrm{tr} \left(Q^{12} Q^{21} \right)$$

$$= \left(V_{1,1} - V_2 \right) \left[\mathrm{tr} \left(\mathbb{1}_{4n \times 4n} \right) - \mathrm{tr} \left(\left(Q^{11} \right)^2 \right) \right]. \tag{3.166}$$

Finally, there is a term of the following type both in Eq. (3.160) and Eq. (3.161):

$$\left\langle (U_1^{-1} Q^{11} U_1)_{ab} (U_1^{-1} Q^{11} U_1)_{cd} \right\rangle_{\mathrm{U}(2n)}$$

$$= \left\langle U_{a\alpha}^{-1} Q_{\alpha\beta}^{11} U_{\beta b} U_{c\gamma}^{-1} Q_{\gamma\mu}^{11} U_{\mu,d} \right\rangle_{\mathrm{U}(2n)}$$

$$= \left\langle U_{\alpha a}^* U_{\beta b} U_{\gamma c}^* U_{\mu d} \right\rangle_{\mathrm{U}(2n)} Q_{\alpha\beta}^{11} Q_{\gamma\mu}^{11}$$

$$= \left[V_{1,1} \left(\delta_{\alpha\beta}\delta_{ab}\delta_{\gamma\mu}\delta_{cd} + \delta_{\alpha\mu}\delta_{ad}\delta_{\gamma\beta}\delta_{cb} \right) + V_2 \left(\delta_{\gamma\beta}\delta_{ab}\delta_{\alpha\mu}\delta_{cd} + \delta_{\alpha\beta}\delta_{ad}\delta_{\gamma\mu}\delta_{cb} \right) \right] Q_{\alpha\beta}^{11} Q_{\gamma\mu}^{22}$$

$$= V_{1,1} \left[(\mathrm{tr}Q^{11})^2 \delta_{ab}\delta_{cd} + \mathrm{tr}(Q^{11}Q^{11}) \delta_{ad}\delta_{cb} \right] + V_2 \left[\mathrm{tr}(Q^{11}Q^{11}) \delta_{ab}\delta_{cd} + (\mathrm{tr}Q^{11})^2 \delta_{ad}\delta_{cb} \right]$$

$$= \left[V_{1,1} \left(\mathrm{tr}Q^{11} \right)^2 + V_2 \mathrm{tr}\left(\left(Q^{11}\right)^2 \right) \right] \delta_{ab}\delta_{cd} + \left[V_{1,1} \mathrm{tr}\left(\left(Q^{11}\right)^2 \right) + V_2 \left(\mathrm{tr}Q^{11} \right)^2 \right] \delta_{ad}\delta_{cb}. \qquad (3.167)$$

In the above transformations, the symmetry property of Q was used,

$$\begin{pmatrix} Q_{11} & Q_{12} \\ Q_{21} & Q_{22} \end{pmatrix} = Q = -\overline{Q} = \begin{pmatrix} -Q_{22}^T & -Q_{12}^T \\ -Q_{21}^T & -Q_{11}^T \end{pmatrix}, \qquad (3.168)$$

as well as the constraints

$$\mathbb{1} = Q^2 = \begin{pmatrix} Q^{11}Q^{11} + Q^{12}Q^{21} & Q^{11}Q^{12} + Q^{12}Q^{22} \\ Q^{21}Q^{11} + Q^{22}Q^{21} & Q^{22}Q^{22} + Q^{21}Q^{12} \end{pmatrix}, \qquad 0 = \mathrm{Tr}Q = \mathrm{Tr}Q^{11} + \mathrm{Tr}Q^{22}. \qquad (3.169)$$

Substituting Eqs. (3.165), (3.166), and (3.167) into Eqs. (3.160) and (3.161), one obtains

$$\left\langle \mathrm{tr}(\Lambda Q_{aa}) \, \mathrm{tr}(\Lambda Q_{bb}) \right\rangle_{\mathrm{U}(2n)} = 2V_{1,1} \left(\mathrm{tr}Q^{11} \right)^2 + 2V_2 \mathrm{tr}\left(\left(Q^{11}\right)^2 \right), \qquad (3.170)$$

$$\left\langle \mathrm{tr}(\Lambda Q_{ab} \Lambda Q_{ba}) \right\rangle_{\mathrm{U}(2n)} = V_2 \left(\mathrm{tr}Q^{11} \right)^2 + (2V_{1,1} - V_2)\mathrm{tr}\left(\left(Q^{11}\right)^2 \right) - \left(V_{1,1} + V_2 \right) \mathrm{tr}\left(\mathbb{1}_{4n \times 4n} \right). \qquad (3.171)$$

In the replica limit $n \to 0$, the last term in Eq. (3.171) vanishes, and one obtains

$$\left\langle \begin{pmatrix} O_{(1,1)}^{ab} \\ O_{(2)}^{ab} \end{pmatrix} \right\rangle_{\mathrm{U}(2n)} = \underbrace{\begin{pmatrix} 2V_{1,1} & 2V_2 \\ V_2 & 2V_{1,1} - V_2 \end{pmatrix}}_{=:K_2} \cdot \begin{pmatrix} O_{(1,1)} \\ O_{(2)} \end{pmatrix}, \qquad (3.172)$$

where notations for basis operators introduced in Eqs. (3.157) and (3.158) were used.

Equation (3.172) is a central result of this subsection. Here its implications are discussed. Consider a K-invariant operator O that is quadratic in Q. One can expand it in the basis $O_{(1,1)}$, $O_{(2)}$ or, alternatively, in the basis $\langle O_{(1,1)}^{ab} \rangle_{\mathrm{U}(2n)}$, $\langle O_{(2)}^{ab} \rangle_{\mathrm{U}(2n)}$:

$$O = c_{(1,1)} O_{(1,1)} + c_{(2)} O_{(2)} = c'_{(1,1)} \langle O_{(1,1)}^{ab} \rangle_{\mathrm{U}(2n)} + c'_{(2)} \langle O_{(2)}^{ab} \rangle_{\mathrm{U}(2n)}. \qquad (3.173)$$

According to Eq. (3.172), the corresponding vectors of coefficients are related by the matrix K_2^T:

$$\begin{pmatrix} c_{(1,1)} \\ c_{(2)} \end{pmatrix} = K_2^T \begin{pmatrix} c'_{(1,1)} \\ c'_{(2)} \end{pmatrix}. \qquad (3.174)$$

It is known from Sec. 3.5.2.2 that, in order for the operator O to be an invariant operator, the vector $(c_{(1,1)}, c_{(2)})^T$ should be an eigenvector of the matrix M_2^T defined in Eq. (3.153). Furthermore, the operation of U$(2n)$ averaging commutes with RG, so that the RG flow of the coefficients $c'_{(1,1)}$, $c'_{(2)}$ is described by the same equation (3.153). Therefore, for O to be an invariant operator, $(c'_{(1,1)}, c'_{(2)})^T$ should also be an eigenvector of M_2^T. In view of Eq. (3.172), both conditions are compatible if and only if the matrix K_2^T has the same eigenvectors as M_2^T. In other words, K_2^T should commute with M_2^T, or, equivalently, K_2 should commute with M_2. To demonstrate that this is indeed the case, the matrix K_2 is represented in the form

$$K_2 = 2(V_{1,1} + V_2) \begin{pmatrix} 1 & \\ & 1 \end{pmatrix} - V_2 \cdot \underbrace{\begin{pmatrix} 2 & -2 \\ -1 & 3 \end{pmatrix}}_{=M_2}, \tag{3.175}$$

which obviously commutes with M_2.

This analysis thus shows that the eigenoperators can be also obtained as eigenvectors of the matrix K_2^T. Explicit verification of the fact that M_2 and K_2 commute serves as a non-trivial check of the calculation.

3.5.3 Generalization to operators of higher degree, $q \equiv |\lambda| > 2$

Her the RG analysis is extended to determine the polynomial pure-scaling operators of higher degree, $q \equiv |\lambda| > 2$.

Begin with considering the basis of K-invariant operators

$$O_{(q_1,\ldots,q_l)} = \prod_{i=1}^{l} \mathrm{tr}\left((\Lambda Q)^{q_i}\right), \tag{3.176}$$

where $(q_1, \ldots, q_l)$ are partitions of q, i.e., $q_1 + q_2 + \ldots + q_l = q$ and $q_1 \geq q_2 \geq \ldots \geq q_l > 0$. This is an extension of the basis (3.157) to arbitrary integer $q \geq 2$. As I am going to discuss, the RG does not mix operators of different degree $q = |\lambda|$. Within given q it acts according to

$$\delta \begin{pmatrix} O_{(1,\ldots 1)} \\ \vdots \\ O_{(q)} \end{pmatrix} = M_q \begin{pmatrix} O_{(1,\ldots 1)} \\ \vdots \\ O_{(q)} \end{pmatrix}. \tag{3.177}$$

I will derive the rules for calculating the matrix M for classes A and C for any q below, and will present it explicitly for $q = 3$ and 4.

Any invariant operator of degree q can be expanded in terms of the basis operators,

$$O = \sum_{(q_1,\ldots,q_l)} c_{(q_1,\ldots,q_l)} O_{(q_1,\ldots,q_l)}, \tag{3.178}$$

where the sum goes over the partitions of q. The RG evolution of the coefficients is determined by the matrix M^T:

$$\delta \begin{pmatrix} c_{(1,\ldots 1)} \\ \vdots \\ c_{(q)} \end{pmatrix} = M_q^T \begin{pmatrix} c_{(1,\ldots 1)} \\ \vdots \\ c_{(q)} \end{pmatrix}. \tag{3.179}$$

Thus, determining eigenvectors of the matrix M_q^T, one finds invariant pure-scaling operators of degree q.

In order to derive the RG rules, it is useful to inspect an example. Consider the operator $\mathrm{tr}\,(AQBQ)\,\mathrm{tr}\,(CQ)$. Splitting Q in slow and fast modes and expanding in fast fields according to Eq. (3.122), and keeping only the terms of zeroth and second order in $\mathcal{X}$, one gets

$$
\mathrm{tr}\,(AQBQ)\,\mathrm{tr}\,(CQ) = \mathrm{tr}\,(AQ_sBQ_s)\,\mathrm{tr}\,(CQ_s)
$$
$$
+ 2\mathrm{tr}\left(Ag_s\Lambda\mathcal{X}^2 g_s^{-1} BQ_s\right)\mathrm{tr}\,(CQ_s) + 2\mathrm{tr}\left(AQ_s Bg_s\Lambda\mathcal{X}^2 g_s^{-1}\right)\mathrm{tr}\,(CQ_s) + 2\mathrm{tr}\,(AQ_s BQ_s)\,\mathrm{tr}\left(Cg_s\Lambda\mathcal{X}^2 g_s^{-1}\right)
$$
$$
+ 4\mathrm{tr}\left(Ag_s\Lambda\mathcal{X} g_s^{-1} Bg_s\Lambda\mathcal{X} g_s^{-1}\right)\mathrm{tr}\,(CQ_s) + 4\mathrm{tr}\left(Ag_s\Lambda\mathcal{X} g_s^{-1} BQ_s\right)\mathrm{tr}\left(Cg_s\Lambda\mathcal{X} g_s^{-1}\right)
$$
$$
+ 4\mathrm{tr}\left(AQ_s Bg_s\Lambda\mathcal{X} g_s^{-1}\right)\mathrm{tr}\left(Cg_s\Lambda\mathcal{X} g_s^{-1}\right). \tag{3.180}
$$

Averaging now over the fast fields $\mathcal{X}$, one finds contributions of three types. In the contributions of the first type, both factors $\mathcal{X}$ originate from the same Q, thus entering as $\mathcal{X}^2$. In the contribution of the second type, two factors of $\mathcal{X}$ come from two different Qs under the same trace. Finally, in the terms of third type, two $\mathcal{X}$s originate from different Qs under different traces. One has already encountered all three types of contributions [see Eq. (3.127)] when developing the RG for $q = 2$ operators in Sec. 3.5.2. By using this, one can generalize the results obtained there, Eqs. (3.151) and (3.138), to the RG rules valid for any q. I do it now separately for classes A and C.

3.5.3.1 Class A

I first derive general RG rules in class A. The contributions $\delta_d(\ldots)$ originating from two $\mathcal{X}$ factors coming from two distinct traces fuse these two traces into a single one, see the first line of Eq. (3.138) :

$$
\delta_d\left[\mathrm{tr}\left((\Lambda Q)^{q_i}\right)\mathrm{tr}\left((\Lambda Q)^{q_j}\right)\right] = 2I_f q_i q_j \cdot \mathrm{tr}\left((\Lambda Q)^{q_i+q_j}\right). \tag{3.181}
$$

The prefactor $q_i q_j$ accounts for q_i places where the fast field $\mathcal{X}$ can occur in $(\Lambda Q)^{q_i}$ and q_j places where another $\mathcal{X}$ can occur in $(\Lambda Q)^{q_j}$. For every of these (identical) $q_i q_j$ terms, one can use the first line of Eq. (3.138) with $A = (\Lambda Q_s)^{q_i-1}\Lambda$ and $B = (\Lambda Q_s)^{q_j-1}\Lambda$, which yields the r.h.s. of Eq. (3.181). If the operator is a product of a larger number of traces, each pair of them will produce such a contribution.

Further, the contributions $\delta_s(\ldots)$ originating from two $\mathcal{X}$ factors coming from the same trace cut this trace into two pieces in all possible ways, see the second line of Eq. (3.138) :

$$
\delta_s\mathrm{tr}\left((\Lambda Q)^{q_i}\right) = \qquad 2I_f \sum_{q_j=1}^{q_i-1} q_j \cdot \mathrm{tr}\left((\Lambda Q)^{q_j}\right)\mathrm{tr}\left((\Lambda Q)^{q_i-q_j}\right)
$$
$$
= \qquad I_f q_i \sum_{q_j=1}^{q_i-1} \mathrm{tr}\left((\Lambda Q)^{q_j}\right)\mathrm{tr}\left((\Lambda Q)^{q_i-q_j}\right). \tag{3.182}
$$

Indeed, the two fast fields can come from Q matrices in arbitrary positions k and $k + q_j$, where $1 \leq k < k + q_j \leq q_i$. For each such contribution, one can use the second line of (3.138) with $A = (\Lambda Q)^{q_j-1}\Lambda$ and $B = (\Lambda Q)^{q_i-q_j-1}\Lambda$. Note that contributions originating from the $\mathcal{X}^2$ factors (i.e. with both $\mathcal{X}$ fields coming from the same Q) vanish in the class A due to the replica limit, see Eq. (3.137) and the comment after it. If the operator is a product of several traces, then each of them will produce a contribution $\delta_s(\ldots)$ according to Eq. (3.182).

Applying these rules, one can find the matrix M_q^A determining the renormalization of operators of degree q, Eq. (3.177). For $q = 3$ and 4 one gets:

$$(M_2^A)^T = (2I_f)\begin{pmatrix} 0 & 1 \\ 1 & 0 \end{pmatrix}, \qquad\qquad (M_3^A)^T = (2I_f)\begin{pmatrix} 0 & 1 & 0 \\ 3 & 0 & 3 \\ 0 & 2 & 0 \end{pmatrix},$$

$$(M_4^A)^T = (2I_f)\begin{pmatrix} 0 & 1 & 0 & 0 & 0 \\ 6 & 0 & 2 & 3 & 0 \\ 0 & 1 & 0 & 0 & 2 \\ 0 & 4 & 0 & 0 & 4 \\ 0 & 0 & 4 & 3 & 0 \end{pmatrix}. \tag{3.183}$$

For convenience, I have also included here the $q = 2$ result, Eq. (3.138). The transposed matrices $(M_q^A)^T$ are listed in Eq. (3.183) since, according to Eq. (3.179), eigenvectors of $(M_q^A)^T$ determine the eigenoperators of RG, i.e., pure-scaling operators. The results for the K-invariant pure scaling operators of class A read

$$\begin{pmatrix} \mathcal{P}_{(1,1)}^A \\ \mathcal{P}_{(2)}^A \end{pmatrix} = \underbrace{\begin{pmatrix} 1 & -1 \\ 1 & 1 \end{pmatrix}}_{\equiv P_2^A}\begin{pmatrix} \mathrm{tr}(\Lambda Q)\mathrm{tr}(\Lambda Q) \\ \mathrm{tr}(\Lambda Q\Lambda Q) \end{pmatrix},$$

$$\begin{pmatrix} \mathcal{P}_{(1,1,1)}^A \\ \mathcal{P}_{(2,1)}^A \\ \mathcal{P}_{(3)}^A \end{pmatrix} = \underbrace{\begin{pmatrix} 1 & -3 & 2 \\ 1 & 0 & -1 \\ 1 & 3 & 2 \end{pmatrix}}_{\equiv P_3^A}\begin{pmatrix} \mathrm{tr}(\Lambda Q)\mathrm{tr}(\Lambda Q)\mathrm{tr}(\Lambda Q) \\ \mathrm{tr}(\Lambda Q)\mathrm{tr}(\Lambda Q\Lambda Q) \\ \mathrm{tr}(\Lambda Q\Lambda Q\Lambda Q) \end{pmatrix},$$

$$\begin{pmatrix} \mathcal{P}_{(1,1,1,1)}^A \\ \mathcal{P}_{(2,1,1)}^A \\ \mathcal{P}_{(2,2)}^A \\ \mathcal{P}_{(3,1)}^A \\ \mathcal{P}_{(4)}^A \end{pmatrix} = \underbrace{\begin{pmatrix} 1 & -6 & 3 & 8 & -6 \\ 1 & -2 & -1 & 0 & 2 \\ 1 & 0 & 3 & 4 & 0 \\ 1 & -2 & 1 & 0 & -2 \\ 1 & 6 & 3 & 8 & 6 \end{pmatrix}}_{\equiv P_4^A}\begin{pmatrix} \mathrm{tr}(\Lambda Q)\mathrm{tr}(\Lambda Q)\mathrm{tr}(\Lambda Q)\mathrm{tr}(\Lambda Q) \\ \mathrm{tr}(\Lambda Q)\mathrm{tr}(\Lambda Q)\mathrm{tr}(\Lambda Q\Lambda Q) \\ \mathrm{tr}(\Lambda Q\Lambda Q)\mathrm{tr}(\Lambda Q\Lambda Q) \\ \mathrm{tr}(\Lambda Q\Lambda Q\Lambda Q)\mathrm{tr}(\Lambda Q) \\ \mathrm{tr}(\Lambda Q\Lambda Q\Lambda Q\Lambda Q) \end{pmatrix}. \tag{3.184}$$

One can fix the freedom in the overall prefactor in each of the eigenoperators by choosing the coefficient in front of $O_{(1,1,\dots,1)}$ to be unity. As proven below in Sec. 3.5.4, eigenvalues $m_{(q_1,\dots,q_n)}^A$ of the one-loop RG matrix $(M_q^A)^T$ are proportional to quadratic Casimir invariants,

$$m_{(q_1,\dots,q_n)}^A = -I_f\sum_j q_j(-c_j^A - q_j), \tag{3.185}$$

where $c_j^A = 1 - 2j$, see Sec. 1.2.1.1. This serves as an additional control of numerical calculations and allows one to unambiguously associate Young diagrams with the eigenvectors of M_q^T.

3.5.3.2 Class C

Now I perform the analysis for class C. For $q = 2$, the RG rules are given by Eq. (3.151). In order to generalize them to operators with higher q, it is useful to trace the origin of various terms in Eq. (3.151)

by inspecting the derivation, Eqs. (3.146)–(3.149). The upper right element -2 of the matrix M_2 in Eq. (3.151) originates from two fast fields $\mathcal{X}$ coming from different traces. It is analogous to class A but contains an additional factor of two. One thus has

$$\delta_d \left[\text{tr} \left((\Lambda Q)^{q_i} \right) \text{tr} \left((\Lambda Q)^{q_j} \right) \right] = 4 I_f q_i q_j \cdot \text{tr} \left((\Lambda Q)^{q_i + q_j} \right). \tag{3.186}$$

The lower left element 1 of the matrix M_2 in Eq. (3.151), as well as the contribution -1 to the lower right element, originate from two fast fields $\mathcal{X}$ coming from the same trace but different Q fields. Finally, the remaining contribution -2 to the lower right element originates from two fast fields $\mathcal{X}$ coming from the same Q matrix. This leads to

$$\delta_s \langle \text{tr} \left((\Lambda Q)^{q_i} \right) \rangle = 2 I_f \sum_{q_j = 1}^{q_i - 1} q_j \, \text{tr} \left((\Lambda Q)^{q_j} \right) \text{tr} \left((\Lambda Q)^{q_i - q_j} \right) - I_f q_i (q_i - 1) \text{tr} \left((\Lambda Q)^{q_i} \right) - 2 I_f q_i \, \text{tr} \left((\Lambda Q)^{q_i} \right)$$

$$= I_f q_i \sum_{q_j = 1}^{q_i - 1} \text{tr} \left((\Lambda Q)^{q_j} \right) \text{tr} \left((\Lambda Q)^{q_i - q_j} \right) - I_f q_i (q_i + 1) \, \text{tr} \left((\Lambda Q)^{q_i} \right). \tag{3.187}$$

In the first line of Eq. (3.187), the first two terms come from a contraction of two $\mathcal{X}$ fields originating from different Q fields, and the last term from the contraction within the $\mathcal{X}^2$ factor originating from a single Q field.

Using these rules, one can determine the matrices M_q that govern the renormalization of operators of degree q in class C according to Eq. (3.177). The results for $q = 3$ and 4 read (the $q = 2$ result found above is also included for completeness):

$$M_2^T = (-2 I_f) \begin{pmatrix} 2 & -1 \\ -2 & 3 \end{pmatrix}, \qquad\qquad M_3^T = (-2 I_f) \begin{pmatrix} 3 & -1 & 0 \\ -6 & 4 & -3 \\ 0 & -4 & 6 \end{pmatrix},$$

$$M_4^T = (-2 I_f) \begin{pmatrix} 4 & -1 & 0 & 0 & 0 \\ -12 & 5 & -2 & -3 & 0 \\ 0 & -2 & 6 & 0 & -2 \\ 0 & -8 & 0 & 7 & -4 \\ 0 & 0 & -8 & -6 & 10 \end{pmatrix}. \tag{3.188}$$

These are class-C counterparts of class-A results given by Eq. (3.183). It is adequate to recall that the matrices M_q^T control the renormalization of coefficients $c_{(q_1, q_2, \dots)}$, see Eq. (3.179). Calculating their

eigenvectors, one finds the eigenoperators:

$$\begin{pmatrix} \mathcal{P}^C_{(1,1)} \\ \mathcal{P}^C_{(2)} \end{pmatrix} = \underbrace{\begin{pmatrix} 1 & -2 \\ 1 & 1 \end{pmatrix}}_{\equiv P^C_2} \begin{pmatrix} \mathrm{tr}(\Lambda Q)\mathrm{tr}(\Lambda Q) \\ \mathrm{tr}(\Lambda Q \Lambda Q) \end{pmatrix},$$

$$\begin{pmatrix} \mathcal{P}^C_{(1,1,1)} \\ \mathcal{P}^C_{(2,1)} \\ \mathcal{P}^C_{(3)} \end{pmatrix} = \underbrace{\begin{pmatrix} 1 & -6 & 8 \\ 1 & -1 & -2 \\ 1 & 3 & 2 \end{pmatrix}}_{\equiv P^C_3} \begin{pmatrix} \mathrm{tr}(\Lambda Q)\mathrm{tr}(\Lambda Q)\mathrm{tr}(\Lambda Q) \\ \mathrm{tr}(\Lambda Q \Lambda Q)\mathrm{tr}(\Lambda Q) \\ \mathrm{tr}(\Lambda Q \Lambda Q \Lambda Q) \end{pmatrix},$$

$$\begin{pmatrix} \mathcal{P}^C_{(1,1,1,1)} \\ \mathcal{P}^C_{(2,1,1)} \\ \mathcal{P}^C_{(2,2)} \\ \mathcal{P}^C_{(3,1)} \\ \mathcal{P}^C_{(4)} \end{pmatrix} = \underbrace{\begin{pmatrix} 1 & -12 & 12 & -32 & 48 \\ 1 & -5 & -2 & -4 & -8 \\ 1 & -2 & 7 & 8 & -2 \\ 1 & 1 & -2 & 2 & 4 \\ 1 & 6 & 3 & -8 & -6 \end{pmatrix}}_{\equiv P^C_4} \begin{pmatrix} \mathrm{tr}(\Lambda Q)\mathrm{tr}(\Lambda Q)\mathrm{tr}(\Lambda Q)\mathrm{tr}(\Lambda Q) \\ \mathrm{tr}(\Lambda Q)\mathrm{tr}(\Lambda Q)\mathrm{tr}(\Lambda Q \Lambda Q) \\ \mathrm{tr}(\Lambda Q \Lambda Q)\mathrm{tr}(\Lambda Q)\mathrm{tr}(\Lambda Q) \\ \mathrm{tr}(\Lambda Q \Lambda Q \Lambda Q)\mathrm{tr}(\Lambda Q) \\ \mathrm{tr}(\Lambda Q \Lambda Q \Lambda Q \Lambda Q) \end{pmatrix}. \tag{3.189}$$

In analogy with class A, the eigenvalues $m_{(q_1,\ldots,q_n)}$ of the class-C one-loop RG matrix $(M_q)^T$ are proportional to quadratic Casimir invariants,

$$m_{(q_1,\ldots,q_n)} = -I_f \sum_j q_j(-c^C_j - q_j), \tag{3.190}$$

where $c^C_j = 1 - 4j$, see Sec. 1.2.1.1. This statement (which I have verified numerically up to the order $q = 15$) will be proven in full generality in Sec. 3.5.4,

3.5.3.3 Invariant operators in class C by U$(2n)$ averaging for $q > 2$.

As was demonstrated in Sec. 3.5.2.3, and alternative way to obtain the K-invariant operators is to perform the $K \equiv \mathrm{U}(2n)$ averaging of fixed-replica operators (replica indices $a_1, \ldots, a_q$). This yields an alternative basis in the space of K-invariant operators. Any K-invariant operator can be expanded in the one and the other basis, and the corresponding coefficients are related by the matrix K_q^T, see Eqs. (3.172), (3.173), and (3.174) for $q = 2$, which are directly extended to arbitrary q:

$$\left\langle \begin{pmatrix} O^{a_1\ldots a_q}_{(1,1,\ldots,1)} \\ \vdots \\ O^{a_1\ldots a_q}_{(q)} \end{pmatrix} \right\rangle_{\mathrm{U}(2n)} = K_q \begin{pmatrix} O_{(1,1,\ldots,1)} \\ \vdots \\ O_{(q)} \end{pmatrix}, \qquad \begin{pmatrix} c_{(1,1,\ldots,1)} \\ \vdots \\ c_{(q)} \end{pmatrix} = K_q^T \begin{pmatrix} c'_{(1,1,\ldots,1)} \\ \vdots \\ c'_{(q)} \end{pmatrix}, \tag{3.191}$$

where

$$O = c_{(1,1,\ldots,1)} O_{(1,1,\ldots,1)} + \ldots + c_{(q)} O_{(q)} = c'_{(1,1,\ldots,1)} \langle O^{a_1,\ldots,a_q}_{(1,1,\ldots,1)} \rangle_{\mathrm{U}(2n)} + c'_{(q)} \langle O^{a_1,\ldots,a_q}_{(q)} \rangle_{\mathrm{U}(2n)}. \tag{3.192}$$

For $q = 3$, one finds

$$K_3^T = \begin{pmatrix} 1 & 0 & 0 \\ 0 & 1 & 0 \\ 0 & 0 & 1 \end{pmatrix} V_{(1,1,1)} + \begin{pmatrix} 0 & \frac{1}{2} & 0 \\ 3 & -\frac{1}{2} & \frac{3}{2} \\ 0 & 2 & -\frac{3}{2} \end{pmatrix} V_{(2,1)} + \begin{pmatrix} 0 & 0 & \frac{1}{4} \\ 0 & 1 & -\frac{3}{4} \\ 2 & -1 & 1 \end{pmatrix} V_{(3)}, \tag{3.193}$$

where, as before, V_λ are Weingarten functions. As was explained in Sec. 3.5.2.3, the consistency requires that K_q^T commutes with the RG matrix M_q^T. Indeed, a straightforward check shows that all the matrices in front of the Weingarten coefficients V_λ in Eq. (3.193) commute with M_3^T, Eq. (3.188).

An analogous calculation for $q = 4$ yields

$$
K_4^T = \begin{pmatrix} 1 & 0 & 0 & 0 & 0 \\ 0 & 1 & 0 & 0 & 0 \\ 0 & 0 & 1 & 0 & 0 \\ 0 & 0 & 0 & 1 & 0 \\ 0 & 0 & 0 & 0 & 1 \end{pmatrix} V_{(1,1,1,1)} + \begin{pmatrix} 0 & \frac{1}{2} & 0 & 0 & 0 \\ 6 & -\frac{1}{2} & 1 & \frac{3}{2} & 0 \\ 0 & 1 & -1 & 0 & 1 \\ 0 & 4 & 0 & -\frac{3}{2} & 2 \\ 0 & 0 & 4 & 3 & -3 \end{pmatrix} V_{(2,1,1)}
$$
$$
+ \begin{pmatrix} 0 & 0 & \frac{1}{4} & 0 & 0 \\ 0 & \frac{1}{2} & -\frac{1}{2} & 0 & \frac{1}{2} \\ 3 & -\frac{1}{2} & \frac{5}{4} & 0 & -\frac{1}{4} \\ 0 & 0 & 0 & \frac{3}{2} & -1 \\ 0 & 2 & -1 & -\frac{3}{2} & \frac{5}{4} \end{pmatrix} V_{(2,2)} + \begin{pmatrix} 0 & 0 & 0 & \frac{1}{4} & 0 \\ 0 & 2 & 0 & -\frac{3}{4} & 1 \\ 0 & 0 & 0 & \frac{3}{2} & -1 \\ 8 & -2 & 4 & \frac{5}{2} & -2 \\ 0 & 4 & -4 & -3 & 4 \end{pmatrix} V_{(3,1)}
$$
$$
+ \begin{pmatrix} 0 & 0 & 0 & 0 & \frac{1}{8} \\ 0 & 0 & 1 & \frac{3}{4} & -\frac{3}{4} \\ 0 & 1 & -\frac{1}{2} & -\frac{3}{4} & \frac{5}{8} \\ 0 & 2 & -2 & -\frac{3}{2} & 2 \\ 6 & -3 & \frac{5}{2} & 3 & -\frac{5}{2} \end{pmatrix} V_{(4)}. \tag{3.194}
$$

Again, it was verified that the matrices multiplying the Weingarten coefficients V_λ in Eq. (3.194) commute with M_4^T, Eq. (3.188). This is an explicit demonstration of the fact that eigenoperators can also be obtained as eigenvectors of K_q^T, see Sec. 3.5.2.3.

3.5.4 Generalized parabolicity of one-loop RG eigenvalues

In Ref. [211], it was shown that the one-loop β function characterizing the RG flow of the coupling constant in non-linear sigma models over Riemannian manifolds $\mathcal{M}$ is given by a purely geometrical property of the manifold—the Ricci curvature. Here I prove that the one-loop RG scaling dimensions describing the flow of gradientless operators $f(Q)$ in sigma models over symmetric spaces G/K are given (up to an overall constant) by Casimir invariants or, equivalently, by eigenvalues of the Laplace-Beltrami operator on G/K [that acts on functions $f(Q)$]. A consequence of this result is the exact generalized parabolicity of one-loop RG scaling dimensions.

Consider an arbitrary function ("composite operator") $f(Q)$, which is a map $G/K \to \mathbb{C}$. I begin the proof by noticing that the one-loop RG operator $\mathcal{D}$ acting on an function $f(Q)$ can be written in the form

$$
\mathcal{D}f(Q) = \frac{1}{2} \int_{\mathfrak{p}} d\mu(\mathcal{X}) \left. \frac{d^2}{dt^2} f(g_s e^{-t\mathcal{X}} \Lambda e^{t\mathcal{X}} g_s^{-1}) \right|_{t=0} e^{-S_f[\mathcal{X}]}, \tag{3.195}
$$

where $S_f[\mathcal{X}]$ is the action (3.123) and the integration runs over the tangent space $\mathfrak{p}$ to the manifold G/K, see Eq. (3.27). The second derivative in t extracts two fast fields $\mathcal{X}$ in all possible ways from all Q fields in $f(Q)$, and the Gaussian integral over the manifold G/K then yields the one-loop contractions.

One can choose a basis $\{\mathcal{X}_i\}$ in $\mathfrak{p}$ satisfying the symmetry constraints of the class-C sigma-model, $\mathcal{X}_i^\dagger = \mathcal{X}_i$ and $\tau_3 \mathcal{X}_i^\dagger \tau_3 = -\mathcal{X}_i$. [A natural choice of this basis was given in Eq. (3.62).] Then $\mathcal{X} = \sum_i y_i \mathcal{X}_i$,

with real and independent coefficients y_i. Further one can demand orthonormality with respect to the trace $\mathrm{tr}\left(\mathcal{X}_i \mathcal{X}_j\right) = \delta_{ij}$. The fast-mode action (3.123) then is diagonal in y_i,

$$S_f[\{y_i\}] = \frac{\pi\sigma_0}{2} \sum_i \left(\nabla y_i \nabla y_i + h^2 y_i y_i\right). \tag{3.196}$$

Using for brevity $e^{t \operatorname{ad}_{\mathcal{X}}} O \equiv e^{-t\mathcal{X}} O e^{t\mathcal{X}}$, one can rewrite Eq. (3.195) as

$$\mathcal{D}f(Q) = \frac{1}{2}\frac{d^2}{dt^2} \int_{\mathfrak{p}} d\mu(\{y_i\}) f(g_s(e^{t\sum_i y_i \operatorname{ad}_{\mathcal{X}_i}}\Lambda)g_s^{-1}) \cdot e^{-S_f[\{y_i\}]}\Bigg|_{t=0}. \tag{3.197}$$

I rewrite the second derivative via

$$\frac{d^2}{dt^2}f(g_s(e^{t\sum_i y_i \operatorname{ad}_{\mathcal{X}_i}}\Lambda)g_s^{-1})\Bigg|_{t=0} = \sum_{ij} y_i y_j \hat{\mathcal{X}}'_i \hat{\mathcal{X}}'_j f(Q), \tag{3.198}$$

where $\hat{\mathcal{X}}'_i$ is the derivative in the direction $\mathcal{X}'_i = g_s \mathcal{X}_i g_s^{-1}$ on the manifold G/K:

$$\hat{\mathcal{X}}'_i f(Q) = \partial_t f(g_s(e^{t \operatorname{ad}_{\mathcal{X}_i}}\Lambda)g_s^{-1})|_{t=0} = \partial_t f(e^{t \operatorname{ad}_{\mathcal{X}'_i}}Q)|_{t=0}. \tag{3.199}$$

It is easy to see that $\{\mathcal{X}'_i\}$ has a meaning of the basis in the tangent space to sigma-model manifold at the point Q.

Substituting Eq. (3.198) into Eq. (3.197), one obtains

$$\mathcal{D}f(Q) = \sum_{ij} \left(\hat{\mathcal{X}}'_i \hat{\mathcal{X}}'_j f(Q)\right) \cdot \int_{\mathfrak{p}} d\mu(\{y_l\})\, y_i y_j\, e^{-S_f[\{y_l\}]} \tag{3.200}$$

The gaussian integral here is exactly the one-loop integral defined by Eq. (3.126),

$$\int_{\mathfrak{p}} d\mu(\{y_l\})\, y_i y_j\, e^{-S_f[\{y_l\}]} = I_f \delta_{ij}, \tag{3.201}$$

so that

$$\mathcal{D} = I_f \sum_i \hat{\mathcal{X}}'_i \hat{\mathcal{X}}'_i. \tag{3.202}$$

Thus, the one-loop RG operator is proportional to the Laplacian $\sum_i \hat{\mathcal{X}}'_i \hat{\mathcal{X}}'_i$. Therefore, the RG eigenvalues are proportional to the quadratic Casimir invariants. It follows that the spectrum of one-loop RG eigenvalues satisfies the generalized parabolicity, as has been already stated (and numerically verified) for classes A and C, Eqs. (3.185) and (3.190). As the above proof is very general, I believe that it is applicable to all ten symmetry classes.

It is crucial to emphasize that the generalized parabolicity of the one-loop RG is violated by higher-loop contributions. In general, the generalized multifractal spectra are not parabolic, see also the discussion in Sec. 3.2.3.

3.6 Wavefunction combinations with one spin component

In this section, I derive eigenfunction correlators that correspond to pure-scaling sigma-model operators determined in Sec. 3.5. Let me emphasize, that this "translation" to the wave-function language is not unique: there are many wave-function observables that correspond to the same sigma-model composite operator, i.e., belong to the same representation and scale in the same way. In the present section, the focus is on correlation functions that involve only one spin component of wave functions (say, spin up). In Sec. 3.6.1, the necessary steps are performed: (i) express correlators of wave functions ψ_σ in terms of retarded and advanced Greens functions; (ii) find linear combinations S_σ of the bosonic action variables ϕ_σ that map one-to-one (in the sense of correlation functions) to ψ_σ; (iii) determine the Q-field combinations that remain after integrating out S and connect them to operators whose RG flow has been derived above. Finally, (iv) one has to take into account connections between the different parametrizations Q and $\tilde{Q}$ of the sigma-model manifold. Overall, one finds that the single-spin wave-function combinations translate into Q-field operators in class C in the same manner as in the class-A sigma-model.

Having derived pure-scaling eigenstate correlation functions (Sec. 3.6.1), one can determine the scaling exponents numerically by simulating the appropriate network model. While this perfectly works at the conventional quantum-Hall transition, it turns out that there is a major computational difficulty for implementing this with a high accuracy at the SQH transition. The point is that, apart from the simplest case of the representations (q) corresponding to the conventional multifractality, the eigenstate correlations for class C obtained in this way have an indefinite sign for an individual disorder realization and exhibit very strong fluctuations. As a result, one has to perform averaging over a very large number of disorder realizations in order to reach a reasonable accuracy for the exponents. This is done for the (1,1) exponent in Sec. 3.6.3. At the same time, for exponents corresponding to Young diagrams with $q > 2$ [such as (2,1), (1,1,1), (3,1), (2,1,1), (2,2), etc] this would require truly outstanding numerical efforts, which go beyond this work. In view of this, I develop two further alternative approaches to determine numerically these exponents.

One of these approaches is presented in Sec. 3.6.2. The focus there is on Young-symmetrized wave function combinations $|\Psi_\lambda|^2$ of $\psi_\uparrow$ that are manifestly positive and show pure scaling of representation λ in class-A systems [87]. This makes them very suitable for numerical averaging. In class C, these combinations [except for LDOS moments $\lambda = (q)$] do not map to pure-scaling operators of the sigma-model. One thus could naively think that studying numerically these correlators does not bring any useful information about the class-C scaling. Luckily, the situation turns out to be much more favorable. Using these results for the coefficients of pure scaling operators $\mathcal{P}_\lambda^A$ (3.184) in class A and $\mathcal{P}_\lambda^C$ (3.189) in class C as obtained in Sec. 3.5.3, in Sec. 3.6.2 mixing matrices relating the two are derived. Remarkably, these matrices have many zero entries, implying that one is able to access numerically some subleading exponents of class C by investigating the scaling of eigenoperators of class A.

In Sec. 3.6.3 numerical results for the exponents accessible within this framework are presented. Since the finite-size effects and the need for ensemble averaging proliferate with increasing q, the numerics is restricted here to $q \leq 4$. The key results are the scaling exponents collected in Table 3.2. Crucially, one finds that the generalized parabolicity is violated strongly: the exponents deviate up to 50% from the values that they would take for a spectrum satisfying the generalized parabolicity. For comparison, the results of the class-A network-model numerics are presented in Table 3.1. There, deviations from parabolicity are much weaker (of the order of several percent).

A second approach for obtaining class-C generalized MF exponents from sign-definite correlation functions is developed in Sec. 3.7 below. The idea is to explore correlation functions that involve both

spin projections on the same site. As is shown there, correlation functions involving the total density $|\psi| = \sqrt{|\psi|_\uparrow^2 + |\psi|_\downarrow^2}$ turn out to be very useful in this connection.

3.6.1 Translation dictionary

In this subsection, I am going to derive a "dictionary" to translate correlations of wave functions ψ into those of bosonic field variables ϕ of the replicated action and further to the sigma-model (Q-field) language. Linear combinations S of the bosonic variables ϕ are chosen, such that the translation of S to ψ is one-to-one. One then restrict the wave-function combination to a singe spin component (e.g., spin up). Mapping the single-spin expressions to Q-field correlation functions and averaging over a certain subgroup U_d of the gauge group $K = U(2n)$, one obtains sigma-model composite operators as studied in Sec. 3.5.

3.6.1.1 From wave functions to Green's functions

One can introduce retarded and advanced Green's function:

$$\hat{G}^{R/A}(\epsilon, r_1, r_2) = \langle r_1 | \frac{1}{\epsilon - \hat{H} \pm i0} | r_2 \rangle. \tag{3.203}$$

The hat indicates the matrix structure representing the two-by-two combined spin and particle-hole space of the Hamiltonian (3.100). To extract eigenstate correlations, one uses a connection between the eigenstates $\psi_{\alpha,\sigma}(r)$ (where σ is the spin index) and the Green's functions in a given disorder configuration

$$G^R_{\sigma_1\sigma_2}(\epsilon, r_1, r_2) - G^A_{\sigma_1\sigma_2}(\epsilon, r_1, r_2) = 2\pi i \sum_\alpha \delta(\epsilon - \omega_\alpha)\psi^*_{\alpha,\sigma_1}(r_1)\psi_{\alpha,\sigma_2}(r_2). \tag{3.204}$$

Here ω_α are exact eigenenergies in that disorder configuration. This implies the correspondence [87, 103]

$$\frac{1}{2\pi i\nu(\epsilon)} \left(G^R_{\sigma_1\sigma_2}(\epsilon, r_1, r_2) - G^A_{\sigma_1\sigma_2}(\epsilon, r_1, r_2) \right) \longleftrightarrow \left. \psi^*_{\alpha,\sigma_1}(r_1)\psi_{\alpha,\sigma_2}(r_2) \right|_{\omega_\alpha \approx \epsilon} \tag{3.205}$$

in averages $\langle \ldots \rangle$ over disorder configurations V. Here $\nu(\epsilon)$ is the average density of states This correspondence is extended to eigenstate composite objects of higher order and allows one to relate the corresponding averages to averaged products of Green's functions [87, 103].

The components of the Green's function are not independent. In view of the particle-hole symmetry (3.101) of the Hamiltonian, the Green's functions satisfy

$$i\sigma_y \hat{G}^R(\epsilon, r_1, r_2) i\sigma_y = \hat{G}^A(-\epsilon, r_2, r_1)^T. \tag{3.206}$$

When written explicitly in terms of the components, this reads

$$\begin{pmatrix} -G^R_{\downarrow\downarrow}(\epsilon, r_1, r_2) & G^R_{\downarrow\uparrow}(\epsilon, r_1, r_2) \\ G^R_{\uparrow\downarrow}(\epsilon, r_1, r_2) & -G^R_{\uparrow\uparrow}(\epsilon, r_1, r_2) \end{pmatrix} = \begin{pmatrix} G^A_{\uparrow\uparrow}(-\epsilon, r_2, r_1) & G^A_{\downarrow\uparrow}(-\epsilon, r_2, r_1) \\ G^A_{\uparrow\downarrow}(-\epsilon, r_2, r_1) & G^A_{\downarrow\downarrow}(-\epsilon, r_2, r_1) \end{pmatrix}. \tag{3.207}$$

One can see that the symmetry operation connects the retarded Green's function at positive energy to the advanced one at negative energy and opposite spin components.

3.6.1.2 From Green's functions to averages over bosonic vector fields

In order to express composite objects built out of Green's functions in terms of field-theoretic averages, it is useful to introduce the following linear combinations of the bosonic integration variables ϕ:

$$
\begin{aligned}
S_{\uparrow,a} &= \phi_{\uparrow,a} + i e^{i\alpha_a} \phi^*_{\downarrow,-a}, \\
S_{\downarrow,a} &= \phi_{\downarrow,a} - i e^{i\alpha_a} \phi^*_{\uparrow,-a},
\end{aligned}
\tag{3.208}
$$

with arbitrary phases α_a. These fields have the useful property of only having "particle-conserving" contractions with respect to the Gaussian action $S_0[\phi^*, \phi; V]$, Eq. (3.103), defined for the Hamiltonian $H = H_0 + V$ in a given disorder configuration V:

$$
\begin{aligned}
i \langle S^*_{\downarrow,a}(r_1) S_{\downarrow,a}(r_2) \rangle_{S_0[\phi^*,\phi;V]} &= G^R_{\downarrow\downarrow}(\omega_a; r_1, r_2) + G^R_{\uparrow\uparrow}(-\omega_a; r_2, r_1) \\
&= G^R_{\downarrow\downarrow}(\omega_a; r_1, r_2) - G^A_{\downarrow\downarrow}(\omega_a; r_1, r_2), \\
i \langle S^*_{\downarrow,a}(r_1) S_{\uparrow,a}(r_2) \rangle_{S_0[\phi^*,\phi;V]} &= G^R_{\downarrow\uparrow}(\omega_a; r_1, r_2) - G^R_{\downarrow\uparrow}(-\omega_a; r_2, r_1) \\
&= G^R_{\downarrow\uparrow}(\omega_a; r_1, r_2) - G^A_{\downarrow\uparrow}(\omega_a; r_1, r_2).
\end{aligned}
\tag{3.209}
$$

Other non-zero contractions can be obtained by complex conjugation and the particle-hole operation. Combining this with Eq. (3.205), one get

$$
\begin{aligned}
\left\langle \left\langle S^*_{\downarrow,a}(r_1) S_{\downarrow,a}(r_2) \right\rangle_{S_0[\phi^*,\phi;V]} \right\rangle_V &= \frac{-1}{2\pi\nu(\epsilon)} \left\langle \psi^*_{\alpha,\downarrow}(r_1) \psi_{\alpha,\downarrow}(r_2) \right\rangle_V \bigg|_{\omega_\alpha \approx \epsilon}, \\
\left\langle \left\langle S^*_{\downarrow,a}(r_1) S_{\uparrow,a}(r_2) \right\rangle_{S_0[\phi^*,\phi;V]} \right\rangle_V &= \frac{-1}{2\pi\nu(\epsilon)} \left\langle \psi^*_{\alpha,\downarrow}(r_1) \psi_{\alpha,\uparrow}(r_2) \right\rangle_V \bigg|_{\omega_\alpha \approx \epsilon}.
\end{aligned}
\tag{3.210}
$$

This shows a one-to-one correspondence between ψ and S (since the interest is only in scaling, the prefactor is omitted):

$$
\psi^*_{\alpha,\sigma_1}(r_1) \psi_{\alpha,\sigma_2}(r_2) \;\longleftrightarrow\; S^*_{\sigma_1,a}(r_1) S_{\sigma_2,a}(r_2).
\tag{3.211}
$$

The correspondence is understood in the sense of averages that are explicitly shown in Eq. (3.210). This correspondence is straightforwardly extended to higher-order products by using the fact that the action $S_0[\phi^*, \phi; V]$ is Gaussian and diagonal in replicas. As an example,

$$
\psi^*_{\alpha,\sigma_1}(r_1) \psi_{\alpha,\sigma_2}(r_2) \psi^*_{\beta,\sigma_3}(r_3) \psi_{\beta,\sigma_4}(r_4) \;\longleftrightarrow\; S^*_{\sigma_1,a}(r_1) S_{\sigma_2,a}(r_2) S^*_{\sigma_3,b}(r_3) S_{\sigma_4,b}(r_4).
\tag{3.212}
$$

Note that the wave-function indices $\alpha, \beta, \gamma, \ldots$ are translated into the replica indices $a, b, c, \ldots$. For this reason, below the replica indices $a, b, c, \ldots$ will be also used as eigenfunction labels.

3.6.1.3 From bosonic vector fields to the sigma-model field Q

The next step is to find the dictionary that translates the vector fields S of the replica field theory into the matrix field Q of the sigma-model. Upon the Hubbard-Stratonovich transformation, one obtains the theory with the action $S[\phi, \phi^*, Q]$, see Eq. (3.109). Intergrating over the fields ϕ, ϕ^*, one translates any composite object $O[\phi, \phi^*]$ into its sigma-model counterpart $\langle O[\phi, \phi^*] \rangle_{S[\phi, \phi^*, Q]}$ expressed in terms

of the field Q. For the objects that are bilinear in S fields (or, equivalently in ϕ fields), one has

$$\langle S^*_{\downarrow,a}(r_1) S_{\downarrow,b}(r_1)\rangle_{S[\phi,\phi^*,Q]} = ie^{-i\alpha_a} Q^{AR}_{-b,-a} - ie^{i\alpha_b} Q^{RA}_{a,b} + Q^{RR}_{a,b} + e^{i\alpha_b - i\alpha_a} Q^{RR}_{-b,-a} \tag{3.213}$$

$$= -ie^{-i\alpha_a} Q^{AR}_{a,b} - ie^{i\alpha_b} Q^{RA}_{a,b} + Q^{RR}_{a,b} - e^{i\alpha_b - i\alpha_a} Q^{AA}_{a,b} \equiv \mathcal{Q}^{00}_{ab}, \tag{3.214}$$

$$\langle S^*_{\uparrow,a}(r_1) S_{\uparrow,b}(r_1)\rangle_{S[\phi,\phi^*,Q]} = -ie^{-i\alpha_a} Q^{AR}_{a,b} + ie^{i\alpha_b} Q^{RA}_{-b,-a} + Q^{RR}_{a,b} + e^{i\alpha_b - i\alpha_a} Q^{RR}_{-b,-a}$$

$$= -ie^{-i\alpha_a} Q^{AR}_{a,b} - ie^{i\alpha_b} Q^{RA}_{a,b} + Q^{RR}_{a,b} - e^{i\alpha_b - i\alpha_a} Q^{AA}_{a,b} \equiv \mathcal{Q}^{00}_{ab}, \tag{3.215}$$

$$\langle S_{\downarrow,a}(r_1) S_{\downarrow,b}(r_1)\rangle_{S[\phi,\phi^*,Q]} = 0, \tag{3.216}$$

$$\langle S^*_{\downarrow,a}(r_1) S^*_{\uparrow,b}(r_1)\rangle_{S[\phi,\phi^*,Q]} = Q^{AR}_{b,-a} e^{-i\alpha_a - i\alpha_b} + Q^{RA}_{a,-b} - ie^{-i\alpha_b} Q^{RR}_{a,-b} + ie^{-i\alpha_a} Q^{RR}_{b,-a}$$

$$= -Q^{AR}_{a,-b} e^{-i\alpha_a - i\alpha_b} + Q^{RA}_{a,-b} - ie^{-i\alpha_b} Q^{RR}_{a,-b} - ie^{-i\alpha_a} Q^{AA}_{a,-b} \equiv \mathcal{Q}^{01}_{ab}, \tag{3.217}$$

$$\langle S_{\downarrow,a}(r_1) S_{\uparrow,b}(r_1)\rangle_{S[\phi,\phi^*,Q]} = Q^{AR}_{-a,b} + Q^{RA}_{-b,a} e^{i\alpha_a + i\alpha_b} - iQ^{RR}_{-a,b} e^{i\alpha_a} + iQ^{RR}_{-b,a} e^{i\alpha_b}$$

$$= Q^{AR}_{-a,b} - Q^{RA}_{-a,b} e^{i\alpha_a + i\alpha_b} - iQ^{RR}_{-a,b} e^{i\alpha_a} - iQ^{AA}_{-a,b} e^{i\alpha_a} \equiv \mathcal{Q}^{10}_{ab}, \tag{3.218}$$

$$\langle S^*_{\downarrow,a}(r_1) S_{\uparrow,b}(r_1)\rangle_{S[\phi,\phi^*,Q]} = 0. \tag{3.219}$$

The right-hand sides can be straightforwardly read off from the coupling (3.107) of Q and ϕ fields in the action $S[\phi,\phi^*;Q]$. One has introduced here the short-hand notations $\mathcal{Q}^{pp'}_{ab}$ with $p, p' = 0, 1$.

Translating composite objects of higher order in S, S^* fields amounts to using Wick's theorem, since the action $S[\phi,\phi^*,Q]$ is Gaussian with respect to ϕ, ϕ^* fields. However, since this action is not diagonal in replicas (due to the coupling to the Q field), many terms arise. A drastic simplification occurs if one assumes (which is fully sufficient for the purposes of calculating scaling exponents) that all r_i are far apart from each other in comparison to the microscopic scale a controlling the decay of averaged single-particle Green's function, $|r_i - r_j| \gg a$. Then one only has to retain contractions that are diagonal in spatial coordinates. In the special case of the network model that is used for numerical simulations in this paper, the condition $r_i \neq r_j$ is sufficient since all contractions between different spatial points are identically equal to zero. With only one spin component, further simplifications occur. First, one only needs the contraction rule (3.214). Second, by averaging over the phases α_a, $\alpha_b, \ldots$, i.e., over the diagonal subgroup $U_d = U(1)^{2n}$ of the gauge group $U(2n)$, one ends up in the space of sigma-model composite operators spanned by products of traces of the type $\mathrm{tr}\,(E_{aa}\Lambda Q E_{bb}\Lambda Q \ldots)$, where E_{aa} is the projector on replica a as defined above. As the simplest example, this is shown for composite operators that are of fourth order in S, S^* fields and thus map on sigma-model composite operators that are quadratic in Q fields (i.e., $q = 2$ operators). There are two such independent composite operators (the spin index is skipped, which is the same for all S fields), $|S_a(r_1)|^2 |S_b(r_2)|^2$ and $S^*_a(r_1) S_b(r_2) S_b(r_1) S^*_a(r_2)$; they will be called the Hartree and Fock terms, respectively, for obvious reason. For the Hartree term one gets, according to Eq. (3.214),

$$\langle \mathcal{Q}^{00}_{aa} \mathcal{Q}^{00}_{bb}\rangle_{U_d} = \int_0^{2\pi}\int_0^{2\pi} \frac{d\alpha_a d\alpha_b}{(2\pi)^2} \left(-ie^{-i\alpha_a} Q^{AR}_{a,a} - ie^{i\alpha_a} Q^{RA}_{a,a} + Q^{RR}_{a,a} - Q^{AA}_{a,a}\right)$$

$$\times \left(-ie^{-i\alpha_b} Q^{AR}_{b,b} - ie^{i\alpha_b} Q^{RA}_{b,b} + Q^{RR}_{b,b} - Q^{AA}_{b,b}\right)$$

$$= \left(Q^{RR}_{a,a} - Q^{AA}_{a,a}\right)\left(Q^{RR}_{b,b} - Q^{AA}_{b,b}\right) = \mathrm{tr}\left(E_{aa}\Lambda Q\right)\mathrm{tr}\left(E_{bb}\Lambda Q\right) \equiv O^{ab}_{(1,1)}. \tag{3.220}$$

Similarly, one has for the Fock term:

$$\langle \mathcal{Q}_{ab}^{00} \mathcal{Q}_{ba}^{00} \rangle_{\mathrm{U}_d} = \int_0^{2\pi} \int_0^{2\pi} \frac{d\alpha_a d\alpha_b}{(2\pi)^2} \left(-ie^{-i\alpha_a} Q_{a,b}^{AR} - ie^{i\alpha_b} Q_{a,b}^{RA} + Q_{a,b}^{RR} - e^{i\alpha_b - i\alpha_a} Q_{a,b}^{AA} \right)$$
$$\times \left(-ie^{-i\alpha_b} Q_{b,a}^{AR} - ie^{i\alpha_a} Q_{b,a}^{RA} + Q_{b,a}^{RR} - e^{i\alpha_a - i\alpha_b} Q_{b,a}^{AA} \right)$$
$$= Q_{a,b}^{RR} Q_{b,a}^{RR} + Q_{a,b}^{AA} Q_{b,a}^{AA} - Q_{a,b}^{AR} Q_{b,a}^{RA} - Q_{a,b}^{RA} Q_{b,a}^{AR} = \mathrm{tr} \left(E_{aa} \Lambda Q E_{bb} \Lambda Q \right) \equiv O_{(2)}^{ab}. \quad (3.221)$$

Thus, after the U_d averaging, one has obtained the operators $O_{(1,1)}^{ab}$ and $O_{(2)}^{ab}$ as defined in Eq. (3.158).

This is straightforwardly generalized to $q > 2$ composite operators, and one obtains a mapping of the composite operators of S fields to the sigma-model operators of the type

$$O_{(i,j,\dots)}^{a_1 \dots a_q} = \mathrm{tr} \left(E_{a_1 a_1} \Lambda Q \cdots E_{a_i a_i} \Lambda Q \right) \mathrm{tr} \left(E_{a_{i+1} a_{i+1}} \Lambda Q \cdots E_{a_{i+j} a_{i+j}} \Lambda Q \right) \dots . \quad (3.222)$$

Recalling the direct correspondence between the S fields and eigenstates ψ, one thus gets a correspondence between eigenstate observables and sigma-model composite operators:

$$O_{(1,1)}^{ab} \longleftrightarrow |\psi_a(r_1)|^2 |\psi_b(r_2)|^2 \,,$$
$$O_{(2)}^{ab} \longleftrightarrow \psi_a^*(r_1) \psi_b(r_1) \psi_b^*(r_2) \psi_a(r_2) \,,$$
$$O_{(1,1,1)}^{abc} \longleftrightarrow |\psi_a(r_1)|^2 |\psi_b(r_2)|^2 |\psi_c(r_3)|^2 \,,$$
$$O_{(2,1)}^{abc} \longleftrightarrow \psi_a^*(r_1) \psi_b(r_1) \psi_b^*(r_2) \psi_a(r_2) |\psi_c(r_3)|^2 \,,$$
$$O_{(3)}^{abc} \longleftrightarrow \psi_a^*(r_1) \psi_b(r_1) \psi_b^*(r_2) \psi_c(r_2) \psi_c^*(r_3) \psi_a(r_3) \,,$$
$$O_{(1,1,1,1)}^{abcd} \longleftrightarrow |\psi_a(r_1)|^2 |\psi_b(r_2)|^2 |\psi_c(r_3)|^2 |\psi_d(r_4)|^2 \,,$$
$$O_{(2,1,1)}^{abc} \longleftrightarrow \psi_a^*(r_1) \psi_b(r_1) \psi_b^*(r_2) \psi_a(r_2) |\psi_c(r_3)|^2 |\psi_d(r_4)|^2 \,,$$
$$O_{(2,2)}^{abcd} \longleftrightarrow \psi_a^*(r_1) \psi_b(r_1) \psi_b^*(r_2) \psi_a(r_2) \psi_c^*(r_3) \psi_d(r_3) \psi_d^*(r_4) \psi_c(r_4) \,,$$
$$O_{(3,1)}^{abcd} \longleftrightarrow \psi_a^*(r_1) \psi_b(r_1) \psi_b^*(r_2) \psi_c(r_2) \psi_c^*(r_3) \psi_a(r_3) |\psi_d(r_4)|^2 \,,$$
$$O_{(4)}^{abcd} \longleftrightarrow \psi_a^*(r_1) \psi_b(r_1) \psi_b^*(r_2) \psi_c(r_2) \psi_c^*(r_3) \psi_d(r_3) \psi_d^*(r_4) \psi_a(r_4) \,. \quad (3.223)$$

The spin index for wave functions is suppressed here (and in the rest of Sec. 3.6) since it is the same for all of them (e.g., all wave functions have spin up). The symmetrized version of the operators $O_{(i,j,\dots)}^{a_1 \dots a_q}$ over the symmetric group S_q is denoted by $O_{(i,j,\dots)}^{S\{a_1 \dots a_q\}}$:

$$O_{(i,j,\dots)}^{S\{a_1 \dots a_q\}} = \frac{1}{q!} \sum_{\sigma \in S_q} \mathrm{tr} \left(E_{\sigma(a_1)\sigma(a_1)} \Lambda Q \cdots E_{\sigma(a_i)\sigma(a_i)} \Lambda Q \right) \mathrm{tr} \left(E_{\sigma(a_{i+1})\sigma(a_{i+1})} \Lambda Q \cdots E_{\sigma(a_{i+j})\sigma(a_{i+j})} \Lambda Q \right) \dots .$$
$$(3.224)$$

(For $q = 2$ the symmetrization is redundant: $O_{(1,1)}^{ab} \equiv O_{(1,1)}^{S\{ab\}}$ and $O_{(2)}^{ab} \equiv O_{(2)}^{S\{ab\}}$.) The symmetrized operators $O_{(i,j,\dots)}^{S\{a_1 \dots a_q\}}$ obey the same RG equations of Sec. 3.5.3.2 as the K-invariant operators. Thus, pure-scaling operators are constructed from them according to Eq. (3.189). At the same time, was just shown, the operators $O_{(i,j,\dots)}^{S\{a_1 \dots a_q\}}$ correspond to eigenstate observables (3.223) (with S_q-symmetrization over energies corresponding to symmetrization over replica indices). Therefore, by using Eq. (3.189), one also obtains the pure-scaling combinations of eigenstates. This is done in Sec. 3.6.2.

There is the following technical subtlety in the above derivation. The choice of the sigma-model manifold that was used in the derivation of the sigma-model in Sec. 3.4 is slightly different from that used in Sec. 3.5.2.2 for derivation of RG equations. The connection was explained in detail in the end of Sec. 3.4 where the former parametrization was denoted Q and the latter $\tilde{Q}$, see Eq. (3.115) for explicit relation between them. In the present section (Sec. 3.6) the Q parametrization is used, since it is most conveneint for the mapping of eigenstate observables to the sigma-model composite operators. At the same time, at the last step, fact that composite operators (3.224) renormalize according to RG equations derived in Sec. 3.5.2.2 is used. To demonstrate this fully rigorously, one should reexpress Eq. (3.224) in terms of the $\tilde{Q}$-field and verify that these operators satisfy the conditions for validity of the RG equations of Sec. 3.5.2.2. This is done in B.2.

3.6.2 Generalized multifractality: Pure-scaling eigenstate observables

Now on is in a position to write down the pure-scaling observables in terms of eigenfunctions. First this is demonstrated for the case of $q = 2$. Then there are two eigenstates (labeled by a and b corresponding to replica indices in the field theory) and two spatial point r_1 and r_2. Two basis combinations are the Hartree (H) and Fock (F) terms, as given by Eq. (3.223) (with symmetrization over indices a, b)

$$
\begin{aligned}
O^{ab}_{(1,1)} &\longleftrightarrow \frac{1}{2}\left(|\psi_a(r_1)|^2|\psi_b(r_2)|^2 + |\psi_b(r_1)|^2|\psi_a(r_2)|^2\right) \equiv H\,, \\
O^{ab}_{(2)} &\longleftrightarrow \frac{1}{2}\left(\psi_a^*(r_1)\psi_b(r_1)\psi_b^*(r_2)\psi_a(r_2) + \psi_b^*(r_1)\psi_a(r_1)\psi_a^*(r_2)\psi_b(r_2)\right) \equiv F\,.
\end{aligned}
\tag{3.225}
$$

Using Eq. (3.156) [the same matrix of coefficients appears also in Eqs. (3.154) and (3.155), and is denoted P_2^C in Eq.(3.189)], one can write down the $q = 2$ pure-scaling observables as combinations of these two basis combinations:

$$
\begin{aligned}
\mathcal{P}^C_{(2)} &\longleftrightarrow & H + F\,, \\
\mathcal{P}^C_{(1,1)} &\longleftrightarrow & H - 2F\,.
\end{aligned}
\tag{3.226}
$$

The operator $\mathcal{P}^C_{(2)}$ is a representative of the conventional multifractality and can be realized also with a single eigenfunction, as $|\psi_a(r)|^4$. On the other hand, the subleading operator $\mathcal{P}^C_{(1,1)}$ goes beyond the conventional multifractality and is a representative of the generalized multifractalty. In the same way, pure-scaling operators for $q > 2$ can be obtained.

By using the class-C network model it is verified numerically, that $\mathcal{P}^C_{(1,1)}$ is realized by $H - 2F$ and determined in this way the corresponding scaling exponent, see Sec. 3.6.3. There is, however, the following computational difficulty in determining the exponents of subleading operators in this way. For an individual realization of disorder, the quantity $H - 2F$ has an indefinite sign, and its typical magnitude is of the same order as H and F. Only after the averaging one obtains $\langle H - 2F\rangle$ that is strongly suppressed with respect to $\langle H\rangle$ and $\langle F\rangle$. This should be contrasted to the case of class A: the operator $\mathcal{P}^A_{(1,1)}$ corresponds to $H - F$ which can be written as an absolute value squared, is thus strictly positive and small for any realization of disorder. In view of this, the numerical evaluation of the scaling exponent $\mathcal{P}^C_{(1,1)}$ by calculating the average $\langle H - 2F\rangle$ requires much larger computational efforts than the analogous calculation (of the average $\langle H - F\rangle$) in class A. For this reason, this approach is numerically implemented in the present work only for the (1,1) operator but not for subleading operators with $q > 2$ for which still more extensive computational efforts are needed. Two alternative

approaches that are used to determine some of subleading exponents with higher q are described below (in this section and in Sec. 3.7).

The first of these alternative approaches is based on expressing the sigma-model scaling operators $\mathcal{P}_\lambda^C$ in terms of a linear combination of the class-A scaling operators $\mathcal{P}_{\lambda'}^A$. According to the analysis of Ref. [87], the wave-function observable $|\Psi_\lambda|^2$, with Ψ_λ obtained by a combination of symmetrization and antisymmetrization of the product of eigenstate amplitudes according to a Young diagram λ ("Young symmetrization"), maps onto $\mathcal{P}_\lambda^A$ in the sigma-model language. Thus, expanding $\mathcal{P}_\lambda^C$ over $\mathcal{P}_{\lambda'}^A$, one simultaneously obtains an expansion of the pure-scaling eigenstate observable of class C corresponding to the diagram λ over the pure-scaling eigenstate observables $|\Psi_{\lambda'}|^2$ of class A. The idea is to invert this expansion and to determine numerically the scaling of $|\Psi_\lambda|^2$, i.e., of $\mathcal{P}_\lambda^A$, in a system of class C. Since $|\Psi_\lambda|^2$ is strictly positive, this can be done quite efficiently. This scaling will be determined by the most relevant (in the RG sense) operator $\mathcal{P}_{\lambda'}^C$ out of those that contribute to $\mathcal{P}_\lambda^A$. This allows one to determine some (although not all) of the subleading scaling expionents in class C.

The construction of $|\Psi_\lambda|^2$ corresponding to a Young diagram λ is briefly sketched; see Appendix A of Ref. [87] for a detailed exposition. Consider a Young diagram $\lambda = (q_1, q_2, \ldots)$ with $|\lambda| = q$, as well as q distinct eigenfunctions $\psi_1, \ldots, \psi_q$ and q points $r_1, \ldots, r_q$. One can put the indices of ψ and r in two Young tableaux of shape λ (i.e., with the first row having the length q_1, the second row the length q_2, and so on). As an illustration, consider the following example for $\lambda = (3, 2, 1)$:

$$T_\psi = \begin{array}{|c|c|c|} \hline \psi_2 & \psi_4 & \psi_6 \\ \hline \psi_1 & \psi_5 \\ \cline{1-2} \psi_3 \\ \cline{1-1} \end{array} \qquad\qquad T_r = \begin{array}{|c|c|c|} \hline \mathbf{r}_6 & \mathbf{r}_2 & \mathbf{r}_3 \\ \hline \mathbf{r}_1 & \mathbf{r}_5 \\ \cline{1-2} \mathbf{r}_4 \\ \cline{1-1} \end{array}. \qquad (3.227)$$

One associates with the pair of these two tableaus the corresponding (unsymmetrized) product $\Psi_{(3,2,1)}(T_\psi, T_r)$ of wave function amplitudes:

$$\Psi_{(3,2,1)}(T_\psi, T_r) = \psi_1(\mathbf{r}_1)\psi_2(\mathbf{r}_6)\psi_3(\mathbf{r}_4)\psi_4(\mathbf{r}_2)\psi_5(\mathbf{r}_5)\psi_6(\mathbf{r}_3).$$

The next step is to introduce the operator a_λ of symmetrization within the rows of a Young tableau and the operator b_λ of antisymmetrization within the columns. The Young symmetrizers are defined as $c_\lambda = b_\lambda a_\lambda$ and $\tilde{c}_\lambda = a_\lambda b_\lambda$. The Young-symmetrized combinations are given by

$$\Psi_\lambda(c_\lambda T_\psi, T_r) = \Psi_\lambda(T_\psi, \tilde{c}_\lambda T_r) \qquad (3.228)$$

and

$$\Psi_\lambda(T_\psi, c_\lambda T_r) = \Psi_\lambda(\tilde{c}_\lambda T_\psi, T_r). \qquad (3.229)$$

As shown in Ref. [87], the squared absolute values of these Young-symmetrized products of eigenfunctions map, in the case of class A, to the pure-scaling sigma-model operator $\mathcal{P}_\lambda^A$.

Absolute values squared of Young-symmetrized eigenstate combinations (which are pure-scaling

observables for class A) are listed for the first few Young diagrams:

$$
|\Psi_{(2)}|^2 = \frac{1}{2} |\psi_a(r_1)\psi_b(r_2) + \psi_b(r_1)\psi_a(r_2)|^2 \,,
$$

$$
|\Psi_{(1,1)}|^2 = \frac{1}{2} |\psi_a(r_1)\psi_b(r_2) - \psi_b(r_1)\psi_a(r_2)|^2 \,,
$$

$$
|\Psi_{(3)}|^2 = \frac{1}{6} |\psi_a(r_1)\psi_b(r_2)\psi_c(r_3) + \psi_b(r_1)\psi_a(r_2)\psi_c(r_3) + \psi_c(r_1)\psi_b(r_2)\psi_a(r_3) \,,
$$

$$
+ \psi_b(r_1)\psi_c(r_2)\psi_a(r_3) + \psi_c(r_1)\psi_a(r_2)\psi_b(r_3) + \psi_a(r_1)\psi_c(r_2)\psi_b(r_3)|^2 \,,
$$

$$
|\Psi_{(2,1)}|^2 = \frac{1}{4} |\psi_a(r_1)\psi_b(r_2)\psi_c(r_3) - \psi_c(r_1)\psi_b(r_2)\psi_a(r_3) + \psi_b(r_1)\psi_a(r_2)\psi_c(r_3) - \psi_c(r_1)\psi_a(r_2)\psi_b(r_3)|^2 \,,
$$

$$
\vdots \tag{3.230}
$$

Since linear combinations of these expressions will be discussed, it is important to comment on their normalization. The symbol $Y(\lambda)$ denotes the number of terms in Ψ_λ produced by the Young symmetrization. Up to order $q = 4$, the values of $Y(\lambda)$ are given in the following table:

λ	$Y(\lambda)$	λ	$Y(\lambda)$
(1,1)	2	(1,1,1,1)	24
(2)	2	(2,1,1)	12
(1,1,1)	6	(2,2)	16
(2,1)	4	(3,1)	12
(3)	6	(4)	24

Writing down $|\Psi_\lambda|^2$ as a sum of monomials, one gets exactly $Y(\lambda)$ terms of modulus-squared type. The prefactor of $|\Psi_\lambda|^2$ in Eq. (3.230) is chosen to be equal to $Y(\lambda)^{-1}$, so that the total prefactor of these terms is unity. This has the consequence that $|\Psi_\lambda|^2$ maps precisely to $\mathcal{P}_\lambda^A$ given by Eq. (3.184). (Recall that all entries in the first column of matrices in Eq. (3.184) have been fixed to be equal to unity.)

The next step is to establish a connection between the class-A eigenoperators $\mathcal{P}_\lambda^A$ and class-C eigenoperators $\mathcal{P}_\lambda^C$. Using Eq. (3.184) for $\mathcal{P}_\lambda^A$ and Eq. (3.189) for $\mathcal{P}_\lambda^C$, one finds

$$
\begin{pmatrix} \mathcal{P}_{(1,1)}^C \\ \mathcal{P}_{(2)}^C \end{pmatrix} = \begin{pmatrix} 1 & -\frac{1}{3} \\ 0 & 1 \end{pmatrix} \begin{pmatrix} \mathcal{P}_{(1,1)}^A \\ \mathcal{P}_{(2)}^A \end{pmatrix} \,,
$$

$$
\begin{pmatrix} \mathcal{P}_{(1,1,1)}^C \\ \mathcal{P}_{(2,1)}^C \\ \mathcal{P}_{(3)}^C \end{pmatrix} = \begin{pmatrix} 1 & -\frac{4}{5} & \frac{1}{5} \\ 0 & 1 & -\frac{1}{4} \\ 0 & 0 & 1 \end{pmatrix} \begin{pmatrix} \mathcal{P}_{(1,1,1)}^A \\ \mathcal{P}_{(2,1)}^A \\ \mathcal{P}_{(3)}^A \end{pmatrix} \,,
$$

$$
\begin{pmatrix} \mathcal{P}_{(1,1,1,1)}^C \\ \mathcal{P}_{(2,1,1)}^C \\ \mathcal{P}_{(2,2)}^C \\ \mathcal{P}_{(3,1)}^C \\ \mathcal{P}_{(4)}^C \end{pmatrix} = \begin{pmatrix} 1 & -\frac{9}{7} & -\frac{4}{35} & \frac{27}{35} & -\frac{1}{7} \\ 0 & 1 & -\frac{2}{9} & -\frac{4}{9} & \frac{1}{9} \\ 0 & 0 & 1 & -\frac{1}{2} & 0 \\ 0 & 0 & 0 & 1 & -\frac{1}{5} \\ 0 & 0 & 0 & 0 & 1 \end{pmatrix} \begin{pmatrix} \mathcal{P}_{(1,1,1,1)}^A \\ \mathcal{P}_{(2,1,1)}^A \\ \mathcal{P}_{(2,2)}^A \\ \mathcal{P}_{(3,1)}^A \\ \mathcal{P}_{(4)}^A \end{pmatrix} \,. \tag{3.231}
$$

Replacing the sigma-model operators $\mathcal{P}_{\lambda'}^A$ on the right-hand side of these equations by $|\Psi_{\lambda'}|^2$, wavefunction combinations that scale like $\mathcal{P}_\lambda^C$ are obtained. For example, for $\lambda = (1,1)$, one gets $\mathcal{P}_{(1,1)}^C \longleftrightarrow$

$|\Psi_{(2)}|^2 - \frac{1}{3}|\Psi_{(1,1)}|^2$. This is, of course, exactly the $H - 2F$ expression from Eq. (3.226) (up to an overall factor). The corresponding numerical results for $\mathcal{P}^C_{(1,1)}$ are shown below in Sec. 3.6.3 (see Fig. 3.1). As has been already explained, this type of numerics suffers from very strong fluctuations, which become even stronger with increasing $|\lambda| \equiv q$. One therefore has to choose a different route for $q = 3, 4$. Inverting the matrices in Eq. (3.231), one finds

$$
\begin{pmatrix} \mathcal{P}^A_{(1,1,1)} \\ \mathcal{P}^A_{(2,1)} \\ \mathcal{P}^A_{(3)} \end{pmatrix} = \begin{pmatrix} \frac{1}{15} & -\frac{1}{10} & 0 \\ 0 & \frac{1}{8} & -\frac{1}{24} \\ 0 & 0 & \frac{1}{6} \end{pmatrix} \begin{pmatrix} \mathcal{P}^C_{(1,1,1)} \\ \mathcal{P}^C_{(2,1)} \\ \mathcal{P}^C_{(3)} \end{pmatrix},
$$
$$
\begin{pmatrix} \mathcal{P}^A_{(1,1,1,1)} \\ \mathcal{P}^A_{(2,1,1)} \\ \mathcal{P}^A_{(2,2)} \\ \mathcal{P}^A_{(3,1)} \\ \mathcal{P}^A_{(4)} \end{pmatrix} = \begin{pmatrix} \frac{1}{35} & -\frac{1}{14} & -\frac{1}{40} & 0 & 0 \\ 0 & \frac{1}{18} & \frac{1}{72} & -\frac{1}{18} & 0 \\ 0 & 0 & \frac{1}{16} & -\frac{1}{20} & \frac{1}{80} \\ 0 & 0 & 0 & \frac{1}{10} & -\frac{1}{40} \\ 0 & 0 & 0 & 0 & \frac{1}{8} \end{pmatrix} \begin{pmatrix} \mathcal{P}^C_{(1,1,1,1)} \\ \mathcal{P}^C_{(2,1,1)} \\ \mathcal{P}^C_{(2,2)} \\ \mathcal{P}^C_{(3,1)} \\ \mathcal{P}^C_{(4)} \end{pmatrix}. \tag{3.232}
$$

Naively, one could expect that, in class C, all $\mathcal{P}^A_\lambda$ will be dominated by the most relevant operator $\mathcal{P}^C_{(q)}$. This is not the case, however, due to zero entries at the upper right corner of the matrix. Equations (3.232) thus lead to non-trivial predictions amenable to numerical investigations. Specifically, when computing the $q = 3$ eigenstate combinations $|\Psi_\lambda|^2$ corresponding to $\mathcal{P}^A_\lambda$ in a system of class C, one should see that $\mathcal{P}^A_{(3)}$ and $\mathcal{P}^A_{(2,1)}$ exhibit both the leading (3) scaling (with the exponent x_λ equal to zero due to Weyl symmetry), while $\mathcal{P}^A_{(1,1,1)}$ has the leading contribution from the representation $(2,1)$. By Weyl symmetry, the scaling exponent x_λ of $(2,1)$ should be identical to the exponent of $(1,1)$ obtained for $q = 2$. For $q = 4$, there should be three operators—$\mathcal{P}^A_{(4)}$, $\mathcal{P}^A_{(3,1)}$, and $\mathcal{P}^A_{(2,2)}$—showing the leading (4) scaling, the operator $\mathcal{P}^A_{(2,1,1)}$ should be dominated by representation $(3,1)$, and the operator $\mathcal{P}^A_{(1,1,1,1)}$ by the representation $(2,2)$.

In Sec. 3.6.3, these predictions are verified and used for determining the scaling exponents by numerical simulations on the network model.

3.6.3 Numerical computations

In this subsection, I present results of numerical evaluation of generalized multifractal exponents by using the Chalker-Coddington network models [U(1) model for class A and its SU(2) generalization for class C]. For class C, two approaches outlined in Sec. 3.6.2 are used: the direct evaluation of a class-C pure scaling operator and the path going through strictly positive Young-symmetrized wave-function combinations $|\Psi_\lambda|^2$. These numerics fully confirms all existing analytical predictions, including those based on Weyl symmetry as well as those resulting from relations between class-A and class-C scaling observables derived in Sec. 3.6.2. Obtained numerical results for the exponents at the SQH transition are summarized in Table 3.2. Remarkably, one finds strong deviations from generalized parabolicity for the subleading exponents [(1,1), (2,1), (3,1), (2,2)]. In Sec. 3.7 these results will be corroborated by an alternative approach (based on obervables involving both spin projections), where also further subleading exponents will be determined numerically.

While the main focus in this work is on class C, all exponents for Young diagrams with $q \leq 4$ for the conventional (class-A) IQH transition are also determined numerically, see Table 3.1 below. At variance with the SQH transition, one finds here only weak deviations from the generalized parabolicity.

3.6.3.1 The Chalker-Coddington network models

An intuitive picture of quantum Hall criticality is imagining the electrons to drift along equipotential lines of the disorder potential. Near saddle points of the potential, tunneling between distinct lines is allowed. The Chalker-Coddington network model [121] adds further simplification to this picture: the random geometry derived from extremal points of the potential landscape is replaced by a square network, with electrons acquiring a random U(1) phase when traveling along a link. The SU(2) version of the Chalker-Coddington network model describes spin quantum hall criticality [54, 56]. The network models have been to be very useful for numerical investigation of localization transitions in 2D systems of various symmetry classes, see the reviews [9, 212] and Sec. 1.5.3.1.

Multifractality of eigenstates of the network scattering matrix $\mathcal{U}$ is analyzed numerically using the conventional sparse-matrix techniques [58, 77, 213]. For each realization of disorder, four eigenstates with lowest positive energies are determined. (When speaking about the energy in the context of the network model, one actually means the quasienergy ϵ corresponding to the eigenvalue $e^{i\epsilon}$ of the network evolution operator $\mathcal{U}$.) The systems studied are of linear size $L = 128\ldots1024$, and the ensemble averaging is performed over at least 10^5 configurations. For each realization of disorder, there also is an average over L^2 positions of the "center of mass" of the set of involved spatial points r_i.

3.6.3.2 Scaling considerations

To investigate the scaling of an operator with $q \leq 4$, I consider eigenstate combinations defined on q lowest-energy eigenstates and at q distinct points $r_1, \ldots, r_q$, see Sec. 3.6.2. The exponents of interest control the power-law scaling of the corresponding observables with L, see general discussion of scaling in Sec. 1.2.2. To improve the statistics, the scaling with the distance r is also considered. All the distances $|r_i - r_j|$ between the involved q points are kept to be of the same order: for $q = 4$ the points form a square, and for $q = 3$ a triangle with approximately equal side lengths. When investigating a combination $\mathcal{O}[\psi]$ of order q that is dominated by a pure-scaling operator $\mathcal{P}_{(q_1, q_2, \ldots)}$, one has (see Sec. 1.2.2)

$$L^{2q}\mathcal{O}[\psi](r_1, r_2, \ldots) \sim \left(\frac{|r_i - r_j|}{L}\right)^{\Delta_{(q_1, q_2, \ldots)}}, \qquad \Delta_{(q_1, q_2, \ldots)} \equiv x_{(q_1, q_2, \ldots)} - q x_\nu, \qquad (3.233)$$

where $x_\nu \equiv x_{(1)}$ is the scaling dimension of the operator Q that controls the scaling of the density of states. In class A (and all other Wigner-Dyson classes) the density of states is not critical, i.e., $x_{(1)} = 0$. For the SQH transition, $x_{(1)}^C = \frac{1}{4}$ is known exactly from mapping to percolation. The slope of the log-log plot of $L^{2q}\mathcal{O}[\psi]$ versus r/L thus yields the exponent $\Delta_{(q_1, q_2, \ldots)}$.

As discussed in Sec. 3.2, if the theory satisfies local conformal invariance, the generalized MF spectrum would obey generalized parabolicity. (The second assumption is the abelian fusion that has been shown explicitly.) For the IQH and SQH transitions, the generalized parabolicity would imply the following form of the dimensions $x_{(q_1, q_2, \ldots)}$ of scaling operators:

$$\text{IQH:} \qquad x_{(q_1, q_2, \ldots)}^{A, \text{para}} = b\left[q_1(1 - q_1) + q_2(3 - q_2) + q_3(5 - q_3) + \ldots\right], \qquad (3.234)$$

$$\text{SQH:} \qquad x_{(q_1, q_2, \ldots)}^{C, \text{para}} = \frac{1}{8}\left[q_1(3 - q_1) + q_2(7 - q_2) + q_3(11 - q_3) + \ldots\right]. \qquad (3.235)$$

For the SQH transition, the exact values of the exponents $x_{(1)}^C = x_{(2)}^C = \frac{1}{4}$ imply that, if the generalized parabolicity (3.235) holds, the prefactor should be exactly 1/8. For the IQH transition, none of the

exponents is rigorously known analytically, which leaves a freedom in the prefactor b. It was conjectured in a recent paper [50] that the IQH critical point is described by a certain model of WZNW type, which would give strict generalized parabolicity with $b = \frac{1}{4}$. As already pointed out in Sec. 1.5.3, high-precision numerical studies reveal small but clear deviations from parabolicity of the standard MF spectrum $x_{(q)}$, both for the IQH [52, 53] and the SQH [58, 59] transitions. For the IQH transition, if one looks for the best parabolic approximation to the spectrum $x_{(q)}$, one finds b in the range $0.26 - 0.27$, depending on the range of q where the fit is performed.

3.6.3.3 Numerical results

In Fig. 3.1numerical results for the scaling of $L^{2q}|\Psi_\lambda|^2$ with r/L are shown, where Ψ_λ are Young-symmetrized eigenstate combinations as defined in Sec. 3.6.2. For class C, the spin projection is fixed, $\psi \equiv \psi_\uparrow$, for all combinations considered here. In both the class A and the class C, these combinations map to the operators $\mathcal{P}_\lambda^A[Q]$ of the sigma-model.

In the case of IQH transition (class A), $\mathcal{P}_\lambda^A[Q]$ are pure-scaling operators. The corresponding results for $L^{2q}|\Psi_\lambda|^2$ are shown in the left panels of Fig. 3.1 for the operators with $q = 2$ (top), $q = 3$ (middle), and $q = 4$ (bottom). The numerical results provide an excellent confirmation of the prediction that $L^{2q}|\Psi_\lambda|^2$ exhibit scaling corresponding to the representation λ: one can observe nice fans representing distinct scaling exponents. The fitted slopes are shown by full lines; the corresponding values of numerically determined exponents $\Delta_\lambda^{A,\mathrm{num}}$ are collected in Table 3.1. For those IQH exponents that have been found numerically previously, the results are in full agreement with previous data. In particular, the value $\Delta_{(2)}^{A,\mathrm{num}} \approx -0.54$ is in excellent agreement with previous values [51–53], which are in the range between -0.54 and -0.55 with error bars within ± 0.01. (In Refs. [52] and [53], the values of $\Delta_{(q)}^{A,\mathrm{num}}/q(1-q)$ were shown only up to $q = 1.5$ and $q = 1.75$, respectively, so that a small extrapolation to $q = 2$ is needed.) For $\lambda = (1, 1)$ one finds $\Delta_{(1,1)}^{A,\mathrm{num}} \approx 0.57$, which is slightly below the value $\Delta_{(1,1)}^{A,\mathrm{num}} \approx 0.62 \pm 0.05$ of Ref. [158] but agrees within the error bars given there. The exponents corresponding to $\lambda = (2, 1)$ and $(2,2)$ represent a very useful test for the numerics, since they are exactly zero by virtue of the Weyl symmetry. Thus, their obtained numerical values provide an estimate for numerical errors associated with finite-size effects and finite statistics. For $\lambda = (2, 1)$ one gets $\Delta_{(2,1)}^{A,\mathrm{num}} \approx 0.01$, indicating an excellent accuracy of the numerics, ± 0.01, for $q \leq 3$. For $\lambda = (2, 2)$ one gets a somewhat larger deviation from the exact value, $\Delta_{(2,2)}^{A,\mathrm{num}} \approx 0.04$, which is not surprising, since errors increase with increasing q. One can see, however, that the numerics remains very good also for $q = 4$.

When compared to the conjecture of Ref. [50] (exact generalized parabolicity with $b = 1/4$), the results for the IQH transition are fully consistent with those of Refs. [52, 53]: the exponents deviate from the spectrum proposed in Ref. [50] by $\sim 10\%$. At the same time, the numerical values of the exponents are rather close to those that would follow from generalized parabolicity with $b \approx 0.27$. Deviations from parabolicity were observed in Refs. [52, 53] where the MF spectrum $\Delta_{(q)}$ was studied with a high accuracy for fractional q in the range from $q = -0.5$ to $q = 1.75$. This is favorable for detecting relatively small deviations, since the numerical accuracy is especially high in this range of q. In principle, this analysis can be extended also to generalized MF exponents with continuously changing q. Since the main focus in this paper is on generalized multifractality at SQH transition, further studies of the IQH transition are left to later work.

In the right panels of Fig. 3.1 the results of numerical simulations for a network model of class C are shown. In the top panel, the scaling of eigenfunction combinations corresponding to class-C
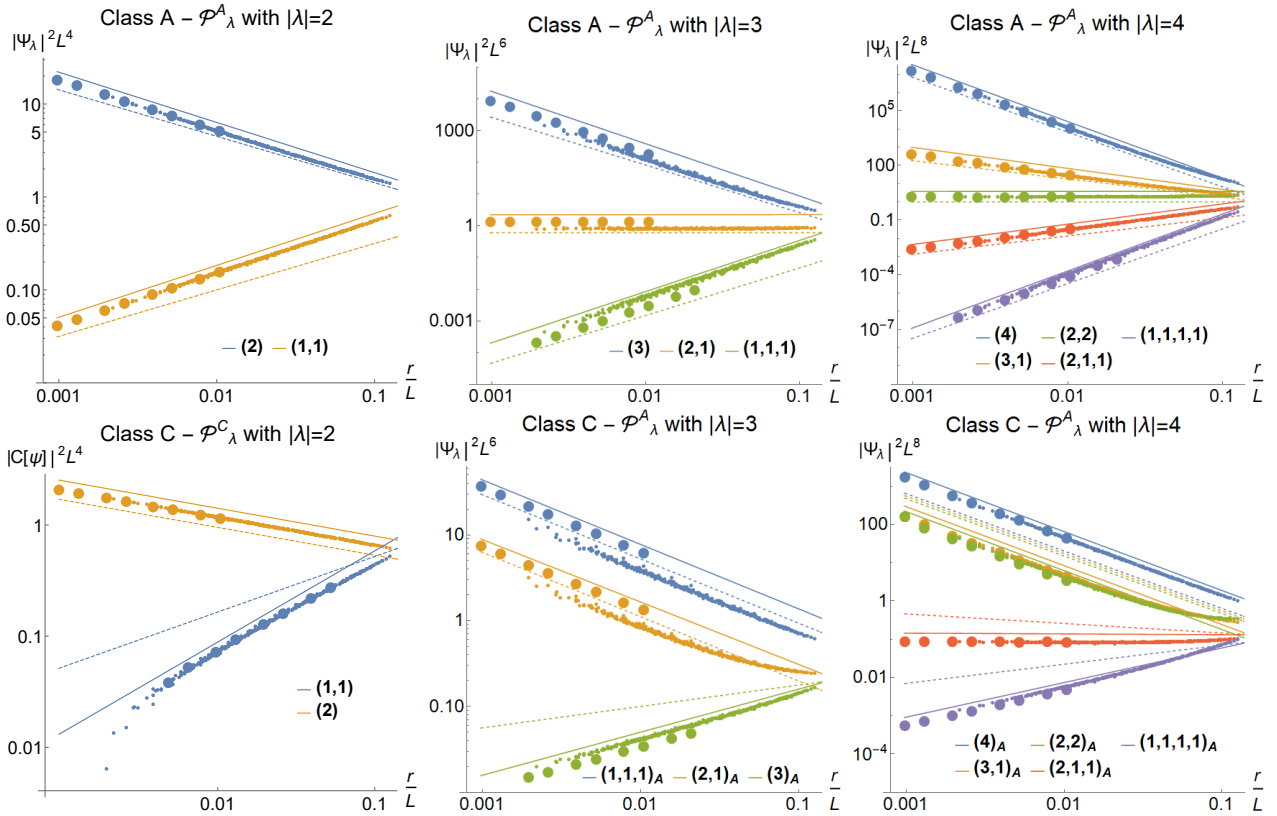
Figure 3.1: Figure taken from Ref. [105]. Numerical determination of generalized parabolicity at IQH (top) and SQH (bottom) transitions, for $q = 2$ (left), $q = 3$ (middle), and $q = 4$ (right) eigenstate observables. Data result from simulations on class-A (top) and class-C (bottom) network models, with averaging over 10^5 realizations of disorder. Top panels show Young-symmetrized eigenstate combinations $L^{2q}|\Psi_\lambda|^2$, which correspond to pure-scaling operators $\mathcal{P}_\lambda^A[Q]$ of class A, collapsed as functions of r/L. Full lines are fits to the data; the corresponding exponents $\Delta_\lambda^{\mathrm{num}}$ are given in Table 3.1. Dashed lines correspond to the generalized parabolic spectrum (3.234) with $b = 1/4$, as would follow from the WZNW model proposed in Ref. [50]; the corresponding values are given in Table 3.1 as $\Delta_\lambda^{\mathrm{para},\,b=1/4}$. For each λ, data points for one fixed value of r of order unity are highlighted as bold dots, in order to visualize the L-dependence at a fixed r. Bottom left panel shows the class-C pure-scaling observables (3.226) with $q = 2$. The bottom middle and right panels display the scaling of Young-symmetrized combinations $L^{2q}|\Psi_\lambda|^2$ (which correspond to $\mathcal{P}_\lambda^A[Q]$) with $q = 3$ and 4 in a class-C network model. They allow to access the class-C exponents for the representations (3), (2,1), (4), (3,1), and (2,2). The extracted exponents $\Delta_\lambda^{\mathrm{num}}$ (full lines) are collected in Table 3.2. The dashed lines in the bottom panels correspond to generalized parabolicity (3.235); the corresponding exponents $\Delta_\lambda^{\mathrm{para}}$ are also listed in Table 3.2. A strong violation of the generalized parabolicity at the SQH transition is evident.

eigenoperators, $H + F \sim \mathcal{P}^C_{(2)}$ and $H - 2F \sim \mathcal{P}^C_{(1,1)}$, is shown, see Eq. (3.226) and the first line of Eq. (3.231). For the subleading operator $\mathcal{P}^C_{(1,1)}$, one can observe stronger fluctuations and deviations from scaling at large L. As explained above, they are related to the fact that the corresponding eigenstate combination $H - 2F$ is sign-indefinite, and, as a result, the averaging becomes insufficient for large L. Since these difficulties become more severe with increasing q, for $q = 3$ (middle panel) and $q = 4$ (bottom panel) the alternative approach outlined in Sec. 3.6.2 is used. Specifically, the r/L dependence of strictly positive Young-symmetrized combinations $L^{2q}|\Psi_\lambda|^2$ are plotted. According to Eq. (3.232), this allows one to access the exponents corresponding to representations (3) and (2,1) for $q = 3$ as well (4), (3,1), and (2,2) for $q = 4$, see the discussion below Eq. (3.232).

The data shown in Fig. 3.1 fully confirm the analytical predictions. The combinations $|\Psi_{(3)}|^2$ and $|\Psi_{(2,1)}|^2$ for $q = 3$, as well as $|\Psi_{(4)}|^2$, $|\Psi_{(3,1)}|^2$, and $|\Psi_{(2,2)}|^2$ for $q = 4$ indeed show the leading scaling. At the same time, the combinations $|\Psi_{(1,1,1)}|^2$, $|\Psi_{(2,1,1)}|^2$ and $|\Psi_{(1,1,1,1)}|^2$ exhibit the subleading scaling, yielding the exponents $\Delta^C_{(2,1)}$, $\Delta^C_{(3,1)}$, and $\Delta^C_{(2,2)}$, respectively.

The values of the class-C exponents are shown in Table 3.2. Recall that the eigenfunction exponents Δ^C_λ are related to the field-theory exponents x^C_λ via $\Delta^C_\lambda = x^C_\lambda - q x^C_{(1)}$, with $x^C_{(1)} = 1/4$ for the SQH transition. One can see that the numerical data very well respect all analytically known exact values and relations (from the mapping to percolation and from Weyl symmetry). These include $x^C_{(2)} = 1/4$, $x^C_{(3)} = 0$, and $x^C_{(1,1)} = x^C_{(2,1)}$. Some deviation between the numerically found $x^C_{(1,1)}$ and $x^C_{(2,1)}$ is due to a somewhat larger error in $x^C_{(1,1)}$ related to strong fluctuations of the $H - 2F$ combination, as explained above. In Sec. 3.7 an alternative (and more accurate) numerical calculation of $x^C_{(1,1)}$ will be presented, which perfectly fulfils the identity $x^C_{(1,1)} = x^C_{(2,1)}$.

The central observation from the obtained values of the exponents is a very strong violation of generalized parabolicity by the subleading exponents [representations (1,1), (2,1), (3,1), and (2,2)]. This will be fully confirmed and reinforced in Sec. 3.7 where these and further exponents will be obtained by a complementary approach. The deviations of numerical values $\Delta^{\mathrm{num}}_\lambda$ from the values $\Delta^{\mathrm{para}}_\lambda$ that would follow from generalized parabolicity (also shown in the table) are very big—of the order of $\Delta^{\mathrm{para}}_\lambda$. These deviations are more than an order of magnitude larger than numerical uncertainties (that can be estimated from the accuracy with which analytically known exponents and Weyl-symmetry relations are reproduced). This strong violation of generalized parabolicity in class C represents one of central results of this paper. As was explained in Sec. 3.2.2.3, it has a very fundamental implication: a violation of local conformal invariance at the SQH transition.

3.7 Modulus square wavefunction combinations

In Sec. 3.6, two approaches to the numerical determination of the exponents characterizing the generalized multifractality in class C were developed. First, exact pure-scaling operators (obtained earlier by RG) were translated to eigenstate expressions. The difficulty with direct application of this approach is that the corresponding subleading eigenstate combinations are sign-indefinite and fluctuate very strongly. It thus used it directly only for the (1,1) operator that has the form $H - 2F$ directly, see upper right panel of Fig. 3.1. Even in this case of the simplest subleading observable, fluctuations are very strong and require very extensive numerical efforts (in Sec. 3.8 L_P $30L_{CC}$ are accessible and the $H - 2F$ cancellation works out beautifully). In view of this, it is intuitive to use a complementary approach for determining other exponents based on studying strictly-positive Young-symmetrized combinations corresponding to pure-scaling operators of class A. However, this way does not allow

	rep. λ	$\Delta_\lambda^{\mathrm{num}}$	$\Delta_\lambda^{\mathrm{para},\,b=1/4}$
$q = 2$	(2)	-0.54	$-\frac{1}{2}$
	(1,1)	0.57	$\frac{1}{2}$
$q = 3$	(3)	-1.66	$-\frac{3}{2}$
	(2,1)	0.01	**0**
	(1,1,1)	1.61	$\frac{3}{2}$
$q = 4$	(4)	-3.12	-3
	(3,1)	-1.10	-1
	(2,2)	0.04	**0**
	(2,1,1)	1.10	1
	(1,1,1,1)	3.12	3

Table 3.1: Table taken from Ref. [105]. Scaling exponents of generalized multifractality at the IQH transition (class A) for eigenstate observables from representations $\lambda = (q_1, q_2, \ldots)$ with $q \equiv q_1 + q_2 + \ldots = 2$, 3, and 4. The exponents $\Delta_\lambda^{\mathrm{num}}$ are determined numerically as shown in the left column of Fig. 3.1. For comparison, the exponents $\Delta_\lambda^{\mathrm{para},\,b=1/4}$ are presented, corresponding to the generalized parabolicity (3.234) with $b = 1/4$, as would result from the WZNW theory conjectured in Ref. [50]. The values $\Delta_{(2,1)} = \Delta_{(2,2)} = 0$ highlighted by boldface are exact (enforced by Weyl symmetry; independent of presence or absence of generalized parabolicity).

	rep. λ	$\Delta_\lambda^{\text{num}}$	$\Delta_\lambda^{\text{num},|\psi|}$	$\Delta_\lambda^{\text{para}}$
$q = 2$	(2)	-0.25	-0.25	$-\mathbf{\frac{1}{4}}$
	(1,1)	0.79	0.74	$\frac{1}{2}$
$q = 3$	(3)	-0.75	-0.75	$-\mathbf{\frac{3}{4}}$
	(2,1)	0.50	0.49	$\frac{1}{4}$
	(1,1,1)	—	1.17	$\frac{3}{2}$
$q = 4$	(4)	-1.5	-1.5	$-\frac{3}{2}$
	(3,1)	-0.01	-0.02	$-\frac{1}{4}$
	(2,2)	0.91	0.86	$\frac{1}{2}$
	(2,1,1)	—	—	$\frac{5}{4}$
	(1,1,1,1)	—	—	3

Table 3.2: Table taken from Ref. [105]. Scaling exponents of generalized multifractality at the SQH transition (class C) for eigenstate observables with $q \equiv |\lambda| \leq 4$. The exponents Δ_λ shown in the table are related to the field-theoretical exponents x_λ via $\Delta_\lambda = x_\lambda - qx_{(1)}$ with $x_{(1)} = 1/4$. The exponents $\Delta_\lambda^{\text{num}}$ are determined numerically by using eigenstate combinations with a single spin projection, see right panels of Fig. 3.1. The exponents $\Delta_\lambda^{\text{num},|\psi|}$ are obtained by a complementary numerical approach using observables involving the total density $|\psi|$ (spin up and spin down), Fig. 3.4. The symbol "—" means that the exponent was not determined by the corresponding approach. The agreement between both sets of numerical exponents is very good. Some deviation between two numerical values of the (1,1) exponent is attributed mainly to the error in the value $\Delta_{(1,1)}^{\text{num}}$ because of strong fluctuations of the corresponding sign-indefinite combination $H - 2F$. The Weyl symmetry implies exact relations $\Delta_{(2,1)} = \Delta_{(1,1)} - 1/4$ and $\Delta_{(2,1,1)} = \Delta_{(1,1,1)} - 1/4$; the first of them is nicely fulfilled by the numerically found exponents. The last column displays the exponents $\Delta_\lambda^{\text{para}}$ corresponding to the generalized parabolic spectrum, Eq. (3.235). The values $\Delta_{(2)} = -1/4$ and $\Delta_{(3)} = -3/4$ shown in boldface are exact and thus independent of the status of generalized parabolicity. Strong deviations from the generalized parabolicity are clearly seen in all subleading exponents that have been determined numerically.

one to access exponents that are on the more RG-irrelevant side of the spectrum, including $(1,1)$. In this section, a third approach is developed that, on one hand, deals with strictly positive observables and, on the other hand, allows one to determine numerically the $(1,1)$ exponent and various other subleading exponents not accessible by the class-A-to-class-C approach of Sec. 3.6. The central idea of the approach developed in this section is to exploit observables built out of $|\psi| = \sqrt{|\psi_\uparrow|^2 + |\psi_\downarrow|^2}$ and thus involving both spin projections at each of the relevant spatial points r_i. Below a physical motivation of this approach is given and justified by establishing a connection with sigma-model pure-scaling operators obtained by the Iwasawa decomposition, and demonstrate numerically its efficiency. For those exponents that are determined numerically by two approaches (i.e., both here and in Sec. 3.6), one finds a very good agreement.

3.7.1 Physical motivation

In class C, the wave function $\psi = (\psi_\uparrow, \psi_\downarrow)$ is an intrinsically two-component object: there is the combined spin and particle-hole space. In Sec. 3.6, only one spin component (say, $\psi_\uparrow$) was used to construct pure-scaling observables. Here I will use the total density

$$|\psi| \equiv \sqrt{|\psi_\uparrow|^2 + |\psi_\downarrow|^2}, \qquad (3.236)$$

where both components at the same spatial point enter simultaneously. [Everywhere below in Sec. 3.7 the notation $|\psi|$ has the meaning defined by Eq. (3.236).] To demonstrate why this is useful, first consider in detail observables that are of fourth order with respect to wave functions (which corresponds to $q = 2$ in this classification). There are two distinct representations (2) and $(1,1)$, and one can construct operators in each of them as linear combinations of Hartree (H) and Fock (F) terms (3.225). In class A the pure-scaling observables are (here ψ abbreviates the two wave functions involved)

$$C_{(2)}^A[\psi] = H[\psi] + F[\psi], \qquad C_{(1,2)}^A[\psi] = H[\psi] - F[\psi], \qquad (3.237)$$

whereas in class C the pure-scaling combinations involving only $\psi_\uparrow$ are

$$C_{(2)}^C[\psi_\uparrow] = H[\psi_\uparrow] + F[\psi_\uparrow], \qquad C_{(1,1)}^C[\psi_\uparrow] = H[\psi_\uparrow] - 2F[\psi_\uparrow]. \qquad (3.238)$$

The only difference here is in the coefficient 2 in the subleading operator: $H - 2F$ in class C instead of $H - F$ in class A. This seemingly small difference, is, however, connected in a profound way with properties of critical eigenstates.

Introduce the ratio R characterizing the local similarity of the two eigenstates involved:

$$R = \frac{\psi_1(r_2)\psi_2(r_1)}{\psi_1(r_1)\psi_2(r_2)}. \qquad (3.239)$$

Note that the U(1) freedom in the definition of the eigenfunctions does not affect R. It is easy to see that the ratio of the Fock and Hartree terms is expressed through R as follows:

$$\frac{F[\psi]}{H[\psi]} = \frac{R + R^*}{1 + RR^*}. \qquad (3.240)$$

Clearly, the ratio F/H satisfies $-1 \leq F/H \leq 1$ and reaches its maximum value unity only for $R = 1$. Thus, the class-A subleading observable $H - F$ satisfies $H - F \geq 0$ and is equal zero only for $R = 1$.

Further, the average value $\langle H - F \rangle$ is suppressed by a power of L in comparison with $\langle H + F \rangle$. It follows that the ratio F/H should be nearly unity, and thus R should be parametrically close to unity, in any disorder realization in class A. This is very well seen in Fig. 3.2, which shows how the distribution of R at the IQH transition point evolves with increasing L. The distribution tends, in the limit $L \to \infty$, to a delta-function at $R = 1$.

The situation in class C is very different. Here $\langle H[\psi_\uparrow] \rangle_V = 2 \langle F[\psi_\uparrow] \rangle_V$ in the limit $L \to \infty$. Since the value $1/2$ is located in the middle of allowed values of F/H, the ratio $\langle F \rangle / \langle H \rangle = 1/2$ does not by itself tell anything about the values of F/H in individual realizations of disorder. As shown in Fig. 3.3, the distribution of the ratio R built out of $\psi_\uparrow$ remains broad (with width of order unity) in the large-L limit. Consequently, the distribution of F/H is broad as well. This is exactly the property that was already emphasized several times: while $H[\psi_\uparrow] - 2F[\psi_\uparrow]$ is parametrically small after disorder averaging, it is of the same order as $H[\psi_\uparrow] + F[\psi_\uparrow]$ in a typical disorder realization.

One thus faces the following observation: while two adjacent-in-energy critical eigenstates are nearly identical locally in class A ($R \approx 1$), this does not hold for class C. At the same time, it is natural to expect that some form of a strong local similarity of eigenstates is a general property of Anderson transitions. A qualitative difference between classes A and C is the existence of the spin degree of freedom in class C. These considerations suggest to look at local correlations between total densities (3.236) of two eigenstates. The corresponding ratio S (which is real and positive) is defined as:

$$S = \frac{|\psi_1(r_2)|\,|\psi_2(r_1)|}{|\psi_1(r_1)|\,|\psi_2(r_2)|}\,, \tag{3.241}$$

with $|\psi|$ being defined by Eq. (3.236). The distribution of S at the SQH critical point is shown in the bottom panel of Fig. 3.3. Remarkably, one can see the same behavior as for the distribution of R in class A: evolution, in the large-L limit, towards the delta-distribution at $S = 1$. Thus, total densities $|\psi_1|$ and $|\psi_2|$ are indeed strongly correlated locally. Broad fluctuations of the ratio R (characterizing one spin component) are therefore related to relative rotations in the spin space between two eigenfunctions.

Since S in class C behaves in the same way as R in class A, it is natural to build Hartree and Fock combinations from total densities. In full analogy with Eq. (3.240),

$$\frac{F[|\psi|]}{H[|\psi|]} = \frac{2S}{1 + S^2}\,. \tag{3.242}$$

In the large-L limit, one has $S \to 1$, and the difference $H[|\psi|] - F[|\psi|]$ yields the subleading combination $(1,1)$. This was exactly the goal: to determine the combination that is expected to scale as $(1,1)$ and is strictly positive in any realization of disorder.

Below it is demonstrated numerically that this approach indeed works very well, can be extended to other subleading combinations, and is supported by an analytical derivation connecting $|\psi|$ observables with the sigma-model operators.

3.7.2 Young-symmetrized combinations of $|\psi|$: Relation to the sigma model

As motivated above, the squared Young-symmetrized combinations are considered. They read $\left| \Psi_\lambda \left[|\psi| \right] \right|^2$ analogous to (3.230) but constructed on absolute values $|\psi|$ of eigenstates that involve both spin projections, Eq. (3.236). For the lowest subleading operator $(1,1)$, this combination is

$$\left| \Psi_{(1,1)} \left[|\psi| \right] \right|^2 = \left(|\psi_a(r_1)|\,|\psi_b(r_2)| - |\psi_b(r_1)|\,|\psi_a(r_2)| \right)^2 \,. \tag{3.243}$$
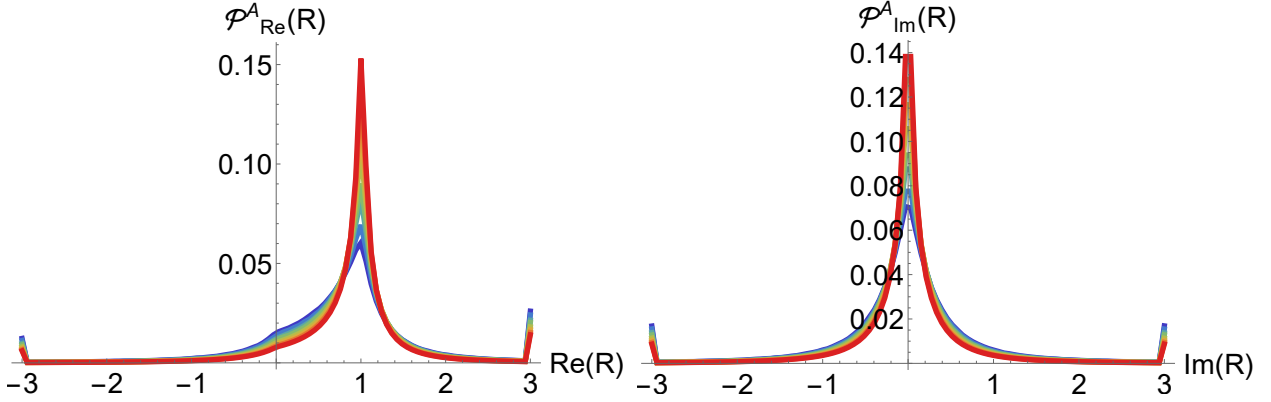
Figure 3.2: Figure taken from Ref. [105]. Distributions of the real part $\mathrm{Re}\,R$ (left) and the imaginary part $\mathrm{Im}\,R$ (right) of the ratio R, Eq. (3.239), characterizing the "local similarity" of two eigenstates at the IQH transition (class A). Different colors correspond to different system sizes, varying from from $L = 96$ (blue) to $L = 1024$ (red). The peak at $R = 1$ becomes sharper with increasing L, implying that $R \to 1$ at $L \to \infty$ with probability unity. This visualizes the suppression of the pure-scaling subleading combination $H - F$ with respect to $H + F$ for any realization of disorder.

In order to rigorously prove analytically that this combination yields the (1,1) scaling, one should map it onto a sigma-model composite operator. While this is in principle possible, the mapping is technically cumbersome in view of the square involved in the definition of $|\psi|$. One can thus restrict to showing how this derivation works in a closely related but technically simpler case.

Consider the Young-symmetrized expression built on $|\psi|$ and corresponding to the Young diagram (3,1):

$$
\begin{aligned}
\left| \Psi_{(3,1)} \left[|\psi| \right] \right|^2 &= \left(|\psi_a(r_1)|^2 |\psi_b(r_2)|^2 - |\psi_b(r_1)|^2 |\psi_a(r_2)|^2 \right)^2 \\
&= \left(|\psi_a(r_1)|^2 \right)^2 \left(|\psi_b(r_2)|^2 \right)^2 + \left(|\psi_b(r_1)|^2 \right)^2 \left(|\psi_a(r_2)|^2 \right)^2 \\
&\quad - 2 |\psi_a(r_1)|^2 |\psi_b(r_1)|^2 |\psi_a(r_2)|^2 |\psi_b(r_2)|^2.
\end{aligned}
\tag{3.244}
$$

Note that it can be written as

$$
\begin{aligned}
\left| \Psi_{(3,1)} \left[|\psi| \right] \right|^2 &= \left| \Psi_{(1,1)} \left[|\psi| \right] \right|^2 \left| \Psi_{(2)} \left[|\psi| \right] \right|^2 \\
&= \left(|\psi_a(r_1)| \, |\psi_b(r_2)| - |\psi_b(r_1)| \, |\psi_a(r_2)| \right)^2 \left(|\psi_a(r_1)| \, |\psi_b(r_2)| + |\psi_b(r_1)| \, |\psi_a(r_2)| \right)^2,
\end{aligned}
\tag{3.245}
$$

i.e., it can be intuitively viewed as a result of fusion of (3.243) with $\left| \Psi_{(2)} \left[|\psi| \right] \right|^2$ that has the leading scaling corresponding to representation (2). By construction, the combination (3.244) is manifestly positive and free of square roots. One can thus translate it to the sigma-model language by using the rules derived above.
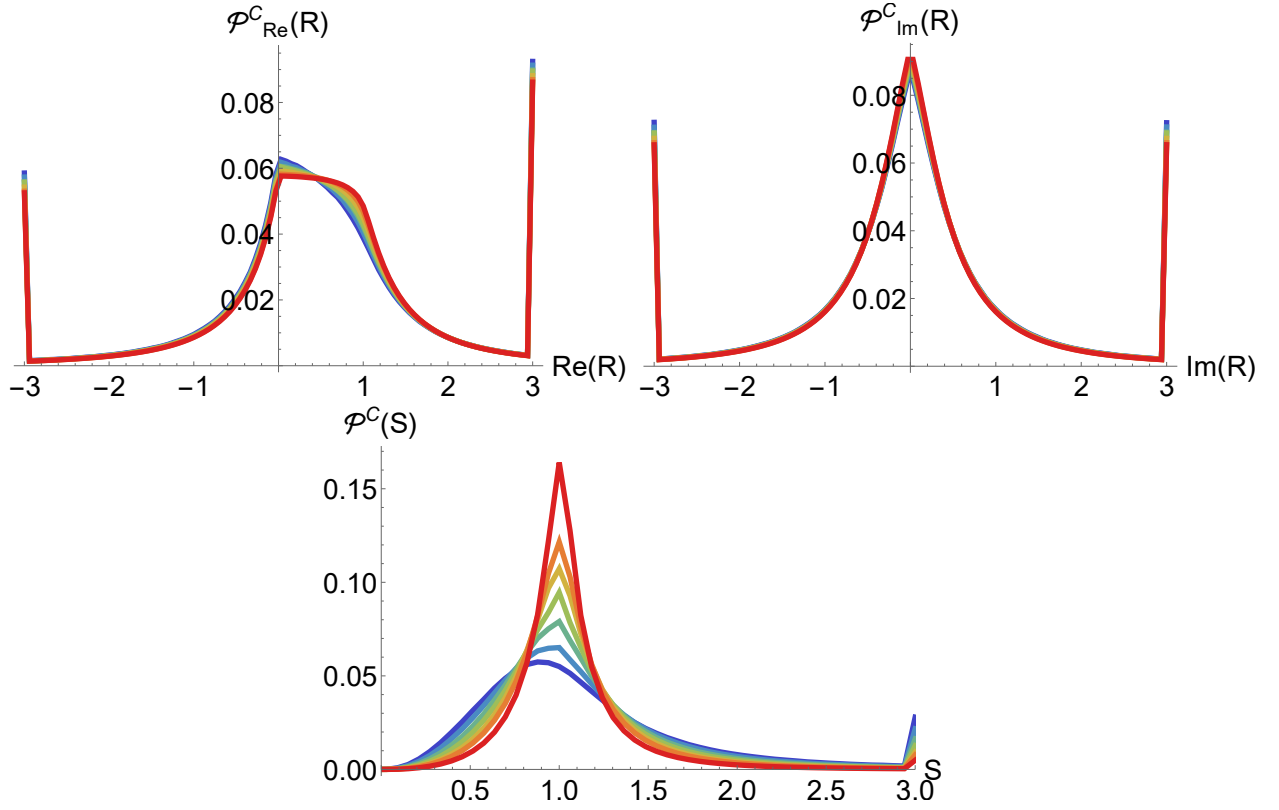
Figure 3.3: Figure taken from Ref. [105]. *Top:* Distributions of the real part Re R (left) and the imaginary part Im R (right) of the ratio R, Eq. (3.239), at the SQH transition (class C). The ratio R is built in this case out of eigenfunctions components with fixed spin projection (all spins up). Different colors correspond to different system sizes, varying from from $L = 96$ (blue) to $L = 1024$ (red). It is seen that the distribution remains broad (with width of order unity) at $L \to \infty$. This illustrates that, while $H - 2F$ is a subleading combination in average, it is typically of the same order as the leading combination $H + F$. *Bottom:* Distribution of the ratio S, Eq. (3.241), characterizing local similarity of total densities (spin up and down) of two eigenstates. The peak at $S = 1$ becomes sharper with increasing L, in close similarity to the behavior of the distribution of R in class A, Fig. 3.2. This implies that the combination $H[|\psi|] - F[|\psi|]$ does not contain the leading operator [Young diagram (2)] and scales according to the subleading one [Young diagram (1,1)], see top left panel of Fig. 3.4.

First, the translation to vector field variables S is performed by using Eq. (3.210):

$$\left\langle \left| \Psi_{(3,1)} \left[|\psi| \right] \right|^2 \right\rangle_V \sim \left\langle \left\langle C_{(3,1)}[S] \right\rangle_{S_0} \right\rangle_V , \text{ where}$$

$$C_{(3,1)}[S] = \left(|S_a|^2(r_1) \right)^2 \left(|S_b|^2(r_2) \right)^2 + \left(|S_b|^2(r_1) \right)^2 \left(|S_a|^2(r_2) \right)^2 - 2|S_a|^2(r_1)|S_b|^2(r_1)|S_b|^2(r_2)|S_a|^2(r_2).$$

$$(3.246)$$

Here $|S|^2 \equiv |S_\uparrow|^2 + |S_\downarrow|^2$. One can further translate this to the sigma-model language as outlined in Sec. 3.6.1.3. Discarding contractions of S variables at different points, one finds:

$$\langle C_{(3,1)}[S] \rangle_{S[\phi,\phi^*,Q]} = 2 \langle \left(|S_a|^2 \right)^2 \rangle_{S[\phi,\phi^*,Q]} \langle \left(|S_b|^2 \right)^2 \rangle_{S[\phi,\phi^*,Q]} - 2 \langle |S_a|^2 |S_b|^2 \rangle_{S[\phi,\phi^*,Q]} \langle |S_a|^2 |S_b|^2 \rangle_{S[\phi,\phi^*,Q]}.$$

$$(3.247)$$

Using Eqs. (3.213)–(3.219), one can translate the building block for generic combinations containing $|\psi|_i^2$ at distinct sites r_i:

$$\langle |S_a|^2 |S_b|^2 \rangle_{S[\phi,\phi^*,Q]} = \sum_{\sigma\sigma'} \left(\langle |S_{a\sigma}|^2 \rangle \langle |S_{b\sigma'}|^2 \rangle + \langle S_{a\sigma}^* S_{b\sigma'} \rangle \langle S_{b\sigma'}^* S_{a\sigma} \rangle + \langle S_{a\sigma}^* S_{b\sigma'}^* \rangle \langle S_{b\sigma'} S_{a\sigma} \rangle \right)$$

$$= 4\mathcal{Q}_{aa}^{00} \mathcal{Q}_{bb}^{00} + 2\mathcal{Q}_{ab}^{00} \mathcal{Q}_{ba}^{00} + 2\mathcal{Q}_{ab}^{01} \mathcal{Q}_{ba}^{10}. \tag{3.248}$$

This is valid also for equal replica indices, $a = b$, in which case the last term vanishes. Substituting Eq. (3.248) into Eq. (3.247), one obtains

$$\langle C_{(3,1)}[S] \rangle_{S[\phi,\phi^*,Q]} = 72 \left(\mathcal{Q}_{aa}^{00} \mathcal{Q}_{bb}^{00} \right)^2 - 8 \left(2\mathcal{Q}_{aa}^{00} \mathcal{Q}_{bb}^{00} + \mathcal{Q}_{ab}^{00} \mathcal{Q}_{ba}^{00} + \mathcal{Q}_{ab}^{01} \mathcal{Q}_{ba}^{10} \right)^2$$

$$= 8 \left(5\mathcal{Q}_{aa}^{00} \mathcal{Q}_{bb}^{00} + \mathcal{Q}_{ab}^{00} \mathcal{Q}_{ba}^{00} + \mathcal{Q}_{ab}^{01} \mathcal{Q}_{ba}^{10} \right) \left(\mathcal{Q}_{aa}^{00} \mathcal{Q}_{bb}^{00} - \mathcal{Q}_{ab}^{00} \mathcal{Q}_{ba}^{00} - \mathcal{Q}_{ab}^{01} \mathcal{Q}_{ba}^{10} \right). \tag{3.249}$$

This contains the operator

$$\mathcal{P}_{(1,1)}^C = \mathcal{Q}_{aa}^{00} \mathcal{Q}_{bb}^{00} - \mathcal{Q}_{ab}^{00} \mathcal{Q}_{ba}^{00} - \mathcal{Q}_{ab}^{01} \mathcal{Q}_{ba}^{10} \tag{3.250}$$

as a factor. It follows from the construction based on the Iwasawa decomposition in Sec. 3.3 that $\mathcal{P}_{(1,1)}^C$ in this form is exactly the (1,1) composite operator that satisfies Abelian fusion. Indeed, according to Eq. (3.96), a complete family of eigenoperators satisfying Abelian fusion is generated by Pfaffians of the matrices

$$\left(\left(T(\tilde{Q}\Lambda) \right)^{AA} \Sigma_2 \right)_m = \begin{pmatrix} \mathcal{Q}^{01} & \mathcal{Q}^{00} \\ -\left(\mathcal{Q}^{00} \right)^T & \mathcal{Q}^{10} \end{pmatrix}_m . \tag{3.251}$$

Here the subscript m indicates a projection to first m replicas (out of their total number of n). On the left-hand side, T is the conjugation defined by Eq. (3.72), which is applied to $\tilde{Q}$ matrix satisfying Eq. (3.118). Since the matrix is restricted to the advanced-advanced block and the first m replicas, its size is $2m \times 2m$. The right-hand side is obtained by computing the action of T explicitly and choosing appropriate phases α_{a_i} in Eqs.(3.213)–(3.219), where $\mathcal{Q}^{ij}$ is introduced. The Pfaffian of the $2m \times 2m$ matrix (3.251) is a scaling operator in the representation $(1, \ldots, 1)_m$. For $m = 2$ one thus finds that

$$\text{Pf} \left(\left(T(\tilde{Q}\Lambda) \right)^{AA} \Sigma_2 \right)_2 = -\mathcal{Q}_{aa}^{00} \mathcal{Q}_{bb}^{00} + \mathcal{Q}_{ab}^{00} \mathcal{Q}_{ba}^{00} + \mathcal{Q}_{ab}^{01} \mathcal{Q}_{ba}^{10} \tag{3.252}$$

is a pure scaling operator in representation $(1,1)$ that satisfies Abelian fusion. This is exactly what was stated below Eq. (3.250).

The other factor in Eq. (3.249) is a linear combination of operators belonging to the representations (2) and $(1,1)$. In view of the Abelian rules, fusion of the $(1,1)$ operator, Eq. (3.250), and the dominant contribution (2) from the other factor yields $(3,1)$. Therefore, the leading behavior of $\left| \Psi_{(3,1)} \left[|\psi| \right] \right|^2$ is indeed governed by an operator from the representation $(3,1)$.

3.7.3 Numerical results

In Fig. 3.4 the results of the numerical study of the r/L dependence of $\left| \Psi_\lambda \left[|\psi| \right] \right|^2$ are presented, where $\Psi_\lambda \left[|\psi| \right]$ are Young-symmetrized combinations of $|\psi|$, on the class-C network model. For $q = 2$ and $q = 3$, one obtains the scaling of all the corresponding class-C operators: (2) and $(1,1)$ for $q = 2$ as well as (3), $(2,1)$, and $(1,1,1)$ for $q = 3$. For $q = 4$ one can only get the scaling of (4), $(3,1)$ and $(2,2)$ in this way. At the same time, one cannot get access to $(2,1,1)$ and $(1,1,1,1)$ scaling, as the corresponding $\left| \Psi_\lambda \left[|\psi| \right] \right|^2$ numerically shows the admixture of the more relevant contribution $(2,2)$. An interesting question is how to improve the construction to get access to all generalized-multifractality exponents via strictly positive observables; I do not have an answer to this question at the present stage.

The exponents $\Delta_\lambda^{\mathrm{num}, |\psi|}$ obtained in this way are presented in Table 3.2 and are in a very good agreement with exponents $\Delta_\lambda^{\mathrm{num}}$ obtained from single-spin observables, Fig. 3.1. For $\lambda = (1,1)$, the accuracy of $\Delta_{(1,1)}^{\mathrm{num}, |\psi|}$ is somewhat higher than that of $\Delta_{(1,1)}^{\mathrm{num}}$ since fluctuations are not so strong because I deal here with a strictly positive observable. The analytically known exponents $\Delta_{(2)}$ and $\Delta_{(3)}$ are perfectly reproduced. Further, the Weyl-symmetry relation $\Delta_{(2,1)} = \Delta_{(1,1)} - 1/4$ is also excellently fulfilled.

In the bottom right panel of Fig. 3.4, the numerical data for $\Psi_{(q/2,q/2)}[|\psi|]$ obtained out of two eigenstates as $(\Psi_{(1,1)}[|\psi|])^{q/2} = (H[|\psi|] - F[|\psi|])^{q/2}$ is shown. Since $\Psi_{(1,1)}[|\psi|]$ is a strictly positive observable corresponding to the representation $(1,1)$, one expects that $(\Psi_{(1,1)}[|\psi|])^{q/2}$ should exhibit the scaling of $(q/2, q/2)$. All numerical tests perfectly confirm this. First, the value of the exponent $\Delta_{(2,2)}$ obtained in this way is in excellent agreement with $\Delta_{(2,2)}^{\mathrm{num}, |\psi|} = 0.86$ found by using four eigenstates. Second, the Weyl symmetry requires that $x_{(q/2,q/2)}$ is invariant with respect to the symmetry transformation $q \to 10 - q$. While I was able to perform the numerics controllably up to $q = 5$ only (for larger q a still larger number of disorder realizations is needed), it is sufficient to see that the behavior of $x_{(q/2,q/2)}^{\mathrm{num}, |\psi|}$ is fully consistent with the required maximum at $q = 5$. In fact, $x_{(q/2,q/2)}^{\mathrm{num}, |\psi|}$ turns out to be approximated rather well by a parabola $\tilde{x}_{(q/2,q/2)}^{\mathrm{para}} = \tilde{b} q(10 - q)/2$ (which clearly satisfies the Weyl symmetry) with $\tilde{b} = 2/13 = 0.154$. For comparison, in the same panel also the conventional (leading) multifractal spectrum $x_{(q)}^{\mathrm{num}, |\psi|}$ obtained from the scaling of $(H[|\psi|] + F[|\psi|])^{q/2}$ is shown. The Weyl symmetry for this spectrum is $q \to 3 - q$ and is again perfectly fulfilled. In the figure one can further see the parabolic approximation $x_{(q)}^{\mathrm{para}} = bq(3 - q)$. While it appears to describe the data rather well, the parabolicity was found to be only approximate in Refs. [58, 59]. Deviations from parabolicity in $x_{(q)}$ are seen more clearly if one plots the ratio $x_{(q)}/q(3 - q)$; it is not necessary to study them here since they were explored recently in great detail and with very high accuracy in Ref. [59].

As was already emphasized above, the numerical results for generalized-miltifractality scaling exponents collected in Table 3.2 demonstrate a strong vioaltion of generalized parabolicity. The exponents
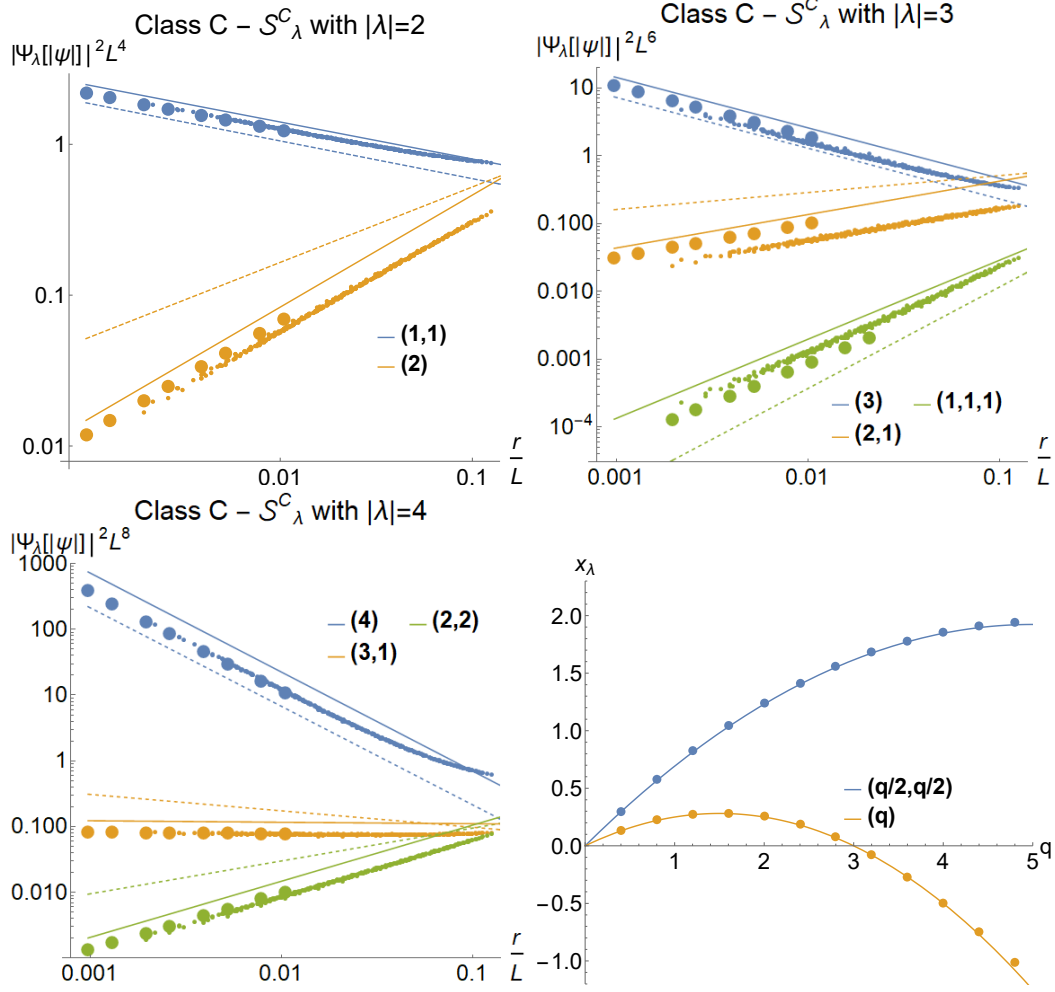
Figure 3.4: Figure taken from Ref. [105]. Generalized multifractality at the SQH transition (class C) studied via Young-symmetrized eigenstate combinations built out of the total density $|\psi|(r)$, Eq. (3.236), for observables of order $q = 2$ (top left), $q = 3$ (top right), and $q = 4$ (bottom left). Full lines are fits to the data; the corresponding exponents $\Delta_\lambda^{\mathrm{num},|\psi|}$ are given in Table 3.2 and are fully consistent with exponents $\Delta_\lambda^{\mathrm{num}}$ obtained from single-spin observables, Fig. 3.1. The dashed lines correspond to generalized parabolicity (3.235); the corresponding exponents $\Delta_\lambda^{\mathrm{para}}$ are also listed in Table 3.2. A strong violation of the generalized parabolicity at the SQH transition is evident. *Bottom right:* Scaling dimensions $x_{(q)}$ and $x_{(q/2,q/2)}$ extracted from eigenstate combinations $|H+F|^{q/2}$ and $|H-F|^{q/2}$, respectively, formed with $|\psi|$. The Weyl symmetry dictates that $x_{(q)}$ is symmetric around $q = 3/2$, and $x_{(q/2,q/2)}$ is symmetric around $q = 5$. Solid lines are parabolas $x_{(q)}^{\mathrm{para}} = bq(3-q)$ and $\tilde{x}_{(q/2,q/2)}^{\mathrm{para}} = \tilde{b}q(10-q)/2$ with $b = 1/8$ and $\tilde{b} = 2/13 = 0.154$. They serve as guides to the eye, illustrating that the numerical data fulfil the Weyl symmetry very well. Note that the parabolicity of $x_{(q)}$ [and, most likely, of $x_{(q/2,q/2)}$ as well] is only approximate. Deviations from parabolicity in $x_{(q)}$ at relatively small q were explored systematically in Refs. [58, 59]; they are seen much better if one plots $x_{(q)}/q(3-q)$. The fact that $\tilde{b}$ [chosen to optimize the fit to $x_{(q/2,q/2)}$] is substantially different from b is a manifestation of strong violation of generalized parabolicity.

corresponding to representations $(1, 1)$, $(2, 1)$, $(3, 1)$ and $(2, 2)$ strongly deviate from their "parabolic values". Another manifestation of this fact is a substantial difference of the prefactors b and $\tilde{b}$ in the parabolic fits in the bottom right panel of Fig. 3.4. Indeed, the generalized parabolicity would imply not only that these parabolic fits are exact but also that $\tilde{b} = b$.

The agreement between different numerical approaches and the fulfilment of all exact analytical results (values of exponents and Weyl-symmetry relations) should make one confident that the numerical results for the exponents are accurate. Thus, the strong violation of generalized parabolicity at the SQH transition observed in the numerics is indeed the genuine property of the SQH critical point and not a finite-size effect. In combinations with the results Sec. 3.2, this means that the local conformal invariance must be violated in the field theory describing the SQH critical point. Indeed, the Abelian fusion was implicitly demonstrated In Sec. 3.3. Thus, as was emphasized in Sec. 3.2.2.3, violation of generalized parabolicity of the generalized-multifractality spectrum of a 2D system implies violation of local conformal invariance.

3.8 Percolation mapping

Certain observables in the SU(2) version of the Chalker-Coddington network model at criticality can be mapped to probabilities of the classical percolation problem. The SU(2) average turns the quantum mechanical coherent sum over all amplitudes into a sum over self-avoiding walks (SAW) with uniform weight. This mapping exists for products of $q = 1, 2, 3$ Green's functions. The scaling dimension of LDOS moments $x_{(1)}, x_{(2)}, x_{(3)}$ can be computed this way. Products of Green's functions with finite level broadening γ also involve products of distinct wave functions that do not behave as pure LDOS powers but show subleading multifractality. Since the mapping to percolation is exact (up to approximations used in the evaluations of probabilities), one should therefore have access to $x_{(1,1)}, x_{(2,1)}, x_{(1,1,1)}$ as well. In this section, I search for these subleading generalized multifractal exponents, which serves as an independent verification of the results in this chapter so far.

For this purpose, first the notation for the correlation functions and classical percolation probabilities is introduced in Sec. 3.8.1. Then in Sec. 3.8.2 the mapping to percolation in the SAW picture from Ref. [58] is applied. Subsequently, the analytical properties of the classical percolation probabilities are reviewed and the consequences for the correlation functions are discussed in Sec. 3.8.3. Numerical simulations of classical percolation are performed (Sec. 3.8.4) in order to verify these analytical calculations. The key result of this section is the relation of the multifractal scaling dimension in SQH systems and scaling dimensions of hull operators in classical percolation.

3.8.1 Notation

For the purposes here, a description of the network model in terms of the "Floquet" operator $\mathcal{U}$ (time evolution over one discrete timestep) is appropriate. Due to the unitarity of $\mathcal{U}$, the eigenvalues lie on the unit circle in the complex plane.

$$\mathcal{U}\psi_i = e^{i\epsilon_i}\psi_i \tag{3.253}$$

Anomalous particle hole symmetry gives the quasienergy ϵ_i a partner $-\epsilon_i$. The wave function $\psi_{i\alpha}(e)$ lives on the links e and carries a spin index α.

One can define the "Floquet" Green's function as

$$G(e', e; z) = \langle e'|(1 - z\mathcal{U})^{-1}|e\rangle. \tag{3.254}$$

Since the evolution operator $\mathcal{U}$ is unitary, its poles lie in the unit circle. For $z < 1$ the von Neumann series for this expression converges.

The defining class C symmetry acts like

$$\left[G(e, e'; z^{-1})\right]^{\dagger} = \mathbb{1} - G(e', e; z^*), \tag{3.255}$$

$$\left[G(e, e'; z)\right]^{\dagger} = -(i\sigma_2)\left[G(e, e'; z)\right]^T (i\sigma_2) \tag{3.256}$$

on the Green's function. Here the Pauli matrix σ_2 acts in spin space. Since it connects the expressions for z^{-1} and z^*, one can use this to extend the series to all $|z| \neq 1$.

Here the correlation functions of $2q$ wave functions ψ_i, ψ_j are studied for $q = 1, 2, 3$. As an example the case $q = 2$ is discussed in more detail in the following. It is convenient to introduce Hartree $\mathcal{D}_{(1,1)}$ and Fock $\mathcal{D}_{(2)}$ term with the following spin structure:

$$\mathcal{D}_{(2)}(e', e; \epsilon_1, \epsilon_2) = \left\langle \sum_{ij\alpha\beta} \psi_{i\alpha}^*(e)\psi_{j\alpha}(e)\psi_{i\beta}(e')\psi_{j\beta}^*(e')\delta(\epsilon_1 - \epsilon_i)\delta(\epsilon_2 - \epsilon_j) \right\rangle, \tag{3.257}$$

$$\mathcal{D}_{(1,1)}(e', e; \epsilon_1, \epsilon_2) = \left\langle \sum_{ij\alpha\beta} |\psi_{i\alpha}(e)|^2 |\psi_{j\beta}|^2 \delta(\epsilon_1 - \epsilon_i)\delta(\epsilon_2 - \epsilon_j) \right\rangle. \tag{3.258}$$

on links e, e' in the network model. Spin indices are denoted by α, β. These expressions are analogous to Hartree and Fock terms introduced in Sec. 3.6.

One can express $\mathcal{D}_{(2)}, \mathcal{D}_{(1,1)}$ in terms of the Green's function (3.254). The results contain traces over the spin space:

$$\mathcal{D}_{(2)}(e', e; \epsilon_1, \epsilon_2) = (2\pi)^{-2} \left\langle \text{Tr}\left[G^R(e, e'; e^{i\epsilon_1}) - G^A(e', e; e^{i\epsilon_1})\right]\left[G^R(e, e'; e^{i\epsilon_2}) - G^A(e', e; e^{i\epsilon_2})\right] \right\rangle, \tag{3.259}$$

$$\mathcal{D}_{(1,1)}(e', e; \epsilon_1, \epsilon_2) = (2\pi)^{-2} \left\langle \text{Tr}\left[G^R(e, e; e^{i\epsilon_1}) - G^A(e, e; e^{i\epsilon_1})\right] \text{Tr}\left[G^R(e', e'; e^{i\epsilon_2}) - G^A(e', e'; e^{i\epsilon_2})\right] \right\rangle. \tag{3.260}$$

The energy arguments $e^{i\epsilon_1} = z = e^{-\gamma}, e^{i\epsilon_2} = w = e^{-\delta}$ are continued analytically to the imaginary axis:

$$\mathcal{D}_{(2)}(e', e; \gamma, \delta) = (2\pi)^{-2} \left\langle \text{Tr}\left[G(e, e'; z) - G(e', e; z^{-1})\right]\left[G(e, e'; w) - G(e', e; w^{-1})\right] \right\rangle, \tag{3.261}$$

$$\mathcal{D}_{(1,1)}(e', e; \gamma, \delta) = (2\pi)^{-2} \left\langle \text{Tr}\left[G(e, e; z) - G(e, e; z^{-1})\right] \text{Tr}\left[G(e', e'; w) - G(e', e'; w^{-1})\right] \right\rangle. \tag{3.262}$$

The calculation is drastically simplified by choosing $\gamma = \delta$ (for generic $\gamma \neq \delta$ the percolation mapping from Ref. [58] no longer applies):

$$(2\pi)^2 \mathcal{D}_{(2)}(e', e; \gamma, \gamma) = \left\langle \sum_{ij\alpha\beta} \psi_{i\alpha}^*(e)\psi_{j\alpha}(e)\psi_{i\beta}(e')\psi_{j\beta}^*(e')\text{Im}\frac{1}{-\epsilon_i + i\gamma}\text{Im}\frac{1}{-\epsilon_j + i\gamma} \right\rangle, \tag{3.263}$$

$$(2\pi)^2 \mathcal{D}_{(1,1)}(e', e; \gamma, \gamma) = \left\langle \sum_{ij\alpha\beta} |\psi_{i\alpha}(e)|^2 |\psi_{j\beta}(e')|^2 \text{Im}\frac{1}{-\epsilon_i + i\gamma}\text{Im}\frac{1}{-\epsilon_j + i\gamma} \right\rangle. \tag{3.264}$$

One can define $\mathcal{D}_\lambda(e, \ldots; \gamma)$ for other Young diagrams λ in an analogous fashion.

3.8.1.1 Scaling of $\mathcal{D}_{(2)}$, $\mathcal{D}_{(1,1)}$

The energy denominator is symmetric under the exchange of i, j. There are two types of contributions one from $i = j$ and one from $i \neq j$ that contains the subleading scaling:

$$
\begin{aligned}
(2\pi)^2 \mathcal{D}_{(2)}(e', e; \gamma, \gamma) = & \left\langle \sum_{i,\alpha\beta} |\psi_{i\alpha}(e)|^2 |\psi_{i\beta}(e')|^2 \left(\mathrm{Im} \frac{1}{-\epsilon_i + i\gamma} \right)^2 \right. \\
& \left. + \sum_{i\neq j,\alpha\beta} \psi_{i\alpha}^*(e)\psi_{j\alpha}(e)\psi_{i\beta}(e')\psi_{j\beta}^*(e') \mathrm{Im} \frac{1}{-\epsilon_i + i\gamma} \mathrm{Im} \frac{1}{-\epsilon_j + i\gamma} \right\rangle, \\
(2\pi)^2 \mathcal{D}_{(1,1)}(e', e; \gamma, \gamma) = & \left\langle \sum_{i,\alpha\beta} |\psi_{i\alpha}(e)|^2 |\psi_{i\beta}(e')|^2 \left(\mathrm{Im} \frac{1}{-\epsilon_i + i\gamma} \right)^2 \right. \\
& \left. + \sum_{i\neq j,\alpha\beta} |\psi_{i\alpha}(e)|^2 |\psi_{j\beta}(e')|^2 \mathrm{Im} \frac{1}{-\epsilon_i + i\gamma} \mathrm{Im} \frac{1}{-\epsilon_j + i\gamma} \right\rangle.
\end{aligned}
\tag{3.265}
$$

The terms with only one eigenstate summation will give pure leading $x_{(2)}$ scaling, there is only one wavefunction in the terms summed over. The terms with two eigenstate summations additionally contain a subleading $x_{(1,1)}$ contribution.

However, the terms with one eigenstate summation are suppressed in the thermodynamic limit $L \to \infty$:

$$
\begin{aligned}
\left\langle \sum_{i,\alpha\beta} |\psi_{i\alpha}(e)|^2 |\psi_{i\beta}(e')|^2 \left(\mathrm{Im} \frac{1}{-\epsilon_i + i\gamma} \right)^2 \right\rangle & \simeq L^2 \int d\epsilon \, \nu(\epsilon) \left(\mathrm{Im} \frac{1}{-\epsilon + i\gamma} \right)^2 \left\langle \sum_{\alpha\beta} |\psi_{i\alpha}(e)|^2 |\psi_{i\beta}(e')|^2 \right\rangle \Bigg|_{\epsilon_i \sim \epsilon} \\
& = aL^{-2} \int d\epsilon \, \nu(\epsilon) \left(\mathrm{Im} \frac{1}{-\epsilon + i\gamma} \right)^2 (r/\xi_\gamma)^{\Delta_{(2)}} \\
& \simeq \frac{7}{6} aL^{-2} \rho(\gamma) \gamma^{-1} (r/\xi_\gamma)^{\Delta_{(2)}},
\end{aligned}
\tag{3.266}
$$

here $\nu(\epsilon) = \nu_0 \epsilon^{-1/7}$ is the density of states, $\xi_\gamma = \gamma^{-\frac{4}{7}}$ the correlation length, and $\left\langle |\psi_{i\alpha}(e)|^2 |\psi_{i\beta}(e')|^2 \right\rangle \Big|_{\epsilon_i \sim \epsilon} = aL^{-4} (r/\xi_\epsilon)^{\Delta_{(2)}}$ holds with a constant a.

The scaling of the correlation functions in the thermodynamic limit $L \to \infty$ is therefore given by $\Delta_{(2)}$ and subleading $\Delta_{(1,1)}$ power laws. The ratios in front of the coefficients of these power laws can be inferred from RG analysis of the class-C NLSM in Sec. 3.5, this is going to be discussed in more detail below Eq. (3.268). All these consideration lead to the result

$$
\mathcal{D}_{(2)}(e', e; \gamma, \gamma) \simeq c\rho(\gamma)^2 L^4 \left\langle \sum_{\alpha\beta} \psi_{i\alpha}^*(e)\psi_{j\alpha}(e)\psi_{i\beta}(e')\psi_{j\beta}^*(e') \right\rangle \Bigg|_{\epsilon_i, \epsilon_j \sim \gamma} \simeq c'\rho(\gamma)^2 \left((r/\xi_\gamma)^{\Delta_{(2)}} - (r/\xi_\gamma)^{\Delta_{(1,1)}} \right),
$$

$$
\mathcal{D}_{(1,1)}(e', e; \gamma, \gamma) \simeq c\rho(\gamma)^2 L^4 \left\langle \sum_{\alpha\beta} |\psi_{i\alpha}(e)|^2 |\psi_{j\beta}(e')|^2 \right\rangle \Bigg|_{\epsilon_i, \epsilon_j \sim \gamma} \simeq c'\rho(\gamma)^2 \left(2(r/\xi_\gamma)^{\Delta_{(2)}} + (r/\xi_\gamma)^{\Delta_{(1,1)}} \right),
$$

$$
\tag{3.267}
$$

where c and c' are constants. In the following it is convenient to switch to the variable $z = e^{-\gamma} < 1$ for $\gamma > 0$ to characterize the uniform broadening.

From Eq. (3.154) in Sec. 3.5, the combinations of $\mathcal{D}_\lambda$ which reveal subleading scaling are known:

$$\begin{pmatrix} \mathcal{P}^C_{(1,1)} \\ \mathcal{P}^C_{(2)} \end{pmatrix} \sim \underbrace{\begin{pmatrix} 1 & -2 \\ 1 & 1 \end{pmatrix}}_{\equiv P^C_2} \begin{pmatrix} \mathcal{D}_{(1,1)}(e, e'; z) \\ \mathcal{D}_{(2)}(e, e'; z) \end{pmatrix}. \tag{3.268}$$

At small r/ξ_γ $2\mathcal{D}_{(2)}(e', e; \gamma, \gamma) \approx \mathcal{D}_{(1,1)}(e', e; \gamma, \gamma)$ holds, subtracting $\mathcal{D}_{(1,1)} - 2\mathcal{D}_{(2)}$ reveals the subleading $\Delta_{(1,1)}$ scaling.

3.8.2 Mapping to percolation

In Ref. [77], it is pointed out that the SU(2) average reduces the coherent quantum mechanical sum over amplitudes appearing in traces over two or three Greens functions to a classical sum over non-intersecting paths. The average over the quantum mechanical expectation value is reduced to a probability of classical self-avoiding walks.

For $q = 1, 2, 3$ Green's functions the mapping obeys the following rules:

- The quantum mechanical average over traces of products of $G(r_i, r'_i; \gamma) - \mathbb{1}$ is replaced by a sum over paths from r_i to r'_i. In the end, there only is a non-vanishing contribution, when each link is traversed exactly 0 or 2 times by the paths.

- Paths of length $2N$ are weighted with a factor z^{2N}.

- Each spin trace gives a factor -1. The negative sign originates from the SU(2) average, since $\langle U^k \rangle_{\text{SU}(2)} = c_k \mathbb{1}$ with $c_2 = -\frac{1}{2} < 0$ and all other $c_k = 0$ for $k > 0$.

The sum over all possible self-avoiding paths traversing these links can then be interpreted as classical percolation partition sum. The full quantum mechanical problem is then re-expressed in terms of the classical percolation probabilities introduced in Tab. 3.3. These are probabilities to find loops (=self avoiding closed paths) of given lengths $N, N', \ldots$ running through certain links $e \to e', \ldots$ in a given order. Sometimes it is useful to specify the path length $N_{ee'}$ between two links traversed. The following identities between the probabilities introduced in Tab. 3.3 are satisfied:

$$\sum_N P(e, e'; N) = \sum_N P_1(e, e'; N) = P(e, e'),$$

$$P(e, e'; N) + \sum_{N'} P(e; N | e'; N') = P(e; N),$$

$$\sum_N P(e; N) = 1. \tag{3.269}$$

The first one relates the probability $P(e, e')$ to find e, e' in the same loop to the sum of P, P_1 over all loop lengths N. The middle one states the probability $P(e; N)$ to find a link e in a loop of length N is equal to the sum of finding e and a fixed e' in the same loop and finding e' in an arbitrary distinct loop of length N'. The last one is normalization of the probability.

In the following, the mapping is applied to SU(2) symmetrized expressions with $q = 1, 2, 3$ Green's functions or $2q = 2, 4, 6$ wavefunctions respectively. These will be labeled by Young diagrams λ with $|\lambda| = q$.

Table 3.3: Probabilities involved in the mapping to classical percolation.

probability	description
$P(e; N)$	loop of length N running through link e
$P(e, e'; N)$	loop of length N running through links $e \to e'$
$P_1(e, e'; N)$	loop running through links $e \to e'$, where $N_{ee'} = N$
$P(e; N \vert e'; N')$	loops of lengths N, N' running through links e, e'
$P(e, e', e''; N)$	loop of length N running through links $e \to e' \to e''$
$P_1(e, e', e''; N)$	loop running through links $e \to e' \to e''$, where $N_{ee''} = N$
$P(e, e'; N \vert e''; N')$	loop of length N running through links $e \to e'$
	and loop of length N' running through link e''
$P_1(e, e'; N \vert e''; N')$	loop of length N running through links $e \to e'$,
	where $N_{ee'} = N$ and loop of length N' running through link e''
$P(e; N \vert e'; N' \vert e''; N')$	loops of lengths N, N', N'' running through links e, e', e''

3.8.2.1 One Green's function: $q = 1$

In this order, there is only one SU(2) symmetrized expression: $\operatorname{Tr} G(e, e; \gamma)$ corresponding to the LDOS $\langle \nu(\gamma, e) \rangle$.

(1) For the average LDOS this means:

$$(2\pi)\mathcal{D}_{(1)}(e; z) = \rho(\gamma) \left\langle \sum_\alpha |\psi_\alpha(e)|^2 \right\rangle = \left\langle \operatorname{Tr}(G(e, e; z)) - \operatorname{Tr}(G(e, e; z^{-1})) \right\rangle. \tag{3.270}$$

The expectation values of the Green's functions can be turned into sums over percolation probabilities:

$$\left\langle \operatorname{Tr}(G(e, e; z)) \right\rangle = 2 - \sum_{N=1}^{\infty} P(e; N) z^{2N},$$

$$\left\langle \operatorname{Tr}(G(e, e; z^{-1})) \right\rangle = \sum_{N=1}^{\infty} P(e; N) z^{2N}. \tag{3.271}$$

The only contribution comes from the loops containing link e traversed exactly twice. The second line is obtained with Eq. (3.256) and assuming $0 < z < 1$ real. The spin trace over the identity gives the constant term in the first line.

Putting everything together and using the normalization of the probability, this yields the percolation expression for the LDOS

$$(2\pi)\mathcal{D}_{(1)}(e; z) = 2 \sum_{N=1}^{\infty} P(e; N)(1 - z^{2N}). \tag{3.272}$$

This expression does not depend on the link e and reveals the well-known $x_1 = \frac{1}{4}$ scaling when one evaluates the percolation sum on the RHS.

3.8.2.2 Two Green's functions: $q = 2$

In the case of two Green's functions or four wavefunctions respectively, the two SU(2) invariant combinations are labeled with $\lambda = (2)$ and $\lambda = (1, 1)$. These correspond to Fock and Hartree term.

(2) First there are the Fock-like terms:

$$\left\langle \mathrm{Tr}(G(e,e';z)G(e',e;z)) \right\rangle = -2 \sum_{N=1}^{\infty} P(e,e';N)z^{2N},$$

$$\left\langle \mathrm{Tr}(G(e,e';z)G(e',e;z^{-1})) \right\rangle = -2 \sum_{N=1}^{\infty} P_1(e,e';N)z^{2N}. \tag{3.273}$$

Since e, e' are distinct, there is no contribution from the unit operator as above. There are two paths contributing: one goes $e \to e' \to e \to e'$ picking up $z^{N_{ee'}}$ with the first G and $e' \to e$ with the second G picking up $z^{N-N_{ee'}}$ or vice versa. The other cases can be obtained with Eq. (3.255).

Ref. [77] uses an invariance argument that requires explicit averages over the link SU(2) groups:

$$\left\langle \mathrm{Tr}(G(e,e';z)G(e,e';z)) \right\rangle = \int_{\mathrm{SU}(2)} d\mu(U_e)d\mu(U_{e'}) \left\langle \mathrm{Tr}(U_e^{\dagger}G(e,e';z)U_{e'}U_e^{\dagger}G(e,e';z)U_{e'}) \right\rangle. \tag{3.274}$$

One then needs the following integral for the average over a link SU(2) appearing in above RHS:

$$\int_{\mathrm{SU}(2)} d\mu(U)U_{\alpha\beta}U_{\gamma\delta} = c_1\delta_{\alpha\beta}\delta_{\gamma\delta} + c_2\delta_{\alpha\delta}\delta_{\gamma\beta}. \tag{3.275}$$

By contracting different indices in this expression, the identities

$$\int_{\mathrm{SU}(2)} d\mu(U)\mathrm{Tr}U\mathrm{Tr}U = 1, \qquad \int_{\mathrm{SU}(2)} d\mu(U)\mathrm{Tr}U^2 = -1, \qquad \int_{\mathrm{SU}(2)} d\mu(U)\mathrm{Tr}UU^T = 0 \tag{3.276}$$

follow and one can infer $c_1 = \frac{1}{2}$ and $c_2 = -\frac{1}{2}$ in Eq. (3.275).

Finally, one finds the desired identity

$$\left\langle \mathrm{Tr}(G(e,e';z)G(e,e';z)) \right\rangle = \frac{1}{2} \left(\mathrm{Tr}(G(e,e';z)G(e,e';z)) - \mathrm{Tr}(G(e,e';z))\mathrm{Tr}(G(e,e';z)) \right) \tag{3.277}$$

from the SU(2) integrals.

One has to express $G(e',e,z^{-1})$ in terms of $G(e,e',z)$ using Eqs. (3.255), (3.256):

$$G(e',e,z^{-1}) = \mathbb{1}(e',e) - \left[G(e',e,z^*)\right]^{\dagger} = \mathbb{1}(e',e) + \varepsilon\left[G(e,e',z^*)\right]^T \varepsilon \tag{3.278}$$

This implies (one can drop $\mathbb{1}$ since e, e' are distinct)

$$\left\langle \mathrm{Tr}\left[G(e,e',z)G(e',e,z^{-1})\right] \right\rangle = \left\langle \mathrm{Tr}\left[G(e,e',z)\varepsilon[G(e,e',z)]^T\varepsilon\right] \right\rangle$$

$$= -\left\langle \mathrm{Tr}(G(e,e';z)G(e,e';z)) - \mathrm{Tr}(G(e,e';z))\mathrm{Tr}(G(e,e';z)) \right\rangle = -2\left\langle \mathrm{Tr}(G(e,e';z)G(e,e';z)) \right\rangle. \tag{3.279}$$

In the second line it has been used that:

$$(i\sigma_2)_{ij}(i\sigma_2)_{kl} = \delta_{ij}\delta_{kl} - \delta_{il}\delta_{kj}. \tag{3.280}$$

Putting all contribution for this correlation function together, one obtains

$$(2\pi)^2 \mathcal{D}_{(2)}(e, e'; z) = -4 \sum_{N=1}^{\infty} P(e, e'; N)z^{2N} + 2 \sum_{N=1}^{\infty} (P_1(e, e'; N) + P_1(e', e; N))z^{2N}$$

$$= 4 \sum_{N=1}^{\infty} \left[P(e, e'; N) - P_1(e, e'; N) \right] (1 - z^{2N}). \tag{3.281}$$

The last line is obtained using $\sum_N P(e, e'; N) = P(e, e') = \sum_N P_1(e, e'; N)$. Note that P_1 appears symmetrized over its argument, this turns out to be the case also for higher correlation functions, where it is convenient to use the convention that all probabilities are symmetrized over the link arguments when they appear as $\bar{P}$ in the equations. For instance $2\bar{P}_1(e', e; N) = P_1(e, e'; N) + P_1(e', e; N)$ here.

(1,1) In the Hartree-like case, due to the traces around each G, the unit operator can contribute giving rise to cross terms. The result reads:

$$\Big\langle \mathrm{Tr}(G(e, e; z)) \mathrm{Tr}(G(e', e'; z)) \Big\rangle = 4 - 2 \sum_{N=1}^{\infty} \left[P(e; N) + P(e'; N) \right] z^{2N}$$

$$+ \sum_{N,N'=1}^{\infty} P_-(e, e'; N, N') z^{2(N+N')} + \sum_N P(e, e'; N) z^{2N},$$

$$\Big\langle \mathrm{Tr}(G(e, e; z)) \mathrm{Tr}(G(e', e'; z^{-1})) \Big\rangle = 2 \sum_{N=1}^{\infty} P(e'; N) z^{2N} - \sum_{N,N'=1}^{\infty} P_-(e, e'; N, N') z^{2(N+N')},$$

$$- \sum_N P(e, e'; N) z^{2N}$$

$$\Big\langle \mathrm{Tr}(G(e, e; z^{-1})) \mathrm{Tr}(G(e', e'; z^{-1})) \Big\rangle = \sum_{N,N'=1}^{\infty} P(e; N|e'; N') z^{2(N+N')} + \sum_N P(e, e'; N) z^{2N}. \tag{3.282}$$

One can use the identity

$$P(e; N) = P(e, e'; N) + \sum_{N'} P(e; N|e', N') \tag{3.283}$$

to rewrite:

$$(2\pi)^2 \mathcal{D}_{(1,1)}(e, e'; z) = 4 \sum_{N=1}^{\infty} P(e, e'; N) z^{2N} + 4 \sum_{N,N'=1}^{\infty} P(e; N|e'; N') z^{2N} z^{2N'}$$

$$- 4 \sum_{N=1}^{\infty} \left[P(e; N) + P(e'; N) \right] z^{2N} + 4$$

$$= 4 \sum_{N=1}^{\infty} \left[P(e, e'; N) + P_-(e, e'; N) \right] (1 - z^{2N}), \tag{3.284}$$

where $P_-(e, e'; N) = \sum_M \Big(P(e; M|e'; N) + P(e; N|e'; M) - P(e; N - M|e'; M) \Big). \tag{3.285}$

The auxiliary function $P_-(e, e'; N)$ introduced here is a linear combination of percolation probabilities, it can assume negative values.

3.8.2.3 Three Green's functions: $q = 3$

There are three SU(2) invariant correlation function in this order that can be labeled with Young diagrams $\lambda = (3)$, $(2, 1)$ and $(1, 1, 1)$:

$$\mathcal{D}_{(3)}(e, e', e''; z) = (2\pi)^{-3} \Big\langle \mathrm{Tr} \Big((G(e, e'; z) - G(e, e'; z^{-1})) \cdot (G(e', e''; z) - G(e', e''; z^{-1}))$$
$$\cdot (G(e'', e; z) - G(e'', e; z^{-1}))) \Big\rangle,$$

$$\mathcal{D}_{(2,1)}(e, e', e''; z) = (2\pi)^{-3} \Big\langle \mathrm{Tr} \Big((G(e, e'; z) - G(e, e'; z^{-1})) \cdot (G(e', e; z) - G(e', e; z^{-1})) \Big)$$
$$\cdot \mathrm{Tr} \Big((G(e'', e''; z) - G(e'', e''; z^{-1})) \Big) \Big\rangle,$$

$$\mathcal{D}_{(1,1,1)}(e, e', e''; z) = (2\pi)^{-3} \Big\langle \mathrm{Tr} \Big((G(e, e; z) - G(e, e; z^{-1})) \Big) \cdot \mathrm{Tr} \Big((G(e', e'; z) - G(e', e'; z^{-1})) \Big)$$
$$\cdot \mathrm{Tr} \Big((G(e'', e''; z) - G(e'', e''; z^{-1})) \Big) \Big\rangle. \tag{3.286}$$

(3) For the trace enclosing all three Green's functions G one has to deal with:

$$\Big\langle \mathrm{Tr}(G(e, e'; z)G(e', e''; z)G(e'', e; z)) \Big\rangle = - \sum_{N=1}^{\infty} \Big[3P(e, e', e''; N) + P(e'', e', e; N) \Big] z^{2N},$$

$$\Big\langle \mathrm{Tr}(G(e, e'; z^{-1})G(e', e''; z^{-1})G(e'', e; z^{-1})) \Big\rangle = \sum_{N=1}^{\infty} \Big[P(e, e', e''; N) + 3P(e'', e', e; N) \Big] z^{2N},$$

$$\Big\langle \mathrm{Tr}(G(e, e'; z)G(e', e''; z)G(e'', e; z^{-1})) \Big\rangle = -2 \sum_{N=1}^{\infty} P_1(e, e', e''; N) z^{2N},$$

$$\Big\langle \mathrm{Tr}(G(e, e'; z)G(e', e''; z^{-1})G(e'', e; z)) \Big\rangle = -2 \sum_{N=1}^{\infty} P_1(e'', e, e'; N) z^{2N},$$

$$\Big\langle \mathrm{Tr}(G(e, e'; z^{-1})G(e', e''; z)G(e'', e; z)) \Big\rangle = -2 \sum_{N=1}^{\infty} P_1(e', e'', e; N) z^{2N},$$

$$\Big\langle \mathrm{Tr}(G(e, e'; z^{-1})G(e', e''; z^{-1})G(e'', e; z)) \Big\rangle = 2 \sum_{N=1}^{\infty} P_1(e'', e', e; N) z^{2N},$$

$$\Big\langle \mathrm{Tr}(G(e, e'; z^{-1})G(e', e''; z)G(e'', e; z^{-1})) \Big\rangle = 2 \sum_{N=1}^{\infty} P_1(e', e, e''; N) z^{2N},$$

$$\Big\langle \mathrm{Tr}(G(e, e'; z)G(e', e''; z^{-1})G(e'', e; z^{-1})) \Big\rangle = 2 \sum_{N=1}^{\infty} P_1(e, e'', e'; N) z^{2N}. \tag{3.287}$$

For the first term with only zs there are four possible paths: in a loop connecting e, e', e'' go from e to e' with one additional loop, then fo from e' to e'' and from e'' to e. There are two other contributions like this where the full loop starts at e', e''. In the fourth contribution, a loop going from e, e'', e' is involved. The second term traverses only the part of the loop connecting e, e', e'' twice, which is why the probability $P_1(e, e', e''; N)$ for e, e', e'' in a loop of arbitrary length appears with N being the distance from e to e''. The prefactor 2 is obtained as in the $q = 2$ case. The definitions of the probabilities appearing in this expression can be found in Tab. 3.3.

This gives

$$(2\pi)^3 \mathcal{D}_{(3)}(e, e', e''; z) = \sum_{N=1}^{\infty} \Big[-4P(e, e', e''; N) - 4P(e, e'', e'; N)$$
$$+ 6P_1(e, e', e''; N) + 6P_1(e, e'', e'; N) \Big] z^{2N} \tag{3.288}$$

for the correlation function. Note that both P and P_1 appear fully symmetrized in their arguments in this expression. It is convenient to use the convention that all probabilities appearing as $\bar{P}$ should be understood as symmetrized over the link arguments.

For $z = 1$, the expression simplifies to:

$$(2\pi)^3 \mathcal{D}_{(3)}(e, e', e''; z) = 4\bar{P}(e, e', e''), \tag{3.289}$$

since $\sum \bar{P}(e, e', e''; N) = \bar{P}(e, e', e'')$ and $\sum \bar{P}_1(e, e', e''; N) = \bar{P}(e, e', e'')$. This implies the interesting decomposition

$$(2\pi)^3 \mathcal{D}_{(3)}(e, e', e''; z) = (2\pi)^3 \mathcal{D}_{(3)}(e, e', e''; z = 1) + \sum_{N=1}^{\infty} \Big[8\bar{P}(e, e', e''; N) - 12\bar{P}_1(e, e', e''; N) \Big] (1 - z^{2N}). \tag{3.290}$$

The first term on the RHS does not scale with energy γ, but has nontrivial $r^{-\frac{3}{4}}$ scaling. This is related to the multifractal scaling dimensions $x_{(3)} = 0$ by Weyl symmetry and $\Delta_{(3)} = -\frac{3}{4}$. As indicated in above remark, the $\bar{P}, \bar{P}_1$ are defined as P, P_1 fully symmetrized over their arguments e, e', e''.

(2,1) In the second case, there are two spin traces:

$$\left\langle \text{Tr}(G(e,e';z)G(e',e;z))\text{Tr}(G(e'',e'';z))\right\rangle = \sum_{N=1}^{\infty} \left[P(e,e',e'';N) + P(e,e'',e';N) \right] z^{2N}$$

$$+ 2\sum_{N=1}^{\infty} P(e,e';N|e'';N'')z^{2N}z^{2N''} - 4\sum_{N} P(e,e';N)z^{2N},$$

$$\left\langle \text{Tr}(G(e,e';z^{-1})G(e',e;z^{-1}))\text{Tr}(G(e'',e'';z))\right\rangle = \sum_{N=1}^{\infty} \left[P(e,e',e'';N) + P(e,e'',e';N) \right] z^{2N}$$

$$+ 2\sum_{N=1}^{\infty} P(e,e';N|e'';N'')z^{2N}z^{2N''} - 4\sum_{N} P(e,e';N)z^{2N},$$

$$\left\langle \text{Tr}(G(e,e';z)G(e',e;z))\text{Tr}(G(e'',e'';z^{-1}))\right\rangle = -\sum_{N=1}^{\infty} \left[P(e,e',e'';N) + P(e,e'',e';N) \right] z^{2N}$$

$$- 2\sum_{N=1}^{\infty} P(e,e';N|e'';N'')z^{2N}z^{2N''},$$

$$\left\langle \text{Tr}(G(e,e';z^{-1})G(e',e;z^{-1}))\text{Tr}(G(e'',e'';z^{-1}))\right\rangle = -\sum_{N=1}^{\infty} \left[P(e,e',e'';N) + P(e,e'',e';N) \right] z^{2N}$$

$$- 2\sum_{N=1}^{\infty} P(e,e';N|e'';N'')z^{2N}z^{2N''},$$

$$\left\langle \text{Tr}(G(e,e';z)G(e',e;z^{-1}))\text{Tr}(G(e'',e'';z))\right\rangle = 2\sum_{N=1}^{\infty} P_1(e,e';N|e'';N'')z^{2N}z^{2N''} - 4\sum_{N} P_1(e,e';N)z^{2N},$$

$$\left\langle \text{Tr}(G(e,e';z^{-1})G(e',e;z))\text{Tr}(G(e'',e'';z))\right\rangle = 2\sum_{N=1}^{\infty} P_1(e,e';N|e'';N'')z^{2N}z^{2N''} - 4\sum_{N} P_1(e,e';N)z^{2N},$$

$$\left\langle \text{Tr}(G(e,e';z)G(e',e;z^{-1}))\text{Tr}(G(e'',e'';z^{-1}))\right\rangle = -2\sum_{N=1}^{\infty} P_1(e,e';N|e'';N'')z^{2N}z^{2N''},$$

$$\left\langle \text{Tr}(G(e,e';z^{-1})G(e',e;z))\text{Tr}(G(e'',e'';z^{-1}))\right\rangle = -2\sum_{N=1}^{\infty} P_1(e,e';N|e'';N'')z^{2N}z^{2N''}. \tag{3.291}$$

Here $P(e,e';N|e'';N'')$ is the probability to find e,e' in a loop of length N and e'' in a distinct loop of length N''. The function $P_1(e,e';N|e'';N'')$ is similar, the length $N_{ee'} = N$ of the path from e to e' is fixed in this case. The prefactor 2 is obtained as in the $q = 2$ case. The definitions of the probabilities appearing in this expression can be found in Tab. 3.3.

This gives

$$(2\pi)^3 \mathcal{D}_{(2,1)}(e,e',e'';z) = 4\sum_{N=1}^{\infty} \left[P(e,e',e'';N) + P(e,e'',e';N) \right] z^{2N}$$

$$+ 8\sum_{N,N''=1}^{\infty} \left[P(e,e';N|e'';N'') - P_1(e,e';N|e'';N'') \right] z^{2N}z^{2N''} - 8\sum_{N=1}^{\infty} \left[P(e,e';N) - P_1(e,e';N) \right] z^{2N}. \tag{3.292}$$

For $z = 1$, the expression simplifies to:

$$(2\pi)^3 \mathcal{D}_{(2,1)}(e, e', e''; z = 1) = 8\bar{P}(e, e', e''),\qquad(3.293)$$

since $\sum_N \left(P(\ldots; N) - P_1(\ldots; N) \right)$ vanishes. One can again split the $z = 1$ part from the correlation function

$$(2\pi)^3 \mathcal{D}_{(2,1)}(e, e', e''; z) = (2\pi)^3 \mathcal{D}_{(2,1)}(e, e', e''; z = 1) - 4 \sum_{N=1}^{\infty} \left[P(e, e', e''; N) + P(e, e'', e'; N) \right] (1 - z^{2N})$$

$$- 8 \sum_{N=1}^{\infty} \left[\sum_M \left(P(e, e'; N - M | e''; M) - P_1(e, e'; N - M | e''; M) \right) \right] (1 - z^{2N})$$

$$+ 8 \sum_{N=1}^{\infty} \left[P(e, e'; N) - P_1(e, e'; N) \right] (1 - z^{2N}).\qquad(3.294)$$

(1,1,1) In the last case, each Green's function is enclosed by a trace:

$$\left\langle \mathrm{Tr}(G(e, e; z)) \mathrm{Tr}(G(e', e'; z)) \mathrm{Tr}(G(e'', e''; z)) \right\rangle = 2^3 - 2^2 \sum_N \left[P(e; N) + P(e'; N) + P(e''; N) \right] z^{2N}$$

$$+ 2 \sum_{NN'} \left[P(e; N | e'; N') + P(e; N | e''; N') + P(e'; N | e''; N') \right] z^{2N} z^{2N'}$$

$$+ 2 \sum_N \left[P(e, e'; N) + P(e', e''; N) + P(e, e''; N) \right] z^{2N} - \sum_{NN'N''} P(e; N | e'; N' | e''; N'') z^{2N} z^{2N'} z^{2N''}$$

$$- \sum_{NN'} \left[P(e, e'; N | e''; N') + P(e, e''; N | e'; N') + P(e', e''; N | e; N') \right] z^{2N} z^{2N'},$$

$$\left\langle \mathrm{Tr}(G(e, e; z)) \mathrm{Tr}(G(e', e'; z)) \mathrm{Tr}(G(e'', e''; z^{-1})) \right\rangle = 2^2 \sum_N \left[P(e''; N) \right] z^{2N}$$

$$- 2 \sum_{NN'} \left[P(e; N | e''; N') + P(e'; N | e''; N') \right] z^{2N} z^{2N'}$$

$$- 2 \sum_N \left[P(e, e'; N) + P(e, e''; N) + P(e, e''; N) \right] z^{2N} + \sum_{NN'N''} P(e; N | e'; N' | e''; N'') z^{2N} z^{2N'} z^{2N''}$$

$$+ \sum_{NN'} \left[P(e, e'; N | e''; N') + P(e, e''; N | e'; N') + P(e', e''; N | e; N') \right] z^{2N} z^{2N'},$$

$$\left\langle \mathrm{Tr}(G(e, e; z)) \mathrm{Tr}(G(e', e'; z^{-1})) \mathrm{Tr}(G(e'', e''; z^{-1})) \right\rangle = 2 \sum_{NN'} P(e'; N | e''; N') z^{2N} z^{2N'}$$

$$+ 2 \sum_N P(e', e''; N) z^{2N} - \sum_{NN'N''} P(e; N | e'; N' | e''; N'') z^{2N} z^{2N'} z^{2N''}$$

$$- \sum_{NN'} \left[P(e, e'; N | e''; N') + P(e, e''; N | e'; N') + P(e', e''; N | e; N') \right] z^{2N} z^{2N'},$$

$$\left\langle \mathrm{Tr}(G(e, e; z^{-1})) \mathrm{Tr}(G(e', e'; z^{-1})) \mathrm{Tr}(G(e'', e''; z^{-1})) \right\rangle = \sum_{NN'N''} P(e; N | e'; N' | e''; N'') z^{2N} z^{2N'} z^{2N''}$$

$$+ \sum_{NN'} \left[P(e, e'; N | e''; N') + P(e, e''; N | e'; N') + P(e', e''; N | e; N') \right] z^{2N} z^{2N'}.\qquad(3.295)$$

As indicated in Tab. 3.3, here $P(e; N)$ stands for the probability of a loop of length N running through the link e. With $P(e; N | e'; N')$ the probability of e, e' being in distinct loops of length N, N' is

meant, whereas $P(e, e'; N)$ is the probability of e, e' being in the same loop of length N. Additionally, $P(e; N|e'; N'|e''; N'')$ is needed where e, e', e'' are in distinct loops. Finally for $P(e, e'; N|e''; N')$ the links e, e' are in a loop of length N and e'' is in a distinct loop of length N'. This means

$$(2\pi)^3 \mathcal{D}_{(1,1,1)}(e, e', e''; z) = 8 - 8 \sum_N \left[P(e; N) + P(e'; N) + P(e''; N) \right] z^{2N}$$

$$+ 8 \sum_{NN'} \left[P(e; N|e'; N') + P(e; N|e''; N') + P(e'; N|e''; N') \right] z^{2N} z^{2N'}$$

$$- 8 \sum_{NN'N''} P(e; N|e'; N'|e''; N'') z^{2N} z^{2N'} z^{2N''} + 8 \sum_N \left[P(e, e'; N) + P(e', e''; N) + P(e, e''; N) \right] z^{2N}$$

$$- 8 \sum_{NN'} \left[P_-(e, e'; N|e''; N') + P_-(e, e''; N|e'; N') + P_-(e', e''; N|e; N') \right] z^{2N} z^{2N'}. \tag{3.296}$$

With the identity

$$\sum_{N'N''} P(e; N|e'; N'|e''; N'') + \sum_{N'} \left[P(e, e'; N|e''; N') + P(e, e''; N|e'; N') + P(e', e''; N|e; N') \right]$$

$$+ P(e, e', e''; N) + P(e, e'', e'; N) = P(e; N) \tag{3.297}$$

stating that a loop running through e of length N can either run through two other points e', e'', one of them, or just through e, one can find:

$$(2\pi)^3 \mathcal{D}_{(1,1,1)}(e, e', e''; 1) = 16 \bar{P}(e, e', e''). \tag{3.298}$$

Once more, one can split off the $z = 1$ contribution in the correlation function to obtain:

$$(2\pi)^3 \mathcal{D}_{(1,1,1)}(e, e', e''; z) = (2\pi)^3 \mathcal{D}_{(1,1,1)}(e, e', e''; 1) + 8 \sum_N \left[P(e; N) + P(e'; N) + P(e''; N) \right] (1 - z^{2N})$$

$$- 8 \sum_N \left[\sum_M \left(P(e; N - M|e'; M) + P(e'; N - M|e''; M) + P(e; N - M|e''; M) \right) \right] (1 - z^{2N})$$

$$- 8 \sum_N \left[P(e, e'; N) + P(e', e''; N) + P(e, e''; N) \right] (1 - z^{2N}) + 8 \sum_{K+M+L=N} P_-(e; L|e', M|e''; K)(1 - z^{2N})$$

$$+ 8 \sum_N \left[\sum_M \left(P(e, e'; N - M|e''; M) + P(e, e''; N - M|e'; M) + P(e', e''; N - M|e; M) \right) \right] (1 - z^{2N}). \tag{3.299}$$

3.8.3 Percolation Analytics

In the following lines the connection of the multifractal exponents $x_{(1)}$, $x_{(1,1)}$ to the scaling dimensions x_n^{hull} of hull operators [214] in classical percolation theory is motivated. For this purpose, the scaling behavior of the probabilities P from Tab. 3.3 needs to be derived.

In Ref.[214] the scaling dimensions of the n-hull operators are introduced as:

$$x_n^{\text{hull}} = \frac{4n^2 - 1}{12}, \qquad x_1^{\text{hull}} = \frac{1}{4}, \qquad x_2^{\text{hull}} = \frac{5}{4}, \qquad x_3^{\text{hull}} = \frac{35}{12}. \tag{3.300}$$

These are related to the probability $P_n \sim (p - p_c)^{\nu x_n^{\mathrm{hull}}}$ for n infinite clusters (their boundaries form the loops of interest here) to touch at a point [214] in a system detuned from the percolation threshold p_c. The P_k can be related to the more complicated conditional probabilities from Tab. 3.3 of interest here. The argument goes as follows: replacing the correlation length introduced due to finite distance from the percolation threshold $\xi_p \sim (p - p_c)^{-\nu}$ by the length scale $\xi_N \sim N^{\frac{4}{7}}$ related to the loop length N, one finds $P_n^{(N)} \sim (\xi_N)^{-x_n^{\mathrm{hull}}}$ for large (compared to (ξ_N)) clusters to touch in a system at criticality. In particular, this means $P_1^{(N)} \sim N^{-\frac{1}{7}}$ and $P_2^{(N)} \sim N^{-\frac{5}{7}}$.

The probability $P_1^{(N)}$ to find a large cluster near a point X includes all long loops $P_1(N) \sim \int_N \mathrm{d}N \, P(e; N)$. Therefore dividing by N relates P_1 to the probability $P(e; N) \sim \frac{1}{N} P_1^{(N)} \sim N^{-\frac{8}{7}}$ for finding a long loop running through a link e. The same argumentation relates $P(e, e'; N_{ee'} \sim N, N_{e'e} \sim N)$ and $P(e; N|e'; N' \sim N)$ to $N^{-2} P_2^{(N)}$. For higher functions analogous arguments exist.

The probabilities $P(e, e'; N)$ and $P_1(e, e'; N)$ can be obtained summing over $P(e, e'; N_{ee'} = N, N_{e'e} = N')$ for different (N, N') domains. This also includes $P(e; N|e'; N' \ll N)$ with $N_r \sim r^{\frac{7}{4}}$, where only one path is part of a large cluster. By above argument, this function is then determined by the one-hull operator $P(e; N|e'; N' \ll N) \sim N^{-\frac{8}{7}}$.

These results were derived in continuum field theory, the probability of a loop of length N going through links $e, e', e'', \ldots$ nearby a node X with separation $r \ll N^{\frac{4}{7}}$ is closely related to the probability of a loop of length N passing the node X: $P(e, e', e'', \ldots; N) \sim N^{-\frac{8}{7}}$. To find the appropriate r scaling, one can eliminate N by integration and repeat above argument. The probabilities $P_n^{(r)} \sim (r)^{-x_n^{\mathrm{hull}}}$ generalize as well to touching clusters large compared to r. This means that $\int_{N_r} \mathrm{d}N P(e, e', e'', \ldots; N) \sim (P_1^{(r)})^n$. As a consequence one finds $P(e, e', e'', \ldots; N) \sim r^{(1-n)x_1^{\mathrm{hull}}} N^{-\frac{8}{7}}$ for $N \gg r^{\frac{7}{4}}$.

As another example consider the function $P(e; N|e'; N' \sim N) \sim N^{-\frac{19}{7}}$ in this regime of large $N \gg N_r$. The integral $\int_{N_r} \mathrm{d}N \mathrm{d}N' P(e; N|e'; N' \sim N)$ is dominated by $N \sim N'$ and scales like $(P_1^{(r)})^2$. This means that $P(e; N|e'; N' \sim N) \sim r^{x_2^{\mathrm{hull}} - 2x_1^{\mathrm{hull}}} N^{-\frac{19}{7}}$.

For all other functions in Tab. 3.3, the scaling properties in the different parameter regimes can be found by applying similar arguments.

3.8.3.1 The case $q = 1$

In Sec. 3.8.2, the derivation of the percolation expression for the LDOS

$$(\pi)\mathcal{D}_{(1)}(e; z) = \sum_N P(e; N)(1 - z^{2N}) \tag{3.301}$$

is sketched.

By the argument given above, $P(e; N) = P(N) \sim N^{-\frac{8}{7}}$ at large $N \gg 1$. One can use the following coarse estimate for the percolation sum, since for $q = 1$ there is only one scaling exponent:

$$\sum_N N^{-\frac{8}{7}} r^{-\frac{1}{4}} (1 - z)^{2N} \sim \int_{\gamma^{-1}}^{\infty} dN \, N^{-\frac{8}{7}} (1 - z^{2N})$$

$$\sim \int_{\gamma^{-1}}^{\infty} dN \, N^{-\frac{8}{7}} \sim \gamma^{-\frac{1}{7}}. \tag{3.302}$$

Hence it holds

$$\mathcal{D}_{(1)}(e; z) \sim \gamma^{\frac{1}{7}} \sim (a/\xi_\gamma)^{x_1^{\mathrm{hull}}}, \tag{3.303}$$

where $\xi_\gamma \sim (1/\gamma)^{\frac{4}{7}}$ is the correlation length, $x_1^{\text{hull}} = \frac{1}{4}$ and a is the lattice constant. From this the relation $x_{(1)} = x_1^{\text{hull}}$ between the multifractal scaling exponent for the LDOS and the one hull operator follows.

3.8.3.2 The case $q = 2$

From the above scaling consideration it follows that $\mathcal{D}_{(2)}, \mathcal{D}_{(1,1)}$ must contain the subleading scaling. One can start from the percolation expressions obtained above:

$$(\pi)^2 \mathcal{D}_\lambda(e', e; z) = \sum_N \mathcal{D}_\lambda^{(N)}(e, e')(1 - z^{2N}),$$

$$\mathcal{D}_{(2)}^{(N)}(e, e') = \left[P(e', e; N) - \frac{1}{2} P_1(e, e'; N) - \frac{1}{2} P_1(e', e; N) \right],$$

$$\mathcal{D}_{(1,1)}^{(N)}(e, e') = \left[P(e', e; N) + P_-(e', e; N) \right]. \tag{3.304}$$

The symbol $P(e, e'; N)$ denotes the probability to find e, e' in the same loop of length N. Similarly $P_1(e, e'; N)$ stands for the probability to find e, e' in the same loop where N is the length from e to e'. One also needs the probability $P(e, N)$ to find e in a loop of length N and $P(e; N|e'; N')$ to find e in a loop of length N and e' in a distinct loop of length N' (see Tab. 3.3).

On the one hand, P and P_1 are the building blocks of the Fock-term $\mathcal{D}_{(2)}$. On the other hand by the argument in the beginning of this section, only x_1^{hull} and x_2^{hull} contribute to P and P_1. Both of these arguments indicate that these functions are linear combinations of two pure power laws. Moreover this holds for P_- appearing in the Hartree term $\mathcal{D}_{(1,1)}$ as well.

Consequently, the following scaling asymptotics must hold:

$$P(e, e'; N) \approx N^{-\frac{8}{7}} r^{-\frac{1}{4}} \left(\#_1 + \#_2 (rN^{-\frac{4}{7}})^y \right),$$

$$P_1(e, e'; N) \approx N^{-\frac{8}{7}} r^{-\frac{1}{4}} \left(\#_3 + \#_4 (rN^{-\frac{4}{7}})^y \right),$$

$$P_-(e, e'; N) \approx N^{-\frac{8}{7}} r^{-\frac{1}{4}} \left(\#_5 + \#_6 (rN^{-\frac{4}{7}})^y \right). \tag{3.305}$$

Here the first term comes from the one hull contributions and the second from the two hull operator, therefore $y = x_2^{\text{hull}} - x_1^{\text{hull}}$. The constants $\#_i$ are numerical coefficients and the second term is a small correction in the scaling limit $r^{\frac{7}{4}} \ll N$ since $y > 0$.

For the leading contributions, one can even make statements about the relations of coefficients:

$$P(e, e'; N) = \sum_{M=0}^\infty P(e, e'; N_{e,e'} = N - M, N_{e',e} = M)$$

$$\approx \sum_{M=0}^{N_r} P(e, e'; N_{e,e'} = N, N_{e',e} = M) + \sum_{M=0}^{N_r} P(e, e'; N_{e,e'} = M, N_{e',e} = N) \sim N^{-\frac{8}{7}},$$

$$P_1(e, e'; N) = \sum_{M=0}^\infty P(e, e'; N_{e,e'} = N, N_{e',e} = M) \approx \sum_{M=0}^{N_r} P(e, e'; N_{e,e'} = N, N_{e',e} = M) \sim N^{-\frac{8}{7}}.$$

$$\tag{3.306}$$

In each sum, only the terms responsible for leading scaling are kept. These originate from the boundaries $N' \sim 1$ or $N \sim 1$ of the summation domains:

$$P(e, e'; N_{e,e'} = N, N_{e',e} = N') \approx c \begin{cases} r^{\frac{3}{4}} N^{-\frac{19}{7}}, & N \sim N' \gg r^{\frac{7}{4}} \\ r^{-\frac{1}{4}} N^{-\frac{8}{7}}, & N' \sim r^{\frac{7}{4}}, N \gg r^{\frac{7}{4}} \\ r^{-\frac{1}{4}} (N')^{-\frac{8}{7}}, & N \sim r^{\frac{7}{4}}, N' \gg r^{\frac{7}{4}} \end{cases} . \tag{3.307}$$

It follows $P(e, e'; N) \approx P_1(e, e'; N) + P_1(e', e; N)$ for large N.

Consequently it holds

$$P(e, e'; N) \approx cN^{-\frac{8}{7}} r^{-\frac{1}{4}} \left(1 + \#_1 (rN^{-\frac{4}{7}}) \right),$$

$$P_1(e, e'; N) \approx cN^{-\frac{8}{7}} r^{-\frac{1}{4}} \left(\frac{1}{2} + \#_2 (rN^{-\frac{4}{7}}) \right), \tag{3.308}$$

here the $\#_i$ are numerical coefficients distinct from those above in Eq. (3.305). The percolation numerics in Sec. 3.8.4 shows that for $r = 1$ these asymptotics describe the actual expressions very well even for small $N \sim 1$.

Similarly to the considerations for $P(e, e'; N_{e,e'} = N, N_{e',e} = N')$, for $P(e; N|e'; N')$ the asymptotic scaling behavior depends on the parameter region:

$$P(e; N|e'; N') \approx c' \begin{cases} r^{\frac{3}{4}} N^{-\frac{19}{7}}, & N \sim N' \gg r^{\frac{7}{4}} \\ r^{-\frac{1}{4}} N^{-\frac{8}{7}}, & N' \sim r^{\frac{7}{4}}, N \gg r^{\frac{7}{4}} \\ r^{-\frac{1}{4}} (N')^{-\frac{8}{7}}, & N \sim r^{\frac{7}{4}}, N' \gg r^{\frac{7}{4}} \end{cases} . \tag{3.309}$$

In the auxiliary function P_- from Eq. (3.285) the leading scaling form the boundaries $N, N' \sim 1$ cancels exactly:

$$P_-(e, e'; N) \approx c'' r^{\frac{3}{4}} N^{-\frac{12}{7}}. \tag{3.310}$$

Having obtained asymptotics for all probabilities occurring in Hartree and Fock term, next one has to think about how to evaluate the sums over loop length N.

With the scaling form (3.308) one finds for sums over N of the power laws occuring in the correlation functions (3.284), (3.281):

$$\sum_N N^{-\frac{8}{7}} r^{-\frac{1}{4}} (rN^{-\frac{4}{7}})^x (1 - z^{2N}) \sim \int_{h\, r^{\frac{7}{4}}}^{\infty} dN \; N^{-\frac{8}{7}} r^{-\frac{1}{4}} (rN^{-\frac{4}{7}})^x (1 - z^{2N})$$

$$= 2^{\frac{1}{7} + \frac{4}{7}x} \Gamma(-\frac{1}{7} - \frac{4}{7}x) \gamma^{\frac{1}{7} + \frac{4}{7}x} r^{-\frac{1}{4} + x} + \mathcal{O}(\gamma\, r^{\frac{5}{4}}) \tag{3.311}$$

Note that the regulator h cutting off the integral at the lower boundary, where the scaling form does not hold any more, does not appear in the result at this order. By choosing small γ the errors in this approximation (conversion of sum to integral, use of asymptotic scaling form) get arbitrarily small. Hence for $x = 0, 1$ (or more precisely $x < \frac{3}{2}$) this calculation justifies the identification of power law terms in N in $\mathcal{D}_\lambda^{(N)}(e, e')$ and power laws in γ in $\mathcal{D}_\lambda(e, e'; z)$.

One can rewrite this introducing the correlation length $\xi_\gamma = \gamma^{-\frac{4}{7}}$ and apply the result directly to the Fock term:

$$\mathcal{D}_{(2)}(e, e'; z) \sim \xi_\gamma^{-\frac{1}{2}} \left(c_0 (r/\xi_\gamma)^{-\frac{1}{4}} + c_1 (r/\xi_\gamma)^{\frac{3}{4}} \right). \tag{3.312}$$

At this stage, one can already read off $\Delta_{(2)} = -\frac{1}{4}$ and $\Delta_{(1,1)} = \frac{3}{4}$. In the Hartree term, this treatment is not sufficient, since it does not include the double sum of the joined probability $P(e, N|e', N')$ hidden in the auxiliary function $P_-(e', e; N)$. The summation there can be treated with

$$\sum_N P_-(e', e; N)(1 - z^{2N}) \sim \int_{\gamma^{-1}}^\infty dN \; N^{-\frac{12}{7}} r^{\frac{3}{4}}$$

$$\sim \gamma^{\frac{5}{7}} r^{-\frac{5}{4}} = \xi_\gamma^{-\frac{1}{2}} (r/\xi_\gamma)^{\frac{3}{4}}. \tag{3.313}$$

As claimed above, the contribution from P_- show subleading $\Delta_{(1,1)} = \frac{3}{4}$ scaling.

Finally this has the consequence:

$$\mathcal{D}_{(1,1)}(e, e'; z) \sim \xi_\gamma^{-\frac{1}{2}} \left(2c_0 (r/\xi_\gamma)^{-\frac{1}{4}} + c_2 (r/\xi_\gamma)^{\frac{3}{4}} \right). \tag{3.314}$$

An improved estimate of the sums is necessary in order to also confirm the ratio $c_1 = -c_2$ expected from the RG analysis (3.268). The percolation analytics nicely confirm $\Delta_{(2)} = -\frac{1}{4}$ and $\Delta_{(1,1)} = \frac{3}{4}$ or $x_{(2)} = \frac{1}{4}$ and $x_{(1,1)} = \frac{5}{4}$ found in the SQH numerics in Sec. 3.7.3, compare Tab. 3.2.

Corrections to the leading scaling of probabilities in classical percolation are common and have been studied in Refs. [215–218] for other observables. An astonishing cancellation mechanism must be in place to let only the pure $\Delta_{(2)}$ and $\Delta_{(1,1)}$ pure power laws expected from the multifractality picture in these correlation functions survive.

3.8.3.3 The case $q = 3$

For the higher order correlation functions, one can proceed with the scaling analysis the same way. The first thing to note is that the correlators in Eqs. (3.290), (3.294) and (3.299) all admit the decomposition:

$$\mathcal{D}_\lambda(e, e', e''; z) = \mathcal{D}_\lambda(e, e', e''; z = 1) + \sum_{N=1}^\infty \mathcal{D}_\lambda^{(N)}(e, e', e'')(1 - z^{2N}). \tag{3.315}$$

The first term

$$\mathcal{D}_\lambda(e, e', e''; z = 1) = c_\lambda \sum_N P(e, e', e''; N) \sim r^{-\frac{3}{4}} \gamma^0 \tag{3.316}$$

does not scale with energy (corresponding to $x_{(3)} = 0$) but with $r^{-\frac{3}{4}}$ (corresponding to $\Delta_{(3)} = -\frac{3}{4}$).

In order to reproduce the expected subleading multifractal exponent $x_{(2,1)} = \frac{5}{4}$, the coefficients $\mathcal{D}_\lambda^{(N)}(e, e', e'')$ have to show $r^{\frac{1}{2}} N^{\frac{12}{7}}$ scaling. However, the leading scaling of probabilities appearing in $\mathcal{D}_\lambda^{(N)}(e, e', e'')$ is $P(e, e', e''; N) \sim r^{-\frac{1}{2}} N^{-\frac{8}{7}}$. These terms must cancel out to be consistent with Weyl symmetry $x_{(2,1)} = x_{(1,1)}$.

In the following, this cancellation in the correlation functions $\mathcal{D}^\lambda$ is shown for $\lambda = (3)$, $(2, 1)$ and $(1, 1, 1)$.

(3) From Eq. (3.290) one can read off the decomposition (3.315) for $\lambda = (3)$:

$$\mathcal{D}_{(3)}^{(N)}(e, e', e'') = 8\bar{P}(e, e', e''; N) - 12\bar{P}_1(e, e', e''; N). \tag{3.317}$$

Here $\bar{P}$ stands for symmetrization over permutations of all links.

One can use an analogous representation of P and P_1 as in the $q = 2$ case:

$$P(e, e', e''; N) = \sum_{MK} P(e, e', e''; N_{ee'} = N - M - K, N_{e'e''} = M, N_{e''e} = K),$$

$$P_1(e, e', e''; N) = \sum_{MK} P(e, e', e''; N_{ee'} = N - M, N_{e'e''} = M, N_{e''e} = K). \tag{3.318}$$

The dominant contributions arises in the region where one summation variable is $\approx N$ and the other two are small $\approx N_r \ll N$. One finds

$$P(e, e', e''; N) \approx \sum_{K, M \approx N_r} P(e, e', e''; N_{ee'} = N, N_{e'e''} = M, N_{e''e} = K)$$

$$+ \sum_{M \approx N_r, K \approx N - N_r} P(e, e', e''; N_{ee'} = N - M, N_{e'e''} = M, N_{e''e} = K)$$

$$+ \sum_{K \approx N_r, M \approx N - N_r} P(e, e', e''; N_{ee'} = K, N_{e'e''} = M, N_{e''e} = N),$$

$$P_1(e, e', e''; N) \approx \sum_{M \approx N_r, K \approx N_r} P(e, e', e''; N_{ee'} = N - M, N_{e'e''} = M, N_{e''e} = K)$$

$$+ \sum_{M \approx N - N_r, K \approx N_r} P(e, e', e''; N_{ee'} = N - M, N_{e'e''} = M, N_{e''e} = K). \tag{3.319}$$

This implies for the ratio of the leading coefficients:

$$2P(e, e', e''; N) \approx P_1(e, e', e''; N) + P_1(e'', e, e'; N) + P_1(e', e'', e; N),$$

$$2P(e, e', e''; N) \approx 3P_1(e, e', e''; N), \tag{3.320}$$

which causes the leading order $r^{-\frac{1}{2}} N^{-\frac{8}{7}}$ cancellation in $\mathcal{D}_{(3)}^{(N)}$ from Eq. (3.317).

(2,1) From Eq. (3.294) one can read off the decomposition (3.315) for $\lambda = (2, 1)$:

$$\mathcal{D}_{(2,1)}^{(N)}(e, e', e'') = -4(\bar{P}(e, e', e''; N) + \bar{P}(e, e'', e'; N))$$

$$- 8 \sum_M \left(\bar{P}'(e, e'; N - M | e''; M) - \bar{P}_1'(e, e'; N - M | e''; M) \right) + 8(P(e, e'; N) - \bar{P}_1(e, e'; N)) \tag{3.321}$$

The symmetrization in this case is more complicated, since this correlation function treats e'' differently than e, e'. In certain cases the symmetrization $\bar{P}'$ over e, e' is needed, in others symmetrization $\bar{P}$ over all links can be used as well.

There are the exact identities:

$$P(e, e'; N) = P(e, e', e''; N) + P(e, e'', e'; N) + \sum_M P(e, e'; N | e''; M),$$

$$P_1(e, e'; N) = P_1(e, e'', e'; N) + P(e, e', e''; N_{ee'} = N) + \sum_M P_1(e, e'; N | e''; M). \tag{3.322}$$

With these, it follows directly that

$$8(P(e, e'; N) - P_1(e, e'; N)) \approx 4P(e, e'; N)$$
$$\approx 4(P(e, e', e''; N) + P(e, e'', e'; N)) + 4\sum_M P(e, e'; N|e''; M). \quad (3.323)$$

As a consequence of this identity, the coefficients of the correlation function then become

$$\mathcal{D}_{(2,1)}^{(N)}(e, e', e'') \approx -4\sum_M \Big(2P(e, e'; N - M|e''; M) - 2P_1(e, e'; N - M|e''; M) - P(e, e'; N|e''; M) \Big)$$

$$\approx -4\sum_M \Big(P(e, e'; N|e''; M) + 2P(e, e'; M|e''; N) - 2P_1(e, e'; N|e''; M) - 2P_1(e, e'; M|e''; N) \Big). \quad (3.324)$$

The leading order term $\sim r^{-\frac{1}{2}} N^{-\frac{8}{7}}$ in this expression cancels, since $2P(e, e'; N|e''; M) \approx P_1(e, e'; N|e''; M)$ and $2P(e, e'; M|e''; N) \approx 2P_1(e, e'; M|e''; N)$ hold for large N and small M.

(1,1,1) From Eq. (3.294) one can read off the decomposition (3.315) for $\lambda = (2,1)$:

$$\mathcal{D}_{(1,1,1)}^{(N)}(e, e', e'') = 24\bar{P}(e; N) - 24\bar{P}(e, e'; N) - 24\sum_M \Big[\bar{P}(e, N - M|e', M) - \bar{P}(e, e'; N - M|e''; M) \Big]$$

$$+ 8\sum_{MK} P(e; N - M - K|e'; M|e''; K) \quad (3.325)$$

The bar $\bar{P}$ of a probability indicates symmetrization over all link permutations.

There are the exact identities:

$$\sum_{N'N''} P(e; N|e'; N'|e''; N'') + 3\sum_{N'} \bar{P}(e, e'; N|e''; N') + 2\bar{P}(e, e', e''; N) = P(e; N),$$

$$\sum_{N''} P(e; N|e'; N'|e''; N'') + P(e, e''; N|e'; N') + P(e; N|e', e''; N') = P(e, N|e', N'). \quad (3.326)$$

These put into each other lead to relations of the probabilities appearing in these coefficients:

$$3P(e; N) - 3P(e, e'; N) = 3\sum_{MK} P(e; N|e'; M|e''; K) + 6\sum_M P(e, e'; N|e''; M),$$

$$3P(e, N|e', N') - 6P(e, e''; N|e'; N') = 3\sum_{N''} P(e; N|e'; N'|e''; N''). \quad (3.327)$$

Using the exact identities, one finds:

$$\mathcal{D}_{(1,1,1)}^{(N)}(e, e', e'') = 24\sum_{MK} \bar{P}(e; N|e'; M|e''; K) + 48\sum_M \bar{P}(e, e'; N|e''; M) - 24\sum_M \bar{P}(e, e'; N - M|e''; M)$$

$$- 24\sum_{MK} \bar{P}(e; N - M|e'; M|e''; K) + 8\sum_{MK} P(e; N - M - K|e'; M|e''; K) \quad (3.328)$$

It is easy to see that the leading order $\sim r^{-\frac{1}{2}} N^{-\frac{8}{7}}$ cancels.

The treatment in this section confirms that $x_{(3)} = 0$ and $x_{(2,1)} = x_2^{\text{hull}} = \frac{5}{4}$. In the multifracality picture, these exponents can be derived directly from lower orders using Weyl symmetry $x_{(3)} = x_{(0)}$ and

$x_{(2,1)} = x_{(1,1)}$. It is intriguing to see how this Weyl symmetry emerges from the classical percolation calculation.

In principle one could try to find $x_{(1,1,1)}$ in this picture as well. However, the cancellations occuring are far more complicated and other corrections than the pure scaling of the hull operators might have to be taken into account. In the percolation simulations performed here, $z = x_{(1,1,1)} - x_{(1)}$ is not accessible due to insufficient averaging and finite size effects. See Tab. 3.4 for a summary.

3.8.4 Percolation Numerics

In this section, numerical simulations supporting the calculations from Sec. 3.8.3 are performed. For this purpose 10000 random disorder configurations in a classical system of linear size $L = 32768$ with periodic boundary conditions are analyzed statistically. A configuration is described by $L \times L$ binary degrees of freedom (black/white). The percolation threshold is $p_c = 0.5$ in 2D, this means black and white dots are to be distributed uniformly with equal probability. One can think about the degrees of freedom to sit at the nodes of the network. Black (white) means, the paths running through this node turn left (right). This is the distinction to the quantum network, where always both paths are taken weighted with different scattering amplitudes for left and right.

In the classical network, one obtains a set of closed loops for each configuration including all $2 \cdot L \cdot L$ links. The probabilities from Tab. 3.3 are then obtained by counting the number of loops satisfying the desired properties and averaging over disorder. These numerically obtained probabilities are compared to the analytical scaling expectations and the correlation functions $\mathcal{D}_\lambda$ are computed numerically.

3.8.4.1 The case $q = 1$

There is only the probability $P(e; N)$ in this order

$$(\pi)\mathcal{D}_{(1)}(e; \gamma) = \sum_N \underbrace{P(e; N)}_{=:\mathcal{D}_{(1)}^{(N)}}(1 - z^{2N}). \tag{3.329}$$

Interestingly, there are virtually no subleading corrections in the numerics (Fig. 3.5), the pure leading $N^{-\frac{8}{7}}$ behavior accurately describes the numerical data up to $N > 12$ very well. This agrees with the hull operator picture, where one does not expect contributions from other than the one-hull operator with dimension $x_1^{\text{hull}} = \frac{1}{4}$. In other words the LDOS scaling is given by $\mathcal{D}_{(1)}(e; \gamma) \sim \gamma^{\frac{1}{7}} = (\xi_\gamma)^{-x_1^{\text{hull}}}$. This implies $x_{(1)} = x_1^{\text{hull}}$ and relates the quantum mechanical multifractal scaling dimension at the SQH transition with a scaling dimension of a hull operator in classical percolation.

3.8.4.2 The case $q = 2$

In this order, one has to analyze:

$$(\pi)^2 \mathcal{D}_{(2)}(e', e; \gamma) = \sum_N \underbrace{\left[\bar{P}_1(e', e; N) - P(e', e; N)\right]}_{=:\mathcal{D}_{(2)}^{(N)}}(1 - z^{2N}), \tag{3.330}$$

$$(\pi)^2 \mathcal{D}_{(1,1)}(e', e; \gamma) \sim \sum_N \underbrace{P(e', e; N) + P_-(e', e; N)}_{=:\mathcal{D}_{(1,1)}^{(N)}}(1 - z^{2N}), \tag{3.331}$$
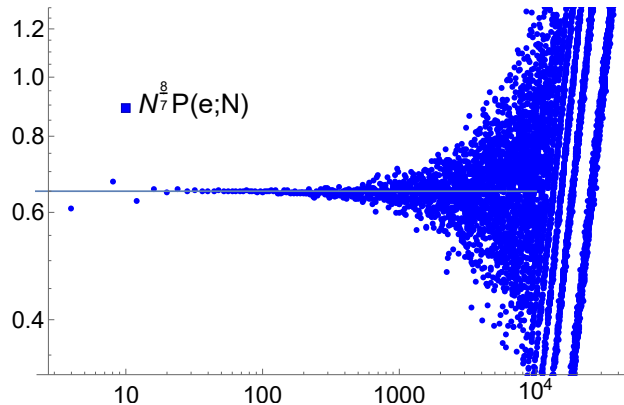
Figure 3.5: Scaling of the probability $P(e; N)$ (blue). Apparently, there are no subleading corrections, only the pure leading $N^{-\frac{8}{7}}$ behavior. The numerics were performed for $L = 32768$ and averaged over $C = 10000 \cdot 2L^2$ configurations (ensemble+system).

Table 3.4: Comparison of numerics in the SU(2) Chalker Coddington network (CCN) model at SQH critical point from Sec. 3.7 with expectations from generalized parabolicity hypothesis and the exact exponents from the percolation mapping assuming subleading scaling. The percolation numerics (see Fig. 3.6) is consistent with the CCN results. Generalized parabolicity is violated strongly in systems with linear size $L \leq 32768$.

	SU(2) CCN numerics	hull operator	percolation numerics	gen. parabolicity
$x_{(1)}$	0.25	$x_1^{\text{hull}} = \frac{1}{4}$	0.25	$\frac{1}{4}$
$x_{(2)}$	0.25	$x_1^{\text{hull}} = \frac{1}{4}$	0.25	$\frac{1}{4}$
$x_{(3)}$	0.0	$\equiv 0$	$\equiv 0$	0
$x_{(1,1)}$	1.25	$x_2^{\text{hull}} = \frac{5}{4}$	1.25	1
$x_{(2,1)}$	1.25	$x_2^{\text{hull}} = \frac{5}{4}$	1.25	1
$x_{(1,1,1)}$	1.91	?	?	$\frac{9}{4}$

compare Eq. (3.284) and Eq. (3.281).

One claim in the analytics section Sec. 3.8.3 is that the auxiliary function $P_-(e, e'; N)$ from Eq. (3.285) scales like $N^{\frac{12}{7}}$ for large N. In Fig. 3.6, data indicating $P_-(e, e'; N) \sim N^{\frac{12}{7}}$ is shown. A linear fit $P_-(e, e'; N) = cN^{y_-}$ is performed that finds $y_- \approx 1.05$. Consequently one can conclude that this numerical result agrees well with the analytic prediction $y = x_2^{\text{hull}} - x_1^{\text{hull}} = 1$.

From the RG analysis of the class-C NLSM, one would expect that $\mathcal{D}_{(1,1)} \approx 2\mathcal{D}_{(2)}$. In Fig. 3.6 the coefficients $\mathcal{D}_\lambda^{(N)}$ in front of $(1 - z^{2N})$ are evaluated numerically for $\mathcal{D}_{(2)}, \mathcal{D}_{(1,1)}$ as functions of loop lengths N. One can clearly observe the cancellation between $\mathcal{D}_{(1,1)}$ and $2\mathcal{D}_{(2)}$. The subleading exponent indeed satisfies $y \approx 0.97$ in agreement with $x_{(1,1)} \approx \frac{5}{4}$ or $\Delta_{(1,1)} \approx \frac{3}{4}$ from the SU(2) CCN model numerics.

Further it holds that the numerical results $y \approx 0.97$ and $y_- \approx 1.05$ and the analytical expectation $y = 1$ are all mutually consistent up to the numerical accuracy. The obtained relations $x_{(1)} = x_1^{\text{hull}} = \frac{1}{4}$ and $x_{(1,1)} = x_2^{\text{hull}} = \frac{5}{4}$ of multifractal scaling dimensions and hull operator dimensions in classical percolation also agree with the CCN numerical simulations performed in Sec. 3.7.3, see Tab. 3.4.
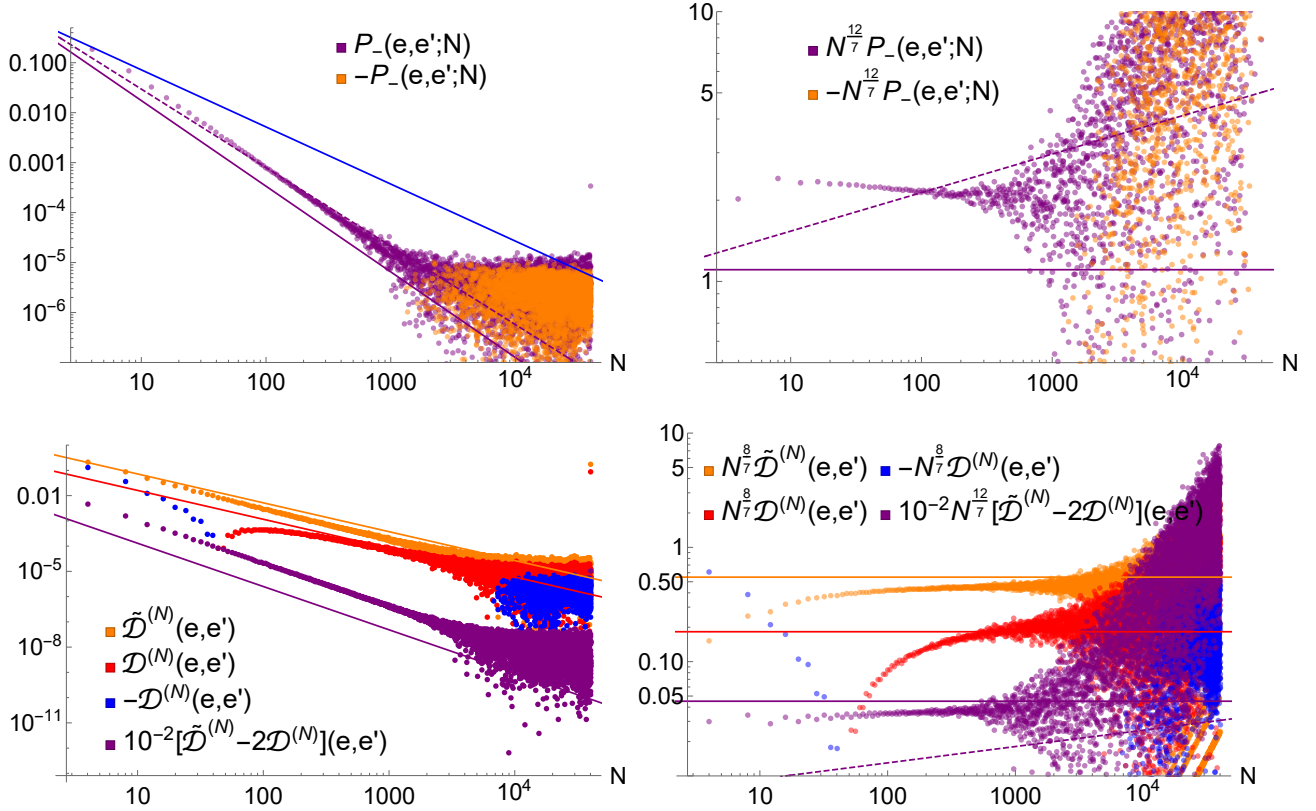
Figure 3.6: *Top panel:* The function $P_-(e, e'; N)$ defined in Eq. (3.284) for e, e' nearest neighbors. This P_- is not a probability and can assume negative values due to finite size effects and insufficient averaging (orange). Left panel: $P_-(e, e'; N)$ compared to different power laws: $N^{-\frac{8}{7}}$, $N^{-\frac{12}{7}}$ corresponding to $y = 1$ and $N^{-\frac{11}{7}}$ corresponding to $y = \frac{3}{4}$. Right panel: $P_-(e, e'; N)N^{\frac{12}{7}}$, deviations from this power law are small (compare to horizontal purple line). Purple dashed line represents $y^{\mathrm{para}} = \frac{3}{4}$ expectation from generalized parabolicity hypothesis, there are strong deviations. A linear fit of P_- yields $y_- \approx 1.05$ for $N < 500$. *Bottom panel:* Coefficients of Hartree $\mathcal{D}_{(1,1)}(e, e')$ term (orange), Fock term $\mathcal{D}_{(2)}(e, e')$ (red/blue) and Hartree minus two Fock (purple). The links e, e' are chosen to be either horizontal or vertical nearest neighbors. Left panel: comparison to $N^{-\frac{8}{7}}$ (orange, blue) $N^{-\frac{12}{7}}$ (purple) scaling. Right panel: the terms are normalized to the expected power law. Deviations for $H - 2F$ from pure $N^{-\frac{12}{7}}$ scaling are small. A linear fit of $H - 2F$ yields $y \approx 0.97$ for $N < 500$. The purple dashed line represents $y_{\mathrm{para}} = \frac{3}{4}$ which would hold for generalized parabolicity.

3.8.4.3 The case $q = 3$

In Sec. 3.8.3, the reader could observe, that each of the $q = 3$ correlation functions can be decomposed as:

$$(2\pi)^3 \mathcal{D}_{(\lambda)}(e, e', e''; z) = (2\pi)^3 \mathcal{D}_{(\lambda)}(e, e', e''; z = 1) + \sum_{N=1}^{\infty} \mathcal{D}_{(\lambda)}^{(N)}(e, e', e'')(1 - z^{2N}). \tag{3.332}$$

The $z = 1$ term is responsible for the leading $x_{(3)} = 0$ scaling. The coefficients $\mathcal{D}_{(\lambda)}^{(N)}(e, e', e'')$ in the second term contain the probabilities $P_1(e, e', e''; N), P(e, e', e''; N) \propto N^{-\frac{8}{7}} r^{-\frac{1}{2}}$ for $r < N^{\frac{4}{7}}$. Naively estimating the sum leads to $x_{(2,1)}^{\text{naive}} = \frac{1}{4}$ scaling, which would violate the Weyl symmetry relation $x_{(2,1)} = x_{(1,1)}$. There must be a cancellation $P(e, e', e'', N) \approx \frac{3}{2} P_1(e, e', e'', N)$ at large N, and the next to leading term must go as $N^{-\frac{12}{7}} r^{\frac{1}{2}}$ determined by x_2^{hull} in order for $x_{(2,1)} = x_{(1,1)}$ to hold.

The percolation simulations in Figs. 3.7 nicely confirm this expectation for the N scaling.

(3) Using the symmetrized notation for the probabilities, one can recast Eq. (3.290) to yield:

$$(2\pi)^3 \mathcal{D}_{(3)}(e, e', e''; z) = (2\pi)^3 \mathcal{D}_{(3)}(e, e', e''; z = 1) + \sum_{N=1}^{\infty} \mathcal{D}_{(3)}^{(N)}(e, e', e'')(1 - z^{2N}),$$

$$\mathcal{D}_{(3)}^{(N)}(e, e', e'') = 8\bar{P}(e, e', e''; N) - 12\bar{P}_1(e, e', e''; N). \tag{3.333}$$

The large N behavior of $\mathcal{D}_{(3)}^{(N)}(e, e', e'')$ is shown in Fig. 3.7. In this regime, $\mathcal{D}_{(3)}^{(N)}(e, e', e'')$ is negative. As expected the probabilities $\bar{P}, \bar{P}_1$ scale like $N^{\frac{8}{7}}$ for large N. Contrarily, $\mathcal{D}_{(3)}^{(N)}(e, e', e'')$ behaves like $N^{\frac{12}{7}}$ for large N, which confirms the cancellation mechanism proposed in Eq. (3.320) in Sec. 3.8.3.

(2,1) In Fig. 3.7, the same analysis for $\mathcal{D}_{(2,1)}^{(N)}(e, e', e'')$ is performed. For the correlation function from Eq. (3.294) one has to be careful, since e'' is not equivalent to e, e' in the definition of $\mathcal{D}_{(2,1)}$. Therefore symmetrization has to be restricted to interchanging e, e'. In case where this difference becomes important the restricted symmetrization is indicated by the symbol $\bar{P}'$. The expression studied numerically reads:

$$(2\pi)^3 \mathcal{D}_{(2,1)}(e, e', e''; z) = (2\pi)^3 \mathcal{D}_{(2,1)}(e, e', e''; z = 1) + \sum_{N=1}^{\infty} \mathcal{D}_{(2,1)}^{(N)}(e, e', e'')(1 - z^{2N}),$$

$$\mathcal{D}_{(2,1)}^{(N)}(e, e', e'') = -4(P(e, e', e''; N) + P(e, e'', e'; N))$$

$$- 8\sum_{M} \left(P(e, e'; N - M|e''; M) - \bar{P}_1'(e, e'; N - M|e''; M) \right) + 8(P(e, e'; N) - \bar{P}_1(e, e'; N)). \tag{3.334}$$

Again $\mathcal{D}_{(2,1)}^{(N)}(e, e', e'')$ is negative for large N. The cancellation mechanism proposed in Eq. (3.324) in Sec. 3.8.3 is operative here as well, since $\mathcal{D}_{(2,1)}^{(N)}(e, e', e'')$ behaves like $N^{\frac{12}{7}}$ for large N. The linear combinations of probabilities appearing in this expression scale like $N^{\frac{8}{7}}$ for large N.
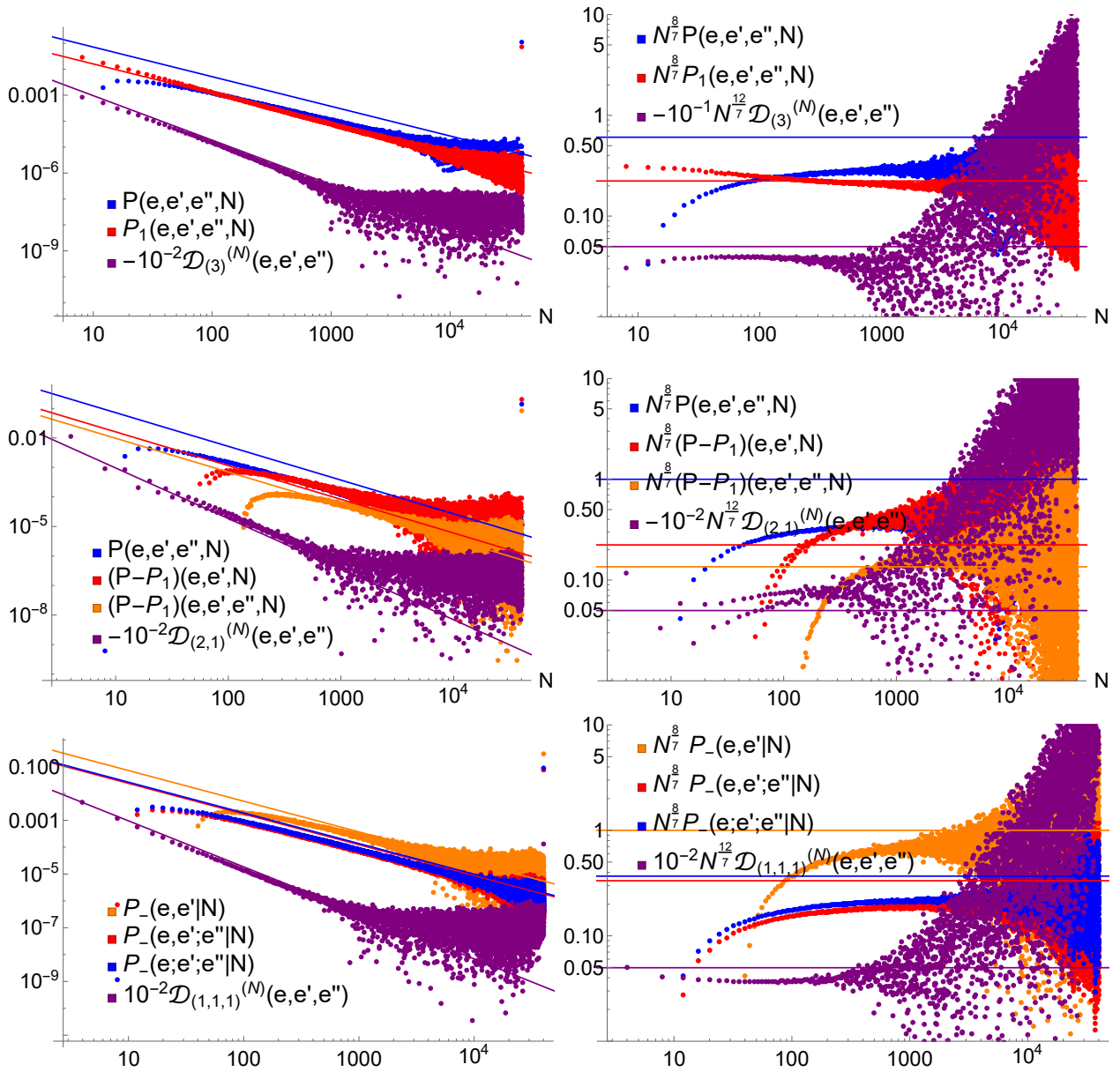
Figure 3.7: Coefficients of $\mathcal{D}_\lambda^{(N)}(e, e', e'')$ term (purple). The links e, e', e'' are chosen to be either horizontal or vertical (next) nearest neighbors. Left hand side: comparison to $N^{-\frac{8}{7}}$ (blue, red, orange) $N^{-\frac{12}{7}}$ (purple) scaling. Right hand side: the terms are normalized to the expected power law. Deviations of $\mathcal{D}_\lambda$ from pure $N^{-\frac{12}{7}}$ scaling are small. This is consistent with $x_{(2,1)} = x_{(1,1)}$ by Weyl symmetry. *Top panel:* Fock like term $\lambda = (3)$ from Eq. (3.333) and the probabilities $P(e, e', e''; N)$ (blue), $P_1(e, e', e''; N)$ (red). *Middle panel:* Coefficients of mixed $\mathcal{D}_{(21)}^{(N)}(e, e', e'')$ term from Eq. (3.334) (purple) and the probabilities $P(e, e', e'', N)$ (blue), $(P - P_1)(e, e', N)$ (red), $(P_- - P_{1,-})(e, e', e'', N)$ (orange). *Bottom panel:* Coefficients of Hartree like $\mathcal{D}_{(111)}^{(N)}(e, e', e'')$ term from Eq. (3.335) (purple) and the probabilities $P_-(e, e'|N) = \sum_M P_-(e; N|e'; M) - P_-(e; N - M|e'; M)$ (orange), $P_-(e, e'; e''|N) = \sum_M P_-(e, e'; N|e''; M) - P_-(e, e'; N - M|e''; M)$ (red) and $P_-(e; e'; e''|N) = \sum_{MK} P_-(e; N - M - K|e'; M|e''; K)$ (blue).

(1,1,1) Finally, numerical data for $\mathcal{D}_{(1,1,1)}^{(N)}(e, e', e'')$ is shown in Fig. 3.7. Here it is convenient to introduce auxiliary functions due to the complexity of the expression:

$$(2\pi)^3 \mathcal{D}_{(1,1,1)}(e, e', e''; z) = (2\pi)^3 \mathcal{D}_{(1,1,1)}(e, e', e''; z = 1) + \sum_N \mathcal{D}_{(1,1,1)}^{(N)}(e, e', e'')(1 - z^{2N}),$$

$$\mathcal{D}_{(1,1,1)}^{(N)}(e, e', e'') = 24\bar{P}(e; N) - 24\sum_M \bar{P}(e; M|e'; N - M) - 24\bar{P}(e, e'; N)$$

$$+ 8\sum_{MK} P(e; N - M - K|e'; M|e''; K) + 24\sum_M \bar{P}(e, e'; N - M|e''; M)$$

$$= P_-(e, e', e''|N) + P_-(e, e'; e''|N) + P_-(e; e'; e''|N), \tag{3.335}$$

$$P_-(e, e', e''|N) = 24\sum_M \left[\bar{P}(e; M|e'; N) - \bar{P}(e; N - M|e'; M) \right],$$

$$P_-(e, e'; e''|N) = 24\sum_M \bar{P}(e, e'; N - M|e''; M),$$

$$P_-(e; e'; e''|N) = 8\sum_{MK} P(e; N - M - K|e'; M|e''; K). \tag{3.336}$$

In this formula $\bar{P}$ indicates symmetrization over all permutations of e, e', e''. All of the auxiliary functions $P_-(\ldots|N)$ show leading $N^{-\frac{8}{7}}$ scaling. One can clearly see the cancellation of these leading $N^{-\frac{8}{7}}$ terms, the coefficients $\mathcal{D}_{(1,1,1)}^{(N)}(e, e', e'')$ scale like $N^{-\frac{12}{7}}$. This confirms the analytical considerations in and around Eq. (3.328).

From Eq. (3.189) one can extract the scaling behavior of $\mathcal{D}_\lambda$

$$\begin{pmatrix} \mathcal{D}_{(1,1,1)}(e, e', e''; z) \\ \mathcal{D}_{(2,1)}(e, e', e''; z) \\ \mathcal{D}_{(3)}(e, e', e''; z) \end{pmatrix} \sim \underbrace{\begin{pmatrix} 4 & 36 & 20 \\ -4 & -6 & 10 \\ 4 & -9 & 5 \end{pmatrix}}_{\sim (P_3^C)^{-1}} \begin{pmatrix} \mathcal{P}_{(1,1,1)}^C \\ \mathcal{P}_{(2,1)}^C \\ \mathcal{P}_{(3)}^C \end{pmatrix}. \tag{3.337}$$

The last column is the leading $\mathcal{P}_{(3)}^C$ scaling. This $x_{(3)} = 0$ or $\Delta_{(3)} = -\frac{3}{4}$ scaling purely comes from $\mathcal{D}_\lambda(e, e', e''; z = 1) \sim r^{-\frac{3}{4}}$. All subleading scaling is contained in $\sum_N \mathcal{D}_\lambda^{(N)}(e, e', e'')(1 - z^{2N})$. The leading coefficients $\mathcal{D}_\lambda^{(N)}(e, e', e'') = c_\lambda N^{-\frac{12}{7}}$ should satisfy $c_{(3)}/c_{(21)} = \frac{3}{2}$ and $|c_{(111)}/c_{(21)}| = 6$. The numerics shows these relations are satisfied approximately, see Fig. 3.8. The cancellation mechanism that is proposed in Sec. 3.8.3 and verified here numerically implies $x_{(2,1)} = \frac{5}{4}$ or $\Delta_{(1,1)} = \frac{1}{2}$ in accordance with the Weyl relation $x_{(2,1)} = x_{(1,1)}$. Up to this order, the percolation analytics and simulations agree perfectly with each other the CCN SQH numerics presented in Sec. 3.7.3.

However, the accuracy of the percolation numerics is not sufficient to find the most subleading exponent $x_{(1,1,1)}$ accessible within this formalism. It is natural to assume, that $x_{(1,1,1)}$ is related to x_3^{hull}. As can be seen in Tab. 3.4, this does not match well the CCN exponent. Many other common [215–218] mechanisms for corrections to such correlation functions are known to exist, which could be responsible for this discrepancy. Further in Eq. (3.311) it can be seen that the one-to-one correspondence between power law scaling of percolation probability P in N and correlation function $\mathcal{D}$ in the broadening γ is only accurate up to $\mathcal{O}(\gamma r^{\frac{7}{4}})$. If this contribution does not cancel out, it would dominate over terms related to x_3^{hull} and lead to $x_{(1,1,1)} = \frac{7}{4}$ matching the CCN numerical result $x_{(1,1,1)} \approx 1.92$ well.
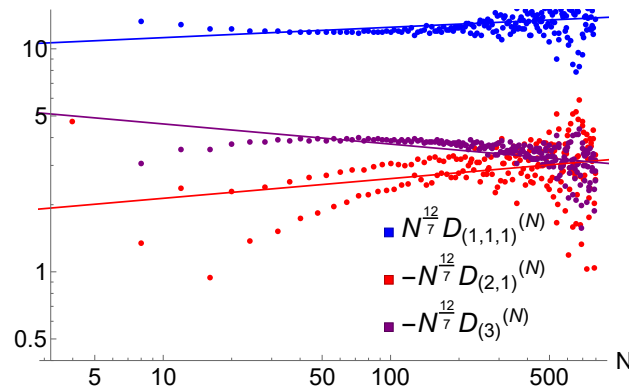
Figure 3.8: Coefficients of third order terms $\mathcal{D}^{(N)}_{(1,1,1)}(e, e', e'')$, $\mathcal{D}^{(N)}_{(2,1)}(e, e', e'')$ and $\mathcal{D}^{(N)}_{(3)}(e, e', e'')$ from Eqs. (3.335) (blue), (3.334) (red) and (3.333) (purple) scaled with $N^{\frac{12}{7}}$. Deviations from $N^{\frac{12}{7}}$ are relatively small, yet large enough to prevent the extraction from the lowest order $(1, 1, 1)$ exponent. Extracting approximate constants from the fits the relations expected from Eq. (3.337) between the coefficients are roughly satisfied: $\mathcal{D}^{(N)}_{(1,1,1)}(e, e', e'') \approx 13 N^{-\frac{12}{7}}$, $\mathcal{D}^{(N)}_{(2,1)}(e, e', e'') \approx -2.7 N^{-\frac{12}{7}}$ and $\mathcal{D}^{(N)}_{(3)}(e, e', e'') \approx -3.1 N^{-\frac{12}{7}}$. The numerics were performed for $L = 32768$ and averaged over $C = 10000 \cdot 2L^2$ configurations (ensemble+system).

3.9 Conclusions

This chapter introduced the notion of generalized multifractality, referring to the scaling exponents of a family of composite wavefunction observables at Anderson-transition criticality. The central attention goes to the SQH transition where I (i) constructed families of pure scaling composite wavefunction observables, (ii) performed numerics extracting the multifractal spectrum, (iii) showed analytically that generalized parabolicity is violated in SQH systems using the percolation mapping. The parts (i), (ii) were performed with the class C NLSM, however the mathematical constructions/numerical algorithms described there generalize straightforwardly to the other symmetry classes.

In more detail, the key results in this part comprise:

1. Me and my collaborators introduced the notion of generalized multifractality and reviewed its description by a field theory possessing conformal invariance. A point to emphasize once more is that one must sharply distinguish between global conformal invariance and the stronger local conformal invariance (LCI) that can occur in 2D. Building on this framework, for 2D systems me and my collaborators have shown that the generalized multifractal spectrum of scaling exponents exhibits generalized parabolicity (parametrized by a single constant) provided that the two conditions are satisfied: (i) existence of a family of pure scaling composite operators and satisfying the Abelian fusion rules, and (ii) local conformal invariance.

2. Within the class C NLSM, I have explicitly constructed pure-scaling composite operators. These are not unique and different operator families have different properties (e.g. positivity, abelian fusion), which is why two approaches were used: (i) The Iwasawa decomposition yields pure scaling operators that are strictly positive and can be raised to arbitrary complex powers and

satisfy abelian fusion. (ii) For composite operators that have polynomial structure in the Q-field of the class C NLSM I have derived one-loop RG rules. This RG approach is a further way towards a family of pure-scaling composite operators. These in general do not have further nice properties, but were directly related to wave function combinations.

3. The link between the NLSM and observables of the system is the translations of polynomials in Q to composite objects of eigenstates. For the polynomial pure-scaling operators obtained from sigma-model RG this "translation" follows the usual rules. For particular cases I managed to relate the pure-scaling operators from the Iwasawa construction to observables composed of total densities in spin space.

4. Knowing the pure scaling observables, I investigated the generalized multifractal spectrum numerically. For this purpose exact diagonalization was applied to network models in classes C and A, revealing the pure scaling exponents at the SQH and IQH transitions. In class C, both two families of wavefunction observables were studied and the exponents were found to agree with each other where ever a comparison was possible. In summary, the validity of the operators found analytically was confirmed by the numerics and a subset of the multifractal exponents was computed numerically.

5. In these lines implications of the IQH transition numerical studies are discussed. Zirnbauer conjectured a WZNW theory in Ref. [50] that implies generalized parabolicity with prefactor $b = 1/4$ for the multifractal spectrum. The numerical results at large $q = 2, 3, 4$ yield relatively small but clear deviations, confirming previous high precision IQH numerics [52, 53].

6. By exploiting the mapping of certain observables in the class C network model to classical percolation, I could find exact analytical expressions (the scaling dimensions of n-hull operators) for certain scaling dimensions. Classical percolation analytics, numerical classical percolation simulations and above mentioned quantum CCN numerical studies all agree nicely on $x_{(1,1)} = x_{(2,1)} = \frac{5}{4}$ and manifestly rule out generalized parabolicity once and for all. Consequently SQH criticality cannot be described by a local conformal invariant field theory.

The work presented in this chapter has a fundamental implication: SQH criticality is not locally conformal invariant! This can be seen by putting above points together: The Iwasawa constuction gives an operator family with abelian fusion. According to the CFT proof reviewed in Sec. 3.2 the existence of such a family in a theory with local conformal invariance (LCI) implies generalized parabolicity. However, both numerically and analytically deviations in the generalized multifractal spectrum from parabolicity were found. Thus LCI is violated at the SQH transition, in particular a WZNW CFT description of SQH criticality is ruled out.

4 Disordered Surfaces of time reversal invariant topological superconductors

Certain two-dimensional (2D) Dirac fermion theories describe the low energy quasiparticles on the surfaces of time-reversal invariant, three-dimensional (3D) topological superconductors (TSCs), exposed to quenched disorder. With my collaborators, I performed numerical studies on these theories, with the remarkable finding that they exhibit a novel to this point not yet fully understood mechanism of topological protection against Anderson localization [75, 88, 89].

Apparently, there is a connection between 3D TSCs in classes AIII, CI, and DIII, and 2D quantum Hall criticality in classes A, C, and D. Neglecting the topological term, from the non-linear σ-model (NLSM) picture one can derive, that most TSC surface states should Anderson localize for arbitrarily weak disorder (CI, AIII), or exhibit weak antilocalizing behavior (DIII).

Contrasting the naive picture sharply, the numerical studies presented in this chapter instead indicate spectrum-wide surface quantum criticality*. This means, there is robust eigenstate multifractality over a whole "energy stack" of critical wave functions. Surprisingly, for class AIII the multifractality spectrum and conductance distribution in the stack matches the phenomenology of the class A integer quantum Hall (IQH) transition. Analogously the surface stacks of class CI TSCs seem to show class C spin quantum Hall (SQH) like criticality. Finally a third kind of critical stacking can be observed in class DIII TSCs. For the lowest winding number, the surface theory is a single Majorana cone with velocity disorder. Restricting to* nematic *disorder, one observes stacking probably corresponding to the class D thermal quantum Hall (TQH) transition.*

By means of bosonization, the disordered Dirac theories under consideration can be represented as perturbed 2D Wess–Zumino–Novikov–Witten (WZNW) sigma models; the conjecture is that these are related to Pruisken models with the topological angle $\Theta = \pi$ at finite energy. A further interesting aspect of the stacked Dirac theories (CI, AIII, DIII) is that they can be used in the description of dirty d-wave quasiparticles in high-T_c cuprates.

The contents of this chapter are published as a review article in Ref. [90] on Refs. [88, 89] written by collaborators and myself. Moreover my numerical work extending Ref. [75] is also presented.

4.1 Motivation

Topological phases of non-interacting fermions are classified according to the "10-fold way" [2–5]. The same scheme (also referred to as the Altland–Zirnbauer or Cartan classification) applies to a seemingly

unrelated problem, that of the Anderson (de)localization in the presence of quenched disorder [7–9]. In fact, topology and disorder are closely intertwined in condensed matter physics. In both cases, one seeks to characterize not the details of a particular band structure or disorder configuration, but the physics that robustly persists under smooth deformations of the Hamiltonian that preserve defining symmetries.

In each spatial dimension, five of the ten classes admit topologically nontrivial phases (see Tab. 1.1). Three of the five topological classes are characterized by an integer-valued winding number $\nu \in \mathbb{Z}$ [3, 4]; the other two classes in each spatial dimension have $\mathbb{Z}_2$ invariants. In two dimensions (2D), the three classes correspond to three different versions of the integer (non-interacting) quantum Hall effect. These are the charge, spin, and thermal quantum Hall effects in classes A, C, and D; the latter two arise in theories of 2D $d+id$ and $p+ip$ topological superconductors (TSCs). In three dimensions (3D), the topological classes with winding numbers $\nu \in \mathbb{Z}$ can describe time-reversal invariant TSCs [2]. The three TSC classes are distinguished by the degree of spin symmetry preserved in every quasiparticle band structure or disorder realization; these are U(1), SU(2), and no spin symmetry for classes AIII, CI, and DIII, respectively. Although TSCs have yet to be conclusively identified in nature, fermionic topological superfluids in classes A and DIII are believed to be realized in thin-film ^{3}He-A and bulk ^{3}He-B, respectively [2, 219, 220].

Topologically nontrivial phases host gapless edge or surface states at the sample boundary [17–19] that are robust to local perturbations. In particular they should be protected from Anderson localization [2, 10, 11]. The topological protection for 1D and 2D boundary modes is in conflict with the natural tendency of low-dimensional states to localize in the presence of arbitrarily weak disorder [9, 16]. For 1D chiral or helical edge modes, the route of escape is that elastic backscattering is strictly prohibited [17, 18, 221, 222]. Surfaces offer a richer variety of possibilities, where topological bands often feature massless 2D Dirac or Majorana fermions. The suppression of pure backscattering for the single 2D Dirac fermion cone is insufficient to prevent quantum interference. Without the restriction to 1D (only forward and backward) in a wire, elastic impurity scattering can still occur at all other angles. In order to resolve the puzzle in this case, it is necessary to use more technical tools like the nonlinear sigma model to gain further insight. For the simplest 3D topological insulator (TI), one finds protection of the 2D surface states from localization throughout the entire bulk energy gap. This is understood as due to weak antilocalization enabled by strong spin-orbit coupling, and the presence of a $\mathbb{Z}_2$ topological term that nullifies the metal-insulator transition in the symplectic class [9, 122, 128, 130, 223, 224].

The 2D surface states of bulk 3D TSCs in classes AIII, CI, and DIII are typically predicted to appear as massless Dirac or Majorana fermions. Different from graphene or TI surface states, time-reversal invariant quenched disorder enters into these surface theories in a peculiar way. Due to the "fractionalization" of the Hilbert space associated with confinement at the sample boundary and the natural particle-hole symmetry present in a superconductor, 2D Dirac TSC surface theories admit only quenched gauge-field disorder [2, 8, 61]. In classes AIII and CI, minimal realizations involve U(1) and SU(2) vector potentials. The minimal realization of a class DIII surface consists of a single Majorana cone; in this case, disorder can only modulate the velocity components of the cone. Since it couples to the stress tensor, this is called "quenched gravitational disorder" (QGD) [89]. Although class CI and AIII 2D Dirac models with gauge disorder could be robustly realized as TSC surface states, these were originally studied two decades ago in the context of the high-T_c cuprate superconductors [62]. Indeed, by suppressing interpair, internode, and/or intranode elastic impurity scattering in a 2D d-wave superconductor, one can realize all three minimal surface models in classes CI [63–66, 225], AIII [67, 226], and DIII [89].
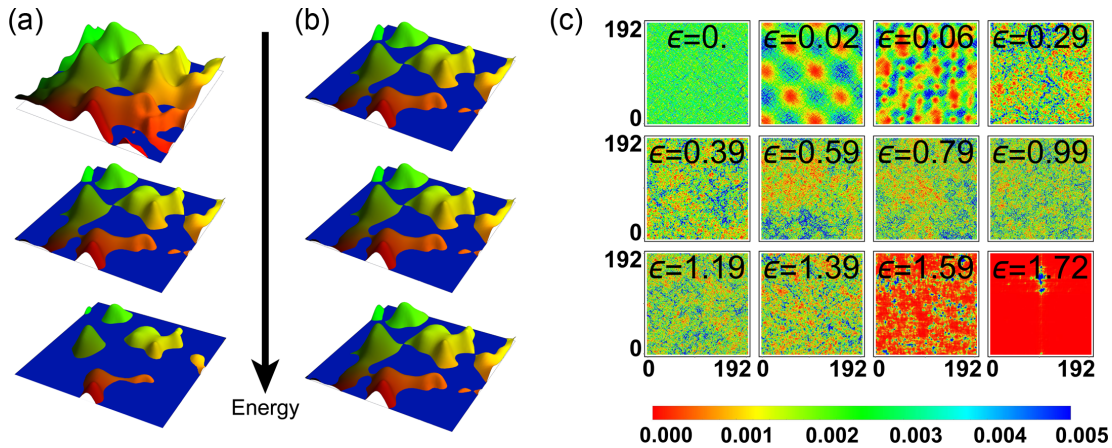
Figure 4.1: Figure taken from Ref. [90]. "Stacked" quantum criticality at the surface of a bulk topological superconductor (TSC). Panel (a) depicts classical geometric critical phenomena in 2D, as can occur when fluid floods a landscape. Criticality arises at the percolation threshold (middle), where fine-tuning of the fluid level makes travel across the landscape equally difficult by land or by sea. By contrast, at the surface of a bulk TSC with quenched disorder that preserves time-reversal symmetry, the numerical studies [75, 88, 89] reviewed in this chapter demonstrate a "stacking" of critical eigenstates throughout the surface energy spectrum, schematically indicated in (b). Panel (c) depicts position-space probability density maps for dirty TSC 2D surface eigenstates, as could be measured in the local density of states probed by scanning tunneling microscopy (STM). Eigenstates at different energies ε are shown for a single class DIII surface Majorana cone, subject to a particular realization of nematic quenched disorder in the components of its velocity (nematic "quenched gravitational disorder" [89]). Eigenenergies ε are measured in units of the momentum cutoff Λ (with average Fermi velocity set equal to one), and lengths are measured in units of $2\pi/\Lambda$. While low-energy states are plane-wave like in this case, states with energies $0.2 < \varepsilon < 1.5$ exhibit quantum critical rarification. The multifractal fluctuations of the wave function intensity appear to be universal, independent of ε and of the disorder strength, forming a "stack" of quantum-critical states. Importantly, evidence for Anderson localization is observed only at high energies, well above the ultraviolet cutoff for TSC surface states in all three classes CI, AIII, and DIII; stacking statistics *improve* for increasing system sizes and disorder strengths [75, 88, 89]. Results are obtained by exact diagonalization of the continuum Dirac theory with periodic boundary conditions, defined in momentum space (so as to avoid fermion doubling) [89]. The "stacked" critical states for class AIII and CI TSC surface states match the known critical statistics of the class A charge and class C spin quantum Hall plateau transitions, respectively [75, 88]. [Since the class C transition shares a few exactly known critical exponents with 2D classical percolation [56], one can say that the stacking in class CI realizes critical percolation without fine-tuning [75], as sketched in panel (b). This mapping between SQH criticality and classical percolation is generalized in Sec. 3.8.] The finite-energy critical fluctuations observed in class DIII, shown in (c), may correspond to the thermal quantum Hall plateau transition in class D.

The recent numerical evidence of Refs. [75, 88, 89] is reviewed, indicating that the class AIII, CI, and DIII Dirac surface theories evade Anderson localization via a highly unusual mechanism. These 2D Dirac models exhibit a "stack" of critical states at finite energies, see Fig. 4.1. The statistics of these states at different energies (away from zero) are identical.

In particular, the multifractal spectrum of wave function fluctuations and the distribution of the Landauer conductance for finite-energy class AIII Dirac surface states appear to match the universal values associated with the integer quantum Hall (IQH) transition in class A [88]. In Chap. 3, the generalized multifractal spectrum of such IQH critical systems is studied. This is surprising for a number of reasons. First, the critical state associated with the IQHE typically obtains only with fine-tuning of the magnetic field or particle density. This is because the IQH effect is a quantum phase transition separating topologically distinct plateaus. Instead, at the surface of a TSC, every finite-energy state appears to feature its own plateau transition. Second, the quantum Hall effect lacks time-reversal symmetry (TRS), yet the findings in Ref. [88] show an energy-stacking of IQH states without TRS breaking. For the TSC with full spin SU(2) symmetry (class CI), the finite-energy surface states [75] mimic the class C *spin* Quantum Hall (SQH) transition phenomenology precisely [9, 54–58, 76, 77]. Finally, for the minimal realization of a class DIII surface with QGD, stacking occurs for a new class of wave function quantum criticality. This is hypothesized to be related to the thermal Quantum Hall (TQH) transition in class D [78–85].

The 2D Dirac surface models studied here are equivalent to Wess–Zumino–Novikov–Witten (WZNW) nonlinear sigma models [8], modified by the addition of the nonzero quasiparticle energy. The latter couples to the trace of the principal chiral field, a strongly relevant perturbation. At zero energy (the surface Dirac point), these models are also quantum critical, and have been long understood thanks to the exact solution via conformal field theory [61–68]. By contrast, there is very little known analytically of the finite-energy behaviour in the perturbed WZNW models. Ludwig *et al.* [67] investigated the minimal single-node class AIII Dirac model (corresponding to the surface of a class AIII TSC with winding number $\nu = 1$). These authors argued that all states at finite energy should Anderson localize. A mechanism for the finite energy states to escape this fate was conjectured by Ostrovsky *et al.* [122]. They showed that a gradient expansion yields the Pruisken model that describes the integer quantum Hall effect. For odd winding numbers ν, the Pruisken model has a theta term with topological angle $\Theta = \pi$, corresponding to the class A IQH transition. This result was confirmed for $\nu = 1$ by numerics [227]. While this argument supports quantum-critical stacking for odd ν, it predicts Anderson localization for even ν (despite the $\mathbb{Z}$ classification for class AIII) [10, 122, 224]. There is no indication of this even/odd effect numerically [88], and both $\nu = 1, 2$ show clear indications of class A IQH criticality in the multifractal spectra and conductance distribution [9, 51, 69–74]. Numerical evidence for class A IQH stacking has also been very recently reported for a single Dirac cone with generic disorder [228].

The key numerical findings for class AIII, CI, and DIII finite-energy surface theories [75, 88, 89] are summarized. For class CI, the previous calculations in Ref. [75] are extended to larger system sizes, and a finite-size scaling analysis of the multifractal spectrum is provided. Further results for the Kubo conductivity for class CI and AIII surface states are presented.

Beyond the connection to the hypothetical class D thermal TQH physics, Ref. [89] found that the single 2D Dirac or Majorana cone subject to *nematic* QGD matches the phenomenology observed in STM studies of the high-T_c cuprate superconductor BSCCO [229–234], see Sec. 4.5.1. The field of experimental studies of disordered superconductors is very rich by itself. Many theoretical scenarios for the disorder-driven superconductor-to-insulator transition involve enhanced Cooper pairing, due to multifractal rarification [61, 124, 168, 169, 172]. Reporting an increase in T_c with increasing disorder,

Ref. [235] recently added experimental support for this. Furthermore there are indications that multifractal superconductor physics provides an adequate description of transition metal dichalcogenides [236–238]. It is also interesting to note that the chiral model for twisted bilayer graphene is effectively described by a class CI surface Dirac Hamiltonian [239–241]. However, the most prominent and well-studied experiments revolve around the mystery of the spatial inhomogeneity in the high-T_c cuprate superconductors [234]; the results reviewed here call for a re-evaluation of the role of disorder in these materials.

4.1.1 Outline

First I give a brief overview about topological surface theories is given in Sec. 4.2.1. Starting with the topological classification an overview about the corresponding σ models (see Table 1.1 in Sec. 1.3) is given, including the conventional expectations for the finite-energy behavior. The key results of WZNW theory relevant for zero-energy states of time-reversal invariant superconducting classes are reviewed in the Fundamentals in Sec. 1.5.5. Here, the role of the energy perturbation and how the modified WZNW model can be deformed "by hand" into the Pruisken model is explained in Sec. 4.2.2.

The main part is organized as a review of the most important numerical results for the class AIII, CI, and DIII surface theories. Each section about these theories covers the numerically obtained multifractal spectra, and for class AIII the Landauer conductance distribution. Additional results [90] include Kubo conductivity computations for classes AIII and CI, as well as larger system sizes and a finite-size analysis for class CI, winding number $\nu = 2$ multifractal spectra.

4.2 Modeling topological surfaces

4.2.1 Dirac surface theories and topological classification

Here 2D surface theories of 3D bulk time reversal ($\mathcal{T}$)-invariant topological superconductors (TSCs) with different degrees of spin symmetry are considered. These reside in classes AIII, CI, or DIII, as indicated in Table 1.1 in Sec. 1.3. For any superconducting realization of a class, *physical* time-reversal symmetry $\mathcal{T}$ corresponds to the *effective* chiral symmetry S in this table. This symmetry transmutation is due to the "automatic" particle-hole invariance associated with the self-conjugate (Balian-Werthammer) spinor formulation of any Bogoliubov-de Gennes Hamiltonian [2, 112]. These bulk phases can be topologically non-trivial, and are indexed with integer-valued winding numbers.

The form of the 2D surface band structure for a clean topological phase in general depends upon some details of the bulk and of the surface orientation. A large class of TSC surface states in classes AIII, CI, and DIII take the form of massless Dirac or Majorana fermions. This has been demonstrated using bulk lattice models in (e.g.) Refs. [125, 242–244]. Generic $\mathcal{T}$-invariant quenched disorder introduced at the surface translates into random abelian and/or nonabelian vector potentials in the low-energy surface Dirac theory. A generic Hamiltonian is [2, 61]

$$H = \hat{\sigma} \cdot \left[(-i\nabla) + \sum_i \mathrm{A}_i(\mathrm{r})\, \hat{\tau}^i \right]. \tag{4.1}$$

Although this is a single–particle Hamiltonian for (2+1)-D surface quasiparticles, it is frequently useful to alternatively interpret H as the Lagrangian density for an imaginary time (2+0)-D theory of 1D relativistic fermions. The pseudospin Pauli matrices $\hat{\sigma}^{1,2}$ then act separately on the spaces of left-

and right-movers [61]. The matrices $\{\hat{\tau}^i\}$ act upon an N-dimensional color space, and couple to the nonabelian vector potential A_i. The color generators have to be compatible with the symmetry of the class. In class AIII, for a bulk winding number $\nu = N$, there can be generic U(N) disorder that encodes elastic scattering between the colors. Thus all Hermitian $N \times N$ generators $\{\hat{\tau}^i\}$ are allowed, including the identity matrix [U(1) abelian vector potential disorder]. For class DIII, these are restricted to antisymmetric generators of SO(N). In class CI, the winding number $\nu = N \equiv 2M$ is always even, and the matrices $\{\hat{\tau}^i\}$ generate the Lie algebra Sp($2M$).

The key defining characteristic of a topological surface is the anomalous representation of a defining bulk symmetry. For surface states of 3D TSCs, this is the chiral/physical time-reversal symmetry. For the Hamiltonian in Eq. (4.1), it is encoded by the condition

$$\hat{\sigma}^3 H + H \hat{\sigma}^3 = 0. \tag{4.2}$$

This version of chiral symmetry is anomalous, i.e. cannot arise without fine-tuning from the continuum Dirac description of a 2D lattice model [2, 61]. It can be shown that Eq. (4.2) implies that the class CI, AIII, or DIII nonlinear sigma model (NLσM) encoding Anderson (de)localization physics [9] is augmented by a Wess–Zumino–Novikov–Witten (WZNW) term [2, 8]. Without the WZNW terms, the NLσMs in these classes are termed "principal chiral models" or principal chiral NLσMs. An introduction and more references to chiral NLσMs with or without WZNW term can be found in Sec. 1.5. The minimal realizations of Eq. (4.1) for topological class CI, AIII, and DIII surfaces have winding numbers $\nu = N = \{2, 1, 1\}$, respectively.

By contrast, the minimal "non-topological" version of class CI possesses four colors of 2D Dirac fermions [62]. Incorporating disorder, the generic continuum Dirac model corresponding to a dirty 2D d-wave superconductor is perturbed by random mass, vector, and scalar potential terms. This model is believed to Anderson localize for arbitrarily weak disorder at all energies; it corresponds to the class CI principal chiral nonlinear sigma model *without* the WZNW term [62, 245]. At the same time, the d-wave model can be fine-tuned to realize any of the three topological models as exemplified by Eq. (4.1) [62, 89]. Suppressing elastic scattering between *pairs* of nodes gives two copies of the $\nu = 2$ class CI WZNW model (nodes in a pair are related by $\mathcal{T}$). Further suppressing scattering between nodes within a pair breaks each $\nu = 2$ CI model into two $\nu = 1$ AIII WZNW models, with only U(1) vector disorder. Suppressing even this still allows random fluctuations of the velocity components, which correspond to "quenched gravitational disorder" in class DIII [89]. This example displays a general rule: a non-topological class CI, AIII, or DIII model (associated e.g. to a 2D lattice model) can always be fragmented into topological components, provided restrictions are placed upon scattering between the different Dirac colors. These restrictions cannot, however, typically be realized exactly in a microscopic 2D model with lattice-scale disorder.

The averages over ensembles of disordered H in Eq. (4.1) can be described by the NLσM theory [9]. Using fermionic replicas, the topological surface-state WZNW Dirac models are associated with the group manifolds $G(2n) \in \{\text{U}(2n), \text{Sp}(4n), \text{O}(2n)\}$ for classes AIII, CI, and DIII, respectively, as shown in Table 1.1. Here $n \to 0$ denotes the number of replicas. The conventional expectation is that any non-standard symmetry class such as these must reduce to a standard Wigner–Dyson class (A, AI, or AII) at finite eigenstate energy $\varepsilon \neq 0$. This is because $\varepsilon \neq 0$ formally breaks the defining particle–hole or chiral symmetry. Classes AIII, CI, and DIII exhibit $G \otimes G$ symmetry at zero energy, but this is reduced to the diagonal subgroup G for $\varepsilon \neq 0$ (see also Sec. 4.2.2). One would therefore expect that finite-energy states in classes AIII, CI, and DIII reside in classes A, AI, and AII, respectively, characterized by the symmetry reduction in the NLσM from the group manifolds to the corresponding

Grassmannians,

$$\frac{G(2n) \otimes G(2n)}{G(2n)} \simeq G(2n) \to \frac{G(2n)}{G(n) \otimes G(n)}, \tag{4.3}$$

see Table 1.1. Class AI always localizes in 2D, as does class A unless fine-tuned to the IQH transition; class AII can exhibit weak antilocalization for sufficiently weak disorder [9, 16].

Although the focus stays limited to Dirac surface theories in this work, there are other possibilities. Bulk TSCs or fermionic topological superfluids that arise by pairing higher-spin fermions (e.g., $S = 3/2$) can give rise to surface Hamiltonians that also exhibit the anomalous chiral symmetry in Eq. (4.2). These have larger minimal winding numbers $|\nu| > 1$, and the bulk winding number can be reflected through nonlinearity of the surface band structure, instead of $N = |\nu|$ colors of linearly-dispersing Dirac fermions [75, 246–249]. Numerical studies suggest that the disorder-induced physics of these surfaces is the same as in the Dirac models studied here [75, 248, 249].

4.2.2 Class AIII, CI, and DIII WZNW models over $\mathbf{U}(2n)$, $\mathbf{Sp}(4n)$, and $\mathbf{O}(2n)$

The statistics of the spatial fluctuations for eigenstates of 2D disordered systems are described by the non-linear sigma model (NLσM) framework [9]. Specifically, for the class AIII, CI, or DIII topological surface-state Hamiltonian in Eq. (4.1), this sigma model becomes a Wess–Zumino–Novikov–Witten (WZNW) model, familiar from conformal field theory (CFT). This class of models is introduced in Sec. 1.5.5. Using non-abelian bosonization [62–68] and conformal embedding theory [61], one can derive exact results for the scaling of generic operators in the energy $\varepsilon \to 0$ limit. In particular, for the density of states (DOS) $\rho(\varepsilon)$ as a function of the surface quasiparticle energy ε, one has

$$\lim_{\varepsilon \to 0} \rho(\varepsilon) \simeq |\varepsilon|^{x_1/z}. \tag{4.4}$$

Here $x_1 = 2 - z$ is the scaling dimension of the operator encoding the first moment of the local density of states at $\varepsilon = 0$, and z denotes the dynamic critical exponent. For surface states of a bulk TSC with winding number ν, the scaling exponent x_1/z is summarized for the different WZNW models in Table 4.1. The multifractal spectrum for the WZNW models at $\varepsilon = 0$ is exactly parabolic:

$$\Delta_q = \theta \, q(1 - q). \tag{4.5}$$

Table 4.1 summarizes how θ depends upon the class and winding number.

The WZNW action for 2D dirty Dirac or Majorana TSC surface states with winding number ν reads

$$S = \frac{\nu}{8\pi l_\phi} \int d^2\mathbf{r} \, \mathrm{Tr}\Big[\nabla \hat{Q}^\dagger \cdot \nabla \hat{Q}\Big] - \frac{i\nu}{12\pi l_\phi} \int d^2\mathbf{r} \, dR \, \epsilon^{abc} \, \mathrm{Tr}\Big[\big(\hat{Q}^\dagger \partial_a \hat{Q}\big)\big(\hat{Q}^\dagger \partial_b \hat{Q}\big)\big(\hat{Q}^\dagger \partial_c \hat{Q}\big)\Big]$$
$$- \frac{\lambda_A \nu^2}{8\pi^2} \int d^2\mathbf{r} \, \mathrm{Tr}\Big[\hat{Q}^\dagger \nabla \hat{Q}\Big] \cdot \mathrm{Tr}\Big[\hat{Q}^\dagger \nabla \hat{Q}\Big] + \frac{i\omega}{2} \int d^2\mathbf{r} \, \mathrm{Tr}\Big[\hat{\Lambda}\big(\hat{Q} + \hat{Q}^\dagger\big)\Big]. \tag{4.6}$$

See e.g. Ref. [61] for a derivation of this action from the disordered Dirac theory defined by Eq. (4.1). The zero-energy surface theory for classes CI and AIII is described by the top line equation (4.6). The WZNW term is the second one on this top line, and requires extending the field configurations from the 2D surface into the 3D bulk [61, 250]; the parameter l_ϕ is the Dynkin index of the corresponding group. For class AIII only, an additional parameter appears even at zero energy, which is the marginal disorder strength λ_A that encodes the strength of abelian vector potential disorder.

The parameter ω on the second line of Eq. (4.6) is the ac frequency at which the conductivity of the NLσM is to be evaluated. With $\omega \neq 0$, states at finite energy can be accessed. This parameter couples to the *imaginary* ("tachyonic") mass term $(i/2)\,\mathrm{Tr}\big[\hat{\Lambda}(\hat{Q}+\hat{Q}^\dagger)\big]$, where $\hat{\Lambda} = \mathrm{diag}\{\hat{1}_n, -\hat{1}_n\}$ grades in the retarded/advanced space [9]. Since it is a strongly relevant perturbation, nonzero ω drives the theory away from quantum critical point described by the WZNW conformal field theory.

The field $\hat{Q}(\mathrm{r})$ is a $(2n)\times(2n)$ $[(4n)\times(4n)]$ element of the matrix group U($2n$), O($2n$), [Sp($4n$)] for classes AIII, DIII [CI]. It satisfies the nonlinear constraint $\hat{Q}^\dagger(\mathrm{r})\,\hat{Q}(\mathrm{r}) = \hat{1}$, where $\hat{1}$ denotes the identity matrix. In the end, the replica limit $n \to 0$ has to be taken [9, 61].

For $\omega = 0$, the WZNW model in Eq. (4.6) is exactly solvable via CFT [61, 63–68, 225, 251]. Exact results for the DOS scaling [Eq. (4.4)], multifractal spectrum [Eq. (4.5)], and conductivity are summarized in Table 4.1.

Finite energy behavior   The ac frequency parameter ω in Eq. (4.6) reduces the $G \otimes G$ group symmetry of the WZNW model down to the diagonal subgroup G. Real nonzero ω gives oscillatory contributions to the functional integral over $\hat{Q}$ unless a further constraint is imposed,

$$\hat{Q} = \hat{Q}^\dagger, \quad \mathrm{Tr}\big[\hat{Q}\big] = 0 \tag{4.7}$$

(after absorbing the matrix $\hat{\Lambda}$ by a left-group translation $\hat{\Lambda}\hat{Q} \to \hat{Q}$). Then, the ω term and the λ_A term (class AIII) on the second line of Eq. (4.6) are projected to zero.

In this constrained case, Bocquet, Serban, and Zirnbauer [79] (see also [62, 224]) derived a deformation of the WZNW term to the topological term in the Pruisken model:

$$S \to \frac{\sigma_{x,x}}{8}\int d^2\mathrm{r}\,\mathrm{Tr}\big[\nabla\hat{Q}\cdot\nabla\hat{Q}\big] - \frac{\sigma_{x,y}}{8}\int d^2\mathrm{r}\,\epsilon^{ij}\,\mathrm{Tr}\big[\hat{Q}\,\partial_i\hat{Q}\,\partial_j\hat{Q}\big], \tag{4.8}$$

where

$$\sigma_{x,x} = \nu/\pi, \quad \sigma_{x,y} = \nu/2. \tag{4.9}$$

In the context of quantum Hall type criticality in 2D, the Pruisken model is discussed in Sec. 1.5.

For classes CI and DIII, the Pruisken model only applies if the target manifold for the constrained $\hat{Q}$ is taken to be that of classes C and D, respectively. Although $\omega \neq 0$ reduces the symmetry of the WZNW action down to the diagonal G subgroup, this information is insufficient to determine the target manifold G/H of the effective NLσM governing the Anderson (de)localization physics of the finite-energy states. In the case of class CI with $G = \mathrm{Sp}(4n)$ (using fermionic replicas, Table 1.1), there are two possible scenarios for the finite-energy NLσM. Either $H = \mathrm{Sp}(2n) \otimes \mathrm{Sp}(2n)$ (the orthogonal Wigner-Dyson class AI), or $H = \mathrm{U}(2n)$ (class C). The former choice is the conventional one that guarantees Anderson localization at all finite energies [9]; the latter is realized in the stacking scenario, wherein Eq. (4.8) describes the *spin* quantum Hall plateau transition [9, 54–58, 76, 77].

Although there is no ambiguity in the target manifold for finite-energy class AIII states (which reside in class A), the "derivation" of Eq. (4.8) from Eq. (4.6) via the imposition of the constraint in Eq. (4.7) poses another problem. Eq. (4.9) implies that the topological angle $\Theta = 2\pi\sigma_{x,y}$ is an odd (even) multiple of 2π for odd (even) winding numbers ν. This even-odd effect is *not* observed in the numerics here and in Refs. [75, 88]. In other words, imposing Eq. (4.7) by hand directly to the fields gives coefficients of the Pruisken model that are not compatible with numerics. This does not rule out this analytical ansatz as a description of the problem, as the following explanation clarifies. The

	AIII	CI	DIII
ν	$\mathbb{Z}$	$2\mathbb{Z}$	$\mathbb{Z}$
x_1/z	$\frac{\pi - \nu^2 \lambda_A}{\pi(2\nu^2 - 1) + \nu^2 \lambda_A}$ [67]	$\frac{1}{2|\nu|+3}$ [63]	$-\frac{1}{2|\nu|-3}$ $(|\nu| \geq 3)$ [61, 123]
$\theta(\varepsilon = 0)$	$\frac{|\nu|-1}{\nu^2} + \frac{\lambda_A}{\pi}$ [64, 65, 67]	$\frac{1}{|\nu|+2}$ [64, 65, 124]	$\frac{1}{|\nu|-2}$ $(|\nu| \geq 3)$ [61]
$\sigma^{xx}(\varepsilon = 0)$	$\frac{\nu}{\pi}$	$\frac{\nu}{\pi}$	$\frac{\nu}{\pi}$
$\theta(\varepsilon \neq 0)$	$\simeq 1/4$ (IQH) [88, 227]	$\simeq 1/8$ (SQH) [75]	$\simeq 1/13$ (TQH?) [89]
$\sigma^{xx}(\varepsilon \neq 0)$	$\simeq 0.58 \pm 0.02$ [74]	$= \frac{\sqrt{3}}{2}$ [76]	?

Table 4.1: Table taken from Ref. [90]. Summary of known properties for the 2D disordered Dirac models [Eq. (4.1)] in classes AIII, CI, DIII that can exhibit Wess–Zumino–Novikov–Witten ("stacked") criticality at zero (nonzero) energy. The zero energy properties of WZNW models are discussed in Sec. 1.5.5. Here these are the allowed bulk TSC winding numbers ν, the scaling of the surface density of states $\rho(\varepsilon) \propto |\varepsilon|^{x_1/z}$, the curvature of the parabola θ controlling the surface multifractal spectrum via $\Delta_q = -\theta\, q(1-q)$, and the longitudinal surface conductivity σ^{xx} (for spin or heat transport at the boundary of the TSC, in units of the appropriate conductance quantum [2, 125]). The top four rows describe the zero or near-zero energy critical features of dirty 2D TSC surface states, which are known analytically from conformal field theory. In class AIII, these results depend on the winding number ν and the abelian disorder strength λ_A, which is defined in Eqs. (4.10) and (4.11). The additional parameter λ_A is RG-marginal and addresses a continuum of distinct zero-energy fixed points [64, 65, 67]. The last two rows detail the recent numerical findings of Refs. [88], [89], and [75]. These characterize the "stacked" criticality of TSC surface states at finite energy, where each state in the stack exhibits identical statistical properties. The results for the finite-energy multifractal spectra and conductance statistics are consistent with a stacking of the class A integer quantum Hall (IQH) and class C spin quantum Hall (SQH) transition states for class AIII and CI Dirac models, respectively. A detailed introduction to quantum Hall criticality can be found in Sec. 1.5.3. The stacked criticality observed for finite-energy class DIII states is conjectured to describe the thermal quantum Hall (TQH) transition in class D [89]. Note that the numerical results for finite-energy class DIII states have only been obtained for quenched gravitational disorder, i.e. modulation of the velocity components for the single Majorana cone associated with winding number $\nu = 1$. The multicolor DIII model with $|\nu| = N > 2$ colors has not yet been studied numerically (but see Refs. [248, 249]).

actual physical RG flow of the full WZNW theory is that ω runs to the strong coupling regime. The other coefficients are likely to receive renormalization well before the $\hat{Q}$ field is reduced to the target manifold associated with Eq. (4.7). Consequently, the physical Pruisken model parameters can deviate from the values stated in Eq. (4.9).

4.3 Axial U(1) spin symmetry: class AIII

In this section the numerical results from Ref. [88] for the 2D Dirac TSC surface theory in class AIII, and the AIII WZNW → A IQH stacking conjecture are reviewed. As pointed out in Sec. 4.2.2, it is important to distinguish between even and odd winding numbers. Computational effort increases quickly with increasing ν, hence the analysis is restricted to $\nu = 1, 2$.

One Dirac node, U(1) vector potential dirt (AIII, $\nu = 1$)   The winding number $\nu = 1$ AIII surface theory can be realized with a single Dirac cone (addressed with Pauli matrices $\hat{\sigma}^{1,2}$).

$$H_{\mathrm{AIII}}^{(1)} = \hat{\sigma} \cdot \left[-i \, \mathbf{v} \, \nabla + \mathrm{A}(\mathrm{r}) \right], \qquad \overline{A^a(\mathrm{r}) \, A^b(\mathrm{r}')} = \lambda_A \, \delta^{ab} \, \delta_\xi^{(2)}(\mathrm{r} - \mathrm{r}'). \tag{4.10}$$

Here $\mathbf{v}$ is the Fermi velocity (which will be set equal to one). Disorder enters as a random abelian $U(1)$ vector potential $\hat{\sigma} \cdot \mathrm{A} = \sigma_1 \, A^1 + \sigma_2 \, A^2$ with disorder strength λ_A; the overline $\overline{\cdots}$ denotes an average over disorder configurations. The delta function $\delta_\xi^{(2)}(\mathrm{r} - \mathrm{r}')$ is smeared out by a correlation length ξ in the numerics described below.

Two Dirac nodes, U(1) $\oplus$ SU(2) vector potential dirt (AIII, $\nu = 2$)   The winding number $\nu = 2$ AIII model can be realized by adding a second Dirac cone (addressed by the color space $\tau_3 = \pm 1$). There is not only the Abelian U(1) vector potential A_0 with strength λ_A, but also a non-abelian SU(2) vector potential A_i ($i \in \{1, 2, 3\}$) with strength λ:

$$H_{\mathsf{AIII}}^{(2)} \equiv \hat{\sigma} \cdot \left[-i \, \mathbf{v} \, \nabla + \mathrm{A}_0(\mathrm{r}) + \mathrm{A}_i(\mathrm{r}) \, \hat{\tau}_i \right],$$
$$\overline{A_0^a(\mathrm{r}) \, A_0^b(\mathrm{r}')} = \lambda_A \, \delta^{ab} \, \delta_\xi^{(2)}(\mathrm{r} - \mathrm{r}'), \qquad \overline{A_i^a(\mathrm{r}) \, A_j^b(\mathrm{r}')} = \lambda \, \delta^{ab} \, \delta_{ij} \, \delta_\xi^{(2)}(\mathrm{r} - \mathrm{r}'). \tag{4.11}$$

In the limiting case of $\lambda_A = 0$, the full SU(2) spin symmetry as well as particle hole symmetry are restored. This puts the model into class CI, identical to the $\nu = 2$ CI Hamiltonian in Eq. (4.18).

4.3.1 Multifractal analysis

For the class AIII dirty Dirac theories described above, at zero energy (the surface quasiparticle Dirac point) the WZNW theory [Eq. (4.6) with $\omega = 0$] predicts exact parabolicity with curvature [Eqs. (1.66), (4.5), and Table 4.1]

$$\theta_\nu = \frac{|\nu| - 1}{\nu^2} + \frac{\lambda_A}{\pi}, \tag{4.12}$$

depending on winding number ν and abelian disorder strength λ_A. With momentum-space exact diagonalization [227], the multifractal statistics of the low-energy states for the $\nu = 1$ Hamiltonian (4.10) were shown to match this expression.

Ref. [88] further analyzes the conductance and the finite-energy multifractal properties. In Fig. 4.2(f) the multifractal spectrum of the $\nu = 1$ model [Eq. (4.10)] with linear size $L = 60\xi$ is analyzed. Here ξ denotes the common correlation length of the disorder potentials, which are taken to be Gaussian distributed [88]. At finite energies, the anomalous multifractal spectrum Δ_q is compared to the parabolic approximation for the class A IQH with $\theta_{\mathsf{IQH}} = 0.25$ [Eqs. (1.66), (4.5), and Table 4.1]. Great agreement is found over a wide energy range. In the high-energy tail $\varepsilon \sim 2\hbar \mathbf{v}/\xi$, there are larger deviations. This can be explained since close to the energy cutoff the system seems untouched by the disorder and

matches the clean DOS [see Fig. 4.2(a)]. Panel (b) in Fig. 4.2 moreover confirms that the low-energy integrated DOS $N(\varepsilon)$ scales as expected from WZNW theory [Eq. (4.4) and Table 4.1].

The results for the $\nu = 2$ surface theory (4.11) with the same linear size $L = 60\xi$ are shown in Fig. 4.3. In panel (f) there is a comparison of finite-energy multifractal spectra to the class A IQH parabola with $\theta_{\mathsf{IQH}} = 0.25$. In the high-energy tail $\varepsilon \sim 2\hbar\mathbf{v}/\xi$ there are deviations for the same reason as in the $\nu = 1$ case.

4.3.2 Landauer conductance

The transport calculations are performed by slicing the system in the x direction and subsequently recasting the time-independent Schrödinger equation $H_{\mathsf{AIII}}^{(1)} \psi = \varepsilon \psi$ in terms of the transfer matrix, using the method of Ref. [223]. Clean, highly doped leads are attached to the system at $x = 0$ and $x = L_x$. The conductance G is then computed from the transmission block t of the scattering matrix S between the leads.

The finite-size resistance normalized to the sample width $L_y/\overline{G}(L_x)$ is expected to depend linearly on L_x

$$L_y/\overline{G}(L_x) = L_y R_0 + \frac{1}{\sigma} L_x. \tag{4.13}$$

Gauge invariance and chiral symmetry force the contact resistance R_0 to zero for each configuration [251, 252]. The data in Fig. 4.2(c) for zero energy $E = 0$ is consistent with the WZNW theory conductivity result $\sigma_{\mathsf{AIII},\nu=1}^{xx} = e^2/h\pi$, see Table 4.1. (Here the quoted conductance quantum e^2/h is appropriate for charged electrons at the surface of a chiral topological insulator in class AIII [243]. At the surface of a class AIII TSC, this should be replaced by the spin conductance quantum $\hbar/8\pi$ [2, 125].)

The finite-energy crossover scale $\zeta(E)$ is defined as the length L_x where $L_y/\overline{G}$ deviates by 5% from the $E = 0$ result. This is shown in Fig. 4.2(d). It follows the scaling $\zeta(E) \sim E^{-1/z}$, consistent with the z determined from the DOS scaling. Physically, $\zeta(E)$ separates class AIII WZNW critical scaling for shorter length scales from class A IQH scaling at larger ones; $\zeta(E) \to \infty$ as $E \to 0$.

Finally the conductivity at finite energy is analyzed in Fig. 4.2(e). For $0 < E \lesssim \hbar\mathbf{v}/\xi$, there is a plateau at $\sigma \simeq 0.55(e^2/h)$ in fair agreement with the value $\sigma_{\mathsf{IQH}}^{xx} = 0.58 \pm 0.02\frac{e^2}{h}$ obtained by Schweitzer and Markoš [74] via the Kubo formula for a lattice model tuned to the class A IQH (Table 4.1). At larger energies E, the conductivity at the accessible length scales increases with energy. This is expected for the semiclassical Drude conductivity, which goes as $\sigma^{xx} \sim (e^2/h)(1/W^2)$, where W^2 is the disorder strength [253]. For these large energies, the available length scales are insufficient to decide which scenario, Anderson localization or IQH criticality, is realized at the largest length scales.

Results for the $\nu = 2$ model are depicted in Fig. 4.3. The largest scattering region of the $\nu = 2$ sample is $(L_x = 350\xi) \times (L_y = 400\xi)$. The consistency check of the crossover length ζ in Fig. 4.3(c) works just as in the $\nu = 1$ case. The dynamical critical exponent z matches with the expected DOS scaling in Fig. 4.3(b). The conductivity as a function of energy shown Fig. 4.3(e) matches $\sigma_{\mathsf{AIII},\nu=2}^{xx}$ for very low energies. At finite energies it slightly drops to $\sigma_{\mathsf{IQH}}^{xx}$. This drop cannot be resolved in the Kubo computations in Fig. 4.6 and is discussed in the next subsection.

A complementary perspective on the results in Fig. 4.3 for the $\nu = 2$ surface theory is the following. Consider ramping up the non-abelian disorder strength W_N from zero. In Fig. 4.4, results for the conductivity are shown for $W_N = 0, 1, 2, 3$ at fixed abelian disorder strength $W_A = 2.1$ and fixed
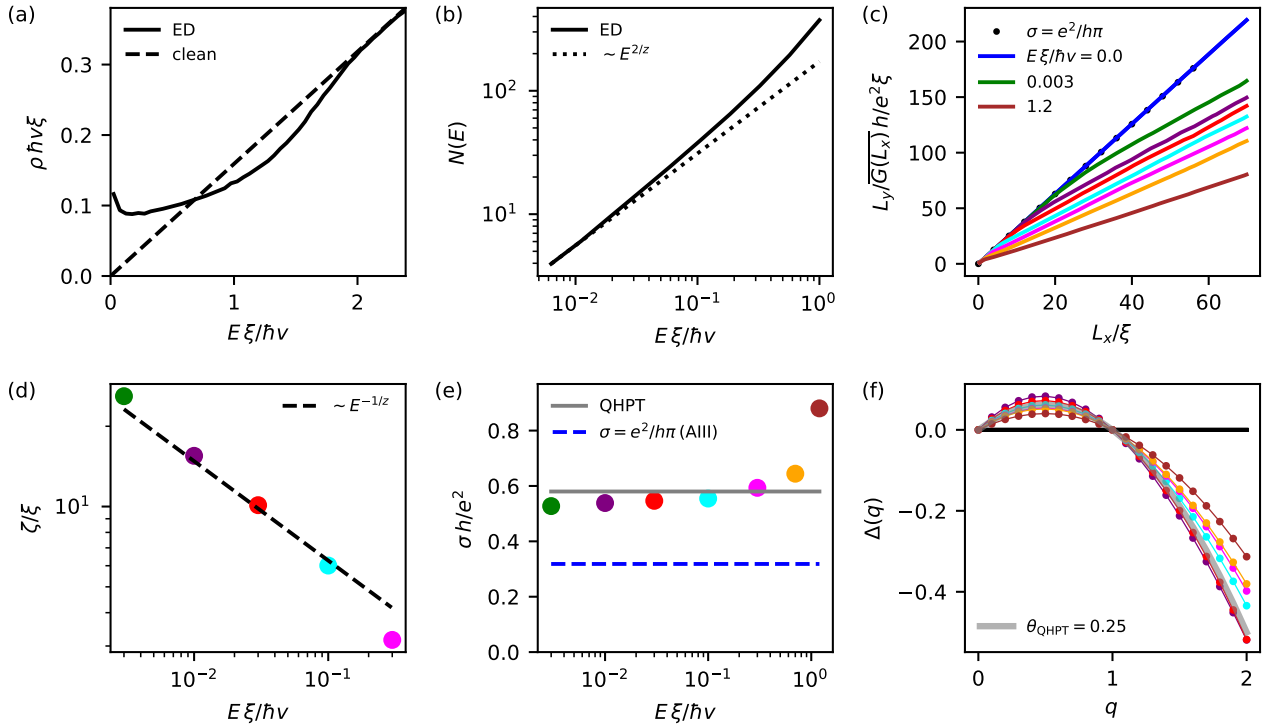
Figure 4.2: Numerical Landauer conductance and multifractal analysis from Ref. [88] for the winding number $\nu = 1$ AIII Hamiltonian, defined by Eq. (4.10). The random abelian vector potential strength is $\sqrt{\lambda_A} \equiv W = 2.3$. (a) The DOS $\rho(E)$ versus energy E, as calculated from momentum-space exact diagonalization (ED), is most strongly affected by disorder around the Dirac point ($E = 0$). (b) The integrated DOS $N(E) = \int_0^E d\varepsilon\, \rho(\varepsilon)$ is plotted versus energy. The predicted scaling form implied by Eq. (4.4) is governed by the disorder-dependent dynamical critical exponent $z = 1 + W^2/\pi$. (c) Quantum transport results for the resistance normalized to system width. The energies are from top to bottom $E\xi/\hbar\mathbf{v} = 0, 0.003, 0.01, 0.03, 0.1, 0.3, 0.7, 1.2$. (d) The *crossover correlation scale* from the transport calculation scales as $\zeta(E) \sim E^{-1/z}$. This scale (not to be confused with the fixed disorder correlation length ξ) governs the crossover at energy E between WZNW and class A IQH criticalities at smaller and larger length scales, respectively. (e) Conductivities extracted from the slope of the curves in panel (c), compared to the established value of the class A IQH critical conductivity (solid gray, see Table 4.1). (f) Anomalous part of the multifractal spectrum $\Delta(q)$ extracted from box-size scaling of ED eigenstates for box sizes beyond the crossover correlation length $\zeta(E)$, as extracted in (d). The data correspond to $E\xi/\hbar\mathbf{v} = 0.01, 0.03, 0.1, 0.3, 0.7, 1.2$ (bottom to top).
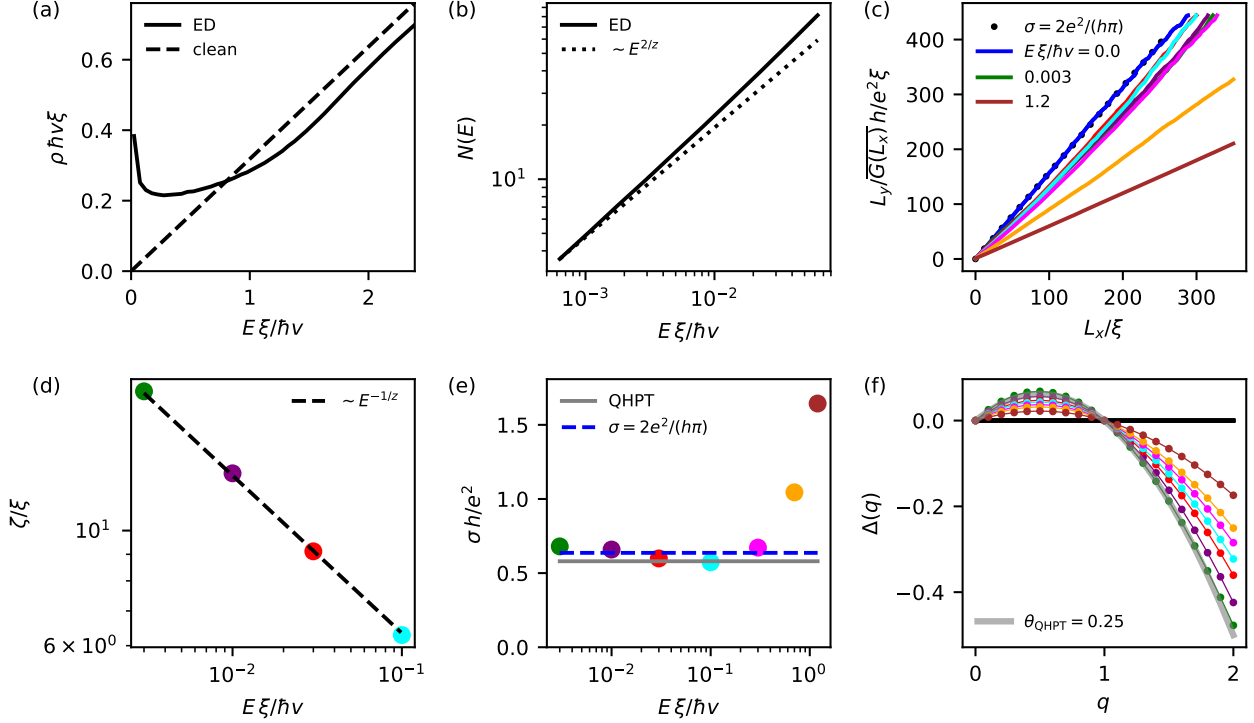
Figure 4.3: Numerical results from Ref. [88] for the topological class AIII surface model with two Dirac nodes ($\nu = 2$), defined by Eq. (4.11). The abelian and non-abelian vector potential disorder strengths are $\sqrt{\lambda_A} \equiv W_A = 2.2$ and $\sqrt{\lambda} \equiv W_N = 1.5$, respectively. (a) The DOS as a function of energy, as calculated from ED. (b) The integrated DOS $N(E) = \int_0^E d\varepsilon\, \rho(\varepsilon)$ plotted versus energy. The predicted scaling form implied by Eq. (4.4) is governed by the dynamical critical exponent $z = 7/4 + W_A^2/\pi$, which depends only on the abelian disorder strength. (c) Quantum transport results for the resistance normalized to system width. The energies are from top to bottom $E\xi/\hbar v = 0, 0.003, 0.01, 0.03, 0.1, 0.3, 0.7, 1.2$. (d) The crossover correlation length from the transport calculation scales as $\zeta(E) \sim E^{-1/z}$. (e) Conductivities extracted from the $L_x \geq 200\xi$ slopes of the curves in panel (c), compared to the established value of the class A IQH critical conductivity (see Table 4.1). (f) Anomalous part of the multifractal spectrum $\Delta(q)$ extracted from box-size scaling of ED eigenstates for box sizes beyond the correlation length $\zeta(E)$ as extracted in (d). The data correspond to $E\xi/\hbar v = 0.003, 0.01, 0.03, 0.1, 0.3, 0.7, 1.2$ (bottom to top).
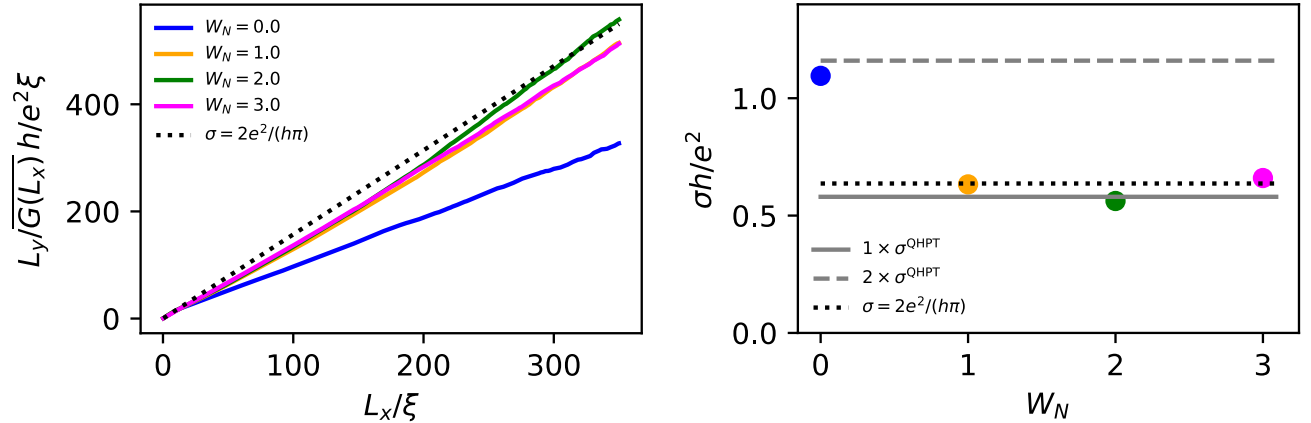
Figure 4.4: Numerical transport results from Ref. [88] for the topological two-node class AIII Dirac model [$\nu = 2$, Eq. (4.11)], with abelian and non-abelian vector potential disorder of strengths $W_A = 2.1$ and increasing $W_N = 0, 1, 2, 3$ at energy $E = 0.03\hbar\mathbf{v}/\xi$. The left panel shows the bare resistance data, while the right panel depicts the bulk conductivities obtained from linear fits to the bare resistance data above $L_x = 200\xi$. These plots establish the crossover of the two-node model from the finite-energy conductivity plateau equal to $2 \times \sigma_{\text{IQH}}^{xx}$ in the absence of internode scattering, to a plateau with value $1 \times \sigma_{\text{IQH}}^{xx}$ in its presence.

energy $E = 0.03\hbar\mathbf{v}/\xi$. For $W_N = 0$, the two nodes are decoupled and the conductivity is close to $2 \times \sigma_{\text{IQH}}^{xx}$, as expected for two replicas of the single node case. For $W_N = 1, 2, 3$ the nodes are coupled and the conductivity is close to the value $1 \times \sigma_{\text{IQH}}^{xx}$.

Finally, there is further numerical evidence for the IQH-stacking scenario obtained in Ref. [88]. First, the full Landauer conductance distribution was computed for both $\nu = 1, 2$ class AIII Dirac models in Ref. [88]. These were calculated for square samples of various sizes, at several energies throughout the surface-state spectrum. The results for both $\nu = 1, 2$ were found to be consistent with the known distribution for the class A IQH [254]. Second, the results for the "anomalous" (WZNW) Dirac models defined by Eqs. (4.10) and (4.11) were benchmarked against identical calculations for nontopological class A and class AIII (Gade) 2D Dirac models. The Gade model [68, 109, 110] arises as the continuum description of a 2D bipartite lattice model with pure intersublattice hopping. These nontopological models were shown to exhibit clear signs of Anderson localization at finite energy, as expected. It is noteworthy that additionally multifractal spectra were computed for surface states of a bulk 3D lattice model for a class AIII TSC in Ref. [88]. The results are consistent with those presented above.

4.3.3 Kubo conductivity

In this subsection, further results testing the AIII WZNW $\rightarrow$ A IQH stacking conjecture are presented, this time computing the dc surface conductivity via the Kubo formula. In natural units $e = 1, \hbar = 1$,
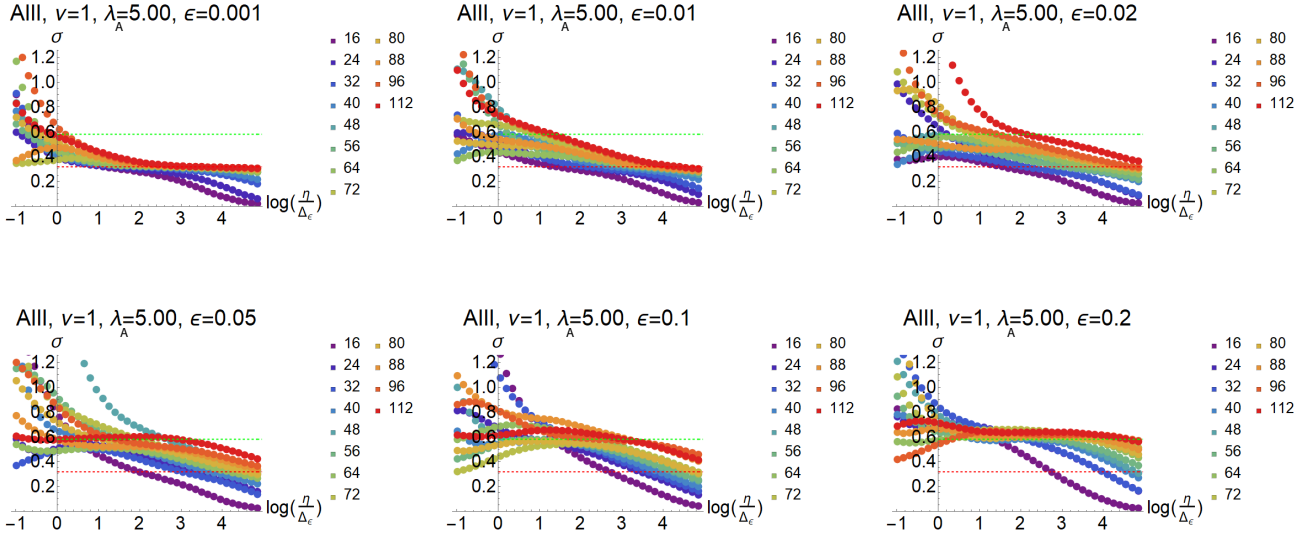
Figure 4.5: Figure taken from Ref. [90]. Numerical Kubo conductivity $\sigma_{\mathsf{dc}}^{xx}$ computed with Eq. (4.17) for the strongly disordered AIII $\nu = 1$ model [Eq. (4.10)], as function of the broadening η. The disorder strength is $\lambda_A = 5$. A logarithmic scale for η in units of the local level spacing Δ_ε is chosen. There is convergence to a plateau of $\sigma_{\mathsf{dc}}^{xx}$ as function η as the linear system size N increases. At small energies $\varepsilon \ll \Lambda$, $\sigma_{\mathsf{dc}}^{xx}$ tends to the WZNW value associated with the zero-energy state of the Dirac theory (red dashed). For finite energies $\varepsilon \lesssim \Lambda$, a value of $\sigma_{\mathsf{dc}}^{xx}$ compatible with the universal IQH result $\sigma_{\mathrm{IQH}}^{xx}$ (green dashed) is found. States at $\varepsilon \approx \Lambda$ are not affected much by the disorder and therefore do not show universal conductance values. This confirms the Landauer computation in Fig. 4.2(e).
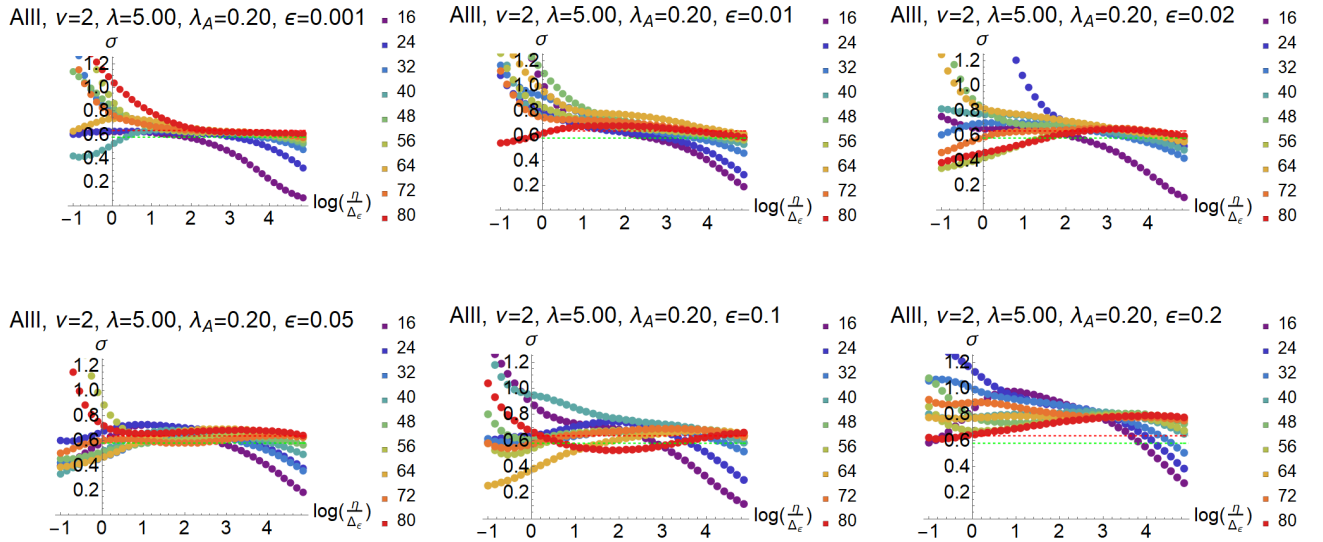
Figure 4.6: Figure taken from Ref. [90]. Same as Fig. 4.5 for the AIII $\nu = 2$ model [Eq. (4.11)]. The nonabelian disorder strength is $\lambda = 5$, while the abelian strength is $\lambda_A = 0.2$. The WZNW value (red dashed) and the universal IQH result (green dashed) are very close to each other. The convergence of $\sigma_{\mathrm{dc}}^{xx}$ is not as clear as in Fig. 4.5. Since the model incorporates the 2D color space [Eq. (4.11)], only systems with $N \leq 80$ are numerically accessible. The data does not show signs of the conventionally expected Anderson localization $\sigma_{\mathrm{dc}}^{xx} \to 0$ at finite energies for this even-winding number class AIII system. In contrast to the more precise Landauer computation presented in Figs. 4.3(e) and 4.4, One cannot distinguish the zero- and finite-energy behavior. States at $\varepsilon \approx \Lambda$ are not affected much by the disorder and therefore do not show universal conductance values.

the Kubo formula relates the dc conductivity $\sigma_{\mathsf{dc}}^{ab}$ to the current-current response function $\mathcal{K}^{ab}(\varepsilon)$:

$$\sigma_{\mathsf{dc}}^{ab} = \frac{1}{4\pi} \int_{-\infty}^{\infty} \left[-\frac{df(\varepsilon)}{d\varepsilon} \right] \mathcal{K}^{ab}(\varepsilon), \tag{4.14}$$

$$\mathcal{K}^{ab}(\varepsilon) \equiv \frac{1}{L^2} \int_{\mathrm{r,r'}} \mathrm{Tr} \left[\hat{\sigma}^a \, \hat{\rho}(\varepsilon; \mathrm{r}, \mathrm{r}') \, \hat{\sigma}^b \, \hat{\rho}(\varepsilon; \mathrm{r}', \mathrm{r}) \right]. \tag{4.15}$$

The finite size conductivity $\sigma_{\mathsf{dc}}^{ab}$ must be evaluated with spectral densities $\hat{\rho}(\varepsilon; \mathrm{r}, \mathrm{r}')$ broadened by a finite η of the order of the level spacing around energy ε:

$$\hat{\rho}(\varepsilon; \mathrm{r}, \mathrm{r}') = i \left[\hat{G}_R(\varepsilon; \mathrm{r}, \mathrm{r}') - \hat{G}_A(\varepsilon; \mathrm{r}, \mathrm{r}') \right] = 2\pi \sum_l \left[\frac{\eta/\pi}{(\varepsilon - \varepsilon_l)^2 + \eta^2} \right] \psi_l(\mathrm{r}) \, \psi_l^\dagger(\mathrm{r}'), \tag{4.16}$$

where $\psi_l(\mathrm{r})$ is an exact eigenstate. One can employ

$$\mathcal{K}^{ab}(\varepsilon) = \left(\frac{2\pi}{L} \right)^2 \sum_{l,m} \left[\frac{\eta/\pi}{(\varepsilon - \varepsilon_l)^2 + \eta^2} \right] \left[\frac{\eta/\pi}{(\varepsilon - \varepsilon_m)^2 + \eta^2} \right] \langle l | \hat{\sigma}^a | m \rangle \langle m | \hat{\sigma}^b | l \rangle \tag{4.17}$$

to compute the Kubo conductivity with eigenenergies ε_l and states $|l\rangle$ from exact diagonalization. The result should be virtually independent of the broadening η chosen around the local level spacing Δ_ε. Calculations are performed for the momentum-space version of the continuum Hamiltonians in Eqs. (4.10) and (4.11), with quantized momenta corresponding to a finite-size torus and an ultraviolet energy cutoff Λ.

The Kubo conductivity $\sigma_{\mathsf{dc}}^{xx}$ is computed via Eq. (4.17) for the strongly disordered AIII $\nu = 1$ model as a function of the level broadening η. A logarithmic scale for η in units of the local level spacing Δ_ε is chosen (the critical DOS $\nu(\varepsilon) \propto \varepsilon^\alpha$ is responsible for the dependence $\Delta_\varepsilon \propto \varepsilon^{-\alpha}$). For large enough systems, $\sigma_{\mathsf{dc}}^{xx}$ as function η should depend only weakly on η. The tendency of $\sigma_{\mathsf{dc}}^{xx}$ to converge towards a plateau value is used as a measure of finite size effects. The results are shown in Fig. 4.5. At small energies $\varepsilon \ll \Lambda$, $\sigma_{\mathsf{dc}}^{xx}$ tends towards the WZNW value $\sigma_{\mathrm{AIII},\nu=1}^{xx} = 1/\pi$ (Table 4.1). For finite energies $\varepsilon \lesssim \Lambda$, one finds a value of $\sigma_{\mathsf{dc}}^{xx}$ compatible with the universal IQH result $\sigma_{\mathrm{IQH}}^{xx} \approx 0.58$ (green dashed). States at high energies $\varepsilon \approx \Lambda$ are only weakly affected by the disorder and therefore do not show universal conductance values. Further this confirms the Landauer computation in Ref. [88], see Fig. 4.2(e).

For the AIII $\nu = 2$ model, the results are shown in Fig. 4.6. The WZNW value $\sigma_{\mathrm{AIII},\nu=2}^{xx} = 2/\pi$ (red dashed) and the IQH result $\sigma_{\mathrm{IQH}}^{xx} \approx 0.58$ (green dashed) are numerically close to each other. The convergence of $\sigma_{\mathsf{dc}}^{xx}$ is not as clear as for the $\nu = 1$ case, Fig. 4.5. Since one needs an additional color space to realize this model [Eq. (4.11)], only systems with $N \leq 80$ are numerically accessible. The data does not show signs of the conventionally expected Anderson localization $\sigma_{\mathsf{dc}}^{xx} \to 0$ in the thermodynamic limit $N \to \infty$ at finite energies for $\nu = 2$ (i.e., even winding numbers). In contrast to the more precise Landauer computation performed in Ref. [88], presented in Figs. 4.3(e) and 4.4, one cannot distinguish the zero- and finite-energy behavior. Finite size effects estimated by the fluctuation of $\sigma_{\mathsf{dc}}^{xx}(\eta)$ are larger than the numerical difference of the expected conductivities $\sigma_{\mathrm{IQH}}^{xx} \sim \sigma_{\mathrm{AIII},\nu=2}^{xx}$. States at $\varepsilon \approx \Lambda$ are not affected much by the disorder and therefore do not show universal conductance values.
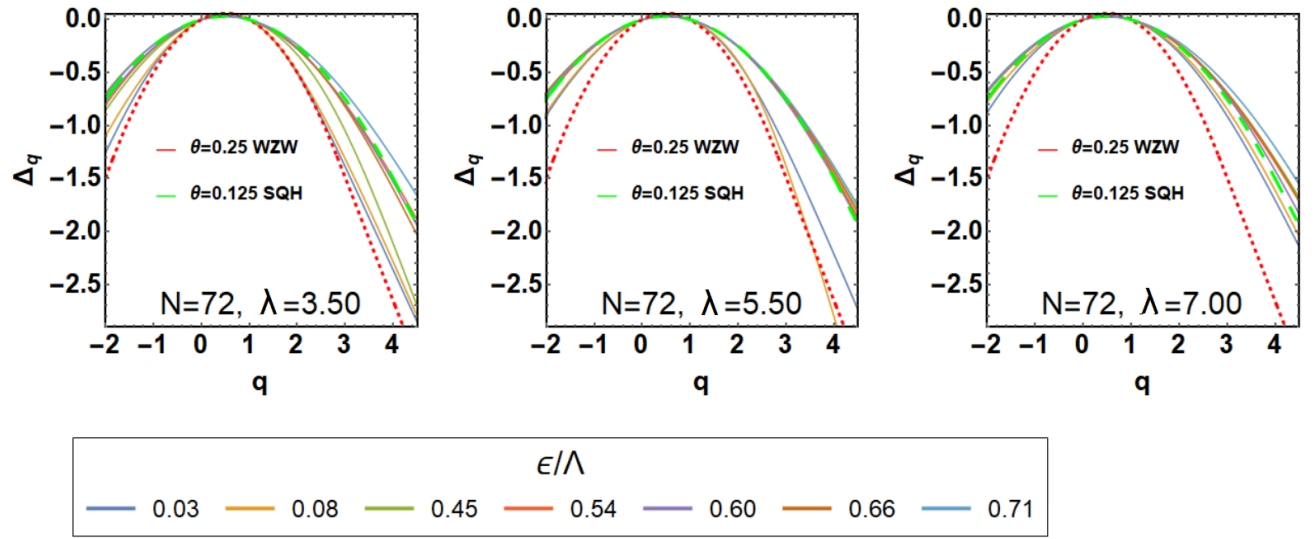
Figure 4.7: Figure taken from Ref. [90]. Multifractality in the CI $\nu = 2$ model, for the largest system size $N = 72$, at weak $\lambda = 3.5$, intermediate $\lambda = 5.5$, and strong disorder $\lambda = 7.0$. The system is a $(2N + 1) \times (2N + 1)$ grid in momentum space; Λ is the ultraviolet energy cutoff for the clean Dirac spectrum. Near-zero energy states and finite-energy states are compared to the class CI-WZNW (red dashed) and class C-SQH parabolic spectra (green dashed). With increasing disorder, there are fewer and fewer states that match the CI-WZNW prediction, and the crossover scale moves towards zero energy. Fig. 4.8 exhibits a finite-size analysis of Δ_q for $q = 2, 3$.
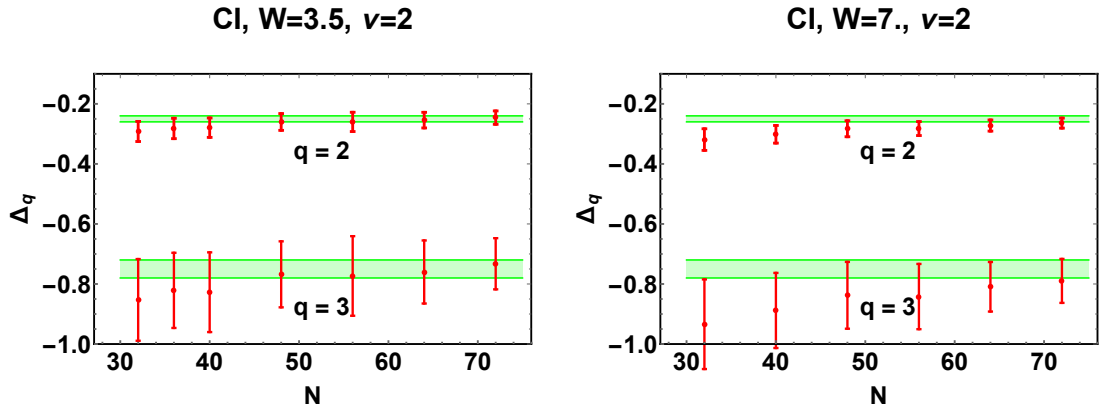
Figure 4.8: Figure taken from Ref. [90]. Finite energy Δ_q for $q = 2, 3$ in the class CI $\nu = 2$ model as function of system size $N = 32, \ldots 72$. The green lines are exact analytical predictions $\Delta_2 = -1/4$, $\Delta_3 = -3/4$ for the class C SQH (see Table 4.1). The red points are average values for Δ_q in the energy range $0.2 \lesssim \varepsilon/\Lambda \lesssim 1$; Λ is the ultraviolet cutoff for the clean Dirac spectrum. Error bars indicate the variance. When increasing N, the Δ_q converge and fluctuations diminish for both intermediate and strong disorder $W \equiv \lambda$.
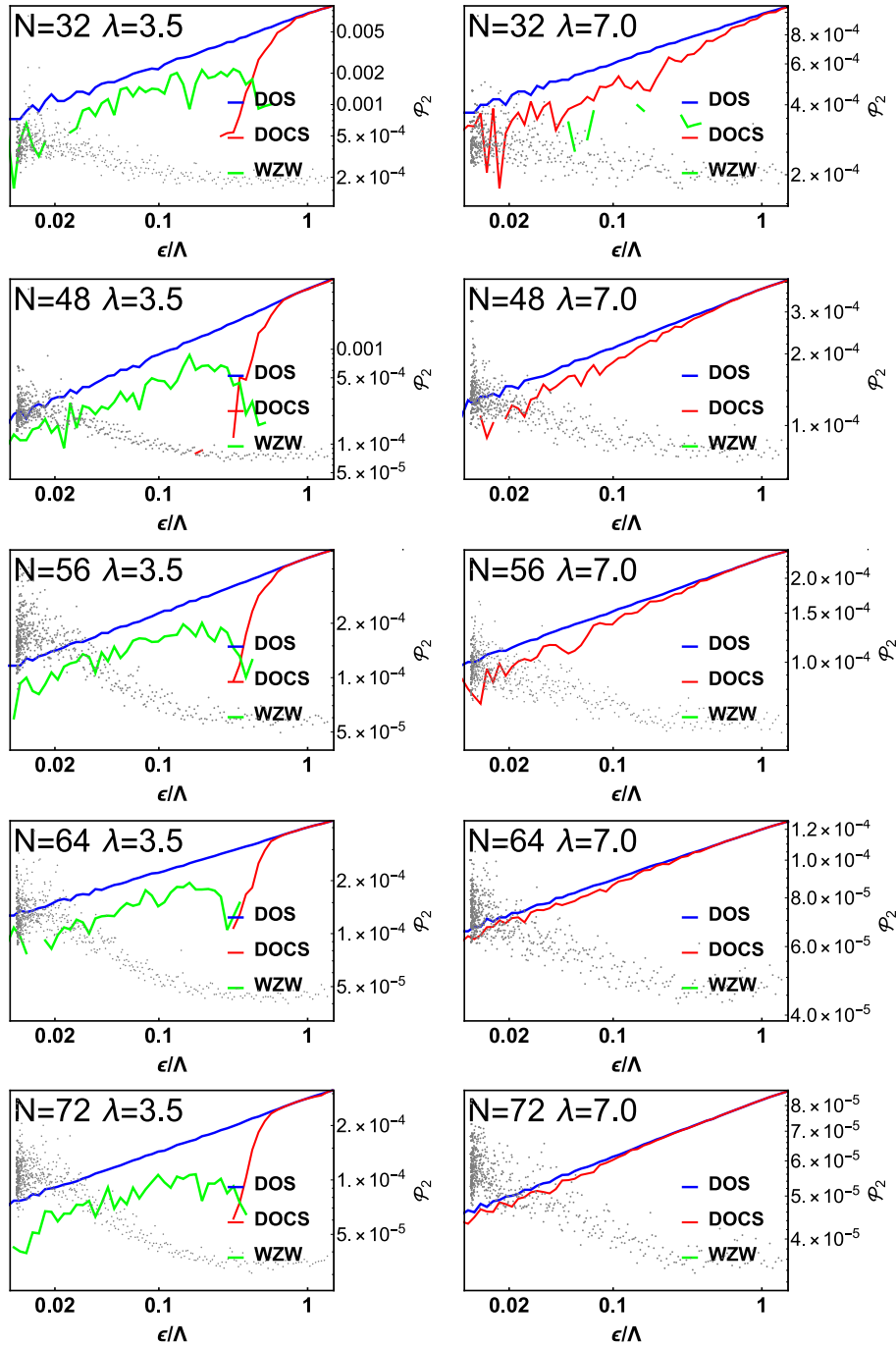
Figure 4.9: Figure taken from Ref. [90]. The density of critical states (DOCS) versus the total density of states (DOS) for the class CI model. A state is termed critical when it matches the expected multifractal spectrum τ_q for the class C-SQH within 4% for at least 75% of the $0 < q < q_c$, where $q_c = 4$. At zero energy one expects class CI WZNW-criticality and at finite energies SQH-criticality, see Fig. 4.8. With increasing system size N or disorder strength λ, the amount of WZNW-critical states decreases in favor of class C-SQH critical finite-energy states. (The green curve labeled "WZW" denotes the density of critical class CI-WZNW states). Superimposed in light gray is the inverse-participation ratio $\mathcal{P}_2$, which shows that states away from zero energy are *less* rarified, as predicted by the stacking conjecture.
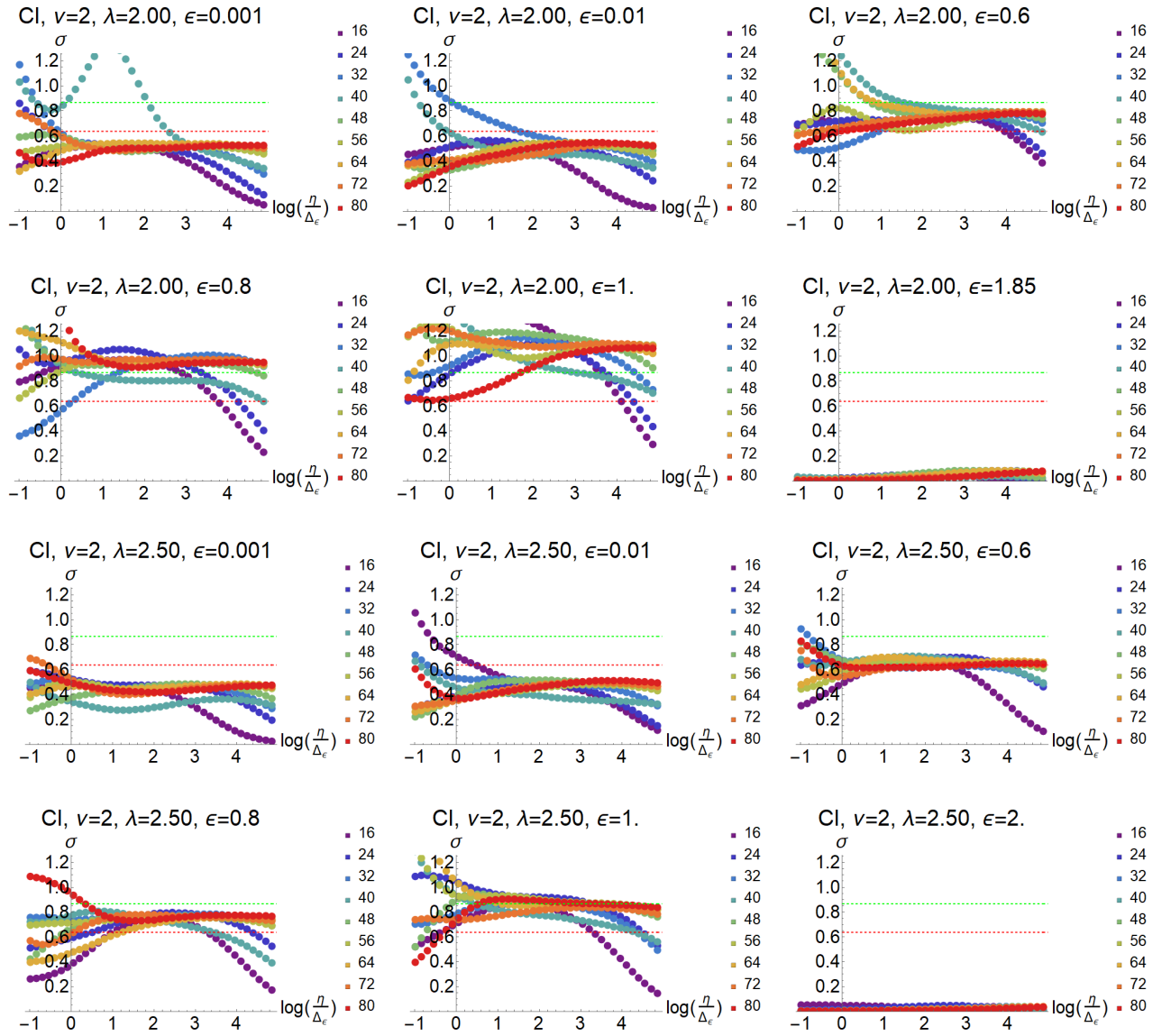
Figure 4.10: Figure taken from Ref. [90]. Numerical Kubo conductivity $\sigma_{\mathrm{dc}}^{xx}$ for the class CI model, computed with Eq. (4.17), for moderate disorder as function of the level broadening η. A logarithmic scale for η in units of the local level spacing Δ_ε is chosen. Numerical results are compared to the exact zero-energy WZNW result $\sigma_{\mathrm{CI},\nu=2}^{xx} = 2/\pi$ (red dashed) and to the exact average value for the class C SQH $\sigma_{\mathrm{SQH}}^{xx} = \sqrt{3}/2$ (green dashed), see Table 4.1. For most energies (except the smallest), there is convergence as a function of η as N increases, and $\sigma_{\mathrm{dc}}^{xx}$ does not depend on η significantly, i.e. shows a plateau. For the purposes here only the finite energies are crucial, but at strong disorder $\lambda \gtrsim 3$ convergence also becomes poor there. The increased finite-size effects near zero energy disable one from going to the strongly disordered regime, where more of the spectrum is SQH-critical, according to the multifractal analysis presented in Figs. 4.7–4.9. Crucially, though, one only observes evidence for Anderson localization deep in the high-energy Lifshitz tail. This again contradicts the conventional picture that all finite-energy states localize in the orthogonal class AI (Secs. 4.2.1 and 4.2.2).

4.4 Full SU(2) spin symmetry: class CI

A class CI topological surface can be described by the following Dirac Hamiltonian:

$$H_{\mathrm{CI}} = \hat{\sigma} \cdot \left[(-i\nabla) + \mathrm{A}_i(\mathrm{r})\,\hat{\tau}^i \right], \quad \overline{A_i^a(\mathrm{r})\,A_j^b(\mathrm{r}')} = \lambda\,\delta^{ab}\,\delta_{ij}\,\delta_{\xi}^{(2)}(\mathrm{r} - \mathrm{r}'), \tag{4.18}$$

where $\hat{\sigma} \equiv \hat{\sigma}^1\,\hat{x} + \hat{\sigma}^2\,\hat{y}$. The winding number $\nu = 2k$ is always even for class CI; disorder that preserves physical time-reversal and spin SU(2) symmetry appears as the color gauge potential A_i, where the $2k \times 2k$ color-space matrices $\{\hat{\tau}^i\}$ generate the color group Sp($2k$) [61, 124, 242]. For the minimal case $k = 1$, Eq. (4.18) is identical to the $\nu = 2$ class AIII Hamiltonian with vanishing abelian disorder [$\lambda_A = 0$ in Eq. (4.11)].

In Ref. [75], extensive studies for several values of ν lead to the class CI WZNW $\to$ C spin quantum Hall plateau transition (SQH) stacking conjecture. Instead of employing Sp($2k$) generators, for $k > 1$ a dispersion-modified version of the Hamiltonian in Eq. (4.11) was used to study class CI with higher winding numbers in [75]. In lieu of reproducing this data, here additional simulations for larger systems ($N_{max} = 72$ vs. $N_{max} = 46$) are shown, with focus on the minimal winding number $\nu = 2$. In this case one can use Eq. (4.18), where the color generators $\{\hat{\tau}^i\}$ are Pauli matrices.

4.4.1 Multifractal analysis

The multifractal spectrum Δ_q is computed numerically [Eqs. (1.67) and (1.66)] using exact diagonalization of the continuum Dirac Hamiltonian in Eq. (4.18) in momentum space. Results are shown for Δ_q, computed for the largest available system size, at various energies in Fig. 4.7. With increasing disorder strength λ, fewer and fewer states match the zero-energy class CI WZNW prediction [Eq. (4.5) with $\theta = 1/4$]. Instead they converge towards the parabolic approximation to the SQH spectrum with $\theta_{\mathsf{SQH}} = 0.125$ (see Table 4.1). In Chap. 3 *deviations* of the SQH spectrum from exact parabolicity are discussed. Strong violations of generalized parabolicity in the subleading multifractal spectrum were found. However, the deviations from parabolicity are small in the leading multifractal spectrum Δ_q in the range of q considered here.

In Fig. 4.8 Δ_q for $q = 2, 3$ at finite energies $\varepsilon/\Lambda \gtrsim 0.2$ are shown. The red dots mark the average values over that part of the spectrum with the standard deviation given by the error bars. With increasing system size, the error bars shrink and there is convergence towards the $\theta_{\mathsf{SQH}} = 1/8$ parabola. In contrast with the conventional reduction to the orthogonal Wigner–Dyson class AI at finite energy (which would imply Anderson localization of all finite-energy states, see Secs. 4.2.1 and 4.2.2), one instead sees evidence for "stacked" universal quantum criticality, consistent with the SQH.

Following Ref. [75], in Fig. 4.9 stacking throughout the energy spectrum is analyzed statistically. In each panel, the total density of states (DOS) is plotted, as well as the *density of critical states* (DOCS). The latter is defined as follows. The DOCS is determined by the proportion of critical states at finite energy matching the class C SQH $\theta_{\mathsf{SQH}} = 1/8$ parabolic ansatz, within the tolerance criterion that 75% of the τ_q with $q \in [0, q_c]$ have to match the parabolic τ_q^θ up to 4% accuracy. Here $q_c(\theta) \equiv \sqrt{2/\theta}$ is the termination threshold [9, 75, 226]. In addition to the DOS and SQH DOCS, in Fig. 4.9 the DOCS for matching the zero-energy class CI WZNW prediction [Eq. (4.5) with $\theta = 1/4$, Table 4.1] is also exhibited. As indicated by the results in Fig. 4.9, more (less) of the spectrum matches the class C SQH (class CI WZNW) prediction as the system size N or disorder strength λ is increased. Since the class C SQH states exhibit *weaker* multifractality than the CI WZNW states, this is strong evidence against Anderson localization.
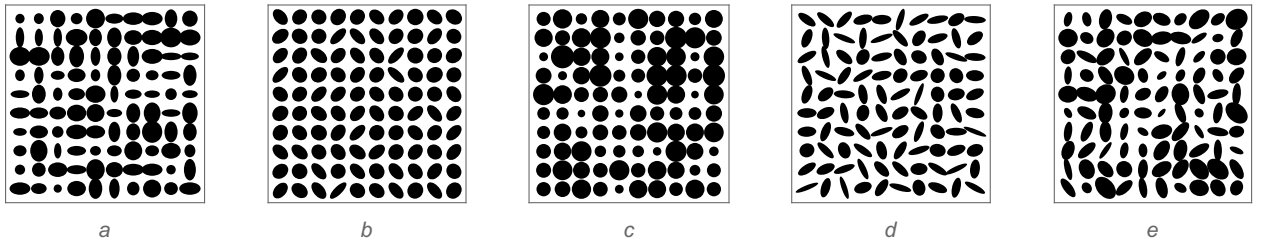
Figure 4.11: Figure taken from Ref. [90]. Visualization of quenched gravitational disorder (QGD): the spatial components of the random metric tensor projected on a flat 2D space. A 2×2 tensor v_{ij} can be visualized by the quadratic form $\{x : v_{ij}x_ix_j = r^2\}$ for some fixed $r > 0$. Different classes of disorder (a)–(e) are considered (see text): (a) flattening/steepening + nematic disorder $v_{21} = v_{12} = 0$, (b) rotations + nematic disorder $\delta v_{11} = \delta v_{22} = 0$, (c) flattening/steepening + rotations $\delta v_{11} = \delta v_{22}$ and $\delta v_{12} = -\delta v_{21}$ (conformal spin $s = 0$), (d) full nematic disorder $\delta v_{11} = -\delta v_{22}$ and $\delta v_{12} = \delta v_{21}$ (conformal spin $s = -2, 2$), (e) generic disorder.

4.4.2 Kubo conductivity

The Kubo conductivity is computed the same way as for the AIII surfaces in Sec. 4.3.3. In Fig. 4.10, the numerical Kubo results for selected energies across the spectrum is shown. Near zero energy, one expects the exact WZNW result $\sigma^{xx}_{\text{CI},\nu=2} = 2/\pi$ (Table 4.1). This result holds for *every* disorder configuration, in the infinite system-size limit. For weak disorder $\lambda \lesssim 1$ one can observe this in the numerics. Finite-size effects seem to grow quickly with increasing disorder, which makes the most interesting regime $\lambda \gtrsim 3$, where SQH multifractality has spread over a wide range of the energy spectrum, difficult to reach numerically. This is the reason for the derivation from the exact WZNW result for $\lambda = 2, 2.5$ shown. At higher energies, the multifractal spectrum suggests class C SQHP criticality. The average value of the conductivity is known to be $\sigma^{xx}_{\text{SQH}} = \sqrt{3}/2$ [76].

Although finite-size effects remain relevant near zero energy, the results indicate convergence towards a finite conductivity, coincident with the Cardy value, at finite energies. This is again in contrast with the conventional expectation of Anderson localization in the orthogonal class AI (Secs. 4.2.1 and 4.2.2). On the other hand, for very high energies $\varepsilon \gtrsim \Lambda$ (in the Lifshitz tail), one observes localization in Δ_q. This is consistent with $\sigma^{xx}_{\text{dc}} \to 0$ observed here, as shown for energy $\varepsilon = 2\Lambda$ in Fig. 4.10.

4.5 Broken spin rotation symmetry: class DIII

4.5.1 Majorana surface fluids, quenched gravitational disorder, and possible relevance to high-T_c cuprates

The simplest bulk topological superconductor resides in class DIII, with the minimal winding number $\nu = 1$; this would be a solid-state analog of ^{3}He-B [2, 219, 220], as has been proposed e.g. in Cu$_x$Bi$_2$Se$_3$ [255–261] Nb$_x$Bi$_2$Se$_3$ [262–265], and β-PdBi$_2$ [266, 267]. In this case, superconductivity and strong spin-orbit coupling imply that neither charge nor spin transport is well-defined at the surface.

The surface theory consists of a single massless Majorana cone. In contrast to the surface Hamiltonian in Eq. (4.1) (which applies for class DIII with winding numbers $|\nu| \geq 3$), the only continuous

symmetry available to gauge by disorder is Poincaré invariance, i.e. "gravitational" coupling to the stress tensor.

Here the results of Ref. [89] are reviewed, in which the effects of "quenched gravitational disorder" (QGD) for a single 2D cone were studied. Time-reversal invariant perturbations, such as a charged impurity, couple only to the spatial–spatial components of the stress–energy tensor T^{ab}, with $a, b \in \{1, 2\}$ [89]. The most generic surface Hamiltonian takes the form

$$H = -\frac{1}{2} \sum_{a,b=1,2} \int d^2r \, v_{ab}(\mathrm{r}) \left(\bar{\psi} i \hat{\sigma}^a \overleftrightarrow{\partial}_b \psi \right), \tag{4.19}$$

where the bidirectional derivative $A \overleftrightarrow{\partial} B = A \partial B - (\partial A) B$. For the Majorana surface theory, $\bar{\psi} = \psi^{\mathsf{T}} \hat{\sigma}^1$. The *four* velocity components are the isotropic Fermi velocity of the clean Majorana cone, perturbed by quenched random fluctuations: $\left\{ v_{11}(\mathrm{r}) \equiv 1 + \delta v_{11}(\mathrm{r}), \, v_{22}(\mathrm{r}) \equiv 1 + \delta v_{22}(\mathrm{r}), \, v_{12}(\mathrm{r}), \, v_{21}(\mathrm{r}) \right\}$. In Ref. [89], five different variants of that model were considered. The variants are visualized in Fig. 4.11,

(a) Independent $\{\delta v_{11}, \delta v_{22}\}$, $v_{12} = v_{21} = 0$. Local isotropic flattening or steepening of the Dirac cone and nematic squishing of the cone.

(b) Independent $\{v_{12}, v_{21}\}$, $\delta v_{11} = \delta v_{22} = 0$. Local pseudospin rotations (antisymmetric part $v_{12a} = -v_{21a}$) and nematic squishing of the Dirac cone (symmetric part $v_{12s} = +v_{21s}$).

(c) Independent $\{\delta v_{11} = \delta v_{22}, \, v_{12} = -v_{21}\}$. Local isotropic flattening or steepening of the Dirac cone and pseudospin rotations.

(d) Independent $\{\delta v_{11} = -\delta v_{22}, \, v_{12} = v_{21}\}$. Local nematic squishing of the Dirac cone.

(e) Independent $\{\delta v_{11}, \delta v_{22}, v_{12}, v_{21}\}$. The generic model.

Without further restrictions, the generic theory (e) is realized. For a fully isotropic bulk superfluid, it can be shown that electric potentials couple only through the isotropic flattening or steepening of the surface Majorana cone, model (c) [89]. Crystal field effects will however generically enable off-diagonal QGD (nonzero $\{v_{12}, v_{21}\}$). Model (d) is another interesting special case, since pure nematic QGD couples only to the holomorphic $T(z)$ and antiholomorphic $\bar{T}(\bar{z})$ stress tensor components (using the language of 2D conformal field theory) [89].

It is important to emphasize that QGD as in Eq. (4.19) will generically be present in *any* 2D massless Dirac material. At zero energy (the Dirac point), short-range correlated QGD is strongly irrelevant. This is why it is typically ignored, compared to mass, scalar, or vector potential perturbations [as in Eq. (4.1)]; short-ranged correlated disorder in the latter is marginal at tree level. The very surprising finding in [89], reviewed below, is that while weak QGD is indeed irrelevant near zero energy, it appears to induce quantum-critical stacking of states with weak, but universal multifractality, similar to the class AIII and CI systems studied above. This occurs because nonzero energy is a strongly relevant perturbation to the (2+0)-D Dirac-point theory. For QGD, the latter can also be cast as a modified version of the WZNW model in Eq. (4.6) with $\nu = 1$ and $\lambda_A = 0$; again $\omega \neq 0$ drives this model away from the zero-energy WZNW fixed point (in this case, equivalent to free fermions), towards some strong coupling regime. The numerical results presented in Figs. 4.13, 4.12 indicate that this is another version of the critical stacking scenario.

QGD might be important in the high-T_c cuprate superconductors [89]. As reviewed in Sec. 4.2.1, the generic Bogoliubov–de Gennes Hamiltonian for a 2D d-wave superconductor with non-magnetic

disorder resides in the non-topological version of class CI; in contrast to Eq. (4.1), the low-energy Dirac theory for the four independent quasiparticle colors features mass, scalar, and vector potentials. This model is known to Anderson localize at all energies [62]. If however one assumes that sufficiently long-wavelength disorder dominates, which does not scatter between the colors, then one obtains four independent copies of the class AIII $\nu = 1$ WZNW Hamiltonian in Eq. (4.10) [62]. Given the class AIII WZNW $\rightarrow$ class A IQH stacking conjecture, this would imply relatively strong multifractality (wave function rarification) at finite energy, along with a strongly renormalized low-energy density of states. This is not seen in experiment. However, *nematic* QGD [as in models (b) and (d), described above] in fact produces a phenomenology similar to that observed in STM maps of the local density of states in BSCCO [89, 229–234]. This includes plane-wave like states at low energy, with a linear-in-energy density of states, but energy-independent, nanometer-scale critical inhomogeneity at finite energies [89]. See also Fig. 4.1 and Table 4.1.

Models (b) and (d) with *nematic* QGD show the most robust stacking of critical eigenstates with universal statistics, as reviewed below. In the context of the cuprates, this is interesting because of the potential role of nematicity in these materials [268, 269]. In particular, evidence for *quenched random nematicity* has emerged in recent studies of the pseudogap phase [270].

The natural generalization of the stacking conjectures in classes AIII and CI is: class DIII WZNW $\rightarrow$ class D thermal quantum Hall (TQH) criticality. As reviewed in Sec. 1.5.3, very little is known about the TQH transition. The multifractal spectra presented in Fig. 4.13 may constitute the first (indirect) results substantiating a universal description of this transition.

4.5.2 Multifractal analysis

In Ref. [89], models (a)–(e) were studied for a large range of $N = 32, \ldots, 96$. In all five models, there are critical states at finite energy matching a $\theta = 1/13$ parabolic ansatz for Δ_q [Eqs. (1.66) and (4.5), Table 4.1]. As for class CI in Sec. 4.4 and Fig. 4.9, one can define the *density of critical states* (DOCS) as follows. This is the proportion of states at finite energy matching the tolerance criterion that 85% of the τ_q within the range $q \in [0, q_c]$ match the parabolic τ_q^θ ansatz with $\theta = 1/13$ up to 4% accuracy; here $q_c = 5.1$ is the termination threshold [9, 89, 226]. The DOCS is plotted for all three models in Fig. 4.12.

As the disorder strength is increased, the critical swath shrinks for model (a) and even more strongly for (c). In Fig. 4.11 and in the definition below Eq. (4.19), one can see that both of these models feature local isotropic flattening and steepening of the Dirac cone. Near zero energy in these models, there are stronger multifractal (rarified) states visible in the superimposed second IPR $\mathcal{P}_2$ (gray) in Fig. 4.12. At high energies near the cutoff there is a crossover to localized Lifshitz tail states.

In the absence of the isotropic flattening and steepening, models (b), (d) instead exhibit an *increasing* number of critical states (improved "stacking") with increasing disorder. Models (b) and (d) are similar, except that for the latter, rarified zero-energy states set in at intermediate disorder, see Fig. 4.12. Indeed models (b) and (d) are related by local diffeomorphisms in the gravitational formulation of the problem [271]. Since there are more independent disorder terms in (d), it is mapped to a (b) with effectively stronger disorder. One must note however that the interpretation of diffeomorphisms is different than in general relativity or 2D quantum gravity [272–274]: at the surface of a dirty class DIII TSC, there is a preferred coordinate system (x, y) that measures physical distances across the surface, given the flatness of physical spacetime. Disorder modulates the Majorana surface fluid in a way that is mathematically identical to gravity, but geodesic distances are not directly measurable.

Model (e) containing generic disorder exhibits a wide swath of critical states for weak disorder.
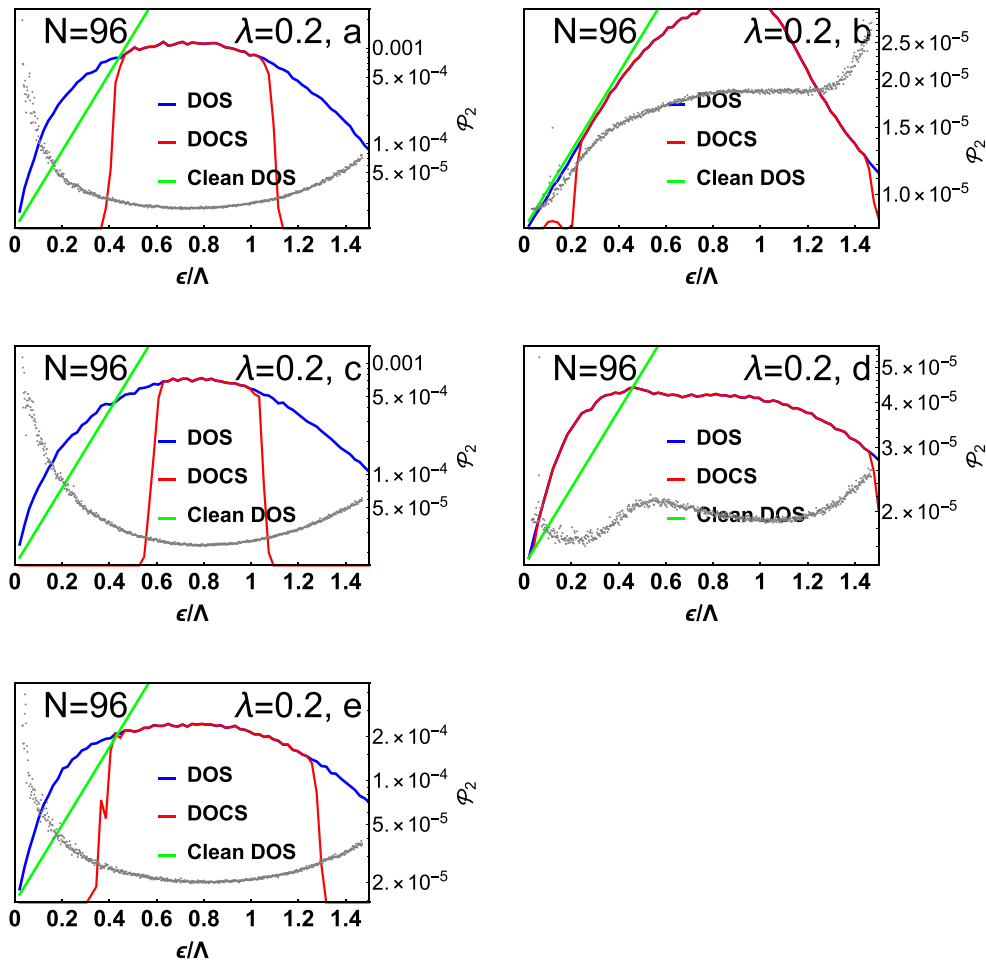
Figure 4.12: This figure shows the total density of states (DOS) and the density of critical states (DOCS) for the QGD, models (a)–(e), defined in and below Eq. (4.19). Results were obtained by diagonalizing the Hamiltonian from Eq. (4.19) over a $(2N + 1) \times (2N + 1)$ grid in momentum space, with cutoff $N = 96$ here [89]. Data is plotted for the five different models at fixed dimensionless disorder strength $\lambda = 0.2$; strong disorder corresponds to $\lambda \gtrsim 0.393$. The DOCS counts the number of states with critical statistics (multifractal spectra) that match a universal ansatz with a certain fitness criterion (see caption of Fig. 4.13). Also plotted is the second IPR $\mathcal{P}_2$ (gray dots), defined by Eq. (1.65). For models (a, c, e), a large swath of the spectrum appears critical for weak disorder. However, as the disorder strength is increased, the swath shrinks [89]. The IPR $\mathcal{P}_2$ shows that states outside of the swath are more rarified or localized than the critical ones. The linear-in-energy DOS of the clean limit is strongly distorted and filled-in at low energies, which happens in models (a, c, e) for all $\lambda \gtrsim 0.2$. These strong disorder effects are likely induced by the velocity component responsible for isotropic flattening or steepening of the cone. By contrast, models (b, d) show plane-wave states near zero energy for weak disorder. Rarification near zero energy sets in for strong disorder; for model (d) the crossover is already visible at $\lambda = 0.2$ shown here. The critical swath is larger and more robust to disorder strength in models (b, d), compared to (a, c, e). Models (b, d) both contain nematic disorder and exclude isotropic flattening.
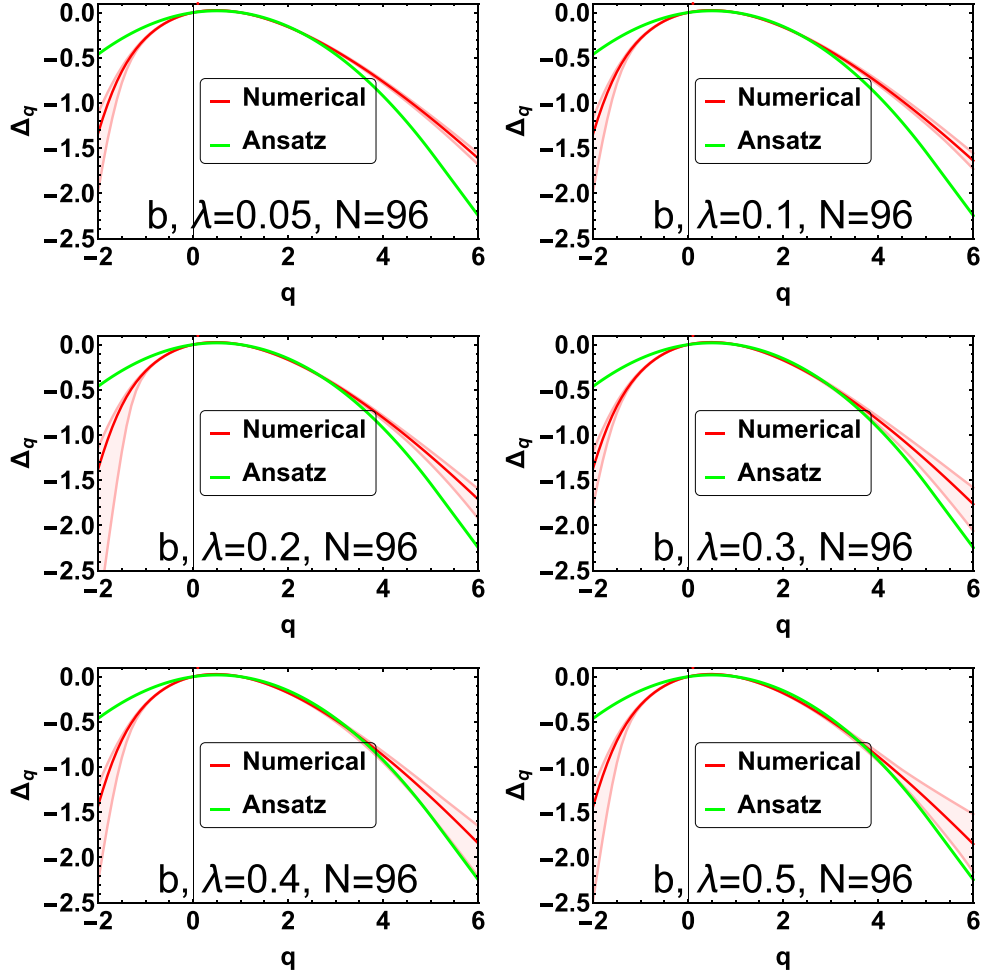
Figure 4.13: Anomalous multifractal spectrum Δ_q [Eq. (1.66)] for an energy bin of states selected from the DOS with the highest percentage of critical states from Ref. [89]. Here the spectrum is shown for model (b), evaluated for the six different disorder strengths. The solid red curve denotes an average over the 15 states in the bin; the shaded red region indicates the standard deviation. The green curve is the parabolic ansatz for $\Delta_q = -\theta\, q(1-q)$, with $\theta = 1/13$. States contributing to the critical count (DOCS) in Fig. 4.12(b) match the parabolic ansatz within a certain threshold (see text) over the range $0 < q \leq q_c = 5.1$.

However, this shrinks with increasing disorder strength, similar to models (a) and (c).

The robustness of the anomalous multifractal spectra selected from an energy bin where the ratio of the DOCS to DOS is maximized with respect to disorder is shown in Fig. 4.13 for the exemplary model (b). Tuning over a whole order of magnitude in the disorder strength, the results are robust for q not to close to the termination threshold q_c. The deviations are easily understood by the absence of ensemble averaging in the numerics.

Excitingly the behavior of models (b), (d) closely parallels observations from STM studies of BSCCO [233, 234]. The cuprate superconductor shows quasiparticle interference at low energies, suggestive of plane wave states modified by rare internode scattering, but strongly inhomogeneous, energy-independent spectra at higher energies. The inhomogeneous, energy-independent spectra could potentially be associated with the "stacked" multifractality, robustly exhibited here for models with *nematic* QGD [89].

4.6 Discussion

Central to this chapter is the quantum-critical stacking conjecture [75] formulated in detail in Sec. 4.2. It states that the surface states of bulk STI in class CI, AIII, and DIII are (i) topologically protected from Anderson localization (ii) closely resemble the phenomenology of Quantum Hall criticality. With my collaborators I was able to gather supporting numerical indications for the conjecture. In Table 4.1, the stacking-conjecture expectations for the conductance distribution and multifractal spectrum and numerical benchmarks of these expectations are summarized in short. In more detail, the results from Secs. 4.3–4.5 for the different symmetry classes are recapitulated in the next paragraphs.

AIII The numerical analysis performed in Ref. [88] clearly confirms the class AIII $\to$ A IQHT stacking conjecture for $\nu = 1, 2$. Multifractality in the surface theory, at the boundary of a bulk lattice model, and in the conductance distribution derived within the scattering matrix formalism were shown to match the universal IQHT characteristics. These impressive results are reviewed in Sec. 4.3.

Ref. [122] gives an analytical argument why this should happen for $\nu = 1$ (or rather all odd ν). Notably, however, the even-odd effect implied by the NLσM-based derivation in Ref. [122] is absent [see also Eqs. (4.6) and (4.8), above]. Remarkably in the numerics, both $\nu = 1, 2$ show a stack of IQHT critical states at finite energy.

My determination of the Kubo $\sigma_{\mathsf{dc}}^{xx}$ conductivity using exact diagonalization of momentum space models in Sec. 4.3.3 additionally supports these remarkable results .

CI Next, the fully spin symmetric case was considered in Sec. 4.4. In Ref. [75], TSC systems in class CI are considered for both small and large ($\nu \geq 8$) winding numbers ν. The stacking conjecture in this case corresponds to: CI WZNW $\to$ class C SQHT. I reproduced some of the results for the minimal winding number $\nu = 2$ in larger ($N = 72$ vs $N = 46$) systems giving stronger indications that the observations are not plagued by finite-size effects.

Additionally with my finite-energy Kubo conductivity computations in Sec. 4.4.2 I was able to show that there is a reasonable agreement with the class-C SQHT conjecture (see Table 4.1). What is most important, the conductivity clearly tends towards a *finite* value, in contradiction with the conventional picture expectation of Anderson localization in this class.

DIII Finally, the generic time-reversal topological superconductor with no spin symmetry at all residing in class DIII also shows clear signs of stacking at finite energy. Only the minimal $\nu = 1$ single Majorana surface cone is considered. This case is special, since time-reversal invariant disorder couples to the stress tensor, producing "quenched gravitational disorder" (QGD). Usually this perturbation is irrelevant and negligible compared to other kinds of disorder.

In this case, the natural stacking conjecture relates DIII WZNW $\rightarrow$ class D thermal quantum Hall transition (TQHT) and is not straightforward to probe numerically. This is due to the absence of observations/calculations of a TQHT with universal multifractal and conductance statistics, see Sec. 1.5.3 for a discussion.

Nevertheless these studies are interesting, since model (b) is similar to the phenomenology of STM observations in the high-T_c cuprate BSCCO [89, 229–234]. This is not a topological material, however the low-energy Dirac quasiparticle description of a 2D d-wave superconductor reduces to independent "topological" components when interpair and/or internode scattering is suppressed by hand [62, 89].

At this point a general comment on the models investigated numerically is in order. It is worth emphasizing that at the surface of a 3D topological phase, at energies of order the gap, the 2D surface states deconfine and merge with the bulk continuum. The pure continuum 2D Dirac theories studied here cannot capture this, for the numerics the spectrum is cut off in momentum space. Eigenstates with energies close to the cutoff show neither stacking nor can they extend into a bulk (since this is a pure surface model). Studies of surface states of a bulk TSC lattice model in [88], show results consistent with the stacking scenarios articulated in this thesis, indicating the pure surface description is not an issue.

The class CI, AIII, and DIII WZNW topological surface theories show a remarkable property: the longitudinal surface charge / spin / thermal conductivity at *zero energy* is quantized. Both disorder and interactions do not break this exact quantization [9, 67, 125, 225, 251]. The results presented here obtained by collaborators and myself indicate the even more stunning correspondence of 2D quantum Hall criticality in classes C, A, and D and surfaces of bulk topological superconductors in classes CI, AIII, and DIII at *finite energy*.

5 **Conclusion and outlook**

5.1 Summary

In this thesis I have studied interacting topological systems in low dimensions in presence of disorder. At the Anderson transition critical points in (effectively) non-interacting theories, there is the infinite spectrum of relevant operator that causes nontrivial multifractal eigenstate correlations. In each chapter the study of eigenstate correlation yielded novel surprising insights on the systems. Remarkably, in certain parameter regimes the low energy of each of the models under consideration here is governed by a Pruisken (type) RG flow. For the quantum Hall like phases in 2D, this is well known. Further, Chiral wires in 1D with staggering show this kind of flow in the "bare" topological index/average conductivity plane, however the fixed points are of infinite randomness type with g^* approaching zero algebraically. Surprisingly, the surface states of disordered time-reversal invariant topological superconductors (TSC) mimic quantum Hall phenomenology at finite energies.

Chapter 2 is devoted to disordered chiral wires. In 1D there are more "tools" available in the sense that (i) with density matrix renormalization group (DMRG) there exists a numerical approach available to study the interacting disordered model directly (ii) employing bosonization one can study the stability of the interacting theory towards disorder. The most remarkable result of this chapter is the difference between Majoranas and complex fermions that emerges when turning on interactions.

In the next chapter of this work (Chap. 3) the focus is on criticality at 2D Quantum Hall type Anderson transitions. In particular the observables allowing access to the generalized multifractal spectrum were studied. Many of the results obtained generalize to all symmetry classes and topological or metal insulator transition, however the main point of concern was the Spin Quantum Hall (SQH) transition. Numerical simulations of the network model and both analytics and numerics on the percolation mapping prove that the multifractal spectrum of the SQH transition is not compatible with a (Virasoro) CFT description of SQH criticality. In particular, this excludes any WZNW description of the SQH critical theory. As can be seen in the next chapter of this work, there apparently is a connection of finite-energy perturbed WZNW models and QH criticality.

Finally the work presented in Chap. 4 is concerned with Wess-Zumino-Novikov-Witten (WZNW) type surface theories of 3D bulk topological superconductors. At zero energy it is well-known that these show a perfectly parabolic multifractal spectrum and quantized conductance, which is robust to disorder and weak interactions. However at the finite energy something even more surprising happens: There is a stack of states whose phenomenology mimics QH criticality. Numerical evidence obtained by my collaborators and myself and heuristic analytical arguments supporting this correspondence are

reviewed. Apparently a finite energy perturbation of the WZNW models breaks the symmetry group of the NLσM action in a way that one ends up in an effective Pruisken model.

In the following lines the key results of the individual chapters are summarized in more detail:

5.1.1 Summary: Disorder and interaction in chiral chains

In this part of the work the chief aim was understanding the behavior of disordered wires of Majoranas and complex fermions in presence of interaction. The models studied both belong to symmetry class BDI and are completely equivalent (except for the smaller Majorana Hilbert space) in the non-interacting limit, the low energy theory is governed by the infinite-randomness fixed point. I could answer the intriguing question whether there is a fundamental difference between the Majorana and complex fermions version of the problem: they behave drastically distinct!

As mentioned above in 1D there are more methods available than in higher dimensions, I could use the full force of DMRG, bosonization, SCBA topological indices with mean field decoupled interaction and infinite randomness RG here in order to find: (1) Together with my collaborators, I have determined phase diagrams and drew conclusions about their observable properties (spin order, criticality). As basis of this, DMRG simulations of the models were employed. This provided access to the entanglement entropy and the spin-spin correlation functions. (2) I performed two kinds of RG analysis to understant these numericals results: (i) First, I have developed a Giamarchi-Schulz like weak-disorder RG. Disorder is strongly relevant, which implies approach (ii) is more appropriate. (ii) The second RG analysis is starting at the non-interacting infinite-randomness fixed point. Using high precision numerics, the correlation functions for both Hartree and Fock term are computed. In certain cases, there is a strong cancellation between the two terms, their difference vanishes rapidly. In the complex fermion chain, this mechanism is operativem the interaction is RG-irrelevant. In the Majorana chain, there is no such cancellation.

This explains the drastic difference of behavior between Majoranas and complex fermions seen in the DMRG numerics.

5.1.2 Summary: Generalized multifractality at the Spin Quantum Hall transition

This chapter introduced the notion of generalized multifractality, referring to the scaling exponents of a family of composite wavefunction observables at Anderson-transition criticality. The central attention goes to the SQH transition where I (i) constructed families of pure scaling composite wavefunction observables, (ii) performed numerics extracting the multifractal spectrum, (iii) showed analytically that generalized parabolicity is violated in SQH systems using the percolation mapping. The parts (i), (ii) were performed with the class C NLSM, however the mathematical constructions/numerical algorithms described there generalize straightforwardly to the other symmetry classes.

The work presented in this chapter has a fundamental implication: SQH criticality is not locally conformal invariant! This can be seen putting above points together: The Iwasawa/HWV constuction give an operator family with abelian fusion. According to the CFT proof the existence of such a family in a theory with LCI implies generalized parabolicity. However, both numerically and analytically deviations in the generalized multifractal spectrum from parabolicity were found.

5.1.3 Summary: Disordered surfaces of time reversal invariant topological superconductors

Central to this chapter is the quantum-critical stacking conjecture formulated in detail in Sec. 4.2. It states that the finite energy surface states of bulk TSC in class CI, AIII, and DIII are (i) topologically protected from Anderson localization (ii) closely match the phenomenology of Quantum Hall criticality. In particular, this conjecture applies to the conductance distribution and multifractal spectrum. In Table 4.1 predictions from the conjecture for these observables are summarized.

Throughout the chapter numerical evidence supporting the conjecture is gathered. Employing exact diagonalization on a Dirac model for the surface states, the multifractal spectrum and the Kubo conductivity for different winding number TSCs in CI, AIII and DIII are computed. Additionally Landauer scattering matrix computations and bulk exact diagonalization studies in class AIII are reviewed.

The class CI, AIII, and DIII WZNW topological surface theories show a remarkable property: the longitudinal surface charge / spin / thermal conductivity at *zero energy* is quantized. Both disorder and interactions do not break this exact quantization. The numerical evidence presented in this chapter indicates the stunning correspondence of 2D quantum Hall criticality in classes C, A, and D and bulk TSC *finite energy* surface states in classes CI, AIII, and DIII. This is an even more suprising property of TSC in these classes!

5.2 Outlook and further directions

Over the course of the work, the main questions posed in the beginning of the thesis could be answered. At the same time, each of the projects has opened many intriguing directions that can be pursued in the future. Especially promising are the chiral wires where the focus in this work has been purely on ground state properties. Recently such systems at finite energy density attracted much attention in the context of topology and MBL [275, 276].

Since the thesis involved numerical studies, one point in all parts is to improve the numerics. The algorithms employed were DMRG (cost $\sim L(\ln L)^\alpha$), exact diagonalization ($\sim L^6$ for 2D) and percolation numerics ($\sim L^2$). All of the computational time / memory costs are faster than linear which is why one cannot just rely on Moore's law (doubling of computational power every $12\ldots48$) months, but should study complementary approaches.

A more exhaustive list on what can be done in the future in the individual parts follows:

5.2.1 Outlook: Disorder and interaction in chiral chains

There are many possible future research directions for this project:

1. Reference [277] is a generalization of the clean interacting Majorana chains to quasi-1D (ladders). One can think about the effect of disorder on these ladder systems and even more general higher dimensions and other lattice types.

2. Instead of changing the spatial dimension one can also look at the other symmetry classes. In particular it is interesting to study interacting Majorana models in 1D, quasi-1D and 2D, since superconducting systems without further symmetries fall in this class. A further related question is, whether the difference between complex fermions and Majoranas persists.

3. Apparently the sign of the interaction in the Majorana model has a drastic impact on the phenomenology. Repulsive interaction leads to localization, attractive interaction to novel criticality. Therefore it is desirable to understand the effect of the sign analytically. Another point is to find out what exactly happens in the novel critical phase. The numerical results yield a central charge larger than the value at infinite randomness and slightly larger than in the clean case.

4. In this work, the ground state properties of the models were explored thoroughly. The spontaneously broken symmetry in the Majorana model is expected to be restored at high temperatures. The system most likely undergoes a many-body (de-)localization (MBL) transition. The field of MBL has prospered well over the last decade [278–281]. More recently the interplay of MBL and topology, which will be observable in this model as well, has attracted a lot of attention [275, 276].

5. Reference [114] predicts a "superuniversality" forcing the critical theories of all five symmetry classes possessing a chiral symmetry (BDI, AIII, CII, D, DIII) to coincide. Therefore a complete analysis of the properties of eigenfunction composite objects at the infinite-randomness fixed point is desirable.

   At this fixed point, the wavefunctions are stretched exponentials, consequently they share properties with trivially localized wavefunctions. On the other hand, most observables show nontrivial critical features. A lot of these closely resemble those observed in MBL transitions on random regular graphs [282].

6. A further possible generalization is to study crossovers to Sachdev-Ye-Kitaev (SYK) type [283] physics. In the model considered in this thesis, the interaction is short range, one would have to add random interaction terms coupling a macroscopic number of sites. In Refs. [284, 285] coupled quantum dots are studied, which can be thought of as an intermediate stage between the original SYK quantum dot and the short range interaction model. By interpolating between the models, a crossover from infinite randomness to SYK phenomena could be studied.

5.2.2 Outlook: Generalized multifractality at the Spin Quantum Hall transition

This work paves the way for further analytical and numerical studies of generalized multifractality at Anderson transitions. Some of the most prospective research directions include:

1. In future projects, one can extend the work in the class C NLSM to the other symmetry classes. Of particular interest is the superconducting class D hosting disordered Majorana systems. Both the conventional metal-insulator transition and the topological thermal quantum Hall transition in 2D are possible in such systems. Exploiting that supersymmetry imposes relations between classes C and D, one can directly obtain the class D pure scaling observables from those explored in this chapter. Moreover preliminary results [120] indicate many other relations between different symmetry classes.

   These superuniversality conjectures are supported by preliminary numerical studies [120] of the metal-insulator transition in the 2D Ando model in the symplectic Wigner-Dyson class AII. The pure scaling operators have the same form as in the class-C NLSM. Duality then extends this result to the orthogonal Wigner-Dyson class AI that was studied in Ref. [207]. Future studies of metal insulator transitions should verify these conjectures for all classes.

2. In Sections 3.6 and 3.7 it is pointed out that the difference between pure-scaling NLSM operators leads to a drastic qualitative distinction in the observables between class A and class C. Even the simplest subleading pure-scaling observables have indefinite sign and fluctuate wildly from one disorder configuration to another. This makes the numerical network model studies computationally challenging. At this point it is important to state again that the complementary investigations of classical percolation in Sec.3.8 show this problem is purely related to insufficient ensemble averaging. This phenomenon is related to the presence of spin in class C and is therefore likely relevant to all spinful symmetry classes. A future challenge is to extensively study the character of eigenstate correlations in critical spinful systems.

3. An intriguing question is whether generalized parabolicity is violated in other 2D Anderson transitions. Preliminary results indicate the violation of generalized parabolicity also in the class AII MIT in the Ando model [120].

4. Finally, many interesting questions arise when one "switches on" the electron-electron interaction. One can closely follow the program set up in Refs. [166] and [207] for the Wigner-Dyson classes. There it was shown within a perturbative RG analysis that generalized multifractality survives the presence of Coulomb interaction. In this context, one should distinguish between a long-range (Coulomb) and a short-range (screened) interaction.

5.2.3 Outlook: Disordered surfaces of time reversal invariant topological superconductors

One can refine and generalize the numerics performed so far:

1. By switching to iterative Arnoldi techniques rather than full diagonalization one may increase the system sizes drastically: The Chalker-Coddington network models for (S)QH effects studied in Chap. 3 have more than an order of magnitude larger linear sizes $L = \mathcal{O}(1000)$. The scattering matrices of these are sparse, every site can scatter only into its nearest neighbors. For the determination of the eigenvectors itself, one does not need sparsity of the Hamiltonian, one just needs to find an efficent way to compute the resolvent map (that is dense in general even for sparse Hamiltonians). For completely generic dense matrices the compotational task of determining the resolvent operators has the same complexity as full diagonalization. The Hamiltonian matrices of the models here are *banded* in k-space. Exploiting the banded structure may lead to a more efficient way of finding the resolvent map.

2. The Landauer conductance for class AIII was computed in Ref. [88]. One should compute this quantity in the other classes CI, DIII as well. From the stacking conjecture one expects to find the analytical result [76] for the SQH network model conductance. The situation in class DIII is more complicated, since there is no clear concept of TQH criticality. Recently the exploration of phase diagrams in 2D class D systems gained new attention [85, 286].

3. A further direction is the analysis of higher winding numbers in class DIII systems. In many aspects, the winding $\nu = 1$ is very different from the higher ν WZNW models. It remains to be checked whether $\theta_{\varepsilon \neq 0} = 0.077$ (Table 4.1) is stable to changes of ν as in the other classes.

4. Finally another point concerning class DIII: One needs to find evidence for the existence of the conjectured TQH plateau transition in class D in the presence of disorder, and check for the

existence of a universal thermal conductivity and multifractal spectrum in order to compare with the stacked criticality in the DIII results.

In the above points the solid numerical evidence for stacking using many different observables is summerized. However the current analytical understanding of this phenomenon is heuristic at best. Therefore one needs to develop novel analytical means:

1. Reference [11] derives an interesting form of bulk-boundary correspondence for all symmetry classes. A winding number of the critical surface states is constructed and shown to be equal to the winding number of the bulk. A fruitful direction of research might be to investigate the applicability of these concepts to the critical stacks at finite energies.

2. Another goal is to improve the NLσM expansion that gives the class AIII WZNW $\rightarrow$ A IQHPT prediction for odd winding numbers.

3. Majoranas in class DIII can also be described as gravitational theory [271], this different perspective may yield new approaches to tackle the problem.

4. Once a candidate field theory is found, one can investigate the effects of interparticle interactions on stacked critical states.

Finally, a key problem is to understand the depth of the relationship implied by the stacking of classes A, C, D topological quantum phase transitions (the Hall plateau transitions) at the surface of classes AIII, CI, and DIII TSCs. Although this connection has been revealed indirectly here, through studies of the effects of disorder on TSC surface theories, it suggests a more intrinsic, topological relationship between these classes (which govern topological phases with integer-valued invariants in two and three dimensions). One idea is the following. Is it possible to reproduce the critical statistics studied here by studying an entanglement cut [287] for a *clean* bulk TSC Hamiltonian? Instead of averaging over disorder configurations at a physical surface, perhaps one can average over *bulk quasiparticle band structures.*

A

Appendix A

Disordered interacting chains

This appendix is based on Ref. [86].

A.1 Weak-disorder RG around the Ising + LL fixed point of the interacting Majorana chain

In this Appendix, details of the weak-disorder RG treatment of the interacting Majorana chain in the Ising+LL fixed point are provided, Sec. 2.4.3. The starting point is the effective mean-field Hamiltonian (2.25) including the third-nearest-neighbor hopping as well as a weak randomness in the nearest-neighbor hopping $t + \delta t_j$, supplemented with the interaction term $g\gamma_j\gamma_{j+1}\gamma_{j+2}\gamma_{j+3}$.

Using the low energy expansion (2.26) for the nearest-neighbor hopping operator $\gamma_j\gamma_{j+1}$ yields oscillatory contributions with wave vectors $k_i = 0$, k_0, $k_0 + \pi$, $2k_0$, $2k_0 + \pi$, and π that can be dropped in the clean case. In the presence of randomness, they couple, however, to the corresponding Fourier harmonics of disorder δt_j. The replica trick is employed to average over disorder. As a result, the following terms in the action representing effective "interactions" between different replica species a, b are generated:

$$
\begin{aligned}
S_{k_0} &= -\frac{8(1 - \cos k_0)}{\pi a} D_{k_0} \int \mathrm{d}x\mathrm{d}\tau\mathrm{d}\tau' \sum_{a,b} \Big[i\gamma_L^a\gamma_L^b \sin(\phi_a + \theta_a - \phi_b - \theta_b) \\
&\quad + i\gamma_R^a\gamma_R^b \sin(\phi_a - \theta_a - \phi_b + \theta_b) - i\gamma_L^a\gamma_R^b \sin(\phi_a + \theta_a - \phi_b + \theta_b) \Big], \\
S_{k_0+\pi} &= -\frac{8(1 + \cos k_0)}{\pi a} D_{k_0+\pi} \int \mathrm{d}x\mathrm{d}\tau\mathrm{d}\tau' \sum_{a,b} \Big[i\gamma_L^a\gamma_L^b \sin(\phi_a - \theta_a - \phi_b + \theta_b) \\
&\quad + i\gamma_R^a\gamma_R^b \sin(\phi_a + \theta_a - \phi_b - \theta_b) - i\gamma_L^a\gamma_R^b \sin(\phi_a - \theta_a - \phi_b - \theta_b) \Big], \\
S_{2k_0} &= -\frac{1}{\pi^2 a^2} D_{2k_0} \int \mathrm{d}x\mathrm{d}\tau\mathrm{d}\tau' \sum_{a,b} \cos(2\phi_a - 2\phi_b) \sin(2\theta_a) \sin(2\theta_b), \\
S_{2k_0+\pi} &= -\frac{1}{(\pi a)^2} D_{2k_0+\pi} \int \mathrm{d}x\mathrm{d}\tau\mathrm{d}\tau' \sum_{a,b} \cos(2\phi_a - 2\phi_b), \\
S_\pi &= -\frac{8}{\pi a} D_\pi \int \mathrm{d}x\mathrm{d}\tau\mathrm{d}\tau' \sum_{a,b} \Big[4\gamma_L^a\gamma_R^a\gamma_R^b\gamma_L^b + \cos^2 k_0 \cos(2\theta_a) \cos(2\theta_b) \Big].
\end{aligned}
\tag{A.1}
$$

Each term S_{k_i} is labeled by the corresponding momentum component k_i. Some of the terms allow for a simple physical explanation. In particular, the action term $S_{2k_0+\pi}$ represents the backscattering between the right and left Fermi-point of the emergent Luttinger-liquid sector, while S_π corresponds to backscattering processes commensurate with the lattice. The RG equations summarized in Table 2.1 and Eq. (2.28) are then inferred in analogy with Ref. [154]. The most relevant terms are $S_{2k_0+\pi}$ and S_π. The contribution of the term $S_{2k_0+\pi}$ to the renormalization of K, Eq. (2.28), is analogous to backscattering in Giamarchi-Schulz RG. For the other term, S_π, the duality exchanging $\phi \leftrightarrow \theta$ and $K \leftrightarrow K^{-1}$ may be used to find the contribution to K.

While the forward scattering can be completely gauged away in the standard Giamarchi-Schulz RG, here the transformation gauging it out generated additional terms. However, a direct inspection shows that they are irrelevant in the RG sense.

The interaction generates a replica-diagonal term that couples the Luttinger-liquid and Majorana sectors:

$$
\begin{aligned}
S_{int} &= -g' \int \mathrm{d}x \mathrm{d}\tau \sum_a \gamma_L^a \gamma_R^a (\Psi_L \Psi_R + \Psi_L^\dagger \Psi_R^\dagger) \\
&= -2g' \int \mathrm{d}x \mathrm{d}\tau \sum_a \gamma_L^a \gamma_R^a \cos(2\theta_a).
\end{aligned}
\tag{A.2}
$$

This term is RG-irrelevant in the range of interest, $K < 1$; the corresponding dimensional coupling is denoted y' in Table 2.1. Higher terms respecting the symmetry are, of course, also generated. It can be checked by dimension counting that all terms arising due to interaction remain irrelevant in the range $1/4 < K < 1$.

A.2 Origin of low-energy suppression of wave function correlations in disordered complex-fermion chain

In this Appendix, analytical arguments are presented explaining the origin of the suppression of eigenstate correlations in a complex-fermion chain at low energies found numerically in Sec. 2.5.2. An eigenvector $U_{i+1,\epsilon}$ of Hamiltonian (2.39) fulfills the following transfer matrix equation:

$$
\begin{pmatrix} U_{i+1,\epsilon} \\ U_{i,\epsilon} \end{pmatrix} = \begin{pmatrix} \epsilon/t_{i+1} & -t_i/t_{i+1} \\ 0 & 1 \end{pmatrix} \begin{pmatrix} U_{i,\epsilon} \\ U_{i-1,\epsilon} \end{pmatrix}
\tag{A.3}
$$

For zero energy, $\epsilon = 0$, two sublattices are decoupled, so that the wave function lives on one sublattice. For finite (but small) ϵ the wave function on the second sublattice is suppressed by ϵ. This implies the suppression of the correlation functions $C_2(\epsilon, r, L)$, $C_H(\epsilon_\alpha, \epsilon_\beta, r, L)$, and $C_F(\epsilon_\alpha, \epsilon_\beta, r, L)$ for odd r by a factor $\sim \epsilon_>^2$, where $\epsilon_>$ is the larger of two energies $\epsilon_\alpha, \epsilon_\beta$. This suppression is indeed numerically observed, see Fig. 2.13 and the right panel of Fig. 2.16 which make evident the $\epsilon_>^2$ scaling of the odd-r correlation functions. As is seen in this figure, for odd r the Fock term is substantially smaller than the Hartree one, so that there is no cancellation between them and $C_{HF} \simeq C_H$.

For even r, an even stronger suppression holds for the Hartree-Fock correlation function. As an

example, consider $r = 2$. Using the transfer-matrix equation (A.3), one gets the relation

$$
\begin{aligned}
&|U_{i,\epsilon_\alpha}|^2|U_{i+2,\epsilon_\beta}|^2 + |U_{i+2,\epsilon_\alpha}|^2|U_{i,\epsilon_\beta}|^2 \\
&- 2U_{i,\epsilon_\alpha}U_{i+2,\epsilon_\alpha}U_{i+2,\epsilon_\beta}U_{i,\epsilon_\beta} \\
&= \frac{1}{t_{2+i}^2}\left(\epsilon_\alpha^2|U_{i+1,\epsilon_\alpha}|^2|U_{i,\epsilon_\beta}|^2\right. \\
&\left. -2\epsilon_\alpha\epsilon_\beta U_{i,\epsilon_\alpha}U_{i+1,\epsilon_\alpha}U_{i+1,\epsilon_\beta}U_{i,\epsilon_\beta} + \epsilon_\beta^2|U_{i,\epsilon_\alpha}|^2|U_{i+1,\epsilon_\beta}|^2\right).
\end{aligned}
\tag{A.4}
$$

The left-hand side of Eq. (A.4) is the difference between the Hartree and Fock terms that enters the correlation function C_{HF} for $r = 2$. On the other hand, the right-hand-side is the linear combination of C_H and C_F terms for $r = 1$, each of them multiplied by a factor quadratic in energies. This proofs that C_{HF} for $r = 2$ is suppressed by an additional factor $\sim \epsilon_>^2$ in comparison with the $r = 1$ correlation function $C_{HF} \simeq C_H$,

$$
C_{HF}(\epsilon_\alpha, \epsilon_\beta, 2, L) \sim \epsilon_>^2 C_{HF}(\epsilon_\alpha, \epsilon_\beta, 1, L).
\tag{A.5}
$$

The same argument holds for other even r. This is fully supported by the numerical data, as shown in Fig. A.1 where the ratio $C_{HF}(\epsilon_1, \epsilon_n, 2, L)/C_{HF}(\epsilon_1, \epsilon_n, 1, L)$ multiplied by ϵ_n^{-2} is plotted for different n, as a function of L. The reader is reminded that ϵ_n scales exponentially as a function of L and n, see Eq. (2.36). Each of the factors $C_{HF}(\epsilon_1, \epsilon_n, 2, L)$, $C_{HF}(\epsilon_1, \epsilon_n, 1, L)$, and ϵ_n^{-2}, when taken separately, changes within an enormous range of many dozens of decades, see, e.g. Figs. 2.15 and 2.16. On the other hand, the product plotted in Fig. A.1 changes only weakly (at most linearly in L, which means logarithmically in ϵ), in full agreement with the analytical argument.

Since it was shown above that the odd-r correlation function in the right-hand side of Eq. (A.5) scales as $\epsilon_>^2$, the even-r Hartree-Fock correlator should scale as $\epsilon_>^4$ according to this equation. The $\epsilon_>^4$ scaling of C_{HF} for even r is indeed observed numerically, see Fig. 2.15.

A.3 Disordered Majorana chain with mean-field treatment of interaction in the Ising + LL phase

In this Appendix, an analysis of the disordered Majorana chain that treats disorder exactly and the interaction on the mean-field level is presented. This approach is in a sense complementary to those in the main text of the paper. In the weak-disorder RG of Sec. 2.4 the interaction was treated exactly and the disorder was considered as a perturbation. Contrary to this, the analysis of Sec. 2.5 considered disorder exactly and the interaction perturbatively. Here, the disorder is treated by using the field-theoretical σ model approach. This treatment is essentially exact, in analogy with Sec. 2.5. The key differences with Sec. 2.5 are that (i) a sufficiently strong repulsive interaction for which the clean system is in the Ising+LL phase is considered, and (ii) the interaction is included on the mean-field level only. This allows one to obtain the phase diagram of the system in the plane spanned by the disorder strength and the staggering. The phase diagram contains four distinct topological phases. Of course, from Sec. 2.5 and from the numerical study in Sec. 2.3.2 it is known that including effects of interaction beyond the mean-field level destabilizes the system on the critical line. This means that the transitions between the topological phases are in fact not of second order (as found in the mean-field treatment below) but rather of first order. On the other hand, the phase diagram is expected to remain applicable also beyond the mean-field level.
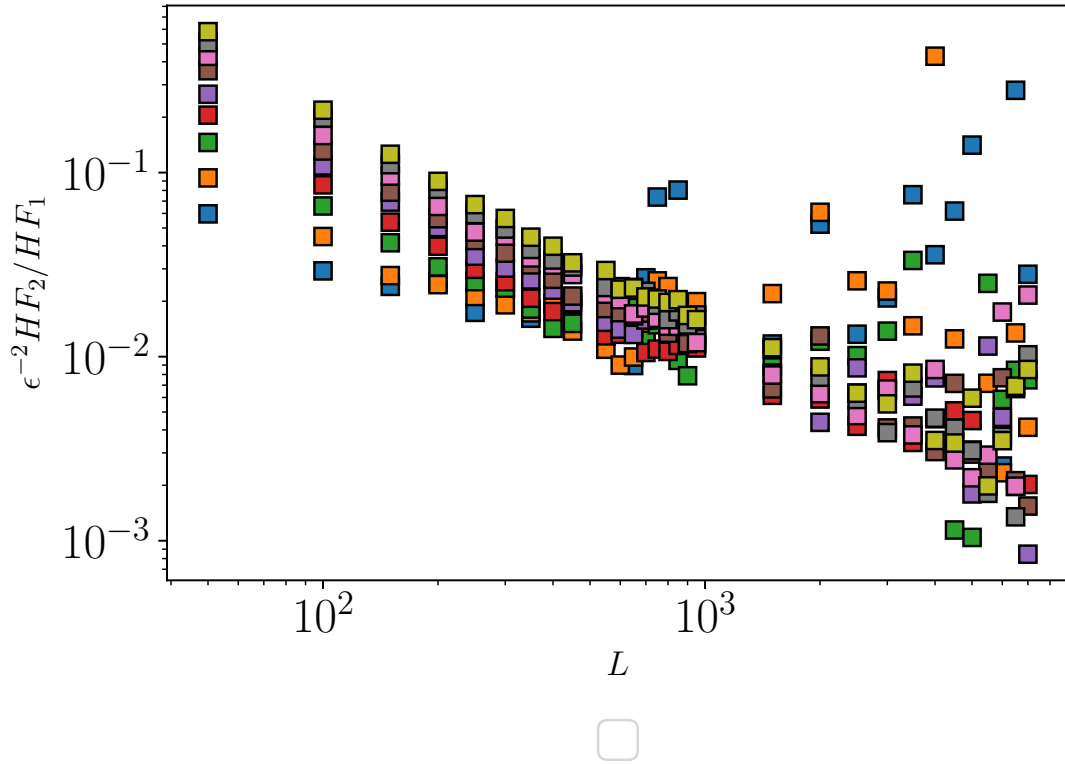
Figure A.1: Ratio $C_{HF}(\epsilon_1, \epsilon_n, 2, L)/C_{HF}(\epsilon_1, \epsilon_n, 1, L)$ multiplied by ϵ_n^{-2} for the first twenty levels n (in distinct colors) as a function of L. The data show only a weak (at most linear) dependence on L (that corresponds to a logarithmic energy dependence), which should be contrasted to the exponential L dependence of both entering correlation functions C_{HF} and of the energy ϵ_n. This confirms the analytic prediction in Eq. (A.5), with possible logarithmic-in-energy corrections.

At mean-field level with respect to the interaction, the third nearest neighbor hoppings are generated and the nearest-neighbor hopping is renormalized. The full mean-field Hamiltonian, including the randomness δt_j in the nearest neighbor hopping, reads

$$H_{I+LL}^{MF} = \frac{i}{2} \sum_j \Big[(t_1 + t_2 + (-1)^j (t_1 - t_2) + 2\delta t_j) \gamma_j \gamma_{j+1}$$
$$+ ((t_1' + t_2') + (-1)^j (t_1' - t_2')) \gamma_j \gamma_{j+3} \Big]. \tag{A.6}$$

By choosing $t_1 \neq t_2$ or $t_1' \neq t_2'$, the system can be staggered. The random component δt_j of the hopping is assumed to have Gaussian statistics, with zero average.

The formalism presented in Refs. [115, 288] for a particular model can be extended to the case of generic banded Hamiltonians. For convenience, the computations were performed in class AIII instead of BDI (i.e., allowing for complex δt_j). The results for AIII shown here remain essentially the same for the class BDI as can be checked numerically using transfer matrices.

The calculations proceed by integrating out the disorder using the supersymmetry formalism. After Hubbard-Stratonovich decomposition and saddle-point expansion (which yields the self-consistent Born approximation), one arrives at a non-linear sigma model describing the disordered wire. The action describes the soft modes $T \in \mathrm{GL}(1|1)$:

$$S[T] = \tilde{\chi} \mathrm{str}(T \partial T^{-1}) - \frac{\tilde{\xi}^2}{4} \mathrm{str}(T \partial^2 T^{-1}). \tag{A.7}$$

There are two coupling constants here: $\tilde{\xi}$ has a meaning of the bare conductance, and $\tilde{\chi}$ of the bare topological index. Under RG, these coupling constants get renormalized. The theory thus exhibits a two-parameter RG flow, which is largely analogous to the Khmelnitskii-Pruisken flow for the 2D theory describing the quantum Hall effect.

Except for the case of half-integer bare values, $\tilde{\chi}$ flows to the nearest integer value, which is the actual topological index χ. Half-integer values of $\tilde{\chi}$ are stable under RG-flow and correspond to critical theories at the boundary of two topologically distinct phases. To determine the phase diagram, one thus should compute the dependence of the bare index $\tilde{\chi}$ on parameters of the chain. These dependences are obtained when one derives the σ model from the microscopic model, as sketched above. Details of this calculation are skipped, since it is analogous to that carried out for a different microscopic model in Ref. [115], which is briefly reviewed in Sec. 1.4. A general 1D non-interacting Hamiltonian H with chiral symmetry and with translational invariance in average can be written as:

$$H = h_n \sum_i a_{i+n}^\dagger b_i + \sum_i r_{n,i} a_{i+n}^\dagger b_i + h.c. \tag{A.8}$$

Here a_i and b_i are operators on two sublattices, h_n are the average hopping matrix elements, and $r_{n,i}$ are random contributions to hopping that are characterized by zero mean and by the variance

$$\langle r_{n,i} r_{m,j}^* \rangle = w_n \delta_{i,j} \delta_{n,m}. \tag{A.9}$$

One finds the following result for the bare index $\tilde{\chi}$ in terms of the parameters of H:

$$\tilde{\chi} = \sum_q \frac{h^-(q) v^+(q)}{\Sigma_0^2 + h^+(q) h^-(q)} + \sum_n n u_n, \tag{A.10}$$

where

$$h^-(q) \;=\; \sum_n h_n e^{-inq}, \tag{A.11}$$

$$h^+(q) \;=\; \sum_n h_n e^{inq}, \tag{A.12}$$

$$v^+(q) \;=\; \sum_{m,n} (n-m) u_n h_m e^{imq}, \tag{A.13}$$

$$u_n \;=\; \frac{w_n^2}{\sum_m w_m^2}, \tag{A.14}$$

and the self-energy Σ_0 is a solution of the equation

$$\left(\sum_n w_n^2 \right) \sum_q \frac{1}{\Sigma_0^2 - h^+(q) h^-(q)} = 1 \tag{A.15}$$

representing the self-consistent Born approximation.

The Hamiltonian (A.6) is a particular case of Eq. (A.8). The nearest and third nearest neighbor hopping of Eq. (A.6) are encoded in terms of Eq. (A.8) in $h_1 = t_1$, $h_2 = t_1'$, $h_0 = t_2$, and $h_{-1} = t_2'$. Further, the randomness in the nearest neighbor hopping of Eq. (A.6) translates into $u_0 = 1/2$ and $u_1 = 1/2$. The resulting phase diagram in the parameter plane spanned by disorder strength w and staggering $t_1' - t_2'$ is shown in Fig. A.2.

The analytical results (black lines show the corresponding phase boundaries) are compared with those of direct transfer matrix numerics in in Fig. A.2. Four topological phases (with $\chi = -1$, 0, 1, and 2) as obtained by the latter approach are shown by different colors in Fig. A.2. An excellent agreement between the analytical and numerical data is observed. This is quite non-trivial since (i) the σ model derivation holds in the limit of large number of channels, $N \gg 1$, whereas this model corresponds to $N = 3$, (ii) the analytical calculation of parameters of the σ model is controlled fir weak disorder, $w/t \ll 1$, whereas a very good agreement also for $w/t \sim 1$ is found here.

The self-duality transformation ensures that the zero-staggering line ($t_2' = -0.7$ in Fig.A.2) is critical within this mean-field analysis. An important observation is that the critical line is adjacent only to 0 (green) and 1 (blue) topological phases for finite disorder.

In the clean DMRG analysis, Sec. 2.3.1, only two distinct topological phases were observed, which correspond to the green and blue phases of Fig. A.2. The other two phases (red and yellow) can only be reached by adding the third nearest neighbor hopping explicitly [31] since otherwise the Hamiltonian (A.6) with the corresponding parameters can not be obtained as a mean-field Hamiltonian of an interacting Majorana chain. When disorder is added to the mean-field model, one can observe that the parameter space for the red and yellow phases shrinks.
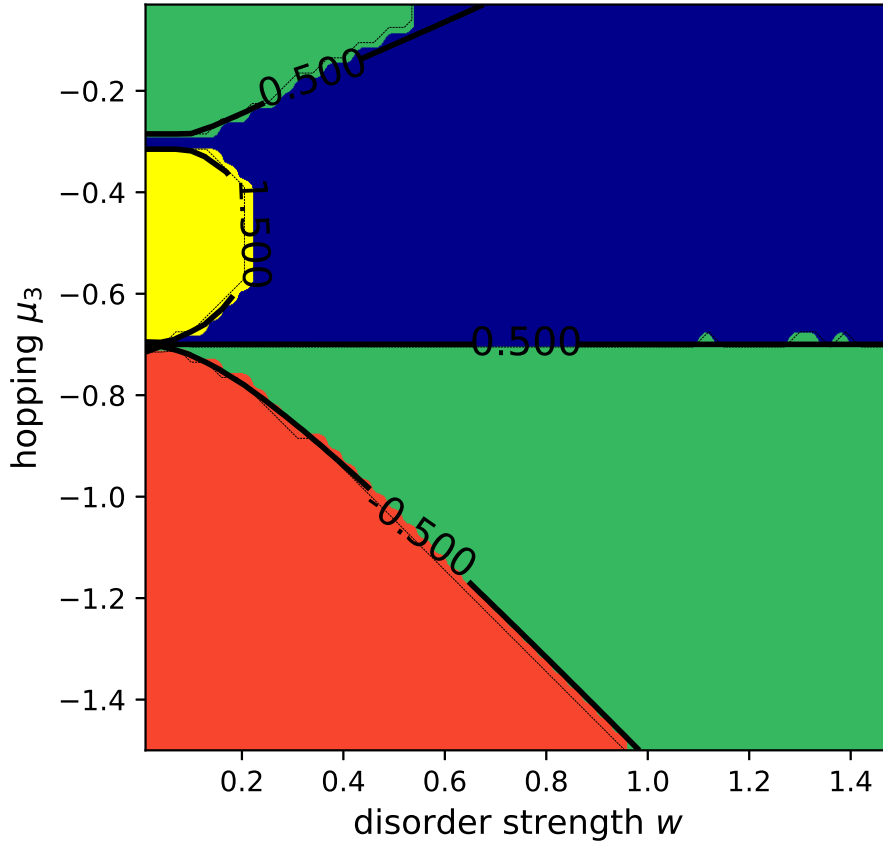
Figure A.2: Phase diagram of the mean-field Hamiltonian (A.6) describing the Ising+LL phase of the disordered Majorana chain. The parameters $t'_1 = -0.7$ and $t_2 = t_1 = t = 1$ are fixed. The phase diagram is shown in the plane spanned by disorder w and the hopping t'_2. The zero staggering corresponds to $t'_2 = t'_1 = -0.7$. Black lines are phase boundaries as obtained analytically via mapping on the σ model from the condition that the bare index $\tilde{\chi}$ is half-integer. Colored regions are four distinct topological phases with the values of the topological index χ equal to -1 (red), 0 (green), 1 (blue), and 2 (yellow), as obtained from the transfer-matrix numerics. A perfect agreement between numerical and analytical results is observed. At zero disorder, $w = 0$, and zero staggering, $t'_1 - t'_2 = 0$, three critical lines meet, yielding a critical theory with central charge $c = 3/2$.

B | Appendix B
Generalized multifractality at the SQH transition

This appendix is based on Ref. [105].

B.1 Class A eigenoperators

In this Appendix, the analytical expressions for the coefficients of the K-invariant scaling operators $\mathcal{P}_\lambda^A$ are derived for arbitrary Young diagrams $\lambda = (q_1, \ldots, q_n)$. These operators for $|\lambda| \equiv q \equiv q_1 + \ldots + q_n = 2, 3$, and 4 are determined in Sec. 3.5.3.1, see Eq. (3.184).

To find $\tilde{\mathcal{P}}_\lambda^A$ analytically, Young-symmetrized expressions for eigenoperators from Ref. [87] are used. Subsequently they are expressed in terms of the characters χ of representations of the symmetric group S_q. These operators (that will be denoted as $\tilde{\mathcal{P}}_\lambda^A$) are plane waves in the Iwasawa construction and also highest-weight vectors, and are not K-invariant. One can then perform the $\mathrm{U}(n) \times \mathrm{U}(n)$-averaging of these combinations to derive the K-invariant operators.

It is convenient to define $\mathcal{Q} = Q^{RR} - Q^{AA} + Q^{RA} - Q^{AR}$ for the following lines. Further, let $\nu_{ij} = \mathrm{tr}\left(E_{ij}\mathcal{Q}\right)$ be matrix elements of $\mathcal{Q}$, and S_q the symmetric group. In Ref. [87], expressions for eigenoperators in terms of Young-symmetrized products of matrix elements ν_{ij} of $\mathcal{Q}$ were derived. As an example, start with the most antisymmetric operators $(1, 1, \ldots, 1)$. According to Ref. [87], the determinant of the $q \times q$ subblock $\hat{\nu}_q$ of the matrix $\hat{\nu}$,

$$\tilde{\mathcal{P}}_{(1,1,\ldots,1)}^A \equiv \det \hat{\nu}_q = \sum_{\sigma \in S_q} \mathrm{sign}(\sigma) \prod_{i=1}^q \nu_{i\,\sigma(i)}\,, \tag{B.1}$$

belongs to the representation $(1, 1, \ldots, 1)$. The opposite extreme is the most symmetrized operator, which is given by the permanent of the same matrix,

$$\tilde{\mathcal{P}}_{(q)}^A = \mathrm{perm}\,\hat{\nu}_q \equiv \sum_{\sigma \in S_q} \prod_{i=1}^q \nu_{i\,\sigma(i)}\,, \tag{B.2}$$

and belongs to the representation (q). For a generic representation (Young diagram) λ, the operator $\tilde{\mathcal{P}}_\lambda^A$ is obtained by applying the corresponding combination of symmetrization and antisymmetrization

operations [87]. One can express the scaling operators $\tilde{\mathcal{P}}_\lambda^A$ in terms of the immanants of the matrix $\hat{\nu}_q$ (multilinear forms invariant under permutations generalizing the determinant):

$$\tilde{\mathcal{P}}_\lambda^A = \mathrm{Imm}_\lambda \, \hat{\nu} \equiv \sum_{\sigma \in S_q} \chi_\lambda(\sigma) \prod_i \nu_{i\,\sigma(i)} \,, \tag{B.3}$$

where χ_λ is the character of the λ representation of S_q. In the special case of $\lambda = (1, 1, \ldots, 1)$, this character reduces to the sign function on S_q. For $\lambda = (q)$ one obtains $\chi_{(q)} = 1$. This formula can be found from mapping the generic Young-symmetrized wave-function combinations in Ref. [87] to sigma-model operators. The Young symmetrization makes the characters $\chi_\lambda(\sigma)$ to appear naturally in the above expression [289].

Now one can perform the $\mathrm{U}(n) \times \mathrm{U}(n)$ averaging of Eq. (B.3) to obtain the K-invariant operators. In the cycle decomposition of S_q, each equivalence class can be labeled by a Young diagram μ with $|\mu| = q$. Let $[\mu]$ be the equivalence class containing σ. Under $\mathrm{U}(n) \times \mathrm{U}(n)$ averaging, and to leading order in the replica limit $n \to 0$, one has

$$\left\langle \prod_{i=1}^q \nu_{i\,\sigma(i)} \right\rangle_{\mathrm{U}(n) \times \mathrm{U}(n)} \simeq n^{-q} O_\mu \,, \tag{B.4}$$

where O_μ are basis K-invariant operators defined in Eq. (3.176). Thus, one obtains for the expansion of K-invariant operators $\mathcal{P}_\lambda^A$ in basis operators O_μ

$$\mathcal{P}_\lambda^A = \sum_\mu \#[\mu] \chi_\lambda(\mu) O_\mu \,, \tag{B.5}$$

where $\#[\mu]$ denotes the number of elements in the equivalence class $[\mu]$. One can read off the matrices of coefficients $(P_q^A)_{\lambda\mu} \equiv \#[\mu] \chi_\lambda(\mu)$ of the K-invariant operators. In Eq. (3.184), these matrices of coefficients, as obtained from RG, were shown for $q = 2$, 3, and 4.

B.2 Transformations of the Q-field

In this Appendix, technical details to the transformation from the sigma-model field Q to the field $\tilde{Q}$ that is most convenient for the derivation of RG equations are provided. This transformation is used in Sec. 3.6.1.3 in course of establishing the mapping between sigma-model composite operators and eigenstate observables. The fields Q and $\tilde{Q}$ represent two different parametrization of G/K [see Eqs. (3.114) and (3.118)]; they are related by the rotation $\tilde{Q} = U_\Sigma Q U_\Sigma$, Eq.(3.115), with the matrix U_Σ given by $U_\Sigma = \mathrm{diag}(1, \Sigma_1)_\tau$, Eq. (3.116). The operators in the Q-representation in Sec. 3.6.1.3 contain products of traces of the type $O = \mathrm{tr}(\cdots E_{a_i a_i} \Lambda Q \cdots)$, see Eq. (3.222) and its S_q-symmetrized version, Eq. (3.224). When transformed to the $\tilde{Q}$-representation, this becomes $O = \mathrm{tr}(\cdots U_\Sigma E_{a_i a_i} \Lambda U_\Sigma \tilde{Q} \cdots)$. When deriving the RG rules above, it was assumed that the matrices multiplying the sigma-model field are odd with respect to the operation (3.141); see Eq. (3.150). A subtlety arises since the matrix $U_\Sigma E_{a_i a_i} \Lambda U_\Sigma$ does not satisfy this requirement. It is shown, however, in this Appendix that this is not essential, and the operators (3.224) undergo the same RG equations as derived in Sec. 3.5.3.2, so that the pure-scaling observables are constructed from them according to Eq. (3.189). To prove this, it is shown that the operators O are equivalent to $\tilde{O} = \mathrm{tr}(\cdots \tilde{E}_{a_i a_i} \Lambda \tilde{Q} \cdots)$ by using gauge transformations $\langle O \rangle_{\mathrm{U}_b} = \tilde{O}$ with a certain subgroup $\mathrm{U}_b \subset K \equiv \mathrm{U}(2n)$. The newly introduced matrices

$$\tilde{E}_{a_i a_i} \Lambda = \frac{1}{2} \mathrm{diag}(E_{a_i, a_i} + E_{-a_i, -a_i}, -E_{a_i, a_i} - E_{-a_i, -a_i})_\tau \tag{B.6}$$

are odd under the symmetry operation (3.141) as required.

The average of O over the subgroup U_b of the full gauge group $K = U(2n)$ is computed:

$$\langle \text{tr}(\cdots E_{a_i a_i} \Lambda Q \cdots) \rangle_{U_b} = \int_{U_b} d\mu(U) \text{tr}(\cdots U_\Sigma U E_{a_i a_i} \Lambda U^\dagger U_\Sigma \tilde{Q} \cdots), \tag{B.7}$$

where μ is the Haar measure on U_b. Choose U_b to be the block-diagonal subgroup $U_b = U(2)_\Sigma^n \subset U(2n)$ with n two-by-two blocks in particle-hole space Σ. These n blocks correspond to n replica indices $1, \ldots n$. Here one needs to distinguish between the matrix $E_{a_i a_i}$ living in $2n \times 2n$ combined replica and particle-hole (Σ) space (that are represented by associating with each replica a_i a replica $-a_i$, see Sec. 3.4) and the matrix $E_{a_i, a_i}^{n \times n}$ living in the $n \times n$ replica space. They are related by $E_{a_i a_i} = E_{a_i, a_i}^{n \times n} \Sigma_+$, where $\Sigma_\pm = (1_\Sigma \pm \Sigma_3)/2$ and 1_Σ is the identity matrix in Σ space. For computing the average over the matrix $U \in U_b$ it is advantageous to simplify:

$$U_\Sigma U E_{a_i a_i} \Lambda U^\dagger U_\Sigma = \begin{pmatrix} 1 & \\ & \Sigma_1 \end{pmatrix}_\tau \begin{pmatrix} U_{a_i} & \\ & U_{a_i}^* \end{pmatrix}_\tau \begin{pmatrix} E_{a_i, a_i}^{n \times n} \Sigma_+ & \\ & E_{a_i, a_i}^{n \times n} \Sigma_+ \end{pmatrix}_\tau \begin{pmatrix} 1 & \\ & -1 \end{pmatrix}_\tau \begin{pmatrix} U_{a_i}^\dagger & \\ & U_{a_i}^T \end{pmatrix}_\tau \begin{pmatrix} 1 & \\ & \Sigma_1 \end{pmatrix}_\tau$$

$$= \begin{pmatrix} E_{a_i, a_i}^{n \times n} U_{a_i} \Sigma_+ U_{a_i}^\dagger & \\ & -E_{a_i, a_i}^{n \times n} \Sigma_1 U_{a_i}^* \Sigma_+ U_{a_i}^T \Sigma_1 \end{pmatrix}_\tau. \tag{B.8}$$

Here U_{a_i} is the two-by-two Σ-space block of the matrix U corresponding to the replicas a_i and $-a_i$.

Now one can integrate over the n independent $U(2)$ subgroups, out of which U_b is composed. Since all a_i are assumed to be distinct in the considered composite operators O, the integrals decouple and one finds $\langle U_{a_i} \Sigma_+ U_{a_i}^\dagger \rangle_{U(2)} = \langle U_{a_i}^* \Sigma_+ U_{a_i}^T \rangle_{U(2)} = \frac{1}{2} 1_\Sigma$. Since $1_\Sigma = \Sigma_+ + \Sigma_-$ and $E_{a_i, a_i}^{n \times n} \Sigma_\pm = E_{\pm a_i, \pm a_i}$, one obtains

$$\langle \text{tr}(\cdots E_{a_i a_i} \Lambda Q \cdots) \rangle_{U_b} = \text{tr}(\cdots \tilde{E}_{a_i a_i} \Lambda \tilde{Q} \cdots), \tag{B.9}$$

with the matrix $\tilde{E}_{a_i a_i} \Lambda$ defined in Eq. (B.6). This proves that the operators $O = \text{tr}(\cdots E_{a_i a_i} \Lambda Q \cdots)$ undergo the same RG flow as $\tilde{O} = \text{tr}(\cdots \tilde{E}_{a_i a_i} \Lambda \tilde{Q} \cdots)$ since they coincide up to terms that vanish upon the averaging over a subgroup of the gauge group. Since $\tilde{E}_{a_i a_i} \Lambda$ is odd under the operation (3.141), the RG flow equations derived in Sec. 3.5.3.2 apply. This completes the justification of applying Eq. (3.189) for pure-scaling operators of class C (derived in $\tilde{Q}$ parametrization) to eigenstate basis combinations corresponding to operators in Q-representation, Eq. (3.223). The corresponding analytical predictions are verified numerically in Sec. 3.6.3.3.

Bibliography

[1] L. Euler, "Solutio problematis ad geometriam situs pertinentis," Comment. Acad. Sci. U. Petrop **8**, 128–40 (1736).

[2] A. P. Schnyder, S. Ryu, A. Furusaki, and A. W. W. Ludwig, "Classification of topological insulators and superconductors in three spatial dimensions," Physical Review B **78**, 195125 (2008).

[3] A. Kitaev, "Periodic table for topological insulators and superconductors," AIP Conference Proceedings **1134**, 22–30 (2009).

[4] S. Ryu, A. P. Schnyder, A. Furusaki, and A. W. W. Ludwig, "Topological insulators and superconductors: tenfold way and dimensional hierarchy," New Journal of Physics **12**, 065010 (2010).

[5] C.-K. Chiu, J. C. Y. Teo, A. P. Schnyder, and S. Ryu, "Classification of topological quantum matter with symmetries," Rev. Mod. Phys. **88**, 035005 (2016).

[6] M. Caselle and U. Magnea, "Random matrix theory and symmetric spaces," Physics Reports **394**, 41 –156 (2004).

[7] A. Altland and M. R. Zirnbauer, "Nonstandard symmetry classes in mesoscopic normal-superconducting hybrid structures," Phys. Rev. B **55**, 1142–1161 (1997).

[8] D. Bernard and A. LeClair, "A classification of 2D random Dirac fermions," Journal of Physics A: Mathematical and General **35**, 2555–2567 (2002).

[9] F. Evers and A. D. Mirlin, "Anderson transitions," Reviews of Modern Physics **80**, 1355 (2008).

[10] A. M. Essin and V. Gurarie, "Delocalization of boundary states in disordered topological insulators," Journal of Physics A: Mathematical and Theoretical **48**, 11FT01 (2015).

[11] A. M. Essin and V. Gurarie, "Bulk-boundary correspondence of topological insulators from their respective Green's functions," Phys. Rev. B **84**, 125132 (2011).

[12] S. D. Sarma, M. Freedman, and C. Nayak, "Majorana zero modes and topological quantum computation," en, npj Quantum Information **1**, 15001 (2015).

[13] J. Alicea, "New directions in the pursuit of Majorana fermions in solid state systems," en, Reports on Progress in Physics **75**, 076501 (2012).

[14] M. Leijnse and K. Flensberg, "Introduction to topological superconductivity and Majorana fermions," en, Semiconductor Science and Technology **27**, 124003 (2012).

[15] C. Beenakker, "Search for Majorana Fermions in Superconductors," Annual Review of Condensed Matter Physics **4**, 113–136 (2013).

[16] P. A. Lee and T. V. Ramakrishnan, "Disordered electronic systems," Rev. Mod. Phys. **57**, 287–337 (1985).

[17] M. Z. Hasan and C. L. Kane, "Colloquium: Topological insulators," Rev. Mod. Phys. **82**, 3045–3067 (2010).

[18] X.-L. Qi and S.-C. Zhang, "Topological insulators and superconductors," Rev. Mod. Phys. **83**, 1057–1110 (2011).

[19] B. A. Bernevig and T. L. Hughes, *Topological Insulators and Topological Superconductors* (Princeton University Press, Princeton, New Jersey, 2013).

[20] A. Rodriguez, L. J. Vasquez, K. Slevin, and R. A. Römer, "Critical Parameters from a Generalized Multifractal Analysis at the Anderson Transition," Phys. Rev. Lett. **105**, 046403 (2010).

[21] A. Rodriguez, L. J. Vasquez, K. Slevin, and R. A. Römer, "Multifractal finite-size scaling and universality at the Anderson transition," Physical Review B **84**, 134209 (2011).

[22] A. Richardella, P. Roushan, S. Mack, B. Zhou, D. A. Huse, D. D. Awschalom, and A. Yazdani, "Visualizing Critical Correlations Near the Metal-Insulator Transition in Ga1-xMnxAs," Science **327**, 665–669 (2010).

[23] B. Sacépé, C. Chapelier, T. I. Baturina, V. M. Vinokur, M. R. Baklanov, and M. Sanquer, "Disorder-Induced Inhomogeneities of the Superconducting State Close to the Superconductor-Insulator Transition," Phys. Rev. Lett. **101**, 157006 (2008).

[24] Y. Noat, V. Cherkez, C. Brun, T. Cren, C. Carbillet, F. Debontridder, K. Ilin, M. Siegel, A. Semenov, H.-W. Hübers, and D. Roditchev, "Unconventional superconductivity in ultrathin superconducting NbN films studied by scanning tunneling spectroscopy," Phys. Rev. B **88**, 014503 (2013).

[25] K. von Klitzing, "The quantized Hall effect," Rev. Mod. Phys. **58**, 519–531 (1986).

[26] L. Fidkowski and A. Kitaev, "Topological phases of fermions in one dimension," Physical Review B **83**, 075103 (2011).

[27] L. Fidkowski and A. Kitaev, "Effects of interactions on the topological classification of free fermion systems," Physical Review B **81**, 134509 (2010).

[28] T. Morimoto, A. Furusaki, and C. Mudry, "Breakdown of the topological classification $\mathbb{Z}$ for gapped phases of noninteracting fermions by quartic interactions," Physical Review B **92**, 125104 (2015).

[29] M. S. Foster and E. A. Yuzbashyan, "Interaction-Mediated Surface-State Instability in Disordered Three-Dimensional Topological Superconductors with Spin SU(2) Symmetry," Physical Review Letters **109**, 246801 (2012).

[30] M. S. Foster, H.-Y. Xie, and Y.-Z. Chou, "Topological protection, disorder, and interactions: Survival at the surface of three-dimensional topological superconductors," Physical Review B **89**, 155140 (2014).

[31] A. Rahmani, X. Zhu, M. Franz, and I. Affleck, "Phase Diagram of the Interacting Majorana Chain Model," Physical Review B **92**, arXiv: 1505.03966 (2015).

[32] A. Kitaev, "Unpaired Majorana fermions in quantum wires," Physics-Uspekhi **44**, arXiv: cond-mat/0010440, 131–136 (2001).

[33] C.-K. Chiu, D. I. Pikulin, and M. Franz, "Strongly interacting Majorana fermions," Physical Review B **91**, 165402 (2015).

[34] D. I. Pikulin, C.-K. Chiu, X. Zhu, and M. Franz, "Interaction-enabled topological phases in topological insulator–superconductor heterostructures," Physical Review B **92**, 075438 (2015).

[35] C.-K. Chiu, D. I. Pikulin, and M. Franz, "Proposed platform to study interaction-enabled topological phases with fermionic particles," Physical Review B **92**, 241115 (2015).

[36] V. Shivamoggi, G. Refael, and J. E. Moore, "Majorana fermion chain at the quantum spin Hall edge," Physical Review B **82**, 041405 (2010).

[37] V. Mourik, K. Zuo, S. M. Frolov, S. R. Plissard, E. P. a. M. Bakkers, and L. P. Kouwenhoven, "Signatures of Majorana Fermions in Hybrid Superconductor-Semiconductor Nanowire Devices," en, Science **336**, 1003–1007 (2012).

[38] D. S. Fisher, "Random antiferromagnetic quantum spin chains," Physical Review B **50**, 3799–3821 (1994).

[39] L. Balents and M. P. A. Fisher, "Delocalization transition via supersymmetry in one dimension," Physical Review B **56**, 12970–12991 (1997).

[40] D. S. Fisher, "Critical behavior of random transverse-field Ising spin chains," Physical Review B **51**, 6411–6461 (1995).

[41] A. Milsted, L. Seabra, I. C. Fulga, C. W. J. Beenakker, and E. Cobanera, "Statistical translation invariance protects a topological insulator from interactions," Physical Review B **92**, arXiv: 1504.07258 (2015).

[42] M. R. Zirnbauer, "Towards a theory of the integer quantum Hall transition: From the nonlinear sigma model to superspin chains," Annalen der Physik **506**, 513–577 (1994).

[43] M. R. Zirnbauer, "Toward a theory of the integer quantum Hall transition: Continuum limit of the Chalker–Coddington model," Journal of Mathematical Physics **38**, 2007–2036 (1997).

[44] M. Janssen, M. Metzler, and M. R. Zirnbauer, "Point-contact conductances at the quantum Hall transition," Phys. Rev. B **59**, 15836–15853 (1999).

[45] M. R. Zirnbauer, *Conformal field theory of the integer quantum Hall plateau transition*, 1999.

[46] S. Kettemann and A. Tsvelik, "Information about the Integer Quantum Hall Transition Extracted from the Autocorrelation Function of Spectral Determinants," Phys. Rev. Lett. **82**, 3689–3692 (1999).

[47] M. J. Bhaseen, I. I. Kogan, O. A. Soloviev, N. Taniguchi, and A. M. Tsvelik, "Towards a field theory of the plateau transitions in the integer quantum Hall effect," Nuclear Physics B **580**, 688–720 (2000).

[48] A. M. Tsvelik, *Wave Functions Statistics at Quantum Hall Critical Point*, 2001.

[49] A. M. Tsvelik, "Evidence for the PSL(2|2) Wess-Zumino-Novikov-Witten model as a model for the plateau transition in the quantum Hall effect: Evaluation of numerical simulations," Phys. Rev. B **75**, 184201 (2007).

[50] M. R. Zirnbauer, "The integer quantum Hall plateau transition is a current algebra after all," Nuclear Physics B **941**, 458–506 (2019).

[51] F. Evers, A. Mildenberger, and A. D. Mirlin, "Multifractality of wave functions at the quantum Hall transition revisited," Phys. Rev. B **64**, 241303 (2001).

[52] H. Obuse, A. R. Subramaniam, A. Furusaki, I. A. Gruzberg, and A. W. W. Ludwig, "Boundary Multifractality at the Integer Quantum Hall Plateau Transition: Implications for the Critical Theory," Phys. Rev. Lett. **101**, 116802, 116802 (2008).

[53] F. Evers, A. Mildenberger, and A. D. Mirlin, "Multifractality at the Quantum Hall Transition: Beyond the Parabolic Paradigm," Phys. Rev. Lett. **101**, 116803 (2008).

[54] V. Kagalovsky, B. Horovitz, Y. Avishai, and J. T. Chalker, "Quantum Hall Plateau Transitions in Disordered Superconductors," Phys. Rev. Lett. **82**, 3516–3519 (1999).

[55] T. Senthil, J. B. Marston, and M. P. A. Fisher, "Spin quantum Hall effect in unconventional superconductors," Phys. Rev. B **60**, 4245–4254 (1999).

[56] I. A. Gruzberg, A. W. W. Ludwig, and N. Read, "Exact Exponents for the Spin Quantum Hall Transition," Phys. Rev. Lett. **82**, 4524–4527 (1999).

[57] E. J. Beamond, J. Cardy, and J. T. Chalker, "Quantum and classical localization, the spin quantum Hall effect, and generalizations," Phys. Rev. B **65**, 214301 (2002).

[58] A. D. Mirlin, F Evers, and A Mildenberger, "Wavefunction statistics and multifractality at the spin quantum Hall transition," Journal of Physics A: Mathematical and General **36**, 3255–3279 (2003).

[59] M. Puschmann, D. Hernangómez-Pérez, B. Lang, S. Bera, and F. Evers, "Quartic multifractality and finite-size corrections at the spin quantum Hall transition," Phys. Rev. B **103**, 235167 (2021).

[60] R. Bondesan, D. Wieczorek, and M. Zirnbauer, "Gaussian free fields at the integer quantum Hall plateau transition," Nuclear Physics B **918**, 52–90 (2017).

[61] M. S. Foster, H.-Y. Xie, and Y.-Z. Chou, "Topological protection, disorder, and interactions: Survival at the surface of three-dimensional topological superconductors," Phys. Rev. B **89**, 155140 (2014).

[62] A. Altland, B. D. Simons, and M. R. Zirnbauer, "Theories of low-energy quasi-particle states in disordered d-wave superconductors," Physics Reports **359**, 283–354 (2002).

[63] A. A. Nersesyan, A. M. Tsvelik, and F. Wenger, "Disorder effects in two-dimensional d-wave superconductors," Phys. Rev. Lett. **72**, 2628–2631 (1994).

[64] C. Mudry, C. Chamon, and X.-G. Wen, "Two-dimensional conformal field theory for disordered systems at criticality," Nuclear Physics B **466**, 383–443 (1996).

[65] J.-S. Caux, I. Kogan, and A. Tsvelik, "Logarithmic operators and hidden continuous symmetry in critical disordered models," Nuclear Physics B **466**, 444–462 (1996).

[66] M. J. Bhaseen, J.-S. Caux, I. I. Kogan, and A. M. Tsvelik, "Disordered Dirac fermions: the marriage of three different approaches," Nuclear Physics B **618**, 465–499 (2001).

[67] A. W. W. Ludwig, M. P. A. Fisher, R. Shankar, and G. Grinstein, "Integer quantum Hall transition: An alternative approach and exact results," Phys. Rev. B **50**, 7526–7552 (1994).

[68] S. Guruswamy, A. LeClair, and A. Ludwig, "gl(N|N) Super-current algebras for disordered Dirac fermions in two dimensions," Nuclear Physics B **583**, 475–512 (2000).

[69] Y. Huo, R. E. Hetzel, and R. N. Bhatt, "Universal conductance in the lowest Landau level," Phys. Rev. Lett. **70**, 481–484 (1993).

[70] B. Huckestein, "Scaling theory of the integer quantum Hall effect," Rev. Mod. Phys. **67**, 357–396 (1995).

[71] S. Cho and M. P. A. Fisher, "Conductance fluctuations at the integer quantum Hall plateau transition," Phys. Rev. B **55**, 1637–1641 (1997).

[72] And Z. Wang, "Conductance Correlations near Integer Quantum Hall Transitions," Phys. Rev. Lett. **81**, 2767–2770 (1998).

[73] X. Wang, Q. Li, and C. M. Soukoulis, "Scaling properties of conductance at integer quantum Hall plateau transitions," Phys. Rev. B **58**, 3576–3579 (1998).

[74]L. Schweitzer, "Universal Conductance and Conductivity at Critical Points in Integer Quantum Hall Systems," Phys. Rev. Lett. **95**, 256805 (2005).

[75]S. A. A. Ghorashi, Y. Liao, and M. S. Foster, "Critical Percolation without Fine-Tuning on the Surface of a Topological Superconductor," Phys. Rev. Lett. **121**, 016802 (2018).

[76]J. Cardy, "Linking Numbers for Self-Avoiding Loops and Percolation: Application to the Spin Quantum Hall Transition," Phys. Rev. Lett. **84**, 3507–3510 (2000).

[77]F. Evers, A. Mildenberger, and A. D. Mirlin, "Multifractality at the spin quantum Hall transition," Phys. Rev. B **67**, 041303 (2003).

[78]T. Senthil and M. P. A. Fisher, "Quasiparticle localization in superconductors with spin-orbit scattering," Phys. Rev. B **61**, 9690–9698 (2000).

[79]M. Bocquet, D. Serban, and M. Zirnbauer, "Disordered 2d quasiparticles in class D: Dirac fermions with random mass, and dirty superconductors," Nuclear Physics B **578**, 628–680 (2000).

[80]N. Read and A. W. W. Ludwig, "Absence of a metallic phase in random-bond Ising models in two dimensions: Applications to disordered superconductors and paired quantum Hall states," Phys. Rev. B **63**, 024404 (2000).

[81]I. A. Gruzberg, N. Read, and A. W. W. Ludwig, "Random-bond Ising model in two dimensions: The Nishimori line and supersymmetry," Phys. Rev. B **63**, 104422 (2001).

[82]J. T. Chalker, N. Read, V. Kagalovsky, B. Horovitz, Y. Avishai, and A. W. W. Ludwig, "Thermal metal in network models of a disordered two-dimensional superconductor," Phys. Rev. B **65**, 012506 (2001).

[83]A. Mildenberger, F. Evers, A. D. Mirlin, and J. T. Chalker, "Density of quasiparticle states for a two-dimensional disordered system: Metallic, insulating, and critical behavior in the class-D thermal quantum Hall effect," Phys. Rev. B **75**, 245321 (2007).

[84]C. R. Laumann, A. W. W. Ludwig, D. A. Huse, and S. Trebst, "Disorder-induced Majorana metal in interacting non-Abelian anyon systems," Phys. Rev. B **85**, 161301 (2012).

[85]I. C. Fulga, Y. Oreg, A. D. Mirlin, A. Stern, and D. F. Mross, "Temperature Enhancement of Thermal Hall Conductance Quantization," Phys. Rev. Lett. **125**, 236802 (2020).

[86]J. F. Karcher, M. Sonner, and A. D. Mirlin, "Disorder and interaction in chiral chains: Majoranas versus complex fermions," Phys. Rev. B **100**, 134207 (2019).

[87]I. A. Gruzberg, A. D. Mirlin, and M. R. Zirnbauer, "Classification and symmetry properties of scaling dimensions at Anderson transitions," Phys. Rev. B **87**, 125144 (2013).

[88]B. Sbierski, J. F. Karcher, and M. S. Foster, "Spectrum-Wide Quantum Criticality at the Surface of Class AIII Topological Phases: An "Energy Stack" of Integer Quantum Hall Plateau Transitions," Phys. Rev. X **10**, 021025 (2020).

[89]S. A. A. Ghorashi, J. F. Karcher, S. M. Davis, and M. S. Foster, "Criticality across the energy spectrum from random artificial gravitational lensing in two-dimensional Dirac superconductors," Phys. Rev. B **101**, 214521 (2020).

[90]J. F. Karcher and M. S. Foster, "How spectrum-wide quantum criticality protects surface states of topological superconductors from Anderson localization: Quantum Hall plateau transitions (almost) all the way down," Annals of Physics **95**, 168439 (2021).

[91] A. Gogolin, A. Nersesyan, and A. Tsvelik, *Bosonization and Strongly Correlated Systems*, Vol. 95 (Cambridge University Press, 2004), p. 256805.

[92] P. Di Francesco, P. Mathieu, and D. Sénéchal, *Conformal Field Theory*, Vol. 95 (Springer-Verlag, 1997), p. 256805.

[93] T. Giamarchi, *Quantum Physics in One Dimension*, Vol. 95, International Series of Monographs on Physics (Clarendon Press, 2003), p. 256805.

[94] A. MacKinnon and B. Kramer, "One-Parameter Scaling of Localization Length and Conductance in Disordered Systems," Phys. Rev. Lett. **47**, 1546–1549 (1981).

[95] I. C. Fulga, F. Hassler, A. R. Akhmerov, and C. W. J. Beenakker, "Scattering formula for the topological quantum number of a disordered multimode wire," Phys. Rev. B **83**, 155429 (2011).

[96] K. Efetov, *Supersymmetry in Disorder and Chaos*, Vol. 95 (Cambridge University Press, 1996), p. 256805.

[97] A. Altland and B. D. Simons, *Condensed Matter Field Theory*, 2nd ed., Vol. 95 (Cambridge University Press, 2010), p. 256805.

[98] M. R. Zirnbauer, "Riemannian symmetric superspaces and their origin in random-matrix theory," Journal of Mathematical Physics **37**, 4986–5018 (1996).

[99] P. W. Brouwer, A. Furusaki, I. A. Gruzberg, and C. Mudry, "Localization and Delocalization in Dirty Superconducting Wires," Physical Review Letters **85**, 1064–1067 (2000).

[100] P. W. Brouwer, C. Mudry, B. D. Simons, and A. Altland, "Delocalization in Coupled One-Dimensional Chains," Physical Review Letters **81**, 862–865 (1998).

[101] M. Titov, P. W. Brouwer, A. Furusaki, and C. Mudry, "Fokker-Planck equations and density of states in disordered quantum wires," Phys. Rev. B **63**, 235318 (2001).

[102] A. D. Mirlin, Y. V. Fyodorov, A. Mildenberger, and F. Evers, "Exact Relations between Multifractal Exponents at the Anderson Transition," Phys. Rev. Lett. **97**, 046803 (2006).

[103] A. D. Mirlin, "Statistics of energy levels and eigenfunctions in disordered systems," Physics Reports **326**, 259–382 (2000).

[104] B. Duplantier and A. W. W. Ludwig, "Multifractals, operator-product expansion, and field theory," Physical Review Letters **66**, 247–251 (1991).

[105] J. F. Karcher, N. Charles, I. A. Gruzberg, and A. D. Mirlin, "Generalized multifractality at spin quantum Hall transition," Annals of Physics **95**, 168584 (2021).

[106] Y. Nakayama, "Scale invariance vs conformal invariance," Physics Reports **569**, 1–93 (2015).

[107] E. P. Wigner, "On a Class of Analytic Functions from the Quantum Theory of Collisions," Annals of Mathematics **53**, 36–67 (1951).

[108] F. J. Dyson, "Statistical Theory of the Energy Levels of Complex Systems. I," Journal of Mathematical Physics **3**, 140–156 (1962).

[109] R. Gade and F. Wegner, "The n = 0 replica limit of U(n) and U(n)SO(n) models," Nuclear Physics B **360**, 213 –218 (1991).

[110] L. Schweitzer, "Anderson localization for sublattice models," Phys. Rev. Lett. **95**, 256805 (2005).

[111] P. Heinzner, A. Huckleberry, and M. Zirnbauer, "Symmetry Classes of Disordered Fermions," Commun. Math. Phys. **257**, 725–771 (2005).

[112] M. S. Foster and A. W. W. Ludwig, "Metal-insulator transition from combined disorder and interaction effects in Hubbard-like electronic lattice models with random hopping," Phys. Rev. B **77**, 165108 (2008).

[113] T. Morimoto and A. Furusaki, "Topological classification with additional symmetries from Clifford algebras," Phys. Rev. B **88**, 125129 (2013).

[114] I. A. Gruzberg, N. Read, and S. Vishveshwara, "Localization in disordered superconducting wires with broken spin-rotation symmetry," Physical Review B **71**, 245124 (2005).

[115] A. Altland, D. Bagrets, and A. Kamenev, "Topology versus Anderson localization: Nonperturbative solutions in one dimension," Physical Review B **91**, 085429 (2015).

[116] A. Altland, D. Bagrets, L. Fritz, A. Kamenev, and H. Schmiedt, "Quantum Criticality of Quasi-One-Dimensional Topological Anderson Insulators," Physical Review Letters **112**, 206602 (2014).

[117] D. Khmel'nitskii, "Quantization of Hall conductivity," JETP Letters **38**, 552 (1983).

[118] A. M. Pruisken, "Quasiparticles in the theory of the integral quantum Hall effect (I)," Nuclear Physics B **285**, 719–759 (1987).

[119] A. M. Pruisken, "Quasi particles in the theory of the integral quantum Hall effect: (II). Renormalization of the Hall conductance or instanton angle theta," Nuclear Physics B **290**, 61–86 (1987).

[120] J. F. Karcher, "Notes on NLσMs," unpublished **95**, 256805 (2021).

[121] J. T. Chalker and P. D. Coddington, "Percolation, quantum tunnelling and the integer Hall effect," Journal of Physics C: Solid State Physics **21**, 2665–2679 (1988).

[122] P. M. Ostrovsky, I. V. Gornyi, and A. D. Mirlin, "Quantum Criticality and Minimal Conductivity in Graphene with Long-Range Disorder," Physical Review Letters **98**, 256801 (2007).

[123] A. LeClair and D. J. a. Robinson, "C and D disorder," J. Phys. A **41**, 452002 (2008).

[124] M. S. Foster and E. A. Yuzbashyan, "Interaction-Mediated Surface-State Instability in Disordered Three-Dimensional Topological Superconductors with Spin SU(2) Symmetry," Phys. Rev. Lett. **109**, 246801 (2012).

[125] H.-Y. Xie, Y.-Z. Chou, and M. S. Foster, "Surface transport coefficients for three-dimensional topological superconductors," Phys. Rev. B **91**, 024203 (2015).

[126] E. J. Dresselhaus, B. Sbierski, and I. A. Gruzberg, "Numerical evidence for marginal scaling at the integer quantum Hall transition," arXiv: **2101**. 01716 (2021).

[127] F. D. M. Haldane, "Nobel Lecture: Topological quantum matter," Reviews of Modern Physics **89**, 040502 (2017).

[128] K. Nomura, M. Koshino, and S. Ryu, "Topological Delocalization of Two-Dimensional Massless Dirac Fermions," Physical Review Letters **99**, 146806 (2007).

[129] J. E. Moore, "The birth of topological insulators," en, Nature **464**, 194–198 (2010).

[130] S. Ryu, C. Mudry, H. Obuse, and A. Furusaki, "${\mathbb{Z}}_{2}$ Topological Term, the Global Anomaly, and the Two-Dimensional Symplectic Symmetry Class of Anderson Localization," Physical Review Letters **99**, 116601 (2007).

[131] A. Altland and R. Merkt, "Spectral and transport properties of quantum wires with bond disorder," Nuclear Physics B **607**, 511–548 (2001).

[132]S. Ryu, A. P. Schnyder, A. Furusaki, and A. W. W. Ludwig, "Topological insulators and superconductors: tenfold way and dimensional hierarchy," en, New Journal of Physics **12**, 065010 (2010).

[133]A. D. Mirlin, F. Evers, I. V. Gornyi, and P. M. Ostrovsky, "Anderson transitions: criticality, symmetries and topologies," International Journal of Modern Physics B **24**, 1577–1620 (2010).

[134]L. Fu and C. L. Kane, "Topological insulators with inversion symmetry," Physical Review B **76**, 045302 (2007).

[135]L. Fu, "Topological Crystalline Insulators," Physical Review Letters **106**, 106802 (2011).

[136]P. M. Ostrovsky, I. V. Gornyi, and A. D. Mirlin, "Interaction-Induced Criticality in ${\mathbb{Z}}_{2}$ Topological Insulators," Physical Review Letters **105**, 036803 (2010).

[137]I. S. Burmistrov, I. V. Gornyi, and A. D. Mirlin, "Enhancement of the Critical Temperature of Superconductors by Anderson Localization," Physical Review Letters **108**, 017002 (2012).

[138]A. M. Finkel'stein, "Disordered electron liquid with interactions," International Journal of Modern Physics B **24**, 1855–1894 (2010).

[139]S. Nadj-Perge, I. K. Drozdov, J. Li, H. Chen, S. Jeon, J. Seo, A. H. MacDonald, B. A. Bernevig, and A. Yazdani, "Observation of Majorana fermions in ferromagnetic atomic chains on a superconductor," en, Science **346**, 602–607 (2014).

[140]A. Bühler, N. Lang, C. V. Kraus, G. Möller, S. D. Huber, and H. P. Büchler, "Majorana modes and p-wave superfluids for fermionic atoms in optical lattices," en, Nature Communications **5**, 4504 (2014).

[141]S. R. White, "Density-matrix algorithms for quantum renormalization groups," Physical Review B **48**, 10345–10356 (1993).

[142]D. Jaschke, M. L. Wall, and L. D. Carr, "Open source Matrix Product States: Opening ways to simulate entangled many-body quantum systems in one dimension," Computer Physics Communications **225**, 59–91 (2018).

[143]C.-K. Chiu, J. C. Teo, A. P. Schnyder, and S. Ryu, "Classification of topological quantum matter with symmetries," Reviews of Modern Physics **88**, 035005 (2016).

[144]A. Luther and I. Peschel, "Calculation of critical exponents in two dimensions from quantum field theory in one dimension," Physical Review B **12**, 3908–3917 (1975).

[145]G. Refael and J. E. Moore, "Entanglement Entropy of Random Quantum Critical Points in One Dimension," Physical Review Letters **93**, 260602 (2004).

[146]G. Refael and J. E. Moore, "Criticality and entanglement in random quantum systems," en, Journal of Physics A: Mathematical and Theoretical **42**, 504010 (2009).

[147]N. Laflorencie, "Scaling of entanglement entropy in the random singlet phase," Phys. Rev. B **72**, 140408 (2005).

[148]R. Kennedy and M. R. Zirnbauer, "Bott Periodicity for $${\mathbb{Z}_2}$$Z2Symmetric Ground States of Gapped Free-Fermion Systems," en, Communications in Mathematical Physics **342**, 909–963 (2016).

[149]U. Schollwoeck, "The density-matrix renormalization group in the age of matrix product states," Annals of Physics **326**, arXiv: 1008.3477, 96–192 (2011).

[150] A. Bazavov, Y. Meurice, S.-W. Tsai, J. Unmuth-Yockey, L.-P. Yang, and J. Zhang, "Estimating the central charge from the R\'enyi entanglement entropy," Physical Review D **96**, arXiv: 1703.10577, 256805 (2017).

[151] P. Sen and B. K. Chakrabarti, "Critical properties of a one-dimensional frustrated quantum magnetic model," Physical Review B **43**, 13559–13565 (1991).

[152] N. M. Gergs, L. Fritz, and D. Schuricht, "Topological order in the Kitaev/Majorana chain in the presence of disorder and interactions," Physical Review B **93**, 075129 (2016).

[153] M. McGinley, J. Knolle, and A. Nunnenkamp, "Robustness of Majorana edge modes and topological order: Exact results for the symmetric interacting Kitaev chain with disorder," Physical Review B **96**, 241113 (2017).

[154] T. Giamarchi and H. J. Schulz, "Anderson localization and interactions in one-dimensional metals," Physical Review B **37**, 325–340 (1988).

[155] I. S. Burmistrov, I. V. Gornyi, and A. D. Mirlin, "Superconductor-insulator transitions: Phase diagram and magnetoresistance," Physical Review B **92**, 014506 (2015).

[156] D.-H. Lee and Z. Wang, "Effects of Electron-Electron Interactions on the Integer Quantum Hall Transitions," Physical Review Letters **76**, 4014–4017 (1996).

[157] Z. Wang, M. P. A. Fisher, S. M. Girvin, and J. T. Chalker, "Short-range interactions and scaling near integer quantum Hall transitions," Physical Review B **61**, 8326–8333 (2000).

[158] I. S. Burmistrov, S. Bera, F. Evers, I. V. Gornyi, and A. D. Mirlin, "Wave function multifractality and dephasing at metal–insulator and quantum Hall transitions," Annals of Physics **326**, 1457–1478 (2011).

[159] F. Evers and A. D. Mirlin, "Anderson Transitions," Reviews of Modern Physics **80**, arXiv: 0707.4378, 1355–1417 (2008).

[160] F. J. Dyson, "The Dynamics of a Disordered Linear Chain," Physical Review **92**, 1331–1338 (1953).

[161] R. H. McKenzie, "Exact Results for Quantum Phase Transitions in Random XY Spin Chains," Phys. Rev. Lett. **77**, 4804–4807 (1996).

[162] M. S. Foster, "Note on scaling arguments," unpublished **95**, 256805 (2018).

[163] S. Bravyi and R. König, "Disorder-Assisted Error Correction in Majorana Chains," en, Communications in Mathematical Physics **316**, 641–692 (2012).

[164] P. W. Anderson, "Absence of diffusion in certain random lattices," Phys. Rev. **109**, 1492 (1958).

[165] L. Schweitzer, *50 Years of Anderson Localization*, edited by E. Abrahams, Vol. 95 (World Scientific, 2010), p. 256805.

[166] I. S. Burmistrov, I. V. Gornyi, and A. D. Mirlin, "Multifractality at Anderson Transitions with Coulomb Interaction," Phys. Rev. Lett. **111**, edited by E. Abrahams, 066601 (2013).

[167] S. Faez, A. Strybulevych, J. H. Page, A. Lagendijk, and B. A. van Tiggelen, "Observation of Multifractality in Anderson Localization of Ultrasound," Phys. Rev. Lett. **103**, edited by E. Abrahams, 155703 (2009).

[168] M. V. Feigel'man, L. B. Ioffe, V. E. Kravtsov, and E. A. Yuzbashyan, "Eigenfunction Fractality and Pseudogap State near the Superconductor-Insulator Transition," Phys. Rev. Lett. **98**, edited by E. Abrahams, 027001 (2007).

169 M. Feigel'man, L. Ioffe, V. Kravtsov, and E Cuevas, "Fractal superconductivity near localization threshold," Annals of Physics **325**, edited by E. Abrahams, 1390–1478 (2010).

170 B. Fan and A. M. García-García, "Superconductivity at the three-dimensional Anderson metal-insulator transition," Phys. Rev. B **102**, edited by E. Abrahams, 184507 (2020).

171 I. Burmistrov, I. Gornyi, and A. Mirlin, "Enhancement of the critical temperature of superconductors by Anderson localization," Physical Review Letters **108**, edited by E. Abrahams, 017002 (2012).

172 I. S. Burmistrov, I. V. Gornyi, and A. D. Mirlin, "Superconductor-insulator transitions: Phase diagram and magnetoresistance," Phys. Rev. B **92**, edited by E. Abrahams, 014506 (2015).

173 J. Mayoh and A. M. García-García, "Global critical temperature in disordered superconductors with weak multifractality," Physical Review B **92**, edited by E. Abrahams, 174526 (2015).

174 B. Fan and A. M. García-García, "Enhanced phase-coherent multifractal two-dimensional super-conductivity," Phys. Rev. B **101**, edited by E. Abrahams, 104509 (2020).

175 I. Burmistrov, I. Gornyi, and A. Mirlin, "Multifractally-enhanced superconductivity in thin films," Annals of Physics **95**, edited by E. Abrahams, 168499 (2021).

176 K. Zhao, H. Lin, X. Xiao, W. Huang, W. Yao, M. Yan, Y. Xing, Q. Zhang, Z.-X. Li, S. Hoshino, J. Wang, S. Zhou, L. Gu, M. S. Bahramy, H. Yao, N. Nagaosa, Q.-K. Xue, K. T. Law, X. Chen, and S.-H. Ji, "Disorder-induced multifractal superconductivity in monolayer niobium dichalcogenides," Nature Physics **15**, edited by E. Abrahams, 904–910 (2019).

177 C. Rubio-Verdu, A. M. Garcia-Garcia, H. Ryu, D.-J. Choi, J. Zaldivar, S. Tang, B. Fan, Z.-X. Shen, S.-K. Mo, J. I. Pascual, and M. M. Ugeda, "Visualization of Multifractal Superconductivity in a Two-Dimensional Transition Metal Dichalcogenide in the Weak-Disorder Regime," Nano Letters **20**, edited by E. Abrahams, 5111–5118 (2020).

178 S. Kettemann, E. R. Mucciolo, I. Varga, and K. Slevin, "Kondo-Anderson transitions," Phys. Rev. B **85**, edited by E. Abrahams, 115112 (2012).

179 S Kettemann, E. Mucciolo, and I Varga, "Critical metal phase at the anderson metal-insulator transition with Kondo impurities," Physical Review Letters **103**, edited by E. Abrahams, 126401 (2009).

180 K. Slevin, S. Kettemann, and T. Ohtsuki, "Multifractality and the distribution of the Kondo temperature at the Anderson transition," The European Physical Journal B **92**, edited by E. Abrahams, 281 (2019).

181 A. D. Mirlin and Y. V. Fyodorov, "Distribution of local densities of states, order parameter function, and critical behavior near the Anderson transition," Physical Review Letters **72**, edited by E. Abrahams, 526 (1994).

182 A. D. Mirlin and Y. V. Fyodorov, "Statistical properties of one-point Green functions in disordered systems and critical behavior near the Anderson transition," Journal de Physique I **4**, edited by E. Abrahams, 655–673 (1994).

183 Y. V. Fyodorov and D. V. Savin, "Statistics of impedance, local density of states, and reflection in quantum chaotic systems with absorption," Journal of Experimental and Theoretical Physics Letters **80**, edited by E. Abrahams, 725–729 (2004).

184 D. V. Savin, H.-J. Sommers, and Y. V. Fyodorov, "Universal statistics of the local Green's function in wave chaotic systems with absorption," Journal of Experimental and Theoretical Physics Letters **82**, edited by E. Abrahams, 544–548 (2005).

[185] Y. V. Fyodorov, D. V. Savin, and H.-J. Sommers, "Scattering, reflection and impedance of waves in chaotic and disordered systems with absorption," Journal of Physics A: Mathematical and General **38**, edited by E. Abrahams, 10731–10760 (2005).

[186] I. A. Gruzberg, A. W. W. Ludwig, A. D. Mirlin, and M. R. Zirnbauer, "Symmetries of Multifractal Spectra and Field Theories of Anderson Localization," Phys. Rev. Lett. **107**, edited by E. Abrahams, 086403 (2011).

[187] D. Höf and F. Wegner, "Calculation of anomalous dimensions for the nonlinear sigma model," Nuclear Physics B **275**, edited by E. Abrahams, 561–579 (1986).

[188] F. Wegner, "Anomalous dimesions for the nonlinear sigma-model in $2 + \epsilon$ dimensions (I)," Nuclear Physics B **280**, edited by E. Abrahams, 193–209 (1987).

[189] F. Wegner, "Anomalous dimensions for the nonlinear sigma-model, in $2 + \epsilon$ dimensions (II)," Nuclear Physics B **280**, edited by E. Abrahams, 210–224 (1987).

[190] D.-H. Lee and Z. Wang, "Effects of Electron-Electron Interactions on the Integer Quantum Hall Transitions," Phys. Rev. Lett. **76**, edited by E. Abrahams, 4014–4017 (1996).

[191] Z. Wang, M. P. A. Fisher, S. M. Girvin, and J. T. Chalker, "Short-range interactions and scaling near integer quantum Hall transitions," Phys. Rev. B **61**, edited by E. Abrahams, 8326–8333 (2000).

[192] R. Bondesan, D. Wieczorek, and M. R. Zirnbauer, "Pure Scaling Operators at the Integer Quantum Hall Plateau Transition," Physical Review Letters **112**, 186803, edited by E. Abrahams, 186803 (2014).

[193] D. C. Lewellen, "Constraints for conformal field theories on the plane: Reviving the conformal bootstrap," Nuclear Physics B **320**, edited by E. Abrahams, 345–376 (1989).

[194] A Mildenberger, F Evers, and A. Mirlin, "Dimensionality dependence of the wave-function statistics at the Anderson transition," Physical Review B **66**, edited by E. Abrahams, 033109 (2002).

[195] A. Rodriguez, L. J. Vasquez, and R. A. Römer, "Multifractal analysis of the metal-insulator transition in the three-dimensional Anderson model. II. Symmetry relation under ensemble averaging," Phys. Rev. B **78**, edited by E. Abrahams, 195107 (2008).

[196] E. Tarquini, G. Biroli, and M. Tarzia, "Critical properties of the Anderson localization transition and the high-dimensional limit," Physical Review B **95**, edited by E. Abrahams, 094204 (2017).

[197] I. M. Suslov, "Strict parabolicity of the multifractal spectrum at the Anderson transition," Journal of Experimental and Theoretical Physics **123**, edited by E. Abrahams, 845–850 (2016).

[198] A. W. Knapp, *Lie Groups Beyond an Introduction*, edited by E. Abrahams, Vol. 95 (Birkhäuser, Boston, Basel, Berlin, 2002), p. 256805.

[199] F. Wegner, "The mobility edge problem: continuous symmetry and a conjecture," Zeitschrift für Physik B **35**, edited by E. Abrahams, 207–210 (1979).

[200] K. Jüngling and R. Oppermann, "Effects of Spin Interactions in Disordered Electronic Systems: Loop Expansions and Exact Relations Among Local Gauge Invariant Models," Zeitschrift für Physik B **35**, edited by E. Abrahams, 207–210 (1979).

[201] K. Efetov, "Supersymmetry and theory of disordered metals," Advances in Physics **32**, edited by E. Abrahams, 53–127 (1983).

[202] K. Efetov, *Supersymmetry in Disorder and Chaos*, edited by E. Abrahams, Vol. 95 (Cambridge University Press, Cambridge, England, 1997), p. 256805.

[203] J. Verbaarschot, H. Weidenmüller, and M. Zirnbauer, "Grassmann integration in stochastic quantum physics: The case of compound-nucleus scattering," Physics Reports **129**, edited by E. Abrahams, 367–438 (1985).

[204] A. Altland, B. D. Simons, and D. Taras Semchuk, "Field theory of mesoscopic fluctuations in superconductor-normal-metal systems," Advances in Physics **49**, edited by E. Abrahams, 321–394 (2000).

[205] D. Taras-Semchuk and A. Altland, "Quantum interference and the formation of the proximity effect in chaotic normal-metal/superconducting structures," Phys. Rev. B **64**, edited by E. Abrahams, 014512 (2001).

[206] Y. Liao, A. Levchenko, and M. S. Foster, "Response theory of the ergodic many-body delocalized phase: Keldysh Finkel'stein sigma models and the 10-fold way," Annals of Physics **386**, edited by E. Abrahams, 97–157 (2017).

[207] E. V. Repin and I. S. Burmistrov, "Mesoscopic fluctuations of the single-particle Green's function at Anderson transitions with Coulomb interaction," Phys. Rev. B **94**, edited by E. Abrahams, 245442 (2016).

[208] I. S. Burmistrov and M. A. Skvortsov, "Magnetic disorder in superconductors: Enhancement by mesoscopic fluctuations," Phys. Rev. B **97**, edited by E. Abrahams, 014515 (2018).

[209] P. A. Mello, "Averages on the unitary group and applications to the problem of disordered conductors," Journal of Physics A: Mathematical and General **23**, edited by E. Abrahams, 4061–4080 (1990).

[210] D. Weingarten, "Asymptotic behavior of group integrals in the limit of infinite rank," Journal of Mathematical Physics **19**, edited by E. Abrahams, 999–1001 (1978).

[211] D. Friedan, "Nonlinear Models in $2 + \epsilon$ Dimensions," Phys. Rev. Lett. **45**, edited by E. Abrahams, 1057–1060 (1980).

[212] B. Kramer, T. Ohtsuki, and S. Kettemann, "Random network models and quantum phase transitions in two dimensions," Physics Reports **417**, edited by E. Abrahams, 211–342 (2005).

[213] R Klesse and M Metzler, "Universal Multifractality in Quantum Hall Systems with Long-Range Disorder Potential," Europhysics Letters (EPL) **32**, edited by E. Abrahams, 229–234 (1995).

[214] H. Saleur and B. Duplantier, "Exact determination of the percolation hull exponent in two dimensions," Phys. Rev. Lett. **58**, edited by E. Abrahams, 2325 (1087).

[215] R. M. Ziff, "Correction-to-scaling exponent for two-dimensional percolation," Phys. Rev. E **83**, edited by E. Abrahams, 020107 (2011).

[216] M. den Nijs, "Extended scaling relations for the magnetic critical exponents of the Potts model," Phys. Rev. B **27**, edited by E. Abrahams, 1674–1679 (1983).

[217] A. Kammerer, F. Höfling, and T. Franosch, "Cluster-resolved dynamic scaling theory and universal corrections for transport on percolating systems," EPL (Europhysics Letters) **84**, edited by E. Abrahams, 66002 (2008).

[218] J. Asikainen, A. Aharony, and B. e. a. Mandelbrot, "Fractal geometry of critical Potts clusters," Eur. Phys. J. B **34**, edited by E. Abrahams, 479–487 (2003).

[219] G. E. Volovik, *The Universe in a Helium Droplet*, edited by E. Abrahams, Vol. 95 (Clarendon Press, Oxford, England, 2003), p. 256805.

[220]T. Mizushima, Y. Tsutsumi, T. Kawakami, M. Sato, M. Ichioka, and K. Machida, "Symmetry-Protected Topological Superfluids and Superconductors —From the Basics to 3He—," Journal of the Physical Society of Japan **85**, edited by E. Abrahams, 022001 (2016).

[221]C. L. Kane and E. J. Mele, "Quantum Spin Hall Effect in Graphene," Phys. Rev. Lett. **95**, edited by E. Abrahams, 226801 (2005).

[222]H.-Y. Xie, H. Li, Y.-Z. Chou, and M. S. Foster, "Topological Protection from Random Rashba Spin-Orbit Backscattering: Ballistic Transport in a Helical Luttinger Liquid," Phys. Rev. Lett. **116**, edited by E. Abrahams, 086603 (2016).

[223]J. H. Bardarson, J. Tworzydło, P. W. Brouwer, and C. W. J. Beenakker, "One-Parameter Scaling at the Dirac Point in Graphene," Phys. Rev. Lett. **99**, edited by E. Abrahams, 106801 (2007).

[224]E. J. König, P. M. Ostrovsky, I. V. Protopopov, I. V. Gornyi, I. S. Burmistrov, and A. D. Mirlin, "Half-integer quantum Hall effect of disordered Dirac fermions at a topological insulator surface," Phys. Rev. B **90**, edited by E. Abrahams, 165435 (2014).

[225]A. M. Tsvelik, "Exactly solvable model of fermions with disorder," Phys. Rev. B **51**, edited by E. Abrahams, 9449–9454 (1995).

[226]C. d. C. Chamon, C. Mudry, and X.-G. Wen, "Localization in Two Dimensions, Gaussian Field Theories, and Multifractality," Phys. Rev. Lett. **77**, edited by E. Abrahams, 4194–4197 (1996).

[227]Y.-Z. Chou and M. S. Foster, "Chalker scaling, level repulsion, and conformal invariance in critically delocalized quantum matter: Disordered topological superconductors and artificial graphene," Phys. Rev. B **89**, edited by E. Abrahams, 165136 (2014).

[228]B. Sbierski, E. J. Dresselhaus, J. E. Moore, and I. A. Gruzberg, "Criticality of Two-Dimensional Disordered Dirac Fermions in the Unitary Class and Universality of the Integer Quantum Hall Transition," Phys. Rev. Lett. **126**, edited by E. Abrahams, 076801 (2021).

[229]S. H. Pan, J. P. O'Neal, R. L. Badzey, C. Chamon, H. Ding, J. R. Engelbrecht, Z. Wang, H. Eisaki, S. Uchida, A. K. Gupta, K.-W. Ng, E. W. Hudson, K. M. Lang, and J. C. Davis, "Microscopic electronic inhomogeneity in the high-Tc superconductor $Bi_2Sr_2CaCu_2O_{8+x}$," Nature **413**, edited by E. Abrahams, 282 (2001).

[230]K. M. Lang, V. Madhavan, J. E. Hoffman, E. W. Hudson, H. Eisaki, S. Uchida, and J. C. Davis, "Imaging the granular structure of high-Tc superconductivity in underdoped $Bi_2Sr_2CaCu_2O_{8+\delta}$," Nature **415**, edited by E. Abrahams, 412 (2002).

[231]K. McElroy, D.-H. Lee, J. E. Hoffman, K. M. Lang, J. Lee, E. W. Hudson, H. Eisaki, S. Uchida, and J. C. Davis, "Coincidence of Checkerboard Charge Order and Antinodal State Decoherence in Strongly Underdoped Superconducting $Bi_2Sr_2CaCu_2O_{8+\delta}$," Phys. Rev. Lett. **94**, edited by E. Abrahams, 197005 (2005).

[232]K. McElroy, J. Lee, J. A. Slezak, D.-H. Lee, H. Eisaki, S. Uchida, and J. C. Davis, "Atomic-Scale Sources and Mechanism of Nanoscale Electronic Disorder in $Bi_2Sr_2CaCu_2O_{8+\delta}$," Science **309**, edited by E. Abrahams, 1048 (2005).

[233]Y. Kohsaka, C. Taylor, P. Wahl, A. Schmidt, J. Lee, K. Fujita, J. W. Alldredge, K. McElroy, J. Lee, H. Eisaki, S. Uchida, D.-H. Lee, and J. C. Davis, "How Cooper pairs vanish approaching the Mott insulator in $Bi_2Sr_2CaCu_2O_{8+\delta}$," Nature **454**, edited by E. Abrahams, 1072 (2008).

[234]K. Fujita, A. R. Schmidt, E.-A. Kim, M. J. Lawler, H. Eisaki, S. Uchida, D.-H. Lee, and J. C. Davis, *Spectroscopic Imaging STM Studies of Electronic Structure in Both the Superconducting and Pseudogap Phases of Underdoped Cuprates*, edited by E. Abrahams, Vol. Conductor-Insulator Quantum Phase Transitions (Oxford University Press, Oxford, England, 2012), p. 256805.

[235]M. Leroux, V. Mishra, J. P. C. Ruff, H. Claus, M. P. Smylie, C. Opagiste, P. Rodière, A. Kayani, G. D. Gu, J. M. Tranquada, W.-K. Kwok, Z. Islam, and U. Welp, "Disorder raises the critical temperature of a cuprate superconductor," Proc. Natl. Acad. Sci. (USA) **116**, edited by E. Abrahams, 10691 (2018).

[236]K. Zhao, H. Lin, X. Xiao, W. Huang, W. Yao, M. Yan, Y. Xing, Q. Zhang, Z.-X. Li, S. Hoshino, J. Wang, S. Zhou, L. Gu, M. S. Bahramy, H. Yao, N. Nagaosa, Q.-K. Xue, K. T. Law, X. Chen, and S.-H. Ji, "Disorder-induced multifractal superconductivity in monolayer niobium dichalcogenides," Nat. Phys. **15**, edited by E. Abrahams, 904 (2019).

[237]C. Rubio-Verdú, A. M. García-García, H. Ryu, D.-J. Choi, J. Zaldívar, S. Tang, B. Fan, Z.-X. Shen, S.-K. Mo, J. I. Pascual, and M. M. Ugeda, "Visualization of multifractal superconductivity in a two-dimensional transition metal dichalcogenide in the weak-disorder regime," arXiv: **1810.** Edited by E. Abrahams, 08222 (2018).

[238]J. Gao, J. W. Park, K. Kim, S. K. Song, F. Chen, X. Luo, Y. Sun, and H. W. Yeom, "Pseudogap and weak multifractality in disordered Mott charge-density-wave insulator," arXiv: **1904.** Edited by E. Abrahams, 04508 (2019).

[239]R. Bistritzer and A. H. MacDonald, "Moiré bands in twisted double-layer graphene," Proc. Natl. Acad. Sci. U.S.A. **108**, edited by E. Abrahams, 12233 (2011).

[240]P. San-Jose, J. González, and F. Guinea, "Non-Abelian Gauge Potentials in Graphene Bilayers," Phys. Rev. Lett. **108**, edited by E. Abrahams, 216802 (2012).

[241]G. Tarnopolsky, A. J. Kruchkov, and A. Vishwanath, "Origin of Magic Angles in Twisted Bilayer Graphene," Phys. Rev. Lett. **122**, edited by E. Abrahams, 106405 (2019).

[242]A. P. Schnyder, S. Ryu, and A. W. W. Ludwig, "Lattice Model of a Three-Dimensional Topological Singlet Superconductor with Time-Reversal Symmetry," Phys. Rev. Lett. **102**, edited by E. Abrahams, 196804 (2009).

[243]P. Hosur, S. Ryu, and A. Vishwanath, "Chiral topological insulators, superconductors, and other competing orders in three dimensions," Phys. Rev. B **81**, edited by E. Abrahams, 045120 (2010).

[244]A. P. Schnyder, P. M. R. Brydon, D. Manske, and C. Timm, "Andreev spectroscopy and surface density of states for a three-dimensional time-reversal-invariant topological superconductor," Phys. Rev. B **82**, edited by E. Abrahams, 184508 (2010).

[245]T. Senthil, M. P. A. Fisher, L. Balents, and C. Nayak, "Quasiparticle Transport and Localization in High-T_c Superconductors," Phys. Rev. Lett. **81**, edited by E. Abrahams, 4704–4707 (1998).

[246]W. Yang, Y. Li, and C. Wu, "Topological Septet Pairing with Spin-$\frac{3}{2}$ Fermions: High-Partial-Wave Channel Counterpart of the $^3\mathrm{He}-B$ Phase," Phys. Rev. Lett. **117**, edited by E. Abrahams, 075301 (2016).

[247]C. Fang, B. A. Bernevig, and M. J. Gilbert, "Tri-Dirac surface modes in topological superconductors," Phys. Rev. B **91**, edited by E. Abrahams, 165421 (2015).

[248] S. A. A. Ghorashi, S. Davis, and M. S. Foster, "Disorder-enhanced topological protection and universal quantum criticality in a spin-$\frac{3}{2}$ topological superconductor," Phys. Rev. B **95**, edited by E. Abrahams, 144503 (2017).

[249] B. Roy, S. A. A. Ghorashi, M. S. Foster, and A. H. Nevidomskyy, "Topological superconductivity of spin-3/2 carriers in a three-dimensional doped Luttinger semimetal," Phys. Rev. B **99**, edited by E. Abrahams, 054505 (2019).

[250] E. J. König, P. M. Ostrovsky, I. V. Protopopov, and A. D. Mirlin, "Metal-insulator transition in two-dimensional random fermion systems of chiral symmetry classes," Physical Review B **85**, edited by E. Abrahams, 195130 (2012).

[251] P. M. Ostrovsky, I. V. Gornyi, and A. D. Mirlin, "Electron transport in disordered graphene," Phys. Rev. B **74**, edited by E. Abrahams, 235443 (2006).

[252] A. Schuessler, P. M. Ostrovsky, I. V. Gornyi, and A. D. Mirlin, "Analytic theory of ballistic transport in disordered graphene," Phys. Rev. B **79**, edited by E. Abrahams, 075405 (2009).

[253] M. S. Foster and I. L. Aleiner, "Graphene via large N: A renormalization group study," Phys. Rev. B **77**, edited by E. Abrahams, 195413 (2008).

[254] B. Jovanović and Z. Wang, "Conductance Correlations near Integer Quantum Hall Transitions," Phys. Rev. Lett. **81**, edited by E. Abrahams, 2767 (1998).

[255] L. Fu and E. Berg, "Odd-Parity Topological Superconductors: Theory and Application to $Cu_xBi_2Se_3$," Phys. Rev. Lett. **105**, edited by E. Abrahams, 097001 (2010).

[256] S. Sasaki, M. Kriener, K. Segawa, K. Yada, Y. Tanaka, M. Sato, and Y. Ando, "Topological Superconductivity in $Cu_xBi_2Se_3$," Phys. Rev. Lett. **107**, edited by E. Abrahams, 217001 (2011).

[257] H. Peng, D. De, B. Lv, F. Wei, and C.-W. Chu, "Absence of zero-energy surface bound states in $Cu_xBi_2Se_3$ studied via Andreev reflection spectroscopy," Phys. Rev. B **88**, edited by E. Abrahams, 024515 (2013).

[258] N. Levy, T. Zhang, J. Ha, F. Sharifi, A. A. Talin, Y. Kuk, and J. A. Stroscio, "Experimental Evidence for s-Wave Pairing Symmetry in Superconducting $Cu_xBi_2Se_3$ Single Crystals Using a Scanning Tunneling Microscope," Phys. Rev. Lett. **110**, edited by E. Abrahams, 117001 (2013).

[259] K. Matano, M. Kriener, K. Segawa, Y. Ando, and G.-q. Zheng, "Spin-rotation symmetry breaking in the superconducting state of $Cu_xBi_2Se_3$," Nat. Phys. **12**, edited by E. Abrahams, 852 (2016).

[260] S. Yonezawa, K. Tajiri, S. Nakata, Y. Nagai, Z. Wang, K. Segawa, Y. Ando, and Y. Maeno, "Thermodynamic evidence for nematic superconductivity in $Cu_xBi_2Se_3$," Nat. Phys. **13**, edited by E. Abrahams, 123 (2017).

[261] R. Tao, Y.-J. Yan, X. Liu, Z.-W. Wang, Y. Ando, Q.-H. Wang, T. Zhang, and D.-L. Feng, "Direct Visualization of the Nematic Superconductivity in $Cu_xBi_2Se_3$," Phys. Rev. X **8**, edited by E. Abrahams, 041024 (2018).

[262] M. P. Smylie, H. Claus, U. Welp, W.-K. Kwok, Y. Qiu, Y. S. Hor, and A. Snezhko, "Evidence of nodes in the order parameter of the superconducting doped topological insulator $Nb_xBi_2Se_3$ via penetration depth measurements," Phys. Rev. B **94**, edited by E. Abrahams, 180510R (2016).

[263] T. Asaba, B. J. Lawson, C. Tinsman, L. Chen, P. Corbae, G. Li, Y. Qiu, Y. S. Hor, L. Fu, and L. Li, "Rotational Symmetry Breaking in a Trigonal Superconductor Nb-doped Bi_2Se_3," Phys. Rev. X **7**, edited by E. Abrahams, 011009 (2017).

[264] M. P. Smylie, K. Willa, H. Claus, A. Snezhko, I. Martin, W.-K. Kwok, Y. Qiu, Y. S. Hor, E. Bokari, P. Niraula, A. Kayani, V. Mishra, and U. Welp, "Robust odd-parity superconductivity in the doped topological insulator $Nb_xBi_2Se_3$," Phys. Rev. B **96**, edited by E. Abrahams, 115145 (2017).

[265] D. Das, K. Kobayashi, M. P. Smylie, C. M. III, T. Takahashi, K. Willa, J.-X. Yin, U. Welp, M. Z. Hasan, A. Amato, H. Luetkens, and Z. Guguchia, "Time-reversal invariant and fully gapped unconventional superconducting state in the bulk of the topological compound $Nb_{0.25}Bi_2Se_3$," Phys. Rev. B **102**, edited by E. Abrahams, 134514 (2020).

[266] A. Kolapo, T. Li, P. Hosur, and J. H. a. Miller, "Transport evidence for three dimensional topological superconductivity in doped β-$PdBi_2$," Sci. Rep. **9**, edited by E. Abrahams, 12504 (2019).

[267] Y. Li, X. Xu, M.-H. Lee, M.-W. Chu, and C. L. Chien, "Observation of half-quantum flux in the unconventional superconductor β-Bi_2Pd," Science **366**, edited by E. Abrahams, 238 (2019).

[268] E. Fradkin, S. A. Kivelson, M. J. Lawler, J. P. Eisenstein, and A. P. Mackenzie, "Nematic Fermi fluids in condensed matter physics," Annu. Rev. Condens. Matter Phys. **1**, edited by E. Abrahams, 153 (2010).

[269] D. F. Agterberg, J. C. S. Davis, S. D. Edkins, E. Fradkin, D. J. V. Harlingen, S. A. Kivelson, P. A. Lee, L. Radzihovsky, J. M. Tranquada, and Y. Wang, "The physics of pair-density waves: Cuprate superconductors and beyond," Annu. Rev. Condens. Matter Phys. **11**, edited by E. Abrahams, 231 (2020).

[270] S. Mukhopadhyay, R. Sharma, C. K. Kim, S. D. Edkins, M. H. Hamidian, H. Eisaki, S.-I. Uchida, E.-A. Kim, M. J. Lawler, A. P. Mackenzie, J. C. S. Davis, and K. Fujita, "Evidence for a vestigial nematic state in the cuprate pseudogap phase," Proc. Natl. Acad. Sci. (USA) **116**, edited by E. Abrahams, 13249 (2019).

[271] S. M. Davis, "Unpublished notes," Phys. Rev. Lett. **95**, edited by E. Abrahams, 256805 (2020).

[272] V. G. Khizhnik, A. M. Polyakov, and A. B. Zamolodchikov, "Fractal structure of $2d$ - quantum gravity," Mod. Phys. Lett. A **3**, edited by E. Abrahams, 819 (1988).

[273] J. Distler and H. Kawai, "Conformal field theory and 2D quantum gravity," Nucl. Phys. **B321**, edited by E. Abrahams, 509 (1989).

[274] A. Zamolodchikov and A. Zamolodchikov, "Lectures on Liouville Theory and Matrix Models," Phys. Rev. Lett. **95**, edited by E. Abrahams, 256805 (2010).

[275] R. Vasseur, A. J. Friedman, S. A. Parameswaran, and A. C. Potter, "Particle-hole symmetry, many-body localization, and topological edge modes," Phys. Rev. B **93**, edited by E. Abrahams, 134207 (2016).

[276] C. M. Duque, H.-Y. Hu, Y.-Z. You, V. Khemani, R. Verresen, and R. Vasseur, "Topological and symmetry-enriched random quantum critical points," Phys. Rev. B **103**, edited by E. Abrahams, L100207 (2021).

[277] A. Rahmani, D. Pikulin, and I. Affleck, "Majorana-Hubbard Ladders," Physical Review B **99**, edited by E. Abrahams, arXiv: 1810.01956, 256805 (2019).

[278] I. V. Gornyi, A. D. Mirlin, and D. G. Polyakov, "Interacting Electrons in Disordered Wires: Anderson Localization and Low-T Transport," Physical Review Letters **95**, edited by E. Abrahams, 206603 (2005).

279 A. Pal and D. A. Huse, "Many-body localization phase transition," Physical Review B **82**, edited by E. Abrahams, 174411 (2010).

280 R. Nandkishore and D. A. Huse, "Many-Body Localization and Thermalization in Quantum Statistical Mechanics," Annual Review of Condensed Matter Physics **6**, edited by E. Abrahams, 15–38 (2015).

281 D. A. Abanin, E. Altman, I. Bloch, and M. Serbyn, "Many-body localization, thermalization, and entanglement," arXiv:1804.11065 [cond-mat, physics:quant-ph] **95**, edited by E. Abrahams, 256805 (2018).

282 K. S. Tikhonov and A. D. Mirlin, "Statistics of eigenstates near the localization transition on random regular graphs," Physical Review B **99**, edited by E. Abrahams, 024202 (2019).

283 S. Sachdev and J. Ye, "Gapless spin-fluid ground state in a random quantum Heisenberg magnet," Physical Review Letters **70**, edited by E. Abrahams, 3339–3342 (1993).

284 A. Altland, D. Bagrets, and A. Kamenev, "SYK non Fermi Liquid Correlations in Nanoscopic Quantum Transport," arXiv:1908.11351 [cond-mat, physics:hep-th] **95**, edited by E. Abrahams, 1908.11351 (2019).

285 A. Altland, D. Bagrets, and A. Kamenev, "Quantum Criticality of Granular Sachdev-Ye-Kitaev Matter," Physical Review Letters **123**, edited by E. Abrahams, 106601 (2019).

286 T. Wang, Z. Pan, T. Ohtsuki, I. A. Gruzberg, and R. Shindou, "Multicriticality of Two-dimensional Class D Disordered Topological Superconductors," arXiv:2108.12133 [cond-mat, physics:dis-nn] **95**, edited by E. Abrahams, 2108.12133 (2021).

287 H. Li and F. D. M. Haldane, "Entanglement Spectrum as a Generalization of Entanglement Entropy: Identification of Topological Order in Non-Abelian Fractional Quantum Hall Effect States," Phys. Rev. Lett. **101**, edited by E. Abrahams, 010504 (2008).

288 A. Altland, D. Bagrets, L. Fritz, A. Kamenev, and H. Schmiedt, "Quantum Criticality of Quasi-One-Dimensional Topological Anderson Insulators," Physical Review Letters **112**, edited by E. Abrahams, 206602 (2014).

289 W. Fulton and J. Harris, *Representation Theory: A First Course*, edited by E. Abrahams, Vol. 95 (Springer, New York, NY, 2004), p. 256805.

290 P. Pöpperl, E. V. Doggen, J. F. Karcher, A. D. Mirlin, and K. S. Tikhonov, "Dynamics of many-body delocalization in the time-dependent Hartree-Fock approximation," Annals of Physics **95**, edited by E. Abrahams, 168486 (2021).

Publications

In the following my publications and their bibliography reference in this thesis are listed:

- Ref. [86]: Jonas F. Karcher, Michael Sonner, and Alexander D. Mirlin, *Disorder and interaction in chiral chains: Majoranas versus complex fermions*, Physical Review B **100** 27, pp. 134207, 2021.

- Ref. [88]: Björn Sbierski, Jonas F. Karcher and Matthew S. Foster, *Spectrum-Wide Quantum Criticality at the Surface of Class AIII Topological Phases: An "Energy Stack" of Integer Quantum Hall Plateau Transitions*, Physical Review X **10** 2, pp. 021025, 2020.

- Ref. [89]: Sayed Ali Akbar Ghorashi, Jonas F. Karcher, Seth M. Davis and Matthew S. Foster, *Criticality across the energy spectrum from random artificial gravitational lensing in two-dimensional Dirac superconductors*, Physical Review B **101** 21, pp. 214521, 2021.

- Ref. [90]: Jonas F. Karcher and Matthew S. Foster, *How spectrum-wide quantum criticality protects surface states of topological superconductors from Anderson localization: Quantum Hall plateau transitions (almost) all the way down*, Annals of Physics, pp. 168439, 2021.

- Ref. [290]: Paul Pöpperl, Elmer V.H. Doggen, Jonas F. Karcher, Alexander D. Mirlin and Konstantin S. Tikhonov, *Dynamics of many-body delocalization in the time-dependent Hartree-Fock approximation*, Annals of Physics, pp. 168486, 2021.

- Ref. [105]: Jonas F. Karcher, Noah Charles, Ilya A. Gruzberg and Alexander D. Mirlin, *Generalized multifractality at spin quantum Hall transition*, Annals of Physics, pp. 168584, 2021.

Acknowledgments

First of all, I need to thank my professor Alexander D. Mirlin for his constant support throughout these three years and for giving me the subject of my thesis that ever grew more interesting, since it took so many turns.
Additionally, I need to thank my second reviewer Jörg Schmalian.

I am very grateful to my collaborators Michael Sonner, Sayid A. A. Ghorashi, Seth M. Davis, Björn Sbierski, Matthew S. Foster, Noah Charles, Paul Pöpperl, Konstantin S. Tikhonov, Elmer V. H. Doggen and Ilya A. Gruzberg.

Special thanks to:
Stefan Backens who made the thesis template compile on my laptop.
Vanessa Gall, Paul Pöpperl, Veronika Stangier, Elmer V. H. Doggen, Charlie Steward and Jonas Gaa for proof-reading.
Katharina Mayer for the constant supply with cupcakes.

Finally I want to thank all my colleagues and friends for their support and suggestions.